# ADVANCES IN TIME-DEPENDENT METHODS FOR NUCLEAR STRUCTURE AND DYNAMICS

EDITED BY: Paul Denis Stevenson, Cedric Simenel, Denis Lacroix, Lu Guo and Nicolas Schunck

PUBLISHED IN: Frontiers in Physics

frontiers Research Topics

# frontiers



ISSN 1664-8714
ISBN 978-2-88966-567-9
DOI 10.3389/978-2-88966-567-9

## About Frontiers

Frontiers is more than just an open-access publisher of scholarly articles: it is a pioneering approach to the world of academia, radically improving the way scholarly research is managed. The grand vision of Frontiers is a world where all people have an equal opportunity to seek, share and generate knowledge. Frontiers provides immediate and permanent online open access to all its publications, but this alone is not enough to realize our grand goals.

## Frontiers Journal Series

The Frontiers Journal Series is a multi-tier and interdisciplinary set of open-access, online journals, promising a paradigm shift from the current review, selection and dissemination processes in academic publishing. All Frontiers journals are driven by researchers for researchers; therefore, they constitute a service to the scholarly community. At the same time, the Frontiers Journal Series operates on a revolutionary invention, the tiered publishing system, initially addressing specific communities of scholars, and gradually climbing up to broader public understanding, thus serving the interests of the lay society, too.

## Dedication to Quality

Each Frontiers article is a landmark of the highest quality, thanks to genuinely collaborative interactions between authors and review editors, who include some of the world's best academicians. Research must be certified by peers before entering a stream of knowledge that may eventually reach the public - and shape society; therefore, Frontiers only applies the most rigorous and unbiased reviews.
Frontiers revolutionizes research publishing by freely delivering the most outstanding research, evaluated with no bias from both the academic and social point of view. By applying the most advanced information technologies, Frontiers is catapulting scholarly publishing into a new generation.

## What are Frontiers Research Topics?

Frontiers Research Topics are very popular trademarks of the Frontiers Journals Series: they are collections of at least ten articles, all centered on a particular subject. With their unique mix of varied contributions from Original Research to Review Articles, Frontiers Research Topics unify the most influential researchers, the latest key findings and historical advances in a hot research area! Find out more on how to host your own Frontiers Research Topic or contribute to one as an author by contacting the Frontiers Editorial Office: frontiersin.org/about/contact

# ADVANCES IN TIME-DEPENDENT METHODS FOR NUCLEAR STRUCTURE AND DYNAMICS

Topic Editors:
**Paul Denis Stevenson,** University of Surrey, United Kingdom
**Cedric Simenel,** Australian National University, Australia
**Denis Lacroix,** UMR8608 Institut de Physique Nucléaire d'Orsay (IPNO), France
**Lu Guo,** University of Chinese Academy of Sciences, China
**Nicolas Schunck,** Lawrence Livermore National Laboratory, United States

**Citation:** Stevenson, P. D., Simenel, C., Lacroix, D., Guo, L., Schunck, N., eds. (2021). Advances in Time-Dependent Methods for Nuclear Structure and Dynamics. Lausanne: Frontiers Media SA. doi: 10.3389/978-2-88966-567-9

# Table of Contents

frontiers in Physics

EDITORIAL
published: 27 January 2021
doi: 10.3389/fphy.2020.629889

# Editorial: Advances in Time-Dependent Methods for Nuclear Structure and Dynamics

*Lu Guo[1], Denis Lacroix[2], Nicolas Schunck[3], Cédric Simenel[4,5] and Paul Stevenson[6]**

[1]School of Nuclear Science and Technology, University of Chinese Academy of Sciences, Beijing, China, [2]Université Paris-Saclay, CNRS/IN2P3, IJCLab, Orsay, France, [3]Nuclear and Chemical Science Division, Lawrence Livermore National Laboratory, Livermore, CA, United States, [4]Department of Theoretical Physics, Research School of Physics and Engineering, Australian National University, Canberra, ACT, Australia, [5]Department of Nuclear Physics, Research School of Physics and Engineering, Australian National University, Canberra, ACT, Australia, [6]Department of Physics, University of Surrey, Guildford, United Kingdom

**Keywords: nuclear physics, computational physics, time-dependent methods, nuclear reactions, nuclear structure**

## Editorial on the Research Topic

### Advances in Time-Dependent Methods for Nuclear Structure and Dynamics

Among non-relativistic approaches to nuclear structure and reactions, the time-dependent Schrödinger equation is the basic equation from which microscopic approaches derive. Historically, stationary state methods which are not explicitly time-dependent have been preferred for describing both structure and reactions. One motivation for not directly solving time-dependent problems has been the computational difficulty, even if the physics case suggests retaining a time-dependent approach. Over time, such computational barriers have been reduced, and a general resurgence in time-dependent methods has occurred. In the last decade development of time-dependent mean-field codes has been substantial. Unrestricted 3D calculations with full effective interactions are now possible [1, 2], and full treatment of superfluidity at the mean-field level has been included [3, 4]. These worldwide efforts were a strong motivation to curate this Special Topic, which was conceived to draw together a snapshot of the current state of the wider field of time-dependent methods and their application in a broad range of problems in nuclear physics.

The article collection includes reviews as well as original material. Some directly address problems in the details of specific nuclei and in specific processes, while others deal with general problems, and general solutions, touching on fields outside nuclear physics.

In their contribution, Tokeida and Hagino address how one deals with open quantum systems. They start with a phenomenological description based on quantum friction and apply it to heavy-ion fusion. They then develop a more microscopic approach, based on a system-plus-bath Hamiltonian, appying it to the Caldeira-Legget model, with a discussion of how a future application to nuclear collisions could be made. Dinh et al. give a review of applications of time-dependent DFT methods to atoms, molecules and atomic clusters, concentrating on issues that are different from typical nuclear scenarios, but which could be relevant for future applications, such as direct laser-nucleus interaction [5].

Tohyama presents a review of the time-dependent density matrix method. This goes beyond the basic self-consistent microsopic approach of time-dependent Hartree-Fock (TDHF) by considering explicitly higher order terms in the BBGKY hierarchy, and Tohyama shows applications to both structure (excited vibrational states) and heavy-ion reactions. Also combining structure and reaction applications is Ebata's contribution, in which the details of the canonical-basis time-dependent Hartree-Fock Bogoliubov approach are reviewed and applied to resonances and heavy-ion reactions. Wang et al.'s review of semiclassical methods based on the time-evolution of the Wigner function

OPEN ACCESS

***Edited and reviewed by:***
*Laura Elisa Marcucci, University of Pisa, Italy*

****Correspondence:***
*Paul Stevenson*
*p.stevenson@surrey.ac.uk*

***Specialty section:***
*This article was submitted to Nuclear Physics, a section of the journal Frontiers in Physics*

***Received:*** *16 November 2020*
***Accepted:*** *26 November 2020*
***Published:*** *27 January 2021*

***Citation:***
*Guo L, Lacroix D, Schunck N, Simenel C and Stevenson P (2021) Editorial: Advances in Time-Dependent Methods for Nuclear Structure and Dynamics. Front. Phys. 8:629889. doi: 10.3389/fphy.2020.629889*

show calculations of giant resonances, presenting results that combine dynamics with excited state structures, demonstrating the importance of nuclear collisions in determining excited state widths.

The topic of fission is covered in a review by Bulgac et al., giving an historical overview of methods used to tackle fission, details of the current state of the art, and a plan for the future. Fission is very much a current focus of time-dependent methods, and the review by Bulgac et al. complements a substantial review published recently elsewhere [6]. A method for describing spontaneous fission from a microscopic approach is given in a review by Sadhukhan. It brings together a WKB-like theory with Langevin dynamics in a framework suitable for making broad predictions of fission observables. An original research paper looking at details of fission is presented by Pancic et al., where the effect of the choice of underlying nuclear interaction is explored. A considerable part of the contribution from Verriere and Regnier concerns fission as described in the time-dependent generator coordinate method (TD-GCM), though they also highlight other processes and extensively review the theories behind different flavors of TD-GCM.

Studies of reaction mechanisms find a natural home in time-dependent approaches, and several contributions are geared toward a better understanding of nuclear reactions. The mini-review of Bao gives a critical analysis of different approaches to fusion reactions for production of superheavy nuclei; Godbey and Umar review some of the detailed observables that can be understood in quasifission reactions using TDHF-based approaches; Jiang and Wang use a TDHF approach followed by a statistical model for deexcitation to look at reactions leading to new neutron rich isotopes.

Using time-dependent methods to link microscopic theories with collective models is a theme of Wen and Nakatsukasa who develop a new method to extract collective masses from microscopic calculations, and also of Washiyama and Sekizawa, who review the links between microscopic time-dependent methods and nucleus-nucleus potentials and friction coefficients in the Dissipation Dynamics-TDHF (DD-TDHF) method.

We mention finally the contribution of Iwata, which brings ideas from the theory of solitons to throw new light on the understanding of nuclear reactions making links to ideas perhaps less familiar in the nuclear theory community.

The response to this special topic has more than matched our expectations in terms of range and quality of contributions from the research community. We think it shows amply the strength and variety of developments and applications of time-dependent methods in nuclear physics, and beyond, and hope the resulting collection and e-book provide a useful reference for future developments.

## AUTHOR CONTRIBUTIONS

All authors listed have made a substantial, direct, and intellectual contribution to the work and approved it for publication.

## REFERENCES


1. Maruhn JA, Reinhard P-G, Stevenson PD, Umar AS. The TDHF code sky3D. *Comput Phys Commun* (2014) 185:2195–216. doi:10.1016/j.cpc.2014.04.008
2. Umar AS, Oberacker VE. Three-dimensional unrestricted time-dependent hartree-fock fusion calculations using the full skyrme interaction. *Phys Rev C* (2006) 73:054607. doi:10.1103/PhysRevC.73.054607
3. Jin S, Bulgac A, Roche K, Wlazłowski G. Coordinate-space solver for superfluid many-fermion systems with the shifted conjugate-orthogonal conjugate-gradient method. *Phys Rev C* (2017) 95:044302. doi:10.1103/PhysRevC.95.044302
4. Scamps G, Hashimoto Y. Density-constrained time-dependent Hartree-Fock-Bogoliubov method. *Phys Rev C* (2019) 100:024623. doi:10.1103/PhysRevC.100.024623
5. von der Wense L, Bilous PV, Seiferle B, Stellmer S, Weitenberg J, Thirolf PG, et al. The theory of direct laser excitation of nuclear transitions. *Eur Phys J A* (2020) 56:176. doi:10.1140/epja/s10050-020-00177-x
6. Bender M, Bernard R, Bertsch G, Chiba S, Dobaczewski J, Dubray N, et al. Future of nuclear fission theory. *J Phys G Nucl Part Phys* (2020) 47:113002. doi:10.1088/1361-6471/abab4f


**Conflict of Interest:** The authors declare that the research was conducted in the absence of any commercial or financial relationships that could be construed as a potential conflict of interest.

frontiers in Physics

ORIGINAL RESEARCH
published: 05 February 2020
doi: 10.3389/fphy.2020.00016

# Collective Inertial Masses in Nuclear Reactions

*Kai Wen*[1]* *and Takashi Nakatsukasa*[1,2,3]

[1] Center for Computational Sciences, University of Tsukuba, Tsukuba, Japan, [2] Faculty of Pure and Applied Sciences, University of Tsukuba, Tsukuba, Japan, [3] RIKEN Nishina Center, Wako, Japan

Toward the microscopic theoretical description for large amplitude collective dynamics, we calculate the coefficients of inertial masses for low-energy nuclear reactions. Under the scheme of energy density functional, we apply the adiabatic self-consistent collective coordinate (ASCC) method, as well as the Inglis' cranking formula to calculate the inertias for the translational and the relative motions, in addition to those for the rotational motion. Taking the scattering between two $\alpha$ particles as an example, we investigate the impact of the time-odd components of the mean-field potential on the collective inertial masses. The ASCC method asymptotically reproduces the exact masses for both the relative and translational motions. On the other hand, the cranking formula fails to do so when the time-odd components exist.

**Keywords: nuclear reaction, inertial mass, nuclear fusion, nuclear collective dynamics, mass parameter**

OPEN ACCESS

***Edited by:***
*Nicolas Schunck,*
*Physical and Life Sciences Directorate, Lawrence Livermore National Laboratory, United States*

***Reviewed by:***
*Peter Ring,*
*Technical University of Munich, Germany*
*Luis Robledo,*
*Autonomous University of Madrid, Spain*

***Correspondence:**
*Kai Wen*
*wenkai@nucl.ph.tsukuba.ac.jp*

***Specialty section:***
*This article was submitted to Nuclear Physics, a section of the journal Frontiers in Physics*

***Received:*** *28 November 2019*
***Accepted:*** *20 January 2020*
***Published:*** *05 February 2020*

***Citation:***
*Wen K and Nakatsukasa T (2020) Collective Inertial Masses in Nuclear Reactions. Front. Phys. 8:16. doi: 10.3389/fphy.2020.00016*

## 1. INTRODUCTION

The time-dependent density functional theory (TDDFT) [1–5] is a general microscopic theoretical framework to study low-energy nuclear reactions. Based on the TDDFT, the mechanisms of nuclear collective dynamics have been extensively studied for decades. The linear approximation of TDDFT leads to the random-phase approximation (RPA) [5–7], which is capable of calculating nuclear response functions and providing us a unified description for both structural and dynamical properties. Despite the detailed microscopic information revealed by TDDFT, it has a difficulty in describing nuclear collective dynamics at low energy [5]. For instance, it cannot describe the sub-barrier fusion and spontaneous fission, due to its semiclassical nature [1, 5, 6].

The description of nuclear dynamics in terms of collective degrees of freedom has been explored in nuclear reaction theories. However, the derivation of the "macroscopic" reaction model based on the microscopic nuclear dynamics has been rarely studied in the past. For the theoretical description in terms of collective degrees of freedom, the collective inertial masses with respect to the collective coordinates are of paramount importance. One of the most commonly used methods to extract the collective mass coefficient is the Inglis' cranking formula [8–10], which can be derived based on the adiabatic perturbation theory.

It is well-known that the cranking formula has a problem that it fails to reproduce the total mass for the translational motion of the center of mass of a nucleus Ring and Schuck [6]. Therefore, it is highly desirable to replace the cranking mass by the one theoretically more advanced and justifiable. We believe that the adiabatic self-consistent collective coordinate (ASCC) method [11–14] suites for this purpose. The method, in the first place, aims at determining the canonical variables on the optimal collective subspace for description of a low-energy collective motion. The masses with respect to those collective coordinates can be extracted by solving a set of the ASCC equations. This method has been applied to many nuclear structure problems with large-amplitude nuclear dynamics with the Hamiltonian of the separable interactions [13–16]. Recently, by combining the

imaginary-time evolution [17] and the finite amplitude method [18–21], we proposed a numerical method to solve the ASCC equations and to determine the optimal collective path for nuclear reaction [22]. At the same time, we obtain the collective inertial mass in a self-consistent manner. In this work, we calculate the collective masses for three modes of collective motion, the translational motion, the relative motion and rotational motion. We compare the ASCC results with those of the cranking formula.

Our calculations are under the scheme of energy density functional theory. In order to guarantee the Galilean symmetry during a collective motion, most of the energy density functionals must include densities that are odd with respect to the time reversal. Under the assumptions of the time-reversal symmetry, these terms vanish and therefore do not contribute to the time-even states, while they have non-zero values in situations of dynamical reactions. It has been found that the time-odd components play an important role in the inertia parameters for nuclear rotations [23, 24]. To investigate this problem in the context of reaction dynamics of light nuclei, we investigate the effects of time-odd terms on the different inertial masses, taking the $\alpha + \alpha$ reaction as the simplest example.

This paper is organized as the following. In section 2, we recapitulate the formulation of the basic ASCC equations in the case of one-dimensional collective motion. We present the method of constructing the collective path and the coordinate transformation procedure to calculate the inertial mass parameter with respect to the relative coordinate. In section 3, we apply the method to the reaction system $\alpha+\alpha \leftrightarrow {}^{8}\mathrm{Be}$. We focus on the influence of the time-odd terms on both the relative and rotational inertias. Summary and concluding remarks are give in section 4.

## 2. THEORETICAL FRAMEWORK

### 2.1. Formulation of ASCC Method

In this section, neglecting the paring correlation, we recapitulate the basic ASCC formulation, and introduce the numerical procedure of constructing the collective path and calculating the inertial mass. The details can be found in Wen and Nakatsukasa [22].

For simplicity, here we consider the collective motion described by only one collective coordinate $q(t)$, which has a conjugate momentum $p(t)$. We assume that the time-dependent mean-field states are parameterized by Slater determinants labeled as $|\psi(p,q)\rangle$. The energy of the system reads

$$H(p,q) = \langle\psi(p,q)|\hat{H}|\psi(p,q)\rangle, \tag{1}$$

which defines a classical collective Hamiltonian. In the ASCC method, the resulting collective path $|\psi(p,q)\rangle$ is determined so as to maximally be decoupled from other intrinsic degrees of freedom. The evolution of $q(t)$ and $p(t)$ obeys the canonical equations of motion with the classical Hamiltonian $H(p,q)$.

In order to consider the adiabatic limit, we assume the momentum $p$ is small and the states are expanded in powers of $p$ about $p = 0$. The states $|\psi(p,q)\rangle$ are written as

$$|\psi(p,q)\rangle = e^{ip\hat{Q}(q)}|\psi(0,q)\rangle = e^{ip\hat{Q}(q)}|\psi(q)\rangle, \tag{2}$$

where the generator $\hat{Q}(q)$ is defined as $\hat{Q}(q)|\psi(q)\rangle = -i\partial_p|\psi(q)\rangle$. The conjugate $\hat{P}(q)$ is introduced as a generator for the infinitesimal translation in $q$, $\hat{P}(q)|\psi(q)\rangle = i\partial_q|\psi(q)\rangle$. $\hat{P}(q)$ and $\hat{Q}(q)$ can be expressed in the form of one-body operator as

$$\begin{aligned}\hat{P}(q) &= i\sum_{n\in p, j\in h} P_{nj}(q)a_n^\dagger(q)a_j(q) + \text{h.c.},\\ \hat{Q}(q) &= \sum_{n\in p, j\in h} Q_{nj}(q)a_n^\dagger(q)a_j(q) + \text{h.c.},\end{aligned} \tag{3}$$

where $i$ in the expression of $\hat{P}(q)$ is simply for convenience. They are locally defined at each coordinate $q$ and will change their structure along the collective path. The particle ($n \in p$) and hole ($j \in h$) states are also defined with respect to the Slater determinant $|\psi(q)\rangle$.

In the adiabatic limit, expanding Equation (2) with respect to $p$ up to second order, the invariance principle of the self-consistent collective coordinate (SCC) method [11] leads to the equations of the ASCC method [5, 12]. Neglecting the curvature terms, it reduces to somewhat simpler equation set:

$$\delta\langle\Psi(q)|\hat{H}_{\mathrm{mv}}|\Psi(q)\rangle = 0, \tag{4}$$

$$\delta\langle\Psi(q)|[\hat{H}_{\mathrm{mv}}, \frac{1}{i}\hat{P}(q)] - \frac{\partial^2 V(q)}{\partial q^2}\hat{Q}(q)|\Psi(q)\rangle = 0, \tag{5}$$

$$\delta\langle\Psi(q)|[\hat{H}_{\mathrm{mv}}, i\hat{Q}(q)] - \frac{1}{M(q)}\hat{P}(q)|\Psi(q)\rangle = 0, \tag{6}$$

with the inertial mass parameter $M(q)$. The mass $M(q)$ depends on the scale of the coordinate $q$. Thus, we can choose it to make $M(q) = 1$ without losing anything. The moving mean-field Hamiltonian $\hat{H}_{\mathrm{mv}}$ and the potential $V(q)$ are, respectively, defined as

$$\hat{H}_{\mathrm{mv}} = \hat{H} - \frac{\partial V(q)}{\partial q}\hat{Q}(q), \quad V(q) = \langle\psi(q)|\hat{H}|\psi(q)\rangle. \tag{7}$$

Note that the collective path is given by $|\psi(q)$, which represents the state $|\psi(q,p)$ with $p = 0$. Equation (4) is similar to a constrained Hartee-Fock problem, however, the constraint operator $\hat{Q}(q)$ depends on the coordinate $q$, which is self-consistently determined by the RPA-like Equations (5) and (6), called "moving RPA equations." The conventional RPA forward and backward amplitude $X_{ni}(q)$ and $Y_{ni}(q)$ can be regarded as the linear combination of $\hat{P}(q)$ and $\hat{Q}(q)$.

$$X_{nj} = \sqrt{\frac{\omega}{2}}Q_{nj} + \frac{1}{\sqrt{2\omega}}P_{nj}, \quad Y_{nj} = \sqrt{\frac{\omega}{2}}Q_{nj} - \frac{1}{\sqrt{2\omega}}P_{nj}, \tag{8}$$

where the RPA eigenfrequency $\omega$ is related to the mass parameter and the second derivative of the potential

$$\omega^2 = \frac{1}{M(q)}\frac{\partial^2 V(q)}{\partial q^2}. \tag{9}$$

As a pair of canonical variables, a weak canonicity condition $\langle\Psi(q)|[i\hat{P}(q),\hat{Q}(q)]|\Psi(q)\rangle = 1$ should be satisfied. This canonicity condition is automatically satisfied if the RPA normalization condition $\sum_{n,j}(X^2_{nj}-Y^2_{nj})=1$ holds.

It should be noted that the ASCC method is applicable to systems with pairing correlations, in principle. However, in this paper, we neglect the pairing correlation to reduce the computational cost, and concentrate our discussion on effects of mean fields of particle-hole channels for the inertial masses. We present results for the $\alpha+\alpha$ reaction in section 3, for which no level crossing at the Fermi surface is involved. Therefore, the pairing plays very little role in this particular case.

For superconducting systems, apart from the collective coordinate and momentum, an additional pair of canonical variables, the particle number and the conjugate gauge angle, are needed to label the nuclear state. Details of the formulation are give in Matsuo et al. [12] and Nakatsukasa et al. [5].

## 2.2. ASCC Collective Path and Inertial Mass

A change in the scale of the collective coordinate $q$ results in a change in the collective mass $M(q)$. Thus, in order to discuss the magnitude of the collective mass, we need to fix its scale. This is normally done by adopting an intuitive choice of the one-body time-even operator $\hat{O}$. One of possible choices is the mass quadrupole operator $Q_{20} = \int d\mathbf{r}\hat{\psi}^\dagger(\mathbf{r})r^2Y_{20}(\hat{\mathbf{r}})\hat{\psi}(\mathbf{r})$. In the present study of nuclear scattering (nuclear fission), it is convenient to adopt the relative distance $\hat{R}$ between two nuclei with the projectile mass number $A_{\rm pro}$ and the target mass number $A_{\rm tar}$. Assuming that the center of mass of the two nuclei are on the $x$ axis ($y=z=0$),

$$\hat{R}\equiv\int d\mathbf{r}\hat{\psi}^\dagger(\mathbf{r})\hat{\psi}(\mathbf{r})x\left[\frac{\theta(x-x_{\rm s})}{A_{\rm pro}}-\frac{\theta(x_{\rm s}-x)}{A_{\rm tar}}\right], \tag{10}$$

where $\theta(x)$ is the step function, and $x = x_{\rm s}$ is the artificially introduced section plane that divides the total space into two, each of which contains the nucleon number of $A_{\rm pro}$ and $A_{\rm tar}$, respectively.

The operator $\hat{R}$ has an evident physical meaning when the projectile and the target are far away to each other. When they touch each other, the distance between two nuclei is no longer a well-defined quantity, thus loses its significance. However, this is not a problem in the present microscopic formulation of the reaction model. We have determined the reaction path and the canonical variables $(q,p)$, through the ASCC method. It is merely a coordinate transformation from $q$ to $R$ with a function $R(q)$. The reaction dynamics do not depend on the choice of $R$, as far as the one-to-one correspondence between $q$ and $R$ is valid.

The coordinate transformation naturally leads to the transformation of the inertial mass from $M(q)$ to $M(R)$;

$$M(R)=M(q)\left(\frac{dq}{dR}\right)^2. \tag{11}$$

The calculation of the derivative $dq/dR$ is straitforward, because the collective path $|\psi(q)$ and the local generator $\hat{P}(q)$ of the coordinate $q$ are obtained by solving the ASCC Equations (5) and (6).

$$\begin{aligned}\left(\frac{dq}{dR}\right)^{-1} &= \frac{dR}{dq}=\frac{d}{dq}\langle\psi(q)\hat{R}|\psi(q)\rangle\\ &= -i\langle\psi(q)\left[\hat{R},\hat{P}(q)\right]|\psi(q)\rangle.\end{aligned} \tag{12}$$

The inertia mass parameter with respect to $R$ or any other coordinate can be easily calculated with this formula.

We solve the moving RPA Equations (5) and (6) by taking advantage of the finite amplitude method (FAM) [18–21], especially the matrix FAM prescription [21]. To solve the ASCC Equations (4), (5), and (6) self-consistently and construct the collective path $|\psi(q)$, we adopt the following procedures:

1. Prepare the Hartree-Fock ground state $|\psi(q=0)$ which can be either the two separated nuclei before fusion, or the ground state of the mother nucleus before fission.
2. Based on $|\psi(q)$, solve the moving RPA Equations (5) and (6), to obtain $\hat{Q}(q)$ and $\hat{P}(q)$. First, we start with an approximation $\hat{Q}(q+\delta q)=\hat{Q}(q)$.
3. Solve the moving HF Equation (4) to calculate the state $|\psi(q+\delta q)$ by imposing the condition

$$\langle\Psi(q+\delta q)|\hat{Q}(q)|\Psi(q+\delta q)\rangle=\delta q, \tag{13}$$

   where we use the approximate relation, $|\psi(q+\delta q)\simeq e^{-i\delta q\hat{P}(q)}|\psi(q)$, to constrain the step size.
4. With this new state $|\psi(q+\delta q)$, update the generators $\hat{Q}(q+\delta q)$ and $\hat{P}(q+\delta q)$ by solving the moving RPA equations again. Then, with these updated generators, go back to the step 2.2. Repeat the steps 2.2 and 2.2 until the self-consistency is achieved at $q+\delta q$.
5. Then, regarding $q+\delta q$ as $q$ with an initial approximation $\hat{Q}(q+\delta q)=\hat{Q}(q)$, go to the step 2.2.

Carrying on this iterative procedure, we determine a series of states $|\psi(0),|\psi(\delta q),|\psi(2\delta q),|\psi(3\delta q),\cdots$ that form the ASCC collective path. Changing the sign of the right hand side of Equation (13), we can also construct the collective path toward the opposite direction $\{|\psi(-\delta q),|\psi(-2\delta q),\cdots\}$. In this way, the collective path $|\psi(q)$, the potential $V(q)$, and the collective mass $M(q)$ are determined self-consistently and no *a priori* assumption is used.

# 3. APPLICATIONS

## 3.1. Solutions for the Translational Motion

First, we calculate the inertial mass for the translational motion, for which we know the exact value $Am$. The calculation is done in the three-dimensional coordinate space discretized in the square grid in a sphere with radius equal to 7 fm. The BKN energy density functional [25] is adopted in the present calculation.

The HF ground state is a trivial solution of Equations (4)–(6), on the collective path since it corresponds to the minimum of the potential surface, $\partial V/\partial q=0$. We calculate the translational inertia mass of the ground state of an alpha particle, and examine

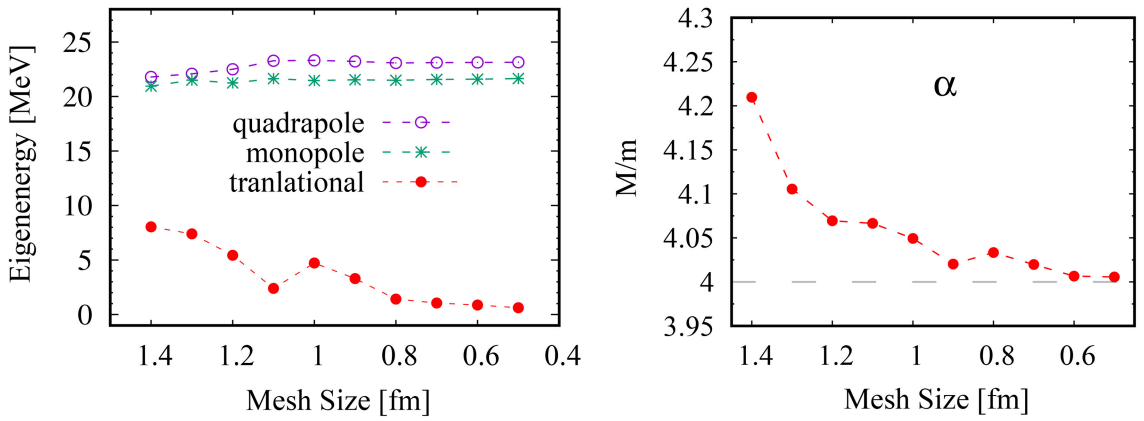


**FIGURE 1 | (Left panel)** Calculated RPA eigenfrequencies based on the ground state of the alpha particle, as a function of mesh size. The red closed circles indicate the values for translational mode, while the green asterisks and purple open circles indicate those for monopole and quadrupole modes, respectively. **(Right panel)** Calculated translational mass $M$ of a single alpha particle in units of nucleon's mass $m$, as a function of the mesh size. The calculated mass with respect to the $y$ direction, perpendicular to the symmetry ($x$) axis, is shown. The one with respect to the $x$ direction is presented in Figure 1 of Wen and Nakatsukasa [22].

its grid size dependence. The left panel of **Figure 1** shows the eigenfrequency $\omega$ in Equation (9) of the lowest several RPA states as a function of the mesh size of the grids. The three translational modes along $x, y, z$ axis are degenerated and shown by the red dots, the absolute value of this eigenfrequency decreases and approaches zero as the mesh size becomes smaller. The value of the translational motion is significantly smaller than all the other collective modes. In the ideal case where the mesh size is sufficiently small, this value is expected to be zero. For other collective modes, the eigenfrequencies stay almost constant as functions of the mesh size. Due to the compact nature of alpha particle, except for the translational zero-modes, the lowest physical excitation mode is calculated to be about 20 MeV, which represents the monopole vibration.

Using Equation (11) we calculate the translational inertia mass of one alpha particle. The right panel of **Figure 1** shows the result as a function of mesh size. As the mesh size decreases, the results approach to the value of 4 in the unit of nucleon mass, which is the exact total mass of the alpha particle. With the simple BKN energy density functional, this exact value for the translation is also obtained with the cranking mass formula of Inglis. However, it underestimates the exact total mass when the energy functional has a effective mass $m^*/m < 1$. On the other hand, the ASCC mass for the translational motion is invariant and exact even with the effective mass. This is due to the Galilean symmetry of the energy density functional which inevitably contains the time-odd components. This will be discussed in section 3.4.

## 3.2. ASCC Reaction Path for $\alpha$+$\alpha \leftrightarrow {}^8$Be

The numerical application of the ASCC method to determine a collective path for the nuclear fusion or fission reactions demands a substantial computational cost. Here, we present the result for the reaction path of $\alpha$+$\alpha \leftrightarrow {}^8$Be, as the simplest example. It can be regarded as either the fusion path of two alpha particles or the fission path of $^8$Be. The model space is the three-dimensional grid space of the rectangular box of size $10 \times 10 \times 18$ fm$^3$ with mesh size equal to 1.0 fm. The standard BKN energy density functional is adopted.

Starting from the two ground states of $\alpha$ particle and carrying out the iterative procedure presented in section 2.2, we obtain a fusion path that connects the two well separated alpha particles to the ground state of $^8$Be. If we start the calculation from the ground state of $^8$Be, the same reaction path, that represents fission of $^8$Be, can be obtained. In the left four panels of **Figure 2**, we show the calculated density distribution of four different points on the obtained collective fusion path. The panel (a) shows the density distribution of two alpha particles at $R = 6.90$ fm, (d) shows that of the ground state of $^8$Be which corresponds to $R = 3.55$ fm. Those of (b) and (c) show those at $R = 5.40$ fm and 4.10 fm, respectively. The collective path smoothly evolves the separated two alpha particles into the ground state of $^8$Be.

The right panel of **Figure 2** shows the potential energy along this collective path, as a function of $R$. The dashed cure shows the point Coulomb potential, $4e/R + 2E_\alpha$, with the ground state energy of a single alpha particle $E_\alpha$. With the BKN energy density functional, the $^8$Be is bound in the mean-field level. The ground state of $^8$Be is located in the potential minimum at $R = 3.55$ fm, while the Coulomb barrier top is at $R = 6.50$ fm. This ASCC collective path is self-consistently generated by the iterative procedure presented in section 2.2. The generators $(\hat{Q}(q), \hat{P}(q))$ for the relative motion are microscopically given. Since the structure of the $^8$Be nucleus is very simple, this potential surface is actually similar to that of the constraint Hartree-Fock calculation.

## 3.3. Inertial Mass for $\alpha$+$\alpha \leftrightarrow {}^8$Be

Upon the collective reaction path obtained, the inertial mass with respect to the relative distance $R$, $M_{\rm ASCC}(R)$, is calculated using Equation (11). In the asymptotic region, we expect the inertial mass to be identical to the reduced mass, $\mu_{\rm red} = A_{\rm pro}A_{\rm tar}m/(A_{\rm pro} + A_{\rm tar})$, where $m$ is the nucleon mass. For the current system $\alpha$+$\alpha \leftrightarrow {}^8$Be, the value of $\mu_{\rm red}$ is expected to be $2\,m$.

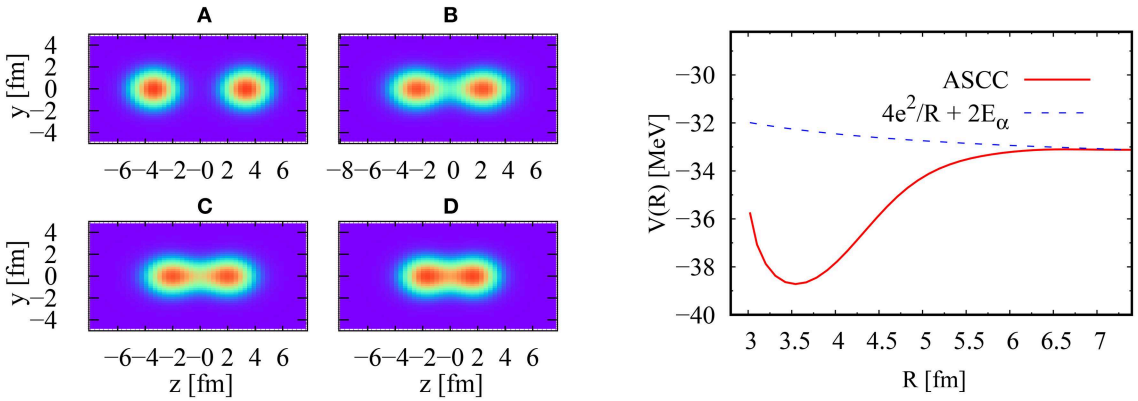


**FIGURE 2 |** (Left panel) Calculated density distributions of four points on the ASCC collective fusion path $\alpha+\alpha\rightarrow{}^{8}$Be. Inset **(A)** shows the density distribution of two well separated alpha particles at $R = 6.90$ fm, inset **(D)** is the ground state of $^{8}$Be at $R = 3.55$ fm. Inset **(B,C)** show the density distributions at $R = 4.10$ fm, 5.40 fm, respectively. Those on the $y - z$ plane are plotted. (Right panel) Potential energy as a function of $R$ shown by the red curve. The blue the dashed line is calculated as $4e^2/R + 2E_\alpha$ for reference.

The reduced mass $\mu_{\rm red}$ is justifiable when two alpha particles are well separated. However, it loses its validity as two particles approach each other. A widely used approach to calculate inertial mass for nuclear collective motion is the "Constrained-Hartree-Fock-plus-cranking" (CHF+cranking) approach [26]. In this approach, the collective path is produced by the CHF calculation with a constraining operator $\hat{O}$ given by hand, and the inertial mass is calculated based on the cranking formula with respect to these CHF states. The formula for the cranking mass can be derived by the adiabatic perturbation [6]. In the present case of the one-dimensional motion, based on the states constructed by the CHF calculation with a given constraining operator $\hat{O}$, the cranking formula reads [26]

$$M_{\rm cr}^{\rm NP}(R) = 2\sum_{n\in p,j\in h}\frac{|\langle\varphi_n(R)|\partial/\partial R|\varphi_j(R)\rangle|^2}{e_n(R)-e_j(R)}, \qquad (14)$$

where the single-particle states $\varphi_\mu$ and their energies $e_\mu$ are defined with respect to $h_{\rm CHF}(\lambda) = h_{\rm HF}[\rho] - \lambda\hat{O}$,

$$h_{\rm CHF}(\lambda)|\varphi_\mu(\lambda)\rangle = e_\mu(\lambda))|\varphi_\mu(\lambda)\rangle, \quad \mu \in p,h. \qquad (15)$$

We may use any operator $\hat{O}$ as a constraint, as far as it can generate the states with all the necessary values of $R = \langle\hat{R}\rangle$. However, obviously the inertial mass $M(R)$ depends on this choice, which is one of drawbacks of the CHF+cranking approach.

In most of the reaction models, the inertial mass with respect to $R$ is assumed to be a constant value of $\mu_{\rm red}$. Our study reveals how the inertia changes as a function of $R$. In **Figure 3**, both the ASCC and the cranking masses are presented. For the cranking mass, since the CHF state needs to be prepared first. We calculate the CHF states in two ways with different constraining operators $\hat{O}$; the mass quadrupole operator $\hat{Q}_{20}$ and the relative distance $\hat{R}$ operator of Equation (10). The model space for both calculations are the same. As we can see from **Figure 3**, at large distance,

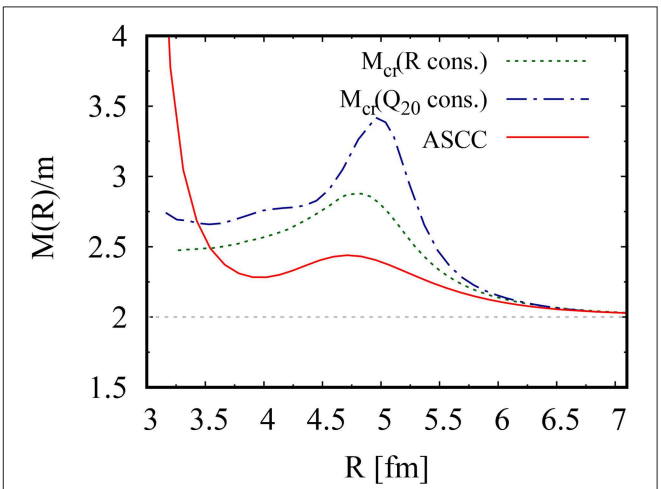


**FIGURE 3 |** (Color online) Inertia masses $M_{\rm R}$ for the reaction $\alpha+\alpha\leftrightarrow{}^{8}$Be as a function of relative distance $R$. The solid (red) curve indicates the result of ASCC. The other curves show the cranking masses of Equation (14) calculated based on CHF states. The dotted (green) and dash-dotted (blue) lines indicate the results with constraints on $\hat{R}$ and $\hat{Q}_{20}$, respectively.

both methods asymptotically reproduce the reduced mass of 2 $m$, which is the exact value for the relative motion between two alpha particles. In the interior region where the two nuclei have merged into one system, these three masses give very different values. Generally the cranking mass is found to be larger than the ASCC mass, especially at around $R = 4.7$ fm where all the three masses develop a bump structure.

The difference between the ASCC and the cranking masses attributes to several factors. One is due to the fact that the cranking formula neglects residual fields induced by the density fluctuation. Another is that the constraining operators affect the single-particle energies $e_\mu(R)$. We also note that the cranking masses obtained with different constraints give very different

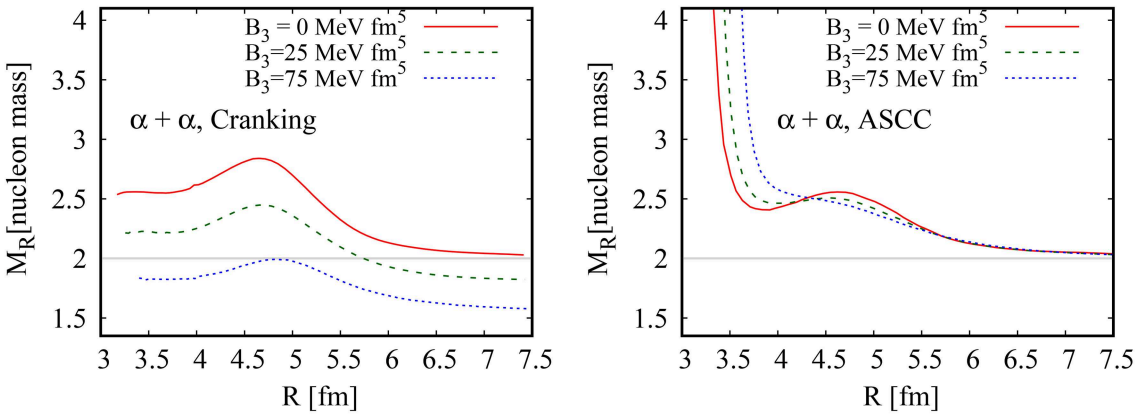


**FIGURE 4 |** Relative inertial masses in the presence of time-odd mean-field potential for the reaction $\alpha+\alpha\leftrightarrow{}^{8}$Be as a function of relative distance $R$. The results of the cranking masses are shown in the left panel and those of the ASCC method are shown in the right panel. The solid (red), dashed (green), and dotted (blue) curves show the results calculated with $B_3 = 0$, 25, and 75 MeV fm$^5$, respectively.

values. This is true even at the HF ground state ($R = 3.55$ fm), in which the single-particle states $|\varphi_\mu(R)$ and their single-particle energies $e_\mu(R)$ are all identical to each other. This is because the derivative $\partial/\partial R$ gives different values, since the different constraint produces different states away from the HF ground state. This ambiguity exposes another drawback of the CHF+cranking approach, while the ASCC mass has an advantage that the collective coordinate as well as the wave functions are self-consistently calculated rather than artificially assumed.

## 3.4. Impact of Time-Odd Potential

All the results shown so far are obtained with the standard BKN energy density functional that has no derivative terms. Therefore, the nucleon's effective mass is identical to the bare nucleon mass. However, most of realistic effective interactions have effective mass smaller than the bare mass, typically $m^*/m \sim 0.7$. In such cases, an improper treatment of the collective dynamics leads to a wrong answer for the collective inertial mass [27]. This change in the effective mass typically comes from the term $\rho\tau$ in the Skyrme energy density functional, which should accompany the term $-\mathbf{j}^2$ to restore the Galilean symmetry [27, 28]. These terms are absent in the standard BKN functional.

To investigate the effect of the time-odd mean-field potential on the collective inertial mass, we add the term $B_3(\rho\tau - \mathbf{j}^2)$ to the original BKN energy density functional. The modified BKN energy density functional reads,

$$\begin{aligned} E[\rho] = & \int \frac{1}{2m}\tau(\mathbf{r})d\mathbf{r} + \int d\mathbf{r}\left\{\frac{3}{8}t_0\rho^2(\mathbf{r}) + \frac{1}{16}t_3\rho^3(\mathbf{r})\right\} \\ & + \int\int d\mathbf{r}d\mathbf{r}'\rho(\mathbf{r})v(\mathbf{r}-\mathbf{r}')\rho(\mathbf{r}') \\ & + B_3\int d\mathbf{r}\left\{\rho(\mathbf{r})\tau(\mathbf{r}) - \mathbf{j}^2(\mathbf{r})\right\} \end{aligned} \tag{16}$$

where $\rho(\mathbf{r})$, $\tau(\mathbf{r})$, and $\mathbf{j}(\mathbf{r})$ are the isoscalar density, the isoscalar kinetic density, and the isoscalar current density, respectively. In Equation (16), $v(\vec{r})$ is the sum of the Yukawa and the Coulomb potentials [25]. The variation of the total energy with respect to the density (or equivalently single-particle wave functions) defines the single-particle (Hartree-Fock) Hamiltonian. In the present case, the single-particle Hamiltonian turns out to be

$$\begin{aligned} h[\rho] = & -\nabla\frac{1}{2m^*(\mathbf{r})}\nabla + \frac{3}{4}t_0\rho(\mathbf{r}) + \frac{3}{16}t_3\rho^2(\mathbf{r}) \\ & + \int d\mathbf{r}'v(\mathbf{r}-\mathbf{r}')\rho(\mathbf{r}'), \\ & + B_3(\tau(\mathbf{r}) + i\nabla\cdot\mathbf{j}(\mathbf{r})) + 2iB_3\mathbf{j}(\mathbf{r})\cdot\nabla \end{aligned} \tag{17}$$

where the effective mass is now deviated from bare nucleon mass

$$\frac{\hbar^2}{2m^*(\mathbf{r})} = \frac{\hbar^2}{2m} + B_3\rho(\mathbf{r}). \tag{18}$$

For the time-even states, such as the ground state of even-even nuclei, the current density disappears, $\mathbf{j} = 0$. Even though, these terms play an important role in the collective inertial mass. The parameter $B_3 \neq 0$ provides the effective mass and the time-odd effect. The rest of the parameters are the same as those in reference [25].

To examine the impact of the time-odd terms on the inertial mass, in **Figure 4** we show $M(R)$ calculated with and without the $B_3$ term. When the time-odd terms are absent, $B3 = 0$, both the ASCC and the cranking formula reproduce the $\alpha + \alpha$ reduced mass in the asymptotic limit ($R \to \infty$). However, the cranking formula fails to do so with $B3 \neq 0$. As the value of $B_3$ increases, the asymptotic cranking mass decreases. This can be naively expected from the reduction of the effective mass from the bare mass. In contrast, the ASCC inertial mass converges to the correct reduced mass, no matter what $B_3$ values are. This means that the ASCC method is capable of taking into account the time-odd effect and recovering the exact Galilean symmetry.

Another inertial mass indispensable in the collective Hamiltonian of nuclear reaction models is the rotational moments of inertia. The rotational motion is a Nambu-Goldstone (NG) mode. To calculate this, we utilize a method

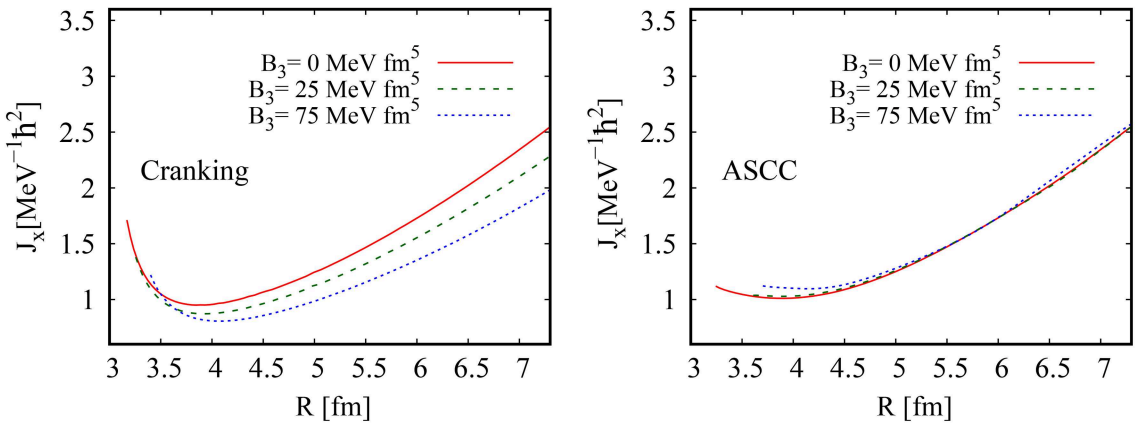


**FIGURE 5 |** Rotational moments of inertias in the presence of time-odd mean-field potential for the system $\alpha$+$\alpha$ as a function of relative distance $R$. The results of cranking formula are shown in the left panel and the results of ASCC are shown in the right panel. The solid (red), dashed (green), and dotted (blue) curves show the results calculated with $B_3 = 0, 25, 75$ MeV fm$^5$, respectively, as labeled in the figure.

proposed in the reference [29], where the inertial masses of the NG modes are calculated from the zero-frequency linear response with the momentum operator of the NG modes. The formulation has been tested in the cases of translational and pairing rotational modes, showing high precision and efficiency. Based on the collective path obtained, we apply this technique to calculate the rotational moments of inertia.

In **Figure 5**, the calculated moments of inertias are presented. With $B_3 = 0$, the moments of inertia calculated with the ASCC and with the cranking formula well agree with each other in the asymptotic region of large $R$. The value is equal to the point-mass approximation in which the point $\alpha$ particles are assumed at the center of mass of each $\alpha$ particle. However, when non-zero $B_3$ comes in, the cranking mass formula can no longer reproduce this asymptotic value. Similar to the case of relative motion, as the value of $B_3$ increases, the asymptotic moments of inertia decrease and deviate from the asymptotic value. In contrast, the ASCC method provides the moments of inertia almost invariant with respect to the $B_3$ values. These results show again that, compared with the cranking formula, the ASCC method gives the collective inertial masses by properly taking into account the time-odd effects.

## 4. SUMMARY AND DISCUSSION

Based on the ASCC theory, we presented a method to determine the collective reaction path for the nuclear reaction as the large amplitude collective motion. This method is applied to the fusion/fission $\alpha$+$\alpha \leftrightarrow {}^8$Be, using the BKN energy density functional. In the three-dimensional coordinate-space representation, the reaction path, the collective potential, as well as the inertial masses are self-consistently calculated. We compare the ASCC results with those of the CHF+cranking method. Since the reaction system is very simple, there is no significant difference between the calculated CHF reaction paths with different constraint operators. Despite of this similarity in the CHF states, the inertial masses calculated with the cranking formula turn out to sensitively depend on the choice of the constraint operator. The ASCC method is able to remove this ambiguity in the inertial mass, by taking into account the residual effects caused by the density fluctuation.

We add a term, which introduce the effective mass and time-odd mean fields, to the standard BKN energy density functional, to examine the effect of these terms on the inertial masses for both the relative and rotational motions. In the presence of time-odd term, the cranking formula fails to preserve the correct asymptotic values, while the validity of ASCC mass is not affected by the introduction of the effective mass. The time-odd mean-fields properly recover the Galilean symmetry, leading to the exact values of the asymptotic inertial mass. This is found to be true in both relative and rotational motions. With this property, we are quite confident that the ASCC method is promising to be applied to the modern nuclear energy density functionals, and make advanced microscopic theoretical analysis on various nuclear reaction models. Another important issue is the inclusion of the paring correlation, which may influence not only static but also dynamical nuclear properties. In order to keep the lowest-energy configuration during the collective motion, the pairing interaction is known to play a key role [30]. Therefore, we may expect significant impact on both the collective inertial masses and the reaction paths. To study the above issues are our future tasks.

## DATA AVAILABILITY STATEMENT

The datasets generated for this study are available on request to the corresponding author.

## AUTHOR CONTRIBUTIONS

The numerical calculation was done by KW. The theoretical part of the work was contributed by TN. KW and TN collaborated to analyze the numerical results and wrote the paper.

## ACKNOWLEDGMENTS

This work was supported in part by JSPS KAKENHI Grant Nos. 19H05142 and 18H01209, and also by JSPS-NSFC Bilateral Program for Joint Research Project on Nuclear mass and life for unraveling mysteries of r-process. This research in part used computational resources provided through the HPCI System Research Project (Project ID: hp190031) and by Multidisciplinary Cooperative Research Program in Center for Computational Sciences, University of Tsukuba.

## REFERENCES

1. Negele JW. The mean-field theory of nuclear structure and dynamics. *Rev Mod Phys.* (1982) **54**:913–1015. doi: 10.1103/RevModPhys.54.913
2. Simenel C. Nuclear quantum many-body dynamics. *Eur Phys J A*. (2012) 48:1–49. doi: 10.1140/epja/i2012-12152-0
3. Nakatsukasa T. Density functional approaches to collective phenomena in nuclei: time-dependent density functional theory for perturbative and non-perturbative nuclear dynamics. *Prog Theor Exp Phys.* (2012) **2012**:01A207. doi: 10.1093/ptep/pts016
4. Maruhn JA, Reinhard PG, Stevenson PD, Umar AS. The TDHF code Sky3D. *Comput Phys Commun*. (2014) 185:2195–216. doi: 10.1016/j.cpc.2014.04.008
5. Nakatsukasa T, Matsuyanagi K, Matsuo M, Yabana K. Time-dependent density-functional description of nuclear dynamics. *Rev Mod Phys.* (2016) **88**:045004. doi: 10.1103/RevModPhys.88.045004
6. Ring P, Schuck P. *The Nuclear Many-Body Problem*. New York, NY: Springer-Verlag (1980).
7. Blaizot JP, Ripka G. *Quantum Theory of Finite Systems*. Cambridge, MA: MIT Press (1986).
8. Baranger M, Kumar K. Nuclear deformations in the pairing-plus-quadrupole model. *Nucl Phys A*. (1968) 110:490–528. doi: 10.1016/0375-9474(68)90370-9
9. Baranger M, Kumar K. Nuclear deformations in the pairing-plus-quadrupole model. *Nucl Phys A*. (1968) 122:241–72. doi: 10.1016/0375-9474(68)90044-4
10. Yuldashbaeva EK, Libert J, Quentin P, Girod M. Mass parameters for large amplitude collective motion: a perturbative microscopic approach. *Phys Lett B*. (1999) **461**:1–8. doi: 10.1016/S0370-2693(99)00836-9
11. Marumori T, Maskawa T, Sakata F, Kuriyama A. Self-consistent collective-coordinate method for the large-amplitude nuclear collective motion. *Prog Theor Phys.* (1980) **64**:1294. doi: 10.1143/PTP.64.1294
12. Matsuo M, Nakatsukasa T, Matsuyanagi K. Adiabatic selfconsistent collective coordinate method for large amplitude collective motion in nuclei with pairing correlations. *Prog Theor Phys.* (2000) **103**:959–79. doi: 10.1143/PTP.103.959
13. Hinohara N, Nakatsukasa T, Matsuo M, Matsuyanagi K. Gauge-invariant formulation of the adiabatic self-consistent collective coordinate method. *Prog Theor Phys*. (2007) **117**:451–78. doi: 10.1143/PTP.117.451
14. Hinohara N, Nakatsukasa T, Matsuo M, Matsuyanagi K. Microscopic description of oblate-prolate shape mixing in proton-rich Se isotopes. *Phys Rev C.* (2009) **80**:014305. doi: 10.1103/PhysRevC.80.014305
15. Hinohara N, Li ZP, Nakatsukasa T, Nikšić T, Vretenar D. Effect of time-odd mean fields on inertial parameters of the quadrupole collective Hamiltonian. *Phys Rev C.* (2012) **85**:024323. doi: 10.1103/PhysRevC.85.024323
16. Sato K, Hinohara N, Yoshida K, Nakatsukasa T, Matsuo M, Matsuyanagi K. Shape transition and fluctuations in neutron-rich Cr isotopes around $N = 40$. *Phys Rev C.* (2012) **86**:024316. doi: 10.1103/PhysRevC.86.024316
17. Davies KTR, Flocard H, Krieger S, Weiss MS. Application of the imaginary time step method to the solution of the static Hartree-Fock problem. *Nucl Phys A*. (1980) **342**:111–23. doi: 10.1016/0375-9474(80)90509-6
18. Nakatsukasa T, Inakura T, Yabana K. Finite amplitude method for the solution of the random-phase approximation. *Phys Rev C.* (2007) **76**:024318. doi: 10.1103/PhysRevC.76.024318
19. Inakura T, Nakatsukasa T, Yabana K. Self-consistent calculation of nuclear photoabsorption cross sections: finite amplitude method with Skyrme functionals in the three-dimensional real space. *Phys Rev C.* (2009) **80**:044301. doi: 10.1103/PhysRevC.80.044301
20. Avogadro P, Nakatsukasa T. Finite amplitude method for the quasiparticle random-phase approximation. *Phys Rev C.* (2011) **84**:014314. doi: 10.1103/PhysRevC.84.014314
21. Avogadro P, Nakatsukasa T. Efficient calculation for the quasiparticle random-phase approximation matrix. *Phys Rev C.* (2013) **87**:014331. doi: 10.1103/PhysRevC.87.014331
22. Wen K, Nakatsukasa T. Self-consistent collective coordinate for reaction path and inertial mass. *Phys Rev C.* (2016) **94**:054618. doi: 10.1103/PhysRevC.94.054618
23. Egido JL, Borrajo M, Rodríguez TR. Collective and single-particle motion in beyond mean field approaches. *Phys Rev Lett*. (2016) **116**:052502. doi: 10.1103/PhysRevLett.116.052502
24. Li ZP, Nikšić T, Ring P, Vretenar D, Yao JM, Meng J. Efficient method for computing the Thouless-Valatin inertia parameters. *Phys Rev C.* (2012) **86**:034334. doi: 10.1103/PhysRevC.86.034334
25. Bonche P, Koonin S, Negele JW. One-dimensional nuclear dynamics in the time-dependent Hartree-Fock approximation. *Phys Rev C.* (1976) **13**:1226–58. doi: 10.1103/PhysRevC.13.1226
26. Baran A, Sheikh JA, Dobaczewski J, Nazarewicz W, Staszczak A. Quadrupole collective inertia in nuclear fission: cranking approximation. *Phys Rev C.* (2011) **84**:054321. doi: 10.1103/PhysRevC.84.054321
27. Thouless DJ, Valatin JG. Time-dependent Hartree-Fock equations and rotational states of nuclei. *Nucl Phys.* (1962) **31**:211–30. doi: 10.1016/0029-5582(62)90741-1
28. Bohr A, Mottelson BR. *Nuclear Structure*. Vol. 2. New York, NY: W. A. Benjamin (1975).
29. Hinohara N. Collective inertia of the Nambu-Goldstone mode from linear response theory. *Phys Rev C.* (2015) **92**:034321. doi: 10.1103/PhysRevC.92.034321
30. Nakatsukasa T, Matsuyanagi K, Matsuzaki M, Shimizu YR. Quantal rotation and its coupling to intrinsic motion in nuclei. *Phys Script*. (2016) **91**:073008. doi: 10.1088/0031-8949/91/7/073008

**Conflict of Interest:** The authors declare that the research was conducted in the absence of any commercial or financial relationships that could be construed as a potential conflict of interest.

frontiers in Physics

ORIGINAL RESEARCH
published: 07 February 2020
doi: 10.3389/fphy.2020.00008

# Time-Dependent Approaches to Open Quantum Systems

*Masaaki Tokieda*[1] *and Kouichi Hagino*[2]*

[1] Department of Physics, Tohoku University, Sendai, Japan, [2] Department of Physics, Kyoto University, Kyoto, Japan

Couplings of a system to other degrees of freedom (that is, environmental degrees of freedom) lead to energy dissipation when the number of environmental degrees of freedom is large enough. Here, we discuss quantal treatments for such energy dissipation. To this end, we discuss two different time-dependent methods. One is to introduce an effective time-dependent Hamiltonian, which leads to a classical equation of motion as a relationship among expectation values of quantum operators. We apply this method to a heavy-ion fusion reaction and discuss the role of dissipation on the penetrability of the Coulomb barrier. The other method is to start with a Hamiltonian with environmental degrees of freedom and derive an equation that the system degree of freedom obeys. For this, we present a new efficient method to solve coupled-channels equations that can be easily applied even when the dimension of the coupled-channels equations is huge.

**Keywords: open quantum systems, quantum friction, Caldeira-Leggett model, barrier transmission, fusion reactions**

OPEN ACCESS

***Edited by:***
*Paul Denis Stevenson,*
*University of Surrey, United Kingdom*

***Reviewed by:***
*Sakir Ayik,*
*Tennessee Technological University, United States*
*Marco La Cognata,*
*Laboratori Nazionali del Sud (INFN), Italy*

***Correspondence:**
*Kouichi Hagino*
*hagino.kouichi.5m@kyoto-u.ac.jp*

***Specialty section:***
*This article was submitted to Nuclear Physics, a section of the journal Frontiers in Physics*

***Received:*** *19 November 2019*
***Accepted:*** *08 January 2020*
***Published:*** *07 February 2020*

***Citation:***
*Tokieda M and Hagino K (2020) Time-Dependent Approaches to Open Quantum Systems. Front. Phys. 8:8. doi: 10.3389/fphy.2020.00008*

## 1. INTRODUCTION

Open quantum systems are ubiquitous in many branches of science. In general, a system is never isolated but couples to other degrees of freedom, which are often referred to as the environment. The couplings to the environmental degrees of freedom can strongly affect the dynamics of the system. When the number of environmental degrees of freedom is huge, the couplings lead to energy dissipation. It has been demonstrated by Caldeira and Leggett that such couplings suppress the tunneling rate [1, 2], going into a transition from quantum to classical regimes. In nuclear physics, it has been well known that a large amount of the relative energy and angular momentum is dissipated during collisions of heavy nuclei at energies close to the Coulomb barrier, known as deep inelastic collisions [3]. In this case, the dissipation occurs due to the couplings between the relative motion of two colliding nuclei and nucleonic degrees of freedom in those nuclei. A classical Langevin equation [4] has been successfully applied to describe such collisions [3]. The Langevin approach has also been employed in order to discuss fusion reactions for syntheses of superheavy elements [5–11].

The classical Langevin approach, by definition, is not applicable at energies around the Coulomb barrier, at which quantum effects play an important role [12, 13]. One can then ask: what is a quantum model that, in the classical Limit, is equivalent to a classical Langevin equation? There are two approaches to address this question. One is to use a phenomenological quantum friction model in which the expectation values of operators obey the classical equation of motion with friction [14–17]. Recently, we solved such quantum friction Hamiltonians with a time-dependent wave packet approach in order to discuss the effect of friction on quantum tunneling [18]. The other approach to a quantum Langevin equation is to start from a system-plus-bath Hamiltonian,

that is, a Hamiltonian that consists of the system and the environmental degrees of freedom and eliminates the environmental degrees of freedom. For instance, one can employ the Caldeira-Leggett Hamiltonian [1] since the classical Langevin equation can be derived from it [3, 4]. This approach is more microscopic, and a computation would thus be more involved than the quantum friction model. It has been known that, in the Markovian limit, the time evolution for the reduced density matrix for the system degree of freedom in general takes the so-called Lindblad form [19, 20].

In this paper, we discuss both of these approaches for open quantum systems from the point of view of the time-dependent method. In the next section, we first discuss the phenomenological quantum friction models using a time-dependent wave packet approach. We apply them to heavy-ion fusion reactions around the Coulomb barrier and discuss a role of friction in fusion dynamics. In section III. we solve the Calderira-Leggett Hamiltonian using a time-dependent coupled-channels approach. Using a quantum damped harmonic oscillator, we discuss how one can deal with a large number of degrees of freedom. A summary of the paper is then given in section IV.

## 2. PHENOMENOLOGICAL QUANTUM FRICTION MODELS

We first considered a phenomenological approach to quantum friction. In this approach, one treats the environmental degrees of freedom implicitly and introduce a phenomenological Hamiltonian with which the classical equation of motion with a frictional force is reproduced as expectation values. For this purpose, several model Hamiltonians have been proposed so far [14–17]. Among these, we focused in this paper on the one introduced by Kostin [16].

Consider a particle of mass $m$ moving in a one-dimensional space $q$ under the influence of a potential $V(q)$. With a friction coefficient $\gamma$, the phenomenological Schrödinger equation in the Kostin model is given by [16]:

$$i\hbar\frac{\partial}{\partial t}\psi(q,t)=\left[-\frac{\hbar^2}{2m}\frac{\partial^2}{\partial q^2}+V(q)+\gamma S(q,t)\right]\psi(q,t), \quad (1)$$

where $S(q,t)$ is the phase of the wave function, $\psi(q,t) = |\psi(q,t)|\exp(iS(q,t)/\hbar)$. From this equation, it is easy to confirm that one can derive the equation of motion with a frictional force:

$$\frac{d}{dt}\langle p\rangle=-\gamma\langle p\rangle-\left\langle\frac{dV}{dq}\right\rangle, \quad (2)$$

as is desired. Here, the expectation value of an operator $\mathcal{O}$ is denoted as $\langle\mathcal{O}\rangle = \int dq\,\psi^*(q,t)\mathcal{O}\psi(q,t)$, and $p$ is the momentum operator.

When one simulates an energy dissipation in heavy-ion collisions by means of friction, a frictional force should be active only when the colliding nuclei are close to each other. In other words, one needs to deal with a coordinate-dependent friction coefficient, $\gamma = \gamma(q)$. An extension of the Kostin model along this line has been proposed in Immele et al. [21], Bargueno and Miret-Artes [22], with which the modified Schrödinger equation is given by:

$$i\hbar\frac{\partial}{\partial t}\psi(q,t)=\left[-\frac{\hbar^2}{2m}\frac{\partial^2}{\partial q^2}+V(q)+\int^q dq_1\,\gamma(q_1)\frac{\partial}{\partial q_1}S(q_1,t)\right]\psi(q,t). \quad (3)$$

To apply the phenomenological model to realistic collision problems, one further needs an extension to a three-dimensional space, $\vec{q} = \vec{q}(r,\theta,\phi)$. To this end, we first must expand the wave function with the Legendre polynomials $P_l(x)$ as $\psi(\vec{q},t) = \sum_{l=0}^{\infty} u_l(r,t)P_l(\cos\theta)/r$. One can then modify the Schrödinger equation for $u_l(r,t)$ in the same way as Equation (3) to incorporate a frictional force,

$$i\hbar\frac{\partial}{\partial t}u_l(r,t)=\left[-\frac{\hbar^2}{2m}\frac{\partial^2}{\partial r^2}+\frac{\hbar^2}{2m}\frac{l(l+1)}{r^2}+V(r)+\int^r dr_1\,\gamma(r_1)\frac{\partial}{\partial r_1}S_l(r_1,t)\right]u_l(r,t), \quad (4)$$

where $S_l(r,t)$ is the phase of the radial wave function $u_l(r,t) = |u_l(r,t)|\exp(iS_l(r,t)/\hbar)$. We have here assumed a spherically symmetric potential, $V(\vec{q}) = V(r)$. Notice that only the radial friction is taken into account here, while the angular momentum dissipation is neglected.

In applying Equation (4) to scattering problems, one needs to use the time-dependent approach since the Hamiltonian depends explicitly on time. To this end, we propagate a wave packet and observe how it bifurcates after it crosses the potential region. Since a wave packet is a superposition of various energy waves, one has to choose the initial condition carefully to get scattering quantities at certain initial energy. Notice that the energy projection approach [23] is inapplicable for our purpose since the energy is not conserved.

In the initial condition, the width of the energy distribution must be small enough to get reasonable results. In this context, the energy refers to the expectation value of the asymptotic Hamiltonian, $H_0$. If we restrict to the s-wave scattering, $l = 0$, and if $V(r)$ rapidly vanishes as $r \to \infty$, one can simply take the kinetic energy operator as $H_0$, that is, $H_0 = -\hbar^2/2m\left(\partial^2/\partial r^2\right)$. The minimum uncertainty wave packet in this case has been discussed in Bracher [24], which reads:

$$u_0^{\min}(r,t=0)\propto re^{-(r-r_0)^2/4\sigma_r^2}e^{ik_0r}, \quad (5)$$

where $r_0$ and $\sigma_r$ are related to the mean position and the width of the wave function in the coordinate space, respectively, and $k_0$ is related to the mean initial energy.

In heavy-ion collisions, on the other hand, the potential is a sum of the nuclear potential $V_N$ and the Coulomb potential $V_C(r) = Z_PZ_Te^2/r$ with the projectile charge $Z_P$ and the target charge $Z_T$. Since the Coulomb potential is a long range potential, the asymptotic Hamiltonian $H_0$ has to include it: $H_0 = -\hbar^2/2m\left(\partial^2/\partial r^2\right) + V_C$. Thus, the minimum uncertainty wave

packet in the form of Equation (5) would not be efficient in this case. Instead, one needs to construct a wave packet from the energy distribution, $f_C(E)$, of $H_0$ in the presence of the Coulomb potential. In analogy to the spherical Bessel functions, we find that this can be achieved as:

$$u_0^C(r, t = 0) \propto \int_0^\infty dk\, F_0(\eta, kr) e^{ikr_0} \sqrt{k f_C(E)}, \tag{6}$$

with $E = \hbar^2 k^2/2m$, where $\eta = mZ_P Z_T e^2/\hbar^2 k$ is the Sommerfeld parameter and $F_0(\eta, kr)$ is the regular Coulomb wave function.

With the initial condition given by Equation (6), we compute the penetrability of the Coulomb barrier for the $^{16}$O + $^{208}$Pb system in the presence of friction. For the nuclear potential, we employ the optical potential in Evers et al. [25]:

$$V_N(r) = \frac{V_0}{1 + \exp\left((r - R_\mathrm{v})/a_\mathrm{v}\right)} + i\frac{W_0}{1 + \exp((r - R_\mathrm{w})/a_\mathrm{w})}, \tag{7}$$

with $V_0 = -901.4$ MeV, $R_\mathrm{v} = 8.44$ fm, $a_\mathrm{v} = 0.664$ fm, $W_0 = -30$ MeV, $R_\mathrm{w} = 6.76$ fm, and $a_\mathrm{w} = 0.4$ fm. With this potential, the Coulomb barrier height $V_B$ is 74.5 MeV.

For a friction coefficient $\gamma(r)$, we employ the surface friction model [3],

$$\gamma(r) = \frac{\gamma_0}{m}\left(V_B \frac{df_\mathrm{WS}}{dr}\right)^2, \tag{8}$$

with the Woods-Saxon from factor $f_\mathrm{WS} = 1/(1 + \exp((r - R_\mathrm{v})/a_\mathrm{v}))$. This is a general form of the friction coefficient obtained perturbatively [26], and it has successfully been applied to the above barrier fusion reactions and to deep inelastic scatterings [3]. We arbitrarily set $\gamma_0 = 4.7 \times 10^{-23}$ s/MeV, and this is used in the classical calculations. We compute the phase of the wave function in the same way as in Tokieda and Hagino [18].

For the initial energy distribution in Equation (6), we assume the Gaussian form,

$$f_C(E) = \frac{1}{\sqrt{2\pi\sigma_E^2}} e^{-(E-E_0)^2/2\sigma_E^2}. \tag{9}$$

where $E_0$ and $\sigma_E$ are the mean and the width of the initial energy distribution. We have confirmed that $\sigma_E = 0.5$ MeV is sufficient in the present parameter set.

**Figure 1** compares the penetrability obtained with and without friction. One finds that the penetrability with friction is shifted to higher energies around the barrier. That is, in the presence of friction, a particle needs additional energy to penetrate the barrier, which originates from the energy dissipation. One can also see that the penetrability does not reach unity at high energies, but it is almost saturated at around 0.9. This means that the exit channel is in a quantum superposition state of absorption and reflection even at sufficiently above-barrier energies. Notice that, in classical mechanics without a random force, the penetrability can be only 0 or 1. In this sense, this is peculiar to the quantum friction model.

For a practical application to fusion reactions, one needs to take into account explicitly low-lying collective excitations, as

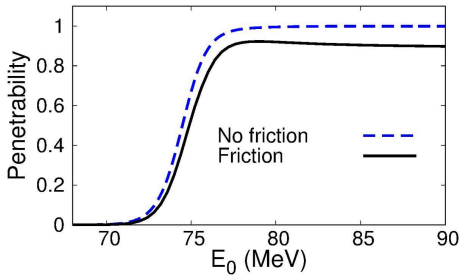


**FIGURE 1 |** Energy dependence of the penetrability of the Coulomb barrier for the $^{16}$O+$^{208}$Pb reaction. The dashed line shows the result without friction, while the solid line is for the result with friction.

they play a crucial role [27]. This can be achieved by extending the above method to the coupled-channels formalism. In that treatment, low-lying collective excitations are taken into account explicitly, while other degrees of freedom, such as non-collective excitations and nucleon transfers, are treated by means of a frictional force.

In Tokieda and Hagino [28], we have applied the method to the $^{16}$O+$^{208}$Pb system. The nuclear potential is the Woods-Saxon form as Equation (7). For low-lying collective states, the first excited state of both $^{16}$O and $^{208}$Pb were taken into account. The channel-coupling effect was treated in the same way as the CCFULL code, and the iso-centrifugal approximation was adopted [29]. The surface friction model was employed for a friction coefficient [with a replacement of $V_B$ with $V_0$ in Equation (8)], treating $\gamma_0$ as an adjustable parameter. See Tokieda and Hagino [28] and reference therein for details of the parameters.

To compute the penetrability at certain energy, we used the same initial condition as Equation (9). It has turned out that $\sigma_E = 0.5$ MeV was sufficient for the employed parameter set. By taking a sum of the penetrability at each angular momentum, one could calculate fusion cross sections, which could then be compared with experimental data.

In **Figure 2**, we compare the energy dependence of fusion cross sections. Notice that the present method is reduced to the conventional coupled-channels method when friction is turned off. Thus, the no-friction result is nothing but the result of the conventional coupled-channels approach. To reproduce the experimental data, we set $\gamma_0 = 0.6 \times 10^{-23}$ s/MeV. In the left panel of **Figure 2**, on one hand, one finds that the fusion cross sections at above barrier energies are suppressed in the friction model (the solid line) compared to that in the no-friction model (the dashed line). In the right panel of **Figure 2**, on the other hand, one sees that the sub-barrier fusion cross sections in both the models give almost the same result. Considering overall energies, the present friction model provided a more consistent description of fusion reactions around the Coulomb barrier as compared to the conventional coupled-channels approach. In this calculation, the same behavior as in **Figure 1** has been found, and this may be a key to achieve a consistent description [28].

In comparison with the classical Langevin approach, the present method did not contain a random force originating from

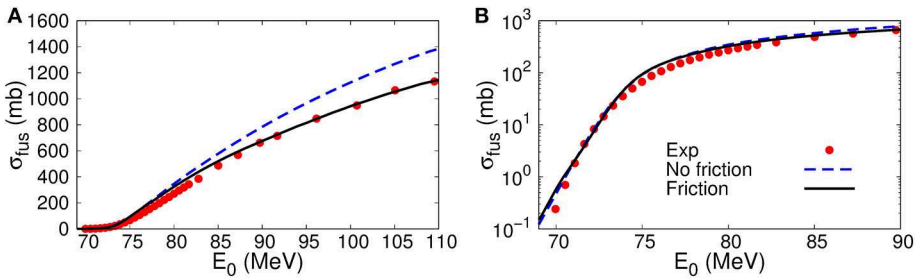


**FIGURE 2 |** Energy dependence of fusion cross sections for the $^{16}$O + $^{208}$Pb system. The results with and without friction are shown by the solid and the dashed lines, respectively, while the experimental data are shown by the circles. The left panel **(A)** is in the linear scale, while the right panel **(B)** is in the logarithmic scale. The experimental data are taken from Morton et al. [30].

thermal fluctuation. For the $^{16}$O+$^{208}$Pb system, the compound nucleus was formed once the projectile and the target nuclei touched each other, and the fluctuation played a much more minor role compared to the massive systems. In that situation, fusion cross sections were given as an averaged quantity, and it was expected that the presence of a random force does not change the result much. However, when one deals with phenomena in which thermal fluctuation plays a crucial role, such as deep inelastic scattering or a synthesis of superheavy elements, the thermal fluctuation should be explicitly taken into account. One could in fact directly add a random force to the Schrödinger equation Equation (1) as was done in the original paper [16]. Alternatively, friction and fluctuation will naturally emerge by explicitly treating environmental degrees of freedom, which we have discussed in the next section.

## 3. SYSTEM-PLUS-BATH MODEL

We next considered a more microscopic model for quantum friction, employing a system-plus-bath model. To be more specific, we considered the Caldeira-Leggett model [1, 2], whose Hamiltonian is given by,

$$H_{\rm tot} = H_S + \sum_i \hbar\omega_i a_i^\dagger a_i + h(q)\sum_i d_i(a_i^\dagger + a_i), \quad (10)$$

$$\equiv H_S + H_B + V_{\rm coup}, \quad (11)$$

where $H_S$ and $H_B$ are the Hamiltonians for the system and the bath degrees of freedom, respectively, while $V_{\rm coup}$ is the coupling Hamiltonian between the system and the bath. Here, the bath degree of freedom is assumed to be a set of harmonic oscillators, whose creation and annihilation operators are denoted by an $a_i^\dagger$ and $a_i$. The coupling Hamiltonian is assumed to be separable between the system and the bath degrees of freedom. In there, $d_i$ is the coupling strength, and $h(q)$ is the coupling form factor, where $q$ is the coordinate of the system.

There are several ways to solve the Calderira-Leggett Hamiltonian. In Caldeira and Leggett [1, 2], the bath degrees of freedom were integrated out using the path integral in order to obtain an effective action for the system degree of freedom [see also Takigawa and Bertsch [31]]. One can also introduce the influence functional [32]. Here we discussed the coupled-channels approach [33].

In the conventional coupled-channels approach [27], one expands the total wave function in terms of the eigen-wave functions of $H_B$:

$$\Psi_{\rm tot}(q,t) = \sum_{\{n_i\}} \psi_{\{n_i\}}(q,t)\,|\{n_i\}\rangle, \quad (12)$$

where the basis states $|\{n_i\}\rangle$ are given by:

$$|\{n_i\}\rangle = \prod_i \frac{1}{\sqrt{n_i!}}\left(a_i^\dagger\right)^{n_i}|0\rangle. \quad (13)$$

Here, $|0\rangle$ is the vacuum state defined as $a_i|0\rangle = 0$. One can derive the coupled equations for $\psi_{\{n_i\}}(q,t)$ by evaluating the equation:

$$\langle\{n_i\}|i\hbar\frac{\partial}{\partial t}|\Psi_{\rm tot}\rangle = \langle\{n_i\}|H_{\rm tot}|\Psi_{\rm tot}\rangle, \quad (14)$$

that is,

$$i\hbar\frac{\partial}{\partial t}\psi_{\{n_i\}}(q,t) = \left(H_S + \sum_i n_i\hbar\omega_i\right)\psi_{\{n_i\}}(q,t) + \sum_{\{n_i'\}}\langle\{n_i\}|V_{\rm coup}|\{n_i'\}\rangle\,\psi_{\{n_i'\}}(q,t). \quad (15)$$

The coupled-channels equations, Equation (15), can be numerically solved when the number of the oscillator modes is not large [27, 29]. However, in general, the number of the oscillator modes can be huge, or the distribution of the frequency of the oscillator may even be given as a continuous function. In that situation, it is almost hopeless to solve the coupled-channels equations directly. In order to overcome this problem, we introduced a more efficient basis to expand the total wave function [33]. To this end, we first expanded the function $\exp(-i\omega t)$ with a finite basis set as:

$$e^{-i\omega t} \sim \sum_{k=1}^{K}\eta_k(\omega)u_k(t), \quad (16)$$

where $u_k(t)$ is a known function such as a Bessel function, and $\eta_k(\omega)$ is the expansion coefficient. We then introduced a new phonon creation operator as:

$$b_k^\dagger = \sum_i \frac{d_i}{\hbar}\eta_k(\omega_i)a_i^\dagger. \tag{17}$$

Notice that the number of $k$ is finite, $k$ running from 1 to $K$, even though the number of $i$ may be infinite. We then constructed the basis states using the operators $b_k^\dagger$ and expanded the total wave function with them. That is, instead of Equation (12), we expanded the total wave function as:

$$\Psi_{\rm tot}(q,t) = \sum_{\{\tilde{n}_k\}} \tilde{\psi}_{\{\tilde{n}_k\}}(q,t)\,|\{\tilde{n}_k\}\rangle, \tag{18}$$

with,

$$|\{\tilde{n}_k\}\rangle = \prod_{k=1}^{K} \frac{1}{\sqrt{\tilde{n}_k!}}\left(b_k^\dagger\right)^{\tilde{n}_k}|0\rangle. \tag{19}$$

One can then obtain the coupled-channels equations similar to Equation (15):

$$\begin{aligned} i\hbar\frac{\partial}{\partial t}\tilde{\psi}_{\{\tilde{n}_k\}}(q,t) &= H_S\,\tilde{\psi}_{\{\tilde{n}_k\}}(q,t) \\ &+ \sum_{\{\tilde{n}'_k\}}\langle\{\tilde{n}_k\}|H_B + V_{\rm coup}|\{\tilde{n}'_k\}\rangle\,\tilde{\psi}_{\{\tilde{n}'_k\}}(q,t). \end{aligned} \tag{20}$$

We once again emphasize that the dimension of the coupled-channels equations, Equation (20), is much smaller than that of the original equations, Equation (15).

The structure of the coupled-channels equations, Equation (20), becomes simple when the basis functions $u_k(t)$ satisfy the following two conditions.

1. The matrix $D$ defined as:

$$D_{kk'} \equiv \frac{1}{\hbar^2}\sum_i d_i^2\eta_k(\omega)\eta_{k'}^*(\omega), \tag{21}$$

is diagonal with respect $k$ and $k'$. That is, $D_{kk'} = \lambda_k\delta_{k,k'}$. Notice that the matrix $D$ can be expressed also as:

$$D_{kk'} \equiv \frac{1}{\hbar}\int_{-\infty}^{\infty} d\omega\, J(\omega)\eta_k(\omega)\eta_{k'}^*(\omega), \tag{22}$$

with the spectral density given by:

$$J(\omega) = \frac{1}{\hbar}\sum_i d_i^2\delta(\omega-\omega_i). \tag{23}$$

2. The basis function $u_k(t)$ is closed under differentiation:

$$\frac{du_k(t)}{dt} = \sum_{k'=1}^{K} C_{kk'}u_{k'}(t). \tag{24}$$

Notice that Bessel functions satisfy this condition since the following relation holds,

$$\frac{d}{dx}J_k(x) = -\frac{1}{2}J_{k+1}(x) + \frac{1}{2}J_{k-1}(x), \tag{25}$$

(with $J_{-k}(x) = (-1)^k J_k(x)$ for an integer value of $k$).

See Equation (31) in Tokieda and Hagino [33] for the explicit form of the coupled-channels equations, Equation (20). Tokieda and Hagino [33] also provides an alternative derivation of the coupled-channels equations, which used the influence functional of the path integral method. This allows one to extend the present formalism to finite temperatures.

Before the present method is applied to heavy-ion collisions, we should make sure that it works in principle. To this end, we considered a damped harmonic oscillator in which the exact solution can be obtained easily [33]. The Hamiltonian for the system, $H_S$ in Equation (10), is now given by:

$$H_S = \frac{p^2}{2M} + \frac{1}{2}M\omega_S^2 q^2 + h^2(q)\sum_i \frac{d_i^2}{\hbar\omega_i}, \tag{26}$$

where $M$ and $\omega_S$ are the mass and the frequency of the system, respectively, and the last term represents the so-called counter term. In the following, we measured the length of the system in units of the oscillator length $q_S$ defined by $q_S \equiv \sqrt{\hbar/M\omega_S}$, and took the coupling form factor, $h(q)$, to be $h(q) = q/q_S$. We assumed that the bath oscillators are distributed according to the spectral density (see Equation 23) as:

$$J(\omega) = V_I\,\frac{\omega}{\Omega}\sqrt{1-\left(\frac{\omega}{\Omega}\right)^2}. \tag{27}$$

In the numerical calculations shown below, we took $\hbar\omega_S = 2$ eV, $V_I = 1$ eV and $\hbar\Omega = 4$ eV.

At $t = 0$, we assumed that $\tilde{\psi}_{\{\tilde{n}_k\}}(q, t=0) = 0$ for $N \equiv \sum_{k=1}^{K}\tilde{n}_k \neq 0$. For $N = 0$, that is, for $\tilde{n}_k = 0$ for all $k$, we assumed that the wave function is given by:

$$\tilde{\psi}_{N=0}(q, t=0) = \frac{1}{\sqrt[4]{2\pi\sigma_0^2}}\,e^{-(q-q_0)^2/4\sigma_0^2}\,e^{ip_0q/\hbar}, \tag{28}$$

with $q_0/q_S = -1$, $\sigma_0/q_S = 1/\sqrt{2}$, and $p_0q_S/\hbar = 0$.

**Figures 3**, **4** show the time evolution. The upper panel of **Figure 3** shows the norm for each phonon state $N$ as a function of $\omega_S t$. Here, the norm is defined as:

$$\mathcal{N}_N(t) \equiv \sum_{\{\tilde{n}_k\}}\int dq\,|\tilde{\psi}_{\{\tilde{n}_k\}}(q,t)|^2\delta_{\sum_k\tilde{n}_k,N}. \tag{29}$$

To draw this figure, we took Bessel functions, $J_k(\Omega t)$, for $u_k(t)$ in Equation (16) with $K = 20$. A new basis was then constructed by diagonalizing the matrix $D$ in Equation (21). With this basis, we solved the coupled-channels equations by including the phonon states with $N \leq 5$. The expectation value of the norm was also shown in the lower panel. As is expected, the number of phonons

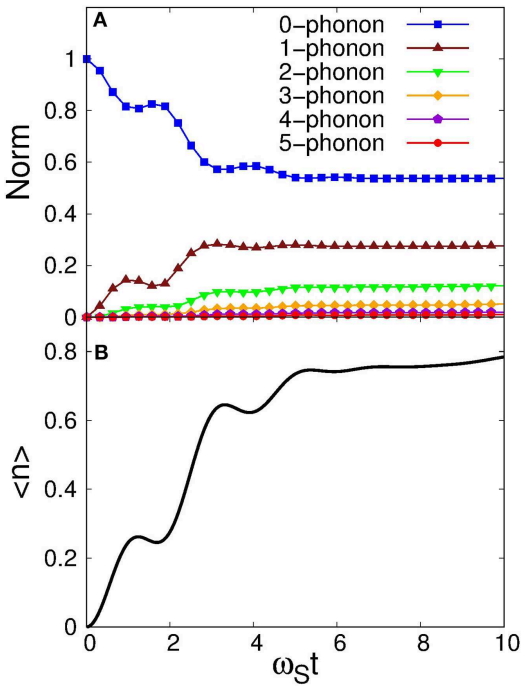


**FIGURE 3 | (A)** The norm for each phonon number, $N = \sum_{k=1}^{K} \tilde{n}_k$. The solid line with squares, triangles, inverted triangles, diamonds, pentagons, and circles are for $N$ = 0, 1, 2, 3, 4, and 5, respectively. These are obtained by solving the coupled-channels equations with the phonon states up to $N_{\max} = 5$, for which the phonon operators are defined with the Bessel function basis with $K = 20$. **(B)** The expectation value of the number of phonon.

in the bath gradually increases as a function of time. Notice that the contribution of the 5-phonon states is small in the whole time range shown in the figure. This justifies the truncation at $N_{\max} = 5$ for the present parameter set. One can also see that the contribution of each phonon reaches its equilibrium at around $\omega_S t = 6$.

**Figure 4** compares the results of the present method with the exact solution for the quantum damped harmonic oscillator. To this end, we evaluated the expectation values for the following four quantities: $\xi_q \equiv \langle q \rangle / q_S$, $\xi_p \equiv \langle p \rangle q_S/\hbar$, $\xi_{qq} \equiv \langle (q - \langle q \rangle)^2 \rangle / q_S^2$, and $\xi_{pp} \equiv \langle (p - \langle p \rangle)^2 \rangle q_S^2/\hbar^2$. We carried out the calculations with three different values of $N_{\max}$, that is, $N_{\max}$ = 3, 4, and 5, and compare them with the exact results shown by the solid lines. One can see that all of the calculations with $N_{\max} = 3$, 4, and 5 reproduce the exact results up to $\omega_S t \sim 5$, for which $J_{20}(\Omega t)$ is negligibly small, and the expansion in Equation (16) with Bessel functions up to $K = 20$ [that is, up to $J_{19}(\Omega t)$] is therefore reasonable. The deviation from the exact results becomes significant for larger values of $\omega_S t$, especially for the second order moments, $\xi_{qq}$ and $\xi_{pp}$. This is a natural consequence of the fact that the larger number of phonon states are required to describe the finer structures.

We would like to make a few comments on an application of the present method to heavy-ion collisions. Unlike the phenomenological quantum friction models discussed in the previous section, the total energy conservation was assured with the Hamiltonian given by Equation (10). Therefore, one can utilize the energy projection method [23] to calculate the penetrability for a given energy. In the present method,

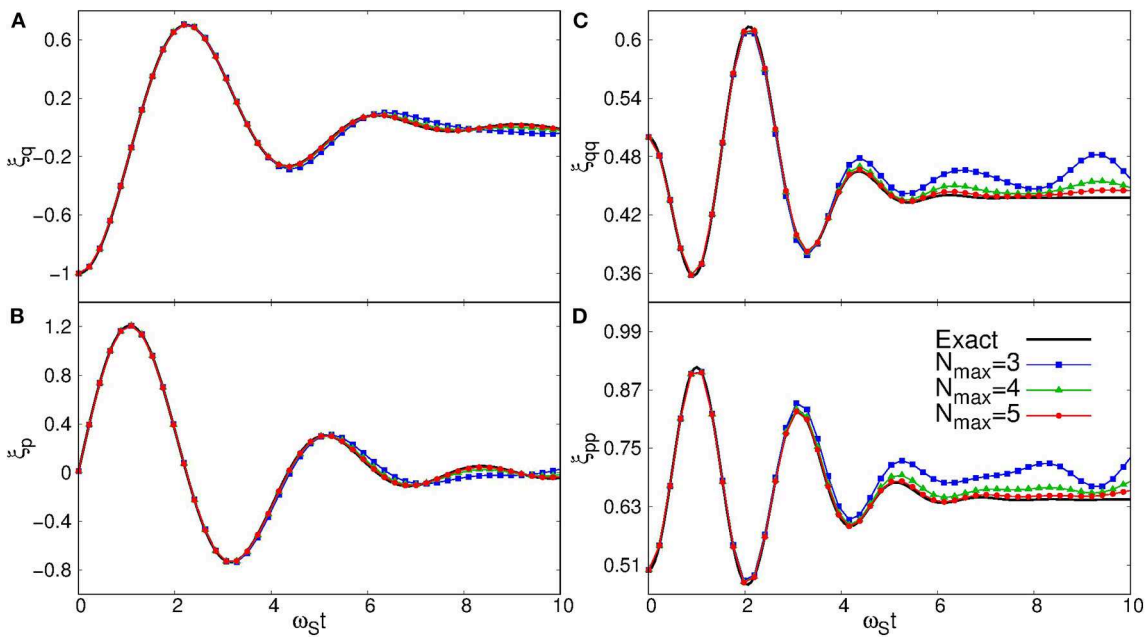


**FIGURE 4 |** Comparison between the present method and the exact results for the expectation values of several quantities, that is, **(A)** $\xi_q = \langle q \rangle / q_S$, **(B)** $\xi_p = \langle p \rangle q_S/\hbar$, **(C)** $\xi_{qq} = \langle (q - \langle q \rangle)^2 \rangle / q_S^2$, and **(D)** $\xi_{pp} = \langle (p - \langle p \rangle)^2 \rangle q_S^2/\hbar^2$. The solid lines show the exact results, while the solid lines with squares, triangles, and circles are the results of the present method with $N_{\max} = 3$, 4, and 5, respectively.

the number of $N_{\max}$ required to achieve convergence was an important parameter that controlled the numerical cost. We expected that $N_{\max}$ was small for collision problems since the system-bath coupling was active only while a wave packet overlapped with the potential region. Another issue in an application to heavy-ion collisions was that one needs to model properly the environmental degrees of freedom. Note that they are described solely by the spectral density (see Equation 23) in the Caldeira-Leggett model. That is, one needs to model a suitable spectral density for heavy-ion collisions. A similar problem has already been discussed in the linear response approach to heavy-ion collisions [34] as well as to fission reactions [35]. We anticipate that these approaches provide a useful means for our future works of an application of the present method to heavy-ion reactions.

## 4. SUMMARY

We have discussed two time-dependent methods for quantum friction. The first method was based on an effective Hamiltonian, which was constructed so that expectation values of operators obey a classical equation of motion with friction. Such Hamiltonian is in general time-dependent, and we have solved it with a time-dependent wave packet method. The other method is to start with a total Hamiltonian with both the system and the environmental degrees of freedom and then eliminate the environmental degree of freedom to derive an equation that the system degree of freedom obeys. For this approach, we have presented a new efficient basis for coupled-channels equations. These two methods were complimentary to each other. In the first method, whereas several parameters had to be determined phenomenologically, a required computational time was much shorter than the second method. On the other hand, the second method was based on a more microscopic Hamiltonian, and fewer empirical inputs were thus required even though the computational time may have been large. By combining these two approaches appropriately, one may be able to achieve a quantum description of heavy-ion deep inelastic collisions as well as fusion reactions to synthesize superheavy elements.

## DATA AVAILABILITY STATEMENT

The datasets generated for this study are available on request to the corresponding author.

## AUTHOR CONTRIBUTIONS

All authors listed have made a substantial, direct and intellectual contribution to the work, and approved it for publication.

## FUNDING

This work was supported by Tohoku University Graduate Program on Physics for the Universe (GP-PU) and JSPS KAKENHI Grant Numbers JP18J20565 and 19K03861.

## ACKNOWLEDGMENTS

We would like to thank Denis Lacroix and Guillaume Hupin for useful discussions.

## REFERENCES

1. Caldeira AO, Leggett AJ. Influence of dissipation on quantum tunneling in macroscopic systems. *Phys Rev Lett.* (1981) **46**:211. doi: 10.1103/PhysRevLett.46.211
2. Caldeira AO, Leggett AJ. Quantum tunnelling in a dissipative system. *Ann Phys.* (1983) **149**:374. doi: 10.1016/0003-4916(83)90202-6
3. Fröbrich P, Lipperheide R. *Theory of Nuclear Reactions*. Oxford: Oxford University Press (1996).
4. Abe Y, Ayik S, Reinhard PG, Suraud E. On stochastic approaches of nuclear dynamics. *Phys Rep.* (1996) **275**:49. doi: 10.1016/0370-1573(96)00003-8
5. Abe Y, Boilley D, Giraud BG, Wada T. Diffusion over a saddle with a Langevin equation. *Phys Rev E.* (2000) **61**:1125. doi: 10.1103/PhysRevE.61.1125
6. Shen CW, Kosenko G, Abe Y. Two-step model of fusion for the synthesis of superheavy elements. *Phys Rev C.* (2002) **66**:061602(R). doi: 10.1103/PhysRevC.66.061602
7. Aritomo Y, Ohta M. Dynamical calculation for fusion - fission probability in superheavy mass region, where mass symmetric fission events originate. *Nucl Phys.* (2004) **A744**:3–14. doi: 10.1016/j.nuclphysa.2004.08.009
8. Swiatecki WJ, Siwek-Wilczynska K, Wilczynski J. Fusion by diffusion. *Acta Phys Pol B.* (2003) **34**:2049–71.
9. Swiatecki WJ, Siwek-Wilczynska K, Wilczynski J. Fusion by diffusion. II. Synthesis of transfermium elements in cold fusion reactions. *Phys Rev C.* (2005) **71**:014602. doi: 10.1103/PhysRevC.71.014602
10. Zagrebaev VI, Greiner W. Cross sections for the production of superheavy nuclei. *Nucl Phys.* (2015) **A944**:257–307. doi: 10.1016/j.nuclphysa.2015.02.010
11. Hagino K. Hot fusion reactions with deformed nuclei for synthesis of superheavy nuclei: an extension of the fusion-by-diffusion model. *Phys Rev C.* (2018) **98**:014607. doi: 10.1103/PhysRevC.98.014607
12. Takigawa N, Ayik S, Washiyama K, Kimura S. Quantum effect in the diffusion along a potential barrier: Comments on the synthesis of superheavy elements. *Phys Rev C.* (2004) **69**:054605. doi: 10.1103/PhysRevC.69.054605
13. Ayik S, Yilmaz B, Gokalp A, Yilmaz O, Takigawa T. Quantum statistical effects on fusion dynamics of heavy ions. *Phys Rev C.* (2005) **71**:054611. doi: 10.1103/PhysRevC.71.054611
14. Caldirola P. Forze non conservative nella meccanica quantistica. *Nuovo Cimento.* (1941) **18**:393–400.
15. Kanai E. On the quantization of the dissipative systems. *Prog Theor Phys.* (1948) **3**:440–2. doi: 10.1143/ptp/3.4.440
16. Kostin MD. On the Schrodinger-Langevin equation. *J Chem Phys.* (1972) **57**:3589. doi: 10.1063/1.1678812
17. Albrecht K. A new class of Schrodinger operators for quantized friction. *Phys Lett B.* (1975) **56**:127–9. doi: 10.1016/0370-2693(75)90283-X
18. Tokieda M, Hagino K. Quantum tunneling with friction. *Phys Rev C.* (2017) **95**:054604. doi: 10.1103/PhysRevC.95.054604
19. Lindblad G. On the generators of quantum dynamical semigroups. *Commun Math Phys.* (1976) **48**:119–130.
20. Pearle P. Simple derivation of the Lindblad equation. *Euro J Phys.* (2012) **33**:805. doi: 10.1088/0143-0807/33/4/805
21. Immele JD, Kan KK, Griffin JJ. Special examples of quantized friction. *Nucl Phys.* (1975) **A241**:47–60. doi: 10.1016/0375-9474(75)90364-4
22. Bargueno P, Miret-Artes S. The generalized Schrodinger-Langevin equation. *Ann Phys.* (2014) **346**:59–65. doi: 10.1016/j.aop.2014.04.004

23. Yabana K. Low energy reactions of halo nuclei in a three-body model. *Prog Theor Phys*. (1997) **97**:437–50. doi: 10.1143/PTP.97.437
24. Bracher C. Uncertainty relations for angular momentum eigenstates in two and three spatial dimensions. *Am J Phys*. (2011) **79**:313. doi: 10.1119/1.3534840
25. Evers M, Dasgupta M, Hinde DJ, Gasques L. Systematic study of the nuclear potential diffuseness through high precision back-angle quasi-elastic scattering. *Phys Rev C*. (2008) **78**:034614. doi: 10.1103/PhysRevC.78.034614
26. Gross DHE, Kalinowski H. Friction model of heavy-ion collisions. *Phys Rep*. (1978) **45**:175–210. doi: 10.1016/0370-1573(78)90031-5
27. Hagino K, Takigawa N. Subbarrier fusion reactions and many-particle quantum tunneling. *Prog Theo Phys*. (2012) **128**:1061–106. doi: 10.1143/PTP.128.1061
28. Tokieda M, Hagino K. Quantum surface friction model for fusion reactions around the Coulomb barrier. to be published in the proceeding of the International Conference on Nucleus-Nucleus collisions (NN2018).
29. Hagino K, Rowley N, Kruppa AT. A program for coupled-channel calculations with all order couplings for heavy-ion fusion reactions. *Comp Phys Comm*. (1999) **123**:143–52. doi: 10.1016/S0010-4655(99)00243-X
30. Morton CR, Berriman AC, Dasgupta M, Hinde DJ, Newton JO, Hagino K, et al. Coupled-channels analysis of the $^{16}$O+$^{208}$Pb fusion barrier distribution. *Phys Rev C*. (1999) **60**:044608. doi: 10.1103/PhysRevC.60.044608
31. Takigawa N, Bertsch GF. Semiclassical theory of quantum tunneling in multidimensional systems. *Phys Rev C*. (1984) **29**:2358. doi: 10.1103/PhysRevC.29.2358
32. Balantekin AB, Takigawa N. Path integral approach to multidimensional quantum tunnelling. *Ann Phys*. (1985) **160**:441–76. doi: 10.1016/0003-4916(85)90152-6
33. Tokieda M, Hagino K. A new approach for open quantum systems based on a phonon number representation of a harmonic oscillator bath. *Ann Phys*. (2020) **412**: 168005. doi: 10.1016/j.aop.2019.168005
34. Adamian GG, Jolos RV, Nasirov AK, Muminov AI. Friction coefficient for deep-inelastic heavy-ion collisions. *Phys Rev C*. (1997) **56**:373. doi: 10.1103/PhysRevC.56.373
35. Ivanyuk FA, Hofmann H. Pairing and shell effects in the transport coefficients of collective motion. *Nucl Phys*. (1999) **A657**:19–58. doi: 10.1016/S0375-9474(99)00324-3


**Conflict of Interest:** The authors declare that the research was conducted in the absence of any commercial or financial relationships that could be construed as a potential conflict of interest.

frontiers in Physics

ORIGINAL RESEARCH
published: 19 February 2020
doi: 10.3389/fphy.2020.00027

# Far Off Equilibrium Dynamics in Clusters and Molecules

*Phuong Mai Dinh*[1]*, *Marc Vincendon*[1], *Jordan Heraud*[1], *Eric Suraud*[1] and *Paul-Gerhard Reinhard*[2]

[1] Laboratoire de Physique Théorique, Université de Toulouse, CNRS, UPS, Toulouse, France, [2] Institut für Theoretische Physik, Universität Erlangen, Erlangen, Germany

This brief review illustrates on a few typical applications fully fledged dynamical simulations of finite electronic systems (atoms, molecules, clusters) using time-dependent density-functional theory (TDDFT). It concentrates on aspects which are different from nuclear applications. These are: the correct handling of electron emission, the self-interaction correction, the enormous versatility of laser excitation to probe systems properties, and with it the exploitation of detailed observables of electron emission as photo-electron angular distributions and photo-electron spectra (PES). Finally, we demonstrate the impact of electronic dissipation putting question marks on the reliability of TDDFT simulations over long times.

**Keywords: time-dependent density-functional theory, molecules, electron emission, photo-electron distributions, dissipation**

OPEN ACCESS

***Edited by:***
*Denis Lacroix,*
*UMR8608 Institut de Physique Nucléaire d'Orsay (IPNO), France*

***Reviewed by:***
*Kazuhiro Yabana,*
*University of Tsukuba, Japan*
*Artur Polls,*
*University of Barcelona, Spain*

***Correspondence:**
*Phuong Mai Dinh*
*dinh@irsamc.ups-tlse.fr*

***Specialty section:***
*This article was submitted to Nuclear Physics, a section of the journal Frontiers in Physics*

***Received:*** *07 January 2020*
***Accepted:*** *30 January 2020*
***Published:*** *19 February 2020*

***Citation:***
*Mai Dinh P, Vincendon M, Heraud J, Suraud E and Reinhard P-G (2020) Far Off Equilibrium Dynamics in Clusters and Molecules. Front. Phys. 8:27. doi: 10.3389/fphy.2020.00027*

## 1. INTRODUCTION

Far-off equilibrium dynamics in quantum many-body systems is since numerous decades a challenging task much studied in experimental and theoretical investigations. In the realm of finite electronic systems, the availability of versatile laser pulses has given way to detailed analysis of the response of clusters and molecules [1–11]. In particular it allows one to explore the properties of electrons emitted after irradiation in correlation with the laser pulse. This has led to detailed analysis of angular- and energy-resolved electron spectra, e.g., their angular distributions and photoelectron spectra (PES) or both simultaneously as angular resolved PES (ARPES) recorded via Velocity Map Imaging techniques [12]. The theoretical description of such far-off equilibrium situations is also demanding. It requires large phase spaces and must cover vastly different time scales ranging from basic processes of excitation over collisional redistribution with subsequent relaxation to ionic motion and possible coupling to environment. They thus require dedicated fully time-dependent approaches, such as the widely used time-dependent density functional theory (TDDFT), often combined with molecular dynamics for the description of ionic motion (see e.g., [13]). This approach is both versatile and robust and allows one to simulate numerous dynamical scenarios with high degree of accuracy. The electronic part, TDDFT, is formally exactly the same as time-dependent Hartree-Fock (TDHF) in the nuclear domain [14]. The difference lies mainly in energy functionals which are constructed by very different strategies, see Dreizler and Gross [15] for electronic systems and Bender et al. [16] for nuclei.

In a typical laser irradiation, electrons immediately react to the external electro-magnetic field driving the system quickly far-off equilibrium long before ionic motion and thermal relaxation processes set on [17]. Thus, the system fully remains in the quantum regime for quite a while, as seen in recent experiments, exhibiting clear quantum and thermal pattern in photoelectron spectra [18–20]. The crucial first stage, i.e., the doorway to any photo-reaction, is predominantly

quantum-mechanical electron dynamics which is (as in nuclear dynamics) well-described by TDDFT and we shall focus on this domain below.

Actual implementations of TDDFT are often based on the Time-Dependent Local Density Approximation (TDLDA) [8, 21, 22] which usually performs well at moderate excitation. However, TDLDA is plagued by a self-interaction error [23] which arises because the local approximation of Coulomb exchange spoils the subtle balance with the direct Coulomb term (which was still maintained in full Hartree-Fock calculations). This is particularly disastrous for simulation of emission properties because the ionization potentials in terms of the energy of the highest occupied single-electron orbital are underestimated. The problem is cured in *ad hoc* manner by augmenting TDLDA with a self-interaction correction (SIC). As this is an aspect which is less important in the nuclear domain and thus ignored, we will address it below. Another aspect which is missing in TDLDA and which becomes important in later stages of the dynamical evolution are dynamical correlations and associated dissipative features. Extensions beyond TDLDA which take dissipation into account are presently under development. We shall address also this question on one example.

The paper is organized as follows. Section 2 provides a brief summary of the formalism, TDDFT in real time with SIC and computation of observables, particularly ionization and PES. Section 3 presents a few selected application examples starting with the impact of SIC and basic features of optical responses as the latter plays a crucial role as doorway to any dynamical scenario. We then illustrate the capabilities of short laser pulses and finally discuss the impact of dissipation.

# 2. THEORETICAL BACKGROUND

## 2.1. Electronic DFT

As in nuclear TDHF, the state of the electronic system is described in terms of single-particle (s.p.) Kohn-Sham (KS) wave functions $\varphi_n (n = 1, \ldots, N)$ from which the key ingredient in DFT, the total electronic density, is built as $\varrho(\mathbf{r}, t) = \sum_{n=1,\ldots,N} |\varphi_n(\mathbf{r}, t)|^2$. The total energy is composed as $E_{\rm tot} = E_{\rm kin} + E_{\rm H} + E_{\rm xc} + E_{\rm ion} + E_{\rm ext}$. The first three terms, namely kinetic energy, Coulomb Hartree energy, and exchange-correlation energy, constitute the purely electronic part and correspond to typical nuclear energy expressions. The last two terms, the ionic energy with its coupling to electrons and a possible external (laser) field, are specific to atoms/molecules. Hartree and exchange-correlation energies are approximated as functionals of $\varrho$: $E_{\rm H} + E_{\rm xc} \simeq E_{\rm TDLDA}[\varrho(\mathbf{r}, t)]$. This constitutes in the dynamic domain the Time-Dependent Adiabatic Local Density Approximation (TDLDA) [15, 24, 25], the electronic analog of nuclear TDHF. Variation with respect to $\varphi_n^*$ yields the KS equations:

$$\mathrm{i}\hbar\partial_t\varphi_n = \left\{-\frac{\hbar^2}{2m}\nabla^2 + v_{\rm LDA}[\varrho] + v_{\rm ion} + v_{\rm ext}\right\}\varphi_n \quad . \tag{1}$$

The LDA potential is obtained as a functional derivative with respect to the local density : $v_{\rm LDA}[\varrho](\mathbf{r}, t) = \left.\frac{\delta E_{\rm LDA}}{\delta\varrho(\mathbf{r},t)}\right|_{[\varrho]}$. The ionic background $v_{\rm ion}$ is described by pseudopotentials [26]. We use the particularly simple and efficient soft local [27] or Goedecker-type [28] pseudopotentials.

An external, coherent laser field is handled as a classical field in the long wavelength limit, adding to the mean-field Hamiltonian the potential

$$\begin{aligned} v_{\rm ext}(\mathbf{r}, t) &= e^2\,\mathbf{r}\cdot\mathbf{e}_{\rm z}\,E_0\,\cos(\hbar\omega_{\rm las}t + \phi_{\rm CEP})f(t) \quad \text{with} \\ f(t) &= \cos^2\left(\pi\frac{t}{T_{\rm pulse}}\right)\theta(t)\theta(T_{\rm pulse} - t) \quad , \end{aligned} \tag{2}$$

$\theta$ being the Heaviside function. The laser characteristics are: linear polarization (here denoted by $\mathbf{e}_{\rm z}$), peak field strength $E_0$ related to laser intensity ($I \propto E_0^2$), photon frequency $\hbar\omega_{\rm las}$, and total pulse length $T_{\rm pulse}$. The full width at half maximum of intensity (FWHM) is given as FWHM $\simeq T_{\rm pulse}/3$. The parameter $\phi_{\rm CEP}$, the so-called carrier-envelop phase, is the phase between the maximum of an oscillation at frequency $\hbar\omega_{\rm las}$ and the maximum of the $\cos^2$ envelope which plays a role particularly for short pulses [29].

## 2.2. Self-Interaction Correction

The KS equations introduce a self-interaction (SI) error because KS mean field $v_{\rm LDA}$ employs the total density which includes also the electron on which $v_{\rm LDA}$ acts. This is particularly disastrous for the long-range Coulomb term which produces thus a shifted single particle energy spectrum and, as a consequence, a wrong ionization potential (IP). To overcome the SI error, the energy-density functional is augmented by a SI correction (SIC) [30]

$$E_{\rm LDA} \longrightarrow E_{\rm LDA}[\varrho(\mathbf{r}, t)] - \sum_n E_{\rm LDA}[\varrho_n(\mathbf{r}, t)] \quad . \tag{3}$$

The price to pay is to deal with a Hamiltonian that is now non-Hermitian and state-dependent, since the variation with respect to $\varphi_n^*$ of the SI-corrected energy explicitly produces a functional of the s.p. density $\varrho_n$ instead of the total electronic density (for a broad overview of orbital-dependent functionals, see Kümmel and Kronik [31]). This difficulty is particularly severe in the time domain and requires elaborate strategies to maintain unitary time evolution [32, 33].

Still, a full solution of dynamical SIC is expensive. Fortunately, there are many situations where one can employ a drastic simplification, namely the average density SIC (ADSIC) which was proposed already in the 1930s [34], and applied since then in clusters [35]. The idea is to assume that all electrons fill about the same region of space and thus contribute about equally to the SI error. This amounts to replace Equation (3) by

$$E_{\rm LDA} \longrightarrow E_{\rm LDA}[\varrho_\uparrow + \varrho_\downarrow] - \sum_{\sigma\in\{\uparrow,\downarrow\}} N_\sigma\,E_{\rm LDA}[\varrho_\sigma/N_\sigma] \quad , \tag{4}$$

where $\varrho_\sigma$ and $N_\sigma$ are the total electronic density and the total number of particles of spin $\sigma$, respectively. This is, again, a functional of the local spin-density only and thus can be treated in the same manner as any LDA scheme. This works nicely in a wide class of compact atomic/molecular systems [36]

and particularly well for metal clusters. It is not applicable to situations with fragmented electron density and to bulk systems (the latter because the particle numbers $N_\sigma$ grow infinite).

## 2.3. Observables

The KS equations are solved in real time on a 3D grid with standard techniques [13, 17, 37]. The predominantly local structure of the KS Hamiltonian allows one to use the very efficient time-splitting scheme for time propagation [38]. The Coulomb field is computed with successive over-relaxation [39] or Fast Fourier Transform techniques [37, 40]. To describe ionization dynamics, we use absorbing boundary conditions [17], which, when properly optimized [41], gently remove outgoing electron flow at the boundaries of the numerical grid. This is a crucial ingredient which is so far not much used in nuclear dynamics. But it is essential in atoms/molecules where observables from electron emission (explained below) are very important.

The analysis of electron dynamics is performed through a set of well-established observables [10, 17, 42, 43] that we briefly recall here. As the laser field couples to the electronic dipole, dipole response is the most prominent observable in many studies [10, 13, 42, 44]. We compute the dipole moment of electrons (with respect to ionic background) from the electronic density as:

$$\mathbf{D}(t) = \int \mathrm{d}^3\mathbf{r}\, \mathbf{r}\, \varrho(\mathbf{r}, t) \quad . \tag{5}$$

Spectral properties are then obtained from the time-frequency Fourier transform $\mathbf{D}(t) \rightarrow \widetilde{\mathbf{D}}(\omega)$ after unfolding the spectrum of the exciting pulse [44]. Spectral analysis becomes particularly simple for excitation by an instantaneous dipole boost. The dipole strength becomes then $\Im\{\widetilde{\mathbf{D}}(\omega)\}$ and the dipole power spectrum $|\widetilde{\mathbf{D}}(\omega)|^2$.

For sufficiently strong excitation, electron emission becomes important. It can be analyzed at various levels of sophistication thanks to the use of absorbing boundary conditions mentioned above. Simplest is the global measure, the total ionization which can be computed from the given density as

$$N_{\mathrm{esc}}(t) = N - \int \mathrm{d}^3\mathbf{r}\, \varrho(\mathbf{r}, t) \tag{6}$$

where $N$ is the initial electron number.

More detailed observables are Photo-Electron Spectra (PES), obtained from measuring the distribution of kinetic energies of the emitted electrons, or their angular distribution. Measuring both simultaneously yields Angular-Resolved PES (ARPES) for which often valuable experimental data exist to compare with [43]. The strategy to compute PES consists in defining a set of "measuring points" $\mathbf{r}_\mathcal{M}$ near the absorbing boundaries, and to record the time evolution of s.p. wave functions $\varphi_n(\mathbf{r}_\mathcal{M}, t)$ at these points. The information thus gathered can be post-processed in two ways. Simple time integration of $|\varphi_n(\mathbf{r}_\mathcal{M}, t)|^2$ yields the amount of ionization at this measuring point. This together with properly accounting for the solid angle $\Omega_{\mathbf{r}_\mathcal{M}}$ associated with the vicinity of the measuring point direction yields the angular distribution of emitted electrons [42, 45]. The PES is obtained by Fourier transforming the s.p. wave functions at the measuring point from time to frequency $\varphi_n(\mathbf{r}_\mathcal{M}, t) \longrightarrow \widetilde{\varphi}_i(\mathbf{r}_\mathcal{M}, E_{\mathrm{kin}})$ and identifying the kinetic energy as $E_{\mathrm{kin}} = k^2/(2m) = \hbar\omega$. This delivers the PES from s.p. state $i$ for emission in direction of the measuring point $\mathbf{r}_\mathcal{M}$. The total PES is then obtained by summing up the contributions from each s.p. state

$$\mathcal{Y}_{\Omega_{\mathbf{r}_\mathcal{M}}}(E_{\mathrm{kin}}) \propto \sum_{n=1}^{N} \left|\widetilde{\varphi}_i(\mathbf{r}_\mathcal{M}, E_{\mathrm{kin}})\right|^2 \ . \tag{7}$$

This simple Fourier transform applies to weak and moderate fields. For stronger field one still needs a phase correction which is explained in detail in [46].

# 3. RESULTS

## 3.1. Impact of SIC

We illustrate the importance of SIC for TDDFT on the example of the $Na_5$ cluster irradiated by a femtosecond (fs) laser pulse with FWHM of 10 fs, intensity $I = 2.2 \times 10^{11}$ W/cm$^2$, and frequency $\omega_{\mathrm{las}} = 10.9$ eV, well above ionization threshold (ionization potential IP= 4.1 eV) and far away from dominant eigenfrequencies of the system. We use the simple ADSIC approximation (which is found to be appropriate for Na systems [35, 36]) and compare it to LDA. **Figure 1** collects the results. The top right part of the figure shows the (planar) ionic configuration. The lower right panel compares the sequence of s.p. energies for LDA and ADSIC. The latter produces a global down-shift of the s.p. levels as compared to those from LDA (by 1.2 eV for the HOMO) due to the enhanced Coulomb attraction (self-interaction neutralizes the asymptotic Coulomb field). The IP can be checked independently by comparing with the difference of energies of $Na_5$ and $Na_5^+$ (Koopman's theorem) and ADSIC matches this energy difference perfectly while LDA fails badly. As a consequence, the s.p. spectrum from ADSIC carries the correct information on the ionization threshold.

The left panels show the dynamical response of the system to the laser pulse. The left lower panel displays the time evolution of the electronic dipole moment along laser polarization ($x$ axis). There is almost no difference between LDA and ADSIC for the dipole signal. This is also found for the optical absorption strength (not shown here) which is no surprise because the optical absorption is another way to look at the dipole response. There is no urgent need to employ SIC when computing these quantities. This is plausible because the dipole signal is a global signal deduced from the density and density is, by construction, well-described in DFT.

The left upper panel shows the time evolution of the total ionization $N_{\mathrm{esc}}$ (see Equation 6). This signal reveals a dramatic difference between ADSIC and LDA. This is no surprise as ADSIC provides a larger IP than LDA (and altogether, more deeply bound levels, see bottom right panel). The reason is that, in TDDFT, ionization is mediated via the actual s.p. energies such that it is crucial to put the s.p. energies right within DFT.

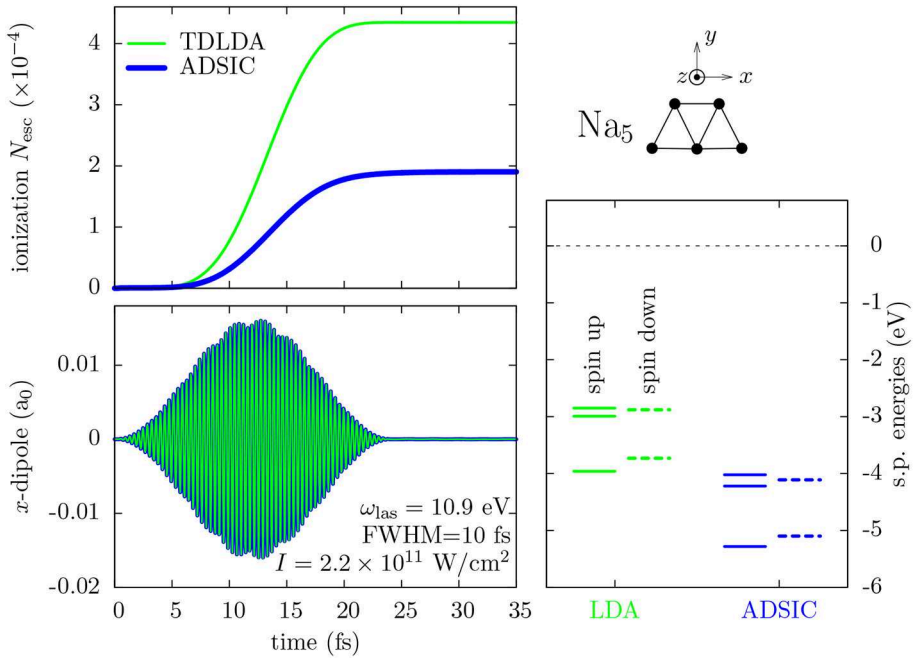


**FIGURE 1 |** Comparison of (TD)LDA and ADSIC for the $Na_5$ cluster. (Top right) Sketch of ionic configuration of $Na_5$. (Bottom right) Single particle (s.p.) energies for spins up (full lines) and down (dashes). (Left) Time evolution of total ionization $N_{esc}$ (top) and of the electronic dipole in the $x$ direction (bottom) after irradiation by a laser pulse polarized along $x$ with $\omega_{las} = 10.9$ eV, $T_{pulse} = 24$ fs, and $I = 2.2 \times 10^{11}$ W/cm$^2$.

## 3.2. Optical Response

Optical response is the most prominent observable for dynamical properties of a system. Its role in nuclear physics and in molecular or cluster physics is similarly important. The conceptually simplest way is to compute it by spectral analysis of a time-dependent simulation (see section 2.3). Traditionally, it has mostly been computed by linearized TDDFT which complicates coding, but simplifies calculations, particularly if a system has certain symmetries (see e.g., [47–49]). The pathway through spectral analysis is competitive in fully 3D calculations and it is more flexible as it also allows one to explore the transition to the non-linear regime [50]. We use that here.

**Figure 2** shows optical absorption strengths for a nucleus, $^{208}$Pb, and three different electronic systems of different bond types, a metal cluster $Na_{40}$, a covalent molecule $H_2O$, and the noble gas Ar atom. The three electronic systems have significantly different spectra. For Ar and $H_2O$, the strength is heavily fragmented over many dipole states, most of them having predominantly the structure of one-particle-one-hole excitations. Quite different is the metallic $Na_{40}$, with one dominating and almost exhaustive peak, the highly collective Mie plasmon [54, 55]. The nuclear spectrum looks very similar to the cluster case. It is dominated by the a strong collective mode, the giant dipole resonance [56]. The similarity is not surprising as both, the metallic electron cloud and the nucleons, have the same bulk limit, namely a Fermi liquid [57].

The nuclear dipole resonance and the cluster's plasmon resonance both have some width. However, the mechanisms producing these widths is different. The nuclear dipole resonance lies in the nucleon continuum and a large part of the width stems from limited lifetime due to nucleon emission. The remaining part is due to dissipative processes from nucleon-nucleon collisions. Both processes also play some role in metal clusters. But here the dominant broadening mechanism is given by thermal fluctuations of the underlying ionic configuration [58, 59].

## 3.3. Laser Excitation

Laser pulses offer a unique and extremely versatile tool for dedicated probing and switching of electronic systems. Coherent pulses in keV and MeV regime, as required for nuclear experiments, appear at the horizon [60–62], but deliver not yet sufficient field strengths to attain the most interesting multi-photon regime. This day will come and thus it is worth having a look at electronic applications and see what experiments with coherent pulses can reveal.

A great deal of information is gained when combining laser excitations with detailed analysis of the emitted electrons. The top panels of **Figure 3** show as an example ARPES produced from the Ar atom (left) and the $Na_9^+$ cluster (right) after irradiation by a few-cycle laser pulse. Cuts along a fixed angle represent the PES and cuts along a fixed kinetic energy the angular distribution. The PES decrease with increasing $E_{kin}$ because more photons have to cooperate to supply the higher emitted energy. And yet, one finds a plateau around 20 eV which is typical for above-threshold ionization spectra [63, 64]. The two different systems deliver different patterns, demonstrating that system properties

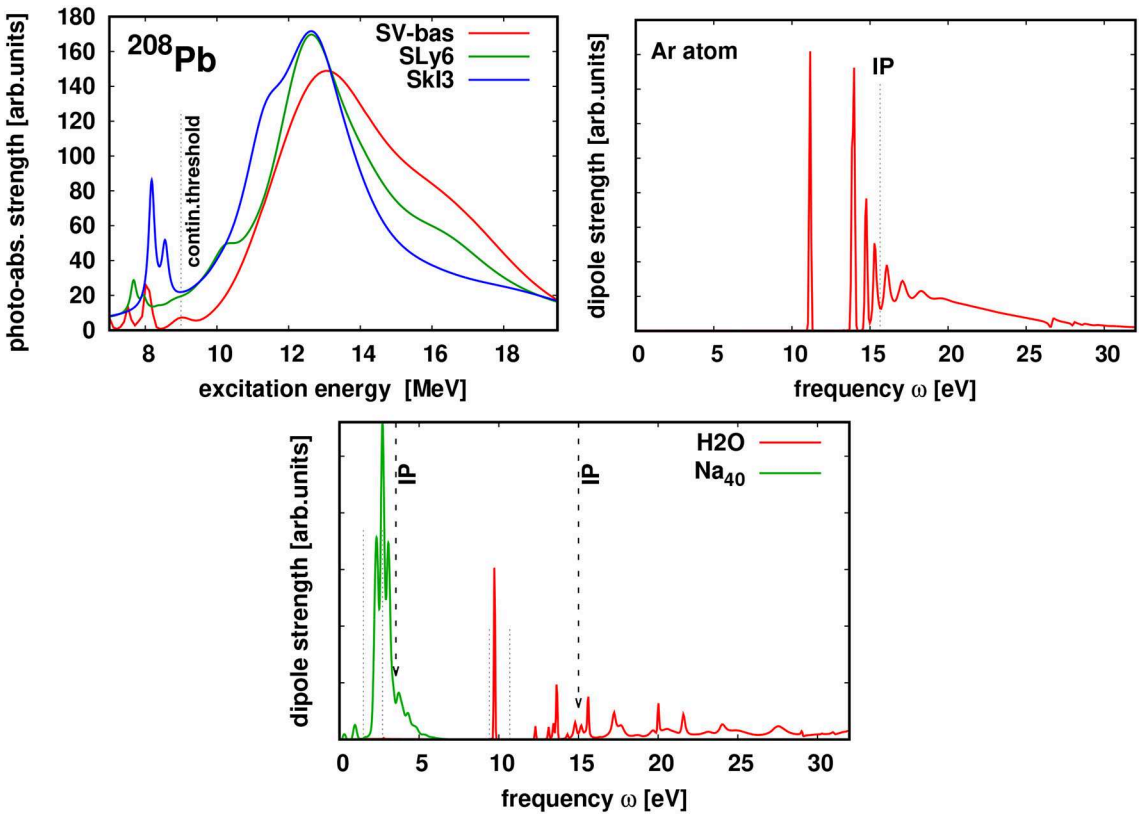


**FIGURE 2 |** Optical absorption spectra for three electronic systems as indicated and the nucleus $^{208}$Pb. The electronic systems are computed with TDLDA + ADSIC as explained in section 2. The nucleus is computed with nuclear TDHF using the code of [37] (for details see Reinhard et al. [50]) and three different Skyrme parameterizations as indicated, SkI3 from [51], SLy6 from [52], and SV-bas from [53]. The vertical dashed lines indicate the particle continuum thresholds in each system, the electronic ionization potential (IP) and the neutron threshold in the nuclear case.

form the signal which, in turn, can be used to analyze a system by ARPES studies.

One of the interesting features in ARPES from very short pulses is the asymmetry of the angular distributions which appears in various energy bins for both systems. Indeed, in such laser pulses, the carrier-envelop phase $\phi_{\rm CEP}$, see Equation (2), becomes a decisive laser parameter because the CEP controls the net momentum exerted on the electron cloud and so impacts the pattern of the pulse dramatically which, in turn, can have a strong impact on laser-induced electron dynamics. For example, photo-electron emission induced by few-cycle laser fields can be controlled by the CEP, leading to a pronounced forward-backward (also called "right-left") asymmetry in the PES. We can quantify this asymmetry by a simple number as

$$\eta(E_{\rm kin}) = \frac{\int_0^{\Theta} d\theta\, \mathcal{Y}(E_{\rm kin},\theta) - \int_{180^\circ-\Theta}^{180^\circ} d\theta\, \mathcal{Y}(E_{\rm kin},\theta)}{\int_0^{\Theta} d\theta\, \mathcal{Y}(E_{\rm kin},\theta) + \int_{180^\circ-\Theta}^{180^\circ} d\theta\, \mathcal{Y}(E_{\rm kin},\theta)} \qquad (8)$$

where $\mathcal{Y}(E_{\rm kin},\theta)$ is the ARPES strength at given kinetic energy and emission angle. For the opening angle in the integration, we take $\Theta = 15^\circ$ in accordance with many experiments in that field (see e.g., [65]). A value of $\eta = +1$ indicates prevailing forward emission and $\eta = -1$ backward dominance. Condensing the angular distribution into one compact number $\eta$ allows one to visualize trends with laser parameter. The lower panel of **Figure 3** shows an energy-integrated asymmetry $\eta$ as a function of $\phi_{\rm CEP}$. The effects are impressive. Tuning $\phi_{\rm CEP}$ allows one to switch emission from forward to backward and vice versa. And we also see a significant system dependence of the trend. The marked difference between both systems can be explained by the difference in their optical response displayed in **Figure 2**. The 1.8 eV laser frequency lies far below any considerable dipole strength for Ar while it comes close to the strong Mie plasmon resonance for the Na cluster. For a detailed discussion with more material see Reinhard et al. [29].

## 3.4. Impact of Dissipation

So far, we have demonstrated the use of TDDFT in electronic systems on a few selected examples. TDDFT has shown to be a robust and versatile tool for simulating dynamical processes. However, the more energy comes into a system, the more likely come dynamical correlations beyond TDDFT into play. This is also well-known in nuclear physics and a variety of methods has been developed to deal with those correlations. They employ all semi-classical concepts and most of them

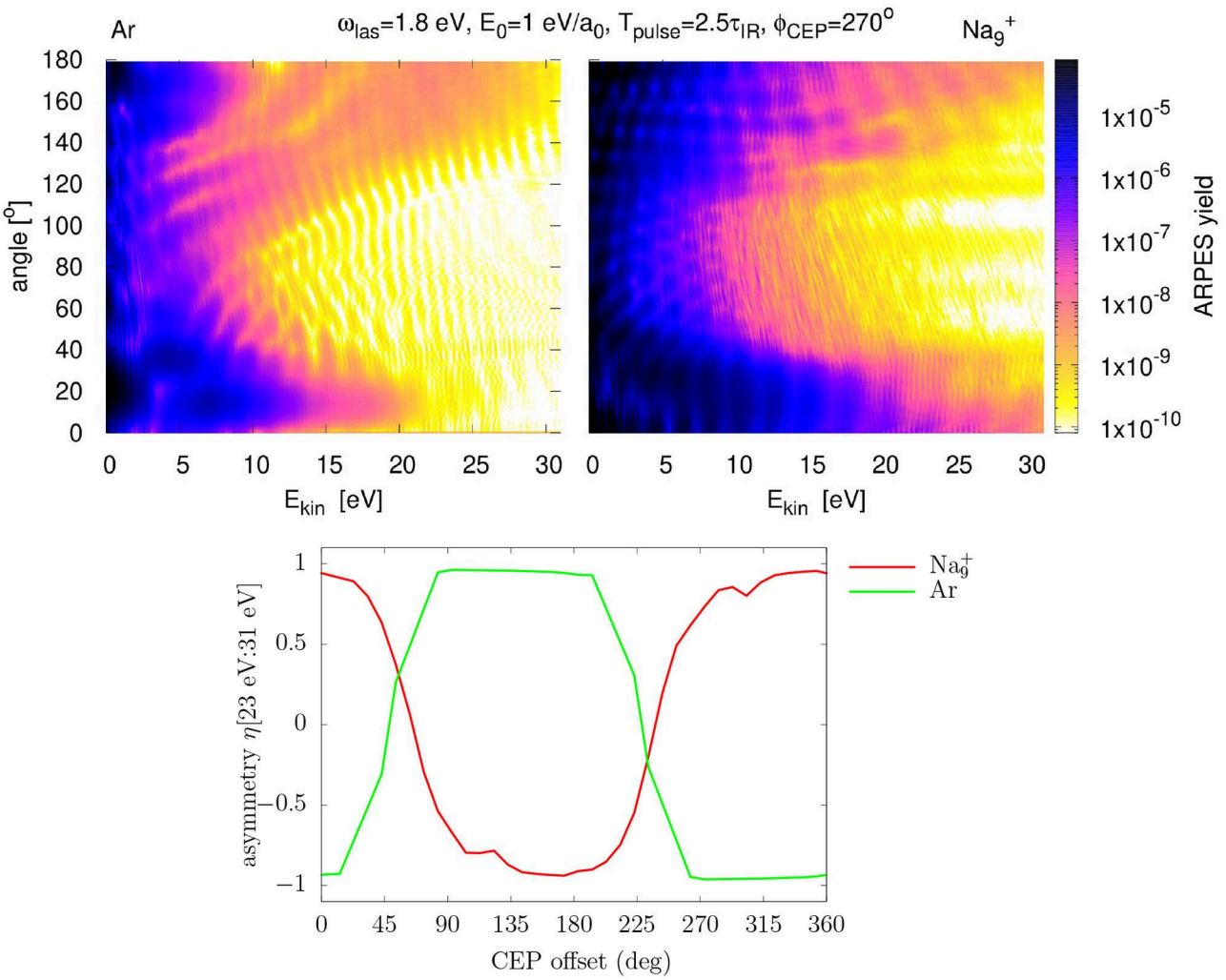


**FIGURE 3 |** Ar atom and $Na_9^+$ cluster excited by a laser with $\omega_{las} = 1.8$ eV, $I = 6 \times 10^{13}$ W/cm$^2$, pulse length $T_{pulse} = 6$ fs (corresponding to 2.5 optical cycles), and $\phi_{CEP} = 270°$. Upper panels: ARPES yield $\mathcal{Y}$ in the plane of kinetic energy $E_{kin}$ and emission angle $\theta$, for Ar (left) and $Na_9^+$ (right). Lower panel: asymmetry parameter $\eta(E_{kin})$ integrated on the $E_{kin}$ interval [23eV : 31eV].

are based on the Vlasov-Ühling-Uhlenbeck collision term [66] (for reviews see [67, 68]). This has also been applied to clusters [10, 69, 70]. But laser excitation processes sail often for a long initial time span through the quantum regime. There is thus a need for a quantum description of dynamical correlations from electron-electron collisions and associated dissipation. Just recently, there were promising moves to develop such approaches, one along the line of stochastic jumps (comparable to the collisions in semi-classical methods) [71–73] and another one with the more empirical relaxation-time approximation (RTA) [74, 75]. Both approaches are based on two-body collisions implying the in-medium electron-electron interaction and take care of the available phase space of final states. RTA, for which we will show an example here, maps cross-section and phase space into a collision rate with which the system relaxes toward local-instantaneous equilibrium, the latter being evaluated at each relaxation step by density- and current-constrained minimization of the free energy. By construction, RTA maintains the continuity equation and energy conservation.

**Figure 4** exemplifies the consequences of the dissipation thus introduced with an application of RTA to resonant laser excitation of a $Na_{40}$ cluster. The lower left panel shows the effect on the dipole signal. The additional damping introduced by RTA is clearly visible. It is interesting to note that the TDLDA signal is also damped, although at lower rate. This damping stems from electron emission which is the dominant cooling mechanism in TDLDA. This is corroborated by the time evolution of ionization shown in the lower right panel. The trends agree up to about 100 fs, the same span where the dipole signals agree. But then the RTA curve levels off whereas TDLDA continues to emit. That happens because RTA has meanwhile converted much of the initial excitation energy into internal heat and so distracted it from moving into direct electron emission.

A comparison of energy balances is detailed in the upper panel of **Figure 4**. It shows the contributions from intrinsic

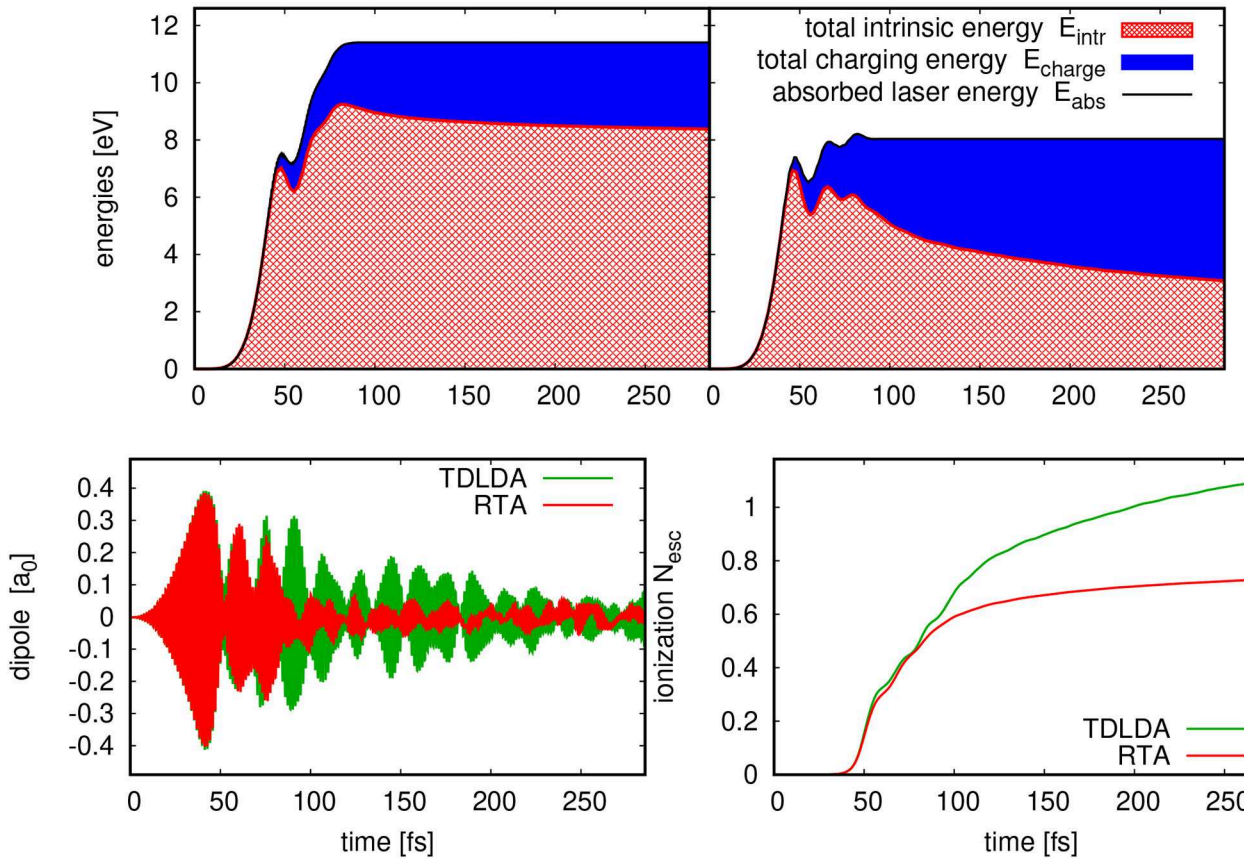


**FIGURE 4 |** Time evolution of ionization (lower right), dipole moment (lower left), and the various contribution to the energy (upper panels) for the case of $Na_{40}$ excited by a laser with frequency $\omega = 2.7$ eV, total pulse length $T_{pulse} = 100$ fs, and intensity $I = 1.3 \times 10^{10}$ W/cm$^2$. Left upper panels show results from RTA and right upper panels from TDLDA.

energy and energy invested in electron emission for TDLDA and RTA (for details of the definition see [75]). It confirms what we have inferred from the ionization trends in the lower right panel. Most interesting is the large difference in the total energy absorbed from the laser pulse (black line). In pure TDLDA, the entrance channel for energy absorption, the dipole channel, has limited capacity as one can see from the onset of oscillations in the absorption signal. Dissipation in RTA clears the entrance channel and thus allows more energy to come in. Altogether, we see that dissipation can make a difference. Note, however, that this example deals with a considerable excitation energy and that deviations from TDLDA develop only slowly. In turn, we can conclude that TDDFT provides a pertinent description of dynamical processes in its early stages. The time scale of validity of TDDFT depends on excitation energy: the lower the excitation is, the longer TDDFT holds.

## 4. CONCLUSIONS

We have presented a couple of typical applications of time-dependent density functional theory (TDDFT) to electronic dynamics in clusters and molecules, as triggered by laser pulses. Basis of our description is TDDFT propagated in real time which delivers a versatile and robust tool for a great variety of dynamical situations. At the numerical side it is important to implement absorbing boundary conditions which then allow a detailed description of electron emission. We have addressed in detail two known defects of TDDFT in the local density approximation, namely the self-interaction error and the lack of dynamical correlations. The first problem is less important in nuclear physics, but highly relevant in electronic systems. It is solved by a self-interaction correction (SIC) which still can be formulated within a mean field theory (thus affordable) and which is particularly crucial if electron emission plays a role. The second problem, also important in nuclear dynamics, requires extensions beyond TDDFT for which manageable quantum mechanical approximations are presently being developed.

We have considered typical examples of applications in clusters and molecules excited by a laser pulses of different strengths. In all cases, the early response of the systems addresses predominantly the electrons and remains fully in the quantum mechanical regime (as properly described by TDDFT). In

particular, we have focused on an analyzing tool which is not yet available in nuclear dynamics, namely widely tunable laser excitation in combination with detailed resolution of the distributions of the emitted electrons with respect to angles and kinetic energies. We have demonstrated that such a setup delivers valuable information on the system and its dynamical response.

Finally, the inclusion of dissipative features is a key step to address the long-time evolution of dynamics far off-equilibrium in which one observes, in addition to ionization, a thermalization of the electron cloud. Formerly, the problem was attacked with semi-classical approaches much similar as done in nuclear dynamics, particularly in heavy-ion collisions. This approach is less justified in connection with laser excitations for which the (electronic) system stays much longer in the quantum regime. Promising and manageable solutions to deal with dissipation in the quantum regime are just presently coming up. First results from treating dynamical correlations in the relaxation-time approximation (RTA) show that dissipation has a crucial impact on the energy balance in the system (internal energy vs. electron emission) and on the energy intake from the laser pulse. Proper treatment of dynamical correlations is still in its infancy and will attract much future development.

## DATA AVAILABILITY STATEMENT

All datasets generated for this study are included in the article/supplementary material.

## AUTHOR CONTRIBUTIONS

All authors listed have made a substantial, direct and intellectual contribution to the work, and approved it for publication.

## ACKNOWLEDGMENTS

We thank Institut Universitaire de France for support during the realization of this work. This work was also granted access to the HPC resources of CalMiP (Calcul en Midi-Pyrénées) under the allocation P1238, and of RRZE (Regionales Rechenzentrum Erlangen).

## REFERENCES

1. Caillat J, Zanghellini J, Kitzler M, Koch O, Kreuzer W, Scrinzi A. Correlated multielectron systems in strong laser fields: a multiconfiguration time-dependent Hartree-Fock approach. *Phys Rev A.* (2005) **71**:012712. doi: 10.1103/PhysRevA.71.012712
2. Ehrmaier J, Picconi D, Karsili TNV, Domcke W. Photodissociation dynamics of the pyridinyl radical: time-dependent quantum wave-packet calculations. *J Chem Phys.* (2017) **146**:124304. doi: 10.1063/1.4978283
3. Greenman L, Ho PJ, Pabst S, Kamarchik E, Mazziotti DA, Santra R. Implementation of the time-dependent configuration-interaction singles method for atomic strong-field processes. *Phys Rev A.* (2010) **82**:023406. doi: 10.1103/PhysRevA.82.023406
4. Hochstuhl D, Hinz C, Bonitz M. Time-dependent multiconfiguration methods for the numerical simulation of photoionization processes of many-electron atoms. *Eur Phys J Spec Top.* (2014) **223**:177–336. doi: 10.1140/epjst/e2014-02092-3
5. Lappas DG, van Leeuwen R. Electron correlation effects in the double ionization of He. *J Phy B.* (1998) **31**:L249. doi: 10.1088/0953-4075/31/6/001
6. Rohringer N, Peter S, Burgdörfer J. Calculating state-to-state transition probabilities within time-dependent density-functional theory. *Phys Rev A.* (2006) **74**:042512. doi: 10.1103/PhysRevA.74.042512
7. Sato T, Ishikawa KL, Brezinova I, Lackner F, Nagele S, Burgdoerfer J. Time-dependent complete-active-space self-consistent-field method for atoms: application to high-order harmonic generation. *Phys Rev A.* (2016) **94**:023405. doi: 10.1103/PhysRevA.94.023405
8. Haken H, Wolf HC. *Time-Dependent Density-Functional Theory: Concepts and Applications*. Oxford: Oxford University Press (2012).
9. Wilken F, Bauer D. Momentum distributions in time-dependent density-functional theory: product-phase approximation for nonsequential double ionization in strong laser fields. *Phys Rev A.* (2007) **76**:023409. doi: 10.1103/PhysRevA.76.023409
10. Fennel T, Meiwes-Broer KH, Tiggesbäumker J, Dinh PM, Reinhard PG, Suraud E. Electro-magnetic signals for analyzing non-linear cluster dynamics. *Rev Mod Phys.* (2010) **82**:1793. doi: 10.1103/RevModPhys.82.1793
11. Gao CZ, Dinh PM, Reinhard PG, Suraud E. Towards the analysis of attosecond dynamics in complex systems. *Phys Chem Chem Phys.* (2017) **19**:19784–93. doi: 10.1039/C7CP00995J
12. Pinaré JC, Baguenard B, Bordas C, Broyer M. Angular distributions in photoelectron spectroscopy of small tungste n clusters: competition between direct and thermionic emission. *Eur Phys J D.* (1999) **9**:21–4. doi: 10.1007/s100530050392
13. Reinhard PG, Suraud E. *Introduction to Cluster Dynamics*. New York, NY: Wiley (2004).
14. Reinhard PG, Suraud E. Comparison of resonance dynamics in metal clusters and nuclei. In: Ekardt W, editor. *Resonance Dynamics in Metal Clusters and Nuclei*. New York, NY: Wiley (1999). p. 211.
15. Dreizler RM, Gross EKU. *Density Functional Theory: An Approach to the Quantum Many-Body Problem*. Berlin: Springer-Verlag (1990).
16. Bender M, Heenen PH, Reinhard PG. Self-consistent mean-field models for nuclear structure. *Rev Mod Phys.* (2003) **75**:121–80. doi: 10.1103/RevModPhys.75.121
17. Calvayrac F, Reinhard PG, Suraud E, Ullrich CA. Nonlinear electron dynamics in metal clusters. *Phys Rep.* (2000) **337**:493–578. doi: 10.1016/S0370-1573(00)00043-0
18. Kjellberg M, Johansson O, Jonsson F, Bulgakov AV, Bordas C, Campbell EEB, et al. Momentum-map-imaging photoelectron spectroscopy of fullerenes with femtosecond laser pulses. *Phys Rev A.* (2010) **81**:023202. doi: 10.1103/PhysRevA.81.023202
19. Hansen K. *Statistical Physics of Nanoparticles in the Gas Phase*. Amsterdam: Springer (2013).
20. Hansen K, Richter R, Alagia M, Stranges S, Schio L, Salen P, et al. Single Photon Thermal Ionization of $C_{60}$. *Phys Rev Lett.* (2017) **118**:103001. doi: 10.1103/PhysRevLett.118.103001
21. Marques MAL, Ullrich CA, Nogueira F, Rubio A, Burke K, Gross EKU. *Time Dependent Density Functional Theory*. Berlin: Springer (2006).
22. Marques MAL, Maitra NT, Nogueira FMS, Gross EKU, Rubio A. *Fundamentals of Time-Dependent Density Functional Theory. Vol. 837 of Lecture Notes in Physics*. Berlin: Springer-Verlag (2012).
23. Yelin S, Arimondo E, Lin CC. *Advances in Atomic, Molecular, and Optical Physics*. Vol. 64. Amsterdam: Elsevier (2015).
24. Gross EKU, Kohn W. Time-dependent density-functional theory. *Adv Quant Chem.* (1990) **21**:255–91. doi: 10.1016/S0065-3276(08)60600-0
25. Gross EKU, Dobson JF, Petersilka M. Density functional of time-dependent phenomena. *Top Curr Chem.* (1996) **181**:81–172. doi: 10.1007/BFb0016643
26. Szasz L. *Pseudopotential Theory of Atoms and Molecules*. New York, NY: Wiley (1985).
27. Kümmel S, Brack M, Reinhard PG. Ionic geometries and electronic excitations of $Na_9^+$ and $Na_{55}^+$. *Eur Phys J D.* (1999) **9**:149–52. doi: 10.1007/s100530050416
28. Goedecker S, Teter M, Hutter J. Separable dual-space Gaussian pseudopotentials. *Phys Rev B.* (1996) **54**:1703. doi: 10.1103/PhysRevB.54.1703
29. Reinhard PG, Suraud E, Meier C. The impact of the carrier envelope phase—dependence on system and laser parameters. *J Phys B.* (2018) **51**:024007. doi: 10.1088/1361-6455/aa9a9c

30. Perdew JP, Zunger A. Self-interaction correction to density-functional approximations for many-electron systems. *Phys Rev B.* (1981) **23**:5048. doi: 10.1103/PhysRevB.23.5048
31. Kümmel S, Kronik L. Orbital-dependent density functionals: theory and applications. *Rev Mod Phys.* (2008) **80**:3–60. doi: 10.1103/RevModPhys.80.3
32. Messud J, Dinh PM, Reinhard PG, Suraud E. Time-dependent density-functional theory with self-interaction correction. *Phys Rev Lett.* (2008) **101**:096404. doi: 10.1103/PhysRevLett.101.096404
33. Messud J, Dinh PM, Reinhard PG, Suraud E. On the exact treatment of time dependent self-interaction correction. *Ann Phys.* (2008) **324**:955–76. doi: 10.1016/j.aop.2008.12.001
34. Fermi E, Amaldi E. Le Orbite Oos Degli Elementi. *Accad Ital Rome.* (1934) **6**:117–49.
35. Legrand C, Suraud E, Reinhard PG. Comparison of self-interaction-corrections for metal clusters. *J Phys B.* (2002) **35**:1115. doi: 10.1088/0953-4075/35/4/333
36. Klüpfel P, Dinh PM, Reinhard PG, Suraud E. Koopmans' condition in self-interaction corrected density functional theory. *Phys Rev A.* (2013) **88**:052501. doi: 10.1103/PhysRevA.88.052501
37. Maruhn JA, Reinhard PG, Stevenson PD, Umar AS. The TDHF code Sky3D. *Comp Phys Comm.* (2014) **185**:2195–216. doi: 10.1016/j.cpc.2014.04.008
38. Feit MD, Fleck JA, Steiger A. *J Comp Phys.* (1982) **47**:412–33. doi: 10.1016/0021-9991(82)90091-2
39. Davies KTR, Koonin SE. Skyrme-force time-dependent Hartree–Fock calculations with axial symmetry. *Phys Rev C.* (1981) **23**:2042–61. doi: 10.1103/PhysRevC.23.2042
40. Lauritsch G, Reinhard PG. An FFT Solver for the Coulomb problem. *Int J Mod Phys C.* (1994) **5**:65–75. doi: 10.1142/S0129183194000064
41. Reinhard PG, Stevenson PD, Almehed D, Maruhn JA, Strayer MR. Role of boundary conditions in dynamic studies of nuclear giant resonances. *Phys Rev E.* (2006) **73**:036709. doi: 10.1103/PhysRevE.73.036709
42. Reinhard PG, Suraud E. Cluster dynamics in strong laser fields. In: Marques MAL, Ullrich CA, Nogueira F, editors. *Time-Dependent Density Functional Theory. Vol. 706 of Lecture Notes in Physics*. Berlin: Springer (2006). p. 391.
43. Wopperer P, Dinh PM, Reinhard PG, Suraud E. Electrons as probes of dynamics in molecules and clusters: a contribution from time dependent density functional theory. *Phys Rep.* (2015) **562**:1. doi: 10.1016/j.physrep.2014.07.003
44. Calvayrac F, Reinhard PG, Suraud E. Spectral signals from electronic dynamics in sodium clusters. *Ann Phys.* (1997) **255**:125–62. doi: 10.1006/aphy.1996.5654
45. Pohl A, Reinhard PG, Suraud E. Angular distribution of electrons emitted from Na clusters. *Phys Rev A.* (2004) **70**:023202. doi: 10.1103/PhysRevA.70.023202
46. Dinh PM, Romaniello P, Reinhard PG, Suraud E. Calculation of photoelectron spectra: a mean-field-based scheme. *Phys Rev A.* (2013) **87**:032514. doi: 10.1103/PhysRevA.87.032514
47. Reinhard PG, Gambhir Y. RPA in wavefunction representation. *Ann Phys.* (1992) **504**:598–631. doi: 10.1002/andp.19925040804
48. Reinhard PG. From sum rules to RPA: 1. Nuclei. *Ann Phys.* (1992) **504**:632–61. doi: 10.1002/andp.19925040805
49. Reinhard PG, Genzken O, Brack M. From sum rules to RPA: 3. Metal clusters. *Ann Phys.* (1996) **508**:576–607. doi: 10.1002/andp.2065080704
50. Reinhard PG, Guo L, Maruhn JA. Nuclear giant resonances and linear response. *Eur Phys J A.* (2007) **32**:19–23. doi: 10.1140/epja/i2007-10366-9
51. Reinhard PG, Flocard H. Nuclear effective forces and isotope shifts. *Nucl Phys A.* (1995) **584**:467–88. doi: 10.1016/0375-9474(94)00770-N
52. Chabanat E, Bonche P, Haensel P, Meyer J, Schaeffer R. A Syrme parametrization from subnuclear to neutron star densities. *Nucl Phys A.* (1997) **627**:710–46. doi: 10.1016/S0375-9474(97)00596-4
53. Klüpfel P, Reinhard PG, Bürvenich TJ, Maruhn JA. Variations on a theme by Skyrme. *Phys Rev C.* (2009) **79**:034310.
54. Mie G. Beiträge zur Optik trüber Medien, speziell kolloidaler Metallösungen. *Ann Phys.* (1908) **25**:377–445. doi: 10.1002/andp.19083300302
55. Kreibig U, Vollmer M. *Optical Properties of Metal Clusters*. Vol. 25. New York, NY; Heidelberg; Berlin: Springer Series in Materials Science (1993).
56. Ring P, Schuck P. *The Nuclear Many-Body Problem*. New York, NY: Heidelberg; Berlin: Springer-Verlag (1980).
57. Pines D, Nozières P. *The Theory of Quantum Liquids*. New York, NY: W. A. Benjamin (1966).
58. Montag B, Reinhard PG. Width of the plasmon resonance in metal clusters. *Phys Rev B.* (1995) **51**:14686. doi: 10.1103/PhysRevB.51.14686
59. Moseler M, Landman U, Yannouleas C. Controllable electrostatic surface guide for cold molecules with a single charged wire. *Phys Rev A.* (2001) **87**:053401. doi: 10.1103/PhysRevLett.87.053401
60. Esirkepov TZ, Bulanov SV, Zhidkov AG, Pirozkov AS, Kando M. High-power laser-driven source of ultra-short X-ray and gamma-ray pulses. *Eur Phys J D.* (2009) **55**:457–63. doi: 10.1140/epjd/e2009-00172-y
61. Kiefer D, Yeung M, Dzelzainis T, Foster PS, Rykovanov SG, Lewis CL, et al. Relativistic electron mirrors from nanoscale foils for coherent frequency upshift to the extreme ultraviolet. *Nat Commun.* (2013) **4**:1763. doi: 10.1038/ncomms2775
62. Li FY, Sheng ZM, Chen M, Wu HC, Liu Y, Meyer-ter Vehn J, et al. Coherent kilo-electron-volt backscattering from plasma-wave boosted relativistic electron mirrors. *Appl Phys Lett.* (2014) **105**:161102. doi: 10.1063/1.4899136
63. Paulus GG, Nicklich W, Xu H, Lambropoulos P, Walther H. Plateau in above threshold ionization spectra. *Phys Rev Lett.* (1994) **72**:2851–54. doi: 10.1103/PhysRevLett.72.2851
64. Wopperer P, Gao CZ, Barillot T, Cauchy C, Marciniak A, Despré V, et al. Progress towards a realistic theoretical description of $C_{60}$ photoelectron-momentum imaging experiments using time-dependent density-functional theory. *Phys Rev A.* (2015) **91**:042514. doi: 10.1103/PhysRevA.91.042514
65. Li H, Mignolet B, Wachter G, Skruszewicz S, Zherebtsov S, Süßmann F, et al. Coherent electronic wave packet motion in $C_{60}$ controlled by the waveform and polarization of few-cycle laser fields. *Phys Rev Lett.* (2015) **114**:123004. doi: 10.1103/PhysRevLett.114.123004
66. Uehling EA, Uhlenbeck GE. Theory of superconductivity. *Phys Rev.* (1932) **108**:1175. doi: 10.1103/PhysRev.108.1175
67. Bertsch GF, Das Gupta S. A guide to microscopic models for intermediate energy heavy ion collisions. *Phys Rep.* (1988) **160**:190. doi: 10.1016/0370-1573(88)90170-6
68. Abe Y, Ayik S, Reinhard PG, Suraud E. On stochastic approaches of nuclear dynamics. *Phys Rep.* (1996) **275**:49–196. doi: 10.1016/0370-1573(96)00003-8
69. Fennel T, Bertsch GF, Meiwes-Broer KH. Ionization dynamics of simple metal clusters in intense fields by the Thomas-Fermi-Vlasov method. *Eur Phys J D.* (2004) **29**:367–78. doi: 10.1140/epjd/e2004-00035-1
70. Domps A, Reinhard PG, Suraud E. Semi-classical electron dynamics in metal clusters beyond mean-field. *Ann Phys.* (2000) **280**:211–35. doi: 10.1006/aphy.1999.5990
71. Lacroix D. Stochastic mean-field dynamics for fermions in the weak coupling limit. *Phys Rev C.* (2006) **73**:044311. doi: 10.1103/PhysRevC.73.044311
72. Suraud E, Reinhard PG. Non equilibrium quantum dynamics with collisional correlations. *New J Phys.* (2014) **16**:063066. doi: 10.1088/1367-2630/16/6/063066
73. Slama N, Reinhard PG, Suraud E. On the inclusion of collisional correlations in quantum dynamics. *Ann Phys.* (2015) **355**:182–203. doi: 10.1016/j.aop.2015.02.008
74. Reinhard PG, Suraud E. A quantum relaxation-time approximation for finite fermion systems. *Ann Phys.* (2015) **354**:183–202. doi: 10.1016/j.aop.2014.12.011
75. Vincendon M, Suraud E, Reinhard PG. Dissipation and energy balance in electronic dynamics of Na clusters. *Eur Phys J D.* (2017) **71**:179. doi: 10.1140/epjd/e2017-80067-0


**Conflict of Interest:** The authors declare that the research was conducted in the absence of any commercial or financial relationships that could be construed as a potential conflict of interest.

frontiers in Physics

ORIGINAL RESEARCH
published: 26 February 2020
doi: 10.3389/fphy.2020.00038

# Predictions of New Neutron-Rich Isotopes at $N = 126$ in the Multinucleon Transfer Reaction $^{136}Xe + ^{194}Ir$

*Xiang Jiang and Nan Wang**

*Department of Physics, College of Physics and Optoelectronic Engineering, Shenzhen University, Shenzhen, China*

Aiming to produce new neutron-rich nuclei at $N = 126$, the multi-nucleon transfer reactions $^{136}$Xe+$^{194}$Ir, $^{208}$Pb are investigated by using the GRAZING model and the three-dimensional time-dependent Hartree-Fock (TDHF) approach. Deexcitation processes of the primary fragments are taken into account in both models. Comparison with the experimental data of $^{136}$Xe+$^{208}$Pb at $E_{c.m.} = 450$ MeV indicates that the isotopic production cross sections around the entrance channel can be well reproduced by both models. The results of GRAZING indicate that $^{136}$Xe+$^{194}$Ir is a promising candidate for producing new neutron-rich isotones with $N = 126$. The limitation of using TDHF to investigate multi-nucleon transfer reactions is also discussed.

**Keywords: multi-nucleon transfer reactions, neutron-rich nuclei, GRAZING, TDHF, particle number projection**

OPEN ACCESS

***Edited by:***
*Lu Guo,*
*University of Chinese Academy of Sciences, China*

***Reviewed by:***
*Andrea Celentano,*
*National Institute of Nuclear Physics, Ministry of Education, Universities and Research, Italy*
*Rosario Gianluca Pizzone,*
*Laboratori Nazionali del Sud (INFN), Italy*

****Correspondence:***
*Nan Wang*
*wangnan@szu.edu.cn*

***Specialty section:***
*This article was submitted to Nuclear Physics, a section of the journal Frontiers in Physics*

***Received:*** *30 November 2019*
***Accepted:*** *06 February 2020*
***Published:*** *26 February 2020*

***Citation:***
*Jiang X and Wang N (2020) Predictions of New Neutron-Rich Isotopes at N = 126 in the Multinucleon Transfer Reaction $^{136}Xe + ^{194}Ir$. Front. Phys. 8:38. doi: 10.3389/fphy.2020.00038*

## 1. INTRODUCTION

Neutron-rich nuclei are of great importance for understanding the astrophysical r-process [1]. For instance, those around the closed neutron shell $N = 126$ can provide information on the solar r-abundance distribution [2]. The neutron-rich radioactive isotopes can also be used as projectiles for synthesizing super-heavy nuclei which is one of the most interesting challenges in nuclear physics. However, new heavy neutron-rich nuclei out of limits of the present nuclear chart are hardly to be produced via traditional ways, such as fusion reactions with stable beams at low energies or fragmentation of heavy projectile at relativistic energies.

In recent years, theoretical predictions indicate that multi-nucleon transfer (MNT) reactions would be a possible route to produce heavy neutron-rich nuclei far away from the stability line [3, 4]. The experimental results of $^{136}$Xe + $^{198}$Pt at the incident energy of 8 MeV/nucleon [2] show that the production cross sections of neutron-rich nuclei with $N = 126$ are orders of magnitude larger than those obtained in fragmentation reaction of $^{208}$Pb (1 AGeV) + Be [5]. But in some other experiments of MNT reactions with stable beams such as $^{64}$Ni + $^{207}$Pb [6] and $^{136}$Xe + $^{208}$Pb [7, 8], no new neutron-rich nuclei is detected. Based on the $N/Z$ equilibrium concept, theoretical predictions show that using neutron-rich radioactive beams can remarkably improve the production cross sections of neutron-rich isotopes along $N = 126$ [9, 10]. However, due to the fact that the experimental intensities of radioactive beams are orders of magnitude lower than stable beams, the advantage of using radioactive beams may be canceled. Opportunities will arise in the near future on the second generation radioactive beam facilities like the European EURISOL [11]. At the present time, to find an optimum stable projectile-target combination are highly appealed.

To describe MNT reactions, many theoretical models are developed. For example, the multidimensional Langevin model shows great success on predicting the isotopic production

cross sections, even for those nuclei far away from projectile and target [3, 4, 12]. Semi-classical GRAZING model [13, 14] and the complex Wentzel-Kramers-Brillouin (CWKB) model [15] can well describe transfer process in peripheral collisions. In GRAZING model, the reactants move on classical trajectories in the combined field of Coulomb repulsion and nuclear surface-surface attraction. Surface modes of the colliding nuclei are taken into account. Independent single nucleon transfer between the projectile-like and target-like nuclei during the collision is governed by the quantum coupled equations [13, 14]. Neutron evaporation is considered for the excited primary fragments. The mass, charge, energy, and angular momentum distributions of the products produced in grazing collisions can be obtained. For details of GRAZING model and its applications (see, e.g., [16–19], and references therein). The dinuclear system model can reproduce the experimental data related with quasi-fission or deep-inelastic collisions [10, 20–23]. The improved quantum molecular dynamics (ImQMD) model [24–26] is capable of describing collisions from central to very peripheral regions on a microscopic basis, the widths of isotopic distributions can be reproduced in ImQMD since stochastic two-body collisions are taken into account [27–29]. The time-dependent Hartree-Fock (TDHF) theory shows success in describing few-nucleon transfer process [30–34]. Recently, the stochastic mean-field (SMF) approach beyond TDHF [35] has been proposed to investigate the damped MNT reaction $^{136}$Xe + $^{208}$Pb, the experimental broad mass distribution can be reproduced.

In this work, the GRAZING model and TDHF theory incorporating with GEMINI++[1] [36] are adopted to investigate the production of neutron-rich nuclei in MNT reactions. The TDHF theory [37] is based on the independent particle picture and is a good approximation to the nuclear many-body problem. It is capable of describing low-energy heavy-ion reactions and provides insight on the average behavior of the dynamics. The state-of-art TDHF calculations are performed in a three-dimensional (3D) framework without any symmetry constraints due to the advances in computational power. It has been applied for investigations on various subjects, for instance, collective vibration [38, 39], fusion reaction [40, 41], fission dynamics [42–44], dissipation mechanism [45–48]. Recently, 3D TDHF is applied to MNT reactions [30–33, 49]. Fluctuation and dissipation can not be properly described in TDHF since two-body collisions and internucleon correlations are not included. Thus, widths of the mass or isotopic distributions in MNT reactions at incident energies above the Coulomb barrier are underestimated in TDHF. To consider these effects in TDHF is beyond the scope of this paper and further studied will be carried out in the future.

This paper is outlined as follows. In section 2, the TDHF approach and particle-number projection (PNP) method as well as the numerical details are introduced. In section 3, numerical results of the isotopic production cross sections in both GRAZING and TDHF approach are shown. Dynamical properties of the reactions are also discussed for TDHF. Finally, a summary is drawn in section 4.

[1]https://bitbucket.org/arekfu/gemini

## 2. BRIEF INTRODUCTION TO TDHF APPROACH

In this section, we briefly introduce TDHF formalism, PNP method and the coupling to GEMINI++. Details of the TDHF theory can be found in, e.g., [50, 51], and references therein. In TDHF approach, time evolution for the single-particle states are described by a set of coupled non-linear equations

$$i\hbar\partial_t\psi_\alpha(\boldsymbol{r},t)=\hat{h}[\psi_\nu(\boldsymbol{r},t)]\psi_\alpha(\boldsymbol{r},t),\quad \alpha,\nu=1,2,\cdots,N, \tag{1}$$

where $\psi_{\alpha,\,\nu}(\boldsymbol{r},t)$ is the single-particle state and $N$ is the total number of states. $\hat{h}$ is the self-consistent mean-field Hamiltonian of single-particle motion and it is always related to Skyrme energy density functional (EDF) which depends on local densities [52]. We underline that there are no adjustable parameters in the TDHF approach. The uncertainty in TDHF calculations may arise from the uncertainty of fundamental nuclear properties, such as the distribution of shape deformation of the reactants in their ground states. This can be obtained by preparing reactants with deformation constraints. The above TDHF equations can be derived from the variation of the action [53]

$$S=\int \mathrm{d}t\langle\Psi|i\partial_t-\hat{H}|\Psi\rangle, \tag{2}$$

where

$$\Psi=\frac{1}{\sqrt{N!}}\det\{\psi_\alpha(\boldsymbol{r},t)\},\quad \alpha=1,2,\cdots,N, \tag{3}$$

is the correlated many-body wave function of the system and is given by a single Slater determinate.

In the present work, the 3D unrestricted TDHF code Sky3D [51] with Skyrme SLy5 parametrization [54] is adopted for both the static and dynamic calculations. The static HF calculations are performed on 32 × 32 × 32 Cartesian grids with 1.0 fm grid spacing in all three directions. In dynamical calculations, the meshes are extended to 70 × 32 × 70 with the same grid spacing in static HF. The projectile and target are initially placed at a separation distance of 24 fm and then boosted with the associated center-of-mass energy $E_{\mathrm{c.m.}}$ and the impact parameter $b$. The time step $\triangle t$ is set to be 0.2 fm/c and six-order Taylor series expansion is employed. The TDHF simulations are stopped when the separation distance of the primary fragments after collision reaches 30 fm. Since single-particle wave functions are partially exchanged between the projectile-like and target-like nuclei in the collision process, the outgoing states are not the eigenstates of the particle-number operators ($\hat{Z}$ for protons and $\hat{N}$ for neutrons) but superpositions of them. One can only get the expectation (mean) values of the charge and mass numbers for each fragment after collision. If one wants to get the distributions of proton or neutron numbers in one of the primary fragments, one should project the many-body states on good particle numbers by introducing the PNP operator [50, 55]

$$\hat{P}_V(N^q)=\frac{1}{2\pi}\int_0^{2\pi}\mathrm{d}\phi e^{i\phi(\hat{N}_V^q-N^q)}, \tag{4}$$

where $q = n, p$ labels the nucleon species, and $N^n$ means $N$ neutrons while $N^p$ means $Z$ protons. The subscript $V$ denotes the region of coordinate space encompassing one of the primary fragments, $\hat{N}_V^q = \sum_{\alpha=1}^{N^q} \Theta_V(\boldsymbol{r})$ and $\Theta_V(\boldsymbol{r}) = 1$ if $\boldsymbol{r} \in$ subspace $V$ and 0 elsewhere. The integral is performed with an $M-$point uniform discretion. For convergence, $M$ is set to be 300.

The probability to find $N^q$ particles in subspace $V$ is then obtained accordingly. The cross section of primary fragment with neutron number $N$ and charge number $Z$ at a certain incident energy is

$$\sigma(N,Z) = 2\pi \int_0^{b_{\max}} P(N,Z;b) b \mathrm{d}b, \tag{5}$$

where $P(N,Z;b) = P(N;b)P(Z;b)$ represents the probability to find $N$ neutrons and $Z$ protons at the impact parameter $b$; $b_{\max}$ is a cutoff impact parameter which depends on the incident energy and should be large enough to guarantee that most of the transfer cross sections are included. But it is not necessary to set $b_{\max}$ to be too large, because the transfer probability is extremely small and elastic collision dominates in very peripheral collisions. In this work, we set it to be 10 fm for $^{136}$Xe+$^{208}$Pb at $E_{\mathrm{c.m.}} = 450$ MeV and 13 fm for $^{136}$Xe+$^{194}$Ir at $E_{\mathrm{c.m.}} = 720$ MeV. $b$ ranges from 0 to $b_{\max}$ with the interval $\Delta\, b = 1$ fm.

Deexcitation of the primary fragments are considered by using the statistical code GEMINI++ with default parameters [36, 56]. All possible sequential binary decay modes, from emission of nucleons and light particles through asymmetric to symmetric fission as well as the $\gamma$-emission are included in GEMINI++. The code needs information of a primary fragment including charge and mass number as well as the excitation energies and the angular momentum as the inputs. Detailed calculations of these quantities can be found in Jiang and Wang [34]. The deexcitation of a certain projectile-like fragment (PLF) or target-like fragment (TLF) should be repeated $M_{\mathrm{trial}}$ times due to the statistical nature of GEMINI++. Here $M_{\mathrm{trial}} = 1,000$ is used. The number of events in which final fragment with $(N_{\mathrm{final}}, Z_{\mathrm{final}})$ is counted and denoted as $M(N_{\mathrm{final}}, Z_{\mathrm{final}})$. Then the final production cross section is given as

$$\sigma(N_{\mathrm{final}}, Z_{\mathrm{final}}) = 2\pi \int_0^{b_{\max}} \sum_{N \geqslant N_{\mathrm{final}},\, Z \geqslant Z_{\mathrm{final}}} P(N,Z;b) \times \frac{M(N_{\mathrm{final}}, Z_{\mathrm{final}})}{M_{\mathrm{trial}}} b \mathrm{d}b. \tag{6}$$

Owing to the intrinsic stochastic nature of the Monte Carlo method employed in GEMINI++, Type A standard uncertainties for the isotopic production cross sections are calculated in the simplest case. The deexcitation process of a certain fragment is performed ten times repeatedly with $M_{\mathrm{trial}} = 1,000$ for each time. Average values of $\sigma(N_{\mathrm{final}}, Z_{\mathrm{final}})$ and the uncertainties can be obtained straightforwardly. We find the uncertainties are very small. For the sake of simplicity, the deexcitation process is performed only once with $M_{\mathrm{trial}} = 1,000$ in this work.

## 3. RESULTS AND DISCUSSIONS

$^{136}$Xe + $^{208}$Pb is a candidate reaction for the production of neutron-rich nuclei at $N = 126$. The experiment at $E_{\mathrm{c.m.}} = 450$ MeV was performed at Argonne in 2015 [8]. In **Figure 1** we plot the calculated isotopic production cross sections of the PLFs in this reaction. The results of GRAZING are shown as blue solid lines while those of TDHF+GEMINI are presented as black dashed lines. The experimental data are shown for comparison. The production cross sections of the TLFs are also calculated but have already been published in another paper [34]. One can find that for $Z = 51 - 53$ and $Z = 55 - 58$, the magnitude of the peak values can be reproduced by TDHF+GEMINI. Whilst those for $Z = 52, 53, 55, 56$ can be reproduced by GRAZING. For $Z = 54$, the peak values are overestimated in both models. This is because the results of (quasi)elastic channels are not excluded in our calculations. One can also find that better predictions are obtained for proton pickup channels than stripping channels in both models. As the number of transferred nucleons increases, discrepancies between model predictions and the experimental data get larger. These isotopes far away from the entrance channel may be produced in strongly damped collisions. Such processes can not be well estimated by the two models: two-body collisions are not considered in TDHF [57, 58] while the GRAZING model only takes grazing collisions into account.

However, no new neutron-rich nuclei were detected in $^{136}$Xe + $^{208}$Pb. The experiment results of $^{136}$Xe+$^{198}$Pt at $E_{\mathrm{c.m.}} = 645$ MeV [2] indicate that this reaction is a better candidate to produce neutron-rich nuclei with $N = 126$. Calculations of this reaction are performed by using both GRAZING and TDHF+GEMINI. Unfortunately, no neutron-rich nuclei with $N = 126$ is obtained in TDHF+GEMINI. The production cross sections of those nuclei predicted by GRAZING are given in **Figure 2**. Detailed discussions about the predictions of TDHF on this reaction will be reported elsewhere. At the end of this section, we will show some results of $^{136}$Xe + $^{194}$Ir given by TDHF+GEMINI and discuss the limits of TDHF approach on investigating MNT reactions when the incident energy is much above the Coulomb barrier. In the following, we concentrate on the predictions of GRAZING on neutron-rich nuclei with $N = 126$.

In order to find another optimum projectile-target combination for producing new exotic neutron-rich nuclei with stable reactants, we carry out a systematic study on 15 MNT reactions with projectile around $^{136}$Xe and target around $^{198}$Pt at various incident energies by using GRAZING. The results indicate that $^{136}$Xe + $^{194}$Ir is a surrogate reaction to produce neutron-rich nuclei around $N = 126$. The production cross sections of isotones with $N = 126$ in $^{136}$Xe + $^{194}$Ir are compared with those of $^{136}$Xe + $^{208}$Pb and $^{136}$Xe + $^{198}$Pt. The center-of-mass energy for all the three systems is set to be $E_{\mathrm{c.m.}} = 645$ MeV (this energy is the same as the experiment of $^{136}$Xe + $^{198}$Pt [2], and we will show later that it is also an optimum energy for $^{136}$Xe + $^{194}$Ir). The simulation results are plotted in **Figure 2** as open symbols. The experimental data of $^{136}$Xe + $^{198}$Pt taken from [2] are shown as black solid squares for comparison. One can first see that more $N = 126$ isotones with charge number

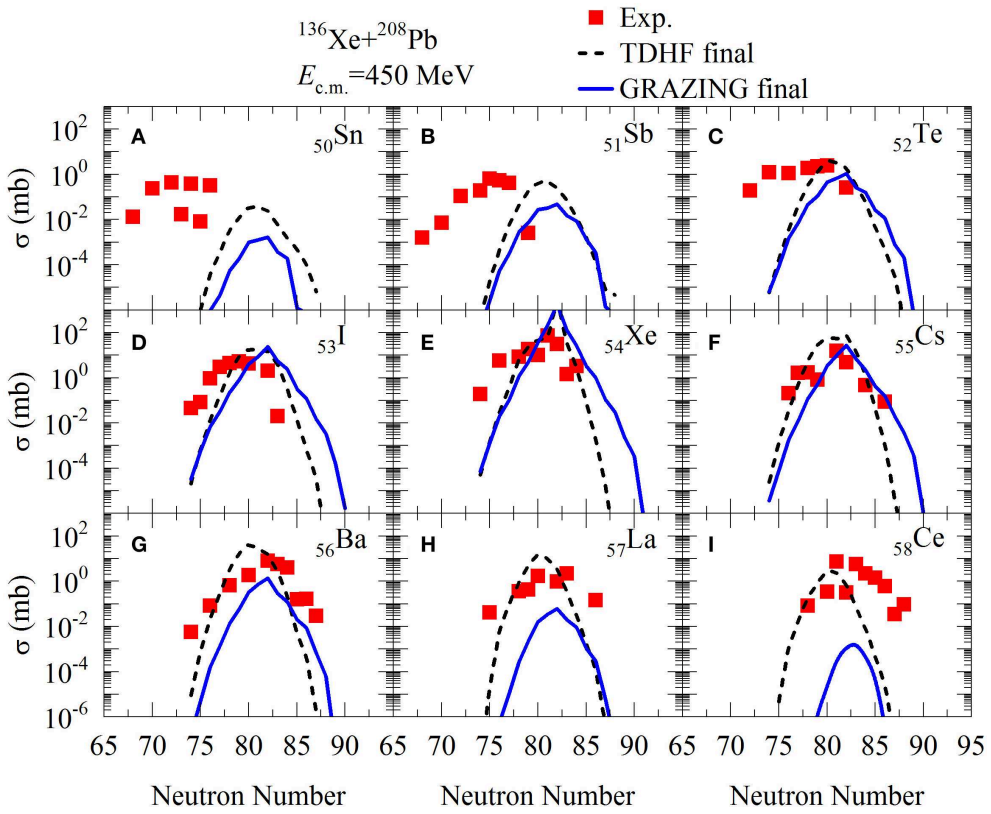


**FIGURE 1 |** (Color online) Isotopic production cross sections of the PLFs for $Z = 50$–58 **(A–I)** in $^{136}$Xe + $^{208}$Pb at $E_{c.m.} = 450$ MeV. The results of GRAZING and TDHF+GEMINI are shown as blue solid and black dashed lines, respectively. The experimental data are taken from Barrett et al. [8] and shown as red solid squares.

$Z \leqslant 78$ can be produced in both $^{136}$Xe + $^{194}$Ir and $^{136}$Xe + $^{198}$Pt rather than $^{136}$Xe + $^{208}$Pb. Particularly, the system $^{136}$Xe + $^{194}$Ir has huge advantages for producing $N = 126$ isotones with $Z \leqslant 74$. Those nuclei are out of the limits of the present nuclear landscape and are of great interest for nuclear and astro-nuclear physics. One can also find that the experimental data are underestimated by GRAZING. This can be understood since only peripheral collisions are treated in GRAZING and those nuclei with large number of nucleon transferred are produced in damped collisions at small impact parameters.

To find an optimum incident energy to produce more neutron-rich nuclei with $N = 126$ in $^{136}$Xe + $^{194}$Ir, the production cross sections of $N = 126$ isotones with $Z = 72 - 77$ at various incident energies from $E_{c.m.} = 1.07V_B$ to $1.85V_B$ ($V_B$ is the Bass barrier [59] and it is around 410 MeV for this reaction) are calculated by using GRAZING. The results are presented in **Figure 3**. It can be seen that very neutron-rich isotones with $Z \leqslant 74$ can not be produced if $E_{lab}/A \leqslant 5.5$ MeV. The cross sections of all these isotones increase with the increasing incident energy when $E_{lab}/A < 6.5$ MeV. However, when $E_{lab}/A$ is in the range of 7–9 MeV, plateau-like structures are observed for all the curves. This phenomenon indicates that the production cross sections of those nuclei are insensitive to the incident energy if $7 \leqslant E_{lab}/A \leqslant 9$ MeV.

In **Figure 4** we show the isotopic production cross sections of the TLFs with $Z = 72 - 77$ in $^{136}$Xe + $^{198}$Pt and $^{136}$Xe + $^{194}$Ir at $E_{c.m.} = 645$ MeV ($E_{lab}/A \approx 8$ MeV) as black dashed and red solid lines, respectively. It can be found that for nuclei on the proton-rich side, larger production cross sections are obtained in $^{136}$Xe + $^{194}$Ir. For isotopes with $Z = 76$ and 77, more neutron-rich ones are produced in $^{136}$Xe + $^{198}$Pt. Whilst for $Z = 75$ the two systems give comparable results for isotopes on the neutron-rich side. As $Z$ decreases, the advantage to produce more neutron-rich nuclei arises in $^{136}$Xe + $^{194}$Ir. Note that the results of $Z = 72$ in $^{136}$Xe + $^{198}$Pt are not given by GRAZING. The above results of the two reactions are difficult to be understood through the $N/Z$ equilibrium process because $N/Z$ is around 1.52 for $^{136}$Xe and $^{194}$Ir while it is about 1.54 for $^{198}$Pt and $^{208}$Pb, respectively. It might be related with the $Q_{gg}$ value effect, where $Q_{gg}$ is the ground state-to-ground state $Q$ value. Other quantum effect like shell effect might also play a role. Further studies should be carried out to check these discussions.

Finally, in **Figure 5** we show the density contour plots of $^{136}$Xe + $^{194}$Ir at some special reaction stages in TDHF for two different initial configurations at $E_{c.m.} = 720$ MeV ($E_{lab}/A \approx 9$) and $b = 6$ fm. Isodensities at half the saturation density ($\rho_0/2 = 0.08$ fm$^{-3}$) is plotted as black solid lines. We should mention

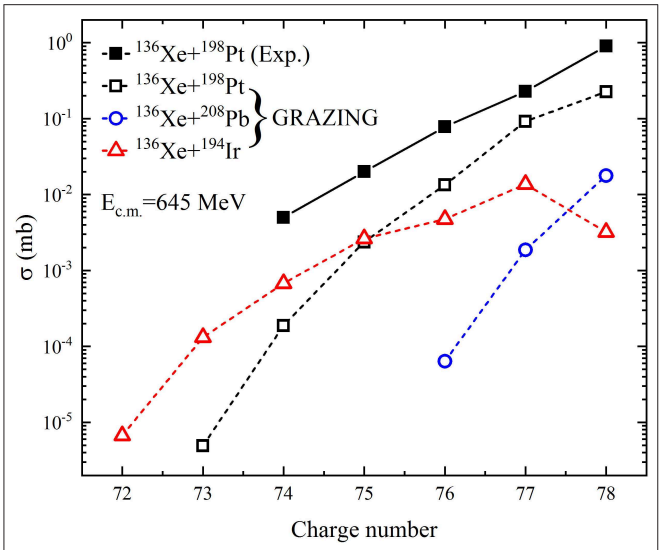


**FIGURE 2 |** (Color online) Production cross sections of $N = 126$ isotones predicted by GRAZING in three different systems at $E_{c.m.} = 645$ MeV. The results of $^{136}$Xe + $^{208}$Pb, $^{198}$Pt, and $^{194}$Ir are presented as blue open circles, black open squares and red open triangles, respectively. The experimental data of $^{136}$Xe + $^{198}$Pt are taken from Watanabe et al. [2] and shown as black solid squares. The lines are drawn to guide the eye.

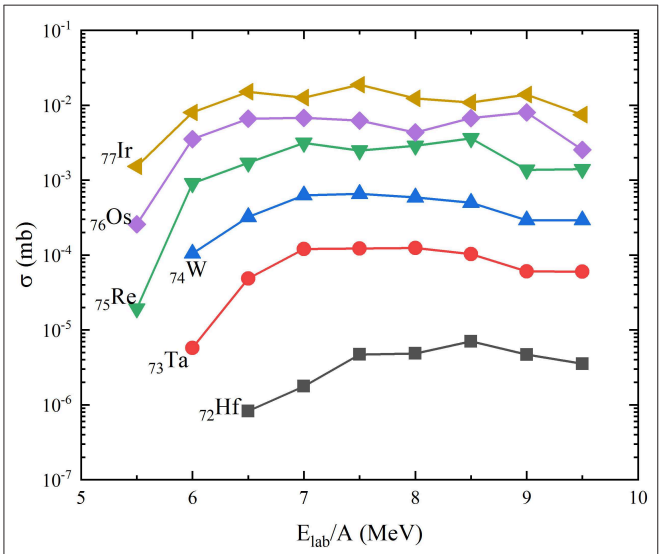


**FIGURE 3 |** (Color online) Production cross sections of neutron-rich $N = 126$ isotones with $Z = 72 - 77$ in $^{136}$Xe + $^{194}$Ir as a function of the incident energy. The lines are drawn to guide the eye.

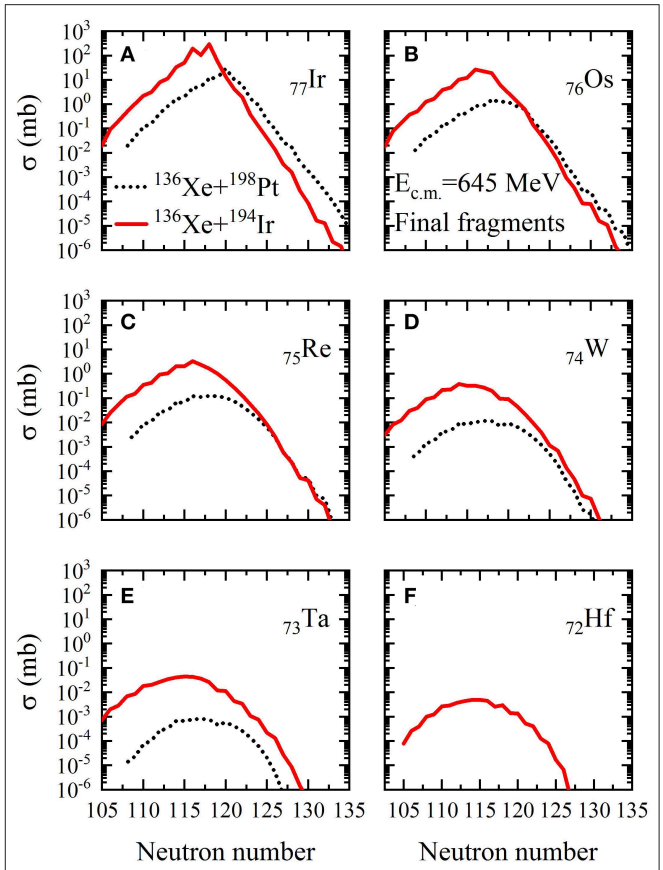


**FIGURE 4 |** (Color online) Isotopic production cross sections of the TLFs with $Z = 72 - 77$ **(A–F)** in $^{136}$Xe + $^{198}$Pt and $^{136}$Xe + $^{194}$Ir at $E_{c.m.} = 645$ MeV, which are plotted as black dotted and red solid lines, respectively.

that in TDHF the projectile and target are both deformed in their ground states with $\beta_2 = 0.064$ and 0.154, respectively. Since the deformation of $^{136}$Xe is very small, we only take into account the orientation effect of the deformed $^{194}$Ir at the beginning of the dynamical calculations. The two initial configurations are named "tip collision" (the symmetry axis of $^{194}$Ir is set parallel to the bombarding direction: $z$-axis) and "side collision" (the symmetry axis of $^{194}$Ir is set parallel to $x$-axis). It can be found that in both configurations, the composite system is strongly elongated before rupture of the neck. The primary fragments produced at the end of the dynamical calculations also have large deformations. Similar results are obtained for TDHF+GEMINI in $^{136}$Xe + $^{198}$Pt at $E_{c.m.} = 645$ MeV. Such large deformation in the exit channel makes the primary fragments have very large excitation energies. This leads to strong evaporation of nucleons in the deexcitation process. So no neutron-rich isotope with $N = 126$ is observed in TDHF+GEMINI for $^{136}$Xe + $^{194}$Ir and $^{136}$Xe + $^{198}$Pt reactions when the incident energy is much larger than the Coulomb barrier. It is well-known that mean-field model such as TDHF is suitable for low-energy reactions, however, the lack of two-body collisions limits the predictive power of TDHF on estimating the yields of MNT reactions when the incident energy is much above the barrier.

## 4. SUMMARY

Employing the semi-classic GRAZING model and the microscopic TDHF approach, we have investigated the MNT reactions of $^{136}$Xe + $^{194}$Ir, $^{208}$Pb. Neutron evaporation is

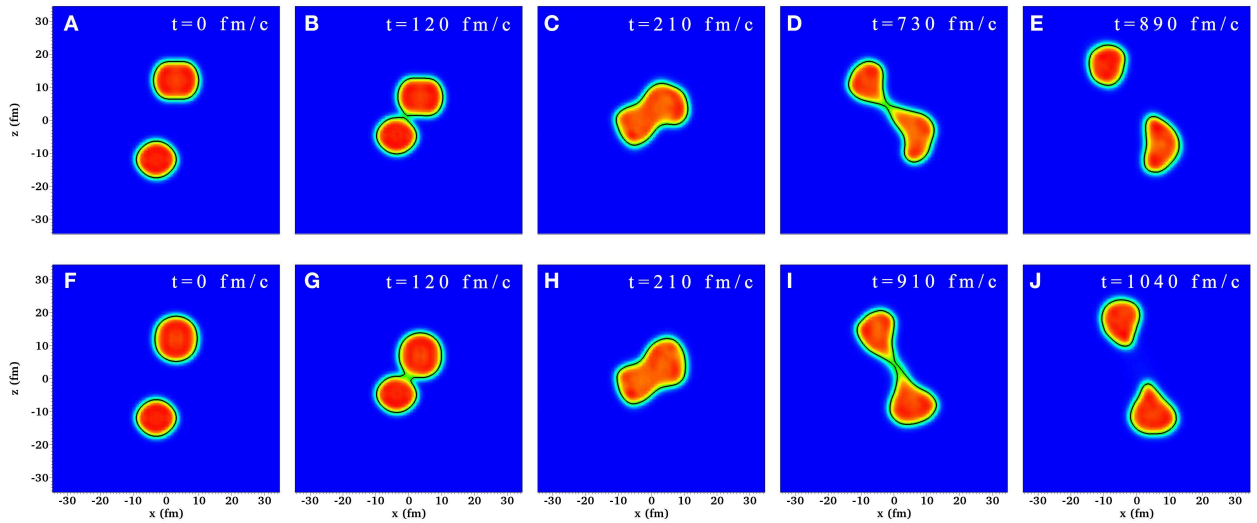


**FIGURE 5 |** (Color online) Density contour plots of $^{136}$Xe + $^{194}$Ir for two different configurations (upper panels: "side collision" and lower panels: "tip collision") at $E_{\text{c.m.}} = 720$ MeV and $b = 6$ fm. Five different reaction stages are given: **(A,F)** the initial stage at $t = 0$ fm/c, **(B,G)** the reactants just contact with each other, **(C,H)** the composite system has the most compact geometric shape, **(D,I)** the neck is going to rupture and **(E,J)** the end of the dynamical calculations. The isodensities of 0.08 fm$^{-3}$ are shown as black solid lines.

considered in GRAZING while GEMINI++ is coupled with TDHF to deal with the deexcitation process. The calculated production cross sections of the PLFs for $^{136}$Xe + $^{208}$Pb at $E_{\text{c.m.}} = 450$ MeV are compared with the experimental data. The model predictions can well describe the yields of nuclei near the projectile. The predictions of GRAZING on $^{136}$Xe + $^{194}$Ir show that this reaction has the advantage to produce more neutron-rich nuclei with $N = 126$ compared with $^{136}$Xe + $^{198}$Pt. The latter one has been carried out at GANIL [2] and the results are inspiring. No new neutron-rich isotope is observed for these two reactions at energies much above the barrier in TDHF+GMINI which might be interpreted as the lack of two-body collisions in the mean-field theory. Further investigations on $^{136}$Xe + $^{194}$Ir by using other theoretical models with two-body collisions included, such as ImQMD, are in progress.

## DATA AVAILABILITY STATEMENT

All datasets generated for this study are included in the article/supplementary material.

## AUTHOR CONTRIBUTIONS

XJ performed numerical calculations. XJ and NW wrote the manuscript.

## FUNDING

This work was supported by the National Natural Science Foundation of China (Projects Nos. 11705118, 11647026, and 11475115) and Natural Science Foundation of SZU (grant no. 2016017).

## REFERENCES

1. Grawe H, Langanke K, Martínez-Pinedo G. Nuclear structure and astrophysics. *Rep Prog Phys.* (2007) **70**:1525. doi: 10.1088/0034-4885/70/9/R02
2. Watanabe YX, Kim YH, Jeong SC, Hirayama Y, Imai N, Ishiyama H, et al. Pathway for the production of neutron-rich isotopes around the $N = 126$ shell closure. *Phys Rev Lett.* (2015) **115**:172503. doi: 10.1103/PhysRevLett.115.172503
3. Zagrebaev V, Greiner W. Production of new heavy isotopes in low-energy multinucleon transfer reactions. *Phys Rev Lett.* (2008) **101**:122701. doi: 10.1103/PhysRevLett.101.122701
4. Zagrebaev VI, Greiner W. Production of heavy and superheavy neutron-rich nuclei in transfer reactions. *Phys Rev C.* (2011) **83**:044618. doi: 10.1103/PhysRevC.83.044618
5. Kurtukian-Nieto T, Benlliure J, Schmidt KH, Audouin L, Becker F, Blank B, et al. Production cross sections of heavy neutron-rich nuclei approaching the nucleosynthesis r-process path around $A = 195$. *Phys Rev C.* (2014) **89**:024616. doi: 10.1103/PhysRevC.89.024616
6. Beliuskina O, Heinz S, Zagrebaev V, Comas V, Heinz C, Hofmann S, et al. On the synthesis of neutron-rich isotopes along the N = 126 shell in multinucleon transfer reactions. *Eur Phys J A.* (2014) **50**:161. doi: 10.1140/epja/i2014-14161-3
7. Kozulin EM, Vardaci E, Knyazheva GN, Bogachev AA, Dmitriev SN, Itkis IM, et al. Mass distributions of the system $^{136}$Xe + $^{208}$Pb at laboratory energies around the Coulomb barrier: a candidate reaction for the production of neutron-rich nuclei at $N = 126$. *Phys Rev C.* (2012) **86**:044611. doi: 10.1103/PhysRevC.86.044611
8. Barrett JS, Loveland W, Yanez R, Zhu S, Ayangeakaa AD, Carpenter MP, et al. $^{136}$Xe +$^{208}$ Pb reaction: a test of models of multinucleon transfer reactions. *Phys Rev C.* (2015) **91**:064615. doi: 10.1103/PhysRevC.91.064615
9. Loveland W. Synthesis of transactinide nuclei using radioactive beams. *Phys Rev C.* (2007) **76**:014612. doi: 10.1103/PhysRevC.76.014612

10. Zhu L, Su J, Xie WJ, Zhang FS. Theoretical study on production of heavy neutron-rich isotopes around the N=126 shell closure in radioactive beam induced transfer reactions. *Phys Lett B*. (2017) **767**:437–42. doi: 10.1016/j.physletb.2017.01.082
11. Bonaccorso A, Prete G. EURISOL: an European Isotope Separation On-Line radioactive ion beam facility. *J Phys Confer Ser*. (2009) **168**:012023. doi: 10.1088/1742-6596/168/1/012023
12. Karpov AV, Saiko VV. Modeling near-barrier collisions of heavy ions based on a Langevin-type approach. *Phys Rev C*. (2017) **96**:024618. doi: 10.1103/PhysRevC.96.024618
13. Winther A. Grazing reactions in collisions between heavy nuclei. *Nucl Phys A*. (1994) **572**:191–235.
14. Winther A. Dissipation, polarization and fluctuation in grazing heavy-ion collisions and the boundary to the chaotic regime. *Nucl Phys A*. (1995) **594**:203–45.
15. Corradi L, Stefanini AM, Ackermann D, Beghini S, Montagnoli G, Petrache C, et al. Multinucleon transfer reactions in $^{32}$S+$^{208}$Pb close to the Coulomb barrier. *Phys Rev C*. (1994) **49**:R2875–9. doi: 10.1103/PhysRevC.49.R2875
16. Dasso CH, Pollarolo G, Winther A. Systematics of isotope production with radioactive beams. *Phys Rev Lett*. (1994) **73**:1907–10. doi: 10.1103/PhysRevLett.73.1907
17. Corradi L, Pollarolo G, Szilner S. Multinucleon transfer processes in heavy-ion reactions. *J Phys G Nucl Part Phys*. (2009) **36**:113101. doi: 10.1088/0954-3899/36/11/113101
18. Montanari D, Corradi L, Szilner S, Pollarolo G, Fioretto E, Montagnoli G, et al. Neutron pair transfer in $^{60}$Ni +$^{116}$ Sn far below the coulomb barrier. *Phys Rev Lett*. (2014) **113**:052501. doi: 10.1103/PhysRevLett.113.052501
19. Wen P, Li C, Zhu L, Lin C, Zhang F. Mechanism of multinucleon transfer reaction based on the GRAZING model and DNS model. *J Phys G Nucl Part Phys*. (2017) **44**:115101. doi: 10.1088/1361-6471/aa8b07
20. Penionzhkevich YE, Adamian GG, Antonenko NV. Towards neutron drip line via transfer-type reactions. *Physics Lett B*. (2005) **621**:119–25. doi: 10.1016/j.physletb.2005.05.085
21. Adamian GG, Antonenko NV, Lukyanov SM, Penionzhkevich YE. Possibility of production of neutron-rich isotopes in transfer-type reactions at intermediate energies. *Phys Rev C*. (2008) **78**:024613. doi: 10.1103/PhysRevC.78.024613
22. Feng ZQ. Production of neutron-rich isotopes around $N = 126$ in multinucleon transfer reactions. *Phys Rev C*. (2017) **95**:024615. doi: 10.1103/PhysRevC.95.024615
23. Guo SQ, Bao XJ, Zhang HF, Li JQ, Wang N. Effect of dynamical deformation on the production distribution in multinucleon transfer reactions. *Phys Rev C*. (2019) **100**:054616. doi: 10.1103/PhysRevC.100.054616
24. Wang N, Li Z, Wu X. Improved quantum molecular dynamics model and its applications to fusion reaction near barrier. *Phys Rev C*. (2002) **65**:064608. doi: 10.1103/PhysRevC.65.064608
25. Wang N, Li Z, Wu X, Tian J, Zhang Y, Liu M. Further development of the improved quantum molecular dynamics model and its application to fusion reactions near the barrier. *Phys Rev C*. (2004) **69**:034608. doi: 10.1103/PhysRevC.69.034608
26. Wang N, Guo L. New neutron-rich isotope production in 154Sm+160Gd. *Phys Lett B*. (2016) **760**:236–41. doi: 10.1016/j.physletb.2016.06.073
27. Welsh T, Loveland W, Yanez R, Barrett JS, McCutchan EA, Sonzogni AA, et al. Modeling multi-nucleon transfer in symmetric collisions of massive nuclei. *Phys Lett B*. (2017) **771**:119–24. doi: 10.1016/j.physletb.2017.05.044
28. Li C, Wen P, Li J, Zhang G, Li B, Xu X, et al. Production mechanism of new neutron-rich heavy nuclei in the Xe136+198Pt reaction. *Phys Lett B*. (2018) **776**:278–83. doi: 10.1016/j.physletb.2017.11.060
29. Desai VV, Loveland W, McCaleb K, Yanez R, Lane G, Hota SS, et al. The $^{136}$Xe +$^{198}$ Pt reaction: A test of models of multi-nucleon transfer reactions. *Phys Rev C*. (2019) **99**:044604. doi: 10.1103/PhysRevC.99.044604
30. Sekizawa K. Microscopic description of production cross sections including deexcitation effects. *Phys Rev C*. (2017) **96**:014615. doi: 10.1103/PhysRevC.96.014615
31. Jiang X, Wang N. Production mechanism of neutron-rich nuclei around N=126 in the multi-nucleon transfer reaction $^{132}$Sn + $^{208}$Pb. *Chinese Phys C*. (2018) **42**:104105. doi: 10.1088/1674-1137/42/10/104105
32. Sekizawa K. TDHF theory and its extensions for the multinucleon transfer reaction: a mini review. *Front Phys*. (2019) **7**:20. doi: 10.3389/fphy.2019.00020
33. Wu Z, Guo L. Microscopic studies of production cross sections in multinucleon transfer reaction $^{58}$Ni +$^{124}$ Sn. *Phys Rev C*. (2019) **100**:014612. doi: 10.1103/PhysRevC.100.014612
34. Jiang X, Wang N. Probing the production mechanism of neutron-rich nuclei in multinucleon transfer reactions. *Phys Rev C*. (2020) **101**:014604. doi: 10.1103/PhysRevC.101.014604
35. Ayik S, Yilmaz B, Yilmaz O, Umar AS. Quantal diffusion approach for multinucleon transfers in Xe + Pb collisions. *Phys Rev C*. (2019) **100**:014609. doi: 10.1103/PhysRevC.100.014609
36. Charity RJ. Systematic description of evaporation spectra for light and heavy compound nuclei. *Phys Rev C*. (2010) **82**:014610. doi: 10.1103/PhysRevC.82.014610
37. Dirac PAM. Note on exchange phenomena in the Thomas atom. *Math Proc Cambridge*. (1930) **26**:376–85.
38. Simenel C, Chomaz P. Nonlinear vibrations in nuclei. *Phys Rev C*. (2003) **68**:024302. doi: 10.1103/PhysRevC.68.024302
39. Umar AS, Oberacker VE. Time-dependent response calculations of nuclear resonances. *Phys Rev C*. (2005) **71**:034314. doi: 10.1103/PhysRevC.71.034314
40. Simenel C, Keser R, Umar AS, Oberacker VE. Microscopic study of 16O+16O fusion. *Phys Rev C*. (2013) **88**:024617. doi: 10.1103/PhysRevC.88.024617
41. Jiang X, Maruhn JA, Yan S. Microscopic study of noncentral effects in heavy-ion fusion reactions with spherical nuclei. *Phys Rev C*. (2014) **90**:064618. doi: 10.1103/PhysRevC.90.064618
42. Umar AS, Oberacker VE, Maruhn JA, Reinhard PG. Microscopic description of nuclear fission dynamics. *J Phys G Nucl Part Phys*. (2010) **37**:064037. doi: 10.1088/0954-3899/37/6/064037
43. Goddard P, Stevenson P, Rios A. Fission dynamics within time-dependent Hartree-Fock: deformation-induced fission. *Phys Rev C*. (2015) **92**:054610. doi: 10.1103/PhysRevC.92.054610
44. Simenel C, Umar AS. Formation and dynamics of fission fragments. *Phys Rev C*. (2014) **89**:031601. doi: 10.1103/PhysRevC.89.031601
45. Maruhn JA, Reinhard PG, Stevenson PD, Strayer MR. Spin-excitation mechanisms in Skyrme-force time-dependent Hartree-Fock calculations. *Phys Rev C*. (2006) **74**:027601. doi: 10.1103/PhysRevC.74.027601
46. Loebl N, Umar AS, Maruhn JA, Reinhard PG, Stevenson PD, Oberacker VE. Single-particle dissipation in a time-dependent Hartree-Fock approach studied from a phase-space perspective. *Phys Rev C*. (2012) **86**:024608. doi: 10.1103/PhysRevC.86.024608
47. Guo L, Simenel C, Shi L, Yu C. The role of tensor force in heavy-ion fusion dynamics. *Phys Lett B*. (2018) **782**:401–5. doi: 10.1016/j.physletb.2018.05.066
48. Wen K, Barton MC, Rios A, Stevenson PD. Two-body dissipation effect in nuclear fusion reactions. *Phys Rev C*. (2018) **98**:014603. doi: 10.1103/PhysRevC.98.014603
49. Umar AS, Simenel C, Ye W. Transport properties of isospin asymmetric nuclear matter using the time-dependent Hartree-Fock method. *Phys Rev C*. (2017) **96**:024625. doi: 10.1103/PhysRevC.96.024625
50. Bender M, Heenen PH, Reinhard PG. Self-consistent mean-field models for nuclear structure. *Rev Mod Phys*. (2003) **75**:121–80. doi: 10.1103/RevModPhys.75.121
51. Maruhn JA, Reinhard PG, Stevenson PD, Umar AS. The {TDHF} code Sky3D. *Comput Phys Commun*. (2014) **185**:2195–216. doi: 10.1016/j.cpc.2014.04.00
52. Vautherin D, Brink DM. Hartree-Fock calculations with Skyrme's interaction. I. Spherical nuclei. *Phys Rev C*. (1972) **5**:626–47. doi: 10.1103/PhysRevC.5.626
53. Negele JW. The mean-field theory of nuclear structure and dynamics. *Rev Mod Phys*. (1982) **54**:913–1015. doi: 10.1103/RevModPhys.54.913
54. Chabanat E, Bonche P, Haensel P, Meyer J, Schaeffer R. A Skyrme parametrization from subnuclear to neutron star densities Part II. Nuclei far from stabilities. *Nucl Phys A*. (1998) **635**:231–56.
55. Simenel C. Particle transfer reactions with the time-dependent Hartree-Fock theory using a particle number projection technique. *Phys Rev Lett*. (2010) **105**:192701. doi: 10.1103/PhysRevLett.105.192701

56. Mancusi D, Charity RJ, Cugnon J. Unified description of fission in fusion and spallation reactions. *Phys Rev C*. (2010) **82**:044610. doi: 10.1103/PhysRevC.82.044610
57. Grangé P, Richert J, Wolschin G, Weidenmüller HA. Influence of a collision term on finite-size one-dimensional TDHF. *Nucl Phys A*. (1981) **356**:260–8.
58. Goeke K, Reinhard PG. Time-Dependent Hartree-Fock and Beyond. *Prog Theor Phys Suppl*. (1983) **171**:33–65.
59. Bass R. Fusion reactions: successes and limitations of a one-dimensional description. In: von Oertzen W, editor. *Deep-Inelastic and Fusion Reactions with Heavy Ions. vol. 117 of Lecture Notes in Physics*. Berlin; Heidelberg: Springer (1980). p. 281–93. doi: 10.1007/3-540-09965-4_23

**Conflict of Interest:** The authors declare that the research was conducted in the absence of any commercial or financial relationships that could be construed as a potential conflict of interest.

frontiers in Physics

ORIGINAL RESEARCH
published: 27 February 2020
doi: 10.3389/fphy.2020.00040

# Quasifission Dynamics in Microscopic Theories

*Kyle Godbey and A. S. Umar**

*Department of Physics and Astronomy, Vanderbilt University, Nashville, TN, United States*

In the search for superheavy elements quasifission reactions represent one of the reaction pathways that curtail the formation of an evaporation residue. In addition to its importance in these searches quasifission is also an interesting dynamic process that could assist our understanding of many-body dynamical shell effects and energy dissipation thus forming a gateway between deep-inelastic reactions and fission. This manuscript gives a summary of recent progress in microscopic calculations of quasifission employing time-dependent Hartree-Fock (TDHF) theory and its extensions.

**Keywords: time-dependent Hartree-Fock, quasifission, superheavy elements, multi-nucleon transfer, time-dependent random phase approximation**

## 1. INTRODUCTION

The ongoing search for discovering new elements in the superheavy regime is perhaps the most exciting but at the same time challenging tasks in low-energy nuclear physics [1]. These searches were historically motivated by theoretical predictions of an *island of stability*, somewhat detached from the far end of the chart-of-nuclides [2–5], due to quantum mechanical shell closures. The experimental search for the so called superheavy elements (SHE) was initially done by using target projectile combinations that minimized the excitation energy of compound nuclei that was formed in reactions studied in the vicinity of the Coulomb barrier. For this reason these reactions are commonly referred to as *cold fusion* reactions and primarily involved closed shell nuclei, such as $^{208}$Pb target and projectiles in the chromium to zinc region. The cold fusion experiments were able to produce elements $Z = 107$–$113$ [6–8], but showed no indication that extending them to heavier elements were feasible. The identification of a SHE is done through the decay properties of a formed evaporation residue. In such reactions involving heavy elements the dominant reaction processes are quasifission (QF) and fusion-fission (FF), which are expected to strongly suppress the formation of an evaporation residue at higher excitation energies. For this reason it was a major surprise to observe that the so called *hot fusion* reactions, despite of their higher excitation energy, were able to synthesize elements $Z = 113$–$118$ [9, 10]. The hot fusion reactions utilized actinide targets with $^{48}$Ca projectiles. To further pursue the hot fusion reactions with heavier projectiles to reach elements $Z > 120$ requires a deeper understanding of the reaction pathways leading to an evaporation residue, particularly QF and FF components. In all of these reactions the evaporation residue cross-section is dramatically reduced due to the quasifission (QF) and fusion-fission (FF) processes. These processes occur during the reactions of heavy systems and correspond to excited fission channels in the classically allowed regime above the barrier and require a combination of statistical and truly dynamical approaches which are not necessarily confined to a collective subspace. Fusion-fission occurs after the formation of a composite system which then fissions due to its excitation, ultimately resulting in a fragment distribution that is peaked at equal mass breakup of the composite system. Quasifission occurs at a considerably shorter time-scale than fusion-fission [11–13] and is characterized by reaction fragments that differ significantly in mass from the original target/projectile nuclei. Quasifission for being one of the

OPEN ACCESS

***Edited by:***
*Paul Denis Stevenson,*
*University of Surrey, United Kingdom*

***Reviewed by:***
*Giuseppe Verde,*
*National Institute for Nuclear Physics, Italy*
*Kazuyuki Sekizawa,*
*Niigata University, Japan*

***Correspondence:**
*A. S. Umar*
*umar@compsci.cas.vanderbilt.edu*

***Specialty section:***
*This article was submitted to Nuclear Physics, a section of the journal Frontiers in Physics*

***Received:*** *03 January 2020*
***Accepted:*** *12 February 2020*
***Published:*** *27 February 2020*

***Citation:***
*Godbey K and Umar AS (2020) Quasifission Dynamics in Microscopic Theories. Front. Phys. 8:40. doi: 10.3389/fphy.2020.00040*

primary reaction mechanism that limits the formation of superheavy nuclei [14–16] has been the subject of intense experimental studies of [11–13, 17–24, 24–34]. Studies have also shown a strong impact of the entrance channel characteristics, including deformation [18, 19, 22, 23, 35–37] and shell structure [28] of the reactants. The final phase of the dynamics is also impacted by the fissility of the composite system [26, 29], its neutron richness [32], and by shell effects in the exit channel [12, 13, 20, 23, 24, 31, 38–40]. A number of theoretical approaches have been developed that describe the quasifission in terms of multi-nucleon transfer (MNT) processes [41–47]. Recently, time-dependent Hartree-Fock (TDHF) theory have proven to be an excellent tool for studying QF dynamics, and in particular mass-angle distributions and final fragment total kinetic energies (TKE) [31, 32, 34, 37, 45, 48–56]. While the fragments produced in TDHF studies are the excited primary fragments [57] a number of extensions based on the use of Langevin dynamics have been successfully applied to de-excite these fragments [55, 56, 58–60]. Theoretical studies of quasifission dynamics have taught us that dynamics themselves may be dominated by shell effects [47, 61]. Despite the apparent strong differences between fission and quasifission, it is interesting to note that similar shell effects are found in both mechanisms [54]. Quasifission can then potentially be used as an alternative mechanisms to probe fission mode properties. For instance, this could provide a much cheaper way than fusion-fission to test the influence of $^{208}$Pb shell effects in super-asymmetric SHE fission.

## 2. MICROSCOPIC APPROACHES

The underlying approach to study quasifission on a microscopic basis is the time-dependent Hartree-Fock (TDHF) theory [61–64]. Alternative approaches employ Langevin dynamics [65–67]. Indeed, the TDHF calculations of the quasifission process have yielded results that not only agree with the broad features of the experimental measurements but also shed insight into the relationship of the data to the properties of the participating nuclei. Such features include static deformation that induces dependence on the orientation of the nuclei with respect to the beam axis, shell effects that can predict the primary fragment charges, as well as the dependence of quasifission on neutron-rich nuclei. TDHF calculations give us the most probable reaction outcome for a given set of initial conditions (e.g., energy, impact parameter, orientation). However, quantum mechanically a collection of outcomes are possible for each of these initial conditions. In order to compute such distributions, one must go beyond TDHF and introduce methods to calculate distribution widths or fluctuations for these reactions. Much effort has been done to improve the standard mean-field approximation by incorporating the fluctuation mechanism into the description. At low energies, the mean-field fluctuations make the dominant contribution to the fluctuation mechanism of the collective motion. Various extensions have been developed to study the fluctuations of one-body observables. These include the time-dependent random phase approximation (TDRPA) approach of Balian and Vénéroni [68–72], the time-dependent generator coordinate method [73], or the stochastic mean-field (SMF) method [74, 75]. The effects of two-body dissipation on reactions of heavy systems using the time-dependent density matrix (TDDM) [76, 77] approach have also been recently reported [78, 79]. It is also possible to compute the probability to form a fragment with a given number of nucleons [80–83], but the resulting fragment mass and charge distributions are often underestimated in dissipative collisions [71, 84]. Recent reviews [47, 61] succinctly summarize the current state of TDHF (and its extensions) as it has been applied to various MNT reactions.

## 3. INSIGHTS FROM TDHF AND BEYOND

Experiments to discover new elements are notoriously difficult, with fusion evaporation residue (ER) cross-sections in pico-barns (for a recent experimental review see [85]). This cross-section is commonly expressed in the product form [86]

$$\sigma_{\rm ER} = \sum_{L=0}^{J_{\rm max}} \sigma_{\rm cap}(E_{\rm c.m.}, L) P_{\rm CN}(E^*, L) W_{\rm sur}(E^*, L), \qquad (1)$$

where $\sigma_{\rm cap}(E_{\rm c.m.}, L)$ is the capture cross-section at center of mass energy $E_{\rm c.m.}$ and orbital angular momentum $L$. $P_{\rm CN}$ is the probability that the composite system fuses into a compound nucleus (CN) rather than breaking up via quasifission, and $W_{\rm sur}$ is the survival probability of the fused system against fission. It is thus clear that to have a good handle on the evaporation residue cross-section estimates it is important to understand each of these terms as well as possible. In this endeavor both theory and experiment can have a complementary role. Among these reaction mechanisms quasifission and fusion-fission can be on the order of millibarns, making it easier to study experimentally. However, the extraction of the $P_{\rm CN}$ requires the proper disentangling of quasifission from fusion-fission [87–89] as it may be given by

$$P_{\rm CN} = \frac{\sigma_{fusion}}{\sigma_{capture}} = \frac{\sigma_{capture} - \sigma_{quasifission}}{\sigma_{capture}} . \qquad (2)$$

Of these cross-sections fusion-fission arises from an excited and equilibrated composite system and therefore peaked around equal mass breakup as calculated in a statistical approach [14, 16, 90–92]. On the other hand, quasifission, which is a faster process and thus not fully equilibrated, could also contribute to the equal breakup regime. Consequently, experimental analysis could use assistance from theory to discern between the two processes. The capture cross-section, being the sum of quasifission, fusion-fission, and evaporation residue is relatively easy to measure or calculate and TDHF predictions using the density-constrained TDHF (DC-TDHF) approach have shown to give a relatively good results [52, 93]. Below, we discuss various aspects of the progress done in studying quasifission using TDHF and its extensions.

### 3.1. Mass Angle Distributions

Study of quasifission together with capture is intimately related to understanding the process for forming a compound nucleus,

the quantity named $P_{\mathrm{CN}}$ in Equation (1) [87]. **Figure 1** shows the time-evolution of the $^{48}$Ca + $^{249}$Bk reaction at $E_{\mathrm{c.m.}} = 234$ MeV and orbital angular momentum $L/\hbar = 60$ [54] and the initial orientation of the $^{249}$Bk with respect to the collision axis $\beta = 135^{\circ}$. For this orbital angular momentum and energy TDHF theory predicts quasifission. As the nuclei approach each other, a neck forms between the two fragments which grows in size as the system begins to rotate. Due to the Coulomb repulsion and centrifugal forces, the dinuclear system elongates and forms a very long neck which eventually ruptures leading to two separated fragments. In this case the final fragments are $^{203}$Au and $^{94}$Sr. While the outcome of such reactions in a single TDHF evolution vary greatly depending on the initial conditions, analysis of the fragments' properties can begin to suggest general behavior for systems undergoing quasifission. For example, the composition of the reaction products can be influenced by shell effects in the outgoing fragments [54] which can be inferred by the slight pear shape of the light outgoing fragment at the point of scission in **Figure 1**.

However, the result from a single TDHF trajectory is difficult to extrapolate to the system as a whole so systematic investigations are often performed. As the reaction products predicted by TDHF give only the most probable outcome for any given collision geometry and energy, quantities like mass angle distributions produced by direct TDHF calculations result in collections of discrete points. By collecting data from large numbers of TDHF evolutions one can reveal deeper insights into the quasifission process. Recent studies of the $^{48}$Ca+$^{249}$Bk reaction at $E_{\mathrm{c.m.}} = 234$ MeV with the TDHF approach went beyond solely considering the extreme orientations of the deformed $^{249}$Bk nucleus by undertaking calculations spanning both a range of orientations and a range of angular momenta. The orientation of the deformed $^{249}$Bk was changed by 15° steps to cover the full range $(0, \pi)$ with orbital angular momentum $L$ changing in units of $10\hbar$ from 0 to quasielastic collisions. A total of 150 TDHF collisions were cataloged and analyzed. This allows for the study of correlations between, e.g., mass, angle, kinetic energy, as well as to predict distributions of neutron and proton numbers at the mean-field level.

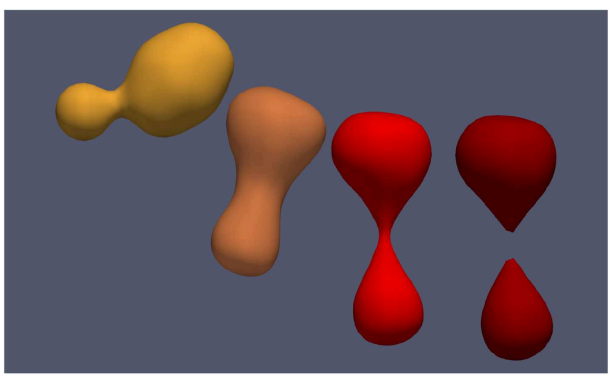

**FIGURE 1 |** Quasifission in the reaction $^{48}$Ca + $^{249}$Bk at $E_{\mathrm{c.m.}} = 234$ MeV and orbital angular momentum $L/h = 60$ and the orientation of the $^{249}$Bk with respect to the collision axis $\beta = 135^{\circ}$. The darkening of tones depict increasing excitation.

In **Figure 2A** we plot the mass angle distribution (MAD) for this reaction. **Figure 2B** shows the corresponding yield in arbitrary units as a function of the mass ratio $M_{\mathrm{R}} = M_1/(M_1 + M_2)$, where $M_1$ and $M_2$ are the masses of the final fragments. We note that the yields are strongly peaked at $M_R \sim 0.33$ and 0.67, with a full width at half maximum FWHM $\simeq 0.1$ corresponding to a standard deviation $\sigma_{M_R} \simeq 0.042$. The purpose of this figure is to compare quantitatively the relative contributions to the yields when going from central to peripheral collisions. For instance, we see that, because of the $2L + 1$ weighting factor, the most central collisions with $L \leq 20\hbar$, which are found at backward angles, have the smallest contribution to the total yield. Despite the discrete nature of the data, the tight grouping of points indicates a peak in production probability in certain mass regions which will be discussed further in the next section.

While nucleon transfer fluctuations can be calculated in TDHF, the ability to compare with experiment is still limited by the fact that TDHF vastly under predicts the widths of these distributions. Ideally, calculations would account for fluctuations in quantities, such as particle transfer, scattering angles, and total kinetic energies in the exit channel to more closely obtain what is observed experimentally. The simplest method for calculating these widths is the particle-number projection for the final fragments [81–83, 94]. However, these widths are still seriously underestimated. This is where extensions, such as TDRPA [68, 70–72] and SMF [74, 75] have proved to be vital theoretical tools for studying deep inelastic and quasifission reactions as both techniques provide methods to calculate both fluctuations and correlations of neutron and proton transfer based on a TDHF trajectory. **Figure 3** shows predicted mass angle and mass energy distributions for the $^{176}$Yb +$^{176}$ Yb system from TDRPA. Production cross-sections are obtained by integrating the probabilities calculated from the predicted fluctuations over a range of impact parameters. Such calculations further extend the insight offered by the base TDHF theory and promise to be of great use for designing future MNT experiments.

An alternate approach to TDRPA calculations for beyond the mean-field approximation can be formulated by incorporating the fluctuations in a manner that is consistent with the quantal fluctuation-dissipation relation, namely the SMF method [75]. In a number of studies it has been demonstrated that the SMF approach improves the description of nuclear collision dynamics by including fluctuation mechanisms of the collective motion. Most applications have been carried out in collisions where a di-nuclear structure is maintained. In this case it is possible to define macroscopic variables by a geometric projection procedure with the help of the window dynamics. The SMF approach gives rise to a Langevin description for the evolution of macroscopic variables. A limited study for central collisions was published in [95]. A general approach for non-central collisions has been developed [96] and used to calculate multi-nucleon transfer and heavy-isotope production in $^{136}$Xe + $^{208}$Pb collisions [97, 98].

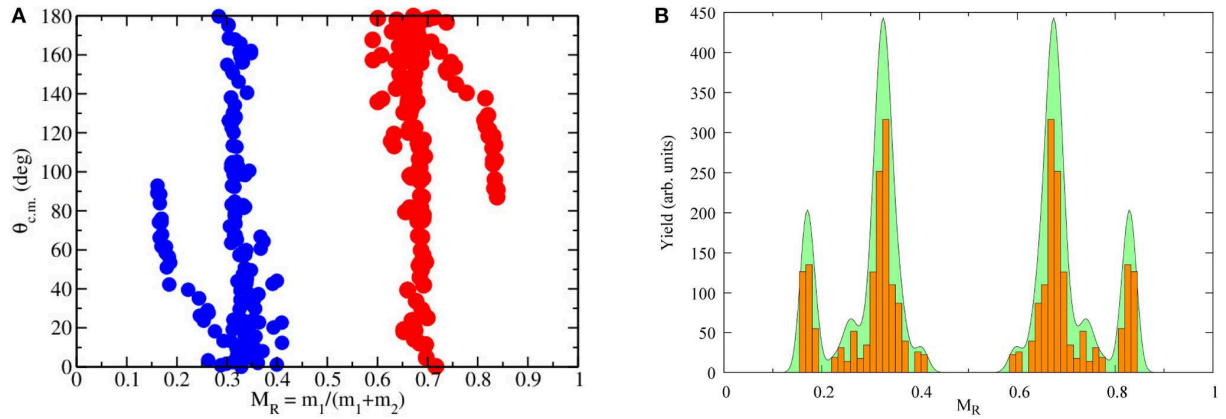


**FIGURE 2 | (A)** TDHF MADs for quasifission in the reaction $^{48}$Ca + $^{249}$Bk at $E_{\text{c.m.}} = 234$ MeV. **(B)** The yield (arb. units) as a function of mass ratio $M_R$ for the same reaction.

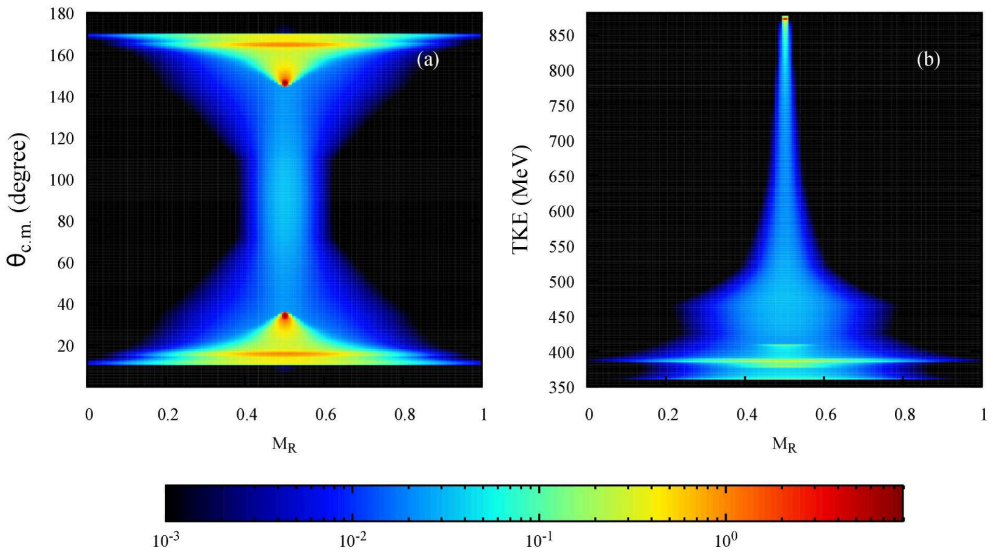


**FIGURE 3 |** Mass angle **(a)** and mass energy **(b)** distributions predicted by TDRPA for the $^{176}$Yb +$^{176}$ Yb collision in the side-side orientation at $E_{\text{c.m.}} = 880$ MeV. Units are in millibarns per degree **(a)** and millibarns per MeV **(b)**.

## 3.2. Deformed Shell Effects in Quasifission

Returning to the inference of shell effects influencing fragment production, this phenomenon can also be seen through thorough TDHF studies of a particular system and systematically analyzing the fragments produced for different impact parameters and deformation orientations. TDHF studies of quasifission dynamics have taught us that the dynamics of a system may be dominated by shell effects [47, 61]. An interesting finding of these TDHF studies is the prediction of the role of shell effects which favor the formation of magic fragments, in particular in the $Z = 82$ region in reactions involving an actinide collision partner [31]. This prediction has been later confirmed experimentally by Morjean et al. [99]. In addition, the calculations show that these shell effects strongly depend on the orientation of deformed actinide. Deformed shell effects in the region of $^{100}$Zr have also been invoked to interpret the outcome of TDHF simulations of $^{40,48}$Ca+$^{238}$U, $^{249}$Bk collisions [37, 52].

Such results are shown in **Figure 4** for the reaction $^{48}$Ca + $^{249}$Bk at $E_{\text{c.m.}} = 234$ MeV. Previous studies of the quasifission dynamics have taught us that dynamics may be dominated by shell effects [47, 54, 61]. These distributions are used to identify potential shell gaps driving quasifission. In **Figure 4A** we plot the charge yield obtained for this reaction. The right frame in **Figure 4B** shows the expected neutron yield distributions. One of the main driving features of this work was to show that shell effects similar to those observed in fission affect the formation of quasifission fragments. For this system the $Z = 82$ shell effect does not seem to play a major role contrary to previous TDHF observations for the Ca+U target projectile combinations. We also point out that mass-angle correlations could be used to experimentally isolate the fragments influenced by $N = 56$

octupole shell gaps [54, 100, 101]. We also find that more peripheral collisions are centered about the proton number $Z = 40$ confirming similar observations from past calculations [37] that the $^{100}$Zr region plays an important role in determining the lighter fragments due to the existence of strongly bound highly deformed Zr isotopes in this region [102].

## 3.3. Mass Equilibration

Due to long reaction times, the quasifission process is also suitable to study the time-scale of mass equilibration. **Figure 5A** shows the mass ratio, $M_R$, of fragment masses as a function of contact time $\tau$ (1 zs $= 10^{-21}$ s) at $E_{c.m.} = 234$ MeV for the $^{48}$Ca+$^{249}$Bk reaction. We define the contact time as the time interval between the time $t_1$ when the two nuclear surfaces (defined as isodensities with half the saturation density $\rho_0/2 = 0.07$ fm$^{-3}$) first merge into a single surface and the time $t_2$ when the surface densities detach again. The dashed line shows a characteristic fit of a function in the form of $c_0 + c_1 exp(-\tau/\tau_0)$. Based on the quality of the fit and whether we exclude some extreme points from the fit or not, we obtain equilibration times between 8 and 10 zs. In **Figure 5B** we plot the ratio of final and initial mass difference between projectile-like fragment, $A_{PLF}$, and target-like fragment, $A_{TLF}$, defined by,

$$\Delta A(\tau) = A_{TLF}(\tau) - A_{PLF}(\tau), \tag{3}$$

as a function of contact time $\tau$ for the $^{48}$Ca $+^{249}$ Bk system at $E_{c.m.} = 234$ MeV. The points correspond to the impact parameters used, ranging from head-on collisions to more peripheral collisions and the full range of orientations angles for $^{249}$Bk. The horizontal lines on the right side of the figure indicate the net number of particles transferred between the target and the projectile. We note that more mass transfer happens at longer contact times as expected. From this figure we can also observe similar time-scale for mass equilibration. From these results (and others not shown here) we can conclude that mass equilibration takes substantially longer in comparison to other quantities, such as the equilibration of total kinetic energy (TKE) or $N/Z$ equilibration. It is also interesting to observe that there is clustering of results around certain mass ratios. This is shown to

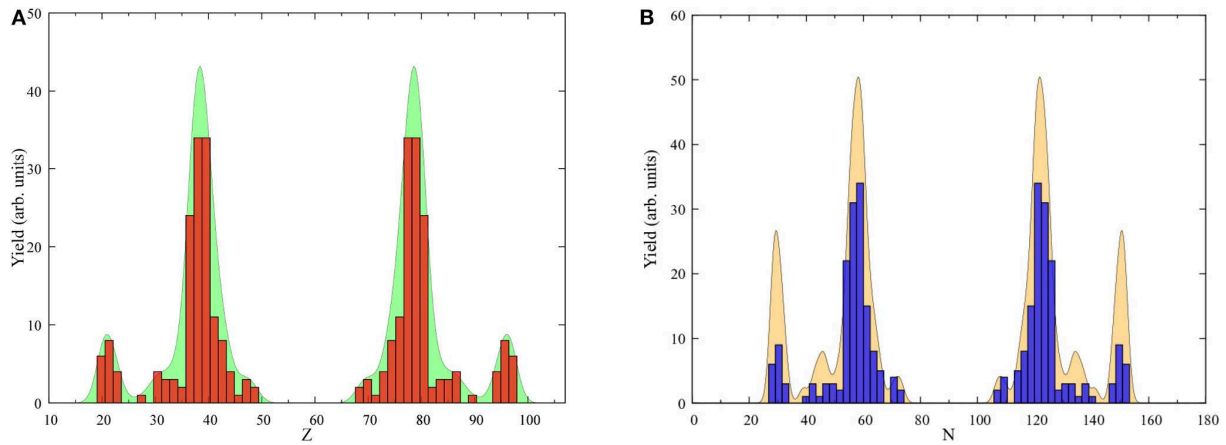


**FIGURE 4 | (A)** Fragment charge yield (histogram) and **(B)** Neutron yields for the reaction $^{48}$Ca + $^{249}$Bk at $E_{c.m.} = 234$ MeV. The smooth representations of the histograms are obtained by using a kernel density estimation with bandwidth 0.012.

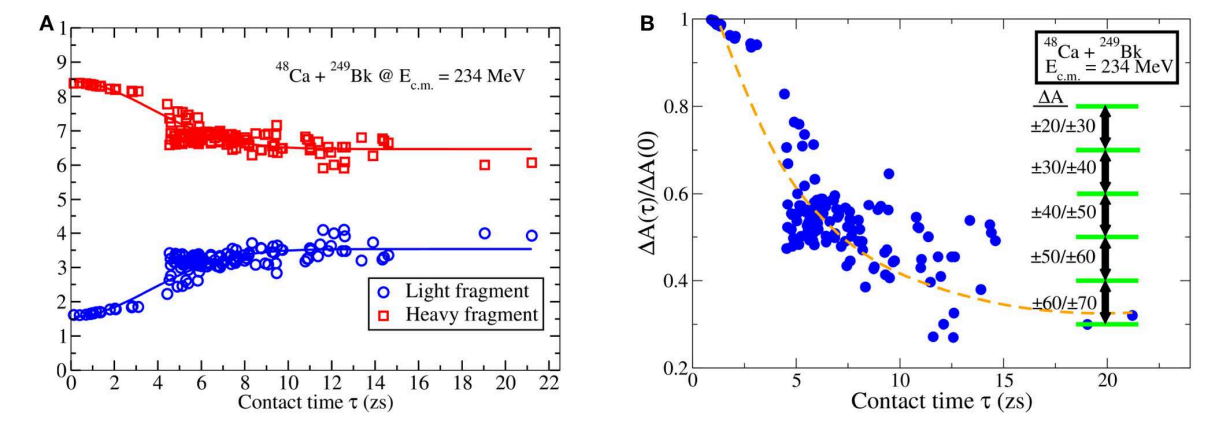


**FIGURE 5 | (A)** Mass ratio of fragment masses as a function of contact time at $E_{c.m.} = 234$ MeV for the reaction $^{48}$Ca + $^{249}$Bk. The solid lines show possible fits. **(B)** The ratio of the final and initial fragment masses as a function of contact time for the same reaction. The dashed line shows one possible fit.

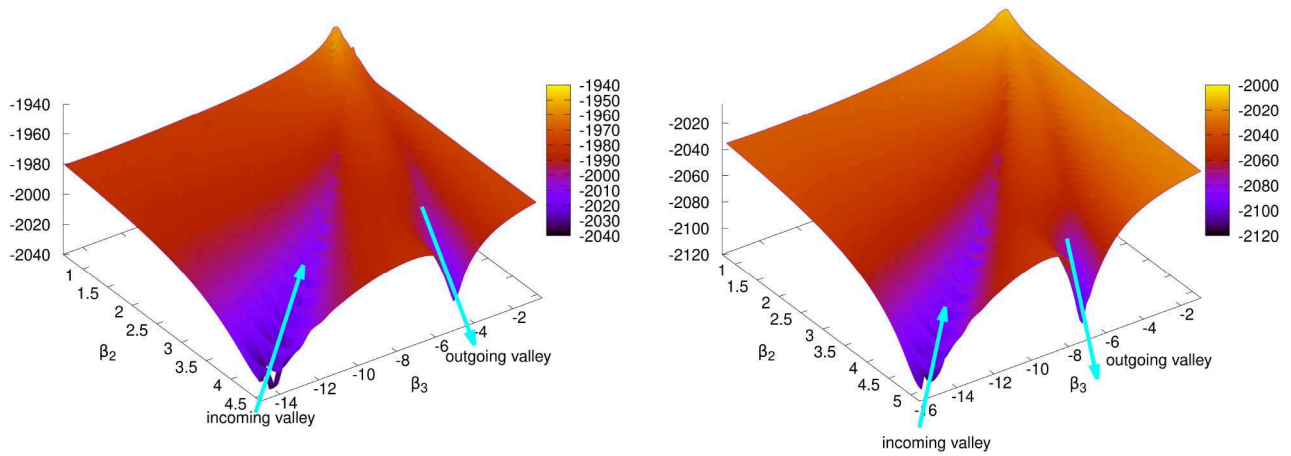


**FIGURE 6 |** Plotted are the PESs calculated, using the DC-TDHF method, for central collisions of $^{40,48}$Ca+$^{238}$U, with the equatorial orientation of $^{238}$U. The PES on the left is for the $^{40}$Ca+$^{238}$U system at $E_{\text{c.m.}} = 211$ MeV, while the PES on the right is for the $^{48}$Ca+$^{238}$U system at $E_{\text{c.m.}} = 203$ MeV.

be related to shell effects influencing the dynamical quasifission process in reference [54].

## 3.4. Collective Landscape

Quasifission and fusion-fission could be used to help map out the non-adiabatic collective landscape between the fusion entrance channel and the fission exit channel. It has been demonstrated that the TDHF theory is able to provide a good simulation of the quasifission process. Calculated time-scales of quasifission indicate that while fast quasifission events are dominant, much slower events resulting in a split with equal mass fragments have also been observed. One of the open experimental questions is how to distinguish quasifission from fusion-fission. This is important for the calculation of the evaporation residue formation probability in superheavy element searches. In **Figure 6** we show two such PESs calculated for the central collisions of the $^{40,48}$Ca+$^{238}$U systems, with the equatorial orientation of the $^{238}$U. The PES on the left of **Figure 6** is for the $^{40}$Ca+$^{238}$U system at $E_{\text{c.m.}} = 211$ MeV, while the PES on the right is for the $^{48}$Ca+$^{238}$U system at $E_{\text{c.m.}} = 203$ MeV. Surfaces in **Figure 6** are obtained by plotting the scattered $\beta_2$, $\beta_3$, and $E$ data obtained from the DC-TDHF calculations for the time-evolution of the nuclear density. Since the scattered plot uses an extrapolation algorithm points far from the valleys may not be precise. A number of observations can be made from the PESs shown in **Figure 6**. First, we clearly see the valley corresponding to the incoming trajectory of the two nuclei. As the system forms a composite the energy rises to maximum, but most likely never makes it to the saddle point. The system spends a lot of time around this area undergoing complex rearrangements and finally starts to proceed down the quasifission valley.

## 4. SUMMARY

Quasifission reactions have emerged as an interesting and vibrant area of research in recent years as they teach us about dynamical many-body effects at much longer time-scales compared to other heavy-ion reactions. The persistence of shell effects for these time-scales has opened the possibility to view quasifission as a doorway process to fusion-fission and perhaps even fission. This wide applicability positions quasifission as a vital process in understanding nuclear reactions across the board. In advancing toward this goal, the TDHF theory and its extensions have emerged as an excellent theoretical tool to study these reactions. The success of TDHF results in replicating experiment is particularly impressive as the calculations contain no free parameters. Through the efforts of both theoretical and experimental study of quasifission, we have been able to identify a number of underlying physical phenomena affecting nuclear reactions, such as the dependence on mass-angle distributions on the orientation of deformed targets and the strong influence of shell effects in determination of reaction products. These predictions take steps toward a more complete understanding of dynamical processes in nuclear reactions and may be crucial in determining such quantities as the $P_{\text{CN}}$ by calibrating experimental angular distributions to that of the theory. To this end methods and techniques to discern between quasifission and fusion-fission may emerge, paving the way for future studies of neutron-rich nuclei and superheavy elements.

## DATA AVAILABILITY STATEMENT

The datasets generated for this study are available on request to the corresponding author.

## AUTHOR CONTRIBUTIONS

All authors listed have made a substantial, direct and intellectual contribution to the work, and approved it for publication.

## FUNDING

This work was supported by the U.S. Department of Energy under grant No. DE-SC0013847.

## REFERENCES


1. Christoph E Düllmann, Rolf–Dietmar Herzberg, Witold Nazarewicz, Yuri Oganessian. Special issue on superheavy elements. *Nucl Phys A.* (2015) **944**:1–690. doi: 10.1016/j.nuclphysa.2015.11.004
2. Bender M, Rutz K, Reinhard PG, Maruhn JA, Greiner W. Shell structure of superheavy nuclei in self-consistent mean-field models. *Phys Rev C.* (1999) **60**:034304. doi: 10.1103/PhysRevC.60.034304
3. Nazarewicz W, Bender M, Ćwiok S, Heenen PH, Kruppa AT, Reinhard PG, et al. Theoretical description of superheavy nuclei. *Nucl Phys A.* (2002) **701**:165–71. doi: 10.1016/S0375-9474(01)01567-6
4. Ćwiok S, Heenen PH, Nazarewicz W. Shape coexistence and triaxiality in the superheavy nuclei. *Nature.* (2005) **433**:705–9. doi: 10.1038/nature03336
5. Pei JC, Nazarewicz W, Sheikh JA, Kerman AK. Fission barriers of compound superheavy nuclei. *Phys Rev Lett.* (2009) **102**:192501. doi: 10.1103/PhysRevLett.102.192501
6. Hofmann S, Heßberger FP, Ackermann D, Münzenberg G, Antalic S, Cagarda P, et al. New results on elements 111 and 112. *Eur Phys J A.* (2002) **14**:147–57. doi: 10.1140/epja/i2001-10119-x
7. Münzenberg G, Morita K. Synthesis of the heaviest nuclei in cold fusion reactions. *Nucl Phys A.* (2015) **944**:3–4. doi: 10.1016/j.nuclphysa.2015.06.007
8. Morita K. SHE research at RIKEN/GARIS. *Nucl Phys A.* (2015) **944**:30–61. doi: 10.1016/j.nuclphysa.2015.10.007
9. Oganessian YT, Utyonkov VK. Superheavy nuclei from $^{48}$Ca-induced reactions. *Nucl Phys A.* (2015) **944**:62–98. doi: 10.1016/j.nuclphysa.2015.07.003
10. Roberto JB, Alexander CW, Boll RA, Burns JD, Ezold JG, Felker LK, et al. Actinide targets for the synthesis of super-heavy elements. *Nucl Phys A.* (2015) **944**:99–116. doi: 10.1016/j.nuclphysa.2015.06.009
11. du Rietz R, Hinde DJ, Dasgupta M, Thomas RG, Gasques LR, Evers M, et al. Predominant time scales in fission processes in reactions of S, Ti and Ni with W: zeptosecond versus attosecond. *Phys Rev Lett.* (2011) **106**:052701. doi: 10.1103/PhysRevLett.106.052701
12. Töke J, Bock R, Dai GX, Gobbi A, Gralla S, Hildenbrand KD, et al. Quasi-fission: the mass-drift mode in heavy-ion reactions. *Nucl Phys A.* (1985) **440**:327–65. doi: 10.1016/0375-9474(85)90344-6
13. Shen WQ, Albinski J, Gobbi A, Gralla S, Hildenbrand KD, Herrmann N, et al. Fission and quasifission in U-induced reactions. *Phys Rev C.* (1987) **36**:115–42. doi: 10.1103/PhysRevC.36.115
14. Sahm CC, Clerc HG, Schmidt KH, Reisdorf W, Armbruster P, Heßberger FP, et al. Hindrance of fusion in central collisions of heavy symmetric nuclear systems. *Z Phys A.* (1984) **319**:113–8. doi: 10.1007/BF01415623
15. Gäggeler H, Sikkeland T, Wirth G, Brüchle W, Bögl W, Franz G, et al. Probing sub-barrier fusion and extra-push by measuring fermium evaporation residues in different heavy ion reactions. *Z Phys A.* (1984) **316**:291–307. doi: 10.1007/BF01439902
16. Schmidt KH, Morawek W. The conditions for the synthesis of heavy nuclei. *Rep Prog Phys.* (1991) **54**:949. doi: 10.1088/0034-4885/54/7/002
17. Hinde DJ, Hilscher D, Rossner H, Gebauer B, Lehmann M, Wilpert M. Neutron emission as a probe of fusion-fission and quasi-fission dynamics. *Phys Rev C.* (1992) **45**:1229–59. doi: 10.1103/PhysRevC.45.1229
18. Hinde DJ, Dasgupta M, Leigh JR, Lestone JP, Mein JC, Morton CR, et al. Fusion-fission versus quasifission: effect of nuclear orientation. *Phys Rev Lett.* (1995) **74**:1295–8. doi: 10.1103/PhysRevLett.74.1295
19. Hinde DJ, Dasgupta M, Leigh JR, Mein JC, Morton CR, Newton JO, et al. Conclusive evidence for the influence of nuclear orientation on quasifission. *Phys Rev C.* (1996) **53**:1290–300. doi: 10.1103/PhysRevC.53.1290
20. Itkis MG, Äystö J, Beghini S, Bogachev AA, Corradi L, Dorvaux O, et al. Shell effects in fission and quasi-fission of heavy and superheavy nuclei. *Nucl Phys A.* (2004) **734**:136–47. doi: 10.1016/j.nuclphysa.2004.01.022
21. Knyazheva GN, Kozulin EM, Sagaidak RN, A Yu Chizhov, Itkis MG, Kondratiev NA, et al. Quasifission processes in $^{40,48}$Ca + $^{144,154}$Sm reactions. *Phys Rev C.* (2007) **75**:064602. doi: 10.1103/PhysRevC.75.064602
22. Hinde DJ, Thomas RG, du Rietz R, Diaz-Torres A, Dasgupta M, Brown ML, et al. Disentangling effects of nuclear structure in heavy element formation. *Phys Rev Lett.* (2008) **100**:202701. doi: 10.1103/PhysRevLett.100.202701
23. Nishio K, Ikezoe H, Mitsuoka S, Nishinaka I, Nagame Y, Watanabe Y, et al. Effects of nuclear orientation on the mass distribution of fission fragments in the reaction of $^{36}$S + $^{238}$U. *Phys Rev C.* (2008) **77**:064607. doi: 10.1103/PhysRevC.77.064607
24. Kozulin EM, Knyazheva GN, Dmitriev SN, Itkis IM, Itkis MG, Loktev TA, et al. Shell effects in damped collisions of $^{88}$Sr with $^{176}$Yb at the Coulomb barrier energy. *Phys Rev C.* (2014) **89**:014614. doi: 10.1103/PhysRevC.89.014614
25. Itkis IM, Kozulin EM, Itkis MG, Knyazheva GN, Bogachev AA, Chernysheva EV, et al. Fission and quasifission modes in heavy-ion-induced reactions leading to the formation of Hs*. *Phys Rev C.* (2011) **83**:064613. doi: 10.1103/PhysRevC.83.064613
26. Lin CJ, du Rietz R, Hinde DJ, Dasgupta M, Thomas RG, Brown ML, et al. Systematic behavior of mass distributions in $^{48}$Ti-induced fission at near-barrier energies. *Phys Rev C.* (2012) **85**:014611. doi: 10.1103/PhysRevC.85.014611
27. Nishio K, Mitsuoka S, Nishinaka I, Makii H, Wakabayashi Y, Ikezoe H, et al. Fusion probabilities in the reactions $^{40,48}$Ca + $^{238}$U at energies around the Coulomb barrier. *Phys Rev C.* (2012) **86**:034608. doi: 10.1103/PhysRevC.86.034608
28. Simenel C, Hinde DJ, du Rietz R, Dasgupta M, Evers M, Lin CJ, et al. Influence of entrance-channel magicity and isospin on quasi-fission. *Phys Lett B.* (2012) **710**:607–11. doi: 10.1016/j.physletb.2012.03.063
29. du Rietz R, Williams E, Hinde DJ, Dasgupta M, Evers M, Lin CJ, et al. Mapping quasifission characteristics and timescales in heavy element formation reactions. *Phys Rev C.* (2013) **88**:054618. doi: 10.1103/PhysRevC.88.054618
30. Williams E, Hinde DJ, Dasgupta M, du Rietz R, Carter IP, Evers M, et al. Evolution of signatures of quasifission in reactions forming curium. *Phys Rev C.* (2013) **88**:034611. doi: 10.1103/PhysRevC.88.034611
31. Wakhle A, Simenel C, Hinde DJ, Dasgupta M, Evers M, Luong DH, et al. Interplay between quantum shells and orientation in quasifission. *Phys Rev Lett.* (2014) **113**:182502. doi: 10.1103/PhysRevLett.113.182502
32. Hammerton K, Kohley Z, Hinde DJ, Dasgupta M, Wakhle A, Williams E, et al. Reduced quasifission competition in fusion reactions forming neutron-rich heavy elements. *Phys Rev C.* (2015) **91**:041602(R). doi: 10.1103/PhysRevC.91.041602
33. Prasad E, Hinde DJ, Ramachandran K, Williams E, Dasgupta M, Carter IP, et al. Observation of mass-asymmetric fission of mercury nuclei in heavy ion fusion. *Phys Rev C.* (2015) **91**:064605. doi: 10.1103/PhysRevC.91.064605
34. Prasad E, Wakhle A, Hinde DJ, Williams E, Dasgupta M, Evers M, et al. Exploring quasifission characteristics for $^{34}$S + $^{232}$Th forming $^{266}$Sg. *Phys Rev C.* (2016) **93**:024607. doi: 10.1103/PhysRevC.93.024607
35. Back BB, Fernandez PB, Glagola BG, Henderson D, Kaufman S, Keller JG, et al. Entrance-channel effects in quasifission reactions. *Phys Rev C.* (1996) **53**:1734–44. doi: 10.1103/PhysRevC.53.1734
36. Umar AS, Oberacker VE. Dynamical deformation effects in subbarrier fusion of $^{64}$Ni + $^{132}$Sn. *Phys Rev C.* (2006) **74**:061601. doi: 10.1103/PhysRevC.74.061601
37. Oberacker VE, Umar AS, Simenel C. Dissipative dynamics in quasifission. *Phys Rev C.* (2014) **90**:054605. doi: 10.1103/PhysRevC.90.054605
38. Morjean M, Jacquet D, Charvet JL, L'Hoir A, Laget M, Parlog M, et al. Fission time measurements: a new probe into superheavy element stability. *Phys Rev Lett.* (2008) **101**:072701. doi: 10.1103/PhysRevLett.101.072701
39. Frégeau MO, Jacquet D, Morjean M, Bonnet E, Chbihi A, Frankland JD, et al. X-ray fluorescence from the element with atomic number $Z = 120$. *Phys Rev Lett.* (2012) **108**:122701. doi: 10.1103/PhysRevLett.108.122701
40. Kozulin EM, Knyazheva GN, Itkis IM, Itkis MG, Bogachev AA, Krupa L, et al. Investigation of the reaction $^{64}$Ni + $^{238}$U being an option of synthesizing element 120. *Phys Lett B.* (2010) **686**:227–32. doi: 10.1016/j.physletb.2010.02.041
41. Adamian GG, Antonenko NV, Scheid W. Characteristics of quasifission products within the dinuclear system model. *Phys Rev C.* (2003) **68**:034601. doi: 10.1103/PhysRevC.68.034601
42. Zagrebaev v, Greiner w. Shell effects in damped collisions: a new way to superheavies. *J Phys G.* (2007) **34**:2265. doi: 10.1088/0954-3899/34/11/004
43. Aritomo Y. Analysis of dynamical processes using the mass distribution of fission fragments in heavy-ion reactions. *Phys Rev C.* (2009) **80**:064604. doi: 10.1103/PhysRevC.80.064604

44. Zhao K, Li Z, Zhang Y, Wang N, Li Q, Shen C, et al. Production of unknown neutron–rich isotopes in $^{238}$U + $^{238}$U collisions at near–barrier energy. *Phys Rev C.* (2016) **94**:024601. doi: 10.1103/PhysRevC.94.024601
45. Sekizawa K, Yabana K. Time-dependent Hartree-Fock calculations for multinucleon transfer and quasifission processes in the $^{64}$Ni + $^{238}$U reaction. *Phys Rev C.* (2016) **93**:054616. doi: 10.1103/PhysRevC.93.054616
46. Sekizawa K. Enhanced nucleon transfer in tip collisions of $^{238}$U + $^{124}$Sn. *Phys Rev C.* (2017) **96**:041601(R). doi: 10.1103/PhysRevC.96.041601
47. Sekizawa K. TDHF theory and its extensions for the multinucleon transfer reaction: a mini review. *Front Phys.* (2019) **7**:20. doi: 10.3389/fphy.2019.00020
48. David J Kedziora, Cédric Simenel. New inverse quasifission mechanism to produce neutron-rich transfermium nuclei. *Phys Rev C.* (2010) **81**:044613. doi: 10.1103/PhysRevC.81.044613
49. Goddard PM, Stevenson PD, Rios A. Fission dynamics within time-dependent Hartree-Fock: deformation-induced fission. *Phys Rev C.* (2015) **92**:054610. doi: 10.1103/PhysRevC.92.054610
50. Umar AS, Oberacker VE, Simenel C. Shape evolution and collective dynamics of quasifission in the time-dependent Hartree-Fock approach. *Phys Rev C.* (2015) **92**:024621. doi: 10.1103/PhysRevC.92.024621
51. Umar AS, Oberacker VE. Time-dependent HF approach to SHE dynamics. *Nucl Phys A.* (2015) **944**:238–56. doi: 10.1016/j.nuclphysa.2015.02.011
52. Umar AS, Oberacker VE, Simenel C. Fusion and quasifission dynamics in the reactions $^{48}$Ca+$^{249}$Bk and $^{50}$Ti+$^{249}$Bk using a time-dependent Hartree-Fock approach. *Phys Rev C.* (2016) **94**:024605. doi: 10.1103/PhysRevC.94.024605
53. Wang N, Guo L. New neutron-rich isotope production in $^{154}$Sm + $^{160}$Gd. *Phys Lett B.* (2016) **760**:236–41. doi: 10.1016/j.physletb.2016.06.073
54. Godbey K, Umar AS, Simenel C. Deformed shell effects in $^{48}$Ca + $^{249}$Bk quasifission fragments. *Phys Rev C.* (2019) **100**:024610. doi: 10.1103/PhysRevC.100.024610
55. Sekizawa K. Microscopic description of production cross sections including deexcitation effects. *Phys Rev C.* (2017) **96**:014615. doi: 10.1103/PhysRevC.96.014615
56. Sekizawa K, Hagino K. Time-dependent Hartree-Fock plus Langevin approach for hot fusion reactions to synthesize the $Z = 120$ superheavy element. *Phys Rev C.* (2019) **99**:051602. doi: 10.1103/PhysRevC.99.051602
57. Umar AS, Oberacker VE, Maruhn JA, Reinhard PG. Microscopic calculation of precompound excitation energies for heavy-ion collisions. *Phys Rev C.* (2009) **80**:041601. doi: 10.1103/PhysRevC.80.041601
58. Umar AS, Simenel C, Ye W. Transport properties of isospin asymmetric nuclear matter using the time-dependent Hartree–Fock method. *Phys Rev C.* (2017) **96**:024625. doi: 10.1103/PhysRevC.96.024625
59. Guo L, Shen C, Yu C, Wu Z. Isotopic trends of quasifission and fusion-fission in the reactions $^{48}$Ca + $^{239,244}$Pu. *Phys Rev C.* (2018) **98**:064609. doi: 10.1103/PhysRevC.98.064609
60. Jiang X, Wang N. Probing the production mechanism of neutron-rich nuclei in multinucleon transfer reactions. *Phys Rev C.* (2020) **101**:014604. doi: 10.1103/PhysRevC.101.014604
61. Simenel C, Umar AS. Heavy-ion collisions and fission dynamics with the time–dependent Hartree-Fock theory and its extensions. *Prog Part Nucl Phys.* (2018) **103**:19–66. doi: 10.1016/j.ppnp.2018.07.002
62. Negele JW. The mean-field theory of nuclear-structure and dynamics. *Rev Mod Phys.* (1982) **54**:913–1015. doi: 10.1103/RevModPhys.54.913
63. Simenel C. Nuclear quantum many-body dynamics. *Eur Phys J A.* (2012) **48**:152. doi: 10.1140/epja/i2012-12152-0
64. Stevenson PD, Barton MC. Low–energy heavy-ion reactions and the Skyrme effective interaction. *Prog Part Nucl Phys.* (2019) **104**:142–64. doi: 10.1016/j.ppnp.2018.09.002
65. Zagrebaev VI, Karpov AV, Greiner W. Possibilities for synthesis of new isotopes of superheavy elements in fusion reactions. *Phys Rev C.* (2012) **85**:014608. doi: 10.1103/PhysRevC.85.014608
66. Karpov AV, Saiko VV. Modeling near-barrier collisions of heavy ions based on a Langevin-type approach. *Phys Rev C.* (2017) **96**:024618. doi: 10.1103/PhysRevC.96.024618
67. Saiko VV, Karpov AV. Analysis of multinucleon transfer reactions with spherical and statically deformed nuclei using a Langevin-type approach. *Phys Rev C.* (2019) **99**:014613. doi: 10.1103/PhysRevC.99.014613
68. Roger Balian, Marcel Vénéroni. Fluctuations in a time-dependent mean-field approach. *Phys Lett B.* (1984) **136**:301–6. doi: 10.1016/0370-2693(84)92008-2
69. Balian R, Vénéroni M. Correlations and fluctuations in static and dynamic mean-field approaches. *Ann Phys.* (1992) **216**:351. doi: 10.1016/0003-4916(92)90181-K
70. Broomfield JMA. *Calculations of Mass Distributions Using the Balian-Vénéroni Variational Approach*. Guildford: University of Surrey (2009).
71. Simenel C. Particle-number fluctuations and correlations in transfer reactions obtained using the Balian-Vénéroni variational principle. *Phys Rev Lett.* (2011) **106**:112502. doi: 10.1103/PhysRevLett.106.112502
72. Williams E, Sekizawa K, Hinde DJ, Simenel C, Dasgupta M, Carter IP, et al. Exploring zeptosecond quantum equilibration dynamics: from deep-inelastic to fusion-fission outcomes in $^{58}$Ni + $^{60}$Ni reactions. *Phys Rev Lett.* (2018) **120**:022501. doi: 10.1103/PhysRevLett.120.022501
73. Goutte H, Berger JF, Casoli P, Gogny D. Microscopic approach of fission dynamics applied to fragment kinetic energy and mass distributions in $^{238}$U. *Phys Rev C.* (2005) **71**:024316. doi: 10.1103/PhysRevC.71.024316
74. Ayik S. A stochastic mean-field approach for nuclear dynamics. *Phys Lett B.* (2008) **658**:174. doi: 10.1016/j.physletb.2007.09.072
75. Lacroix D, Ayik S. Stochastic quantum dynamics beyond mean field. *Eur Phys J A.* (2014) **50**:95. doi: 10.1140/epja/i2014-14095-8
76. Tohyama M. Two-body collision effects on the low-L fusion window in $^{16}$O + $^{16}$O reactions. *Phys Lett B.* (1985) **160**:235–8. doi: 10.1016/0370-2693(85)91317-6
77. Tohyama M, Umar AS. Quadrupole resonances in unstable oxygen isotopes in time-dependent density-matrix formalism. *Phys Lett B.* (2002) **549**:72–8. doi: 10.1016/S0370-2693(02)02885-X
78. Assié M, Lacroix D. Probing neutron correlations through nuclear breakup. *Phys Rev Lett.* (2009) **102**:202501. doi: 10.1103/PhysRevLett.102.202501
79. Tohyama M, Umar AS. Two-body dissipation effects on the synthesis of superheavy elements. *Phys Rev C.* (2016) **93**:034607. doi: 10.1103/PhysRevC.93.034607
80. Koonin SE, Davies KTR, Maruhn-Rezwani V, Feldmeier H, Krieger SJ, Negele JW. Time-dependent Hartree-Fock calculations for $^{16}$O + $^{16}$O and $^{40}$Ca + $^{40}$Ca reactions. *Phys Rev C.* (1977) **15**:1359–74. doi: 10.1103/PhysRevC.15.1359
81. Simenel C. Particle transfer reactions with the time-dependent Hartree-Fock theory using a particle number projection technique. *Phys Rev Lett.* (2010) **105**:192701. doi: 10.1103/PhysRevLett.105.192701
82. Sekizawa K, Yabana K. Time-dependent Hartree-Fock calculations for multinucleon transfer processes in $^{40,48}$Ca + $^{124}$Sn, $^{40}$Ca + $^{208}$Pb, and $^{58}$Ni + $^{208}$Pb reactions. *Phys Rev C.* (2013) **88**:014614. doi: 10.1103/PhysRevC.88.014614
83. Scamps G, Lacroix D. Effect of pairing on one- and two-nucleon transfer below the Coulomb barrier: a time-dependent microscopic description. *Phys Rev C.* (2013) **87**:014605. doi: 10.1103/PhysRevC.87.014605
84. Dasso CH, Dossing T, Pauli HC. On the mass distribution in time-dependent Hartree-Fock calculations of heavy-ion collisions. *Z Phys A.* (1979) **289**:395–8. doi: 10.1007/BF01409391
85. Vardaci E, Itkis MG, Itkis IM, Knyazheva G, Kozulin EM. Fission and quasifission toward the superheavy mass region. *J Phys G.* (2019) **46**:103002. doi: 10.1088/1361-6471/ab3118
86. Loveland W. Synthesis of transactinide nuclei using radioactive beams. *Phys Rev C.* (2007) **76**:014612. doi: 10.1103/PhysRevC.76.014612
87. Yanez R, Loveland W, Barrett JS, Yao L, Back BB, Zhu S, et al. Measurement of the fusion probability, $P_{CN}$, for hot fusion reactions. *Phys Rev C.* (2013) **88**:014606. doi: 10.1103/PhysRevC.88.014606
88. Zhu L, Su J, Xie WJ, Zhang FS. Study of the dynamical potential barriers in heavy ion collisions. *Nucl Phys A.* (2013) **915**:90–105. doi: 10.1016/j.nuclphysa.2013.07.003
89. Schmitt C, Mazurek K, Nadtochy PN. New procedure to determine the mass-angle correlation of quasifission. *Phys Rev C.* (2019) **100**:064606. doi: 10.1103/PhysRevC.100.064606
90. Back BB. Complete fusion and quasifission in reactions between heavy ions. *Phys Rev C.* (1985) **31**:2104–12. doi: 10.1103/PhysRevC.31.2104
91. Back BB, Esbensen H, Jiang CL, Rehm KE. Recent developments in heavy-ion fusion reactions. *Rev Mod Phys.* (2014) **86**:317–60. doi: 10.1103/RevModPhys.86.317

92. Schmidt KH, Jurado B. Review on the progress in nuclear fission–experimental methods and theoretical descriptions. *Rep Prog Phys.* (2018) **81**:106301. doi: 10.1088/1361-6633/aacfa7
93. Umar AS, Oberacker VE, Maruhn JA, Reinhard PG. Entrance channel dynamics of hot and cold fusion reactions leading to superheavy elements. *Phys Rev C.* (2010) **81**:064607. doi: 10.1103/PhysRevC.81.064607
94. Scamps G, Hashimoto Y. Transfer probabilities for the reactions $^{14,20}$O+$^{20}$O in terms of multiple time-dependent Hartree-Fock-Bogoliubov trajectories. *Phys Rev C.* (2017) **96**:031602. doi: 10.1103/PhysRevC.96.031602
95. Ayik S, Yilmaz O, Yilmaz B, Umar AS. Quantal nucleon diffusion: central collisions of symmetric nuclei. *Phys Rev C.* (2016) **94**:044624. doi: 10.1103/PhysRevC.94.044624
96. Ayik S, Yilmaz B, Yilmaz O, Umar AS. Quantal diffusion description of multinucleon transfers in heavy–ion collisions. *Phys Rev C.* (2018) **97**:054618. doi: 10.1103/PhysRevC.97.054618
97. Ayik S, Yilmaz B, Yilmaz O, Umar AS. Quantal diffusion approach for multinucleon transfers in Xe+Pb collisions. *Phys Rev C.* (2019) **100**:014609. doi: 10.1103/PhysRevC.100.014609
98. Ayik S, Yilmaz O, Yilmaz B, Umar AS. Heavy-isotope production in $^{136}$Xe + $^{208}$Pb collisions at $E_{\mathrm{c.m.}} = 514$ MeV. *Phys Rev C.* (2019) **100**:044614. doi: 10.1103/PhysRevC.100.044614
99. Morjean M, Hinde DJ, Simenel C, Jeung DY, Airiau M, Cook KJ, et al. Evidence for the role of proton shell closure in quasifission reactions from X-ray fluorescence of mass-identified fragments. *Phys Rev Lett.* (2017) **119**:222502. doi: 10.1103/PhysRevLett.119.222502
100. Scamps G, Simenel C. Impact of pear-shaped fission fragments on mass-asymmetric fission in actinides. *Nature.* (2018) **564**:382–5. doi: 10.1038/s41586-018-0780-0
101. Scamps G, Simenel C. Effect of shell structure on the fission of sub-lead nuclei. *Phys Rev C.* (2019) **100**:041602. doi: 10.1103/PhysRevC.100.041602
102. Blazkiewicz A, Oberacker VE, Umar AS, Stoitsov M. Coordinate space Hartree-Fock-Bogoliubov calculations for the zirconium isotope chain up to the two-neutron drip line. *Phys Rev C.* (2005) **71**:054321. doi: 10.1103/PhysRevC.71.054321


**Conflict of Interest:** The authors declare that the research was conducted in the absence of any commercial or financial relationships that could be construed as a potential conflict of interest.

The handling editor declared a past co-authorship with one of the authors AU.

frontiers in Physics

MINI REVIEW
published: 28 February 2020
doi: 10.3389/fphy.2020.00014

# Fusion Dynamics of Low-Energy Heavy-Ion Collisions for Production of Superheavy Nuclei

*Xiao Jun Bao**

*Department of Physics, Collaborative Innovation Center for Quantum Effects, and Key Laboratory of Low Dimensional Quantum Structures and Quantum Control of Ministry of Education, Hunan Normal University, Changsha, China*

One of the major motivations for low-energy heavy-ion collision is the synthesis of superheavy nuclei. Based on the following two main aspects, various theoretical and experimental studies have been performed to explore the fusion dynamical process of superheavy nuclei production. The first reason is to elucidate and analyze the synthesis mechanism of superheavy nuclei; the other is to search the favorable incident energy and the best combination of projectile and target to produce new superheavy elements and isotopes of superheavy elements.

**Keywords: low-energy heavy-ion collisions, superheavy nuclei production, fusion dynamics, transport theory, TDHF model**

OPEN ACCESS

***Edited by:***
*Cedric Simenel,*
*Australian National University, Australia*

***Reviewed by:***
*Sait Umar,*
*Vanderbilt University, United States*
*Nikolai Antonenko,*
*Joint Institute for Nuclear Research (JINR), Russia*

***Correspondence:**
*Xiao Jun Bao*
*baoxiaojun@hunnu.edu.cn*

***Specialty section:***
*This article was submitted to Nuclear Physics, a section of the journal Frontiers in Physics*

***Received:*** *21 November 2019*
***Accepted:*** *16 January 2020*
***Published:*** *28 February 2020*

***Citation:***
*Bao XJ (2020) Fusion Dynamics of Low-Energy Heavy-Ion Collisions for Production of Superheavy Nuclei. Front. Phys. 8:14. doi: 10.3389/fphy.2020.00014*

## 1. INTRODUCTION

The maximum mass and charge of a nucleus is a long-standing fundamental problem in nuclear physics [1, 2]. Pioneer studies have theoretically predicted the "island of stability" of superheavy nuclei (SHN). The macroscopic-microscopic models predicted $^{298}$Fl to be the double magic nucleus [3–7]. However, results of the self-consistent models showed that the closed shell of $Z = 114$ becomes weaker, and $Z = 114$ is replaced by $Z = 120$ or 126 [8–13].

The production process of superheavy nuclei is a very complicated dynamical problem [14]. Many theoretical models have been developed to explain the experimental data. On one hand, the synthesis mechanism of superheavy nuclei needs to be elucidated [15–21]. Different approaches are devoted to calculate and analyze the fusion probability and the distribution of quasifission fragments [15–41]. However, none of them has absolute advantage. On the other hand, in order to produce the new superheavy elements, or isotopes of superheavy elements, the favorable incident energy and the best combination of projectile and target should be evaluated.

The extended nuclear landscape allows us to investigate the nuclear structure of superheavy nuclei and the nuclear reaction mechanism. To search for the optimal condition of synthesis, the influence of the entrance channel [29, 42, 43] and the isospin of heavy colliding nuclei [44–46] on the evaporation residual cross section have been studied systematically in many works. The predictions of the possible way to synthesize the new superheavy elements $Z = 119$ and 120 have also been carried out [17, 47–52].

## 2. EXPERIMENTAL PROGRESS

Producing superheavy nuclei in the laboratory is one of the major motivations of low-energy heavy-ion physics [1, 2, 53–55]. Over the past 30 years, great progress has been achieved for superheavy nuclei production in experimental studies [53–55]. The experimental trends $\alpha$ decay half-lives, and the evaporation residue cross sections of the superheavy nuclei show

that the stability of superheavy nuclei increases as the neutron number approaches the closed neutron shell closure $N = 184$. However, the location of the "island of stability" has not been determined by experiment. Up until now, based on the fusion-evaporation reaction, the superheavy nuclei with charge numbers in the range of $Z = 104118$ have been synthesized successfully.

The superheavy elements $Z = 107 - 112$ was first synthesized by using the cold fusion reactions [1, 53, 54, 56, 57]. The excitation energy range of the formed compound nucleus was 10–18 MeV. The measurement of the evaporation residue cross section decreased dramatically from $Z = 107$ to $Z = 113$. Moreover, the final evaporated residual nuclei were extremely neutron deficient. Experiments of producing superheavy nuclei by cold fusion have been repeated and verified by other laboratories [54, 58, 59].

The $^{48}$Ca-induced hot-fusion reactions were used to synthesize $Z = 112 - 118$ superheavy nuclei in experiment [54, 55, 60]. From the measurement of evaporation residue cross sections, we found that there was no significant difference from $Z = 112$–118, and the values of the evaporation residual cross sections were all in the order of picobarn. Experiments based on hot fusion for synthesizing $Z = 112$ and 114–117 superheavy nuclei have been verified by other laboratories [60].

To search for the optimal condition of the superheavy nuclei production, various experiments have been performed to study the entrance channel effect on the evaporation residual cross section [61–65]. Recently, the isospin effect of the target nucleus on the evaporation residue cross section has been explored [66–68]. Some laboratories have also attempted to synthesize the $Z = 119$ and 120 superheavy elements by using hot fusion [69, 70].

Experimentally, the measurement of fusion probability is required to distinguish quasifission between fusion-fission and fast fission [71–76]. The experimental characteristics of the quasifission process are different from the fusion-fission process [77]. Therefore, it is important to distinguish the fusion and quasifission fragments for a better understanding of the fusion mechanism.

## 3. THEORETICAL DESCRIPTION OF FUSION REACTIONS

Theoretically, the synthesis process of superheavy nuclei can be divided into three stages [39]. A schematic diagram for this process is shown in **Figure 1**. The first stage is the capture process, which can be evaluated by the capture cross section. The second stage is that the dinuclear system evolves from the touching configuration to the formation of the compound nucleus, which can be evaluated by the fusion probability. The last stage is where the excited compound nucleus cools down through emitting neutrons or fission, and this can be evaluated by the survival probability. Finally, a very small evaporation residue cross section is obtained for the superheavy nuclei production. The evaporation residue cross section can be expressed as [39],

$$\sigma_{ER}(E_{c.m.}) = \sum_{J} \sigma_{cap}(E_{c.m.}, J) P_{CN}(E_{c.m.}, J) W_{sur}(E_{c.m.}, J), \quad (1)$$

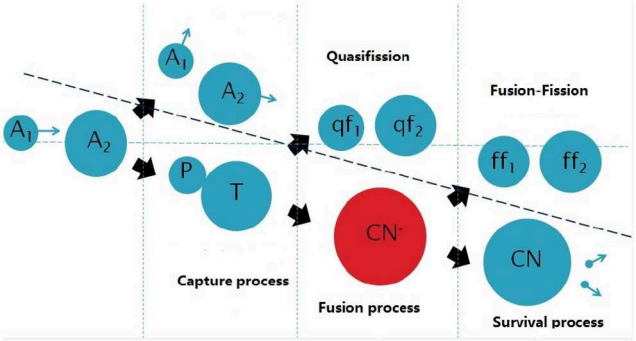


**FIGURE 1 |** (Color online) Schematic diagram of production of superheavy nuclei.

where $E_{c.m.}$ is the incident energy in the center-of-mass frame.

### 3.1. Capture Cross Sections

For the low-energy heavy-ion collision, the capture cross section from the sub-barrier region to above the Coulomb barrier is an important issue for theoretical and experimental studies [78–83]. One of reasons is that the overall uncertainties in predicting superheavy nuclei production are associated with the calculations of capture cross sections [50, 84, 85].

The capture process is closely related to the nuclear structure of the interacting nuclei [86–97]. This is because the nucleus-nucleus potential contains nuclear structure information. To precisely describe the measurements of capture cross sections, the nucleus-nucleus interaction potential is the most important input quantity. In addition, the heavy-ion capture process is intimately linked to nuclear deformation [87, 88]. Thus, the nuclear deformation must be reliable to some extent.

Theoretically, the capture cross section is one of the important components in the synthesis of superheavy nuclei. The capture cross section have been explored extensively [82–84] from light to superheavy by averaging the penetration probability over barrier heights. Most of them have tested a number of experimental data of capture cross sections, however, these experimental data do not contain the capture cross sections of superheavy nuclei [84]. Therefore, it is very important to examine carefully the capture process for the study of the synthesis mechanism of superheavy nuclei.

Usually, the capture cross section $\sigma_{cap}$ is mainly calculated with an empirical coupled-channel approach for the superheavy nuclei production [17, 44–52]. From a theoretical point of view, one of the powerful methods is to solve coupled-channels equations numerically. This may help us to understand the influence of the couplings between nuclear intrinsic degrees of freedom and the relative motion on capture cross sections.

Recently, the quantum diffusion approach [98–101] has also been used to calculate capture cross sections. This model takes into consideration the influence of fluctuations and dissipation effects on capture cross sections. The nuclear deformation effects and mutual orientations of the colliding nuclei are taken into account through using a double folding potential, and

the influence of two neutrons transfer onto the sub-barrier capture through the change of the deformations of the colliding nuclei [100].

Another powerful theoretical tool is to calculate the capture cross section by the time-dependent Hartree Fock (TDHF) method. Recently, the pioneering work of studying capture cross section based on TDHF has been completed for the $^{40}$Ca+$^{238}$U reaction [102]. In addition, Umar et al. found that the capture cross sections calculated by TDHF method agreed with the experimental data within 20% [103].

## 3.2. Fusion Dynamics

In order to explain the fusion dynamics process (the second stage), various theoretical approaches and models have been developed. The simplification can be made in different ways, and, as a result, we can obtain different theoretical pictures for the same real nuclear process. Some of the models can be roughly divided into two types. The first type is based on transport equations to describe the fusion dynamics process [15–41]. The second one is based on the time-dependent Hartree Fock method to describe the mainly experimental features in the process of fusion dynamics [104–115].

The first approach is that the multitude of degrees of freedom are decomposed into a dominating collective degree of freedom and other degrees (non-collective) of freedom. Therefore, the dissipative processes are introduced to account for the coupling between the collective motions and the intrinsic motions of the freedom of the system. Many models based on transport equations have been developed, and they assumed that the main characteristics of fusion dynamics process can be described by using the main collective degrees of freedom.

On the one hand, after eliminating the intrinsic motion, a stochastic equation can be derived theoretically. Many models adopted the Langevin forces (Langevin equation) to describe stochastic characteristics of the coupling between collective motions and intrinsic degrees of freedom. One can calculate a bundle of trajectories by solving a stochastic equation [16, 17, 28, 31, 35, 36].

On the other hand, through eliminating the intrinsic degrees of freedom, a diffusion equation can be derived theoretically to describe the distribution of collective degrees of freedom in the phase space [19–21, 27, 29, 29, 30, 32, 41–43, 46, 47, 49, 51, 116, 117]. Diffusion equations (the master equation, Smoluchowski equation, etc.,) may be used to describe the transport process of collective degrees of freedom in phase space.

The second approach is the time-dependent Hartree Fock method. The basic idea of this method is that the mean field produced by all nucleons not only determines the intrinsic motion of a single particle but also describes the evolution characteristics of collective degrees. TDHF calculations may be used to compute the ratio of fusion cross sections to capture cross sections. In addition, the TDHF method may be used to explore the effect of the orientation of the projectile and the target at the contact point, and the role of the nuclear shell structure and tensor force [104–115].

## 3.3. Fusion Mechanism

For the real fusion dynamics process, a theoretical model may be considered as a collection of theoretical assumptions. Up to now, there have been proposed fusion mechanisms that are incompatible with the compound nucleus formation. One assumption is that all the nucleons are immediately collectivized into one superdeformed mononucleus. Then, the dynamic evolution behavior of the superdeformed mononucleus can be described by the equation of motion or transport theory [15–17, 33, 34, 118]. The macroscopic dynamical model is the first model to describe the fusion mechanism based on the idea of forming one superdeformed mononucleus [15]. However, it encountered serious difficulties in attempts to describe evaporation residue cross sections for the synthesis of superheavy nuclei.

As the macroscopic dynamical models, the same approximations are used in the fluctuation-dissipation model [16, 118], the two-step model [17], and the fusion-by-diffusion model [33, 34]. But two significant improvements are taken into account for the description of the fusion-dynamics mechanism: shell effects in the calculation of the potential energy surface of the reaction system and statistical fluctuations in the interaction of colliding nuclei. These improvements permit one to describe the evaporation residue cross section of superheavy nuclei, the mass distribution of quasifission, and fusion-fission products [16, 17, 33, 34, 118, 119].

Another assumption is that two touching nuclei always keeps its own identity with their ground state characteristics and deformations (dinuclear system model) [19–21, 29], fusion is achieved by means of nucleon transfer. However, the real situation is due to strong Coulomb and nuclear interactions between projectile and target; the dinuclear system should be gradually deformed [30, 48]. This assumption has recently been improved upon. The coupling of the deformations evolution of project and target and the nucleon transfer has been studied numerically [120, 121]. The calculated results for the cold and hot fusion reactions by using the dinuclear system model match well with the available experimental data [20, 27, 29, 29, 30, 32, 41–43, 46, 47, 49, 51, 116, 117]. The fusion probability and the distribution of the quasifission fragments can be reasonably described based on the dinuclear system model [120–122].

A new fusion mechanism on compound nucleus formation was proposed by Zagrebaev [18]. The concept of a nucleon collectivization model assumes that two nuclei gradually lose their individualities through increasing the number of collectivized nucleons [18]; the reliability of the theoretical hypothesis needs further demonstration [123]. The nucleon collectivization model allows us to describe reasonably the fusion probability as well as the charge and mass distributions of the quasifission products [124].

## 3.4. Selection of Collective Degree and Calculation of Related Input Quantity in Transport or Diffusion Equations

To theoretically describe fusion dynamics and the mechanism based on transport equations as mentioned above, one needs to assume that several important degrees of freedoms can be

used to describe the main characteristics of fusion dynamics process [15–21]. These important degrees of freedoms include the distance between the nuclear centers, the neutron and proton asymmetries of projectile-target combinations, deformations, and corresponding orientation effects, which influence the dynamics from touching the configuration to the compound nucleus.

Because equations of motion contain time derivatives up to the second order, there are three quantities in each equations of motion. The first quantity is the conservative potential. The second and third are the friction tensor (friction force) and the inertia tensor (inertia parameter), respectively. For the conservative potential, two different approaches have been taken into account to calculate the potential energy surface. The two assumptions of calculating potential energy surface are frozen density or sudden approximation [19–21] and the adiabatic approximation [15–18].

Recently, Diaz-Torres showed that the gradual transition of potential energy surface from the diabatic to the adiabatic should be more realistic for describing the fusion or quasifission [125, 126]. In addition, one needs to consider how the shell structure evolutes with excitation energy and deformation. The excitation energy dissipated from kinetic energy of relative motion makes the individual shell structure of nuclei become damped [127–131], and deformation tends to be spherical [132]. Thus, the dynamical potential energy surface has to be further studied. However, a small amount of research work has involved the shell correction energy employed in the fusion process being temperature dependent [133] and the potential energy surface from diabatic approximation to adiabatic approximation to describe the whole dynamic evolution process.

The dissipation tensor arises from the distinction between collective motion and intrinsic motion. The dissipation tensor accounts for the coupling between the collective degrees of freedom and other degrees (non-collective) of freedom. When equations of motion or stochastic equations are used to describe the dynamic process, the friction coefficients are mainly treated by the phenomenological approaches for the description of the fusion dynamics process [16, 124].

The inertial tensor describes the response of the system to small changes in the collective degrees of freedom. The macroscopic approach, macroscopic-microscopic approach, and microscopic approach are used to calculate the inertia tensor of the fission dynamics process [134–137]. However, in the low-energy heavy-ion collisions process, it seems that the proper calculation on inertial parameters has not been paid enough attention compared to the fission dynamics process. In the stochastic equation, the inertia parameter is calculated by the Werner-Wheeler approach [124, 127]. In the diffusion equation, the inertia parameter is treated as a reduced mass of relative motion [138]. From the theoretical point of view, the inertia parameters and friction coefficient of theoretical calculations have to match our understanding of the potential energy surface in the transport equations.

### 3.5. Survival Probabilities

The last important factor is the survival probability of the compound nucleus against fission in the deexcitation process. For exciting compound nuclei, there are two methods to describe the fission process: the statistical approach and the dynamical approach. Based on the statistical model, two different approaches are taken into account for the excitation energy dependent shell structure. The first one is to introduce the influence of excitation energy on the shell structure through the energy level density parameter [139]. The second one is to ensure the excitation energy-dependent shell effect is taken into account by the effective potential energy surface [140].

The uncertainty of survival probability calculation based on statistical model mainly comes from two aspects. On one hand, a number of approximations are adapted in the calculation of survival probability. One the other hand, the survival probabilities for the *xn* evaporation channels are very sensitive to the model input. The level densities, fission barriers, neutron-separation energies, as well as the transmission coefficients have to be known with sufficient accuracy. Only systematic calculations based on the same assumptions and parameters can help to confirm the validity and reliability of the theoretical approximations and input quantities [28, 117].

## 4. THE OPTIMUM PROJECTILE-TARGET COMBINATION AND BOMBARDING ENERGY

### 4.1. Influence of Entrance Channel on ERCSs

Systematic studies of the existing experimental ERCSs are helpful to reveal reaction mechanisms. In addition, searching the optimal combination of the projectile and target and the range of the favorable beam energy is essential.

Some work systematically studies the influence of the neutron number of a target or projectile on the evaporation residue cross section [32, 36, 44–46]. Many researchers have found that the fusion probability and survival probability are sensitive to the neutron number of the target or projectile nuclei [32, 36, 44–46]. For $^{48}$Ca-induced hot fusion, the excess neutron of target nucleus is beneficial to the increase of the evaporation residue cross section of the synthesized superheavy nuclei [32, 45, 46].

Using a different combination of projectile and target to produce the same compound nucleus may help us to reveal the effect of the ground-state deformations, the reaction *Q* value, the asymmetry of charge and mass of target and projectile, and the Coulomb barrier on the evaporation residual cross section [33, 138, 141]. The results calculated by Liu et al. show that the *Q* value of reaction has a significant effect on the capture cross section and fusion probability [142].

### 4.2. The ERCS of Production Using Radioactive Beams

In order to investigate the possibility of neutron-rich superheavy nuclei production with radioactive beams, some calculations have been made [25, 116, 143, 144]. The evaporation residue

cross section by using radioactive beams are comparable with a stable beam for some superheavy nuclei production [116, 143]. However, the choice of reaction channels is determined by the product of beam intensity and evaporation residue cross section [143].

The intensities of stable beams, in most of the cases, are significantly larger than those of the radioactive beams [143], and the results have shown that the calculated evaporation residue cross section based on stable beam is more favorable for the production of many superheavy nuclei [116, 143]. In addition, due to small evaporation residue cross sections and low radioactive beam intensities, the synthesis of higher charge number superheavy nuclei by using the neutron-rich radioactive beams seems impossible based on today's experimental conditions [116, 143].

### 4.3. Prediction ERCS $Z$ = 119 and 120

By comparing evaporation residue cross sections for production $Z = 119$ and 120, we found that the calculations from different models were obviously different [17, 47–52, 124]. On one hand, the survival probability of the compound nucleus was very sensitive to the fission barrier. However, the difference in fission barriers of superheavy nuclei calculated by different models was obvious not only due to the absolute values but also the trends with charge number $Z$ [2, 85]. On the other hand, due to different assumptions, the fusion probability calculated by different models was significantly different for synthesis $Z = 119$ and 120 [84].

According to our calculation and other theoretical predictions, almost all the models that predicted evaporation residue cross sections to produce superheavy new element $Z = 119$ are generally greater than those in producing $Z = 120$ [17, 47–52].

## 5. THE FUTURE

The synthesis of SHN in the laboratory has made great progress, and all the elements up to $Z$=118 have been synthesized successfully. However, the location of the island of stability has not been confirmed in experiments. Although many theoretical approaches were used to study the fusion mechanism, there are still many problems that have not been solved properly. In my opinion, the transport theory is the least developed one due to three factors: (i) the neck formation itself and the relationship between dynamic deformation and neck formation should be included to improve the theoretical description of fusion dynamic mechanism; (ii) the gradual transition of the potential energy surface from the diabatic approximation to the adiabatic approximation needs to be further explored; and (iii) the further study of inertia and damping coefficients to match our understanding of the potential energy surface in the transport equations should be performed.

## 6. SUMMARY

The evaporation residue cross section of superheavy nuclei depends on three factors: the capture cross section $\sigma_{cap}$, the fusion probability $P_{CN}$, and the survival probability $W_{sur}$. We found that the reasonable description of the capture cross section near the Coulomb barrier is very important. The coupled channel or TDHF can be better approached to calculate the value, especially for superheavy nuclei calculations.

I think the fusion probability $P_{CN}$ for producing superheavy nuclei is still not well understood. Not only the magnitude of the fusion probability $P_{CN}$ but also the dependence of $P_{CN}$ on the excitation energy and the entrance channel are lacking in clarity. The fusion mechanism must be further studied.

The uncertainty of survival probability calculation based on a statistical model mainly comes from theoretical approximations and input quantities. Systematic calculations based on the same assumptions and parameters can help to confirm the validity and reliability of the theoretical approximations and input quantities.

## AUTHOR CONTRIBUTIONS

The author confirms being the sole contributor of this work and has approved it for publication.

## FUNDING

This work was supported by the National Natural Science Foundation of China (Grants 11705055) and Hunan Provincial Natural Science Foundation of China (2018JJ3324).

## REFERENCES

1. Hofmann S, Münzenberg G. The discovery of the heaviest elements. *Rev Mod Phys.* (2000) **72**:733. doi: 10.1103/RevModPhys.72.733
2. Giuliani SA, Matheson Z, Nazarewicz W, Olsen E, Reinhard PG, Sadhukhan J, et al. Colloquium: superheavy elements: oganesson and beyond. *Rev Mod Phys.* (2019) **91**:011001. doi: 10.1103/RevModPhys.91.011001
3. Sobiczewski A, Gareev FA, Kalinkin BN. Closed shells for Z>82 and N>126 in a diffuse potential well. *Phys Lett.* (1966) **22**:500. doi: 10.1016/0031-9163(66)91243-1
4. Mosel U, Greiner W. On the stability of superheavy nuclei against fission. *Z Phys.* (1969) **222**:261. doi: 10.1007/BF01392125
5. Nilsson SG, Tsang CF, Sobiczewski A, Szymanski Z, Wycech S, Gustafson C, et al. On the nuclear structure and stability of heavy and superheavy elements. *Nucl Phys A.* (1969) **131**:1. doi: 10.1016/0375-9474(69)90809-4
6. Moller P, Nix JR, Myers WD, Swiatecki WJ. Nuclear ground-state masses and deformations. *At Data Nucl Data Tables.* (1995) **59**:185. doi: 10.1006/adnd.1995.1002
7. Smolańczuk R. Properties of the hypothetical spherical superheavy nuclei. *Phys Rev C.* (1997) **56**:812. doi: 10.1103/PhysRevC.56.812
8. Decharge J, Berger JF, Dietrich K, Weiss MS. Superheavy and hyperheavy nuclei in the form of bubbles or semi-bubbles. *Phys Lett B.* (1999) **451**:275–82. doi: 10.1016/s0370-2693(99)00225-7
9. Bender M, Nazarewicz W, Reinhard PG. Shell stabilization of super- and hyperheavy nuclei without magic gaps. *Phys Lett B.* (2001) **515**:42–8. doi: 10.1016/S0370-2693(01)00863-2
10. Ring P. Relativistic mean field theory in finite nuclei. *Prog Part Nucl Phys.* (1996) **37**:193–263. doi: 10.1016/0146-6410(96)00054-3
11. Meng J, Toki H, Zhou SG, Zhang SQ, Long WH, Geng LS. Relativistic continuum Hartree Bogoliubov theory for ground-state

properties of exotic nuclei. *Prog Part Nucl Phys*. (2006) **57**:470–563. doi: 10.1016/j.ppnp.2005.06.001
12. Li JJ, Long WH, Margueron J, Van Giai N. Superheavy magic structures in the relativistic HartreeCFockCBogoliubov approach. *Phys Lett B*. (2014) **732**:169–73. doi: 10.1016/j.physletb.2014.03.031
13. Cwiok S, Dobaczewski J, Heenen PH, Magierski P, Nazarewicz W. Shell structure of the superheavy elements. *Nucl Phys A*. (1996) **611**:211–46. doi: 10.1016/S0375-9474(96)00337-5
14. Swiatecki WJ. Three lectures on macroscopic aspects of nuclear dynamics. *Prog Part Nucl Phys*. (1980) **4**:383. doi: 10.1016/0146-6410(80)90014-9
15. Swiatecki WJ. The dynamics of the fusion of two nuclei. *Nucl Phys A*. (1982) **376**:275. doi: 10.1016/0375-9474(82)90065-3
16. Aritomo Y, Wada T, Ohta M, Abe Y. Fluctuation-dissipation model for synthesis of superheavy elements. *Phys Rev C*. (1999) **59**:796. doi: 10.1103/PhysRevC.59.796
17. Shen CW, Abe Y, Boilley D, Kosenko G, Zhao EG. Isospin dependence of reactions 48Ca+243−251Bk. *Int. J. Mod. Phys. E*. (2008) **17**:66. doi: 10.1142/S0218301308011768
18. Zagrebaev VI. Synthesis of superheavy nuclei: nucleon collectivization as a mechanism for compound nucleus formation. *Phys Rev C*. (2001) **64**:034606. doi: 10.1103/PhysRevC.64.034606
19. Adamian GG, Antonenko NV, Scheid W, Volkov VV. Treatment of competition between complete fusion and quasifission in collisions of heavy nuclei. *Nucl Phys A*. (1997) **627**:361. doi: 10.1016/S0375-9474(97)00605-2
20. Feng ZQ, Jin GM, Fu F, Li JQ. Production cross sections of superheavy nuclei based on dinuclear system model. *Nucl Phys A*. (2006) **771**:50. doi: 10.1016/j.nuclphysa.2006.03.002
21. Diaz-Torres A, Adamian GG, Antonenko NV, Scheid W. Quasifission process in a transport model for a dinuclear system. *Phys Rev C*. (2001) **64**:024604. doi: 10.1103/PhysRevC.64.024604
22. Zagrebaev V, Greiner W. Synthesis of superheavy nuclei: a search for new production reactions. *Phys Rev C*. (2008) **78**:034610. doi: 10.1103/PhysRevC.78.034610
23. Smolańczuk R. Synthesis of transactinide nuclei in cold fusion reactions using radioactive beams. *Phys Rev C*. (2010) **81**:067602. doi: 10.1103/PhysRevC.81.067602
24. Wang N, Tian J, Scheid W. Systematics of fusion probability in hot fusion reactions. *Phys Rev C*. (2011) **84**:061601(R). doi: 10.1103/PhysRevC.84.061601
25. Wu ZH, Zhu L, Li F, Yu XB, Su J, Guo CC. Synthesis of neutron-rich superheavy nuclei with radioactive beams within the dinuclear system model. *Phys Rev C*. (2018) **97**:064609. doi: 10.1103/PhysRevC.97.064609
26. Shen CW, Kosenko G, Abe Y. Two-step model of fusion for the synthesis of superheavy elements. *Phys Rev C*. (2002) **66**:061602. doi: 10.1103/PhysRevC.66.061602
27. Wang N, Li JQ, Zhao EG. Orientation effects of deformed nuclei on the production of superheavy elements. *Phys Rev C*. (2008) **78**:054607. doi: 10.1103/PhysRevC.78.054607
28. Siwek-Wilczyńska K, Cap T, Kowal M, Sobiczewski A, Wilczyński J. Predictions of the fusion-by-diffusion model for the synthesis cross sections of Z=114-120 elements based on macroscopic-microscopic fission barriers. *Phys Rev C*. (2012) **86**:014611. doi: 10.1103/PhysRevC.86.014611
29. Nasirov AK, Giardina G, Mandaglio G, Manganaro M, Hanappe F, Heinz S, et al. Quasifission and fusion-fission in reactions with massive nuclei: Comparison of reactions leading to the Z = 120 element. *Phys. Rev. C*. (2009) **79**:024606. doi: 10.1103/PhysRevC.79.024606
30. Bao XJ, Gao Y, Li JQ, Zhang HF. Influence of the nuclear dynamical deformation on production cross sections of superheavy nuclei. *Phys Rev C*. (2015) **91**:011603(R). doi: 10.1103/PhysRevC.91.011603
31. Litnevsky VL, Pashkevich VV, Kosenko GI, Ivanyuk FA. Description of synthesis of super-heavy elements within the multidimensional stochastic model. *Phys Rev C*. (2014) **89**:034626. doi: 10.1103/PhysRevC.89.034626
32. Adamian GG, Antonenko NV, Scheid W. Isotopic trends in the production of superheavy nuclei in cold fusion reactions. *Phys Rev C*. (2004) **69**:011601. doi: 10.1103/PhysRevC.69.011601
33. Liu ZH, Bao JD. Isotopic dependence of the evaporation residue cross section in the synthesis of superheavy nuclei. *Phys Rev C*. (2007) **76**:034604. doi: 10.1103/PhysRevC.76.034604
34. Liu ZH, Bao JD. Synthesis of superheavy element 120 via50Ti+ACf hot fusion reactions. *Phys Rev C*. (2009) **80**:054608. doi: 10.1103/PhysRevC.80.054608
35. Zagrebaev VI, Karpov AV, Greiner W. Possibilities for synthesis of new isotopes of superheavy elements in fusion reactions. *Phys Rev C*. (2012) **85**:014608. doi: 10.1103/PhysRevC.85.014608
36. Cap T, Wilczynska KS, Kowal M, Wilczynski J. Calculations of the cross sections for the synthesis of new 293-296118 isotopes in 249-252Cf(48Ca,xn) reactions. *Phys Rev C*. (2013) **88**:037603. doi: 10.1103/PhysRevC.88.037603
37. Wang N, Zhao EG, Scheid W. Synthesis of superheavy nuclei with Z=118 in hot fusion reactions. *Phys Rev C*. (2014) **89**:037601. doi: 10.1103/PhysRevC.89.037601
38. Li W, Wang N, Jia F, Xu H, Zuo W, Li JQ et al. Fusion probability in heavy-ion collisions by a dinuclear-system model. *J Phys G Nucl Phys*. (2006) **32**:1143. doi: 10.1209/epl/i2003-00622-0
39. Antonenko N, Cherepanov E, Nasirov A, Permjakov V, Volkov V. Competition between complete fusion and quasi-fission in reactions between massive nuclei. The fusion barrier. *Phys Lett B*. (1993) **319**:425. doi: 10.1016/0370-2693(93)91746-A
40. Antonenko NV, Cherepanov EA, Nasirov AK, Permjakov VP, Volkov VV. Compound nucleus formation in reactions between massive nuclei: fusion barrier. *Phys Rev C*. (1995) **51**:2635. doi: 10.1103/PhysRevC.51.2635
41. Huang MH, Gan ZG, Feng ZQ, Zhou XH, Li JQ. Neutron and proton diffusion in fusion reactions for the synthesis of superheavy nuclei. *Chin Phys Lett*. (2008) **25**:1243. doi: 10.1088/0256-307X/25/4/022
42. Nasirov A, Fukushima A, Toyoshima Y, Aritomo Y, Muminov A, Kalandarov S, et al. The role of orientation of nucleus symmetry axis in fusion dynamics. *Nucl Phys A*. (2005) **759**:342–69. doi: 10.1016/j.nuclphysa.2005.05.152
43. Hong J, Adamian GG, Antonenko NV. Possibilities of production of transfermium nuclei in charged-particle evaporation channels. *Phys Rev C*. (2016) **94**:044606. doi: 10.1103/PhysRevC.94.044606
44. Feng ZQ, Jin GM, Li JQ, Scheid W. Formation of superheavy nuclei in cold fusion reactions. *Phys Rev C*. (2007) **76**:044606. doi: 10.1103/PhysRevC.76.044606
45. Mandaglio G, Giardina G, Nasirov AK, Sobiczewski A. Investigation of the 48Ca+249-252Cf reactions synthesizing isotopes of the superheavy element 118. *Phys Rev C*. (2012) **86**:064607. doi: 10.1103/PhysRevC.86.064607
46. Bao XJ, Gao Y, Li JQ, Zhang HF. Isotopic dependence of superheavy nuclear production in hot fusion reactions. *Phys Rev C*. (2015) **92**:034612. doi: 10.1103/PhysRevC.92.034612
47. Liu ZH, Bao JD. Possibility to produce element 120 in the 54Cr+248 Cm hot fusion reaction. *Phys Rev C*. (2013) **87**:034616. doi: 10.1103/PhysRevC.87.034616
48. Wang N, Zhao EG, Scheid W, Zhou SG. Theoretical study of the synthesis of superheavy nuclei with Z=119 and 120 in heavy-ion reactions with trans-uranium targets. *Phys Rev C*. (2012) **85**:041601(R). doi: 10.1103/PhysRevC.85.041601
49. Zhu L, Xie WJ, Zhang FS. Production cross sections of superheavy elements Z=119 and 120 in hot fusion reactions. *Phys Rev C*. (2014) **89**:024615. doi: 10.1103/PhysRevC.89.024615
50. Bao XJ, Guo SQ, Li JQ, Zhang HF. Influence of hexadecapole deformation on production cross sections of superheavy nuclei. *J Phys G Nucl Part Phys*. (2016) **43**:125105. doi: 10.1088/0954-3899/43/12/125105
51. Huang MH, Zhang ZY, Gan ZG, Zhou XH, Li JQ, Scheid W. Dynamical deformation in heavy ion collisions and formation of superheavy nuclei. *Phys Rev C*. (2011) **84**:064619. doi: 10.1103/PhysRevC.84.064619
52. Wang N, Liu M, Wu XZ. Modification of nuclear mass formula by considering isospin effects. *Phys Rev C*. (2010) **81**:044322. doi: 10.1103/PhysRevC.81.044322
53. Hofmann S. Synthesis of superheavy elements by cold fusion. *Radiochim Acta*. (2011) **99**:405. doi: 10.1524/ract.2011.1854
54. Kosuke M, Kouji M, Daiya K, Takahiro A, Sin-ichi G, Hiromitsu H, et al. Experiment on Synthesis of an Isotope 277112 by 208Pb+70Zn Reaction. *J. Phys. Soc. Japan*. (2007) **76**:043201. doi: 10.1143/JPSJ.76.043201

55. Oganessian YT. Synthesis of the heaviest elements in 48Ca-induced reactions. *Radiochim Acta*. (2011) **99**:429. doi: 10.1524/ract.2011.1860
56. Münzenberg G. Recent advances in the discovery of transuranium elements. *Rep Prog Phys.* (1988) **51**:57. doi: 10.1088/0034-4885/51/1/002
57. Hofmann S. New elements-approaching Z=114. *Rep Prog Phys.* (1998) **61**:639.
58. Kosuke M, Kouji M, Daiya K, Takahiro A, Sin-ichi G, Hiromitsu H, et al. Experiment on the synthesis of element 113 in the reaction 209Bi(70Zn,n)278113. *J Phys Soc Jpn*. (2004) **73**:2593. doi: 10.1143/JPSJ.73.2593
59. Morita K, Morimoto K, Kaji D, Haba H, Ozeki K, Kudou Y, et al. New result in the production and decay of an isotope, 278113, of the 113th Element. *J Phys Soc Jpn*. (2012) **81**:103201. doi: 10.1143/JPSJ.81.103201
60. Oganessian YT, Utyonkov VK. Super-heavy element research. *Rep Prog Phys*. (2015) **78**:036301. doi: 10.1088/0034-4885/78/3/036301
61. Dvorak J, Bruchle W, Dullmann Ch E, Dvorakova Z, Eberhardt K, Eichler R, et al. Cross section limits for the 248Cm(25Mg,4n-5n)268,269Hs reactions. *Phys Rev C*. (2009) **79**:037602. doi: 10.1103/PhysRevC.79.037602
62. Graeger R, Ackermann D, Chelnokov M, Chepigin V, Dullmann Ch. E, Dvorak J, et al. Experimental study of the 238U(36S,3-5n)269-271Hs reaction leading to the observation of 270 Hs. *Phys Rev C*. (2010) **8**:061601(R). doi: 10.1103/PhysRevC.81.061601
63. Nishio K, Hofmann S, Heberger FP, Ackermann D, Antalic S, Aritomo Y, et al. Nuclear orientation in the reaction 34S+238U and synthesis of the new isotope 268 Hs. *Phys Rev C*. (2010) **82**:024611. doi: 10.1103/PhysRevC.82.024611
64. Oganessian Yu Ts, Utyonkov VK, Abdullin FS, Dmitriev SN, Graeger R, Henderson RA, et al. Synthesis and study of decay properties of the doubly magic nucleus 270Hs in the 226Ra +48Ca reaction. *Phys Rev C*. (2013) **87**:034605. doi: 10.1103/PhysRevC.87.034605
65. Dvorak J, Bruchle W, Chelnokov M, Dullmann Ch E, Dvorakova Z, Eberhardt K, et al. Observation of the 3n evaporation channel in the complete hot-fusion reaction 26Mg+248Cm leading to the new superheavy nuclide 271 Hs. *Phys Rev Lett*. (2008) **100**:132503. doi: 10.1103/PhysRevLett.100.132503
66. Utyonkov VK, Brewer NT, Oganessian Yu Ts, Rykaczewski KP, Abdullin F, Dmitriev SN, et al. Experiments on the synthesis of superheavy nuclei 284Fl and 285Fl in the 239,240Pu+48Ca reactions. *Phys Rev C*. (2015) **92**:034609. doi: 10.1103/PhysRevC.92.034609
67. Brewer NT, Utyonkov VK, Rykaczewski KP, Oganessian Yu Ts, Abdullin F, Boll RA, et al. Search for the heaviest atomic nuclei among the products from reactions of mixed-Cf with a 48Ca beam. *Phys Rev C*. (2018) **98**:024317. doi: 10.1103/PhysRevC.98.024317
68. Nishio K, Mitsuoka S, Nishinaka I, Makii H, Wakabayashi Y, Ikezoe H, et al. Fusion probabilities in the reactions40,48Ca+238U at energies around the Coulomb barrier. *Phys Rev C*. (2012) **86**:034608. doi: 10.1103/PhysRevC.86.034608
69. Oganessian YT, Utyonkov VK, Lobanov Yu V, Abdullin F, Polyakov AN, Sagaidak RN, et al. Attempt to produce element 120 in the 244Pu+58Fe reaction. *Phys Rev C*. (2009) **79**:024603. doi: 10.1103/PhysRevC.79.024603
70. Hofmann S, et al. *2012 GSI Anuual Report GSI Report vol 2012-C1*. (2011). p. 205.
71. Heusch B, Volant C, Freiesleben H, Chestnut RP, Hildenbrand KD, Puhlhofer F, et al. The reaction mechanism in the system132Xe+56Fe at 5.73 MeV/u: evidence for a new type of strongly damped collisions. *Z Phys A*. (1978) **288**:391. doi: 10.1007/BF01417723
72. Toke J, Bock R, Dai GX, Gobbi A, Gralla S, Hildenbrand KD, et al. Quasi-fission — The mass-drift mode in heavy-ion reactions. *Nucl Phys A*. (1985) **440**:327. doi: 10.1016/0375-9474(85)90344-6
73. du Rietz R, Williams E, Hinde DJ, Dasgupta M, Evers M, Lin CJ, et al. Mapping quasifission characteristics and timescales in heavy element formation reactions. *Phys Rev C*. (2013) **88**:054618. doi: 10.1103/PhysRevC.88.054618
74. Itkis MG, Bogachev AA, Itkis IM, Kliman J, Knyazheva GN, Kondratiev NA, et al. The processes of fusion-fission and quasi-fission of superheavy nuclei. *Nucl Phys A*. (2007) **787**:150c. doi: 10.1016/j.nuclphysa.2006.12.026
75. Itkis IM, Kozulin EM, Itkis MG, Knyazheva GN, Bogachev AA, Chernysheva EV, et al. Fission and quasifission modes in heavy-ion-induced reactions leading to the formation of Hs. *Phys Rev C*. (2011) **83**:064613. doi: 10.1103/PhysRevC.83.064613
76. Kozulin EM, Knyazheva GN, Novikov KV, Itkis IM, Itkis MG, Dmitriev SN, et al. Fission and quasifission of composite systems with Z=108-120: transition from heavy-ion reactions involving S and Ca to Ti and Ni ions. *Phys Rev C*. (2014) **94**:054613. doi: 10.1103/PhysRevC.94.054613
77. Banerjee K, Hinde DJ, Dasgupta M, Simpson EC, Jeung DY, Simenel C, et al. Mechanisms suppressing superheavy element yields in cold fusion reactions. *Phys Rev Lett*. (2019) **122**:232503. doi: 10.1103/PhysRevLett.122.232503
78. Dasgupta M, Hinde DJ, Rowley N, Stefanini AM. Measuring barriers to fusion. *Annu Rev Nucl Part Sci.* (1998) **48**:401. doi: 10.1146/annurev.nucl.48.1.401
79. Hagino K, Takigawa N. Subbarrier fusion reactions and many-particle quantum tunneling. *Prog Theor Phys*. (2012) **128**:1061. doi: 10.1143/PTP.128.1061
80. Back BB, Esbensen H, Jiang CL, Rehm KE. Recent developments in heavy-ion fusion reactions. *Rev Mod Phys*. (2014) **86**:317. doi: 10.1103/RevModPhys.86.317
81. Montagnoli G, Stefanini AM. Recent experimental results in sub- and near-barrier heavy-ion fusion reactions. *Eur Phys J A*. (2017) **53**:169. doi: 10.1140/epja/i2017-12350-2
82. Wang N, Wu XZ, Li ZX, Liu M, Scheid W. Applications of Skyrme energy-density functional to fusion reactions for synthesis of superheavy nuclei. *Phys Rev C*. (2006) **74**:044604. doi: 10.1103/PhysRevC.74.044604
83. Wang B, Wen K, Zhao WJ, Zhao EG, Zhou SG. Systematics of capture and fusion dynamics in heavy-ion collisions. *At Data Nucl. Data Tables*. (2017) **114**:281. doi: 10.1016/j.adt.2016.06.003
84. Loveland W. An experimentalist's view of the uncertainties in understanding heavy element synthesis. *Eur Phys J A*. (2015) **51**:120. doi: 10.1140/epja/i2015-15120-2
85. Bao XJ, Guo SQ, Zhang HF, Li JQ. Influence of proton shell closure on the evaporation residue cross sections of superheavy nuclei. *J Phys G Nucl Part Phys*. (2017) **44**:045105. doi: 10.1088/1361-6471/aa53e8
86. Diaz-Torres A, Hinde DJ, Dasgupta M, Milburn GJ, Tostevin JA. Dissipative quantum dynamics in low-energy collisions of complex nuclei. *Phys Rev C*. (2008) **78**:064604. doi: 10.1103/PhysRevC.78.064604
87. Sargsyan VV, Kanokov Z, Adamian GG, Antonenko NV, Scheid W. Capture process in nuclear reactions with a quantum master equation. *Phys Rev C*. (2009) **80**:034606. doi: 10.1103/PhysRevC.80.034606
88. Sargsyan VV, Adamian GG, Antonenko NV, Scheid W, Zhang HQ. Effects of nuclear deformation and neutron transfer in capture processes, and fusion hindrance at deep sub-barrier energies. *Phys Rev C*. (2011) **84**:064614. doi: 10.1103/PhysRevC.84.064614
89. Esbensen H, Stefanini AM. Influence of multiphonon excitations and transfer on the fusion of Ca+Zr. *Phys Rev C*. (2014) **89**:044616. doi: 10.1103/PhysRevC.89.044616
90. Jiang CL, Rehm KE, Back BB, Esbensen H, Janssens VF, Stefanini AM, et al. Influence of heavy-ion transfer on fusion reactions. *Phys Rev C*. (2014) **89**:051603(R). doi: 10.1103/PhysRevC.89.051603
91. Jia HM, Lin CJ, Yang F, Xu XX, Zhang HQ, Liu ZH, et al. Fusion of 32S+94Zr: further exploration of the effect of the positive Qxn value neutron transfer channels. *Phys Rev C*. (2014) **89**:064605. doi: 10.1103/PhysRevC.89.064605
92. Rachkov VA, Karpov AV, Denikin AS, Zagrebaev VI. Examining the enhancement of sub-barrier fusion cross sections by neutron transfer with positive Q values. *Phys Rev C*. (2014) **90**:014614. doi: 10.1103/PhysRevC.90.014614
93. Misicu S, Greiner W. Influence of hexadecupole deformation and role of orientation in capture reactions with 48Ca projectiles leading to superheavy nuclei. *Phys Rev C*. (2004) **69**:054601. doi: 10.1103/PhysRevC.69.054601
94. Misicu S, Esbensen H. Hindrance of heavy-ion fusion due to nuclear incompressibility. *Phys Rev Lett*. (2006) **96**:112701. doi: 10.1103/PhysRevLett.96.112701

95. Wong CY. Interaction Barrier in charged-particle nuclear reactions. *Phys Rev Lett*. (1973) **31**:766. doi: 10.1103/PhysRevLett.31.766
96. Stokstad RG, Switkowski ZE, Dayras RA, Wieland RM. Measurements of fusion cross sections for heavy-ion systems at very low energies. *Phys Rev Lett*. (1976) **37**:888. doi: 10.1103/PhysRevLett.37.888
97. Rowley N, Satchler GR, Stelson PH. On the "distribution of barriers" interpretation of heavy-ion fusion. *Phys Lett B*. (1991) **254**:25. doi: 10.1016/0370-2693(91)90389-8
98. Sargsyan VV, Adamian GG, Antonenko NV, Scheid W. Peculiarities of the sub-barrier fusion with the quantum diffusion approach. *Eur Phys J A*. (2010) **45**:125. doi: 10.1140/epja/i2010-10978-x
99. Sargsyan VV, Adamian GG, Antonenko NV, Scheid W, Zhang HQ. Sub-barrier capture with quantum diffusion approach: actinide-based reactions. *Eur Phys J A*. (2011) **47**:38. doi: 10.1140/epja/i2011-11038-y
100. Sargsyan VV, Adamian GG, Antonenko NV, Scheid W, Zhang HQ. Role of neutron transfer in capture processes at sub-barrier energies. *Phys Rev C*. (2012) **85**:024616. doi: 10.1103/PhysRevC.85.024616
101. Sargsyan VV, Adamian GG, Antonenko NV, Scheid W, Zhang HQ. Influence of neutron transfer in reactions with weakly and strongly bound nuclei on the sub-barrier capture process. *Phys Rev C*. (2012) **86**:014602. doi: 10.1103/PhysRevC.86.014602
102. Wakhle A, Simenel C, Hinde DJ, Dasgupta M, Evers M, Luong DH, et al. Interplay between quantum shells and orientation in quasifission. *Phys Rev Lett*. (2014) **113**:182502. doi: 10.1103/PhysRevLett.113.182502
103. Umar AS, Oberacker VE, Maruhn JA, Reinhard PG. Entrance channel dynamics of hot and cold fusion reactions leading to superheavy elements. *Phys Rev C*. (2010) **81**:064607. doi: 10.1103/PhysRevC.81.064607
104. Simenel C, Hinde DJ, du Rietz R, Dasgupta M, Evers M, Lin CJ. Influence of entrance-channel magicity and isospin on quasi-fission. *Phys Lett B*. (2012) **710**:607. doi: 10.1016/j.physletb.2012.03.063
105. Simenel C. Nuclear quantum many-body dynamics: from collective vibrations to heavy-ion collisions. *Eur Phys J A*. (2012) **48**:152. doi: 10.1140/epja/i2012-12152-0
106. Oberacker VE, Umar AS, Simenel C. Energy dependence of potential barriers and its effect on fusion cross sections. *Phys Rev C*. (2014) **89**:034611. doi: 10.1103/PhysRevC.89.034611
107. Umar AS, Oberacker VE, Simenel C. Shape evolution and collective dynamics of quasifission in the time-dependent Hartree-Fock approach. *Phys Rev C*. (2015) **92**:024621. doi: 10.1103/PhysRevC.92.024621
108. Sekizawa K, Yabana K. Time-dependent Hartree-Fock calculations for multinucleon transfer and quasifission processes in the 64Ni+238U reaction. *Phys Rev C*. (2016) **93**:054616. doi: 10.1103/PhysRevC.93.054616
109. Umar AS, Oberacker VE, Simenel C. Fusion and quasifission dynamics in the reactions 48Ca+249Bk and 50Ti+249Bk using a time-dependent Hartree-Fock approach. *Phys Rev C*. (2016) **94**:024605. doi: 10.1103/PhysRevC.94.024605
110. Umar AS, Simenel C, Ye W. Transport properties of isospin asymmetric nuclear matter using the time-dependent Hartree-Fock method. *Phys Rev C*. (2017) **96**:024625. doi: 10.1103/PhysRevC.96.024625
111. Sekizawa K. Enhanced nucleon transfer in tip collisions of 238U+124Sn. *Phys Rev C*. (2017) **96**:041601(R). doi: 10.1103/PhysRevC.96.041601
112. Guo L, Simenel C, Shi L, Yu C. The role of tensor force in heavy-ion fusion dynamics. *Phys Lett B*. (2018) **782**:401. doi: 10.1016/j.physletb.2018.05.066
113. Guo L, Godbey K, Umar AS. Influence of the tensor force on the microscopic heavy-ion interaction potential. *Phys Rev C*. (2018) **98**:064607. doi: 10.1103/PhysRevC.98.064607
114. Simenel C, Umar AS. Heavy-ion collisions and fission dynamics with the time-dependent HartreeCFock theory and its extensions. *Prog Part Nucl Phys*. (2018) **103**:19. doi: 10.1016/j.ppnp.2018.07.002
115. Godbey K, Umar AS, Simenel C. Deformed shell effects in Ca48+Bk249 quasifission fragments. *Phys Rev C*. (2019) **100**:024610. doi: 10.1103/PhysRevC.100.024610
116. Bao XJ, Gao Y, Li JQ, Zhang HF. Theoretical study of the synthesis of superheavy nuclei using radioactive beams. *Phys Rev C*. (2015) **91**:064612. doi: 10.1103/PhysRevC.91.064612
117. Bao XJ, Gao Y, Li JQ, Zhang HF. Influence of nuclear basic data on the calculation of production cross sections of superheavy nuclei. *Phys Rev C*. (2015) **92**:014601. doi: 10.1103/PhysRevC.92.014601
118. Swiatecki WJ, Siwek-Wilczynska K, Wilczynski J. Fusion by diffusion. II. Synthesis of transfermium elements in cold fusion reactions. *Phys Rev C*. (2005) **71**:014602. doi: 10.1103/PhysRevC.71.014602
119. Hagino K. Hot fusion reactions with deformed nuclei for synthesis of superheavy nuclei: an extension of the fusion-by-diffusion model. *Phys Rev C*. (2018) **98**:014607. doi: 10.1103/PhysRevC.98.014607
120. Bao XJ, Guo SQ, Zhang HF, Li JQ. Dynamics of complete and incomplete fusion in heavy ion collisions. *Phys Rev C*. (2018) **97**:024617. doi: 10.1103/PhysRevC.97.024617
121. Guo SQ, Gao Y, Li JQ, Zhang HF. Dynamical deformation in heavy ion reactions and the characteristics of quasifission products. *Phys Rev C*. (2017) **96**:044622. doi: 10.1103/PhysRevC.96.044622
122. Adamian GG, Antonenko NV, Scheid W. Characteristics of quasifission products within the dinuclear system model. *Phys Rev C*. (2003) **68**:034601. doi: 10.1103/PhysRevC.68.034601
123. Volkov VV. The mechanism of compound nucleus formation in complete fusion of two massive nuclei. *Phys Atom Nuclei*. (2003) **66**:1065. doi: 10.1134/1.1586419
124. Zagrebaev VI, Greiner W. Cross sections for the production of superheavy nuclei. *Nucl Phys A*. (2015) **944**:257–307. doi: 10.1016/j.nuclphysa.2015.02.010
125. Diaz-Torres A. Modeling of compound nucleus formation in the fusion of heavy nuclei. *Phys Rev C*. (2004) **69**:021603(R). doi: 10.1103/PhysRevC.69.021603
126. Diaz-Torres A. Competition between fusion and quasifission in a heavy fusing system: diffusion of nuclear shapes through a dynamical collective potential energy landscape. *Phys Rev C*. (2006) **74**:064601. doi: 10.1103/PhysRevC.74.064601
127. Aritomo Y. Analysis of dynamical processes using the mass distribution of fission fragments in heavy-ion reactions. *Phys Rev C*. (2009) **80**:064604. doi: 10.1103/PhysRevC.80.064604
128. Bao XJ. Possibility to produce 293,295,296Og in the reactions 48Ca+249,250,251Cf. *Phys Rev C*. (2019) **100**:011601(R). doi: 10.1103/PhysRevC.100.011601
129. Schmidtt KH, Morawekt W. The conditions for the synthesis of heavy nuclei. *Rep Prog Phys*. (1991) **54**:949–1003. doi: 10.1088/0034-4885/54/7/002
130. Ivanyuk FA, Ishizuka C, Usang MD, Chiba S. Temperature dependence of shell corrections. *Phys Rev C*. (2018) **97**:054331. doi: 10.1103/PhysRevC.97.054331
131. Zhu L, Wen PW, Lin CJ, Bao XJ, Su J, Li C, et al. Shell effects in a multinucleon transfer process. *Phys Rev C*. (2018) **97**:044614. doi: 10.1103/PhysRevC.97.044614
132. Sauer G, Chandra H, Mosel U. Thermal properties of nuclei. *Nucl Phys A*. (1976) **264**:221. doi: 10.1016/0375-9474(76)90429-2
133. Fröbrich P. On the dynamics of fission of hot nuclei. *Nucl Phys A*. (2007) **787**:170c. doi: 10.1016/j.nuclphysa.2006.12.028
134. Brack M, Jens D, Jensen AS, Pauli HC, Strutinsky VM, Wong CY. Funny hills: the shell-correction approach to nuclear shell effects and its applications to the fission process. *Rev Mod Phys*. (1972) **44**:320. doi: 10.1103/RevModPhys.44.320
135. Davies KTR, Sierk AJ, Nix JR. Effect of viscosity on the dynamics of fission. *Phys Rev C*. (1976) **13**:2385. doi: 10.1103/PhysRevC.13.2385
136. Schunck N, Robledo LM. Microscopic theory of nuclear fission: a review. *Rep Prog Phys*. (2016) **79**:116301. doi: 10.1088/0034-4885/79/11/116301
137. Schmidt KH, Jurado B. Review on the progress in nuclear fission-experimental methods and theoretical descriptions. *Rep Prog Phys*. (2018) **81**:106301. doi: 10.1088/1361-6633/aacfa7
138. Bao XJ. Possibilities for synthesis of new neutron-deficient isotopes of superheavy nuclei. *Chin Phys C*. (2019) **43**:054105. doi: 10.1088/1674-1137/43/5/054105
139. Ignatyuk AV, Smirenkin GN, Tishin AS. *Yad Fiz*. (1975) **21**:485. [*Sov. J. Nucl. Phys*. (1975) **29**:255].
140. Vandenbosch R, Huizenga JR. *Nuclear Fission*. New York, NY: Academic (1973).

141. Bao XJ, Guo SQ, Zhang HF, Li JQ. Influence of entrance channel on production cross sections of superheavy nuclei. *Phys Rev C*. (2017) **96**:024610. doi: 10.1103/PhysRevC.96.024610
142. Liu ZH, Bao JD. Q-value effects on the production of superheavy nuclei. *Phys Rev C*. (2006) **74**:057602. doi: 10.1103/PhysRevC.74.057602
143. Loveland W. Synthesis of transactinide nuclei using radioactive beams. *Phys Rev C*. (2007) **76**:014612. doi: 10.1103/PhysRevC.76.014612
144. Loveland W. The synthesis of new neutron-rich heavy nuclei. *Front Phys*. (2019) **7**:23. doi: 10.3389/fphy.2019.00023

**Conflict of Interest:** The author declares that the research was conducted in the absence of any commercial or financial relationships that could be construed as a potential conflict of interest.

frontiers in Physics

ORIGINAL RESEARCH
published: 18 March 2020
doi: 10.3389/fphy.2020.00063

# Nuclear Fission Dynamics: Past, Present, Needs, and Future

*Aurel Bulgac*[1]*, *Shi Jin*[1] and *Ionel Stetcu*[2]

[1] Department of Physics, University of Washington, Seattle, WA, United States, [2] Los Alamos National Laboratory, Theoretical Division, Los Alamos, NM, United States

Significant progress in the understanding of the fission process within a microscopic framework has been recently reported. Even though the complete description of this important nuclear reaction remains a computationally demanding task, recent developments in theoretical modeling and computational power have brought current microscopic simulations to the point where they can provide guidance and constraints to phenomenological models, without making recourse to parameters. An accurate treatment compatible with our understanding of the inter-nucleon interactions should be able to describe the real-time dynamics of the fissioning system and could justify or rule out assumptions and approximations incompatible with the underlying universally accepted quantum-mechanical framework. Of particular importance are applications to observables that cannot be directly measured in experimental setups (such as the angular momentum distribution of the fission fragments, or the excitation energy sharing between the fission fragments, or fission of nuclei formed during the *r*-process), and their dependence of the excitation energy in the fissioning system. Even if accurate predictions are not within reach, being able to extract the trends with increasing excitation energy is important in various applications. The most advanced microscopic simulations of the fission process do not support the widely used assumption of adiabaticity of the large amplitude collective motion in fission, in particular for trajectories from the outer saddle toward the scission configuration. Hence, the collective potential energy surface and inertia tensor, which are the essential elements of many simplified microscopic theoretical approaches, become irrelevant. In reality, the dynamics of the fissioning system is slower than in the case of pure adiabatic motion by a factor of three to four times and is strongly overdamped. The fission fragment properties are defined only after the full separation, while in most of the current approaches no full separation can be achieved, which increases the uncertainties in describing fission-related observables in such methods.

**Keywords: nuclear fission, total kinetic energy, total excitation energy, overdamped collective motion, adiabatic collective motion, average neutron multiplicity**

OPEN ACCESS

***Edited by:***
*Paul Denis Stevenson, University of Surrey, United Kingdom*

***Reviewed by:***
*Giuseppe Verde, National Institute for Nuclear Physics, Italy*
*Armen Sedrakian, Frankfurt Institute for Advanced Studies, Germany*

***Correspondence:**
*Aurel Bulgac*
*bulgac@uw.edu*

***Specialty section:***
*This article was submitted to Nuclear Physics, a section of the journal Frontiers in Physics*

***Received:*** *30 November 2019*
***Accepted:*** *27 February 2020*
***Published:*** *18 March 2020*

***Citation:***
*Bulgac A, Jin S and Stetcu I (2020) Nuclear Fission Dynamics: Past, Present, Needs, and Future. Front. Phys. 8:63. doi: 10.3389/fphy.2020.00063*

## 1. THE PAST

In a matter of days after Hahn and Strassmann [1] communicated their yet unpublished results to Lise Meitner, she and her nephew Otto Frisch [2] understood that an unexpected and qualitatively new type of nuclear reaction has been put in evidence and they dubbed it nuclear fission, in analogy to cell divisions in biology. Until that moment in time nuclear fission was considered a totally

unthinkable process [3, 4], "as excluded by the small penetrability of the Coulomb barrier [5], indicated by the Gamov's theory of alpha-decay" [2]. Meitner and Frisch [2] also gave the correct physical interpretation of the nuclear fission mechanism. They understood that Bohr's compound nucleus [6] is formed after the absorption of a neutron, which eventually slowly evolves in shape, while the volume remains constant, and that the competition between the surface energy of a nucleus and its Coulomb energy leads to the eventual scission. Meitner and Frisch [2] also correctly estimated the total energy released in this process to be about 200 MeV. A few months later Bohr and Wheeler [7] filled in all the technical details and the long road to developing a microscopic theory of nuclear fission ensued. In the years since, a few more crucial theoretical results have been firmly established: (i) the defining role of quantum shell effects [8, 9] and in particular the special role played by the pairing type of nucleon-nucleon interaction in shape evolution [10, 11]; (ii) the fact that the subsequent emission of neutrons and gammas can be described quite accurately using statistical methods [12, 13]; (iii) and that the non-relativistic Schrödinger equation should be adequate as well, as no genuine relativistic effects, such a retardation, are expected to play any noticeable role in fission dynamics.

Whether a fissioning nucleus undergoes either spontaneous fission or induced fission the time it takes the nucleus to evolve from its ground state shape until outside the barrier or past the outer saddle is very long in case of neutron induced fission $\approx \mathcal{O}(10^{-15})$ s. in comparison with the time the nucleus slides downhill until scission, which is estimated to be $\mathcal{O}(10^{-20})$ s. Therefore, the saddle-to-scission stage of nuclear shape evolution is the fastest and arguably the most non-equilibrium stage of the nucleus dynamics from the moment a neutron has been captured and the stage which plays a crucial role in in determining the FFs properties. The many intricacies of the fission process, the multitude of aspects, which required a deep theoretical understanding, ultimately rooted in the quantum nature of this phenomenon defied the efforts of many generations of theorists, and a huge plethora of mostly phenomenological models have been put forward, often based on contradictory assumptions between models. The extensive range of assumptions, range from adiabatic evolution on top of which one adds (relatively weak) dissipation and fluctuations, to strongly overdamped motion, when the role of the collective inertia becomes irrelevant, to full statistical equilibrium near the scission configuration, and to mixing quantum and classical descriptions.

Microscopically inspired models are typically based on the (ill suited choice of words, as the our analysis shows) adiabatic approximation, which is often conflated with slow motion. The class of adiabatic transformations, during which only mechanical work is performed and no heat transfer or entropy production occurs, are only a subclass of slow motion or quasistatic processes. Theorists believed that the nuclear shape evolution until the moment of scission was so slow that individual nucleons had a sufficient time to adapt to avoided single-particle level crossings [14] and the entire nucleus would follow the lowest "molecular term," using the Born-Oppenheimer chemical terminology [15] (see **Figure 1**). Following this assumption at first the generator coordinate method (GCM) has been introduced by Hill and Wheeler [14] and Griffin and Wheeler [18] and later on a related alternative approach, the adiabatic time-dependent Hartree-Fock (ATDHF) method [19–22]. GCM is still one of the most popular tools still in use in the microscopic theories of fission [22–29]. The GCM and ATDHF method have been shown to be basically equivalent [30], when GCM is defined with complex generator coordinates [31]. As however Goeke and Reinhard [30] succinctly state: "Usually the $|q\rangle$ is obtained by an educated guess using the preconceived knowledge of the process." (Typically $|q\rangle$ stands for a generalized Slater determinant, aka Hartree-Fock-Bogoliubov many-nucleon wave function.) Even though many efforts have been dedicated to find a better way to choose the collective or generator coordinates the methods proved to be too difficult to implement in practice and the quality of the decoupling between collective and intrinsic degrees of freedom either too not very good or difficult to assess [32]. An exact separation between collective and intrinsic degrees of freedom (DoF) it is equivalent to an adiabatic evolution of the set of collective DoF. Then the collective DoF would always follow the lowest "molecular orbital" and only work would be performed on the intrinsic DoF, and thus with no heat transfer, and the intrinsic system would remain "cold" during the entire evolution.

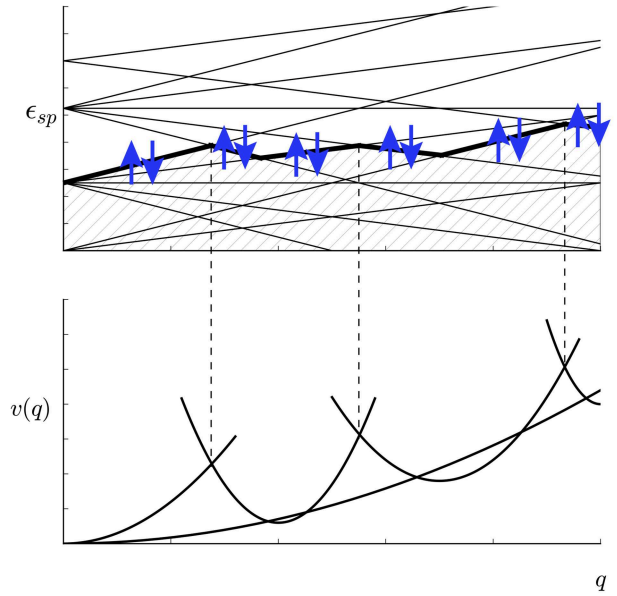


**FIGURE 1 |** The schematic evolution of the single-particle nucleons levels **(Upper panel)** and of the total nuclear energy **(Lower panel)** as a function of deformation parameter $q$ [10, 16, 17]. The thick line represents the Fermi level and the up/down arrows depict the Cooper pairs of nucleons on the Fermi level only, in time-reversed orbits $(m, -m)$. This figure is reproduced from Bulgac et al. [17] under the terms of the American Physical Society copyright agreement.

## 2. THE PRESENT

Unfortunately until recently this crucial aspect of large amplitude collective nuclear dynamics, whether the large amplitude collective motion in fission is indeed adiabatic was never tested and, as our results unequivocally show, the adiabatic assumption is strongly violated. Surprisingly at first glance, we have recently shown that the evolution of the nuclear shape is in reality significantly slower that the adiabatic assumption would predict. One would naively expect that if the motion is even slower then at an avoided level crossing (see **Figure 1**), the probability that the system would follow the lower "molecular term" is even greater and thus the adiabatic assumption would be even more likely be valid. An analogy with a classical system can help and demonstrate just the opposite. If a railroad car is released on top of a hill, it will convert basically all the gravitational potential energy difference when reaching the bottom of the hill into kinetic energy. Thus, only pure mechanical work on the intrinsic DoF of the railroad car will occur with essentially no heat transfer or entropy production. This is an adiabatic process. However, if one were instead to block the wheels of the railroad car, the friction will slow down the car and almost the entire gravitational potential energy difference will be converted into heat, the wheels will get red hot, thus increasing the "intrinsic energy" of the car, and the speed of the car at the bottom of the hill would be rather small.

The only practical theoretical framework to consider in the treatment of the dynamics of large nuclei is the (Time-Dependent) Density Function Theory [(TD)DFT], which has been formulated a long time ago [33–38]. One of the main difficulties consist in constructing the energy density functional, for which no rigorous recipes exist, DFT and TDDFT arrive at the mathematical conclusion that the stationary or time-dependent solution of the many-body Schrödinger equation is in a one-to-one-to-one correspondence with the number density, an (arbitrary) applied one-body external potential, and that the number density can be obtained by solving the much simpler DFT or TDDFT equations. There is a continual debate in nuclear physics that DFT is not applicable to nuclei, which are self-bound isolated systems. At the same time however, no one would argue that DFT cannot describe neutrons and protons in the neutron star crust and deeper into the star. Neutrons are delocalized in the neutron star crust and below it. In the rod, slab, and tube phases in the neutron star crust and below both protons and neutrons are delocalized and in this respect they are similar to electrons in solids. One can imagine that in the future one might produce a nuclear trap using some kind of $\gamma$-lasers, similarly to what nowadays experiments are made with cold atoms. Until then one can mentally imagine that one can put an isolated nucleus in a spherical infinite square well-potential with a radius about $3\ldots5\times$ the nuclear radius (or even a harmonic potential) and compare the results of such a DFT treatment of the nucleus with the widely accepted DFT *alter ego*, the NEDF approach, a tool of choice in theoretical nuclear calculations. The results of the these two approaches are numerically indistinguishable under these conditions, and therefore the debate alluded above is merely pedantic. One deficiency of a pure DFT approach is that the number density alone cannot disentangle between a normal and a superfluid system, and one needs an order parameter, as one does in the case of magnetization. The practical local density approximation (LDA) [34], which is the local formulation of DFT, has to be augmented with the anomalous density [39, 40], and it was dubbed the superfluid LDA (SLDA). In Bulgac [39, 40] one can find detailed reviews of the developments, verification, and validation of TDSLDA for a variety of physical systems, ranging from cold atoms, nuclei, and to neutron star crust.

A (TD)DFT framework for nuclear structure and dynamics should satisfy several requirements (in this order of importance): (i) the DFT and the Schrödinger description of observables should be identical, as both in ultimate instance rely on the same inter particle interactions; (ii) both DFT and Schrödinger equations should describe correctly Nature, thus we need accurate interactions between nucleons; (iii) the numerical implementation of the (TD)DFT should faithfully reproduce the theory. At present we definitely do not have acceptable answers to the requirements (i) and (ii) and rely instead to a significant amount of phenomenology. The numerical implementation of DFT without any drastic physical restrictions became possible only relatively recently, with the advent of supercomputers [39, 40].

The TDSLDA is formulated in terms of Bogoliubov quasi-particle wave functions (qpwfs). The evolution of the qpwfs is governed by the equations:

$$i\hbar\frac{\partial}{\partial t}\begin{pmatrix} u_{k\uparrow} \\ u_{k\downarrow} \\ v_{k\uparrow} \\ v_{k\downarrow} \end{pmatrix} = \begin{pmatrix} h_{\uparrow\uparrow} & h_{\uparrow\downarrow} & 0 & \Delta \\ h_{\downarrow\uparrow} & h_{\downarrow\downarrow} & -\Delta & 0 \\ 0 & -\Delta^* & -h^*_{\uparrow\uparrow} & -h^*_{\uparrow\downarrow} \\ \Delta^* & 0 & -h^*_{\downarrow\uparrow} & -h^*_{\downarrow\downarrow} \end{pmatrix}\begin{pmatrix} u_{k\uparrow} \\ u_{k\downarrow} \\ v_{k\uparrow} \\ v_{k\downarrow} \end{pmatrix}, \quad (1)$$

where we have suppressed the spatial $\boldsymbol{r}$ and time coordinate $t$, and $k$ labels the qpwfs (including the isospin) $[u_{k\sigma}(\boldsymbol{r},t), v_{k\sigma}(\boldsymbol{r},t)]$, with $\sigma = \uparrow, \downarrow$ the z-projection of the nucleon spin. The single-particle (sp) Hamiltonian $h_{\sigma\sigma'}(\boldsymbol{r},t)$, and the pairing field $\Delta(\boldsymbol{r},t)$ are functionals of various neutron and proton densities, which are computed from the qpwfs, see Jin et al. [41] for technical details. No proton-neutron pairing is assumed in the present study, and the pairing field is singlet in character. A TDSLDA extension to a more complex pairing mechanisms is straightforward.

While a nuclear system evolves in time one can uniquely separate the energy into collective kinetic energy and intrinsic energy contributions [17] using the nuclear energy density functional (NEDF) $\mathcal{E}\left(\tau(\mathbf{r},t), n(\mathbf{r},t), ...\right)$, in a similar manner as in hydrodynamics:

$$E_{\rm tot} = E_{\rm coll}(t) + E_{\rm int}(t) \equiv \int d\mathbf{r}\frac{mn(\mathbf{r},t)\mathbf{v}^2(\mathbf{r},t)}{2} + \int d\mathbf{r}\,\mathcal{E}\left(\tau(\mathbf{r},t) - n(\mathbf{r},t)m^2\mathbf{v}^2(\mathbf{r},t), n(\mathbf{r},t), ...\right). \quad (2)$$

Above $n(\mathbf{r},t)$ is the number density, $\tau(\mathbf{r},t)$ is the kinetic density energy, and $\mathbf{p}(\mathbf{r},t) = mn(\mathbf{r},t)\mathbf{v}(\mathbf{r},t)$ are linear momentum and local collective/hydrodynamic velocity densities, and ellipses stand for various other densities. $\mathbf{p}(\mathbf{r},t)/n(\mathbf{r},t)$ is the position of

the center of the local Fermi sphere in momentum space. The first term in Equation (2) is the collective/hydrodynamic energy flow $E_{\rm coll}$ and the second term is the intrinsic energy $E_{\rm int}$ in the local rest frame. For the sake of simplicity we have suppressed the spin and isospin DoF, even though they are included in all the actual calculations. The collective energy $E_{\rm coll}(t)$ is not vanishing only in the presence of currents and vanishes exactly for stationary states. The inertia tensor in $E_{\rm coll}(t)$ in the case of irrotational collective motion is fully equivalent to the Werner-Wheeler inertial tensor [23]. The intrinsic energy $E_{\rm int}(t)$ is determined only by the fermionic matter distribution. The qualitative new result established in Bulgac et al. [17] and also illustrated here in **Figure 2** is that in an fully unrestricted TDSLDA the collective flow energy is almost negligible until scission, in total discrepancy with what one would have naively expected if the adiabatic assumptions would be satisfied.

Our simulations point to an unexpectedly small $E_{\rm coll}$ from saddle-to-scission, corresponding to a collective speed $v_{\rm coll}/c \approx 0.002 \cdots 0.004$, significantly smaller than the Fermi velocity $v_F/c \approx 0.25$ (see **Figure 2**). Since in TDSLDA one simulates the one-body dynamics exactly, it is natural to discuss adiabaticity at the mean-field level. The transition rate between sp states is suppressed if the time to cross an avoided level-crossing configuration satisfies the restriction $\Delta t \ll \hbar/\Delta\epsilon \approx 400$ fm/c, where $\Delta\epsilon = 1/\rho_{\rm sp}(\epsilon_F)$ is the average sp energy level spacing at the Fermi level. Since on the way from saddle-to-scission the time required is $1 \ldots 3 \times 10^3$ fm/c and several dozen of avoided level crossings occur [16, 43], this condition is clearly violated. Somewhat surprisingly, the adiabatic assumption is also violated even in the case of SLy4 NEDF (see Bulgac et al. [42] and **Figure 2**), when the saddle-to-scission time is $\mathcal{O}(10^4)$ fm/c as well. The collective motion is thus expected to be strongly overdamped. From saddle-to-scission the nucleus behaves as a very viscous fluid, the role of collective inertia is strongly suppressed, and the trajectories follow predominantly the direction of the steepest descent with the terminal velocity determined by the balance between the friction and the driving conservative forces (see **Figure 2**).

This result serves as the first microscopic justification for the assumption of the overdamped Brownian motion model [44–49] and partially to the scission-point model [50–53]. In both these phenomenological models it is assumed that the preformed FFs are in statistical equilibrium and that the collective energy flow is either vanishing or very small. The main difference is that in the scission-point model there is no mechanism to ensure that all equilibrium scission configurations could be reached dynamically, while the nucleus evolves from the saddle-to-scission. Moreover, the relaxed FF properties are defined only after the FFs become sufficiently well-separated, see below. It is equally unexpected that in the case of enhanced pairing, when the pairing condensates retain their long-range order throughout the entire saddle-to-scission evolution, the collective dynamics remains strongly overdamped.

While evolving from saddle-to-scission a nucleus encounters a large number of avoided level crossings and instead of following the lowest potential energy surface, as would happen in an adiabatic evolution, many transitions to higher excited levels occur. Similarly to what is known for decades in chemistry [54–56], one should consider not only the lowest potential energy surface, when initially the system could be found on the lowest with unit probability, but all "molecular terms," which become populated during the evolution (see **Figure 3**). The separation

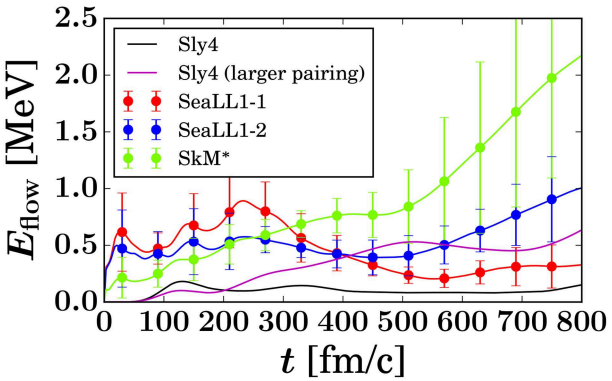


**FIGURE 2 |** (Color online) the collective flow energy evaluated for NEDFs [42] realistic pairing SLy4 (dash-dot line), enhanced pairing SLy4* (dash line), and for SkM* (dotted and dash-dot lines with error bars), and SeaLL1 (solid and dashed lines with errors bars) sets [17]. The error bars illustrate the size of the variations due to different initial conditions in case of various SeaLL1-1,2 and SkM*-1,2 NEDFs used. In the case of realistic pairing NEDF Sly4 (larger pairing) the time has been scaled by a factor of 1/10. This figure is adapted from the results published in Bulgac et al. [17] under the Creative Commons CC BY license.

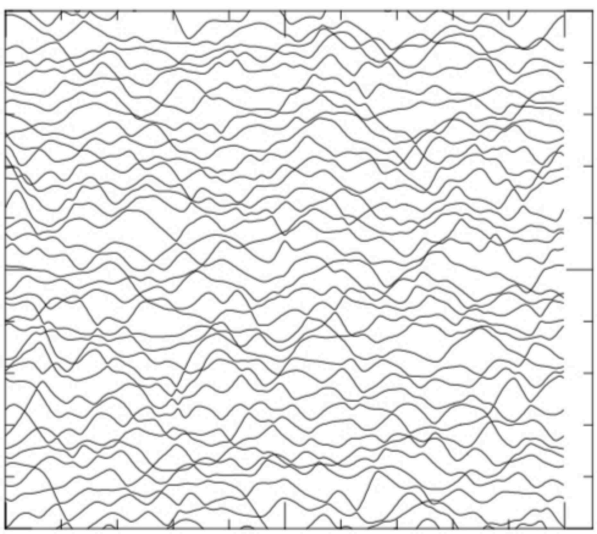

**FIGURE 3 |** In nuclei the level density increases with the excitation energy quite fast, practically exponentially at energies of the order of the neutron separation energy, when $\rho(E^*) \propto \exp\left(\sqrt{2aE^*}\right)$ [57, 58], and it reaches values of $\mathcal{O}(10^5)$ MeV$^{-1}$ and various potential energy surfaces, corresponding to different "molecular terms" display a large number of avoided level crossings. Here we illustrate the generic behavior of the collective energy levels ($y$-axis) as a function of a collective coordinate ($x$-axis), see Bulgac et al. [59] for details and a similar figure.

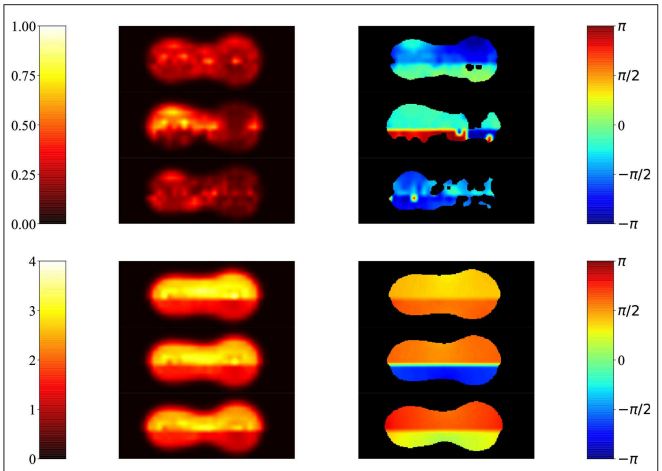


**FIGURE 4 |** These are some selected snapshots of the neutron/proton magnitudes **(Left)** and phases **(Right)** of pairing gaps (upper half/lower/half of each frame) in the case of realistic pairing strengths (upper panels) and enhanced pairing strength (lower panels), obtained in the case of SLy4 NEDF. This figure is adapted from the results published in Bulgac et al. [17] under the Creative Commons CC BY license.

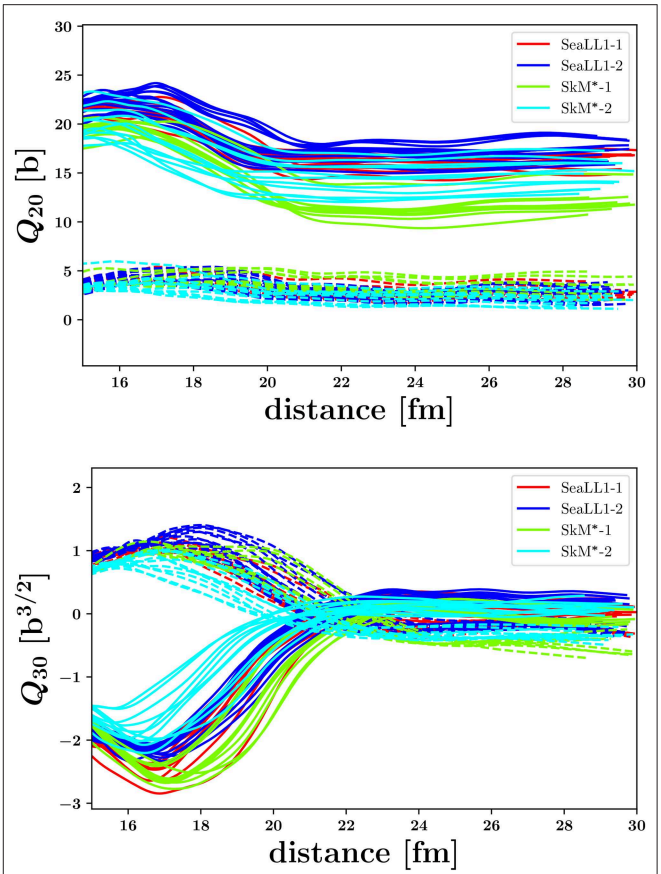


**FIGURE 5 |** The evolution of the quadrupole and octupole moments of the FFs as a functions of their separation after scission [17]. Different lines correspond to different initial conditions and different NEDFs, see Bulgac et al. [17] more details. The solid/dashed lines are for the light/heavy FFs, respectively. This figure is adapted from the results published in Bulgac et al. [17] under the Creative Commons CC BY license.

between such potential energy surfaces reaches values of order $\mathcal{O}(10)$ keV or even less, and only if the system traverses a level crossing in a time much longer than $\approx \hbar/10\,\text{keV} \approx 20,000$ fm/c or longer the nucleus will remain on the lowest potential energy surface. On the other hand the saddle-to-scission time is $\mathcal{O}(10^3)$ fm/c and this is why the adiabatic assumption is in the final analysis strongly violated.

Why do pairing correlations play an important role in fission dynamics? In a static nuclear configuration each single-particle level is doubly-degenerate, due to the Kramers degeneracy. At the level crossing both nucleons on the highest occupied level (homo—highest occupied molecular orbital) would have to transition simultaneously to the lowest down-sloping level (lumo—lowest unoccupied molecular orbital) to ensure that the local momentum distribution remains approximately spherical, as otherwise it would acquire an oblate shape [10, 11, 14], while the shape of the nucleus becomes more prolate. Nucleon-nucleon interactions at low momentum transfer can be modeled with a reasonable accuracy with a zero-range $\delta$-interaction, which favors the transitions between pairs of time-reversed orbitals, exactly as the Kramers degenerate orbitals (see **Figure 1**). The up-sloping levels are characterized by larger projections of the angular momentum on the fission axis, $|m| \approx k_F r_0 A^{1/3}$, and these levels should be depopulated, since in a FF the largest angular momenta are smaller, $\approx k_F r_0 (A/2)^{1/3}$. While evolving from one level crossing to the next, the entire evolution is likely rather well-reproduced by a simple one-body dynamics, as each single-particle level occupation probability changes little. What one-body dynamics lacks is the contributions arising from the Boltzmann collision integral. However, at each level crossing the two-correlated nucleon pairs will undergo a collision, and at low energies transitions between pairs of time-reversed orbitals expected to dominate the collision rate. One should take with a grain of salt this simplistic picture of "collisions" and jumps between sp levels, as nothing happens instantaneously or at one point in space in quantum mechanics. In the presence of a Bose-Einstein condensate of nucleon Cooper pairs the nucleus has a superfluid component and pair transfers are enhanced due to the Bose enhancement factor. The dynamics of the nuclear systems then approaches the evolution of classical inviscid (no viscosity) or perfect fluid. An illustration of this behavior was exemplified in Figure 4 in Bulgac [40] and in **Figure 4**. When the magnitude of the pairing field was artificially increased from a realistic value to a value $3\ldots4\times$ larger the evolution time from saddle-to-scission decreased by a factor of $\approx 10$ and at the same time the long range coherence of the pairing field across the entire nucleus survived. For realistic values of pairing strengths during the descent from the saddle-to-scission both proton and neutron pairing fields fluctuate both in space and time, long range order basically vanishes, but quite often it is revived.

Another important aspect which emerged from our TDSLDA fission simulations [17, 42], which is of significant importance

in the implementation of various phenomenological models, concerns the shapes of FFs at scission and when they reach their relaxed shapes (see **Figure 5**). This behavior is apparently confirmed indirectly by experiments. In Langevin or Fokker-Planck [60–65], TDGCM [26, 66], and scission-point [50–53] models the calculation of the FFs yields consider only a very limited range of nuclear shapes. In particular in such simulations one never introduces the octupole FF moments. Our results, as well recent analysis by Scamps and Simenel [67], clearly demonstrate that the FFs emerge at scission octupole deformed and also with a significantly larger quadrupole deformation than the relaxed values. Moreover, even after scission the FFs there is a significant Coulomb interaction between them, which leads to the excitation of both low energy and giant resonances in FF [68, 69]. This interaction enables additional excitation energy exchange between the FFs after scission, and it also affects their total kinetic energy, a behavior also seen in our simulation, but yet not documented. In statistical scission-point models there is no dynamics, and only the competition between FFs configurations at the scission point are considered [50–53], a model to which our results lend partial support. However, the only shapes considered are quadrupole deformation of the relaxed FFs, which clearly is not what our dynamical simulation demonstrate.

Our simulations put in evidence another very important aspect, the mechanism of the excitation energy sharing between the FFs. As a rule the heavy FF emerges in the end cooler than the light FF, even though they have been in contact for quite a long time before scission. Moreover, when increasing the initial energy excitation of the fissioning nucleus we have established that only the heavy FF becomes hotter and that is reflected in the average neutron multiplicity number of emitted, and results which is in apparent agreement with experimental findings (see **Figure 6**). Experimentally it is extremely difficult to infer the excitation energies of the FFs, which are a crucial input in various statistical codes [70, 72, 73]. Bertsch et al. [74] argue that the FFs spin distribution, which determines the prompt gamma angular distribution, can be used to infer information of the excitation energy sharing between FFs. Randrup et al. [73] point to a pronounced anti-correlation between $\bar{\nu}(A)$ and mean total kinetic energy $\overline{TKE}$, which can be used reduce uncertainties in data analysis. Schmidt and Jurado [75, 76] suggested a phenomenological model, the "energy-sorting" mechanism based on the empirical constant temperature parametrization of the nuclear level densities due to Gilbert and Cameron [77]. In this "energy-sorting" model the FFs before scission have different temperatures, with a lower temperature of the heavy fragment, which would generate an energy flow from the light/hotter to the heavy/cooler fragment. Our simulations demonstrate however that the near scission the two FFs have properties quite different (shape, excitation energy, pairing correlations) from the properties of relaxed fragments. It is therefore problematic to relate the properties of excited isolated nuclei with the properties of FFs in contact before rupture.

As we have mentioned above, the number of collective DoF and their character is a long standing problem in microscopic inspired theoretical and phenomenological models. The choice of collective DoF and their character is guided by the authors' intuition, their computational and other abilities, educated guess, imagination, and/or available resources [30]. It was never proven or demonstrated that a GCM representation of the nuclear

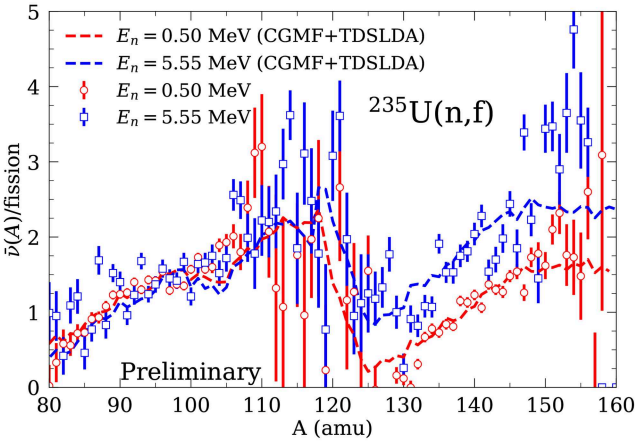


**FIGURE 6 |** We compare here the average neutron multiplicity $\bar{\nu}(A)$ emitted by FFs using a CGMF simulation [70], which assumes an $E_n$ dependence for the energy sharing extracted using the excitation energy sharing between the FFs in our calculation with NEDF SeaLL1, as a function of the equivalent incident neutron energy in $^{235}$U(n,f) reaction along with available experimental data [71]. Note that in this figure the parametrization was based on $^{240}$Pu calculations, while $^{236}$U calculations are in progress.

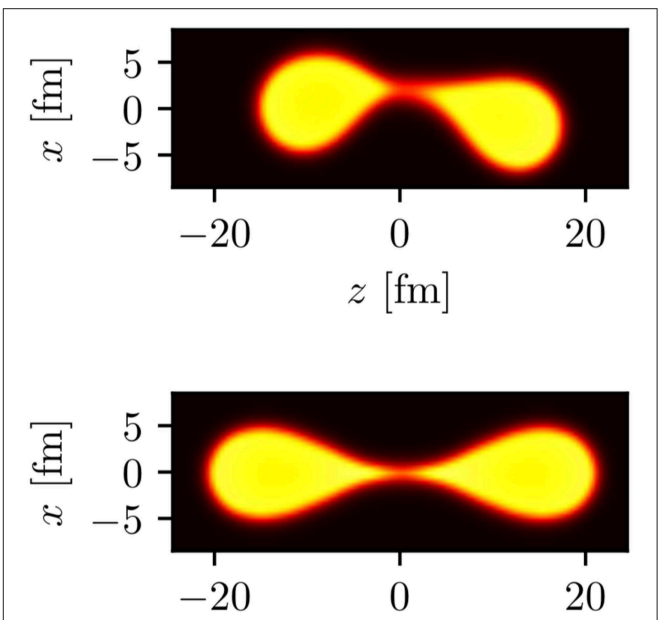


**FIGURE 7 |** In the upper panel we show a typical scission configuration when unlimited type of fluctuations are allowed as compared to a typical TDSLDA scission configuration, in which axial symmetry is assumed in this case for 258Fm. This figure is reproduced form Bulgac et al. [81] under the terms of the American Physical Society copyright agreement.

wave function is ever accurate. The wave function of a many-fermion system in TDGCM is constructed according to the following prescription

$$\Psi_{\rm GCM}(\mathbf{x},t) = \int d\mathbf{q} f(\mathbf{q},t)\Phi(\mathbf{x}|\mathbf{q}), \quad (3)$$

where $\Phi(\mathbf{x}|\mathbf{q})$ are (generalized) Slater determinants depending on nucleon spatial coordinates, spin, and isospin $\mathbf{x} = (x_1,\ldots,x_A)$, $x_k = (\mathbf{r}_k,\sigma_k,\tau_k)$ and parameterized by the collective coordinates $\mathbf{q} = (q_1,\ldots,q_n)$, and where $f(\mathbf{q},t)$ is the collective wave function. There is no criterion or small parameter which controls the accuracy of such a representation, that is

$$1 - |\langle\Psi_{\rm GCM}|\Psi_{\rm exact}\rangle| \ll \epsilon. \quad (4)$$

We have presented rather simple arguments that most likely such an accurate representation does not exist in general, particularly in fission large amplitude collective motion [17]. A rather simple estimate of the possible number of different shapes, and therefore of independent terms in Equation (3), shows that it is basically infinitely small in comparison with the number of possible terms in an exact multi-configurational Slater determinant representation of $\Psi_{\rm exact}$. Can we check whether GCM is a good approximation for the saddle-to-scission evolution? Now we definitely can and we have the answer, and since

$$E_{\rm total} = E_{\rm coll}(t) + E_{\rm int}(t) \approx E_{\rm int}(q,T) \approx V(q,T) \approx const. \quad (5)$$

where $T$ is the temperature of the intrinsic system, we know that the collective motion is strongly overdamped, that there is an irreversible energy flow from the collective/shape DoF to the intrinsic DoF, and that during the saddle-to-scission evolution the temperature of the intrinsic system increases, as does its (entanglement) entropy as well. We should also remember, that the evolution of the fissioning nucleus from saddle-to-scission is a truly non-equilibrium one, and the notion of a "slowly evolving" nuclear temperature $T$ might be questionable. This suggest that in phenomenological calculations a more physically motivated choice for the potential energy surface would be one in which with increasing deformation one would increase the "temperature $T$," so as to keep the "collective potential" energy $V(q,T)$ essentially equal to the initial excitation energy of the compound nucleus. Basically this is the prescription that Randrup et al. [48, 49] have implemented lately.

There were indirect indication in microscopic approaches that the number of collective DoF can vary along the fission path. In the overwhelming majority of fission studies the only deformation of the nucleus close to the ground state is the axial symmetric quadrupole moment $Q_{20}$, in spite of the fact that the Bohr-Mottelson five-dimensional collective Hamiltonian is one tool of choice to describe the low energy structure of open-shell nuclei [58, 78, 79]. Ryssens et al. [80] have shown in a beyond mean field calculation of the 1-dimensional fission path the nucleus $^{240}$Pu is axially deformed around the ground state configuration, it becomes triaxially deformed when it reaches the fission isomer region, and before it reaches the outer fission barrier it breaks the axial symmetry as well. We have recently developed a framework into which one can include fluctuations and dissipation in a quantum approach [81], which allows for shape fluctuations of any kind. What we observed that by allowing a bending mode to become active (see **Figure 7**), the mass and TKE distributions acquire shapes in quite nice agreement with observations. It was discussed quite some time ago that such bending modes might be responsible for the angular distributions of the FFs [82] and this type of distributions can be also extracted from TDSLDA calculations in the near future [74, 83]. Phenomenological or even TDGCM approaches do not consider so far such bending modes, which are definitely physically relevant for a large number of observables.

## 3. WHAT ARE THE NEEDS?

Nuclear fission is a complex process, in which a heavy nucleus evolves from a compact shape to a configuration in which two or more fragments are produced, and is accompanied by emission of prompt neutrons and gamma rays (and, eventually, electrons and antineutrinos). Most of the energy is released in form of kinetic energy of the fragments, while prompt neutrons emitted before beta decays play the main role in applications like energy production.

The dynamics of the nuclear system from the formation of compound nucleus until after the acceleration of FFs and prompt particle emission is too rapid to be experimentally resolved. On the other hand, the time scale of the weak interaction, which governs the decay of FFs in experiments toward stability ranges from seconds to minutes, and thus the dynamics involving beta decay toward stability, including delayed neutron and gamma emissions, can be decoupled from the initial more rapid part that is only governed by the strong interactions. Consequently, the fragment properties directly influence the properties of prompt fission and gamma rays, which have been the subject of comprehensive, albeit not exhaustive, experimental investigations over the years. Thus, at Los Alamos National Laboratory, experimental campaigns have investigated the prompt fission neutron spectra for neutron-induced fission of major actinides ($^{235,238}$U, $^{239}$Pu) for a large range of incident neutron energies using the ChiNu experimental setup [84, 85]. On the other hand, experiments that measure the average neutron multiplicity as a function of pre-fission neutron mass [86–91], which can be used to guide energy sharing in fission fragments, are more scarce, and for a limited number of reactions (usually spontaneous fission or neutron-induced fission with thermal neutrons). The surrogate reaction technique is used by Lawrence Livermore National Lab and Texas A&M to measure the $^{239}$Pu and $^{241}$Pu prompt fission neutron multiplicity (average and distribution) as a function of equivalent incident neutron energy [92, 93]. Complementary, significant resources have been devoted toward measuring the prompt fission gamma rays produced in the decay of fission fragments, after the neutron emission, at Los Alamos, using the DANCE calorimeter [94–97], and worldwide employing high-resolution detectors [98–102]. Such measurements complement existing measurements of prompt-gamma rays by Verbinski et al.

[103], and many others [104–106]. Furthermore, data on total gamma production can be useful in evaluating the prompt fission gamma properties, if no other data exist, fission dominates, and the other gamma-producing channels can be modeled with reasonable accuracy [107].

In addition to detecting and measuring the products of decay of FFs, a concerted effort has been directed toward the direct measurement of the FF distributions. While simpler, the "2E" measurements [108–111] have the shortcoming that additional information is required to identify the mass of the fragment, hence the poor 4-6 amu resolution. Reducing such large uncertainties was the main argument for the construction of the SPIDER "2E–2v" experimental setup [112, 113] at the Los Alamos Neutron Science Center, which should start taking data in the near future. In this setup the two fragment kinetic energies and velocities are measured simultaneously and can achieve one mass unit resolution, as also demonstrated by similar setups, COSI FAN TUTTE at ILL, France and VERDI at JRC-Geel, Belgium. The Sofia experiment [114] at GSI has produced an extensive amount of experimental data with accuracies in mass and charge $<1$ mass unit, but suffer from the fact that a large range of excitation energies that cannot be disentangled is produced in Coulomb excitations. LLNL and LANL activation measurements at TUNL have provided invaluable data on the incident energy dependence of cumulative fission product yields [93, 115], and ongoing efforts are directed toward testing the Bohr hypothesis of independence between entrance and outgoing channels in a compound reaction by comparing fission yields in the $^{239}$Pu(n,f) and $^{240}$Pu($\gamma$,f) reactions [116] that lead to the same fissioning system, at least in mass and charge. At CARIBOU, two projects are underway: (i) measurement of fission product properties (isomeric yield ratios, gamma-ray decay branching ratios, and $\beta$-delayed neutron emission properties) and (ii) improvements of the antineutrino spectrum simulations by performing measurements of the $\beta$-decay data using GAMASPHERE [117]. Other experiments related to the properties of FFs have concentrated on measuring the average total kinetic energy (TKE) of the fission fragments at the LANSCE WNR facility for energy from a few hundred keVs to 200 MeV [111, 113]. The High Rigidity Spectrometer [118] at FRIB [119] will allow to explore the fissioning of very neutron-rich nuclei, study their shell structure, the presence of superheavy, the limits of stability and the equation of state of neutron-rich nuclear matter, the neutron skins, and shed light on the nature of the *r*-process, so far an unknown territory.

Treating the evolution of a heavy nucleus from a compact configuration until the start of beta decays in the FFs, including prompt neutron and gamma emissions, is a complicated task, computationally unfeasible within a unified microscopic approach. Within this reality, one has to consider a mixture of approaches, in which the initial part of the fission process is treated within a microscopic framework that can inform more phenomenological treatments that model the emission of prompt neutrons and gamma rays, and whose results can be directly compared against a large set of experimental data. And the input from microscopic models does not necessarily need to be restricted to the fission process. The systematics of several physical quantities used in the phenomenological models of neutron and gamma emission is based on data for stable nuclei. Since the FFs are nuclei far from stability, it is important to investigate within more microscopic models the validity of various systematics far from stability, as prompt neutron and gamma observables are sensitive to ingredients like level densities, optical models, or gamma strength functions.

Several models have been proposed to describe the shape dynamics, and to some extent many of them are able to reproduce experimental quantities like the pre-neutron emission mass distributions, irrespective of the approximations involved. But, as noted above, the direct measurement of the FFs before neutron emission is not possible. Therefore, even before one goes into details regarding the validity of the approximations involved in theoretical models, one needs to consider the corrections involved in the analysis of the experimental data. The post-neutron emission FF mass distributions are obtained using information on average prompt neutron multiplicity as a function of the fragment mass, $\bar{\nu}(A)$, either from measurements, where available, or from phenomenological models. Given the scarcity of the data, and the fact that these phenomenological models have been built in a systematics based on little data, the uncertainties arising from $\bar{\nu}(A)$ could be considerable. Another assumption is that no neutrons are emitted during scission or at neck rupture. It is conceivable that the number of neutrons emitted during the scission dynamics is not necessarily large, but how large is large? If the fraction of scission neutrons is significant, as some phenomenological models predict, citing the experimental prompt fission spectrum as evidence to support the claim [120–125], what is the impact on the experimental analysis? While these models are not universally accepted, a microscopic approach should be able to answer such a question, and the assumption of small numbers of neutrons emitted during scission should not be implicitly included in the model. Moreover, it would be rather impossible to asses the fraction of scission neutrons if the model does not follow the dynamics of the process until full separation.

All the codes that model the prompt neutron and gamma emissions have been built in the assumption that the neutron emission proceeds after the full acceleration of the fission fragments [70, 126–130]. This assumption can have significant consequences, as at full acceleration the neutrons are maximally boosted. If the emission occurs instead during the acceleration, then the prompt neutron spectrum in the lab frame can noticeably be altered.

In addition to validating assumptions in phenomenological codes, a reliable theoretical model should provide information on observables that cannot be measured, but are essential in modeling the neutron and gamma emission. Thus, while the total excitation energy available in the fragments can be determined from the Q-value and TKE, no additional constrains on how this energy is shared between the FFs are available. As the most efficient way to lower the energy in FFs is via neutron emission, $\bar{\nu}(A)$ can be used to parameterize the excitation energy sharing. However, such data are scarcely available, usually for a limited number of spontaneous and neutron-induced fission with thermal neutrons, and thus guidance from microscopic models

on how the excitation energy is shared with increasing incident neutron energy is required not only for minor actinides, but even for induced fission reaction of major actinides $^{235,238}$U and $^{239}$Pu isotopes.

Gamma emission competes with the neutron emission when the excitation energy in the nucleus is around the neutron separation energy. The spin of the fragments, which cannot be directly measured experimentally, determines the exact strength on the neutron-gamma competition. Only indirect information can be extracted regarding the spin distribution of the FFs from properties of prompt gamma rays, like average multiplicity, prompt gamma fission spectra [131], or isomeric ratios [132]. The measurements of gamma rays are also scarce with increasing the incident neutron energy. Experimentally, one observes an increase of the total prompt fission gamma energy released in fission [133], which has been interpreted as an increase of the average spin with the incident energy. However, only little experimental data exist and no microscopic model has been able to reproduce such trends.

The main message of this section is that experimentally one cannot isolate and measure properties of post-scission FFs, and any full model will have to include simulations of prompt neutron and gamma emission, in order to compare and validate against experimental data. Given that many quantities used in the modeling of prompt neutron and gamma emission are taken from data systematics, which in general is available only for nuclei close to stability, the reliability of the theoretical model near scission and beyond, until full separation, is very important. Such models should allow for a full separation of the fragments, and employ approximations that are validated and under control, as to reduce any uncertainties regarding the FF properties.

## 4. WHAT LESSONS HAVE WE LEARNED SO FAR AND WHAT IS THE MOST LIKELY PATH TO THE FUTURE?

While pairing is not the engine driving the fission dynamics, pairing provides the essential lubricant, without which the evolution may arrive rather quickly to a screeching halt [134–136]. So far we have not considered whether proton-neutron pairing might have a role in fission. It is very unlikely that a condensate of proton-neutron pairs exists in heavy nuclei, but as we have learned from our simulations, proton-neutron transitions with L = 0 between single-particle orbitals could be important as the neutron-neutron and proton-proton transitions with (S,L,T) = (0,0,1) at low excitation energies, even in the absence of a condensate of such pairs, see the discussion concerning **Figures 1**, **4**.

TDSLDA framework for fission dynamics, while it does not incorporate fluctuations, has provided a lot of insight into the real quantum dynamics, and it revealed extremely valuable information into nuclear processes and quantities, which are either not easy or impossible to obtain in laboratory or observations: FFs excitation energies and angular momenta distributions prior to neutron and gamma emission, element formation in astrophysical environments, as well as other nuclear reactions in a parameter free approach. In particular, the excitation energy sharing mechanism between FFs and its evolution with the initial excitation energy of the compound nucleus was not accessible until now within a dynamic approach. Fluctuations, which are essential in order to reproduce mass and charge yields for example, can be now incorporated into a pure quantum framework [81].

The quality of the agreement with experimental data is surprisingly good, especially taking into account the fact that no attempt was made to reproduce any fission data. Basically all phenomenological NEDFs satisfy the most important requirements to describe the gross properties of nuclear fission: saturation, realistic surface tension and symmetry energy, Coulomb energy, realistic pairing and shell corrections energy. Nevertheless, the quality of existing NEDFs needs improving. One can make a strong argument that we have now a clear path from more phenomenology and adjusted parameters to more fundamental theory and increased predictive power [137].

Perhaps the most important aspect we have observed in all our simulations is the strong violation of the adiabatic assumption in fission large amplitude collective motion. Basically since the 1950's the adiabatic assumption was the main simplification included in all microscopic frameworks, GCM, ATDHF and a large majority of phenomenological models as well, such as the Langevin and the Fokker-Planck equations, where one needs to introduce a potential energy surface and an inertia tensor in the space of the collective variables. If the collective motion is overdamped, the inertia tensor becomes irrelevant, and moreover, considering only the lowest potential energy surface is physically unacceptable (see **Figures 3**, **2**) and the corresponding discussion in section 2. As we have established in Bulgac et al. [81] the fluctuations, or equivalently the role of two-body collisions, does not affect this conclusion.

A somewhat unexpected result was the character of the energy sharing mechanism between the fission fragments, the fact that the heavy fragment is cooler than the light fragment and it has less excitation energy [17, 42]. And this conclusion is not a result of the fact that the heavy FF is closer to the double magic $^{132}$Sn nucleus. In the original experiment of Hahn and Strassmann [1] the heavy fragment had a charge closer to $Z \approx 52 - 56$, a fact recognized also by Meitner and Frisch [2, 138], and explained by Scamps and Simenel [67], this is due to a stabilization of the octupole deformation in FFs, also observed in our simulations [17, 42]. With increasing excitation energy of the fissioning nucleus the heavy FF appears to be the only one who absorb the increase and emits more neutrons (see **Figure 6**) and the accompanying discussion. The character of the excitation energy sharing mechanism has major consequences on the predicted spectrum of emitted neutrons and gammas.

Another important outcome was the clear indications that many more collective DoF appear to be relevant in fission than have ever been considered in either phenomenological or microscopically inspired models, such as GCM and ATDHF frameworks. At scission, both FFs are octupolly deformed. Moreover, the FFs attain their relaxed shapes only after the separation between them is $\approx$ 5...6 fm. No phenomenological or microscopically inspired approach on the market follow the

FFs to such large separations. As we stressed in section 3 the spectrum of emitted neutrons is affected by the number of neutrons emitted before the full FFs acceleration. Another DoF, which appears to be relevant as well is the bending mode (see **Figure 7** and Bulgac et al. [81]), the inclusion of which likely is going to influence the angular momentum distributions of the FFs [82].

We have pointed to several directions into which phenomenological models and theoretical models, such as GCM and ATDHF would have to be altered, in order to describe nuclear fission in a manner more consistent with theoretical expectations inferred from unrestricted quantum mechanical simulations (see section 3). We did not cover or mention all phenomenological models on the market and not all microscopically inspired theoretical frameworks, as this is not a review of such approaches, for which we recommend [129, 139].

## DATA AVAILABILITY STATEMENT

The datasets generated for this study are available on request to the corresponding author.

## AUTHOR CONTRIBUTIONS

All authors listed have made a substantial, direct and intellectual contribution to the work, and approved it for publication.

## FUNDING

The work of AB and SJ was supported by U.S. Department of Energy, Office of Science, Grant No. DE-FG02-97ER41014 and in part by NNSA cooperative agreement DE-NA0003841. The work of IS was supported by the US Department of Energy through the Los Alamos National Laboratory. Los Alamos National Laboratory is operated by Triad National Security, LLC, for the National Nuclear Security Administration of U.S. Department of Energy (Contract No. 89233218CNA000001).

## ACKNOWLEDGMENTS

We thank many people with whom we had discussion over the years and for their input: I. Abdurrahman, G. F. Bertsch, P. Magierski, K. J. Roche, and N. Schunck. We thank G. F. Bertsch and J. Randrup who made a number of suggestions on our manuscript, which has been released as a preprint [140]. The TDSLDA calculations have been performed at the OLCF Summit and Titan, and CSCS Piz Daint, and for generating initial configurations for direct input into the TDSLDA code at OLCF Titan and Summit and NERSC Edison. This research used resources of the Oak Ridge Leadership Computing Facility, which was a U.S. DOE Office of Science User Facility supported under Contract No. DE- AC05-00OR22725 and of the National Energy Research Scientific computing Center, which was supported by the Office of Science of the U.S. Department of Energy under Contract No. DE-AC02-05CH11231. We acknowledge PRACE for awarding us access to resource Piz Daint based at the Swiss National Supercomputing Centre (CSCS), decision No. 2018194657. This work was supported by High Performance Computing Infrastructure in Japan, Project ID: hp180048. A series of simulations were carried out on the Tsubame 3.0 supercomputer at Tokyo Institute of Technology. This research used resources provided by the Los Alamos National Laboratory Institutional Computing Program.

## REFERENCES

1. Hahn O, Strassmann F. Über den Nachweis und das Verhalten der bei der Bestrahlung des Urans mittels Neutronen entstehenden Erdalkalimetalle. *Naturwissenschaften.* (1939) **27**:11.
2. Meitner L, Frisch OR. Disintegration of uranium by neutrons: a new type of nuclear reaction. *Nature.* (1939) **143**:239. doi: 10.1038/143239a0
3. Stuewer R. *An Act of Creation: The Meitner–Frisch Interpretation of Nuclear Fission*. Berlin: Neopubli GmbH (2010). Available online at: http://edition-open-access.de/proceedings/5/11/index.html
4. Pearson JM. On the belated discovery of fission. *Phys Today.* (2015) **68**:40. doi: 10.1063/PT.3.2817
5. Fermi E, Amaldi E, d'Agostino O, Rasetti F, Segre E. Artificial radioactivity produced by neutron bombardment. *Proc R Soc A.* (1934) **146**:249.
6. Bohr N. Neutron capture and nuclear constitution. *Nature.* (1936) **137**:344, 351.
7. Bohr N, Wheeler JA. The mechanism of nuclear fission. *Phys Rev.* (1939) **56**:426.
8. Strutinsky VM. Shell effects in nuclear masses and deformation energies. *Nucl Phys A.* (1967) **95**:420.
9. Brack M, Damgaard J, Jensen AS, Pauli HC, Strutinsky VM, Wong CY. Funny Hills: the shell-correction approach to nuclear shell effects and its applications to the fission process. *Rev Mod Phys.* (1972) **44**:320.
10. Bertsch G. The nuclear density of states in the space of nuclear shapes. *Phys Lett B.* (1980) **95**:157.
11. Bertsch GF, Bulgac A. Comment on "spontaneous fission: a kinetic approach". *Phys Rev Lett.* (1997) **79**:3539.
12. Weisskopf V. Statistics and nuclear reactions. *Phys Rev.* (1937) **52**:295.
13. Hauser W, Feshbach H. The inelastic scattering of neutrons. *Phys Rev.* (1952) **87**:366.
14. Hill DL, Wheeler JA. Nuclear constitution and the interpretation of fission phenomena. *Phys Rev.* (1953) **89**:1102.
15. Born M, Oppenheimer JR. Zur Quantentheorie der Molekeln. *Ann Phys.* (1927) **389**:457.
16. Barranco F, Bertsch GF, Broglia RA, Vigezzi E. Large-amplitude motion in superfluid Fermi droplets. *Nucl Data Sheets Phys A.* (1990) **512**:253.
17. Bulgac A, Jin S, Roche KJ, Schunck N, Stetcu I. Fission dynamics of $^{240}$Pu from saddle to scission and beyond. *Phys Rev C.* (2019) **100**:034615. doi: 10.1103/PhysRevC.100.034615
18. Griffin JJ, Wheeler JA. Collective motions in nuclei by the method of generator coordinates. *Phys Rev.* (1957) **108**:311.
19. Baranger M. Microscopic view of nuclear collective properties. *J Phys.* (1972) **33**:C5.
20. Baranger M, Véneroni M. An adiabatic time-dependent Hartree-Fock theory of collective motion in finite systems. *Ann Phys.* (1978) **114**:123.
21. Villars F. Adiabatic time-dependent Hartree-Fock theory in nuclear physics. *Nucl Phys A.* (1978) **285**:269.
22. Ring P, Schuck P. *The Nuclear Many-Body Problem*. 1st ed. No. 17 in Theoretical and Mathematical Physics Series. Berlin; Heidelberg; New York, NY: Springer-Verlag (2004).

23. Krappe JK, Pomorski K. *Theory of Nuclear Fission*. Heidelberg: Springer (2012).
24. Schunck N, Robledo LM. Microscopic theory of nuclear fission: a review. *Rep Prog Phys.* (2016) **79**:116301. doi: 10.1088/0034-4885/79/11/116301
25. Goutte H, Berger JF, Casoli P, Gogny D. Microscopic approach of fission dynamics applied to fragment kinetic energy and mass distributions in $^{238}$U. *Phys Rev C.* (2005) **71**:024316. doi: 10.1103/PhysRevC.71.024316
26. Regnier D, Dubray N, Schunck N, Verrière M. Fission fragment charge and mass distributions in $^{239}$Pu$(n,f)$ in the adiabatic nuclear energy density functional theory. *Phys Rev C.* (2016) **93**:054611. doi: 10.1103/PhysRevC.93.054611
27. Zdeb A, Dobrowolski A, Warda M. Fission dynamics of $^{252}$**Cf**. *Phys Rev C.* (2017) **95**:054608. doi: 10.1103/PhysRevC.95.054608
28. Schunck N, editor. *Energy Density Functional Methods for Atomic Nuclei*. Bristol: IOP Publishing (2019).
29. Younes W, Gogny DM, Berger JF. *A Microscopic Theory of Fission Based on the Generator Coordinate Method. Vol. 950 of Lectures Notes in Physics*. Berlin: Springer (2019).
30. Goeke K, Reinhard PG. The generator-coordinate-method with conjugate parameters and the unification of microscopic theories for large amplitude collective motion. *Ann Phys.* (1980) **124**:249.
31. Peierls RE, Thouless DJ. Variational approach to collective motion. *Nucl Phys.* (1962) **38**:154.
32. Dang GD, Klein A, Walet NR. Self-consistent theory of large-amplitude collective motion: applications to approximate quantization of nonseparable systems and to nuclear physics. *Phys Rep.* (2000) **335**:93. doi: 10.1016/S0370-1573(99)00119-2
33. Hohenberg P, Kohn W. Inhomogeneous electron gas. *Phys Rev.* (1964) **136**:B864–71.
34. Kohn W, Sham LJ. Self-consistent equations including exchange and correlation effects. *Phys Rev.* (1965) **140**:A1133–8.
35. Kohn W. Nobel lecture: electronic structure of matter—wave functions and density functionals. *Rev Mod Phys.* (1999) **71**:1253–66.
36. Dreizler RM, Gross EKU. *Density Functional Theory: An Approach to the Quantum Many–Body Problem*. Berlin: Springer-Verlag (1990).
37. Marques MAL, Ullrich CA, Nogueira F, Rubio A, Burke K, Gross EKU, editors. *Time-Dependent Density Functional Theory. Vol. 706 of Lecture Notes in Physics*. Berlin: Springer-Verlag (2006).
38. Marques MAL, Maitra NT, Nogueira FMS, Gross EKU, Rubio A, editors. *Fundamentals of Time-Dependent Density Functional Theory. Vol. 837 of Lecture Notes in Physics*. Heidelberg: Springer (2012).
39. Bulgac A. Time-dependent density functional theory and the real-time dynamics of Fermi superfluids. *Ann Rev Nucl Part Sci.* (2013) **63**:97. doi: 10.1146/annurev-nucl-102212-170631
40. Bulgac A. Time-dependent density functional theory for fermionic superfluids: from cold atomic gases, to nuclei and neutron star crust. *Phys Status Solidi B.* (2019) **2019**:1800592. doi: 10.1002/pssb.201800592
41. Jin S, Bulgac A, Roche K, Wlazłowski G. Coordinate-space solver for superfluid many-fermion systems with the shifted conjugate-orthogonal conjugate-gradient method. *Phys Rev C.* (2017) **95**:044302. doi: 10.1103/PhysRevC.95.044302
42. Bulgac A, Magierski P, Roche KJ, Stetcu I. Induced fission of $^{240}$Pu within a real-time microscopic framework. *Phys Rev Lett.* (2016) **116**:122504. doi: 10.1103/PhysRevLett.116.122504
43. Bertsch GF, Younes W, Robledo LM. Scission dynamics with $K$ partitions. *Phys Rev C.* (2018) **97**:064619. doi: 10.1103/PhysRevC.97.064619
44. Weidenmüller HA, Zhang JS. Nuclear fission viewed as a diffusion process: case of very large friction. *Phys Rev C.* (1984) **29**:879. doi: 10.1103/PhysRevC.29.879
45. Randrup J, Möller P. Brownian shape motion on five-dimensional potential-energy surfaces: nuclear fission-fragment mass distributions. *Phys Rev Lett.* (2011) **106**:132503. doi: 10.1103/PhysRevLett.106.132503
46. Randrup J, Möller P, Sierk AJ. Fission-fragment mass distributions from strongly damped shape evolution. *Phys Rev C.* (2011) **84**:034613. doi: 10.1103/PhysRevC.84.034613
47. Randrup J, Möller P. Energy dependence of fission-fragment mass distributions from strongly damped shape evolution. *Phys Rev C.* (2013) **88**:064606. doi: 10.1103/PhysRevC.88.064606
48. Ward DE, Carlsson BG, Døssing T, Möller P, Randrup J, Åberg S. Nuclear shape evolution based on microscopic level densities. *Phys Rev C.* (2017) **95**:024618. doi: 10.1103/PhysRevC.95.024618
49. Albertsson M, Carlsson BG, Døssing T, Møller P, Randrup J, Åberg S. Excitation energy partition in fission. *Phys Lett B.* (2020) **803**:135276. doi: 10.1016/j.physletb.2020.135276
50. Wilkins BD, Steinberg EP. Semi-empirical interpretation of nuclear fission based on deformed-shell effects. *Phys Lett B.* (1972) **42**:141.
51. Wilkins BD, Steinberg EP, Chasman RR. Scission-point model of nuclear fission based on deformed-shell effects. *Phys Rev C.* (1976) **14**:1832.
52. Lemaître JF, Panebianco S, Sida JL, Hilaire S, Heinrich S. New statistical scission-point model to predict fission fragment observables. *Phys Rev C.* (2015) **92**:034617. doi: 10.1103/PhysRevC.92.034617
53. Lemaître JF, Goriely S, Hilaire S, Sida JL. Fully microscopic scission-point model to predict fission fragment observables. *Phys Rev C.* (2019) **99**:034612. doi: 10.1103/PhysRevC.99.034612
54. Tully JC, Preston RK. Trajectory surface hopping approach to nonadiabatic molecular collisions: the reaction of $H^+$ with $D_2$. *J Chem Phys.* (1971) **55**:562.
55. Tully JC. Molecular dynamics with electronic transitions. *J Chem Phys.* (1990) **93**:1061.
56. Hammes-Schiffer S, Tully JC. Proton transfer in solution: molecular dynamics with quantum transitions. *J Chem Phys.* (1994) **101**:4657.
57. Bethe HA. An attempt to calculate the number of energy levels of a heavy nucleus. *Phys Rev.* (1936) **50**:332–41.
58. Bohr A, Mottelson BR. *Nuclear Structure, Vols. I and II*. New York, NY: Benjamin Inc. (1969).
59. Bulgac A, Dang GD, Kusnezov D. Stochastic aspects of large amplitude collective motion. *Phys Rep.* (1996) **264**:67.
60. Grangé P, Li JQ, Weidenmüller HA. Induced nuclear fission viewed as a diffusion process: transients. *Phys Rev C.* (1983) **27**:2063.
61. Fröbrich P, Gontchar II. Langevin description of fusion, deep-inelastic collisions and heavy-ion-induced fission. *Phys Rep.* (1998) **292**:131.
62. Sierk AJ. Langevin model of low-energy fission. *Phys Rev C.* (2017) **96**:034603. doi: 10.1103/PhysRevC.96.034603
63. Ishizuka C, Usang MD, Ivanyuk FA, Maruhn JA, Nishio K, Chiba S. Four-dimensional Langevin approach to low-energy nuclear fission of $^{236}$**U**. *Phys Rev C.* (2017) **96**:064616. doi: 10.1103/PhysRevC.96.064616
64. Sadhukhan J, Nazarewicz W, Schunck N. Microscopic modeling of mass and charge distributions in the spontaneous fission of $^{240}$Pu. *Phys Rev C.* (2016) **93**:011304. doi: 10.1103/PhysRevC.93.011304
65. Sadhukhan J, Zhang C, Nazarewicz W, Schunck N. Formation and distribution of fragments in the spontaneous fission of $^{240}$**Pu**. *Phys Rev C.* (2017) **96**:061301. doi: 10.1103/PhysRevC.96.061301
66. Regnier D, Dubray N, Schunck N. From asymmetric to symmetric fission in the fermium isotopes within the time-dependent generator-coordinate-method formalism. *Phys Rev C.* (2019) **99**:024611. doi: 10.1103/PhysRevC.99.024611
67. Scamps G, Simenel C. Impact of pear-shaped fission fragments on mass-asymmetric fission in actinides. *Nature.* (2018) **564**:382. doi: 10.1038/s41586-018-0780-0
68. Mustafa MG, Schmitt HW, Mosel U. Dipole excitations in fission fragments. *Nucl Phys A.* (1971) **178**:9.
69. Simenel C, Umar AS. Formation and dynamics of fission fragments. *Phys Rev C.* (2014) **89**:031601. doi: 10.1103/PhysRevC.89.031601
70. Becker B, Talou P, Kawano T, Danon Y, Stetcu I. Monte Carlo Hauser-Feshbach predictions of prompt fission gamma rays: application to n+235U, n+239Pu, and 252Cf (sf). *Phys Rev C.* (2013) **87**:014617. doi: 10.1103/PhysRevC.87.014617
71. Müller R, Naqvi AA, Käppeler F, Dickmann F. Fragment velocities, energies, and masses from fast neutron induced fission of $^{235}$U. *Phys Rev C.* (1984) **29**:885.
72. Randrup J, Vogt R. Calculation of fission observables through event-by-event simulation. *Phys Rev C.* (2009) **80**:024601. doi: 10.1103/PhysRevC.80.024601
73. Randrup J, Talou P, Vogt R. Sensitivity of neutron observables to the model input in simulations of $^{252}$Cf(sf). *Phys Rev C.* (2019) **99**:054619. doi: 10.1103/PhysRevC.99.054619

74. Bertsch GF, Kawano T, Robledo LM. Angular momentum of fission fragments. *Phys Rev C.* (2019) **99**:034603. doi: 10.1103/PhysRevC.99.034603
75. Schmidt KH, Jurado B. Entropy driven excitation energy sorting in superfluid fission dynamics. *Phys Rev Lett.* (2010) **104**:212501. doi: 10.1103/PhysRevLett.104.212501
76. Schmidt KH, Jurado B. Final excitation energy of fission fragments. *Phys Rev C.* (2011) **83**:061601. doi: 10.1103/PhysRevC.83.061601
77. Gilbert A, Cameron AGW. A composite nuclear-level density formula with shell correction. *Can J Phys.* (1965) **43**:1446.
78. Bertsch GF, Girod M, Hilaire S, Delaroche JP, Goutte H, Péru S. Systematics of the first $2^+$ excitation with the Gogny interaction. *Phys Rev Lett.* (2007) **99**:032502. doi: 10.1103/PhysRevLett.99.032502
79. Delaroche JP, Girod M, Libert J, Goutte H, Hilaire S, Péru S, et al. Structure of even-even nuclei using a mapped collective Hamiltonian and the D1S Gogny interaction. *Phys Rev C.* (2010) **81**:014303. doi: 10.1103/PhysRevC.81.014303
80. Ryssens W, Heenen PH, Bender M. Numerical accuracy of mean-field calculations in coordinate space. *Phys Rev C.* (2015) **92**:064318. doi: 10.1103/PhysRevC.92.064318
81. Bulgac A, Jin S, Stetcu I. Unitary evolution with fluctuations and dissipation. *Phys Rev C.* (2019) **100**:014615. doi: 10.1103/PhysRevC.100.014615
82. Moretto LG, Peqaslee GF, Wozniak GJ. Angular-momentum-bearing modes in fission. *Nucl Phys A.* (1989) **502**:453c.
83. Bulgac A. Projection of good quantum numbers for reaction fragments. *Phys Rev C.* (2019) **100**:034612. doi: 10.1103/PhysRevC.100.034612
84. Haight RC, Wu CY, Lee HY, Taddeucci TN, Perdue BA, O'Donnell JM, et al. The LANL/LLNL prompt fission neutron spectrum program at LANSCE and approach to uncertainties. *Nucl Data Sheets.* (2015) **123**:130–4. doi: 10.1016/j.nds.2014.12.023
85. Kelly KJ, Devlin M, Gomez JA, O´Donnell JM, Taddeucci TN, Haight RC, et al. Measurements of the prompt fission neutron spectrum at LANSCE: the Chi-Nu experiment. *EPJ Web Conf.* (2018) **193**:03003. doi: 10.1051/epjconf/201819303003
86. Maslin EE, Rodgers AL, Core WGF. Prompt neutron emission from $U^{235}$ fission fragments. *Phys Rev.* (1967) **164**:1520–7.
87. Nishio K, Nakagome Y, Yamamoto H, Kimura I. Multiplicity and energy of neutrons from 235U(nth,f) fission fragments. *Nucl Phys A.* (1998) **632**:540–58.
88. Tsuchiya C, Nakagome Y, Yamana H, Moriyama H, Nishio K, Kanno I, et al. Simultaneous measurement of prompt neutrons and fission fragments for 239Pu(nth,f). *J Nucl Sci Tech.* (2000) **37**:941. doi: 10.1080/18811248.2000.9714976
89. Batenkov OA, Boykov GA, Hambsch FJ, Hamilton JH, Jakovlev VA, Kalinin VA, et al. Prompt neutron emmision in the neutron-induced fission of $^{239}$Pu and $^{235}$U. *AIP Conf Proc.* (2005) **769**:1003. doi: 10.1063/1.1945175
90. Göök A, Hambsch FJ, Vidali M. Prompt neutron multiplicity in correlation with fragments from spontaneous fission of $^{252}$Cf. *Phys Rev C.* (2014) **90**:064611. doi: 10.1103/PhysRevC.90.064611
91. Göök A, Hambsch FJ, Oberstedt S, Vidali M. Prompt neutrons in correlation with fission fragments from $^{235}$U$(n,f)$. *Phys Rev C.* (2018) **98**:044615. doi: 10.1103/PhysRevC.98.044615
92. Akindele OA, Alan BS, Burke JT, Casperson RJ, Hughes RO, Koglin JD, et al. Expansion of the surrogate method to measure the prompt fission neutron multiplicity for $^{241}$Pu. *Phys Rev C.* (2019) **99**:054601. doi: 10.1103/PhysRevC.99.054601
93. Wang BS, Harke JT, Akindele OA, Casperson RJ, Hughes RO, Koglin JD, et al. Determining the average prompt-fission-neutron multiplicity for $^{239}$Pu$(n,f)$ via a $^{240}$Pu$(\alpha,\alpha' f)$ surrogate reaction. *Phys Rev C.* (2019) **100**:064609. doi: 10.1103/PhysRevC.100.064609
94. Ullmann JL, Bond EM, Bredeweg TA, Couture A, Haight RC, Jandel M, et al. Prompt $\gamma$-ray production in neutron-induced fission of $^{239}$Pu. *Phys Rev C.* (2013) **87**:044607. doi: 10.1103/PhysRevC.87.044607
95. Chyzh A, Wu CY, Kwan E, Henderson RA, Gostic JM, Bredeweg TA, et al. Systematics of prompt $\gamma$-ray emission in fission. *Phys Rev C.* (2013) **87**:034620. doi: 10.1103/PhysRevC.87.034620
96. Chyzh A, Wu CY, Kwan E, Henderson RA, Bredeweg TA, Haight RC, et al. Total prompt $\gamma$-ray emission in fission of $^{235}$U, $^{239,241}$Pu, and $^{252}$Cf. *Phys Rev C.* (2014) **90**:014602. doi: 10.1103/PhysRevC.90.014602
97. Jandel M, Rusev G, Bond EM, Bredeweg TA, Chadwick MB, Couture A, et al. Prompt fission gamma-ray studies at DANCE. *Phys Proc.* (2014) **59**:101–6. doi: 10.1016/j.phpro.2014.10.016
98. Billnert R, Hambsch FJ, Oberstedt A, Oberstedt S. New prompt spectral $\gamma$-ray data from the reaction $^{252}$Cf(sf) and its implication on present evaluated nuclear data files. *Phys Rev C.* (2013) **87**:024601. doi: 10.1103/PhysRevC.87.024601
99. Oberstedt A, Belgya T, Billnert R, Borcea R, Bryś T, Geerts W, et al. Improved values for the characteristics of prompt-fission $\gamma$-ray spectra from the reaction $^{235}$U$(n_{\rm th},f)$. *Phys Rev C.* (2013) **87**:051602. doi: 10.1103/PhysRevC.87.051602
100. Lebois M, Wilson JN, Halipré P, Oberstedt A, Oberstedt S, Marini P, et al. Comparative measurement of prompt fission $\gamma$-ray emission from fast-neutron-induced fission of $^{235}$U and $^{238}$U. *Phys Rev C.* (2015) **92**:034618. doi: 10.1103/PhysRevC.92.034618
101. Gatera A, Belgya T, Geerts W, Göök A, Hambsch FJ, Lebois M, et al. Prompt-fission $\gamma$-ray spectral characteristics from $^{239}$Pu$(n_{\rm th},f)$. *Phys Rev C.* (2017) **95**:064609. doi: 10.1103/PhysRevC.95.064609
102. Makii H, Nishio K, Hirose K, Orlandi R, Léguillon R, Ogawa T, et al. Effects of the nuclear structure of fission fragments on the high-energy prompt fission $\gamma$-ray spectrum in $^{235}$U$(n_{\rm th},f)$. *Phys Rev C.* (2019) **100**:044610. doi: 10.1103/PhysRevC.100.044610
103. Verbinski VV, Weber H, Sund RE. Prompt gamma rays from $^{235}$U$(n,f)$, $^{239}$Pu$(n,f)$, and spontaneous fission of $^{252}$Cf. *Phys Rev C.* (1973) **7**:1173–85.
104. Peelle RW, Maienschein FC. Spectrum of photons emitted in coincidence with fission of $^{235}$U by thermal neutrons. *Phys Rev C.* (1971) **3**:373–90.
105. Pleasonton F, Ferguson RL, Schmitt HW. Prompt gamma rays emitted in the thermal-neutron-induced fission of $^{235}$U. *Phys Rev C.* (1972) **6**:1023–39.
106. Pleasonton F. Prompt $\gamma$-rays emitted in the thermal-neutron induced fission of $^{233}$U and $^{239}$Pu. *Nucl Phys A.* (1973) **213**:413–25.
107. Stetcu I, Chadwick MB, Kawano T, Talou P, Capote R, Trkov A. Evaluation of the prompt fission gamma properties for neutron induced fission of $^{235;238}$U and $^{239}$Pu. *Nucl Data Sheets.* (2020) **163**:261–79. doi: 10.1016/j.nds.2019.12.007
108. Straede C, Budtz-Jørgensen C, Knitter HH. 235U(n, f) Fragment mass-, kinetic energy- and angular distributions for incident neutron energies between thermal and 6 MeV. *Nucl Phys A.* (1987) **462**:85–108.
109. Vivès F, Hambsch FJ, Bax H, Oberstedt S. Investigation of the fission fragment properties of the reaction 238U(n,f) at incident neutron energies up to 5.8 MeV. *Nucl Phys A.* (2000) **662**:63–92. doi: 10.1016/S0375-9474(99)00413-3
110. Birgersson E, Oberstedt A, Oberstedt S, Hambsch FJ. Properties of the reaction 238U at the vibrational resonances. *Nucl Phys A.* (2009) **817**:1–34. doi: 10.1016/j.nuclphysa.2008.12.001
111. Duke DL, Tovesson F, Laptev AB, Mosby S, Hambsch FJ, Bryś T, et al. Fission-fragment properties in $^{238}$U$(n,f)$ between 1 and 30 MeV. *Phys Rev C.* (2016) **94**:054604. doi: 10.1103/PhysRevC.94.054604
112. Tovesson F, Arnold CW, Bredeweg T, Jandel M, Laptev AB, Meierbachtol K, et al. SPIDER: a new instrument for fission yield measurement. In: Hamilton JH, Ramayya AV, editors. *Proceedings of the Fifth International Conference on ICFN5*. Singapore: World Scientific (2013). p. 361.
113. Meierbachtol K, Tovesson F, Duke DL, Geppert-Kleinrath V, Manning B, Meharchand R, et al. Total kinetic energy release in $^{239}$Pu$(n,f)$ post-neutron emission from 0.5 to 50 MeV incident neutron energy. *Phys Rev C.* (2016) **94**:034611. doi: 10.1103/PhysRevC.94.034611
114. Pellereau E, Taïeb J, Chatillon A, Alvarez-Pol H, Audouin L, Ayyad Y, et al. Accurate isotopic fission yields of electromagnetically induced fission of $^{238}$U measured in inverse kinematics at relativistic energies. *Phys Rev C.* (2017) **95**:054603. doi: 10.1103/PhysRevC.95.054603
115. Gooden ME, Arnold CW, Becker JA, Bhatia C, Bhike M, Bond EM, et al. Energy dependence of fission product yields from 235U, 238U and 239Pu for incident neutron energies between 0.5 and 14.8 MeV. *Nucl Data Sheets.* (2016) **131**:319–56. doi: 10.1016/j.nds.2015.12.006
116. Silano J, Tonchev A, Henderson R, Schunck N, Tornow W, Howell C, et al. Comparing fission-product yields from photon-induced fission of $^{240}$Pu and neutron-induced fission of $^{239}$Pu as a test of the Bohr hypothesis in nuclear fission. In: *Proceedings of the Santa Fe Workshop on Fission Product Yields*. Los Alamos, NM (2019).

117. Savard G. Fission product yield measurements using $^{252}$Cf spontaneous fission and neutron-induced fission on actinide targets at CARIBU. In: *Talk at the International Workshop on Fission Product Yields*. Los Alamos, NM (2019).
118. *A High Rigidity Spectrometer fro FRIB*. Available online at: hrs.lbl.gov/documents/HRS-WhitePaper122017.pdf
119. *Facility for Rare Isotopes Beams*. Available online at: www.frib.msu.edu
120. Carjan N, Rizea M. Scission neutrons and other scission properties as function of mass asymmetry in $^{235}$U($n_{\rm th}$,$f$). *Phys Rev C.* (2010) **82**:014617. doi: 10.1103/PhysRevC.82.014617
121. Carjan N, Hambsch FJ, Rizea M, Serot O. Partition between the fission fragments of the excitation energy and of the neutron multiplicity at scission in low-energy fission. *Phys Rev C.* (2012) **85**:044601. doi: 10.1103/PhysRevC.85.044601
122. Rizea M, Carjan N. Dynamical scission model. *Nucl Phys A.* (2013) **909**:50–68. doi: 10.1016/j.nuclphysa.2013.04.014
123. Carjan N, Rizea M. Similarities between calculated scission-neutron properties and experimental data on prompt fission neutrons. *Phys Lett B.* (2015) **747**:178–81. doi: 10.1016/j.physletb.2015.05.050
124. Capote R, Carjan N, Chiba S. Scission neutrons for U, Pu, Cm, and Cf isotopes: relative multiplicities calculated in the sudden limit. *Phys Rev C.* (2016) **93**:024609. doi: 10.1103/PhysRevC.93.024609
125. Carjan N, Rizea M. Structures in the energy distribution of the scission neutrons: finite neutron-number effect. *Phys Rev C.* (2019) **99**:034613. doi: 10.1103/PhysRevC.99.034613
126. Vogt R, Randrup J. Event-by-event modeling of prompt neutrons and photons from neutron-induced and spontaneous fission with FREYA. *Phys Proc.* (2013) **47**:82–7. doi: 10.1016/j.phpro.2013.06.013
127. Litaize O, Serot O, Berge L. Fission modelling with FIFRELIN. *Eur Phys Jour A.* (2015) **51**:177. doi: 10.1140/epja/i2015-15177-9
128. Schmidt KH, Jurado B, Amouroux C, Schmitt C. General description of fission observables: GEF model code. *Nucl Data Sheets.* (2016) **131**:107–221. doi: 10.1016/j.nds.2015.12.009
129. Schmidt KH, Jurado B. Review on the progress in nuclear fission–experimental methods and theoretical descriptions. *Rep Prog Phys.* (2018) **81**:106301. doi: 10.1088/1361-6633/aacfa7
130. Talou P, Vogt R, Randrup J, Rising ME, Pozzi SA, Verbeke J, et al. Correlated prompt fission data in transport simulations. *Eur Phys J A.* (2018) **54**:9. doi: 10.1140/epja/i2018-12455-0
131. Stetcu I, Talou P, Kawano T, Jandel M. Properties of prompt-fission $\gamma$ rays. *Phys Rev C.* (2014) **90**:024617. doi: 10.1103/PhysRevC.90.024617
132. Stetcu I, Talou P, Kawano T, Jandel M. Isomer production ratios and the angular momentum distribution of fission fragments. *Phys Rev C.* (2013) **88**:044603. doi: 10.1103/PhysRevC.88.044603
133. Fréhaut J, Bertin A, Bois R. Mesure de $\bar{\nu}_p$ pour la fission de $^{232}$Th, $^{235}$U et $^{237}$Np induite par des neutrons d'energie comprise entre 1 et 15 MeV. In: *International Conference on Nuclear Data for Science and Technology*. Antwerp; Dordrech: Reidel (1983). p. 78.
134. Goddard P, Stevenson P, Rios A. Fission dynamics within time-dependent Hartree-Fock: deformation-induced fission. *Phys Rev C.* (2015) **92**:054610. doi: 10.1103/PhysRevC.92.054610
135. Goddard P, Stevenson P, Rios A. Fission dynamics within time-dependent Hartree-Fock. II. Boost-induced fission. *Phys Rev C.* (2016) **93**:014620. doi: 10.1103/PhysRevC.93.014620
136. Tanimura Y, Lacroix D, Scamps G. Collective aspects deduced from time-dependent microscopic mean-field with pairing: application to the fission process. *Phys Rev C.* (2015) **92**:034601. doi: 10.1103/PhysRevC.92.034601
137. Bulgac A, Jin S, Magierski P, Roche KJ, Schunck N, Stetcu I. Nuclear fission: from more phenomenology and adjusted parameters to more fundamental theory and increased predictive power. *EPJ Web Conf.* (2017) **163**:00007. doi: 10.1051/epjconf/201716300007
138. Meitner L, Frisch OR. Products of the fission of the uranium nucleus. *Nature.* (1939) **143**:471.
139. Andreyev AN, Nishio K, Schmidt KH. Nuclear fission: a review of experimental advances and phenomenology. *Rep Prog Phys.* (2018) **81**:016301.
140. Bulgac A, Jin S, Stetcu I. Nuclear fission dynamics: past, present, needs, and future. *arXiv.* (2019) 1912:00287v1.


**Conflict of Interest:** The authors declare that the research was conducted in the absence of any commercial or financial relationships that could be construed as a potential conflict of interest.

frontiers in Physics

REVIEW
published: 25 March 2020
doi: 10.3389/fphy.2020.00067

# Applications of Time-Dependent Density-Matrix Approach

*Mitsuru Tohyama**

*Faculty of Medicine, Kyorin University, Tokyo, Japan*

The equations of motion for reduced density matrices form a coupled chain known as the Bogoliubov-Born-Green-Kirkwood-Yvon (BBGKY) hierarchy. To close the coupled chain at the two-body level, approximations for a three-body density matrix with one-body and two-body density matrices are needed. The time-dependent density-matrix theory (TDDM) assumes that the three-body density matrix is given by the antisymmetrized products of the one-body and two-body density matrices. In this review the truncation schemes of the BBGKY hierarchy beyond TDDM are discussed and a formulation for the study of excited states which is derived from the time-dependent approach is explained. The truncation schemes and the formulation for excited states are applied to the Lipkin model and the Hubbard model to corroborate their validity. Two realistic applications of the TDDM approaches are also presented. One is the dipole and quadrupole excitations of $^{40}$Ca and $^{48}$Ca and the other the fusion reactions of $^{16}$O + $^{16}$O.

**Keywords: extended TDHF, extended RPA, Lipkin model, Hubbard model, giant resonances, fusion**

OPEN ACCESS

***Edited by:***
*Denis Lacroix,*
*UMR8608 Institut de Physique Nucléaire d'Orsay (IPNO), France*

***Reviewed by:***
*Marcella Grasso,*
*UMR8608 Institut de Physique Nucléaire d'Orsay (IPNO), France*
*Gianluca Colò,*
*University of Milan, Italy*

***Correspondence:**
*Mitsuru Tohyama*
*tohyama@ks.kyorin-u.ac.jp*

***Specialty section:***
*This article was submitted to Nuclear Physics, a section of the journal Frontiers in Physics*

***Received:*** *22 November 2019*
***Accepted:*** *28 February 2020*
***Published:*** *25 March 2020*

***Citation:***
*Tohyama M (2020) Applications of Time-Dependent Density-Matrix Approach. Front. Phys. 8:67. doi: 10.3389/fphy.2020.00067*

## 1. INTRODUCTION

The time-dependent Hartree-Fock theory (TDHF) is the basis of the mean-field theories such as the Hartree-Fock theory (HF) and the random-phase approximation (RPA): The HF ground state is given as a stationary solution of the TDHF equation and RPA can be formulated as the small amplitude limit of the TDHF equation. HF and RPA have extensively been used as standard theories to study nuclear structure problem [1]. Extensive TDHF simulations have also been performed for heavy-ion collisions [2, 3]. However, most experimental data suggest that beyond-mean field theories are required for a more realistic description of nuclear structure and reactions. In this paper an approach to extend the mean-field theories based on the equations of motion for reduced density matrices is reviewed. The equations of motion for reduced density matrices form a coupled chain known as the Bogoliubov-Born-Green-Kirkwood-Yvon (BBGKY) hierarchy [4] where the time evolution of an $n$-body density matrix depends on $n$-body and $n + 1$-body density matrices. The advantage of such a time-dependent density-matrix approach (TDDMA) is that it is directly connected to TDHF in the lowest-level approximation: The truncation of the BBGKY hierarchy at the level of the one-body density matrix by approximating the two-body density matrix with the antisymmetrized product of the one-body density matrices gives TDHF. A beyond TDHF is obtained by the truncation of the BBGKY hierarchy at the two-body level and it needs approximations for the three-body density matrix. A few truncations schemes have been proposed. The simplest truncation scheme is to replace the three-body density matrix with the antisymmetrized products of the one-body and two-body density matrices, neglecting the correlated part of the three-body density matrix [the three-body correlation matrix ($C_3$)] [5, 6]. This truncation scheme has been called the time-dependent density-matrix theory (TDDM). TDDM has been applied to heavy-ion collisions [7–9] and collective excitations [6, 10–12]. A

simplified TDDM called TDDM$^{\mathrm{p}}$ [13] where two-body correlations are consider only for a pair of time reversed single-particle (s.p.) states have also been employed to simulate heavy-ion collisions [13, 14]. It was found that TDDM sometimes overestimates ground-state correlations in a solvable model [15], gives unphysical s.p. occupation probabilities in dynamical simulations [16, 17] and causes divergent dynamical behaviors in highly excited and (or) strongly interacting cases [18, 19]. Obviously the problems originate in the neglect of $C_3$ and are related to the loss of $N$-representability [20] which refers to the properties of reduced density matrices derived from an $N$-body total wavefunction and is completely fulfilled only in the case of the untruncated BBGKY hierarchy. To remedy the difficulties of the naive truncation scheme in the description of ground states, an approximation for $C_3$ has been proposed based on perturbative consideration [21], where $C_3$ is given by the traced products of the correlated part of the two-body density matrix ($C_2$). This truncation scheme is referred to as TDDM1 hereafter. The correlation matrices $C_2$ and $C_3$ are also called the two-body and three-body cumulants and the above approximation for $C_3$ corresponds to taking the leading-order terms of the three-body cumulant [22, 23]. It has been demonstrated that TDDM1 improves the TDDM results for the ground states of model Hamiltonians [21, 23] and also $^{16}$O [24]. In the case of the Lipkin model [25], however, TDDM1 was found to overestimate $C_3$ in strongly interacting regions. There, another truncation scheme [26] where $C_3$ in TDDM1 is divided by a reduction factor was introduced. This truncation scheme is referred to as TDDM2. In this paper three truncation schemes TDDM, TDDM1 and TDDM2 are explained and their applications are presented.

The small amplitude limit of the TDDMA equations gives an extended RPA (ERPA) which is used for the study of excited states, as is the case of RPA which is formulated as the small amplitude limit of TDHF. RPA and ERPA are also formulated by using the equation of motion approach [27, 28]. ERPA consists of the coupled equations for the one-body and two-body amplitudes and include the effects of ground-state correlations through the fractional occupation probability $n_\alpha$ of a s.p. state $\alpha$ and $C_2$. ERPA is related to so far proposed beyond-RPA theories. When the coupling to the two-body amplitude is omitted, the ERPA equation for the one-body amplitude is the same as the self-consistent RPA (SCRPA) [29, 30] equation which includes both $n_\alpha$ and $C_2$. The neglect of $C_2$ in the SCRPA equation corresponds to the renormalized RPA (rRPA) [27, 28] which includes the ground-state correlation effect via $n_\alpha$. When the HF ground state is assumed, the equations in ERPA are reduced to those in the second RPA (SRPA) [31]. If particle-hole correlations included in the two-body amplitudes were expressed by phonons, ERPA would be connected the particle-vibration coupling or quasiparticle-phonon models [32]. ERPA has been applied to solvable models [23, 33]. Realistic cases have also been studied in ERPA [34–36]. Main results of the ERPA applications are presented in this paper.

The TDDM truncation scheme has been used for simulations of heavy-ion collisions [7–9] where the TDDM equations are formulated by using the time-dependent s.p. states which obey a TDHF-like equation. The application of such a TDDM approach to the fusion reactions of $^{16}$O + $^{16}$O is also presented.

The paper is organized as follows: The equations of motion for the one-body and two-body density matrices formulated by using a time-independent s.p. basis are given in section 2 and the truncation schemes of the BBGKY hierarchy and the formulation of ERPA are discussed. The applications are made to two model Hamiltonians, the Lipkin model [25] and the one-dimensional Hubbard model [37] in section 2 and the obtained results are compared with the exact solutions. The ERPA results for the dipole and quadrupole excitations in $^{40}$Ca and $^{48}$Ca are presented in section 2 as realistic applications of ERPA. The TDDM formulation using a time-dependent s.p. basis and its application to the fusion reactions of $^{16}$O + $^{16}$O are given in section 3. Section 4 is devoted to summary and outlook.

## 2. FORMULATION IN TIME-INDEPENDENT SINGLE-PARTICLE BASIS

The TDDMA equations are formulated for an $N$ fermion system described by the Hamiltonian $H$ consisting of a one-body part $t$ (the kinetic energy term) and a two-body interaction $v$

$$H = \sum_{\alpha\alpha'} \langle \alpha | t | \alpha' \rangle a^+_\alpha a_{\alpha'} + \frac{1}{2} \sum_{\alpha\beta\alpha'\beta'} \langle \alpha\beta | v | \alpha'\beta' \rangle a^+_\alpha a^+_\beta a_{\beta'} a_{\alpha'},$$

where $a^+_\alpha$ and $a_\alpha$ are the creation and annihilation operators of a particle at a s.p. state $\alpha$ and the s.p. states are assumed time-independent.

### 2.1. Time-Dependent Density-Matrix Theory and Truncation Schemes

The TDDMA equations given in Tohyama and Schuck [21] are explained below. They consist of the coupled equations of motion for the one-body density matrix (the occupation matrix) $n_{\alpha\alpha'}$ and the correlated part of the two-body density matrix $C_{\alpha\beta\alpha'\beta'}$ ($C_2$). These matrices are defined as

$$n_{\alpha\alpha'}(t) = \langle \Phi(t) | a^+_{\alpha'} a_\alpha | \Phi(t) \rangle, \tag{1}$$

$$C_{\alpha\beta\alpha'\beta'}(t) = \rho_{\alpha\beta\alpha'\beta'}(t) - \mathcal{A}(n_{\alpha\alpha'}(t) n_{\beta\beta'}(t)), \tag{2}$$

where $|\Phi(t)\rangle$ is the time-dependent total wavefunction $|\Phi(t)\rangle = \exp[-iHt]|\Phi(t=0)\rangle$, $\rho_{\alpha\beta\alpha'\beta'}$ is the two-body density matrix ($\rho_{\alpha\beta\alpha'\beta'}(t) = \langle \Phi(t) | a^+_{\alpha'} a^+_{\beta'} a_\beta a_\alpha | \Phi(t) \rangle$) and $\mathcal{A}$ is an operator which properly antisymmetrizes $n_{\alpha\alpha'} n_{\beta\beta'}$ under the exchange of the s.p. indices such as $\alpha \leftrightarrow \beta$ and $\alpha' \leftrightarrow \beta'$. Units $\hbar = 1$ are used hereafter. The equations of motion for $n_{\alpha\alpha'}$ and $C_{\alpha\beta\alpha'\beta'}$ are derived from

$$i\dot{n}_{\alpha\alpha'} = \langle \Phi(t) | [a^+_{\alpha'} a_\alpha, H] | \Phi(t) \rangle \tag{3}$$

$$i\dot{\rho}_{\alpha\beta\alpha'\beta'} = \langle \Phi(t) | [a^+_{\alpha'} a^+_{\beta'} a_\beta a_\alpha, H] | \Phi(t) \rangle, \tag{4}$$

by evaluating the commutation relations. They are written as

$$i\dot{n}_{\alpha\alpha'} = \sum_{\lambda}(\epsilon_{\alpha\lambda}n_{\lambda\alpha'} - n_{\alpha\lambda}\epsilon_{\lambda\alpha'}) + \sum_{\lambda_1\lambda_2\lambda_3}[\langle\alpha\lambda_1|v|\lambda_2\lambda_3\rangle C_{\lambda_2\lambda_3\alpha'\lambda_1} - C_{\alpha\lambda_1\lambda_2\lambda_3}\langle\lambda_2\lambda_3|v|\alpha'\lambda_1\rangle], \quad (5)$$

$$i\dot{C}_{\alpha\beta\alpha'\beta'} = \sum_{\lambda}(\epsilon_{\alpha\lambda}C_{\lambda\beta\alpha'\beta'} + \epsilon_{\beta\lambda}C_{\alpha\lambda\alpha'\beta'} - \epsilon_{\lambda\alpha'}C_{\alpha\beta\lambda\beta'} - \epsilon_{\lambda\beta'}C_{\alpha\beta\alpha'\lambda}) + B_{\alpha\beta\alpha'\beta'} + P_{\alpha\beta\alpha'\beta'} + H_{\alpha\beta\alpha'\beta'} + T_{\alpha\beta\alpha'\beta'}, \quad (6)$$

where $\epsilon_{\alpha\alpha'}$ is the s.p. energy including the mean field and is given by

$$\epsilon_{\alpha\alpha'} = \langle\alpha|t|\alpha'\rangle + \sum_{\lambda_1\lambda_2}\langle\alpha\lambda_1|v|\alpha'\lambda_2\rangle_A n_{\lambda_2\lambda_1}. \quad (7)$$

Here the subscript $A$ means that the corresponding matrix is antisymmetrized. The term $B_{\alpha\beta\alpha'\beta'}$ in Equation (6) consists of only the occupation matrices and describes 2 particle (p) – 2 hole (h) and 2h–2p excitations, while $P_{\alpha\beta\alpha'\beta'}$ and $H_{\alpha\beta\alpha'\beta'}$ contain $C_2$ and express p–p (and h–h) and p–h correlations to infinite order, respectively [6]. The $T_{\alpha\beta\alpha'\beta'}$ term gives the coupling to the three-body correlation matrix ($C_3$)

$$T_{\alpha\beta\alpha'\beta'} = \sum_{\lambda_1\lambda_2\lambda_3}[\langle\alpha\lambda_1|v|\lambda_2\lambda_3\rangle C_{\lambda_2\lambda_3\beta\alpha'\lambda_1\beta'} + \langle\lambda_1\beta|v|\lambda_2\lambda_3\rangle C_{\lambda_2\lambda_3\alpha\alpha'\lambda_1\beta'} - \langle\lambda_1\lambda_2|v|\alpha'\lambda_3\rangle C_{\alpha\lambda_3\beta\lambda_1\lambda_2\beta'} - \langle\lambda_1\lambda_2|v|\lambda_3\beta'\rangle C_{\alpha\lambda_3\beta\lambda_1\lambda_2\alpha'}], \quad (8)$$

where $C_{\alpha\beta\gamma\alpha'\beta'\gamma'}$ ($C_3$) is given by

$$C_{\alpha\beta\gamma\alpha'\beta'\gamma'} = \langle\Phi(t)|a^+_{\alpha'}a^+_{\beta'}a^+_{\gamma'}a_\gamma a_\beta a_\alpha|\Phi(t)\rangle - \mathcal{A}(n_{\alpha\alpha'}\rho_{\beta\gamma\beta'\gamma'}) \quad (9)$$

Approximations for $C_3$ are needed to close the equations of motion within $n_{\alpha\alpha'}$ and $C_2$. Three truncation schemes TDDM, TDDM1 and TDDM2 have been proposed. In TDDM, $C_3$ is simply omitted [5, 6]. In TDDM1, $C_3$ is given by [21]

$$C_{\mathrm{p_1p_2h_1p_3p_4h_2}} = \sum_{\mathrm{h}} C_{\mathrm{hh_1p_3p_4}}C_{\mathrm{p_1p_2h_2h}}, \quad (10)$$

$$C_{\mathrm{p_1h_1h_2p_2h_3h_4}} = \sum_{\mathrm{p}} C_{\mathrm{h_1h_2p_2p}}C_{\mathrm{p_1ph_3h_4}}, \quad (11)$$

where p and h refer to particle and hole states, respectively. These expressions were derived from perturbative consideration using the Coupled-Cluster-Doubles (CCD)-like ground state wavefunction [38]. In a time-independent density-matrix approach in quantum chemistry, known as the contracted Schrödinger equation [20], Mazziotti [22] has proposed a method for constructing the three-body cumulant ($C_3$) with $n_{\alpha\alpha'}$ and $C_2$. Equations (10) and (11) describe the leading-order terms in the three-body cumulant [23]. TDDM2 [26] is the most effective in the large $N$ and strongly interacting limits of the Lipkin model and gives

$$C_{\mathrm{p_1p_2h_1p_3p_4h_2}} = \frac{1}{\mathcal{N}}\sum_{\mathrm{h}} C_{\mathrm{hh_1p_3p_4}}C_{\mathrm{p_1p_2h_2h}}, \quad (12)$$

$$C_{\mathrm{p_1h_1h_2p_2h_3h_4}} = \frac{1}{\mathcal{N}}\sum_{\mathrm{p}} C_{\mathrm{h_1h_2p_2p}}C_{\mathrm{p_1ph_3h_4}}, \quad (13)$$

where $\mathcal{N}$ is

$$\mathcal{N} = 1 + \frac{1}{4}\sum_{\mathrm{pp'hh'}} C_{\mathrm{pp'hh'}}C_{\mathrm{hh'pp'}}. \quad (14)$$

The factor $\mathcal{N}$ was introduced to simulate many-body effects which reduce $C_3$ in large $N$ systems and (or) strongly interacting regions of the Lipkin model. In the perturbative region where the second term on the right-hand side of Equation (26) is smaller than unity, $\mathcal{N}$ has the meaning of the normalization factor of the total wavefunction.

The conservation of the total energy and total particle number is not affected by the truncation schemes for $C_3$ as long as its symmetry and anti-symmetry properties under the exchange of s.p. indices is respected. However, the trace relation between the one-body and two-body density matrices $n_{\alpha\alpha'} = \sum_\lambda \rho_{\alpha\lambda\alpha'\lambda}/(N-1)$ is not conserved when any approximation is made for $C_3$. This is an example of the loss of $N$-representability [20]. It was pointed out [21] that the fulfillment of the trace relation is drastically improved by going from TDDM to TDDM1. In an attempt to conserve the trace relation, Cassing and Pfitzner [39] proposed an approximation for $C_3$ which also contains quadratic terms of $C_2$. However, $C_3$ is not uniquely determined only by the requirement of the trace relation conservation. In contrast to TDDM1 their quadratic terms do not have the leading-order terms (Equations 10, 11) of the three-body cumulant [22, 23] and the dynamical effect of $C_3$ was found small in one-dimensional heavy-ion simulations [39]. $C_3$ in Reference [39] is not anti-symmetric under the exchange of s.p. indices, which may violate even the conservation of the trace relation as was pointed out by Gherega et al. [17]. There is another attempt [40] to conserve the trace relation, where the equation motion for $C_3$ was solved by truncating the BBGKY hierarchy at the three-body level. However, the application of such an approach was limited to model Hamiltonians [40].

## 2.2. Ground-State Calculation

The ground state in TDDMA is given as a stationary solution of the time-dependent equations (Equations 5, 6) which satisfies $\dot{n}_{\alpha\alpha'} = 0$ and $\dot{C}_2 = 0$. Two methods have been employed to obtain the stationary solution. One is the adiabatic method: Equations (5) and (6) are solved by starting from the HF configuration and gradually increasing the strength of the residual interaction such as $v(\vec{r}-\vec{r}') \times t/T$. This method is based on the Gell-Mann-Low theorem [41] and has often been used to obtain approximate ground states with various time-dependent functionals [11, 13, 14, 42, 43]. To suppress oscillating components which come from the mixing of excited

states, $T$ must be much larger than the longest period in the system considered. The other method is a usual iterative gradient method which is useful to obtain a rigorously stationary solution. Since it involves matrix inversion, the application of the gradient method is limited to small systems: The gradient method has been employed to obtain the ground states of the Lipkin model [15] and the oxygen, calcium and tin isotopes [34–36] using several s.p. states around the Fermi level [34, 36] or the valence neutron s.p. states [35].

## 2.3. Excited-States Calculation

The formulation for excited states can be derived by either taking the small amplitude limit of the TDDM equations or using the equation of motion approach [1, 27]. Here the formulation based on the equation of motion approach is presented. Let us consider a generalized RPA operator with one-body and two-body sectors

$$\mathcal{Q}_\mu^+ = \sum_{\lambda\lambda'} x^\mu_{\lambda\lambda'} a^+_\lambda a_{\lambda'} + \sum_{\lambda_1\lambda_2\lambda'_1\lambda'_2} X^\mu_{\lambda_1\lambda_2\lambda'_1\lambda'_2} a^+_{\lambda_1} a^+_{\lambda_2} a_{\lambda'_2} a_{\lambda'_1}, \quad (15)$$

where there is no restriction on the s.p. indices: They can be both p and h. As usual with the equation of motion approach, the properties of the excitation operator $\mathcal{Q}_\mu^+|\Phi_0\rangle = |\Phi_\mu\rangle$ and $\mathcal{Q}_\mu|\Phi_0\rangle = 0$ are assumed and the following equations of motion satisfied by exact states are taken into account

$$\langle\Phi_0|[a^+_\lambda a_{\lambda'}, H]|\Phi_\mu\rangle = \omega_\mu \Phi_0|a^+_\lambda a_{\lambda'}|\Phi_\mu\rangle \quad (16)$$

$$\langle\Phi_0|[a^+_{\lambda_1} a^+_{\lambda_2} a_{\lambda'_2} a_{\lambda'_1}, H]|\Phi_\mu\rangle = \omega_\mu \langle\Phi_0|a^+_{\lambda_1} a^+_{\lambda_2} a_{\lambda'_2} a_{\lambda'_1}|\Phi_\mu\rangle, \quad (17)$$

where $\omega_\mu$ is the excitation energy of an excited state $|\Phi_\mu\rangle$. The equations for $x^\mu_{\lambda\lambda'}$ and $X^\mu_{\lambda_1\lambda_2\lambda'_1\lambda'_2}$ are obtained by inserting Equation (15) into the above equations. They are written in matrix form [15, 40]

$$\begin{pmatrix} A & B \\ C & D \end{pmatrix} \begin{pmatrix} x^\mu \\ X^\mu \end{pmatrix} = \omega_\mu \begin{pmatrix} S_1 & T_1 \\ T_2 & S_2 \end{pmatrix} \begin{pmatrix} x^\mu \\ X^\mu \end{pmatrix}. \quad (18)$$

The Hamiltonian matrices $A$, $B$, $C$ and $D$ are given by

$$A(\alpha\alpha' : \lambda\lambda') = \langle\Phi_0|[[a^+_{\alpha'} a_\alpha, H], a^+_\lambda a_{\lambda'}]|\Phi_0\rangle, \quad (19)$$

$$B(\alpha\alpha' : \lambda_1\lambda_2\lambda'_1\lambda'_2) = C^+ = \langle\Phi_0|[[a^+_{\alpha'} a_\alpha, H], a^+_{\lambda_1} a^+_{\lambda_2} a_{\lambda'_2} a_{\lambda'_1}]|\Phi_0\rangle, \quad (20)$$

$$D(\alpha\beta\alpha'\beta' : \lambda_1\lambda_2\lambda'_1\lambda'_2) = \langle\Phi_0|[[a^+_{\alpha'} a^+_{\beta'} a_\beta a_\alpha, H], a^+_{\lambda_1} a^+_{\lambda_2} a_{\lambda'_2} a_{\lambda'_1}]|\Phi_0\rangle. \quad (21)$$

The norm matrices $S_1$, $T_1$, $T_2$, and $S_2$ are given as

$$S_1(\alpha\alpha' : \lambda\lambda') = \langle\Phi_0|[a^+_{\alpha'} a_\alpha, a^+_\lambda a_{\lambda'}]|\Phi_0\rangle, \quad (22)$$

$$T_1(\alpha\alpha' : \lambda_1\lambda_2\lambda'_1\lambda'_2) = T_2^+ = \langle\Phi_0|[a^+_{\alpha'} a_\alpha, a^+_{\lambda_1} a^+_{\lambda_2} a_{\lambda'_2} a_{\lambda'_1}]|\Phi_0\rangle, \quad (23)$$

$$S_2(\alpha\beta\alpha'\beta' : \lambda_1\lambda_2\lambda'_1\lambda'_2) = \langle\Phi_0|[a^+_{\alpha'} a^+_{\beta'} a_\beta a_\alpha, a^+_{\lambda_1} a^+_{\lambda_2} a_{\lambda'_2} a_{\lambda'_1}]|\Phi_0\rangle. \quad (24)$$

These matrices are evaluated by assuming $|\Phi_0\rangle$ to be the ground state in TDDMA. This means that the effects of ground-state correlations are included in the above matrices through $n_{\alpha\alpha'}$ and $C_2$. All matrix elements in Equation (18) are given in Tohyama and Schuck [40]. The one-body sector of Equation (18), $Ax^\mu = \omega_\mu S_1 x^\mu$, is explicitly shown below to explain how $n_{\alpha\alpha'}$ and $C_2$ are included. The matrix $S_1$ is given by

$$S_1(\alpha\alpha' : \lambda\lambda') = (n_{\alpha'\alpha'} - n_{\alpha\alpha})\delta_{\alpha\lambda}\delta_{\alpha'\lambda'} \quad (25)$$

and $A$ by

$$\begin{aligned} A(\alpha\alpha' : \lambda\lambda') &= (\epsilon_\alpha - \epsilon_{\alpha'})(n_{\alpha'\alpha'} - n_{\alpha\alpha})\delta_{\alpha\lambda}\delta_{\alpha'\lambda'} \\ &+ (n_{\alpha'\alpha'} - n_{\alpha\alpha})(n_{\lambda'\lambda'} - n_{\lambda\lambda})\langle\alpha\lambda'|v|\alpha'\lambda\rangle_A \\ &- \delta_{\alpha'\lambda'} \sum_{\gamma\gamma'\gamma''} \langle\alpha\gamma|v|\gamma'\gamma''\rangle C_{\gamma'\gamma''\lambda\gamma} \\ &- \delta_{\alpha\lambda} \sum_{\gamma\gamma'\gamma''} \langle\gamma\gamma'|v|\alpha'\gamma''\rangle C_{\lambda'\gamma''\gamma\gamma'} \\ &+ \sum_{\gamma\gamma'} (\langle\alpha\gamma|v|\lambda\gamma'\rangle_A C_{\lambda'\gamma'\alpha'\gamma} + \langle\lambda'\gamma|v|\alpha'\gamma'\rangle_A C_{\alpha\gamma'\lambda\gamma}) \\ &- \sum_{\gamma\gamma'} (\langle\alpha\lambda'|v|\gamma\gamma'\rangle C_{\gamma\gamma'\alpha'\lambda} + \langle\gamma\gamma'|v|\alpha'\lambda\rangle C_{\alpha\lambda'\gamma\gamma'}), \end{aligned} \quad (26)$$

where $\epsilon_{\alpha\alpha'}$ and $n_{\alpha\alpha'}$ are assumed to be diagonal for simplicity. The first two terms on the right-hand side of Equation (22) are of the same form as the RPA and rRPA euqations, the next two terms with $C_2$ and the Kronecker delta $\delta_{\alpha\alpha'}$ describe the self-energies of the $\alpha$–$\alpha'$ configurations due to ground-state correlations [29, 44], and the other terms with $C_2$ are interpreted as the vertex corrections [29, 44]. Equation (18) has the most general form of beyond RPA theories: It is reduced to SRPA when the ground-state correlations are neglected and the one-body sector of Equation (18) $Ax^\mu = \omega_\mu S_1 x^\mu$ is formally the same as the equation in SCRPA. Equation (18) is referred to as the extended RPA (ERPA) hereafter.

Although ERPA has great advantages over other extended RPA theories, it is worth pointing out its limitations. The numbers of the matrix elements of $C_2$ and $X^\mu_{\alpha\beta\alpha'\beta'}$ increase rapidly with increasing number of the s.p. states. Therefore, truncation of the s.p. space is required in realistic applications. As shown below, basic effects of two-body correlations can be described with rather small s.p. space, however. The other limitation is concerned with hermiticity of $D$ in Equation (18), which is related to the truncation of the BBGKY hierarchy. Equation (21) contains $C_3$ and it is approximated depending on the truncation scheme. Hermiticity of $D$ which is guaranteed only when all the matrix elements of $C_3$ satisfy the stationary condition as those of $n_{\alpha\alpha'}$ and $C_2$ do is not fulfilled [40] when any approximated is made for $C_3$. The non-hermiticity has not caused serious problems in the applications thus far considered, though. In the case of the Lipkin model, an attempt [40] to obtain Hermitian $D$ was carried out by solving the equation of motion for $C_3$.

## 2.4. Applications

TDDMA's in the time-independent s.p. basis have been applied to model Hamiltonians [23, 33] to corroborate their validity:

The Lipkin model [25] was used to compare three truncation schemes TDDM, TDDM1 and TDDM2. Comparison of ERPA with other beyond-RPA theories, rRPA, SCRPA and SRPA was performed for the one-dimensional Hubbard model [37]. As realistic applications of ERPA, the quadrupole excitations of oxygen isotopes [34], the low-lying quadrupole states in tin isotopes [35] and the dipole and quadrupole excitations of $^{40}$Ca and $^{48}$Ca [36] have been studied. In the following some of the results are presented.

### 2.4.1. Lipkin Model

The Lipkin model [25] has extensively been used to test theoretical models. It describes an $N$-fermions system with two $N$-fold degenerate levels. The upper (lower) levels have energies $\epsilon/2$ ($-\epsilon/2$) and quantum number $p$ ($-p$) with $p = 1, 2, ..., N$. The Hamiltonian is given by

$$H = \epsilon J_z + \frac{V}{2}(J_+^2 + J_-^2), \tag{27}$$

where the operators are the followings

$$J_z = \frac{1}{2}\sum_{p=1}^{N}(c_p^+ c_p - c_{-p}{}^+ c_{-p}), \tag{28}$$

$$J_+ = J_-^+ = \sum_{p=1}^{N} c_p^+ c_{-p}. \tag{29}$$

For $\chi = |V|(N-1)/\epsilon \leq 1$ the HF ground state is given by $|\mathrm{HF}\rangle = \prod_{p=1}^{N} c_{-p}^+|0\rangle$, where $|0\rangle$ is the true vacuum. For $\chi > 1$ the lowest s.p. states are obtained by the transformation

$$\begin{pmatrix} a_{-p}^+ \\ a_p^+ \end{pmatrix} = \begin{pmatrix} \cos\alpha & \sin\alpha \\ -\sin\alpha & \cos\alpha \end{pmatrix} \begin{pmatrix} c_{-p}^+ \\ c_p^+ \end{pmatrix}, \tag{30}$$

where $\alpha$ satisfies $\cos 2\alpha = 1/\chi$. The HF ground state in this case is often called the "deformed" HF (DHF) state and is given by $|\mathrm{DHF}(\alpha)\rangle = \prod_{p=1}^{N} a_{-p}^+|0\rangle$.

The truncation schemes TDDM, TDDM1 and TDDM2 have been applied to the Lipkin model and it was found that the simplest scheme TDDM gives the exact solutions in the limits of large $N$ and $\chi$ [45]. This is due to the unique property of the Lipkin model that the ground-state energy in DHF becomes exact in such limits [1]. The relation between the density-matrices in DHF and TDDM is discussed below. The occupation matrix in DHF is given by $n_{-p-p} = \cos^2\alpha$, $n_{pp} = 1 - n_{-p-p} = \sin^2\alpha$, and $n_{p-p} = \cos\alpha\sin\alpha$. The two-body and three-body density matrices in DHF are given by the above elements of the occupation matrix. For example the 2p–2h and ph–ph elements of the two-body density matrix are expressed as

$$\begin{aligned}\rho_{pp'-p-p'} &= \langle \mathrm{DHF}(\alpha)|c_{-p}^+ c_{-p'}^+ c_{p'} c_p|\mathrm{DHF}(\alpha)\rangle \\ &= \cos^2\alpha\sin^2\alpha = n_{p-p}n_{p'-p'} = \rho_{p-p'-pp'}(p \neq p').\end{aligned} \tag{31}$$

Similarly, the three-body density matrix is given by

$$\rho_{p-p'p''pp'-p''} = \cos^2\alpha\sin^4\alpha = n_{pp}\rho_{-p'p''p'-p''}. \tag{32}$$

This means that the correlated part ($C_{p-p'p''pp'-p''}$) of the three-body density matrix vanishes in DHF. The "spherical" total wavefunction $|\Psi\rangle$ in DHF which does not have the mixing of the $p$ and $-p$ states is given by the two DHF solutions as

$$|\Psi\rangle = \frac{1}{\sqrt{2}}(|\mathrm{DHF}(\alpha)\rangle + |\mathrm{DHF}(-\alpha)\rangle). \tag{33}$$

Since the overlap between $|\mathrm{DHF}(\alpha)\rangle$ and $|\mathrm{DHF}(-\alpha)\rangle$ is negligibly in the large $\chi$ and $N$ limits, the three-body density matrix calculated with $|\Psi\rangle$ has also no correlated part. This is the reason why the results in TDDM approach the exact solutions in the large $\chi$ and $N$ limits.

The ground-state energy $E_0$ calculated in TDDM (solid line) for $N = 12$ and 50 is presented respectively in **Figures 1**, **2** as a function of $\chi$. The dashed and green (gray) lines denote the results in TDDM1 and TDDM2, respectively. In the case of $N = 50$ the results in TDDM2 are not displayed because they lie between the TDDM results and the exact values. The dotted and dot-dashed lines depict the results in HF and DHF ($\chi > 1$) and the exact values, respectively. As seen in **Figures 1**, **2**, the factor $\mathcal{N}$ in Equations (12) and (13) plays a role in greatly reducing $C_3$, making TDDM2 almost equivalent to TDDM for $N = 50$. In the limits of large $N$ and $\chi$ both TDDM and DHF results become close to the exact solutions. In the transitional region $\chi \approx 1$, however, TDDM1 and TDDM2 were found better than TDDM and DHF [45]. In the case of $N = 12$ this extends to $\chi \approx 2$ as seen in **Figure 1**.

The excitation energies of the first and second excited states calculated from the small oscillations of the TDDM solutions (dots) are compared with the exact solutions (dot-dashed line) in **Figures 3**, **4** for $N = 200$ where TDDM is supposed to give the nearly exact ground state. The dotted lines in **Figures 3**, **4** depict the results in RPA and the "deformed" RPA ($\chi > 1$) for the first excited state. In contrast to RPA and the deformed RPA TDDM reproduces the smoothly decreasing excitation energy of the first excited state with increasing interaction strength beyond $\chi = 1$. **Figure 4** shows that TDDM also gives good description of the second excited state. As seen in **Figure 4**, the excitation energies for the first excited state calculated in the deformed RPA become close to the exact values for the second excited state [1] with increasing $\chi$. The excited states were also calculated for a small system with $N$ = 4 by using the ground states in TDDM [15] and TDDM1 [23], and it was found that the TDDM1 ground state gives much better results.

As was pointed out above, the fact that TDDM becomes exact in large $N$ and $\chi$ limits is due to the unique feature of the Lipkin model that the mean-field theory DHF gives the exact solutions in such limits. In the transitional region $\chi \approx 1$ TDDM1 and TDDM2 give better description of the exact solutions than TDDM, and the applications to the ground states of other solvable models [23, 26] and $^{16}$O [24] also showed that TDDM1 largely improves TDDM whereas the improvement

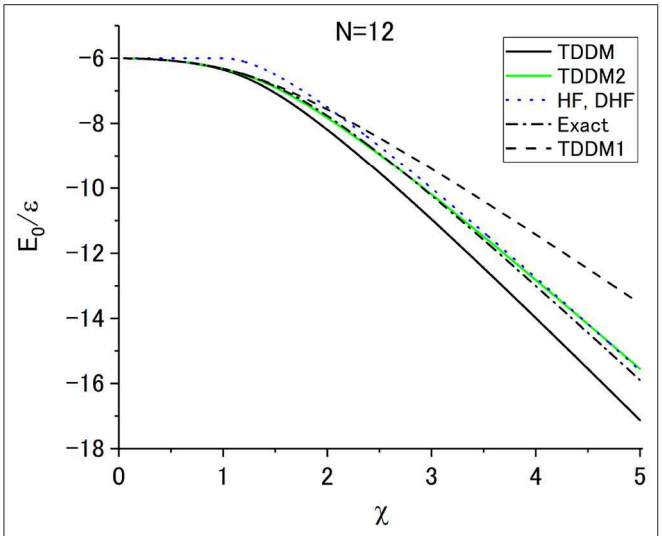


**FIGURE 1 |** Ground-state energy in TDDM (solid line) as a function of $\chi = |V|(N-1)/\epsilon$ for $N = 12$. The results in TDDM1 where the three-body correlation matrix is given by Equations (10) and (11) are shown with the dashed line. The green (gray) line depicts the results in TDDM2 where the three-body correlation matrix is given by Equations (12) and (13). The results in HF and DHF($\chi > 1$) are depicted with the dotted line. The exact values are given by the dot-dashed line. Adapted from Tohyama and Schuck [45] with permission from Società Italiana di Fisica/Springer-Verlag GmbH Germany.

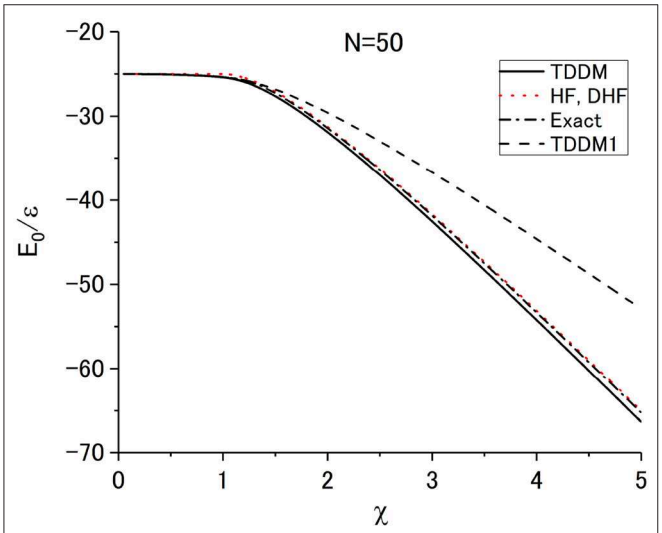


**FIGURE 2 |** Ground-state energy in TDDM (solid line) as a function of $\chi$ for $N = 50$. The exact values are given with the dot-dashed line. The dashed line depicts the results in TDDM1. The results in TDDM2 lie between the TDDM results and the exact values and are not displayed here. The results in HF and DHF($\chi > 1$) are shown with the dotted line but cannot be distinguished from the exact values in the scale of the figure except for the region $\chi \approx 1$. Adapted from Tohyama and Schuck [45] with permission from Società Italiana di Fisica/Springer-Verlag GmbH Germany.

from TDDM1 to TDDM2 is not large [26]. Therefore, TDDM1 or TDDM2 may be a useful truncation scheme to be applied to realistic cases except for strongly interacting regions.

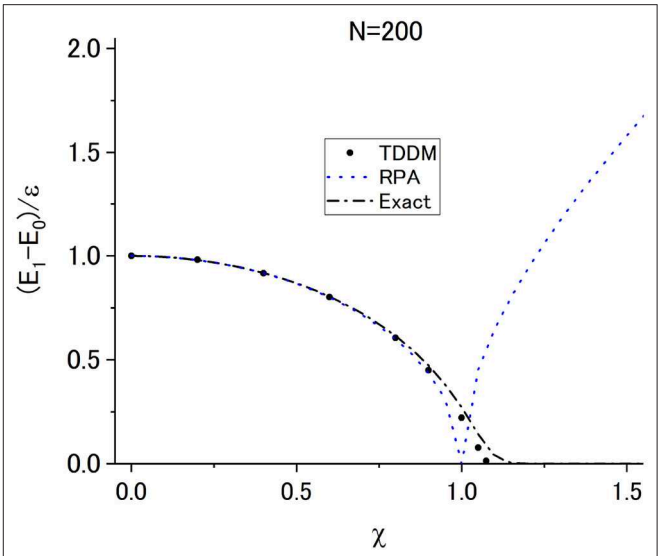


**FIGURE 3 |** Excitation energy of the first excited state calculated in TDDM (dots) as a function of $\chi$ for $N = 200$. The exact values are shown with the dot-dashed line. The dotted line depicts the results in RPA. Adapted from Tohyama and Schuck [45] with permission from Società Italiana di Fisica/Springer-Verlag GmbH Germany.

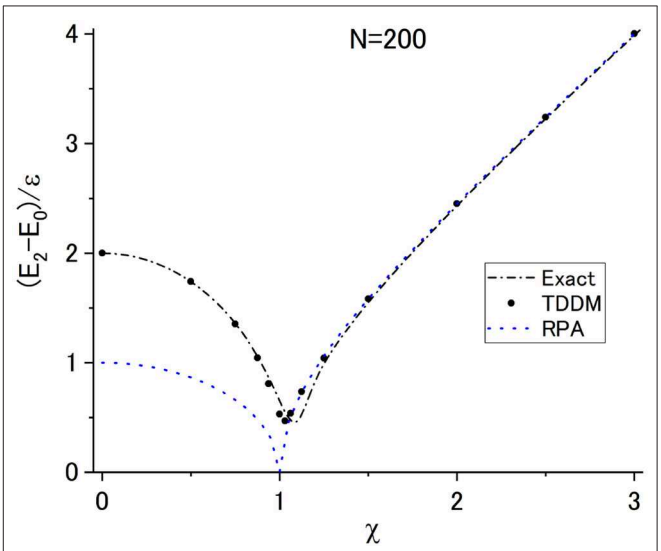


**FIGURE 4 |** Same as **Figure 3** but for the second excited state. The dotted line depicts the RPA results for the first excited state. Adapted from Tohyama and Schuck [45] with permission from Società Italiana di Fisica/Springer-Verlag GmbH Germany.

### 2.4.2. One-Dimensional Hubbard Model

ERPA based on the TDDM1 ground state has been applied to the one-dimensional (1-D) Hubbard model [37] to compare with other beyond RPA theories [33]. The Hubbard model is one of the most widespread models to investigate strong electron correlations and has often been used to corroborate the validity of beyond RPA theories [46]. In momentum space the Hamiltonian

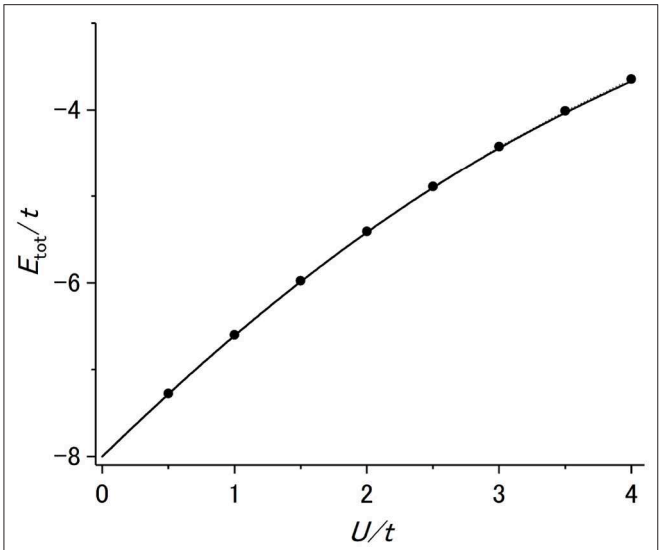


**FIGURE 5 |** Ground-state energy $E_{tot}$ calculated in TDDM1 (dots) as a function of $U/t$ for $N = 6$ with half-filling. The exact solutions are displayed with the solid line. Adapted from Tohyama [33] under the Creative Commons CCBY license.

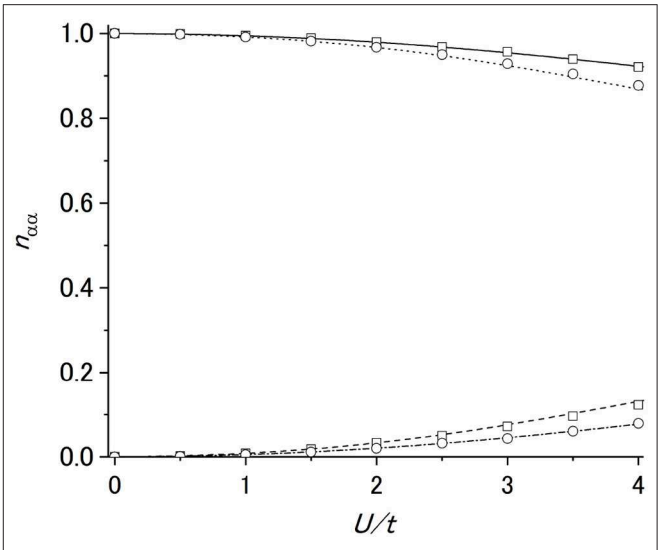


**FIGURE 6 |** Occupation probability of each s.p. state calculated in TDDM1 (circles and squares) as a function of $U/t$. The exact solutions are depicted with the solid, dotted, dashed and dot-dashed lines. Adapted from Tohyama [33] under the Creative Commons CCBY license.

is given by [46]

$$H = \sum_{k,\sigma} \epsilon_k a^+_{k,\sigma} a_{k,\sigma} + \frac{U}{2N} \sum_{k,p,q,\sigma} a^+_{k,\sigma} a_{k+q,\sigma} a^+_{p,-\sigma} a_{p-q,-\sigma}, \quad (34)$$

where $U$ is the matrix element of the on-site repulsive Coulomb interaction, $\sigma$ spin projection and the s.p. energies are given by $\epsilon_\alpha = -2t \cos k_\alpha$ with the nearest-neighbor hopping potential $t$. In the case of the six sites at half filling considered here, there are the following six wave numbers

$$k_1 = 0, \quad k_2 = \frac{\pi}{3}, \quad k_3 = -\frac{\pi}{3},$$
$$k_4 = \frac{2\pi}{3}, \quad k_5 = -\frac{2\pi}{3}. \quad k_6 = -\pi. \quad (35)$$

The s.p. energies are $\epsilon_1 = -2t$, $\epsilon_2 = \epsilon_3 = -t$, $\epsilon_4 = \epsilon_5 = t$, and $\epsilon_6 = 2t$. In HF the lower states with $\epsilon_1$, $\epsilon_2$ and $\epsilon_3$ are fully occupied by 6 particles.

The ground state energy calculated in TDDM1 (dots) with the adiabatic method is displayed in **Figure 5** as a function of $U/t$. It was found [21] that TDDM1 gives much better ground states of this model Hamiltonian than TDDM and that the improvement from TDDM1 to TDDM2 is minor [26]. The exact values obtained in exact diagonalization approach are depicted with the solid line. The TDDM1 results agree well with the exact values. The occupation probabilities of the four s.p. states in TDDM1 (circles and squares) given in **Figure 6** as functions of $U/t$ also have reasonable agreement with the exact solutions (solid, dotted, dashed and dot-dashed lines). The deviation of the occupation probabilities from the HF values ($n_{\alpha\alpha} = 1$ or 0) exceeds 10% at $U/t = 4$.

ERPA is compared with other beyond RPA theories for the spin mode with the momentum transfer $q = \pi/3$ which is excited mainly by the one-body operator $a^+_{k_4\uparrow} a_{k_2\uparrow} - a^+_{k_4\downarrow} a_{k_2\downarrow}$. Since the s.p. states are partially occupied, the h–h and p–p transitions such as $k_1 \rightarrow k_2$ and $k_6 \rightarrow k_5$ also contribute in rRPA, SCRPA and ERPA. In **Figure 7** the excitation energies in ERPA (dots), RPA (open triangles), rRPA (filled triangles), SCRPA (squares) and SRPA (crosses) are shown as functions of $U/t$. The exact solutions are given with the solid line. The rRPA and SCRPA results are calculated with $n_{\alpha\alpha}$ and $C_{\alpha\beta\alpha'\beta'}$ which are not self-consistently determined by the p–h and h–p amplitudes [28, 29] but given by the TDDM1 calculations. In the case of a repulsive interaction, the excitation energy of a spin mode where the s.p. transitions between spin-up states and spin-down states destructively interfere decreases with increasing $U$. The results in RPA agree rather well with the exact solutions. In rRPA there are two states below $E/t < 2$. The main components of the lower state at $E/t \approx 1$ are the p–p and h–h transitions and the higher state consists of the p–h and h–p components. Thus in rRPA the configurations consisting of the p–p and h–h components appear as the lowest state as if it is a physical state. This indicates that it is not appropriate to include the ground-state correlation effects only through $n_\alpha$. In SCRPA the states originating from the p–p and h–h transitions gain self energies and move to the high energy region ($E/t > 10$). This is because the terms in Equation (26) with $C_2$ are divided by the small values $n_{pp} - n_{p'p'}$ or $n_{hh} - n_{h'h'}$ when $Ax^\mu = S_1 x^\mu$ is solved. Thus in SCRPA the states consisting of the p–p and h–h components are energetically separated from the lowest state. The excitation energies of the lowest state calculated in SCRPA, however, exceed significantly the exact values. This is due to the neglect of the coupling to the two-body amplitudes. SRPA includes the coupling to the two-body amplitudes though the ground-state correlation effects are neglected. As shown in **Figure 7** with the crosses, the coupling to

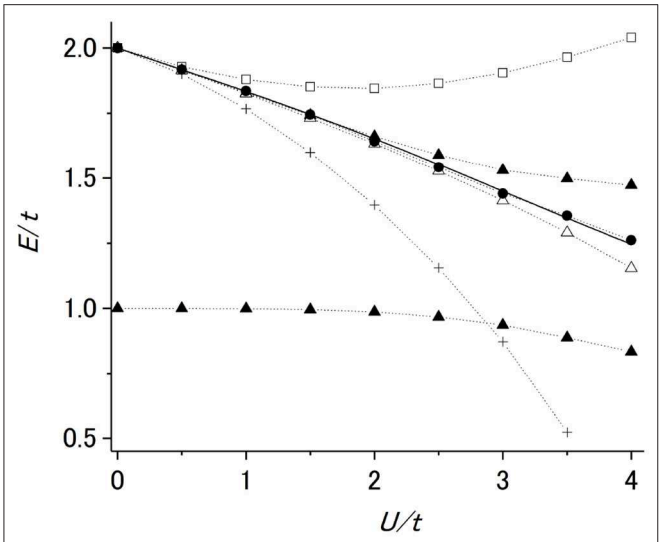


**FIGURE 7 |** Excitation energy of the spin mode with momentum transfer $q = \pi/3$ as a function of $U/t$ calculated in ERPA (dots). The results in RPA, rRPA, SCRPA, and SRPA are denoted with the open triangles, filled triangles, squares and crosses, respectively. The exact solutions are depicted with the solid line. Adapted from Tohyama [33] under the Creative Commons CCBY license.

the 2p–2h amplitudes considered in SRPA downwardly shift the RPA results with increasing $U$ and SRPA collapses at $U/t = 3.9$. The results in ERPA have reasonable agreement with the exact solutions. The coupling to the two-body amplitudes included in ERPA plays a role in bringing down the results in SCRPA.

From the application to the 1-D Hubbard model it was clarified that when the couping to the two-body amplitude is considered, the effects of ground-state correlations should also be included, and vice versa. Therefore, rRPA, SCRPA and SRPA which only include either the ground-state correlations effects or the coupling to the two-body amplitude cannot give satisfactory results.

### 2.4.3. Dipole and Quadrupole Excitations of $^{40}$Ca and $^{48}$Ca

In this subsection the applications of ERPA to the dipole excitation of $^{48}$Ca and the quadrupole excitation of $^{40}$Ca [36] are presented. It is demonstrated that the effects of ground-state correlations which are not fully incorporated in other beyond RPA theories play a significant role in the fragmentation of transition strengths.

Since the numbers of $C_2$ and $X^{\mu}_{\alpha\beta\alpha'\beta'}$ increase rapidly with the number of the s.p. states, rather sever truncation of the s.p. space is required in realistic applications. The occupation probability $n_{\alpha\alpha}$ and $C_2$ were calculated within TDDM by using the truncated s.p. basis consisting of the $2s$–$1d$ and $1f$–$2p$ states, and only the 2p–2h and 2h–2p elements of $C_2$ were included to reduce the dimension size. It was pointed out in Reference [24] that TDDM with this truncation of $C_2$ gives as good results for the ground state of $^{16}$O as TDDM1 with all components of $C_2$. The Skyrme III force [47] was used to obtain the s.p. wavefunctions which satisfy a HF-like $n_{\alpha\alpha}$-dependent equation. In Pfitzner et al. [11] and Peter et al. [12] a fixed harmonic oscillator basis was chosen to facilitate the calculations of two-body matrix elements when the TDDM equations were applied to the study of giant resonances. A simplified interaction which contains only the $t_0$ and $t_3$ terms of the Skyrme III force was used as the residual interaction. The ground states were calculated with the iterative gradient method [15]. The one-body amplitudes $x^{\mu}_{\alpha\alpha'}$ in Equation (18) were defined with a large number of s.p. states including those in the continuum to satisfy the energy-weighted sum rule: The continuum states were discretized by confining the wavefunctions in a sphere with radius 15 fm and all the s.p. states with $\epsilon_\alpha \leq 50$ MeV and $j_\alpha \leq 11/2\hbar$ were included. The residual interaction in Equation (18) was assumed to have the same form as that used in the ground-state calculations. Since the residual interaction differs from the effective interaction used in the calculation of the s.p. states, it is necessary to reduce the strength of the residual interaction. The reduction factors 0.66 and 0.69 for $^{40}$Ca and $^{48}$Ca, respectively, were determined so that the spurious mode corresponding to the center-of-mass motion has zero excitation energy in RPA. To reduce the number of the two-body amplitudes, only the 2p–2h and 2h–2p components of $X^{\mu}_{\alpha\beta\alpha'\beta'}$ were considered for the $2s$–$1d$ and $2p$–$1f$ states.

**TABLE 1 |** Single-particle energies $\epsilon_\alpha$ and occupation probabilities $n_{\alpha\alpha}$ calculated in TDDM for $^{40}$Ca.

| | $\epsilon_\alpha$ [MeV] | | $n_{\alpha\alpha}$ | |
|---|---|---|---|---|
| **Orbit** | **Proton** | **Neutron** | **Proton** | **Neutron** |
| $1d_{5/2}$ | −15.6 | −22.9 | 0.923 | 0.924 |
| $1d_{3/2}$ | −9.4 | −16.5 | 0.884 | 0.884 |
| | | | (0.65 ± 0.05) | (0.80 ± 0.11) |
| $2s_{1/2}$ | −8.5 | −15.9 | 0.846 | 0.846 |
| $1f_{7/2}$ | −3.4 | −10.4 | 0.154 | 0.154 |

*Observed occupation probabilities [48] are shown for the $1d_{3/2}$ states.*

The occupation probabilities calculated in TDDM for $^{40}$Ca and $^{48}$Ca are given in **Tables 1**, **2**, respectively. They deviate more than 10% from the HF values ($n_{\alpha\alpha}$=1 or 0) in $^{40}$Ca. This indicates that the ground state of $^{40}$Ca is highly correlated as an RPA study [49] and perturbative calculations [31, 50] have already shown. Since the occupation of the neutron $1f_{7/2}$ state in $^{48}$Ca blocks some 2p–2h excitations, the ground-state correlations are weaker in $^{48}$Ca than in $^{40}$Ca. As will be discussed below, the fractional occupation of the $2p$–$1f$ states plays an important role in the fragmentation of dipole and quadrupole transition strengths. Occupation probabilities deduced from ground-state-to-ground-state $(p, d)$ and $(e, e'p)$ reactions [48] are also shown for some s.p. states in **Tables 1**, **2** (values in parentheses). These values also strongly deviate from the HF value ($n_\alpha = 1$). The TDDM results cannot be directly compared with these data, however. A more appropriate formalism such as the odd-particle number RPA [51] which deals with odd particle systems is needed to compare with experiment.

The strength function for the isovector dipole excitation in $^{48}$Ca calculated in ERPA (solid line) is displayed in **Figure 8**.

**TABLE 2 |** Same as **Table 1** but for $^{48}$Ca.

| | $\epsilon_\alpha$ [MeV] | | $n_{\alpha\alpha}$ | |
|---|---|---|---|---|
| **Orbit** | **Proton** | **Neutron** | **Proton** | **Neutron** |
| $1d_{5/2}$ | −22.6 | −22.4 | 0.963 | 0.965 |
| $1d_{3/2}$ | −17.1 | −17.0 | 0.952 | 0.940 |
| $2s_{1/2}$ | −15.1 | −16.4 | 0.905 | 0.932 |
| | | | (0.54 ± 0.04) | |
| $1f_{7/2}$ | −10.6 | −10.6 | 0.059 | 0.919 |
| | | | | (0.73 ± 0.14) |
| $2p_{3/2}$ | −1.7 | −3.8 | – | 0.103 |
| $2p_{1/2}$ | 0.1 | −2.0 | – | 0.064 |
| $1f_{5/2}$ | −2.2 | −1.9 | 0.022 | 0.116 |

*Observed occupation probabilities [48] are shown for the proton $2s_{1/2}$ and neutron $1f_{7/2}$ states.*

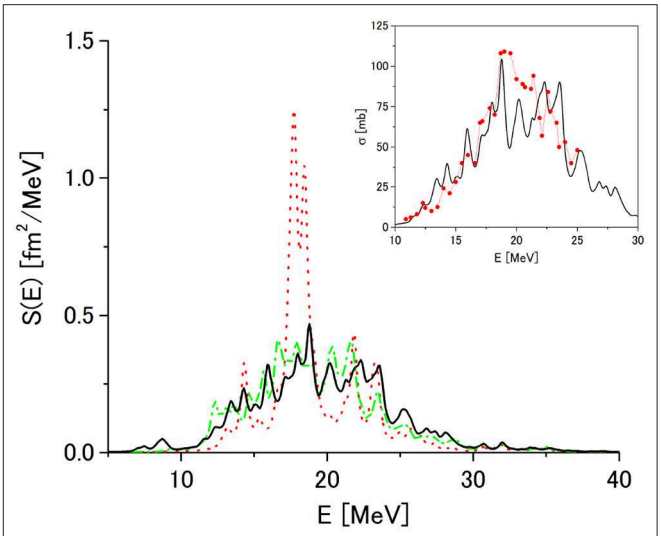


**FIGURE 8 |** Strength functions calculated in RPA (dotted line), SRPA (dot-dashed line) and ERPA (solid line) for the isovector dipole excitation in $^{48}$Ca. The distributions are smoothed with an artificial width $\Gamma = 0.5$ MeV. In the inset the photo absorption cross section in ERPA (solid line) is compared with experimental data [52] (dots). Readapted from Tohyama [36] under the Creative Commons CCBY license.

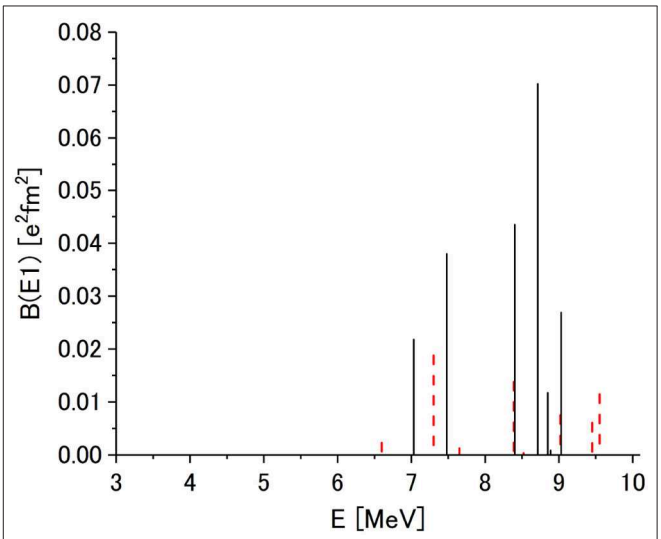


**FIGURE 9 |** Distribution of $B(E1)$ strength below 10 MeV calculated in ERPA for $^{48}$Ca. Experimental data (dashed line) are taken from Hartmann et al. [54]. Adapted from Tohyama [36] under the Creative Commons CCBY license.

The dotted and dot-dashed lines depict the results in RPA and SRPA, respectively. An artificial width $\Gamma = 0.5$ MeV is used to smooth the distributions. The strength distributions in **Figure 8** exhaust about 90% of the energy-weighted-sum-rule (EWSR) value including the enhancement term given by the $t_1$ and $t_2$ parameters of the Skyrme III force. A better treatment of the residual interaction and the continuum states is required to fulfill the EWSR value. The sharp peak in RPA corresponds to the giant dipole resonance (GDR). GDR strongly couples to the 2p–2h states and it is damped both in SRPA and ERPA. The occupation of the neutron $1f_{7/2}$ state in $^{48}$Ca allows the 2p–2h states which include the neutron $1f_{7/2}$ state as a hole state. Since these states have energies close to the energy of GDR, GDR is strongly damped due to the coupling to the 2p–2h states. The SRPA result in **Figure 8** dose not show a strong downward shift of the dipole strength which has been reported in large scale SRPA calculations [53]. This is due to fact that a rather small number of the s.p. states are used to define the 2p–2h amplitudes. The peak position and width of GDR in ERPA are comparable with the experimental photo absorption cross section [52] as shown in the inset of **Figure 8**.

ERPA gives 7 states below 10 MeV, which are compared with experiment [54] in **Figure 9**. These states involve the transitions from the partially occupied neutron $2p_{1/2}$, $2p_{3/2}$ and $1f_{5/2}$ states and the p–p transition components exhaust 15 − 39% of the transition amplitude $(x^\mu, X^\mu)$. The summed strength below 10 MeV is 213 $\times 10^{-3} e^2\text{fm}^2$, which somewhat overestimates the experimental value 61.5 ± 7.8 $\times 10^{-3} e^2\text{fm}^2$. SRPA gives two dipole states at 9.2 MeV and 9.3 MeV with the summed strength $21 \times 10^{-3} e^2\text{fm}^2$. The study of low-lying dipole strength distribution has been attracting strong interests and various theoretical approaches such as the large scale SRPA [55, 56] and the quasi-particle phonon coupling models [57, 58] have been successfully applied to calcium isotopes.

The strength function for the isoscalar quadrupole excitation in $^{40}$Ca calculated in ERPA (solid line) is shown in **Figure 10**. The dotted and dot-dashed lines depict the results in RPA and SRPA, respectively. The distributions are smoothed with an artificial width $\Gamma = 0.5$ MeV. The energy-weighted sums of the strength distributions in **Figure 10** exceed the EWSR value by about 10% due to the simple approximations for the residual interaction and the continuum states. The main peak in RPA corresponds to the giant quadrupole resonance (GQR). ERPA brings much larger fragmentation of the quadrupole strength than SRPA especially to the low energy region, indicating the importance of the ground-state correlations effects included in ERPA. The large fragmentation of the quadrupole strength is consistent with experiment [59, 60]. The p–p transitions allowed

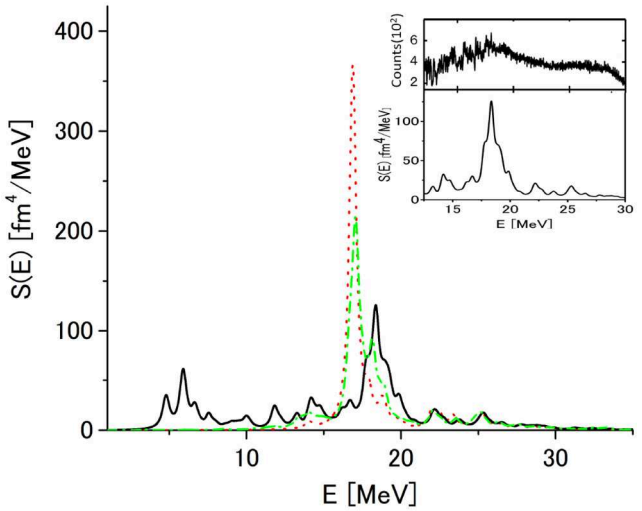


**FIGURE 10 |** Strength functions calculated in RPA (dotted line), SRPA (dot-dashed line) and ERPA (solid line) for the isoscalor quadrupole excitation in $^{40}$Ca. The distributions are smoothed with an artificial width $\Gamma = 0.5$ MeV. In the inset the ERPA strength distribution (lower part) is compared with the experimental data from $(p, p')$ experiments at $E_p = 200$ MeV and $\theta_{\rm Lab} = 11°$ [59] (upper part). Redapted from Tohyama [36] under the Creative Commons CCBY license.

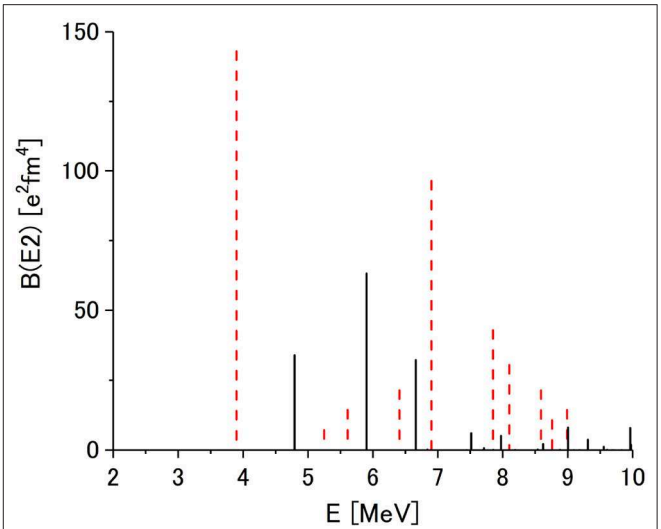


**FIGURE 11 |** Distribution of $B(E2)$ strength below 10 MeV for $^{40}$Ca. Experimental data (dashed line) are taken from Hartmann et al. [54]. Adapted from Tohyama [36] under the Creative Commons CCBY license.

by the fractional occupation of the $1f_{7/2}$ states and the coupling of the 2p–2h amplitudes to the h–h or p–p amplitudes through $C_2$ were found to play an important role in the large fragmentation of the quadrupole strength [34, 36]. The importance of the coupling of the one-body amplitude to $C_2$ in the fragmentation of GQR in $^{40}$Ca was also pointed out by the 1p–1h⊗phonon configurations model [61, 62]. A large scale SRPA calculation [63] shows a downward shift of the quadrupole strength and larger fragmentation of GQR than the SRPA result in **Figure 10**. This difference again originates from the difference in the number of the 2p–2h configurations used. In the inset the ERPA strength distribution in the GQR region (lower part) is compared with the experimental data from $(p, p')$ experiments [59] (upper part). Although the peak position in ERPA corresponds to the experimental data, ERPA cannot describe the large fragmentation of GQR. The result of the large scale SRPA calculation [63] suggests the importance of higher configurations.

There are 19 sates below 10 MeV in ERPA, which are compared with experiment [54] in **Figure 11**. The first $2^+$ state in $^{40}$Ca cannot be described in RPA and ERPA because it mainly consists of 4p–4h states [64] as in the case of $^{16}$O [65]. The summed strength below 10 MeV is 166 $e^2$fm$^4$ in ERPA, which is about two thirds of the experimental value $263 \pm 46$ $e^2$fm$^4$ where the first $2^+$ state is excluded.

From the applications of ERPA to the dipole and quadrupole excitations of $^{48}$Ca and $^{40}$Ca it was clarified that the ground state correlation effects should be included to explain the large fragmentation of the dipole and quadrupole strengths in doubly-magic nuclei. The ground-state correlation effects in magic nuclei have extensively been studied for spin-isospin modes [31, 50, 66–68].

## 3. FORMULATION IN TIME-DEPENDENT SINGLE-PARTICLE BASIS

The first applications of the time-dependent density-matrix approach were based on the TDDM truncation scheme and the TDDM calculations [6, 7] were performed by using the time-dependent s.p. wavefunctions obtained from the then available TDHF code with axial symmetry and without spin-orbit force [69]. More advanced TDHF codes with spin-orbit force, unconstrained symmetry and improved effective interactions have been used to solve the TDDM equations [8, 13]. Since the calculation of the two-body matrix elements is time-consuming, a simpler approximation called TDDM$^{\rm P}$ [13, 14] has also been employed in heavy-ion collisions, where two-body correlations are considered only for a pair of time reversed s.p. states to reduce the number of matrix elements of $C_2$. The TDDM approaches based on the time-dependent s.p. basis have been applied to study the particle transfers in heavy-ion collisions [7], the fusion reactions [8, 9] and the damping of giant resonances at zero [6, 70, 71] and finite temperatures [10]. TDDM$^{\rm P}$ has been applied to the particle transfers in heavy-ion collisions [13] and the fusion reactions [14]. In the following the TDDM formulation in the time-dependent s.p. basis is given and the application to the fusion reactions of $^{16}$O + $^{16}$O is presented in some detail as an example.

### 3.1. TDDM Equations

The one-body density matrix $\rho$ and the correlated part $C_2$ of the two-body density matrix $\rho_2$ are expanded with a finite number of time-dependent s.p. states $\psi_\alpha$

$$\rho(11', t) = \sum_{\alpha\alpha'} n_{\alpha\alpha'}(t)\psi_\alpha(1, t)\psi^*_{\alpha'}(1', t), \tag{36}$$

$$C_2(121'2',t) = \rho_2 - \mathcal{A}(\rho\rho)$$
$$= \sum_{\alpha\beta\alpha'\beta'} C_{\alpha\beta\alpha'\beta'}(t)\psi_\alpha(1,t)\psi_\beta(2,t)\psi^*_{\alpha'}(1',t)\psi^*_{\beta'}(2',t), \quad (37)$$

where the numbers denote space, spin and isospin coordinates. The equations of motion of TDDM in the time-dependent basis consist of the following three coupled equations [6]:

$$i\frac{\partial}{\partial t}\psi_\alpha(1,t) = h(1,t)\psi_\alpha(1,t), \quad (38)$$

$$i\dot{n}_{\alpha\alpha'} = \sum_{\beta\gamma\delta}[\langle\alpha\beta|v|\gamma\delta\rangle C_{\gamma\delta\alpha'\beta} - C_{\alpha\beta\gamma\delta}\langle\gamma\delta|v|\alpha'\beta\rangle], \quad (39)$$

$$i\dot{C}_{\alpha\beta\alpha'\beta'} = B_{\alpha\beta\alpha'\beta'} + P_{\alpha\beta\alpha'\beta'} + H_{\alpha\beta\alpha'\beta'}, \quad (40)$$

where $h$ is the mean-field Hamiltonian given by $\rho$. When the time-dependent s.p. states are chosen, the terms with the s.p. energies on the right-hand side of Equations (5) and (6) are incorporated into the equation for the s.p. wavefunctions [6]. In TDDM$^{\rm P}$ [13, 14] $H_{\alpha\beta\alpha'\beta'}$ is neglected and two-body correlations are considered only for a pair of time reversed s.p. states.

## 3.2. Fusion Reactions of $^{16}$O + $^{16}$O

The fusion reactions of $^{16}$O + $^{16}$O studied in TDDM with the time-dependent s.p. basis are explained below. This work Tohyama and Umar [8] finally solved the longstanding problem of fusion window anomaly. Early TDHF calculations showed that the colliding heavy ions do not fuse in a small impact parameter region when incident energy is higher than a certain relatively low threshold value $E_{\rm th}$ [2]. This is known as the fusion window anomaly. Experimental search for the fusion window anomaly has found no evidence [72–75]. It was found that the inclusion of spin-orbit force introduced enough one-body dissipation to $^{16}$O + $^{16}$O collisions [76] because the degeneracy of the $1p_{3/2}$ and $1p_{1/2}$ states is lifted. It was also found [77] that the effects of two-body dissipation taken in TDDM resulted in the doubling of $E_{\rm th}$ without incorporating spin-orbit force. This is due to the inclusion of additional unoccupied s.p. states in TDDM. In Tohyama and Umar [8] the combined effects of spin-orbit force and two-body dissipation were studied for $^{16}$O + $^{16}$O. In this study the Skyrme II force (SKII) [78] was chosen as an effective interaction to calculate the s.p. wavefunctions since SKII has often been used in TDHF calculations [69]. The s.p. states were restricted to the $1s$–$1p$ and $2s$–$1d$ states and the simple force of the $\delta$ function form $v = v_0\delta^3(\vec{r} - \vec{r}')$ with $v_0 = -350$ MeV·fm$^3$ was used as the residual interaction to facilitate the calculation of the matrix elements. The threshold energy $E_{\rm th}$ was searched for four different calculation schemes for the head-on collisions of $^{16}$O + $^{16}$O: TDHF with and without spin-orbit force, and TDDM with and without spin-orbit force.

The obtained results for $E_{\rm th}$ in the center-of-mass (c.m.) frame are summarized in **Table 3**. The inclusion of either spin-orbit force or two-body dissipation dramatically increases $E_{\rm th}$.

**TABLE 3 |** Threshold energy $E_{\rm th}$ in the center-of-mass frame for the head-on collisions of $^{16}$O + $^{16}$O.

| Method | $E_{\rm th}$ [MeV] |
|---|---|
| TDHF without $\vec{\ell}\cdot\vec{s}$ | 30 |
| TDDM without $\vec{\ell}\cdot\vec{s}$ | 66 |
| TDHF with $\vec{\ell}\cdot\vec{s}$ | 69 |
| TDDM with $\vec{\ell}\cdot\vec{s}$ | 80 |

*Fusion occurs below $E_{th}$.*

However, two-body dissipation increases $E_{\rm th}$ only about 10 MeV when spin-orbit force is included. It was also found that the translational motion damps faster in TDDM than in TDHF [8] below $E_{\rm c.m.} = 69$ MeV where the colliding system fuses both in TDHF and TDDM. The fusion reactions of $^{16}$O + $^{16}$O below $E_{\rm th}$ were also studied by Wen et al. [14] using the TDDM$^{\rm P}$ approach and a paring interaction as the residual interaction and it was found that extracted friction coefficients are enhanced by about 20% due to two-body dissipation.

In the case of heavy-ion collisions the TDDM (and TDDM$^{\rm P}$) equations ostensibly do not conserve the total energy because of the truncation of the s.p. space [7, 14]. Wen et al. [14] has proposed a method to recover the energy conservation within the truncated s.p. space.

# 4. SUMMARY AND OUTLOOK

An approach which extends the time-dependent Hartree-Fock theory (TDHF) based on the equations of motion for reduced density matrices was presented. The equations of motions for reduced density matrices form a coupled chain known as the Bogoliubov-Born-Green-Kirkwood-Yvon (BBGKY) hierarchy. In this time-dependent density-matrix approach (TDDMA) the truncation of the BBGKY hierarchy is applied at the two-body level by approximating the correlated part of the three-body density matrix ($C_3$). TDDMA has great advantages that a correlated ground state is obtained as a stationary solution of the TDDMA equations and that the small amplitude limit of the TDDMA equations gives the most general form of beyond the random-phase approximation (RPA). TDDMA was applied to the Lipkin model to test the approximations for $C_3$. It was found that the simplest approximation where $C_3$ is neglected becomes exact in the limits of large number of particles and strong interaction. The extended RPA (ERPA) derived from the TDDMA equations was applied to the one-dimensional Hubbard model to compare with other beyond RPA theories. It was pointed out that when the effects of ground-state correlations are included, the coupling to the two-body amplitudes should also be considered, and vice versa. As the realistic applications of ERPA, the dipole and quadrupole excitations of $^{40}$Ca and $^{48}$Ca were studied. It was found that the effects of ground-state correlations play an important role in fragmenting the dipole and quadrupole strengths. The TDDMA study for the fusion reactions of $^{16}$O + $^{16}$O was also presented as an application of the TDDMA formulation with a time-dependent singe-particle

basis. It was pointed out that the two-body dissipation plays a role in further damping the translational motion of $^{16}O + ^{16}O$.

Although the obtained results indicate that TDDMA provides a promising beyond mean-field framework to include two-body correlation effects which are missing in TDHF, TDDMA has limitations and issues to be resolved. One limitation is the fact that the number of matrix elements of the two-body density matrix rapidly increases with increasing number of the s.p. states, which forces us to use small s.p. space around the Fermi level in realistic applications, though the obtained results show that basic effects of two-body correlations can be described with rather small s.p. space. In the realistic applications, simple residual interactions of the $\delta$ function form were used to facilitate the calculations of two-body matrix elements whereas the s.p. wavefunctions were obtained from the Skyrme interactions included in TDHF codes. The consistent treatment of the effective interactions is a subject to be addressed in TDDMA. Another point is the truncation scheme of the BBGKY hierarchy itself. In TDDMA the BBGKY hierarchy is truncated at the two-body level by making approximations for $C_3$. The truncation violates the properties of reduced density matrices which should be fulfilled if they are derived from an $N$-body total wavefunction. It was pointed out that the TDDM1 truncation scheme where $C_3$ is given by the traced products of the 2p–2h elements of the two-body correlation matrix largely improves the simple scheme where $C_3$ is neglected. However, the validity of TDDM1 cannot be simply extended to highly excited cases such as heavy-ion collisions. The study of the truncation schemes in such cases remains a difficult but interesting subject to be investigated.

## AUTHOR CONTRIBUTIONS

The author confirms being the sole contributor of this work and has approved it for publication.

## REFERENCES


1. Ring P, Schuck P. *The Nuclear Many-Body Problem*. Berlin: Springer-Verlag (2000).
2. Davies KTR, Devi KRS, Koonin SE, Strayer MR. TDHF calculations of heavy-ion collisions. In: Bromley DA, editor. *Treatise on Heavy Ion Science*, Vol. 3. New York, NY: Plenum Press (1985).
3. Sekizawa K. TDHF Theory and its extensions for the multinucleon transfer reaction: a mini review. *Front Phys*. (2019) **7**:20. doi: 10.3389/fphy.2019.00020
4. Bonitz M. *Quantum Kinetic Theory, 2nd Edn*. Berlin: Springer (2016). doi: 10.1007/978-3-319-24121-0
5. Wang SJ, Cassing W. Explicit treatment of N-body correlations within a density-matrix formalism. *Ann Phys*. (1985) **159**:328–50. doi: 10.1016/0003-4916(85)90116-2
6. Gong M, Tohyama M. Application of a time-dependent density-matrix formalism. *Z Phys A*. (1990) **335**:153–61. doi: 10.1007/BF01294470
7. Gong M, Tohyama M, Randrup J. Time-dependent density matrix theory II. Mass dispersion in damped nuclear reactions. *Z Phys A*. (1990) **335**:331–40. doi: 10.1007/BF01304712
8. Tohyama M, Umar AS. Fusion window problem in time-dependent Hartree-Fock theory revisited. *Phys Rev C*. (2002) **65**:037601. doi: 10.1103/PhysRevC.65.037601
9. Tohyama M, Umar AS. Two-body dissipation effects on the synthesis of superheavy elements. *Phys Rev C*. (2016) **93**:034607. doi: 10.1103/PhysRevC.93.034607
10. De Blasio FV, Cassing W, Tohyama M, Bortignon PF, Broglia RA. Non-perturbative study of the damping of giant resonances in hot nuclei. *Phys Rev Lett*. (1992) **68**:1663–6. doi: 10.1103/PhysRevLett.68.1663
11. Pfitzner A, Cassing W, Peter A. Vibrations versus collisions and the iterative structure of two-body dynamics. *Nucl Phys A*. (1994) **577**:753–72. doi: 10.1016/0375-9474(94)90943-1
12. Peter A, Cassing W, Hauser JM, Pfitzner A. Microscopic analysis of two-body correlations in light nuclei. *Nucl Phys A*. (1994) **573**:93–129. doi: 10.1016/0375-9474(94)90016-7
13. Assiee M, Lacroix D. Probing neutron correlations through nuclear breakup. *Phys Rev Lett*. (2009) **102**:202501. doi: 10.1103/PhysRevLett.102.202501
14. Wen K, Barton MC, Rios A, Stevenson PD. Two-body dissipation in nuclear fusion reactions. *Phys Rev C*. (2018) **98**:014603. doi: 10.1103/PhysRevC.98.014603
15. Takahara S, Tohyama M, Schuck P. Extended RPA with ground-state correlations in a solvable model. *Phys Rev C*. (2004) **70**:057307. doi: 10.1103/PhysRevC.70.057307
16. Schmitt K-J, Reinhard P-G, Toepffer C. Truncation of time-dependent many-body theories. *Z Phys A*. (1990) **336**:123–31. doi: 10.1007/BF01290612
17. Gherega T, Krieg R, Reinhard P-G, Toepffer C. Dynamics of correlations in a solvable model. *Nucl Phys A*. (1993) **560**:166–86. doi: 10.1016/0375-9474(93)90090-K
18. Akbari A, Hashemi MJ, Rubio A, Nieminen RM, van Leeuwen R. Challenges in truncating the hierarchy of time-dependent reduced density matrices equations. *Phys Rev B*. (2012) **85**:23512. doi: 10.1103/PhysRevB.85.235121
19. Tohyama M. Time-dependent density-matrix approach to collective excitations of a quantum dot. *J Phys Soc Jpn*. (2012) **81**:054707. doi: 10.1143/JPSJ.81.054707
20. Coleman AJ, Yukalov VI. *Reduced Density Matrices: Coulson's Challenge*. Berlin: Springer-Verlag (2000). doi: 10.1007/978-3-642-58304-9
21. Tohyama M, Schuck P. Truncation scheme of time-dependent density-matrix approach. *Eur Phys J A*. (2014) **50**:77. doi: 10.1140/epja/i2014-14077-x
22. Mazziotti DA. Pursuit of $N$-representability for the contracted Schrödinger equation through density-matrix reconstruction. *Phys Rev A*. (1999) **60**:3618–26. doi: 10.1103/PhysRevA.60.3618
23. Schuck P, Tohyama M. Progress in many-body theory with the equation of motion method: time-dependent density matrix meets self-consistent RPA and applications to solvable models. *Phys Rev B*. (2016) **93**:165117. doi: 10.1103/PhysRevB.93.165117
24. Tohyama M. New truncation scheme for a time-dependent density-matrix approach applied to the ground state of $^{1}6O$. *Phys Rev C*. (2015) **91**:017301. doi: 10.1103/PhysRevC.91.017301
25. Lipkin HJ, Meshkov N, Glick AJ. Validity of many-body approximation methods for a solvable model: (I). Exact solutions and perturbation theory. *Nucl Phys*. (1965) **62**:188–98. doi: 10.1016/0029-5582(65)90862-X
26. Tohyama M, Schuck P. Truncation scheme of time-dependent density-matrix approach II. *Eur Phys J A*. (2017) **53**:186. doi: 10.1140/epja/i2017-12377-3
27. Rowe DJ. Equations-of-Motion method and the extended shell model. *Rev Mod Phys*. (1968) **40**:153. doi: 10.1103/RevModPhys.40.153
28. Rowe DJ. Methods for calculating ground-state correlations of vibrational nuclei. *Phys Rev*. (1968) **175**:1283–92. doi: 10.1103/PhysRev.175.1283
29. Schuck P, Ethofer S. Self-consistent (nuclear) phonons. *Nucl Phys A*. (1973) **212**:269–86. doi: 10.1016/0375-9474(73)90563-0
30. Dukelsky J, Schuck P. Towards a variational theory for RPA-like correlations and fluctuations. *Nucl Phys A*. (1990) **512**:466–82. doi: 10.1016/0375-9474(90)90081-V

31. Drożdż S, Nishizaki S, Speth J, Wambach J. The nuclear response within extended RPA theories. *Phys Rep*. (1990) **197**:1–65. doi: 10.1016/0370-1573(90)90084-F
32. Litvinova E, Schuck P. Toward an accurate strongly coupled many-body theory with in the equation-of-motion framework. *arXiv[Preprint]*.arXiv:1908.05384.
33. Tohyama M. Role of small-norm components in extended random-phase approximation. *Prog Theor Exp Phys*. (2017) **2017**:093D06. doi: 10.1093/ptep/ptx128
34. Tohyama M. Damping of collective states in an extended random-phase approximation with ground-state correlations. *Phys Rev C*. (2007) **75**:044310. doi: 10.1103/PhysRevC.75.044310
35. Tohyama M. Quadrupole excitation of tin isotopes in extended random-phase approximation. *Prog Theor Phys*. (2012) **127**:1121–30. doi: 10.1143/PTP.127.1121
36. Tohyama M. Effects of ground-state correlations on dipole and quadrupole excitations of $^{4}$0Ca and $^{4}$8Ca. *Prog Theor Exp Phys*. (2018) **2018**:043D02. doi: 10.1093/ptep/pty035
37. Hubbard J. Electron correlations in narrow energy bands. *Proc Roy Soc (London)*. (1963) **276**:238–57. doi: 10.1098/rspa.1963.0204
38. Shavitt I, Bartlett RJ. *Many-Body Methods in Chemistry and Physics*. Cambridge: Cambridge University Press (2009). doi: 10.1017/CBO9780511596834
39. Cassing W, Pfitzner A. Self-consistent truncation of the BBGKY hierarchy on the two-body level. *Z Phys A*. (1992) **342**:161–7. doi: 10.1007/BF01288464
40. Tohyama M, Schuck P. Extended random-phase approximation with three-body ground-state correlations. *Eur Phys J A*. (2008) **36**:349–57. doi: 10.1140/epja/i2008-10596-3
41. Gell-Mann M, Low F. Bound states in quantum field theory. *Phys Rev*. (1951) **84**:350–4. doi: 10.1103/PhysRev.84.350
42. Tohyama M. Stationary solution of a time dependent density matrix formalism. *Prog Theor Phys*. (1994) **92**:905–8. doi: 10.1143/ptp/92.4.905
43. Tohyama M. Mean-field approach to excitations of a trapped Bose-Einstein condensate gas at finite temperatures. *Phys Rev A*. (2005) 71:043613. doi: 10.1103/PhysRevA.71.043613
44. Janssen D, Schuck P. On some aspects of selfconsistent RPA theory. *Z Phys A*. (1991) **339**:43–50. doi: 10.1007/BF01282932
45. Tohyama M Schuck P. Truncation scheme of time-dependent density-matrix approach III. *Eur Phys J A*. (2019) **55**:74. doi: 10.1140/epja/i2019-12746-x
46. Jemaï M, Schuck P, Dukelsky J, Bennaceur R. Self-consistent random phase approximation: application to the Hubbard model for finite number of sites. *Phys Rev B*. (2005) **71**:085115. doi: 10.1103/PhysRevB.71.085115
47. Beiner M, Flocard H, Van Giai N, Quentin P. Nuclear ground-state properties and self-consistent calculations with the skyrme interaction: (I). Spherical description. *Nucl Phys A*. (1975) **238**:29–69. doi: 10.1016/0375-9474(75)90338-3
48. Lee J, Tostevin JA, Brown BA, Delaunay F, Lynch WG, Saelim MJ, et al. Reduced neutron spectroscopic factors when using potential geometries constrained by Hartree-Fock calculations. *Phys Rev C*. (2006) **73**:044608. doi: 10.1103/PhysRevC.73.044608
49. Agassi D, Gillet V, Lumbroso A. RPA description of the ground state of $^{1}$2C, $^{1}$6O, $^{4}$0Ca and $^{2}$08Pb. *Nucl Phys A*. (1969) **130**:129–45. doi: 10.1016/0375-9474(69)90966-X
50. Adachi S, Lipparini E, Nguyen van Giai. Gamow-Teller and M1 strengths in closed-shell nuclei. *Nucl Phys A*. (1985) **438**:1–14. doi: 10.1016/0375-9474(85)90115-0
51. Tohyama M, Schuck P. Odd particle number random-phase approximation and extensions: applications to particle and hole states around $^{1}$6O. *Phys Rev C*. (2013) **87**:044316. doi: 10.1103/PhysRevC.87.044316
52. O'Keefe GJ, Thompson MN, Assafiri YI, Pywell RE. The photonuclear cross sections of $^{4}$8Ca. *Nucl Phys A*. (1987) **469**:239–52. doi: 10.1016/0375-9474(87)90108-4
53. Gambacurta D, Grasso M, Catara F. Collective nuclear excitations with Skyrme-second random-phase approximation. *Phys Rev C*. (2010) **81**:054312. doi: 10.1103/PhysRevC.81.054312
54. Hartmann T, Enders J, Mohr P, Vogt K, Volz S, Zilges A. Measurement of the dipole and electric quadrupole strength distributions up to 10 MeV in the doubly magic nuclei $^{4}$0Ca and $^{4}$8Ca. *Phys Rev Lett*. (2000) **85**:274–7. doi: 10.1103/PhysRevLett.85.274
55. Gambacurta D, Grasso M, Catara F. Low-lying dipole response in the stable $^{4}$0, 48Ca nuclei with the second random-phase approximation. *Phys Rev C*. (2011) **84**:034301. doi: 10.1103/PhysRevC.84.034301
56. Gambacurta D, Grasso M, Vasseur O. Electric dipole strength and dipole polarizability in $^{4}$8Ca within a fully self-consistent second random-phase approximation. *Phys Lett B*. (2018) **777**:163–8. doi: 10.1016/j.physletb.2017.12.026
57. Hartmann T, Babilon M, Kamerdzhiev S, Litvinova E, Savran D, Volz S, et al. Microscopic nature of the pygmy dipole resonance: the stable Ca isotopes. *Phys Rev Lett*. (2004) **93**:192501. doi: 10.1103/PhysRevLett.93.192501
58. Egorova I A, Litvinova E. Electric dipole response of neutron-rich calcium isotopes in relativistic quasiparticle time blocking approximation. *Phys Rev C*. (2016) **94**:034322. doi: 10.1103/PhysRevC.94.034322
59. Usman I, Buthelezia Z, Carterb J, Cooper GRJ, Fearickd RW, Förtsch SV, et al. Fine structure of the isoscalar giant quadrupole resonance in $^{4}$0Ca due to Landau damping? *Phys Lett B*. (2011) **698**:191–5. doi: 10.1016/j.physletb.2011.03.015
60. Diesener H, Helm U, Herbert G, Huck V, von Neumann-Cosel P, Rangacharyulu C, et al. Excitation and decay of giant resonances in the $^{4}$0Ca $(e, e'x)$ reaction. *Phys Rev Lett*. (1994) **72**:1994–7. doi: 10.1103/PhysRevLett.72.1994
61. Kamerdzhiev S, Speth J, Tertychny G. Splitting of the isoscalar *E*2 giant resonance and evidence of low-lying *E*0 strength in $^{4}$0Ca. *Phys Rev Lett*. (1995) **74**:3943–6. doi: 10.1103/PhysRevLett.74.3943
62. Kamerdzhiev S, Speth J, Tertychny G. Microscopic description of the E0, E2 and E1 giant resonances in $^{4}$0Ca, $^{4}$8Ca and $^{5}$6Ni. *Nucl Phys A*. (1997) **624**:328–48. doi: 10.1016/S0375-9474(97)00315-1
63. Vasseur O, Gambacurta D, Grasso M. Systematic study of giant quadrupole resonances with the subtracted second random-phase approximation: Beyond-mean-field centroids and fragmentation. *Phys Rev C*. (2018) **98**:044313. doi: 10.1103/PhysRevC.98.044313
64. Caurier E, Menéndez J, Nowacki F, Poves A. Coexistence of spherical states with deformed and superdeformed bands in doubly magic $^{4}$0Ca: a shell-model challenge. *Phys Rev C*. (2007) **75**:054317. doi: 10.1103/PhysRevC.75.054317
65. Zuker AP, Buck B, McGrory JB. Structure of O$^{1}$6. *Phys Rev Lett*. (1968) **21**:39–43. doi: 10.1103/PhysRevLett.21.39
66. Gross W, Meuer D, Richter A, Spamer E, Titze O, Knüpfer W. A strong magnetic dipole excitation in $^{4}$0Ca observed in high-resolution inelastic electron scattering and coherent spin-flip transitions due to cground-state correlations. *Phys Lett B*. (1979) **84**:296–300. doi: 10.1016/0370-2693(79)90043-1
67. Takayanagi K, Shimizu K, Arima A. A theoretical study of magnetic dipole transitions in $^{4}$8Ca. *Nucl Phys A*. (1988) **481**:313–32. doi: 10.1016/0375-9474(88)90499-X
68. Robin C, Litvinova E. Time-reversed particle-vibration loops and nuclear Gamow-Teller response. *Phys Rev Lett*. (2019) **123**:202501. doi: 10.1103/PhysRevLett.123.202501
69. Davies KTR, Koonin SE. Skyrme-force time-dependent Hartree-Fock calculations with axial symmetry. *Phys Rev C*. (1981) **23**:2042–61. doi: 10.1103/PhysRevC.23.2042
70. Tohyama M, Umar AS. Dipole resonances in oxygen isotopes in time-dependent density-matrix theory. *Phys Lett B*. (2001) **516**:415–9. doi: 10.1016/S0370-2693(01)00925-X
71. Tohyama M, Umar AS. Quadrupole resonances in unstable oxygen isotopes in time-dependent density-matrix formalism. *Phys Lett B*. (2002) **549**:72–8. doi: 10.1016/S0370-2693(02)02885-X
72. Lazzarini A, Doubre H, Lesko KT, Metag V, Seamster A, Vandenbosch R, et al. Search for a fusion $L$ window in the $^{1}$6O + $^{1}$6O system at $E_{c.m.} = 34$ MeV. *Phys Rev C*. (1981) **24**:309–12. doi: 10.1103/PhysRevC.24.309
73. Kox S, Cole AJ, Ost R. Determination of limiting angular momenta for fusion from statistical-model fits to mass distributions of evaporation residues. *Phys Rev Lett*. (1980) **44**:1204–6. doi: 10.1103/PhysRevLett.44.1204
74. Szanto de Toledo A, Cormier TM, Herman M, Lin B, Stwertka PM, Coimbra MM, et al. Limiting angular momenta for light heavy-ion fusion at high energy. *Phys Rev Lett*. (1981) **47**:1881–4. doi: 10.1103/PhysRevLett.47.1881

75. Ikezoe H, Shikazono N, Tomita Y, Ideno K, Sugiyama Y, Takekoshi E, et al. Measurements of evaporation residues to investigate lower limiting angular momenta in fusion reactions. *Nucl Phys A*. (1986) **456**:298–316. doi: 10.1016/0375-9474(86)90395-7
76. Umar AS, Strayer MR, Reinhard P-G. Resolution of the fusion window anomaly in heavy-ion collisions. *Phys Rev Lett*. (1986) **56**:2793–6. doi: 10.1103/PhysRevLett.56.2793
77. Tohyama M. Application of quantum theory of particle collisions to $^{1}$6O + $^{1}$6O reactions. *Phys Rev C*. (1987) **36**:187–92. doi: 10.1103/PhysRevC.36.187
78. Vautherin D, Brink DM. Hartree-Fock calculations with Skyrme's interaction. I. Spherical nuclei. *Phys Rev C*. (1972) **5**:626–47. doi: 10.1103/PhysRevC.5.626

**Conflict of Interest:** The author declares that the research was conducted in the absence of any commercial or financial relationships that could be construed as a potential conflict of interest.

frontiers in Physics

MINI REVIEW
published: 03 April 2020
doi: 10.3389/fphy.2020.00093

# TDHF and a Macroscopic Aspect of Low-Energy Nuclear Reactions

*Kouhei Washiyama*[1]* *and Kazuyuki Sekizawa*[2,3]

[1] *Research Center for Superheavy Elements, Kyushu University, Fukuoka, Japan,* [2] *Center for Transdisciplinary Research, Institute for Research Promotion, Niigata University, Niigata, Japan,* [3] *Division of Nuclear Physics, Center for Computational Sciences, University of Tsukuba, Ibaraki, Japan*

Time-dependent Hartree–Fock (TDHF) method has been applied to various low-energy nuclear reactions, such as fusion, fission, and multinucleon transfer reactions. In this Mini Review, we summarize recent attempts to bridge a microscopic nuclear reaction theory, TDHF, and a macroscopic aspect of nuclear reactions through nucleus–nucleus potentials and energy dissipation from macroscopic degrees of freedom to microscopic ones obtained from TDHF in various colliding systems from light to heavy mass regions.

**Keywords: heavy-ion fusion reactions, TDHF, nucleus–nucleus potential, energy dissipation, fusion hindrance, quasifission**

OPEN ACCESS

***Edited by:***
*Denis Lacroix,*
*UMR8608 Institut de Physique Nucléaire d'Orsay (IPNO), France*

***Reviewed by:***
*Sait Umar,*
*Vanderbilt University, United States*
*Chen Ji,*
*Central China Normal University, China*

***Correspondence:**
*Kouhei Washiyama*
*washiyama@phys.kyushu-u.ac.jp*

***Specialty section:***
*This article was submitted to Nuclear Physics, a section of the journal Frontiers in Physics*

***Received:*** *31 January 2020*
***Accepted:*** *12 March 2020*
***Published:*** *03 April 2020*

***Citation:***
*Washiyama K and Sekizawa K (2020) TDHF and a Macroscopic Aspect of Low-Energy Nuclear Reactions. Front. Phys. 8:93. doi: 10.3389/fphy.2020.00093*

## 1. INTRODUCTION

Time-dependent Hartree–Fock (TDHF) method has been widely used in analyzing low-energy nuclear reactions since Bonche and his coworkers applied TDHF to collision of slabs in one-dimensional space as the first application of TDHF to nuclear physics [1]. Since then TDHF has been improved in several respects, e.g., including all terms in recent energy density functionals (EDF) such as Skyrme [2] and Gogny [3] functionals and breaking symmetries such as space (from one-dimensional to three-dimensional space).

It is well-known that the coupling between relative motions of colliding nuclei (macroscopic degrees of freedom) and internal excitations of them (microscopic degrees of freedom) plays an important role for describing low-energy nuclear reactions at energies around the Coulomb barrier. To include such couplings, coupled-channel models [4–7] have been developed and widely used. TDHF automatically includes couplings between relative motion and internal excitations since TDHF describes the dynamics of single particles. Moreover, TDHF provides an intuitive picture of nuclear dynamics through the time evolution of one-body densities constructed from single-particle wave functions in nuclei. Recently, TDHF has been applied to nuclear collective excitations [3, 8–15] and to nuclear reactions such as fusion [16–22], quasifission [23–25], fission [26–29], and multinucleon transfer reactions [30–34], some of which include pairing correlations.

In this Mini Review, however, we do not discuss the development of TDHF itself (see recent review articles on the development of TDHF in [35–40]). Instead, we focus on a macroscopic aspect of low-energy nuclear reactions described by TDHF. To this end, we show various applications of the method called "dissipative-dynamics TDHF" (DD-TDHF) developed in Washiyama and Lacroix [19], Washiyama et al. [20], and Washiyama [41].

## 2. DISSIPATIVE-DYNAMICS TDHF

The basic idea of DD-TDHF is to combine microscopic dynamics of nuclear reactions described by TDHF and a macroscopic aspect of nuclear reactions through a mapping from microscopic TDHF

evolution to a set of macroscopic equations of motion. We briefly summarize DD-TDHF by the following steps: (1) We first solve the TDHF equation to obtain time evolution of single-particle wave functions for nuclear reactions:

$$i\hbar\frac{\partial\phi_i(t)}{\partial t} = \hat{h}[\rho(t)]\phi_i(t), \tag{1}$$

where $\phi_i(t)$ is the single-particle wave functions with index $i$ (including spin and isospin degrees of freedom), and $\hat{h}[\rho(t)]$ is the single-particle Hamiltonian as a functional of one-body density $\rho(t)$, obtained from an EDF $E[\rho]$ by an appropriate functional derivative $\hat{h}[\rho(t)] = \delta E/\delta\rho$. (2) The next step is to define macroscopic two-body dynamics from microscopic TDHF simulations. Macroscopic two-body dynamics can be constructed once collective coordinate is defined from TDHF simulations. To do so in TDHF, we introduce a separation plane which divides the density $\rho(\boldsymbol{r}, t)$ of a colliding system to two subsystems, $\rho_1(\boldsymbol{r}, t)$ and $\rho_2(\boldsymbol{r}, t)$, corresponding to projectile-like and target-like densities. This separation plane is perpendicular to the collision axis, and at the position where the two densities $\rho_P(\boldsymbol{r}, t)$ and $\rho_T(\boldsymbol{r}, t)$ constructed from the single-particle wave functions initially in the projectile and in the target, respectively, cross (see Figure 1 of [19] for an illustrative example). We then compute the coordinate $R_i$ and its conjugated momentum $P_i$ for each subsystem $i = 1, 2$ from $\rho_1(\boldsymbol{r}, t)$ and $\rho_2(\boldsymbol{r}, t)$. Also, we compute the masses of the two subsystems by $m_i = P_i/\dot{R}_i$. From these, two-body dynamics for the relative distance $R$ as a collective coordinate and its conjugated momentum $P$, and reduced mass $\mu$ that may depend on $R$ is constructed. (3) For the case of central collisions, we assume that the trajectory of the two-body dynamics obtained from TDHF follows a one-dimensional equation of motion for relative motions,

$$\frac{dR}{dt} = \frac{P}{\mu}, \tag{2}$$

$$\frac{dP}{dt} = -\frac{dV}{dR} - \frac{d}{dR}\left(\frac{P^2}{2\mu}\right) - \gamma\frac{P}{\mu}, \tag{3}$$

where $V(R)$ and $\gamma(R)$ denote the nucleus–nucleus potential and friction coefficient expressing energy dissipation from the relative motion of colliding nuclei to internal excitations in nuclei, respectively. An important point is that these two quantities $V(R)$ and $\gamma(R)$ are unknown in TDHF simulations. (4) To obtain those two unknown quantities we prepare a system of two equations from two trajectories at slightly different energies. Then, we solve the system of two equations at each $R$ to obtain $V(R)$ and $\gamma(R)$. The details of numerical procedures for the calculations described above can be found in Washiyama and Lacroix [19], Washiyama et al. [20], and Washiyama [41]. In the following results, we used the SLy4d Skyrme EDF [16] without pairing interactions.

# 3. NUCLEUS–NUCLEUS POTENTIAL AND ENERGY DISSIPATION

## 3.1. Light and Medium-Mass Systems

In light and medium-mass systems, whose charge product $Z_1Z_2$ is smaller than $\approx$ 1,600, it is known that fusion occurs once two nuclei contact each other after passing the Coulomb barrier. Indeed, TDHF simulations for head-on collisions at energies above the Coulomb barrier lead to fusion, keeping a compound system compact for sufficiently long time. We first provide selected results of nucleus–nucleus potential and energy dissipation obtained from DD-TDHF and discuss their properties.

In **Figure 1A**, we show obtained nucleus–nucleus potentials as a function of relative distance $R$ near the Coulomb barrier radius for $^{40}$Ca + $^{40}$Ca. The lines show the nucleus–nucleus potentials at different center-of-mass energies ($E_{\mathrm{c.m.}}$) by DD-TDHF, while the filled circles show the potential obtained by the frozen-density approximation, where the energy of the system is calculated with the same EDF except that the dynamical effect during the collision is neglected and the density of each fragment is fixed to be its ground-state one. Moreover, in the frozen-density approximation, the Pauli principle is neglected between nucleons in the projectile and in the target, leading to worse approximation as the overlap of projectile and target nuclei becomes significant. Important remarks from this figure are: (1) Potentials obtained at higher energies ($E_{\mathrm{c.m.}} = 90$, 100 MeV) agree with the frozen-density one, indicating the convergence of the potentials obtained by DD-TDHF at higher energies. (2) DD-TDHF potentials express an $E_{\mathrm{c.m.}}$ dependence at lower energies $E_{\mathrm{c.m.}} = 55$, 57 MeV. (3) The height of DD-TDHF potential decreases with decreasing $E_{\mathrm{c.m.}}$. The Coulomb barrier height decreases from $\approx$ 54.5 MeV at $E_{\mathrm{c.m.}} = 90$, 100 MeV of DD-TDHF and of the frozen-density approximation to $\approx$ 53.4 MeV at $E_{\mathrm{c.m.}} = 55$ MeV of DD-TDHF. The above remarks can be understood by the dynamical reorganization of the TDHF density profile of each TDHF trajectory. **Figure 1B** shows the TDHF density $\rho(x, y, z = 0, t)$ at each $R$ for $E_{\mathrm{c.m.}} = 55$ (top panels) and 90 MeV (bottom panels). At $E_{\mathrm{c.m.}} = 90$ MeV, the shape of each $^{40}$Ca density keeps its shape spherical, while at $E_{\mathrm{c.m.}} = 55$ MeV the shape of each $^{40}$Ca density deviates from its ground-state spherical shape as $R$ becomes smaller. This is a dynamical reorganization of density during fusion reactions. This dynamical reorganization changes the shape of each nucleus when two nuclei approach sufficiently, then reduces the height of the nucleus–nucleus potential obtained by DD-TDHF. This dynamical reduction of the nucleus–nucleus potential is seen in various light- and medium-mass systems in Washiyama and Lacroix [19].

We would like to note that, in the density-constrained TDHF (DC-TDHF) method [17], in which constrained Hartree–Fock calculation is performed to obtain the nucleus–nucleus potential under the condition that the density is constrained to the density obtained from TDHF at each time, similar $E_{\mathrm{c.m.}}$ dependence of nucleus–nucleus potentials is seen in various colliding systems reported, e.g., in Umar and Oberacker [18], Umar et al. [42], Oberacker et al. [43], and Umar et al. [44]. Moreover, in the

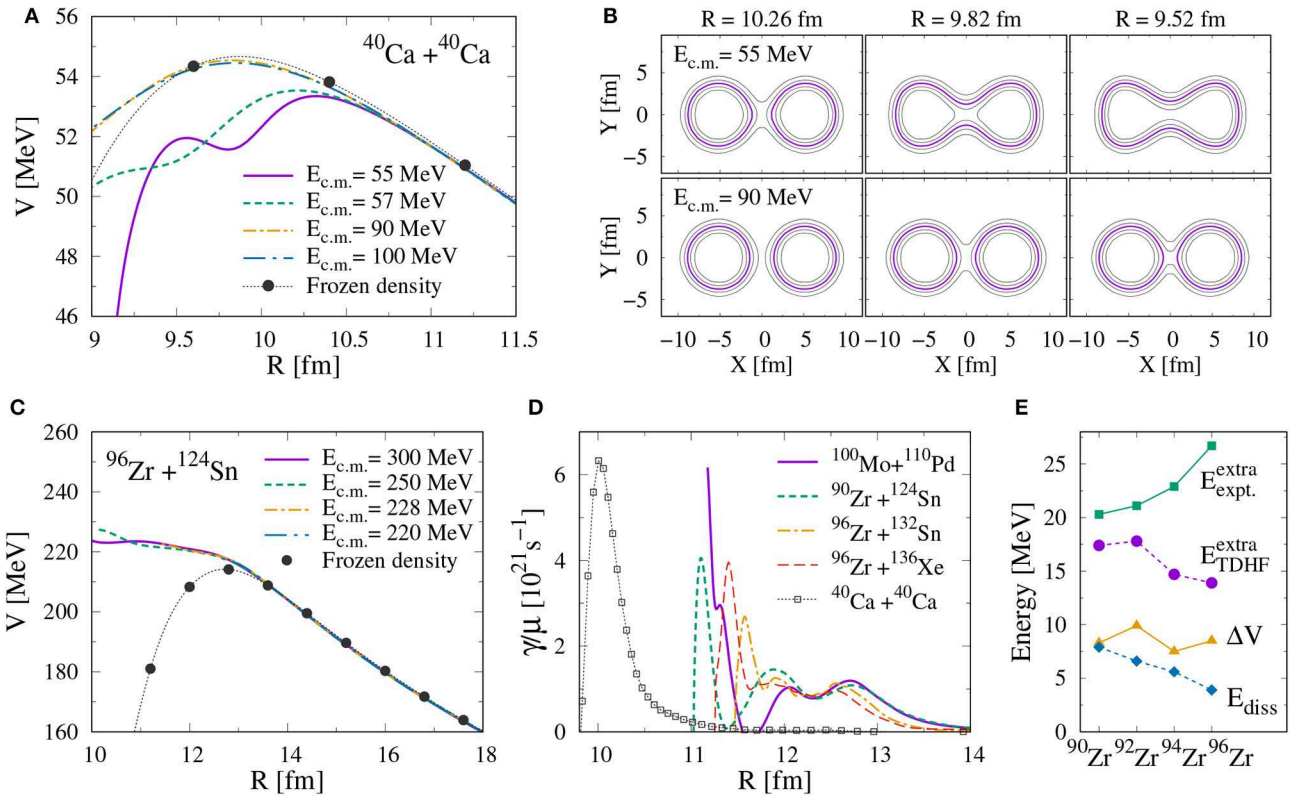


**FIGURE 1 | (A)** Nucleus–nucleus potentials denoted by lines obtained by DD-TDHF at different energies and by the frozen-density approximation by filled circles with the dotted line as a function of $R$ in $^{40}$Ca + $^{40}$Ca. **(B)** Contour plots of density profile $\rho(X, Y, 0)$ obtained from TDHF at $E_{\text{c.m.}} = 55$ MeV (upper panels) and at $E_{\text{c.m.}} = 90$ MeV (lower panels), at $R = 10.26$ fm (left panels), 9.82 fm (middle), and 9.52 fm (right) in $^{40}$Ca + $^{40}$Ca. The isodensities (contour lines) are plotted at each 0.025 fm$^{-3}$. **(C)** Same as **(A)** but for $^{96}$Zr + $^{124}$Sn. **(D)** Friction coefficient divided by reduced mass, $\gamma/\mu$, from DD-TDHF. **(E)** Extra-push energy from experiments ($E^{\text{extra}}_{\text{expt.}}$) and from TDHF ($E^{\text{extra}}_{\text{TDHF}}$) together with potential increase $\Delta V$ and dissipated energy $E_{\text{diss}}$ for $^{90,92,94,96}$Zr + $^{124}$Sn (see text for detail). **(A,B)** adopted from Washiyama and Lacroix [19], **(C,D)** adopted from Washiyama [41], and **(E)** adopted from Washiyama [41] with slight change with permission from APS and SciPris.

$^{40}$Ca + $^{40}$Ca system, we find no significant difference in the potential extracted by DD-TDHF and the one by DC-TDHF [44].

## 3.2. Heavy Systems

Contrary to light and medium-mass systems described in section Light and Medium-Mass Systems, it was experimentally observed that fusion probability at energies near the Coulomb barrier is strongly hindered in heavy systems ($Z_1Z_2 \geq 1,600$) [45, 46]. The main origin of this hindrance has been considered as the presence of the quasifission process, where a composite system of two colliding nuclei reseparates before forming an equilibrated compound nucleus. This fusion hindrance indeed has been observed in TDHF e.g., in Simenel [35], Washiyama [41], Simenel et al. [47], and Guo and Nakatsukasa [48]. Namely, TDHF simulations for head-on collisions at energies above the Coulomb barrier lead to touching configuration of a composite system, and then to reseparation after a while (several to tens of zeptoseconds). In Washiyama [41], the extra-push energy $E^{\text{TDHF}}_{\text{extra}} = E^{\text{TDHF}}_{\text{thres}} - V^{\text{FD}}_B$ in TDHF was systematically obtained in heavy systems, where $E^{\text{TDHF}}_{\text{thres}}$ and $V^{\text{FD}}_B$ denote the fusion threshold energy above which fusion occurs in TDHF and the Coulomb barrier energy obtained in the frozen-density approximation, respectively. We show in **Figure 1E** extra-push energies in TDHF for $^{90,92,94,96}$Zr + $^{124}$Sn, compared with those deduced from experimental data, $E^{\text{extra}}_{\text{expt.}}$, taken from Schmidt and Morawek [49], where the Bass barrier $V_{\text{Bass}}$ [50] was employed as the Coulomb barrier height. We found that the difference between $V^{\text{FD}}_B$ and $V_{\text{Bass}}$ in $^{90,92,94,96}$Zr + $^{124}$Sn is at most $\approx$ 1 MeV. These obtained extra-push energies in TDHF reasonably reproduce observations.

One may think why the fusion hindrance in heavy systems appears in both experiments and TDHF simulations. In Washiyama [41], we address this question and analyze where finite extra-push energies arise. For the analysis, we first derive the nucleus–nucleus potential and energy dissipation by DD-TDHF because we think that these two quantities are strongly related to the appearance of finite extra-push energy. In **Figure 1C**, we show an example of nucleus–nucleus potentials extracted in heavy systems, which is for the $^{96}$Zr + $^{124}$Sn system for three different energies in DD-TDHF and the frozen-density one. One can clearly see the difference between the potentials in $^{40}$Ca + $^{40}$Ca (**Figure 1A**) and $^{96}$Zr + $^{124}$Sn (**Figure 1C**): the potentials in $^{96}$Zr + $^{124}$Sn extracted by DD-TDHF monotonically increases as the relative distance decreases while the potentials in

$^{40}$Ca + $^{40}$Ca and by the frozen-density approximation in $^{96}$Zr + $^{124}$Sn show a barrier structure at a certain relative distance. We have observed monotonic increase in potential in other heavy systems [41]. We consider the increase in potential in heavy systems as the transition from two-body dynamics of colliding nuclei to one-body dynamics of a composite system with strong overlap of the densities of colliding nuclei in TDHF and as the appearance of the conditional saddle point inside the Coulomb barrier in heavy systems [51–54].

We would like to note here that this is different property from the one obtained from the DC-TDHF method in the same colliding system in Oberacker et al. [43]. This difference comes from a different interpretation of the nucleus–nucleus potential between the two methods. In the DC-TDHF method energy minimization is carried out at a given density of a system obtained from TDHF to deduce a nucleus–nucleus potential that eliminates internal excitations in this system. In the DD-TDHF method the potential is deduced under the assumption that TDHF evolution is reduced to a one-dimensional equation of motion for relative motion. We consider that the DD-TDHF potential can include a part of the DC-TDHF internal excitation energy. We make a comment on the origin of the difference between the two potentials in the following: In heavy systems with larger Coulomb replusion, larger overlap of projectile and target densities during a collsion in TDHF is achieved at a short relative distance. In TDHF, diabatic level crossings can occur more in larger overlap region, leading to a part of internal excitations and to a transition from two-body to one-body picture of a system. This part of internal excitations is interpreted as potential energy in DD-TDHF, while this is treated as excitation energy in DC-TDHF. In the DC-TDHF method, the flattening of the potential at short distances inside the Coulomb barrier radius is seen in heavier systems leading to the synthesis of superheavy elements in Umar et al. [42].

In **Figure 1D**, reduced friction coefficient ($\gamma/\mu$), the friction coefficient divided by the reduced mass extracted from Equation (2), are plotted for selected systems. The friction coefficient increases as $R$ decreases, and shows oscillations in heavy systems. We consider that the fact that the friction coefficient becomes negative indicates breakdown of the assumption that the TDHF trajectory follows a macroscopic one-dimensional equation of motion for relative motion of a two-body colliding system.

Finally, we consider the origin of the fusion hindrance in heavy systems through the analysis with DD-TDHF. As mentioned above, nucleus–nucleus potential and energy dissipation are main contribution to the appearance of finite extra-push energy. We evaluate the potential increase at short distances and the accumulated dissipation energy from the friction coefficient using the formula [41],

$$E_{\rm diss}(t) = \int_0^t dt' \gamma[R(t')]\dot{R}(t')^2, \tag{4}$$

up to time $t$ when the kinetic energy of the relative motion of the system is completely dissipated. In **Figure 1E**, we also show the contribution of potential increase $\Delta V$ and dissipated energy $E_{\rm diss}$ to the extra-push energy in the $^{90,92,94,96}$Zr + $^{124}$Sn systems. The result $\Delta V > E_{\rm diss}$ indicates that the potential increase is a main origin for the appearance of the finite extra-push energy, i.e., fusion hindrance. Though the energy dissipation is known to play an important role in this fusion hindrance, it is not sufficient to explain the amount of the extra-push energy in the analysis with the DD-TDHF method.

## 3.3. Off-Central Collisions

So far, the applications of the DD-TDHF method has been limited to central collisions. Here we discuss a possible extension of the method to off-central collisions. Regarding $(R, P)$ and $(\varphi, L)$ as sets of canonical coordinates, where $\varphi$ represents a rotation angle of the colliding system in the reaction plane and $L = \mu R^2\dot{\varphi}$ is the angular momentum of the relative motion, we obtain a set of macroscopic equations of motion:

$$\frac{{\rm d}R}{{\rm d}t} = \frac{P}{\mu}, \tag{5}$$

$$\frac{{\rm d}\varphi}{{\rm d}t} = \frac{L}{\mu R^2}, \tag{6}$$

$$\frac{{\rm d}P}{{\rm d}t} = -\frac{{\rm d}V}{{\rm d}R} + \frac{1}{2}\left(\frac{P^2}{\mu^2} + \frac{L^2}{\mu^2 R^2}\right)\frac{{\rm d}\mu}{{\rm d}R} + \frac{L^2}{\mu R^3} - \gamma_R\frac{P}{\mu}, \tag{7}$$

$$\frac{{\rm d}L}{{\rm d}t} = -\gamma_\varphi\frac{L}{\mu}. \tag{8}$$

Here, $\gamma_R(R)$ and $\gamma_\varphi(R)$ denote the radial and tangential (or "sliding") friction coefficients, respectively, where the former already appeared in Equation (3), the case of central collisions, and the latter governs the angular momentum dissipation (cf. Equation 8).

At first sight, there are three unknown quantities: the nucleus–nucleus potential $V$, the radial friction coefficient $\gamma_R$, and the tangential friction coefficient $\gamma_\varphi$. However, since time evolution of $\varphi(t)$ and $L(t)$ can be obtained from TDHF, a single TDHF simulation already provides the tangential friction coefficient by

$$\gamma_\varphi(R) = -\mu(t)\frac{\dot{L}(t)}{L(t)}. \tag{9}$$

Thus, there are only two unknown quantities in Equations (5)–(8), i.e., $V(R)$ and $\gamma_R(R)$, and we can apply the same procedure applied for central collisions.

In **Figure 2**, we show the results for the $^{16}$O+$^{16}$O reaction at $E/V_{\rm B} = 1.4$ including off-central collisions, as an illustrative example. In **Figure 2A**, the nucleus–nucleus potential is shown as a function of the relative distance, $R$. We also show the potential in the frozen-density approximation by open circles, for comparison. **Figure 2A** clearly shows that the method provides almost identical nucleus–nucleus potentials $V(R)$ irrespective of the impact parameters. In **Figure 2B**, the effective potential $V_{\rm eff}(R)$, the sum of nuclear, Coulomb, and centrifugal potentials, is shown. It can be seen that, for $b = 6$ fm, the closest distance is achieved at around $R = 10$ fm, at which the effective potential coincides with the incident relative energy. In **Figures 2C,D**, the reduced radial and tangential friction coefficients, $\beta_R = \gamma_R/\mu$ and $\beta_\varphi = \gamma_\varphi/\mu$, are shown as a function of the relative distance.

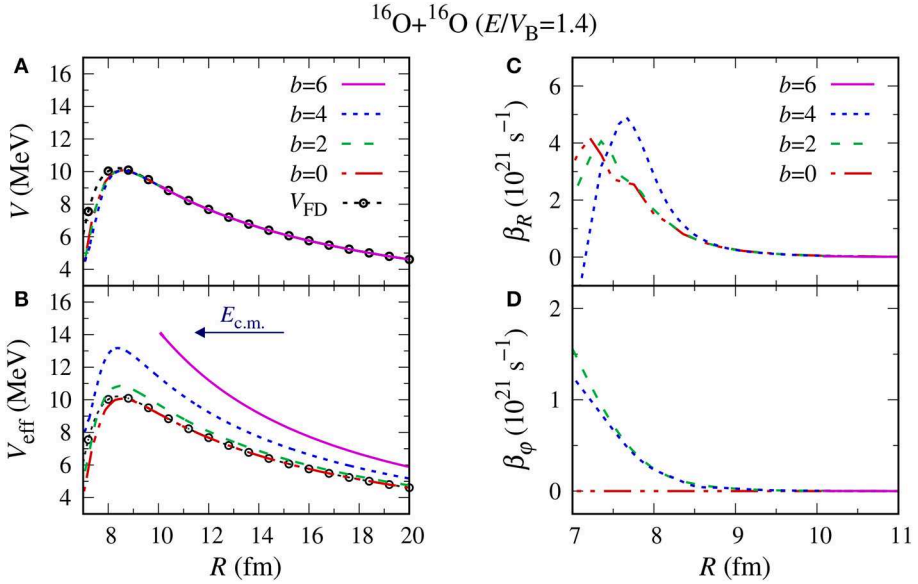


**FIGURE 2 |** Results of DD-TDHF calculations for the $^{16}$O+$^{16}$O reaction at $E/V_B = 1.4$ at various impact parameters. The nucleus–nucleus potentials and the effective potential $V_{\rm eff}(R) = V(R) + L^2/2\mu R^2$ are shown in **(A,B)**, respectively, as a function of the relative distance, $R$. The reduced radial friction coefficients, $\beta_R = \gamma_R/\mu$, are shown in **(C)**, while the reduced tangential friction coefficients, $\beta_\varphi = \gamma_\varphi/\mu$, are shown in **(D)**.

We found no significant dependence of the friction coefficients on the impact parameters in this system. In this way, this approach enables us to access the angular momentum dissipation mechanism and a systematic calculation is in progress.

Note that non-central effects on nucleus–nucleus potentials and effective mass parameters in fusion reactions have been studied in TDHF and DC-TDHF in Jiang et al. [21]. It is interesting to make detailed comparison between those and our DD-TDHF in a future work.

## 4. SUMMARY

The macroscopic aspect of TDHF dynamics for low-energy nuclear reactions at energies near the Coulomb barrier was discussed within the DD-TDHF method. We showed that the dynamical reorganization of single-particle wave functions inside the colliding nuclei affects the macroscopic nucleus–nucleus potential that leads to dynamical reduction of the potential around the Coulomb barrier radius in light- and medium-mass systems. In heavy systems, the dynamical reorganization leads to the fusion hindrance, increase in potential compared with the potential obtained from the frozen-density approximation in which the dynamical reorganization effect is neglected. By extending the DD-TDHF method to off-central collisions, the tangential friction coefficient was extracted in the $^{16}$O+$^{16}$O reaction in addition to the nucleus–nucleus potential and the radial friction. As expected, the nucleus–nucleus potentials do not show a significant dependence of the initial angular momentum. The strength of the tangential friction is in the same order of magnitude as the radial one. From this extension, one can access the mechanism of angular momentum dissipation from microscopic reaction models. Possible future extension would be a systematic study of angular momentum dissipation mechanism in various systems, especially in heavy systems to address the fusion hindrance problem. Another possible extension would be a systematic study of collisions with deformed nuclei. It is interesting to study an orientation effect, a dependence of an angle between the collision axis and the principle axis of a deformed nucleus, on the nucleus–nucleus potential and the friction coefficient. It would be important to investigate how orbital angular momentum dissipation couples to a rotation of deformed nucleus during collision.

## AUTHOR CONTRIBUTIONS

All authors listed have made a substantial, direct and intellectual contribution to the work, and approved it for publication.

## FUNDING

This work was supported in part by QR Program of Kyushu University, by JSPS-NSFC Bilateral Program for Joint Research Project on Nuclear mass and life for unravelling mysteries of r-process, and by JSPS Grant-in-Aid for Early-Career Scientists No. 19K14704.

## ACKNOWLEDGMENTS

The authors acknowledge Denis Lacroix and Sakir Ayik for the collaboration to this work. This work used computational resources of the Oakforest-PACS Supercomputer System provided by Multidisciplinary Cooperative Research Program

in Center for Computational Sciences (CCS), University of Tsukuba (Project ID: NUCLHIC), and computational resources of the HPCI system (Oakforest-PACS) provided by Joint Center for Advanced High Performance Computing (JCAHPC) through the HPCI System Project (Project ID: hp190002).

## REFERENCES


1. Bonche P, Koonin S, Negele JW. One-dimensional nuclear dynamics in the time-dependent Hartree-Fock approximation. *Phys Rev C*. (1976) **13**:1226–58. doi: 10.1103/PhysRevC.13.1226
2. Umar AS, Strayer MR, Reinhard PG. Resolution of the fusion window anomaly in heavy-ion collisions. *Phys Rev Lett*. (1986) **56**:2793–6. doi: 10.1103/PhysRevLett.56.2793
3. Hashimoto Y. Linear responses in time-dependent Hartree-Fock-Bogoliubov method with Gogny interaction. *Eur Phys J A*. (2012) **48**:55. doi: 10.1140/epja/i2012-12055-0
4. Reisdorf W, Hessberger FP, Hildenbrand KD, Hofmann S, Münzenberg G, Schmidt KH, et al. Influence of collective surface motion on the threshold behavior of nuclear fusion. *Phys Rev Lett*. (1982) **49**:1811–5. doi: 10.1103/PhysRevLett.49.1811
5. Dasso CH, Landowne S, Winther A. Channel-coupling effects in heavy-ion fusion reactions. *Nucl Phys A*. (1983) **405**:381–96.
6. Balantekin AB, Takigawa N. Quantum tunneling in nuclear fusion. *Rev Mod Phys*. (1998) **70**:77–100. doi: 10.1103/RevModPhys.70.77
7. Hagino K, Takigawa N. Subbarrier fusion reactions and many-particle quantum tunneling. *Prog Theor Phys*. (2012) **128**:1001–60. doi: 10.1143/PTP.128.1061
8. Simenel C, Chomaz P, de France G. Quantum calculation of the dipole excitation in fusion reactions. *Phys Rev Lett*. (2001) **86**:2971–4. doi: 10.1103/PhysRevLett.86.2971
9. Simenel C, Chomaz P. Nonlinear vibrations in nuclei. *Phys Rev C*. (2003) **68**:024302. doi: 10.1103/PhysRevC.68.024302
10. Nakatsukasa T, Yabana K. Linear response theory in the continuum for deformed nuclei: Green's function vs. time-dependent Hartree-Fock with the absorbing boundary condition. *Phys Rev C*. (2005) **71**:024301. doi: 10.1103/PhysRevC.71.024301
11. Maruhn JA, Reinhard PG, Stevenson PD, Stone JR, Strayer MR. Dipole giant resonances in deformed heavy nuclei. *Phys Rev C*. (2005) **71**:064328. doi: 10.1103/PhysRevC.71.064328
12. Avez B, Simenel C, Chomaz P. Pairing vibrations study with the time-dependent Hartree-Fock-Bogoliubov theory. *Phys Rev C*. (2008) **78**:044318. doi: 10.1103/PhysRevC.78.044318
13. Ebata S, Nakatsukasa T, Inakura T, Yoshida K, Hashimoto Y, Yabana K. Canonical-basis time-dependent Hartree-Fock-Bogoliubov theory and linear-response calculations. *Phys Rev C*. (2010) **82**:034306. doi: 10.1103/PhysRevC.82.034306
14. Stetcu I, Bulgac A, Magierski P, Roche KJ. Isovector giant dipole resonance from the 3D time-dependent density functional theory for superfluid nuclei. *Phys Rev C*. (2011) **84**:051309. doi: 10.1103/PhysRevC.84.051309
15. Scamps G, Lacroix D. Systematics of isovector and isoscalar giant quadrupole resonances in normal and superfluid spherical nuclei. *Phys Rev C*. (2013) **88**:044310. doi: 10.1103/PhysRevC.88.044310
16. Kim KH, Otsuka T, Bonche P. Three-dimensional TDHF calculations for reactions of unstable nuclei. *J Phys G*. (1997) **23**:1267.
17. Umar AS, Oberacker VE. Heavy-ion interaction potential deduced from density-constrained time-dependent Hartree-Fock calculation. *Phys Rev C*. (2006) **74**:021601. doi: 10.1103/PhysRevC.74.021601
18. Umar AS, Oberacker VE. Density-constrained time-dependent Hartree-Fock calculation of $^{16}$O+$^{208}$Pb fusion cross-sections. *Eur Phys J A*. (2009). **39**:243–7. doi: 10.1140/epja/i2008-10712-5
19. Washiyama K, Lacroix D. Energy dependence of the nucleus-nucleus potential close to the Coulomb barrier. *Phys Rev C*. (2008) **78**:024610. doi: 10.1103/PhysRevC.78.024610
20. Washiyama K, Lacroix D, Ayik S. One-body energy dissipation in fusion reactions from mean-field theory. *Phys Rev C*. (2009) **79**:024609. doi: 10.1103/PhysRevC.79.024609
21. Jiang X, Maruhn JA, Yan S. Microscopic study of noncentral effects in heavy-ion fusion reactions with spherical nuclei. *Phys Rev C*. (2014) **90**:064618. doi: 10.1103/PhysRevC.90.064618
22. Hashimoto Y, Scamps G. Gauge angle dependence in time-dependent Hartree-Fock-Bogoliubov calculations of $^{20}$O + $^{20}$O head-on collisions with the Gogny interaction. *Phys Rev C*. (2016) **94**:014610. doi: 10.1103/PhysRevC.94.014610
23. Kedziora DJ, Simenel C. New inverse quasifission mechanism to produce neutron-rich transfermium nuclei. *Phys Rev C*. (2010) **81**:044613. doi: 10.1103/PhysRevC.81.044613
24. Wakhle A, Simenel C, Hinde DJ, Dasgupta M, Evers M, Luong DH, et al. Interplay between quantum shells and orientation in quasifission. *Phys Rev Lett*. (2014) **113**:182502. doi: 10.1103/PhysRevLett.113.182502
25. Sekizawa K, Yabana K. Time-dependent Hartree-Fock calculations for multinucleon transfer and quasifission processes in the $^{64}$Ni + $^{238}$U reaction. *Phys Rev C*. (2016) **93**:054616. doi: 10.1103/PhysRevC.93.054616
26. Simenel C, Umar AS. Formation and dynamics of fission fragments. *Phys Rev C*. (2014) **89**:031601. doi: 10.1103/PhysRevC.89.031601
27. Scamps G, Simenel C, Lacroix D. Superfluid dynamics of $^{258}$Fm fission. *Phys Rev C*. (2015) **92**:011602(R). doi: 10.1103/PhysRevC.92.011602
28. Goddard P, Stevenson P, Rios A. Fission dynamics within time-dependent Hartree-Fock: Deformation-induced fission. *Phys Rev C*. (2015) **92**:054610. doi: 10.1103/PhysRevC.92.054610
29. Bulgac A, Magierski P, Roche KJ, Stetcu I. Induced fission of $^{240}$Pu within a real-time microscopic framework. *Phys Rev Lett*. (2016) **116**:122504. doi: 10.1103/PhysRevLett.116.122504
30. Simenel C. Particle transfer reactions with the time-dependent Hartree-Fock theory using a particle number projection technique. *Phys Rev Lett*. (2010) **105**:192701. doi: 10.1103/PhysRevLett.105.192701
31. Sekizawa K, Yabana K. Time-dependent Hartree-Fock calculations for multinucleon transfer processes in $^{40,48}$Ca + $^{124}$Sn, $^{40}$Ca + $^{208}$Pb, and $^{58}$Ni + $^{208}$Pb reactions. *Phys Rev C*. (2013) **88**:014614. doi: 10.1103/PhysRevC.88.014614
32. Scamps G, Lacroix D. Effect of pairing on one- and two-nucleon transfer below the Coulomb barrier: a time-dependent microscopic description. *Phys Rev C*. (2013) **87**:014605. doi: 10.1103/PhysRevC.87.014605
33. Wu Z, Guo L. Microscopic studies of production cross sections in multinucleon transfer reaction $^{58}$Ni +$^{124}$ Sn. *Phys Rev C*. (2019) **100**:014612. doi: 10.1103/PhysRevC.100.014612
34. Jiang X, Wang N. Probing the production mechanism of neutron-rich nuclei in multinucleon transfer reactions. *Phys Rev C*. (2020) **101**:014604. doi: 10.1103/PhysRevC.101.014604
35. Simenel C. Nuclear quantum many-body dynamics. *Eur Phys J A*. (2012) **48**:152. doi: 10.1140/epja/i2012-12152-0
36. Nakatsukasa T. Density functional approaches to collective phenomena in nuclei: Time-dependent density functional theory for perturbative and non-perturbative nuclear dynamics. *Prog Theor Exp Phys*. (2012) **2012**:01A207. doi: 10.1093/ptep/pts016
37. Nakatsukasa T, Matsuyanagi K, Matsuo M, Yabana K. Time-dependent density-functional description of nuclear dynamics. *Rev Mod Phys*. (2016) **88**:045004. doi: 10.1103/RevModPhys.88.045004
38. Simenel C, Umar AS. Heavy-ion collisions and fission dynamics with the time-dependent Hartree-Fock theory and its extensions. *Prog Part Nucl Phys*. (2018) **103**:19–66. doi: 10.1016/j.ppnp.2018.07.002
39. Sekizawa K. TDHF theory and its extensions for the multinucleon transfer reaction: a mini review. *Front Phys*. (2019) **7**:20. doi: 10.3389/fphy.2019.00020
40. Stevenson PD, Barton MC. Low-energy heavy-ion reactions and the Skyrme effective interaction. *Prog Part Nucl Phys*. (2019) **104**:142–64. doi: 10.1016/j.ppnp.2018.09.002
41. Washiyama K. Microscopic analysis of fusion hindrance in heavy nuclear systems. *Phys Rev C*. (2015) **91**:064607. doi: 10.1103/PhysRevC.91.064607

42. Umar AS, Oberacker VE, Maruhn JA, Reinhard PG. Entrance channel dynamics of hot and cold fusion reactions leading to superheavy elements. *Phys Rev C*. (2010) **81**:064607. doi: 10.1103/PhysRevC.81.064607
43. Oberacker VE, Umar AS, Maruhn JA, Reinhard PG. Microscopic study of the $^{132,124}$Sn+$^{96}$Zr reactions: Dynamic excitation energy, energy-dependent heavy-ion potential, and capture cross section. *Phys Rev C*. (2010). **82**:034603. doi: 10.1103/PhysRevC.82.034603
44. Umar AS, Simenel C, Oberacker VE. Energy dependence of potential barriers and its effect on fusion cross sections. *Phys Rev C*. (2014) **89**:034611. doi: 10.1103/PhysRevC.89.034611
45. Gäggeler H, Sikkeland T, Wirth G, Brüchle W, Bögl W, Franz G, et al. Probing sub-barrier fusion and extra-push by measuring fermium evaporation residues in different heavy ion reactions. *Z Phys A*. (1984) **316**:291–307. doi: 10.1007/BF01439902
46. Sahm CC, Clerc HG, Schmidt KH, Reisdorf W, Armbruster P, Heßberger FP, et al. Hindrance of fusion in central collisions of heavy, symmetric nuclear systems. *Z Phys A*. (1984) **319**:113–8. doi: 10.1007/BF01415623
47. Simenel C, Avez B, Golabek C. Microscopic description of heavy ion collisions around the barrier (2009). arXiv: 0904.2653.
48. Guo L, Nakatsukasa T. Time-dependent Hartree-Fock studies of the dynamical fusion threshold. *EPJ Web Conf*. (2012) **38**:09003. doi: 10.1051/epjconf/20123809003
49. Schmidt KH, Morawek W. The conditions for the synthesis of heavy nuclei. *Rep Prog Phys*. (1991) **54**:949.
50. Bass R. Fusion of heavy nuclei in a classical model. *Nucl Phys A*. (1974) **231**:45–63.
51. Swiatecki WJ. The Dynamics of Nuclear Coalescence or Reseparation. *Phys Scr*. (1981) **24**:113–22.
52. Swiatecki WJ. The dynamics of the fusion of two nuclei. *Nucl Phys A*. (1982) **376**:275–91.
53. Bjornholm S, Swiatecki WJ. Dynamical aspects of nucleus-nucleus collisions. *Nucl Phys A*. (1982) **391**:471–504.
54. Swiatecki WJ, Siwek-Wilczynska K, Wilczynski J. Fusion by diffusion. II. Synthesis of transfermium elements in cold fusion reactions. *Phys Rev C*. (2005) **71**:014602. doi: 10.1103/PhysRevC.71.014602


**Conflict of Interest:** The authors declare that the research was conducted in the absence of any commercial or financial relationships that could be construed as a potential conflict of interest.

frontiers in Physics

MINI REVIEW
published: 09 April 2020
doi: 10.3389/fphy.2020.00102

# Studies on Nuclear Structure and Nuclear Dynamics Using Cb-TDHFB

*Shuichiro Ebata**

*Graduate School of Science and Engineering, Saitama University, Saitama, Japan*

In this paper, we briefly review the studies on nuclear structure and nuclear dynamics using the Canonical-basis time-dependent Hartree-Fock-Bogoliubov (Cb-TDHFB) theory which is one of the time-dependent mean-field models which deal with nuclear pairing correlation. At first, after a brief introduction of the time-dependent mean-field models, we explain the derivation and the properties of Cb-TDHFB equations. Next, we introduce the methods to study the nuclear linear responses and to simulate the nuclear collision in terms of the time-dependent mean-field models. Then, we display parts of the results obtained by using the time-dependent methods; Strength functions of electric dipole ($E1$) excitation mode of $^{172}$Yb, Systematic study of low-energy $E1$ mode, and Comparison of the simulations of the fusion reactions using time-dependent mean-field models with and without pairing correlation. Finally, we summarize the Cb-TDHFB activities and discuss its perspectives.

**Keywords: TDHF, TDHFB, Cb-TDHFB, nuclear structure, nuclear dynamics**

OPEN ACCESS

***Edited by:***
*Cedric Simenel,*
*Australian National University, Australia*

***Reviewed by:***
*Yukio Hashimoto,*
*University of Tsukuba, Japan*
*Scamps Guillaume,*
*Université Libre de Bruxelles, Belgium*

***Correspondence:**
*Shuichiro Ebata*
*ebata@mail.saitama-u.ac.jp*

***Specialty section:***
*This article was submitted to Nuclear Physics, a section of the journal Frontiers in Physics*

***Received:*** *31 January 2020*
***Accepted:*** *18 March 2020*
***Published:*** *09 April 2020*

***Citation:***
*Ebata S (2020) Studies on Nuclear Structure and Nuclear Dynamics Using Cb-TDHFB. Front. Phys. 8:102. doi: 10.3389/fphy.2020.00102*

## 1. INTRODUCTION

Our subject is the atomic nucleus which is a self-binding finite quantum many-body system composed of two kinds of particles (nucleon: proton and neutron). The nuclear system in which the nucleons are the primary degree of freedom has various aspects depending on its nucleon number and its energy. To describe the structure and the dynamics of the finite quantum many-body system from the degree of freedom of nucleon is the core aim of nuclear physics.

The existence of mean-field is a unique and essential property in the nucleus, which is supported by the nuclear magic numbers. The independent-particle model, like the Hartree-Fock (HF) approximation, is based on the mean-field aspect of the nucleus and expresses the many-body wave function in terms of the single-particle states. The HF is a useful method in the Fermi particle system, in which the anti-symmetrization of the single-particle wave functions are necessary to satisfy the Pauli principle. Furthermore, the pairing correlation is also an important nuclear aspect [1]. The ground-state properties of a nucleus with the pairing correlation is successfully described by the well-known theory [2] proposed by Bardeen-Cooper-Schrieffer (BCS) in the condensed matter physics.

The time-dependent (TD) mean-filed models, such as TD Hartree-Fock-Bogoliubov (TDHFB) theory [3], have been proposed with the aim at describing the nuclear structure and dynamics, taking account of the mean-field property as well as including the pairing correlations. However, the number of TDHFB applications is not so large. It is because huge computational costs are required in the TDHFB calculations. Hence, several methods have been proposed to solve the TDHFB equation, not in its full size but some approximate ways. The canonical-basis TDHFB (Cb-TDHFB) is one of such approximation methods [4] of solving the TDHFB equation. In this mini-review, we introduce the framework of the Cb-TDHFB, which is a feasible TD model dealing with nuclear pairing correlation, together with the results obtained by the Cb-TDHFB to demonstrate its possibilities.

## 2. TIME-DEPENDENT MEAN-FIELD MODELS

In order to obtain to the Cb-TDHFB equations, we will briefly follow the naive derivation of TD Hartree-Fock (TDHF) and TDHFB equations, from time-dependent many-body Schrödinger equation (1). When a time-dependent many-body wave function is written as $|\Phi(t)\rangle$, the time evolution of $|\Phi(t)\rangle$ which obeys the many-body Schrödinger equation, is given by,

$$|\Phi(t)\rangle = e^{-iHt/\hbar}|\Phi(0)\rangle. \tag{1}$$

Here the Hamiltonian $H$ is assumed as the sum of a kinetic and a two-body interaction terms for the Fermion system, which is described by a Fermion creation and annihilation operators ($c^\dagger$, $c$). The time-dependent density matrix $\rho(t)$ and pairing tensor $\kappa(t)$ are defined with the $|\Phi(t)\rangle$ as $\rho_{ij}(t) \equiv \langle\Phi(t)|c_j^\dagger c_i|\Phi(t)\rangle$ and $\kappa_{ij}(t) \equiv \langle\Phi(t)|c_j c_i|\Phi(t)\rangle$. The subscripts $i, j$ mean the label of the particle states. The equations to describe the time-dependence of $\rho(t)$ and $\kappa(t)$ are written as follows, using Equation (1):

$$\begin{aligned} i\hbar\frac{\partial}{\partial t}\rho_{ij}(t) &= \langle\Phi(t)|[c_j^\dagger c_i, H]|\Phi(t)\rangle, \\ i\hbar\frac{\partial}{\partial t}\kappa_{ij}(t) &= \langle\Phi(t)|[c_j c_i, H]|\Phi(t)\rangle. \end{aligned} \tag{2}$$

The TDHF (TDHFB) equation is derived by replacing $|\Phi(t)\rangle$ in the Equation (2) with the HF state $|\Phi_{\rm HF}(t)\rangle$ (the HFB state $|\Phi_{\rm HFB}(t)\rangle$), respectively. The $|\Phi_{\rm HF}(t)\rangle$ is written as a single Slater-determinant composed of single-particle states $\phi_l$. The number of the single-particle states in the HF state is usually the same as the particle number of the system. The $|\Phi_{\rm HFB}(t)\rangle$ is the vacuum of the quasi-particles whose creation and annihilation operators ($\beta^\dagger$, $\beta$) are composed of particle operators ($c^\dagger$, $c$) and the coefficient matrices $U$ and $V$; $\beta_k^\dagger \equiv \sum_\alpha U_{\alpha k}c_\alpha^\dagger + V_{\alpha k}c_k$. The matrices $U$ and $V$ are the general form of the BCS factors and are defined under the normalization and the unitary condition. The number of the quasi-particle basis is infinite in principle.

### 2.1. Cb-TDHFB Equation

There was an attempt to develop a time-dependent method that incorporates the nuclear pair correlation without directly solving the TDHFB equation [6]. Blocki and Flocard [6] proposed the equation of motion for the canonical basis $\phi_l$ and their BCS factors $u_l$ and $v_l$ with a simple effective interaction and a very schematic pairing functional. In Cusson et al. [7], Scamps et al. [8], and Magierski et al. [9], the equation of motion is called TDHF+BCS which is essentially equivalent to the Cb-TDHFB. The difference between their formulation and the Cb-TDHFB is in the derivation of the basic set of equations. The equations in Blocki and Flocard [6] were derived from the time-dependent variational principle with constraint terms for the norm conservation of particle wave functions and the number conservation. The constraint for the norm conservation finally induces the phase term in the equation of motion of the canonical basis, which is written as $\varepsilon_l$ in Blocki and Flocard [6]. The Cb-TDHFB equation is derived from the TDHFB equation with the canonical basis representation, in which the density matrix is diagonal. This is equivalent to replacing the HFB state by a state with the ordinary BCS form under an assumption for the functional form of the pair potential. In the Cb-TDHFB derivation, the phase term is naturally induced from the orthonormal property of the canonical basis. The phase term is essential to connect the canonical basis with pair probability $\kappa_l$ [4] and to keep the total energy conservation in the time evolution. The Cb-TDHFB equations are composed of three types of differential equations with respect to the time of the canonical basis, the occupation provability $\rho_l$ and the pair probability $\kappa_l$.

The BCS state can always be derived from the HFB state as a special solution, which is guaranteed by the Bloch-Messiah theorem. On the other hand, in the dynamical cases, the time dependence of the unitary transformation from HFB to BCS state is unclear on the way of time evolution. This leads to the fact that the canonical basis can not be guaranteed to keep their property in general. This is the most crucial key point in the formulation of the Cb-TDHFB derivation. The major factor that disturbs the canonical basis is the non-diagonal elements of pair potential $\Delta$. Therefore, the assumption is introduced in the formulation of the Cb-TDHFB that the pair potential should be of the diagonal form: $\Delta_{l\bar{k}} \equiv -\Delta_k\delta_{kl}$, which is equal to the ordinary BCS approximation.

The number of canonical basis in the Cb-TDHFB equation is about twice the particle number at most, although it depends on the nucleus and the energy cutoff for the pairing channel. On the other hand, the TDHFB needs an infinite number of quasi-particle orbitals in principle. This property that the number of dynamical variables in the Cb-TDHFB is much smaller is a significant advantage of the Cb-TDHFB compared with the other time-dependent method which deals with pairing correlation. Therefore, the computational costs of the Cb-TDHFB and the TDHF applications are comparable, and it is computationally feasible to employ the three-dimensional (3D) representation of the orbitals: e.g., $\phi_l(\boldsymbol{r}, t) = \langle\boldsymbol{r}|\phi_l(t)\rangle$.

Here, let us mention two major concerns for the particle "gas" problem and the continuity equation in the Cb-TDHFB application. The gas problem is famous in the BCS treatment for the finite nuclear system, which is reported in previous studies [10, 11]. The problem is caused by the expression of the many-body wave function in the BCS approximation, which is well-checked and summarized by a recent study in Anguiano et al. [12] from the practical point of view. The single-particle states with the positive energy near the Fermi surface cause the unphysical particle gas. Because the initial state of the Cb-TDHFB is also HF+BCS state, we should avoid the nuclei near the drip-line.

In Scamps et al. [8], the problem of the continuity equation in the Cb-TDHFB calculation is studied relating with the particle transport phenomena. The Cb-TDHFB satisfies the conservation laws for the orthonormality of the canonical states, the average particle number, and the average total energy. The local density of HF+BCS and Cb-TDHFB is given by sum of $|v_l(t)|^2|\phi_l(\boldsymbol{r}, t)|^2$ in which the coefficients depend on time only. The separable expression of the density and the lack of the spatial degree of freedom in the occupation probability cause the unphysical

density oscillation, which is the same reason as the particle gas problem and is unavoidable as long as the BCS expression is adopted. And the expression also causes the difficulty in describing the relative gauge angle between the superfluid nuclei in the collision reaction, which is well-explained in the supplemental material of Magierski et al. [9]. However, we know the source of the unphysical results, and we can find a method to address it. The frozen occupation approximation is suggested in Scamps et al. [8]. We should use the Cb-TDHFB as a feasible and beneficial tool while knowing the matters stated above.

## 2.2. Linear Response Calculation Using TD Mean-Field Model

There are many models to study nuclear excitation modes, such as the random phase approximation (RPA) or quasi-particle RPA (QRPA) formalism, which are the most used mean-field methods for nuclear excitation. The (Q)RPA formalism can be derived as the small-amplitude limit of the TDHF(B) method, which is the so-called linear response theory [3, 5]. The strength function calculated with the (Q)RPA can be reproduced by the TDHF(B) calculations of the small-amplitude oscillation.

The procedure to calculate the strength function is as follows [13–17]. (A) We prepare the initial states of the TD method and add a weak and instantaneous external field $V_{\rm ext}(t) = -\eta\hat{F}\delta(t)$ to them. The $\eta$ stands for a strength of the external filed, and $\hat{F}$ is an operator to excite the oscillations with a set of quantum numbers like multipolarity $L$, projection $K$, parity $\pi$, etc. The $\eta$ should be small to guarantee the linearity throughout the numerical iteration, since we consider the linear response. In practice, the size of the $\eta$ depends on the operator $\hat{F}$. (B) We calculate the time-evolution of $|\Phi(t)\rangle$ by using the time-dependent method and calculate the time-dependent expectation value of $\hat{F}$: $f(t) \equiv \langle\Phi(t)|\hat{F}|\Phi(t)\rangle$. After the calculation of $|\Phi(t)\rangle$, the strength function $S(E;\hat{F})$ can be obtained from the Fourier transformation of $f(t)$.

Here, it is to be noted that some operators $\hat{F}$ are related with the spurious mode of excitation. For instance, the operators isoscalar-compressional dipole and the quadrupole mode $Q_{21}$, induce the spurious modes of translational and rotational modes, respectively.

## 2.3. Collision Simulation by Means of TD Mean-Field Model

There have been many studies for the low-energy heavy-ion collisions by means of several types of TD mean-field models [18–25]. In the procedure to apply the TD mean-field models to the nuclear collision simulations, however, there is no essential difference among the models. The typical procedure for the collision simulation is as follows; (A) Set the wave functions of the target and the projectile to the positions with an impact parameter $b$, (B) Boost the wave functions with the incident energy $E_{\rm in}$, (C) Calculate the time-evolution of the wave functions which are within the common mean-field.

The $b$ and $E_{\rm in}$ are values when the relative distance between the two nuclei is infinite. Then, they must be changed due to the Coulomb field in the calculation space, which obeys the Rutherford's trajectory. This is realized by setting the initial wave functions at the positions where the interaction between projectile and target can be regarded as Coulomb force only. The frozen density approximation is well reasonable to indicate the initial positions. Indeed it is applied to the simple estimation of the Coulomb barrier [26–28]. When setting the wave functions for projectile and target to the initial positions, it is safe in practice to avoid the overlaps of them because the duplications cause complex interference in the phase of each other state.

# 3. APPLICATIONS

## 3.1. Electric Dipole Excitation in the Linear Response Theory

In this and the next subsection, we show examples of the linear response calculations using the Cb-TDHFB. Following the procedure described in section 2.2, we investigate the strength functions for the electric dipole ($E1$) excitation of ytterbium-172 ($^{172}$Yb, $Z$=70). $^{172}$Yb is an open-shell nucleus with the nuclear pairing correlation and has a prolate deformed shape in its ground state, which is calculated with SkM* Skyrme parameter set.

The characteristic structure of the quadrupole deformed nucleus appears in the shape of the $E1$ strength function of $^{172}$Yb in **Figure 1I**, in which two peaks corresponding to the $K$=0 and 1 modes appear. The photo-absorption cross-section of $^{172}$Yb can be deduced from the strength function. The experimental data [29, 30] were well-reproduced by the cross section.

Furthermore, the strength function can be compared with the HFB+QRPA results shown in Figure 7 of Terasaki and Engel [31]. The peak positions of the strength functions are almost the same, although the small difference in the shapes of the peaks appears in the width and height of $K = 0$ mode. The results illustrate that the Cb-TDHFB works well in dealing with the pairing correlation at the small-amplitude limit.

The Cb-TDHFB calculations can be performed in the 3D Cartesian coordinate space, with a single-core computer and several hundred hours. The HFB+QRPA calculations had been performed in axial symmetric space using the many-core parallel computer (about 10,000 cores), which could be estimated from the proposal [32]. If we restrict ourselves only to the strength functions, the Cb-TDHFB can significantly reduce the computational cost compared with the other TDHFB methods, which is one of the practical benefits of using the Cb-TDHFB. Taking advantage of the benefit of the Cb-TDHFB, we can carry out the systematic study of the linear responses of a large number of nuclei on the nuclear chart. Here we note that the finite amplitude method (FAM) is also an effective method to calculate the excitation energies [33–36] within the (Q)RPA theory.

## 3.2. Systematic Study of *E*1 Excitation Modes

We have performed a systematic investigation of the $E1$ strength functions using the Cb-TDHFB represented in the 3D Cartesian coordinate [37]. The purpose of the systematic study was to clarify the excitation mechanism of low-energy dipole (LED)

resonances, which have been called the pygmy dipole resonance (PDR). The PDR has been considered as the excited modes which is deeply connected with the characteristic structure of the neutron-rich nucleus [38, 39]. However, the systematic study showed that the PDR is not a unique excitation mode of the unstable nucleus, but can also be found in a stable nucleus, which suggests the PDR has a composite mechanism [37].

The comparison between the results of unstable heavy nuclei with and without a self-consistent residual interaction indicates that the PDR has the composite mechanism. The residual interaction can be excluded from the real-time calculation by using the single-particle Hamiltonian with the fixed density at the ground state. In the mechanism, there are the pure single-particle excitation mode and the decoupling modes from the giant dipole resonance. The decoupling modes might have a collective isoscalar character [37].

**Figure 1II** shows the neutron number dependence of the LED ratio $f_{\rm LED}$ of nickel, zirconium, and tin isotopes. The $f_{\rm LED}$ is defined as $m_1(E_{\rm low})/m_1$ where $m_1(E_{\rm low})$ is the energy weighted sum of the $E1$ strength function up to the energy $E_{\rm low}$=10 MeV, and $m_1$ is the value of the energy weighted sum rule of $E1$ mode. The panel shows the characteristic behavior of $f_{\rm LED}$ at

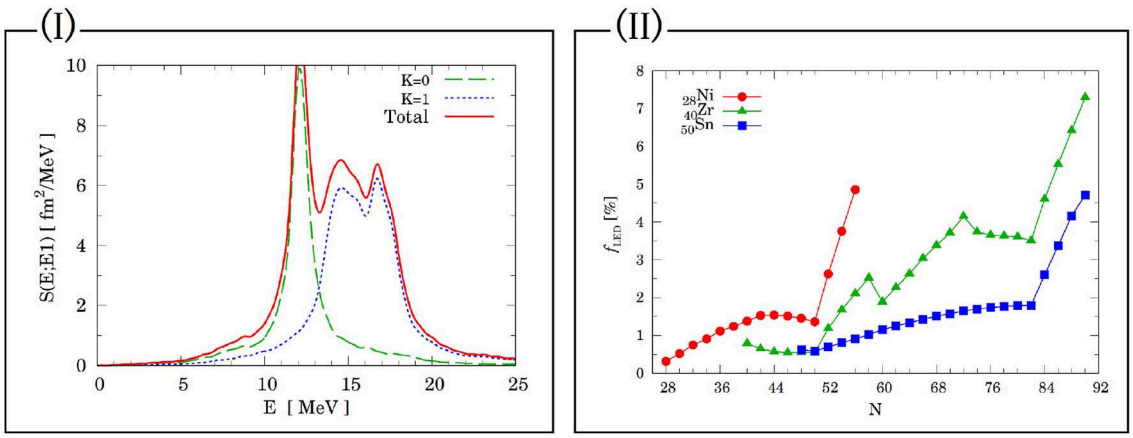


**FIGURE 1 |** Example for linear response calculations: **(I)** $E1$ strength function of $^{172}$Yb calculated by Cb-TDHFB with SkM$^*$, **(II)** Systematics of the LED ratio in the energy weighted sum rule for $E1$ of (circle) Ni, (triangle) Zr, and (square) Sn isotopes with respect to neutron number.

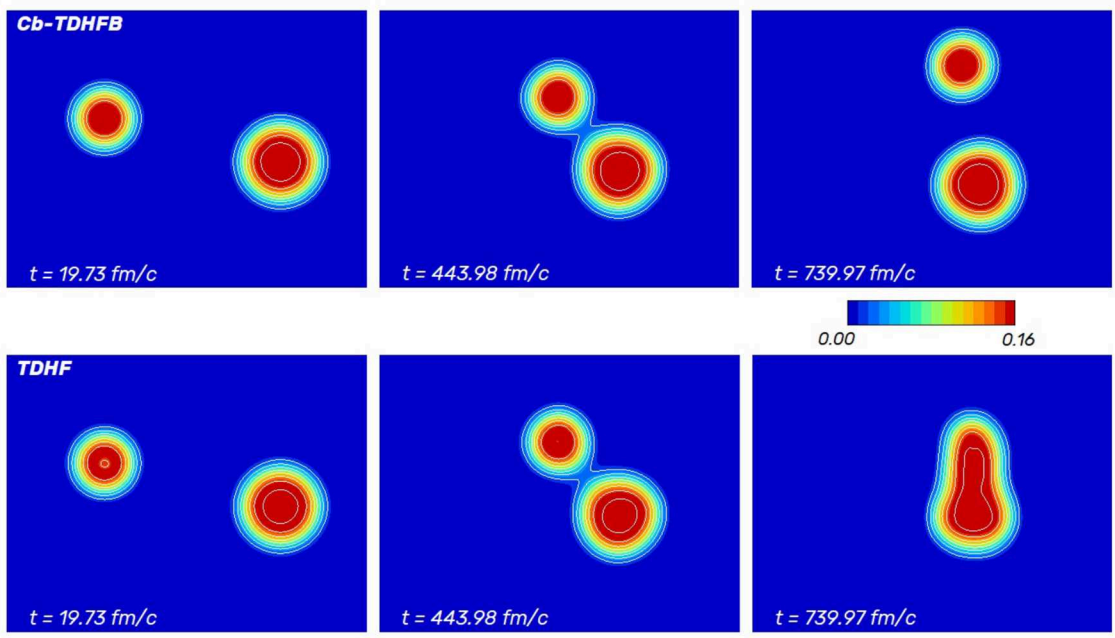


**FIGURE 2 |** Time-evolution of nucleon density for the $^{22}$O+$^{52}$Ca collision reactions which are calculated by **(Upper panels)** Cb-TDHFB and **(Lower panels)** TDHF. The calculations are performed with the parameters $b$=4.1 fm and $E_{\rm in}$=35.6 MeV.

the neutron numbers which correspond to the magic numbers ($N = 28, 50, 82$) of the spherical nuclei as well as those of the deformed nuclei ($N = 60 - 74$).

The systematic application of the Cb-TDHFB is carried out also for the quadrupole type excitations [40, 41], including modes with $K = 0, 1$, and 2. As mentioned in section 2.2, the quadrupole excitation with $K = 1$ induces the spurious mode. The authors in Scamps and Lacroix [41] employ an excellent practical method to avoid the spurious mode. The systematic study of the nuclear linear responses performed by using the TD method is significantly useful to prospect for understanding the nuclear structure of the broad range of nuclear mass number, although several techniques are necessary to extract physical quantities from the calculated data.

### 3.3. Fusion Reaction

The pairing effect on the large amplitude collective motion is one of the most exciting topics in nuclear physics. Many studies for nuclear collision and fission by using the mean-field models, including the pairing correlation, have been performed [7, 9, 42–50]. We performed the Cb-TDHFB and TDHF calculations for symmetric and asymmetric collisions; $^{22}$O+$^{22}$O, $^{52}$Ca+$^{52}$Ca, and $^{22}$O+$^{52}$Ca, in Ebata and Nakatsukasa [46]. In **Figure 2**, we show examples of the simulations of the fusion reactions. Upper and lower panels show the snapshots of the time-evolutions of nucleon densities calculated by Cb-TDHFB and TDHF, respectively.

The Cb-TDHFB results indicate the repulsive effects of pairing correlation in the fusion reaction. The nuclear pairing correlation attractively acts in the ground state basically, although the discussions of the pairing role for the anti-halo effect have not yet converged [51–53]. The strength dependence of pairing correlation is reported for the fission reaction using full TDHFB calculations [50]. The pairing correlation might not be wholly clarified yet in the static and the dynamic processes.

## 4. SUMMARY AND PERSPECTIVES

We have introduced the studies using Cb-TDHFB [4] and the points to note for its applications. The problems due to the BCS treatment are pointed out: the particle gas and the continuity equation. The linear response study for $E1$ excitation of $^{172}$Yb is simply explained, in which the comparisons between the strength functions obtained by HFB+QRPA and by Cb-TDHFB are mentioned, including the computational cost. The systematic studies with the strength function and the collision simulation for fusion reaction have also been shown to introduce the future possibilities of the Cb-TDHFB.

The TD mean-field study might be extended more and more in the future because there are large amounts of relevant regions that will be studied by using the TD mean-field model. The research for the large amplitude collective motion, such as fusion or fission, will especially increase, due to the continuous developments of nuclear theory and the numerical resource. The fusion and fission reactions are significantly important topics not only in nuclear physics but also in other fields: nuclear engineering, nuclear astrophysics.

Furthermore, the wave function in the TD mean-field model might be extended to the superposition of several wave functions such as the multi-Slater determinants, with the aim at expressing the stochastic phenomena [54–56]. There are upcoming trends of practical applications of the extended framework of mean-field among the recent researchers. At the same time, new effective interaction is demanded, just as the Skyrme interaction has been refined in the nuclear dynamics. Some new effective interactions have been suggested in Reinhard and Nazarewicz [57] and Bulgac et al. [58]. The feedback from many applications is necessary for the refinement and improvement of the effective interactions. The Cb-TDHFB application will be increasing to construct a next-generation mean-field model as one of the methods to treat nuclear pairing correlation.

## AUTHOR CONTRIBUTIONS

The author confirms being the sole contributor of this work and has approved it for publication.

## ACKNOWLEDGMENTS

I would like to express thanks to P. D. Stevenson, C. Simenel, D. Lacroix, L. Guo, and N. Schunk for giving an opportunity to write our works. This work was supported by Leading Initiative for Excellent Young Researchers, MEXT, Japan.

## REFERENCES

1. Bohr A, Mottelson BR, Pines D. Possible analogy between the excitation spectra of nuclei and those of the superconducting metallic state. *Phys Rev.* (1958) **110**:936–8. doi: 10.1103/PhysRev.110.936
2. Bardeen J, Cooper LN, Schrieffer JR. Theory of superconductivity. *Phys Rev.* (1957) **108**:1175–204. doi: 10.1103/PhysRev.108.1175
3. Jean-Paul B, Ripka G. *Quantum Theory of Finite Systems.* Cambridge: MIT Press (1986).
4. Ebata S, Nakatsukasa T, Inakura T, Yoshida K, Hashimoto Y, Yabana K. Canonical-basis time-dependent Hartree-Fock-Bogoliubov theory and linear-response calculations. *Phys Rev C.* (2010) **82**:034306. doi: 10.1103/PhysRevC.82.034306
5. Ring P, Schuck P. *The Nuclear Many-Body Problems.* Berlin; Heidelberg: Springer Verlag (1980).
6. Blocki J, Flocard H. Simple dynamical models including pairing residual interaction. *Nuclear Phys A.* (1976) **273**:45–60.
7. Cusson RY, Maruhn JA, Stocker H. Collision of $^{238}$U+$^{238}$U using a three-dimensional TDHF − BCS model. *Z Phys A Atoms Nuclei.* (1980) **294**:257–60. doi: 10.1007/BF01438163
8. Scamps G, Lacroix D, Bertsch GF, Washiyama K. Pairing dynamics in particle transport. *Phys Rev C.* (2012) **85**:034328. doi: 10.1103/PhysRevC.85.034328
9. Magierski P, Sekizawa K, Wlazłowski G. Novel role of superfluidity in low-energy nuclear reactions. *Phys Rev Lett.* (2017) **119**:042501. doi: 10.1103/PhysRevLett.119.042501
10. Dobaczewski J, Flocard H, Treiner J. Hartree-Fock-Bogolyubov description of nuclei near the neutron-drip line. *Nucl Phys A.* (1984) **422**:103–39.

11. Dobaczewski J, Nazarewicz W, Werner TR, Berger JF, Chinn CR, Dechargé J. Mean-field description of ground-state properties of drip-line nuclei: pairing and continuum effects. *Phys Rev C.* (1996) **53**:2809–40. doi: 10.1103/PhysRevC.53.2809
12. Anguiano M, Lallena AM, Bernard R, Co' G. Neutron gas and pairing. *Phys Rev C.* (2019) **99**:034302. doi: 10.1103/PhysRevC.99.034302
13. Chinn CR, Umar AS, Vallieres M, Strayer MR. Mean field studies of exotic nuclei. *Phys Rep.* (1996) **264**:107–21.
14. Nakatsukasa T, Yabana K. 3D real-space calculation of the continuum response. *Prog Theor Phys Suppl.* (2002) **146**:447–51. doi: 10.1143/PTPS.146.447
15. Simenel C, Chomaz P. Nonlinear vibrations in nuclei. *Phys Rev C.* (2003) **68**:024302. doi: 10.1103/PhysRevC.68.024302
16. Nakatsukasa T, Yabana K. Linear response theory in the continuum for deformed nuclei: green's function vs time-dependent Hartree-Fock with the absorbing boundary condition. *Phys Rev C.* (2005) **71**:024301. doi: 10.1103/PhysRevC.71.024301
17. Maruhn JA, Reinhard PG, Stevenson PD, Stone JR, Strayer MR. Dipole giant resonances in deformed heavy nuclei. *Phys Rev C.* (2005) **71**:064328. doi: 10.1103/PhysRevC.71.064328
18. Bonche P, Koonin S, Negele JW. One-dimensional nuclear dynamics in the time-dependent Hartree-Fock approximation. *Phys Rev C.* (1976) **13**:1226–58. doi: 10.1103/PhysRevC.13.1226
19. Koonin SE, Davies KTR, Maruhn-Rezwani V, Feldmeier H, Krieger SJ, Negele JW. Time-dependent Hartree-Fock calculations for $^{16}$O + $^{16}$O and $^{40}$Ca + $^{40}$Ca reactions. *Phys Rev C.* (1977) **15**:1359–74. doi: 10.1103/PhysRevC.15.1359
20. Davies KTR, Feldmeier HT, Flocard H, Weiss MS. Comparisons of two- and three-dimensional time-dependent Hartree-Fock calculations of the reactions $^{16}$O + $^{16}$O and $^{40}$Ca + $^{40}$Ca. *Phys Rev C.* (1978) **18**:2631–40. doi: 10.1103/PhysRevC.18.2631
21. Davies KTR, Koonin SE. Skyrme-force time-dependent Hartree-Fock calculations with axial symmetry. *Phys Rev C.* (1981) **23**:2042–61. doi: 10.1103/PhysRevC.23.2042
22. Negele JW. The mean-field theory of nuclear structure and dynamics. *Rev Mod Phys.* (1982) **54**:913–1015. doi: 10.1103/RevModPhys.54.913
23. Kim KH, Otsuka T, Bonche P. Three-dimensional TDHF calculations for reactions of unstable nuclei. *J Phys G Nucl Part Phys.* (1997) **23**:1267–73. doi: 10.1088/0954-3899/23/10/014
24. Umar AS, Oberacker VE. Three-dimensional unrestricted time-dependent Hartree-Fock fusion calculations using the full Skyrme interaction. *Phys Rev C.* (2006) **73**:054607. doi: 10.1103/PhysRevC.73.054607
25. Maruhn JA, Reinhard PG, Stevenson PD, Umar AS. The TDHF code Sky3D. *Comput Phys Commun.* (2014) **185**:2195–216. doi: 10.1016/j.cpc.2014.04.008
26. Denisov VY, Norenberg W. Entrance channel potentials in the synthesis of the heaviest nuclei. *Eur Phys J A.* (2002) **15**:375–88. doi: 10.1140/epja/i2002-10039-3
27. Washiyama K, Lacroix D. Energy dependence of the nucleus-nucleus potential close to the Coulomb barrier. *Phys Rev C.* (2008) **78**:024610. doi: 10.1103/PhysRevC.78.024610
28. Washiyama K. Microscopic analysis of fusion hindrance in heavy nuclear systems. *Phys Rev C.* (2015) **91**:064607. doi: 10.1103/PhysRevC.91.064607
29. Goryachev AM, Zalesnyy GN. Photoneutron cross sections for Yb-170,171,172,173,174, and 176 in the region of giant resonance. *Voprosy Teoreticheskoy i Yadernoy Fiziki* (1976) **1976**:42.
30. Ebata S, Nakatsukasa T, Inakura T, Yoshida K, Hashimoto Y, Yabana K. *Cb-TDHFB Calculations for Isovector Dipole Mode of Heavy Nucleus.* RIKEN Accelerator Progress Report (2010). Available online at: http://www.nishina.riken.jp/researcher/APR/Document/ProgressReport_vol_44.pdf (accessed September 30, 2011).
31. Terasaki J, Engel J. Self-consistent Skyrme quasiparticle random-phase approximation for use in axially symmetric nuclei of arbitrary mass. *Phys Rev C.* (2010) **82**:034326. doi: 10.1103/PhysRevC.82.034326
32. Engel J, Terasaki J. *Systematics of Nuclear Surface Vibrations in Deformed Nuclei.* Available online at: http://unedf.mps.ohio-state.edu/content/projects/engel_qra_teragrid_proposal.pdf (accessed Jun 18, 2010).
33. Nakatsukasa T, Inakura T, Yabana K. Finite amplitude method for the solution of the random-phase approximation. *Phys Rev C.* (2007) **76**:024318. doi: 10.1103/PhysRevC.76.024318
34. Inakura T, Nakatsukasa T, Yabana K. Self-consistent calculation of nuclear photoabsorption cross sections: finite amplitude method with Skyrme functionals in the three-dimensional real space. *Phys Rev C.* (2009) **80**:044301. doi: 10.1103/PhysRevC.80.044301
35. Avogadro P, Nakatsukasa T. Finite amplitude method for the quasiparticle random-phase approximation. *Phys Rev C.* (2011) **84**:014314. doi: 10.1103/PhysRevC.84.014314
36. Washiyama K, Nakatsukasa T. Multipole modes of excitation in triaxially deformed superfluid nuclei. *Phys Rev C.* (2017) **96**:041304. doi: 10.1103/PhysRevC.96.041304
37. Ebata S, Nakatsukasa T, Inakura T. Systematic investigation of low-lying dipole modes using the canonical-basis time-dependent Hartree-Fock-Bogoliubov theory. *Phys Rev C.* (2014) **90**:024303. doi: 10.1103/PhysRevC.90.024303
38. Suzuki Y, Ikeda K, Sato H. New type of dipole vibration in nuclei. *Prog Theor Phys.* (1990) **83**:180–4. doi: 10.1143/PTP.83.180
39. Van Isacker P, Nagarajan MA, Warner DD. Effect of the neutron skin on collective states of nuclei. *Phys Rev C.* (1992) **45**:R13–6. doi: 10.1103/PhysRevC.45.R13
40. Scamps G, Lacroix D. Systematics of isovector and isoscalar giant quadrupole resonances in normal and superfluid spherical nuclei. *Phys Rev C.* (2013) **88**:044310. doi: 10.1103/PhysRevC.88.044310
41. Scamps G, Lacroix D. Systematic study of isovector and isoscalar giant quadrupole resonances in normal and superfluid deformed nuclei. *Phys Rev C.* (2014) **89**:034314. doi: 10.1103/PhysRevC.89.034314
42. Cusson RY, Meldner HW. Time-dependent Hartree-Fock-Bogoliubov calculations of heavy-element fusion and fission phenomena. *Phys Rev Lett.* (1979) **42**:694–6. doi: 10.1103/PhysRevLett.42.694
43. Mirea M. Time-dependent pairing equations for seniority-one nuclear systems. *Phys Rev C.* (2008) **78**:044618. doi: 10.1103/PhysRevC.78.044618
44. Mirea M. Energy partition in low energy fission. *Phys Rev C.* (2011) **83**:054608. doi: 10.1103/PhysRevC.83.054608
45. Ebata S. Simulation of heavy ion collision using a time-dependent density functional theory including nuclear superfluidity. *J Phys.* (2013) **454**:012054. doi: 10.1088/1742-6596/454/1/012054
46. Ebata S, Nakatsukasa T. Repulsive aspects of pairing correlation in nuclear fusion reaction. *J Phys Soc Jpn.* (2015) **6**:020056. doi: 10.7566/JPSCP.6.020056
47. Bulgac A, Magierski P, Roche KJ, Stetcu I. Induced fission of $^{240}$Pu within a real-time microscopic framework. *Phys Rev Lett.* (2016) **116**:122504. doi: 10.1103/PhysRevLett.116.122504
48. Hashimoto Y, Scamps G. Gauge angle dependence in time-dependent Hartree-Fock-Bogoliubov calculations of $^{20}$O +$^{20}$ O head-on collisions with the Gogny interaction. *Phys Rev C.* (2016) **94**:014610. doi: 10.1103/PhysRevC.94.014610
49. Scamps G, Simenel C. Impact of pear-shaped fission fragments on mass-asymmetric fission in actinides. *Nature.* (2018) **564**:382–5. doi: 10.1038/s41586-018-0780-0
50. Bulgac A, Jin S, Roche KJ, Schunck N, Stetcu I. Fission dynamics of $^{240}$Pu from saddle to scission and beyond. *Phys Rev C.* (2019) **100**:034615. doi: 10.1103/PhysRevC.100.034615
51. Bennaceur K, Dobaczewski J, Poszajczak M. Pairing anti-halo effect. *Phys Lett B.* (2000) **496**:154–60. doi: 10.1016/S0370-2693(00)01292-2
52. Zhang Y, Chen Y, Meng J, Ring P. Influence of pairing correlations on the radius of neutron-rich nuclei. *Phys Rev C.* (2017) **95**:014316. doi: 10.1103/PhysRevC.95.014316
53. Hagino K, Sagawa H. New concept for the pairing anti-halo effect as a localized wave packet of quasiparticles. *Phys Rev C.* (2017) **95**:024304. doi: 10.1103/PhysRevC.95.024304
54. Lacroix D, Ayik S. Stochastic quantum dynamics beyond mean field. *Eur Phys J A.* (2014) **50**:95. doi: 10.1140/epja/i2014-14095-8
55. Tanimura Y, Lacroix D, Ayik S. Microscopic phase-space exploration modeling of $^{258}$Fm Spontaneous Fission. *Phys Rev Lett.* (2017) **118**:152501. doi: 10.1103/PhysRevLett.118.152501

56. Simenel C, Umar AS. Heavy-ion collisions and fission dynamics with the time-dependent Hartree-Fock theory and its extensions. *Prog Part Nucl Phys*. (2018) **103**:19–66. doi: 10.1016/j.ppnp.2018.07.002
57. Reinhard PG, Nazarewicz W. Toward a global description of nuclear charge radii: exploring the Fayans energy density functional. *Phys Rev C.* (2017) **95**:064328. doi: 10.1103/PhysRevC.95.064328
58. Bulgac A, Forbes MM, Jin S, Perez RN, Schunck N. Minimal nuclear energy density functional. *Phys Rev C.* (2018) **97**:044313. doi: 10.1103/PhysRevC.97.044313

**Conflict of Interest:** The author declares that the research was conducted in the absence of any commercial or financial relationships that could be construed as a potential conflict of interest.

frontiers in Physics

ORIGINAL RESEARCH
published: 30 June 2020
doi: 10.3389/fphy.2020.00154

# Solitons in Nuclear Time-Dependent Density Functional Theory

*Yoritaka Iwata**

*Faculty of Chemistry, Materials and Bioengineering, Kansai University, Osaka, Japan*

The soliton existence in sub-atomic many-nucleon systems will be discussed. In many nucleon dynamics represented by the nuclear time-dependent density functional formalism, much attention is paid to energy and mass dependence of the soliton existence. In conclusion, the existence of nuclear soliton is clarified if the temperature of nuclear system ranges from 10 to 30 MeV. With respect to the mass dependence $^{4}$He and $^{16}$O are suggested to be the candidates for the self-bound states exhibiting the property of nuclear soliton.

**Keywords: TDDFT, multi-dimensional solition, full skyrme interaction, many-nucleon system, ion collisions**

## 1. INTRODUCTION

The concept of nuclear soliton is proposed by its existence in the three-dimensional nuclear time-dependent density functional formalism. The solitons in this article are the waves stably traveling without changing shape and velocity even after collisions between waves (**Figure 1**). In this sense, as for the terminologies of classical and quantum field theory, what we study in this article is not similar to the topological soliton [1, 2], but rather corresponds to the non-topological soliton [3]. From here on, we refer simply to "soliton" for a kind of non-topological soliton. The mathematically common property of a soliton (for example, see Ablowitz [4]) has been clarified as

- Non-linearity
- Dispersive property

being independent of the size and medium of wave. The common properties of solitons are essential to the solitons existence, and several uncommon properties specific to nuclear solitons such as

- Quantum effect with the fermi statistics
- Many-body effect leading to the collectivity

can modify the conditions of soliton existence, where a competition between them possibly appears. In most soliton research mentioned here, the size and model dependent additional properties are not seriously considered. Here we employ the nuclear time-dependent density functional theory (TDDFT) in which all the above four properties are included in a self-consistent manner. In particular the collectivity of many-nucleon systems has been successfully treated by the nuclear DFT with and without time-dependence (for example, see Greiner and Maruhn [5]).

The solitons are observed in any scale, if the mathematically common property is held by the master equation. This fact has something to do with the size and model dependence of the two common properties. The nuclear soliton is found in sub-atomic femto-meter scales whose energy is at the order of MeV (mega electron volt). Such a specific scale arises from the effective unit of motion: the nucleon degree of freedom in the case of a nuclear soliton. For example, the effective unit of motion for the optical soliton is the photon. In other words, as is known in nuclear physics, the motion of the nucleus at the energy order of MeV is governed by the independent nucleon motion (for example, see Ring and Schuck [6]).

OPEN ACCESS

***Edited by:***
*Lu Guo,*
*University of Chinese Academy of Sciences, China*

***Reviewed by:***
*Giuseppe Verde,*
*National Institute for Nuclear Physics, Italy*
*Nikolai Antonenko,*
*Joint Institute for Nuclear Research (JINR), Russia*

***Correspondence:**
*Yoritaka Iwata*
*iwata_phys@08.alumni.u-tokyo.ac.jp*

***Specialty section:***
*This article was submitted to Nuclear Physics, a section of the journal Frontiers in Physics*

***Received:*** *04 February 2020*
***Accepted:*** *15 April 2020*
***Published:*** *30 June 2020*

***Citation:***
*Iwata Y (2020) Solitons in Nuclear Time-Dependent Density Functional Theory. Front. Phys. 8:154. doi: 10.3389/fphy.2020.00154*

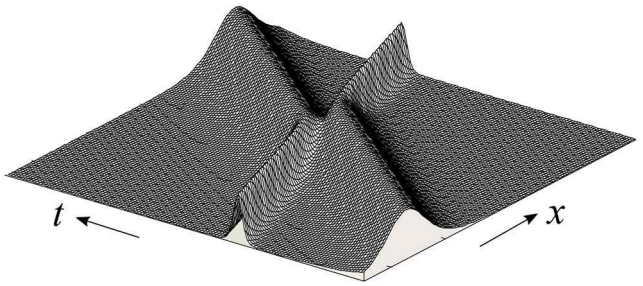


**FIGURE 1 |** Two soliton solution of KdV equation ($\alpha = 1$). Although the momentum and shape are exactly conserved, time delay appears due to the collision (around $(t, x) = (0, 0)$).

The soliton is a wave with both individuality and stability. On the other hand, the nuclear soliton is also regarded as bringing about a nuclear matter state with perfect fluidity. It is worth mentioning here that perfect fluidity can be rephrased as inertness in the context of reaction theory. Accordingly, the nuclear soliton is expected to be associated with some important physics if its existence is established. Indeed, perfect fluidity leads to the conservation of the number of vortexes. Since celestial bodies consist of nuclear matter, the quantitative understandings of the nuclear soliton are able to show a new aspect of the matter/heat transportation inside the (compact) stars. Furthermore, perfect fluidity is associated with the dissipation property of low-energy heavy-ion collisions that has been a long standing open problem in microscopic nuclear reaction theory. Perfect fluidity is also associated with the conservation of nuclear matter without the loss of any information: i.e., isentropic property arising from the time-reversal symmetry [7]. As the conservation property of the soliton has already been utilized in the optical fiber, the preservation property of nuclear matter is expected to be utilized in the nuclear engineering for preserving and condensing a certain projectile nucleus. In particular, the well-preserved nuclear matter is expected to be used for the reduction of nuclear waste by the nuclear transmutation, with the extremely high intensity/density projectile of reactions, which is not only to make a high intensity/density beam but also high projectile-density matter in the nuclear reactor.

This article is organized as follows. The basic concepts of wave propagation are introduced in section 2. The general definition of solitary wave and soliton is shown in section 3. The existence of nuclear soliton is discussed in section 4. The summary and perspectives are presented in section 5.

## 2. EQUATION OF WAVES

This section is devoted to introducing the basic concepts for wave propagation, which provides a working area of the soliton research. For the purpose of introducing the concept of dispersive property, we begin with the linear wave:

$$u(t, x) = A \exp(i(kx - \omega t + \alpha)), \tag{1}$$

in one-dimensional space, where $k$ means the wave number, $\omega$ the angular frequency, and $\alpha$ the phase. This wave is also referred to as the plane wave in the multi-dimensional case, and to a traveling wave in more general fields. The first order linear hyperbolic equation (advection equation) is written by

$$\partial_t u + c\partial_x u = 0 \tag{2}$$

in one-dimensional space $\mathbb{R}$, where $c$ is a real constant, meaning the propagation speed. It is well-known that this equation holds the solution represented by the d'Alembert's formula, so that the plane wave (1) satisfies this equation. The linear dispersion relation $\omega = ck$ is satisfied by the plane wave solution. The plane wave solution can also be associated with the second order linear wave equations, more closely to the present interest, the Klein-Gordon equation:

$$\partial_t^2 u - c^2 \partial_x^2 u + \left(\frac{mc^2}{\hbar}\right)^2 u = 0 \tag{3}$$

describing a quantum scalar or pseudoscalar fields [8]. By considering the same plane wave solution, another relation $\omega^2 = c^2(k^2 + m^2c^2/\hbar^2)$ is obtained, which is asymptotically equal to $\omega = \pm ck$ (**Figure 2**). Note that the dispersion relation in the massless case ($m = 0$) also becomes $\omega = \pm ck$.

The Schrödinger equation is known to describe the non-relativistic quantum physics. The linear dispersion relation $\omega = ck$ is violated in case of Schrödinger type waves. On the other hand, it is readily confirmed that the plane-wave solution is also the solution of the linear Schrödinger equation:

$$i\partial_t u + c\partial_x^2 u = 0 \tag{4}$$

in one-dimensional space $\mathbb{R}$, where $c$ is a real constant being represented by $c = -\hbar/2m$ using the Dirac constant $\hbar$ and the mass $m$. In this case another dispersion relation $\omega = ck^2$ is satisfied instead. Such waves, without satisfying the linear dispersion relation $\omega = ck$, are called the dispersive wave. It is worth noting here that the non-relativistic approximation of Klein-Gordon equation corresponds to the Schrödinger equation. As a result, the Schrödinger equation is a typical example of dispersive wave equations.

## 3. NON-LINEAR DISPERSIVE WAVES

### 3.1. Korteweg-de Vries Equation

The concepts of solitary wave and soliton are introduced. For verifying the soliton existence in sub-atomic quantum equations, we focus on two relevant equations: the Korteweg-de Vries equation and non-linear Schrödinger equation. These equations are not only dispersive wave equations but also non-linear evolution equations.

First, in the flow of shallow water, the concept of a solitary wave was introduced by Scott-Russel [9] in 1844. Indeed, they observe that

- A single wave moves stably on the flat surface without changing the shape and velocity.

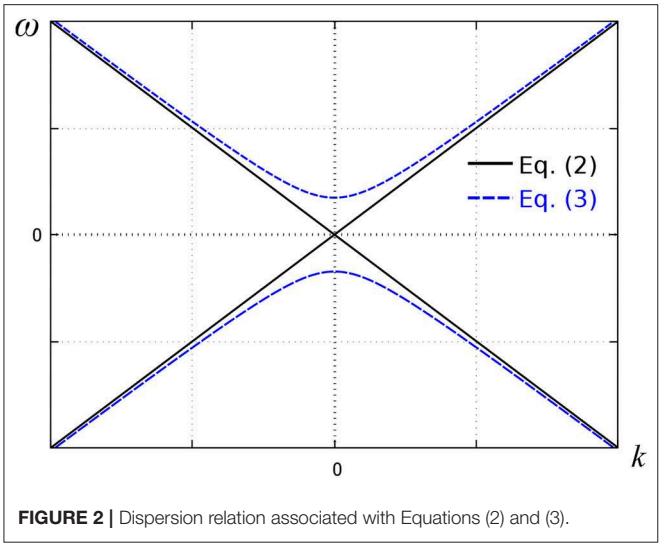


**FIGURE 2 |** Dispersion relation associated with Equations (2) and (3).

This is the essential property of the solitary wave. Here the single wave means the wave without undergoing any collisions with the other waves. Although such a property is common in linear cases, this should not be true in non-linear cases. If solitary waves preserve their shape and speed after a collision, the solitary waves holding a transparency is called the soliton. In particular, the terminology "soliton" is introduced by Zabusky and Kruskal [10]. Indeed, for the initially given sine waves, they are split into several solitary waves, and

- The Solitary wave moves stably by preserving momentum and shape even after the collisions.
- The Solitary wave possibly experiences a phase shift and time delay during the collision.

These are the properties to be satisfied by the soliton wave. That is, the solitary wave is called soliton if it satisfies the above properties. The transparency leading to the individuality is often called the particle-like property in the soliton theory. In particular, by comparing soliton waves before and after collision, there are no changes in the momentum and shape, but there is for the phase.

The equations holding the soliton as a solution are called the soliton equation, and the Korteweg-de-Vries equation (KdV equation, for short) is known as a soliton equation. In a mathematical sense the concept of a solitary wave was initially studied by the KdV equation [11]

$$\partial_t u + \alpha u \partial_x u + \partial_x^3 u = 0, \quad x \in \mathbb{R}, \tag{5}$$

where $\alpha$ is a real constant. In the second term $\alpha u$ plays a role of propagation speed (cf. Equation 2), so that the propagation speed depends on the state of the wave. This non-linear equation models the shallow water waves including both the non-linearity and the dispersive property, but not the dissipation leading to the non-unitary time evolution. It is worth noting here that the KdV equation is obtained by approximating the incompressible Navier-Stokes equation (for example, see Lamb [12]).

The plane wave (1) can be the solution at small amplitude oscillation limit, and then $\omega = ck - k^3$ is approximately satisfied. On the other hand, KdV equation admits some exact traveling wave solutions:

$$u = \frac{3c}{\alpha}\mathrm{sech}^2\left[\frac{\sqrt{c}}{2}(x - ct)\right] \tag{6}$$

where $c$ means the speed of wave propagation. It is remarkable that Equation (6) holds the form of d'Alembert's solution for the wave equation. This solution corresponds to the solitary wave solution (one-soliton solution) whose amplitude depends on the propagation speed $c$. The solitary wave solution can hold the soliton property that has been examined by obtaining the exact two-soliton solution (**Figure 1**).

$$u = \frac{72}{\alpha}\frac{3 + 4\cosh(2x - 8t) + \cosh(4x - 64t)}{\{3\cosh(x - 28t) + \cosh(3x - 36t)\}^2} \tag{7}$$

asymptotically equal to the superposition of two solitons for large $t$

$$u = \frac{12\kappa_i}{\alpha}\mathrm{sech}^2\left[\kappa_i(x - 4\kappa_i^2 t) + \delta_i\right], \tag{8}$$

where $i = 1, 2, \kappa_1 = 1, \kappa_2 = 2$, and $\delta_i$ are constants. The existence of the two-soliton solution ensures the existence of soliton in a given theoretical framework. In several equations the two-soliton solutions are extended to $N$-soliton solutions (for example, see Scott et al. [13]).

## 3.2. Non-linear Schrödinger Equation

A typical soliton equation for non-relativistic quantum dynamics is the non-linear Schrödinger equation (NLS equation, for short). It reads

$$i\partial_t u + \partial_x^2 u + k|u|^2 u = 0, \tag{9}$$

where a real number $k$ means the interaction constant, and also the height/depth of potential hill/well. Indeed, in the case of positive $k$, $V(u) = -k|u|^2$ provides a potential well. Indeed, it holds a solution

$$u(t,x) = \sqrt{\frac{u_e^2 - 2u_e u_c}{2k}}\,\mathrm{sech}\left[\sqrt{\frac{u_e^2 - 2u_e u_c}{4}}(x - u_c t)\right] \exp\left[i(u_0/2)(x - u_c t)\right],$$

where the amplitude of $u$ depends on the constant $k$, which is a specific feature arising from the angular speed $u_c$ and the wave propagation speed $u_e$. Contrary to the previous KdV equation, the amplitude is proportional to $k^{-1/2}$ and $u_e$. Consequently, the two factors have been considered to be essential to the soliton propagation: the dispersive property and the non-linearity.

## 3.3. Sturm-Liouville Formalism

Following Lax [14], the relation between the KdV and the Schrödinger type equations are understood by a simplified Sturm Liouville equation:

$$Ly := \partial_x^2 y - U(x,t)y = \lambda y, \tag{10}$$

where the periodic boundary condition is imposed, for instance. This equation can be regarded as the Schrödinger equation with the potential $-\lambda + U(x,t)$. It is readily seen that

$$\partial_t(Ly) = (\partial_t L)y + L(\partial_t y) = (\partial_t\lambda)y + \lambda(\partial_t y) = -(\partial_t U(x,t))y + (\partial_x^2 - U(x,t))(\partial_t y) \tag{11}$$

leads to

$$(\partial_t L)y = -(\partial_t U(x,t))y. \tag{12}$$

If $t$-independence of parameter $\lambda$: $\partial_t\lambda = 0$ is further assumed,

$$\begin{aligned}(\partial_t\lambda)y &= -(\partial_t U(x,t))y + L(\partial_t y) - (\partial_t\lambda y)\\ &= -(\partial_t U(x,t))y + L(\partial_t y) - (\partial_t L y)\\ &= -(\partial_t U(x,t))y + [L,\partial_t]y\end{aligned} \tag{13}$$

is obtained, where $[\cdot,\cdot]$ denotes the commutator product. After generalizing this equation as

$$(\partial_t\lambda)y = -(\partial_t U(x,t))y + [L,D]y, \tag{14}$$

the KdV equation with the potential $U$ and $\alpha = -6$ is obtained by $-(\partial_t U(x,t)) + [L,D] = 0$ with $D = f\partial_x^3 + g\partial_x + h$, $g = -3Uf/2$ and $h = -3(\partial_x u)f/4$. Consequently, KdV and Schrödinger equations are associated not only with having a soliton solution, but with holding a common mathematical structure. An interesting reminder here is the relation between Schrödinger, Heisenberg, and interaction pictures in quantum field theory (for a textbook, see Fetter and Warecka [15]).

# 4. SOLITONS IN NUCLEAR TDDFT

## 4.1. Many-Nucleon System

Atomic nucleus is a finite-body many-nucleon system consisting of nucleons: protons and neutrons. Proton numbers range from 1 to 120 (at the present), and neutron numbers from 1, roughly, to 200. It is thought that almost 300 stable nuclei exist in nature, and the theoretical calculations such as nuclear density functional calculations simulate those nuclei as being sufficiently comparable to the experiments.

We are interested in the soliton propagation at the scale of atomic nuclei. The size of one nucleus ranges from $10^{-15}$ to $10^{-13}$ m, and the corresponding energy is below several 10s of MeV per nucleon. One of the unique features of the many-nucleon system is found in their finite-body property, which is quite different from most of many-electron systems being treated as infinite matter. This feature brings about the fact that the self-bound state (the localized wave) is naturally realized in both nature and theory of many-nucleon systems. Following the general usage of low-energy nuclear physics, the terminology "low-energy" is used for energy below 30 MeV per nucleon. The relativistic effect plays a considerable role, only if the relative velocity of the collision is over 30% of the speed of light, and it roughly corresponds to the collision energy 30 MeV per nucleon.

Ground states and some excited states of stable nuclei (in the following, self-bound nuclei) are classified to the localized self-bound system. Each self-bound system is the solitary wave in the soliton theory because it is satisfied that

- A self-bound nucleus moves stably without changing the shape

if there is no collision with the other nuclei/particles. Therefore, the existence of a solitary wave is trivially true for many-nucleon systems, where this issue should be examined by the non-linear framework with the ultimately determined density functional. In other words, all the self-bound nuclei are candidates of soliton. All we have to do to verify the soliton existence is to check that

- [Conditional] a nucleus moves stably by preserving momentum and shape even after the collisions.
- The nucleus possibly experiences the phase shift and the time delay.

The first condition is expected to be satisfied conditionally. On the other hand, the second condition is trivially satisfied in case of atomic nuclei, as phase shifts have been observed and theoretically calculated in nuclear reactions, as well as the time delay. One of the general motivations is to find a valid condition for the existence of the nuclear soliton.

## 4.2. Theoretical Framework

Among several theoretical models in nuclear physics, nuclear time-dependent density functional theory [16, 17] (TDDFT, for short), which describes the nuclear collision dynamics with the nucleon degree of freedom, is a unique theory including time dependence, non-linearity, and the dispersive property simultaneously. The solution of the TDDFT shows the unitary time evolution, which is preferable because of exact conservation of the total energy. The dispersive property is satisfied by the non-relativistic theory, while it is violated in the massless relativistic theories. In this context, we remind that the sine-Gordon equation is known as a soliton equation. Furthermore, it is worth noting here that, among sub-atomic theories except for the TDDFT, it is not easy to find a calculationally-feasible theoretical framework including the time-dependence. Note that the TDDFT is also called nuclear time-dependent Hartree-Fock theory, and nuclear reaction is often referred to as heavy-ion collision or ion collision. The theory with nucleon degree of freedom is called the microscopic treatment, because a nucleus is a smaller component that builds up a nucleus. The TDDFT is usually calculated in three-dimensional space, and the TDDFT have many stable localized stationary solutions corresponding to the self-bound nuclei. Non-linearity, dispersive property, and the unitary time-dependence realized in the TDDFT are preferable for examining the soliton existence. Furthermore, nuclear saturation property brings about rather universal shallow potential well with a depth of 50 MeV at the deepest, whose environmental setting is ideal for the existence of certain kinds of shallow water waves.

Before moving on to the nuclear theoretical models, a few remarks are made on the multi-dimensional treatment. There is limited knowledge on the multi-dimensional soliton, where

the shape of colliding waves plays more roles. In the multi-dimensional case, the soliton existence depends on whether the waves are spatially finite or not, and whether the waves are spherical or deformed. As a multi-dimensional version of KdV equation, Kadomtsev-Petviashvili equation (KP equation, for short) is known. In particular the multi-dimensional version of NLS equation (2) cannot have the self-bound solution, while the multi-dimensional NLS type equation

$$\begin{aligned} &i\partial_t u + \partial_x^2 u + \partial_y^2 u + k|u|^2 u = u\partial_x v, \\ &\partial_x^2 v - \partial_y^2 v = -2\partial_x(|u|^2) \end{aligned} \tag{15}$$

is known to have the soliton (or dromion) solution instead [18–20], where $v$ means the velocity potential. Roughly speaking, the addition of a non-linear term contributes to keeping the soliton property in this case.

#### 4.2.1. One-Dimensional Soliton Model

Let us begin with reviewing the preceding work on soliton propagation in nuclear physics. In one-dimensional space, the Hamiltonian of $N$ bosons interacting through a $\delta$-force is represented by

$$H = -\frac{1}{2}\sum_{i=1}^{N}\partial_{x_i}^2 - \nu\sum_{i<j=1}^{N}\delta(x_i - x_j). \tag{16}$$

The corresponding stationary and non-stationary problems are known to be exactly solvable for bound states and for scattering states [21–26]. Application of the variational principle to

$$\begin{aligned} < \Psi|\partial_t\ -H|\Psi > = N\int dx\Big( &\psi^* i\partial_t\psi + \tfrac{1}{2}\psi^*\partial_x^2\psi \\ &+\tfrac{\nu}{2}(N-1)\psi^*\psi^*\psi\psi\Big) \end{aligned} \tag{17}$$

leads to

$$i\partial_t\psi + \tfrac{1}{2}\partial_x^2\psi + \tfrac{\nu}{2}(N-1)|\psi|^2\psi = 0, \tag{18}$$

where $\Psi$ means the many-nucleon wave function and $\psi$ denotes single-nucleon wave function. The similarity to the NLS equation (2) is clear, so that the soliton solution follows. The static solution is

$$\psi_i(x) = \frac{\sqrt{(N-1)\nu}}{2\cosh((N-1)\nu x/2)} \tag{19}$$

with the energy

$$E_H = -\frac{N(N-1)^2\nu^2}{24} \tag{20}$$

and the density

$$\rho(x) = \frac{N(N-1)\nu}{4\cosh^2((N-1)\nu x/2)}. \tag{21}$$

For the $2N$ particle case, a two-soliton solution is obtained. The two-soliton solution is represented by

$$\psi(t,x) = \frac{\sqrt{2(N-1)\nu}}{2}e^{-(i/2)(K^2-a^2)t}\frac{e^{iKx}\{e^{-a(x-Kt)}+(K^2/(K-ia)^2)e^{-a(3x+Kt)}\}+(K\leftrightarrow -K)}{1+2e^{-2ax}\cosh(2aKt)-2a^2e^{-2ax}\mathrm{Re}(e^{2iKx}/(K+ia)^2)+(K^4/(K^2+a^2)^2)e^{-4ax}}. \tag{22}$$

The existence of the two-soliton solution ensures the existence soliton in a given theoretical framework.

#### 4.2.2. Three-Dimensional Model

A two-dimensional model is realized as the axial symmetric model in nuclear density functional theory dealing with finite quantum systems, and the axis of symmetry is taken as the collision axis in the time-dependent collision calculations. In this sense two dimensional calculation computes one-dimensional colliding motion along the center axis. One and two-dimensional models are toy models for simulating the collision, because the effect described by the outer product (vector product) cannot be rigorously incorporated. Consequently spin effect on the dynamics such as spin-orbit force effect cannot be rigorously treated in one and two dimensional models (cf. the representation of spin current $\boldsymbol{J}(\boldsymbol{r})$ in Equation (24)). Note that spin-orbit force in the non-relativistic framework arises from the special relativity theory. In particular the spin orbit force is well-known to play a decisive role in the structure of nuclei (cf. magic numbers of nuclear structure [6]).

Let us consider the three-dimensional case. It is remarkable that the nuclear medium as a nucleon degree of freedom consists of two different kinds of fermions: protons and neutrons. In the following, the formalism of TDDFT [11, 16] for low-energy nuclear reactions are introduced based on [27], where the Skyrme interaction [28] is utilized as the effective nuclear force in most of the TDDFT calculations. The Skyrme interaction is a zero-range formalism of effective nucleon-nucleon interaction. The TDDFT with Skyrme type zero-range interaction is represented by several densities

$$\begin{aligned} \rho(\boldsymbol{r}) &= \textstyle\sum_{i,\sigma}(\psi_i^*(\boldsymbol{r},\sigma)\psi_i(\boldsymbol{r},\sigma)), \\ \tau(\boldsymbol{r}) &= \textstyle\sum_{i,\sigma}(\nabla\psi_i^*(\boldsymbol{r},\sigma)\cdot\nabla\psi_i(\boldsymbol{r},\sigma)), \\ \boldsymbol{j}(\boldsymbol{r}) &= \tfrac{1}{2i}\textstyle\sum_{i,\sigma}(\psi_i^*\nabla\psi_i(\boldsymbol{r},\sigma) - \psi_i\nabla\psi_i^*(\boldsymbol{r},\sigma)), \end{aligned} \tag{23}$$

and

$$\begin{aligned} \boldsymbol{s}(\boldsymbol{r}) &= \textstyle\sum_{i,\sigma,\sigma'}(\psi_i^*(\boldsymbol{r},\sigma)\psi_i(\boldsymbol{r},\sigma')\langle\sigma|\hat{\sigma}|\sigma'\rangle), \\ \boldsymbol{T}(\boldsymbol{r}) &= \textstyle\sum_{i,\sigma}(\nabla\psi_i^*(\boldsymbol{r},\sigma)\cdot\nabla\psi_i(\boldsymbol{r},\sigma')\langle\sigma|\hat{\sigma}|\sigma'\rangle), \\ \boldsymbol{J}(\boldsymbol{r}) &= \tfrac{1}{2i}\textstyle\sum_{i,\sigma}(\psi_i^*\nabla\psi_i(\boldsymbol{r},\sigma) - \psi_i\nabla\psi_i^*(\boldsymbol{r},\sigma))\times\langle\sigma|\hat{\sigma}|\sigma'\rangle), \end{aligned} \tag{24}$$

where $\psi_i(\boldsymbol{r},\sigma)$ and $\psi_i^*(\boldsymbol{r},\sigma)$ are $i$-th single wave functions and its complex conjugate, respectively, $\rho(\boldsymbol{r})$, $\tau(\boldsymbol{r})$, and $\boldsymbol{j}(\boldsymbol{r})$ denote the density, the kinetic energy density, and the momentum density, respectively, and $\boldsymbol{s}(\boldsymbol{r})$, $\boldsymbol{T}(\boldsymbol{r})$, and $\boldsymbol{J}(\boldsymbol{r})$ stand for the spin density, the spin kinetic density, and the spin current density, respectively. Single wave functions depend on both spatial variable $\boldsymbol{r} \in \mathbf{R}^3$ and the spin $\sigma$, while the spin dependence is summed up in each density. By assuming wave functions and densities as depending also on the time variable $t \in \mathbf{R}$, each single-nucleon satisfies the equation of the form.

$$i\hbar\partial_t\psi_i(t,\boldsymbol{r},\sigma) = h\psi_i(t,\boldsymbol{r},\sigma) \tag{25}$$

with

$$
\begin{aligned}
h\psi_i(t,\boldsymbol{r},\sigma) = \sum_{\sigma'} \Big[ & -\nabla\cdot\frac{\hbar^2}{2m_q^*}\nabla\delta_{\sigma,\sigma'} + U_q(\boldsymbol{r})\delta_{\sigma,\sigma'} \\
& + \boldsymbol{V}_q(\boldsymbol{r})\cdot\langle\sigma|\hat{\sigma}|\sigma'\rangle + iC_q(\boldsymbol{r})\cdot\nabla\delta_{\sigma,\sigma'} \\
& + i\boldsymbol{W}_q(\boldsymbol{r})\cdot(\langle\sigma|\hat{\sigma}|\sigma'\rangle\times\nabla)\Big]\psi_i(t,\boldsymbol{r},\sigma'),
\end{aligned} \tag{26}
$$

where $h$ is the single-particle Hamiltonian, $m_q^*$ denotes the effective mass, and $U_q$, $\boldsymbol{V}_q$, $C_q$, and $\boldsymbol{W}_q$ mean the spin scalar potential, the spin vector potential, the current potential, and the spin orbit potential, respectively. The isospin index $q$ distinguishes protons ($q = p$) from neutrons ($q = n$). For realizing the fermionic statistical property, single wave functions are assumed to form the single Slater determinant, where this assumption is necessary to derive Equation (26). First, the nucleon-nucleon interaction is fully represented by the densities. Here the reason this formalism is called the nuclear TDDFT. Second, this formalism tells us that each single nucleon does not interact directly with the other nucleon, but with the force field described by the collectively summed-up densities (23) and (24). This is the reason the nuclear TDDFT is claimed to be the theory, based on the mean-field description of the many-body interaction (in the same context, the nuclear TDDFT is also called the nuclear TDHF). Furthermore one-body dissipation with the unitarity appears mainly due to the internal excitation of nucleus. Note that the concept of one-body dissipation is a kind of dissipation, but it does not violate the unitarity of time evolution. The details are given by

$$
\begin{aligned}
&\frac{\hbar^2}{2m_q^*} = \frac{\hbar^2}{2m_q} + B_3\rho + B_4\rho_q, \\
&U_q(\boldsymbol{r}) = 2B_1\rho + 2B_2\rho_q + B_3(\tau + i\nabla\cdot\boldsymbol{j}) + B_4(\tau_q + i\nabla\cdot\boldsymbol{j}_q) \\
&\quad +2B_5\triangle\rho + 2B_2\triangle\rho_q + (2+\alpha)B_7\rho^{\alpha+1} \\
&\quad +B_8\left\{\alpha\rho^{\alpha-1}(\rho_n^2+\rho_p^2) + 2\rho^\alpha\rho_q + B_9(\nabla\cdot\boldsymbol{J} + \nabla\cdot\boldsymbol{J}_q)\right\} \\
&\quad +\alpha\rho^{\alpha-1}\{B_{12}\boldsymbol{s}^2 + B_{13}\boldsymbol{s}_n^2(\boldsymbol{s}_n^2 + \boldsymbol{s}_p^2)\} \\
&\quad +\left[e^2\int\frac{\rho_p(\boldsymbol{r}')}{|\boldsymbol{r}-\boldsymbol{r}'|}d\boldsymbol{r}' - e^2\left(\frac{3\rho_p}{\pi}\right)^{1/3}\right]\delta_{q,p}, \\
&\boldsymbol{V}_q(\boldsymbol{r}) = B_9(\nabla\times\boldsymbol{j} + \nabla\times\boldsymbol{j}_q) + 2B_{10}\boldsymbol{s} + 3B_{11}\boldsymbol{s}_q \\
&\quad +2\rho^\alpha(2B_{12}\boldsymbol{s} + 2B_{13}\boldsymbol{s}_q) + B_9(\nabla\times\boldsymbol{J} + \nabla\times\boldsymbol{J}_q), \\
&\boldsymbol{C}_q(\boldsymbol{r}) = 2B_3\boldsymbol{j} + 2B_4\boldsymbol{j}_q - B_9(\nabla\times\boldsymbol{s} + \nabla\times\boldsymbol{s}_q), \\
&\boldsymbol{W}_q(\boldsymbol{r}) = -B_9(\nabla\rho + \nabla\rho_q),
\end{aligned} \tag{27}
$$

where a part shown inside the parenthesis $[\cdot]$ in $U_q(\boldsymbol{r})$ shows the Coulomb interaction acting only on protons. Thirteen different coefficients $(B_1, B_2, \cdots, B_{13})$ must be determined, while they are reduced to only 10 parameters $(t_0, t_1, \cdots, x_3, \alpha)$. For the derivation of the above effective nuclear interaction, see [27, 29].

Although more than 100 parameter sets are proposed for the Skyrme-type effective nuclear interaction (the values for $\{t_0, t_1, t_2, t_3, W_0, x_0, x_1, x_2, x_3, \alpha\}$), the ultimate parameter set is not known to include such an existence. Here we take SV-bas parameter set (**Table 1**). The SV-bas parameter set is known well for reproducing the neutron skin thickness of heavy nuclei such as $^{208}$Pb (for a compilation of experimental and theoretical results, see von Neumann-Cosel [31]). The quality of SV-bas in some relevant heavy nuclei can be found in Iwata and Stevenson [7]. On the other hand, the description of light ions (helium isotopes) using SV-bas is also confirmed to be sufficiently good [32]. The pairing interaction is not introduced in the present density functional, as the collision energy of the present study is sufficiently high for pairing interaction not to play a significant role. Indeed, from an energetic point of view, the nuclear pairing is the effect of less than a few 100s of keV per nucleon. A set of equations (25), (26), and (27) are called the nuclear TDDFT or the nuclear TDHF equations. The nuclear TDDFT is known to reproduce the result rather sufficiently nowadays (for recent reviews, see [33–35]).

**TABLE 1 |** Parameter setting in the TDDFT.

| (a) Reduced coefficients | (b) Skyrme parameter set (SV-bas) [30] |
|---|---|
| $B_1 = t_0(1 + x_0/2)/2$ | $t_0 = -1879.640018$ [MeV · fm$^3$] |
| $B_2 = -t_0(x_0 + 1/2)/2$ | $t_1 = 313.7493427$ [MeV · fm$^5$] |
| $B_3 = (t_1 + t_2)/4 + (t_1x_1 + t_2x_2)/8$ | $t_2 = 112.6762700$ [MeV · fm$^5$] |
| $B_4 = (t_2 - t_1)/8 - (t_2x_2 - t_1x_1)/4$ | $t_3 = 12527.38921$ [MeV · fm$^{3+3\alpha}$] |
| $B_5 = (t_2 - 3t_1)/16 + (t_2x_2 - 3t_1x_1)/32$ | $W_0 = 124.6333000$ [*rmMeV · fm*$^5$] |
| $B_6 = (3t_1 + t_2)/32 + (t_1x_1 + t_2x_2)/16$ | $x_0 = 0.2585452462$ |
| $B_7 = t_3(1 + x_3/2)/12$ | $x_1 = -0.3816889952$ |
| $B_8 = -t_3(x_3 + 1/2)/12$ | $x_2 = -2.823640993$ |
| $B_9 = -W_0/2$ | $x_3 = 0.1232283530$ |
| $B_{10} = -t_0x_0/4$ | $\alpha = 0.3$ |
| $B_{11} = -t_0/4$ | |
| $B_{12} = -t_3x_3/24$ | |
| $B_{13} = -t_3/24$ | |

*The reduced coefficients (a) and a Skyrme parameter set (b) are shown. Among many parameter sets (models for the effective nuclear force), the SV-bas model is taken in this paper.*

## 4.3. Solitons in Many-Nucleon Systems

### 4.3.1. Similarity of Master Equations

To verify the soliton existence, we begin by finding similarities between NLS (4) and the nuclear TDDFT. For one-dimensional cases, as the soliton solution has been obtained, Equation (18) is essentially identical to Equation (9). For three-dimensional cases, a term with $\hbar^2/2m_q^*$ in the TDDFT corresponds to the second term of the left hand side of Equation (9). Here we see that the TDDFT is a Schrödinger type equation. Meanwhile the nonlinear term $|u|^2u$ in Equation (9) corresponds to terms with the coefficients $B_1$ and $B_2$ (depending essentially on the parameter $t_0$). The terms with the coefficients $B_7$ and $B_8$ (depending essentially on the parameter $t_3$), which are known to be indispensable to reproduce the nuclear saturation properties [29], are also relevant, because they introduce additional fractional power contributions (cf. $\alpha$ in the Skyrme parameter set: the

fractional power). The dominance of $t_0$ and $t_3$ terms has been confirmed for the binding energies of $^4$He and $^8$He [32], where the experimental binding energy is 28.30 MeV and 31.40 for $^4$He and $^8$He respectively. No self-bound states of $^4$He and $^8$He are obtained if the $t_0$ term is turned off, and even in the presence of the $t_0$ term the calculated binding energies are at the order of 1,000 MeV which are far from the realistic binding energy. More quantitatively, with respect to the bindings of $^4$He, a large binding (due to the attractive force property of $t_0$ term) at the order of 1,000 MeV is obtained only by the $t_0$ term, it is substantially modified by the $t_3$ term (due to the repulsive force property of $t_3$ term) as 63.80 MeV, and the momentum density contribution ($t_1$ term) reduces it to a realistic value of 27.71 MeV, where the binding energy calculated by including all the terms is 27.73 MeV. Note that the spin-orbit contribution is known to be important in the nuclear structure, but it does not play a prominent role in this case because $^4$He is a spin-saturated system. A rough estimation tells us that the interaction part of the TDDFT with the SV-bas model (the inhomogeneous term of non-linear Schrödinger type equation) is dominated by the $t_0$ and $t_3$ terms with the percentage:

$$\frac{|63.80|}{|63.80| + |63.80 - 27.71| + |27.71 - 27.73|} \times 100 = 63.9\%,$$

where the amplitudes of the $t_0$ and $t_3$ terms, $t_1$ term and the other terms are estimated as $|63.80|$, $|63.80 - 27.71|$, and $|27.71 - 27.73|$, respectively. Dominance of those terms in the nuclear density functional implies the validity of an energy-dependent soliton existence in which the $t_0$ and $t_3$ terms are responsible for the soliton existence and energy dependence, respectively. This similarity between NLS and the nuclear TDDFT provides a sound motivation to investigate the soliton propagation in nuclear TDDFT.

### 4.3.2. Mechanism of Soliton Propagation in the TDDFT

Some specific physics associated with many-nucleon systems are presented with respect to the soliton propagation. In three-dimensional nuclear TDDFT, the existence of a solitary wave corresponds to the existence of self-bound stationary states. For low-energy nuclear reactions, fusion, deep inelastic collision, and collision-fission such as fusion-fission and quasi-fission may appear. Particularly, in case of fusion, the solitary waves are totally destroyed. It implies that a solitary wave cannot necessarily be the soliton, and the soliton existence is inevitably conditional. Let us begin with the collision between $^4$He and $^8$He. Following the usage of nuclear reaction representation, the fusion reaction realized by collision between two self-bound nucleus $^4$He (helium 4: 2 protons and 2 neutrons) and $^8$He (helium 8: 2 protons and 6 neutrons) is represented by

$$^8\mathrm{He} + ^4\mathrm{He} \rightarrow {}^{12}\mathrm{Be}, \tag{28}$$

where $^{12}$Be (beryllium 12: 4 protons and 8 neutrons) is produced as a result of fusion reaction. Fusion reaction is generally an exothermic or endothermic reaction according to the total binding energy difference between reactants and products, where a chemical element iron ($Z = 26$) is the most stable element. On the other hand, if self-bound states $^4$He and $^8$He hold the soliton property,

$$^8\mathrm{He} + ^4\mathrm{He} \rightleftharpoons {}^4\mathrm{He} + ^8\mathrm{He} \tag{29}$$

takes place in which the total energy is conserved before and after the collision. In the context of reaction theory, the soliton property is included in a class of reactions with the time-reversal symmetry. The goal is to find the condition for the appearance of soliton events shown by Equation (29). The time reversal symmetry arises from the energy conservation, according to Noether's theorem, and the total energy is strictly conserved by the nuclear TDDFT framework. For each collision there are two controllable parameters: the relative velocity of collision (i.e., the collision energy) and the impact parameter of collision (usually denoted by $b$ fm). The condition for soliton existence is expected to be written by these two control parameters (i.e., the initial condition).

The soliton existence is confirmed by systematically calculating collision events. The fast charge equilibration mechanism, which is the generalized concept of fusion reaction, has been suggested to govern the mixing of protons and neutrons, including fusion and deep inelastic collisions [36]. Under the appearance of fast charge equilibration, the mixing between protons and neutrons is known to take place quite rapidly within the order of $10^{-22}$ s [36] that should be compared to the typical duration time of low-energy nuclear reactions ($\sim 10^{-20}$ s). The charge equilibrating wave propagates at around 90% of the fermi velocity of many-nucleon systems (corresponding to the speed of zero sound propagation [37]), so that the propagation speed of the charge equilibrating wave is roughly equal to a quarter of the speed of light. Soliton existence is false if we observe the charge equilibration. Consequently, the soliton propagation is realized by the competition between the fast charge equilibration and the transparency, originally due to a certain non-linearity ($t_0$ and $t_3$ terms) of the TDDFT. The fast charge equilibrating wave has been confirmed to play a role only if the collision energy is below the charge equilibration upper-limit energy [36].

In the lower energies less than a few MeV per nucleon, nuclear fusion appears, and soliton cannot survive. In higher energies larger than 50 MeV per nucleon, the nucleus breaks up into small pieces. On the other hand, the fast charge equilibration wave can exist only below the upper-limit energy, where the upper energy is almost 80% of the fermi energy which is in accordance with the fact that the propagation speed is almost 90% of the fermi velocity. In case of nuclear collisions, this energy is roughly equal to 10 MeV per nucleon. This fact may contain a hint for finding the soliton existence condition, i.e., it is reasonable to search for the energy just above the fast charge equilibration upper-limit energy.

### 4.3.3. Numerical Experiment

The heuristic aspect of the numerical experiment plays important roles in the past and present soliton theory (e.g., Fermi-Pasta-Ulam [38]). In this section systematic large-scale calculation

**TABLE 2 |** Self-binding energies of the ground states [7] are calculated using the SV-bas effective nuclear force.

| $(A,Z)$ | $B(^{A}Z)$ | $B(^{A+4}Z)$ | $B(^{2A+4}2Z)$ |
|---|---|---|---|
| (4,2) | 6.93(7.08) | 4.48(3.93) | 6.07(7.06) |
| (16,8) | 8.21(7.98) | 7.84(7.57) | 8.75(8.58) |

*Binding energy per nucleon (MeV) of the initial nuclei are compared to those of the intermediate fused system, and the corresponding experimental values are shown in parenthesis [40].*

of the nuclear collision dynamics is carried out based on the TDDFT. Three-dimensional nuclear TDDFT calculations with the fully-introduced Skyrme-type interaction (10 parameters, as in the present calculations) were initiated in the 1990's [39]. On the other hand, many self-bound stationary states have already been calculated (theoretically found) by static calculations ($\partial\psi_i(t,\boldsymbol{r},\sigma) = 0$ in the TDDFT) in the 1980's, and they are compared to the experiments. The impact parameter dependence of the soliton existence is systematically considered in three-dimensional calculations.

Before moving on to the main discussion, we briefly review the preceding results [7, 32]. According to the calculations dealing with $^{8}$He+$^{4}$He, $^{20}$O+$^{16}$O, $^{44}$Ca+$^{40}$Ca, $^{52}$Ca+$^{48}$Ca, $^{104}$Sn+$^{100}$Sn, $^{124}$Sn+$^{120}$Sn reactions, the energy-dependence of soliton emergence has been clarified only for lighter cases: $^{8}$He+$^{4}$He, and $^{20}$O+$^{16}$O (cf. **Figure 4** of Iwata and Stevenson [7]). For those lighter cases, a rough sketch of the energy-dependence is as follows: the soliton property is not so active for low energies less than a few MeV per nucleon; soliton property becomes active around 10 MeV per nucleon, it achieves almost the perfect transparency around 10–30 MeV per nucleon, and the transparency again decreases for much higher energies (**Figures 2**, **3** of Iwata and Stevenson [7]). For a mass dependence, the most decisive factor for the soliton propagation in heavier collisions has been clarified to be the appearance of the fragmentation including the nucleon emissions (mostly neutron emission). On the other hand, massive momentum equilibration leading to the momentum equilibrium of each spatial point are activated around 80–100 MeV per nucleon, and those energies are too high to be relevant to the suppression of nuclear soliton propagation. In this article, by focusing on the stability of $N = Z$ nucleus of the two colliding nuclei, we clarify the energy-dependent soliton property of $^{4}$He and $^{16}$O.

The initial state of the non-stationary problem is prepared by the two stationary solutions. Let $A$ and $Z$ be mass number and the proton number of a colliding nucleus $^{A}Z$. We consider a set of collisions:

$$^{A}Z + {}^{A+4}Z \tag{30}$$

as a generalization of Equation (28), where $(A,Z) = (4,2)$, $(16,8)$, $(40,20)$, $(48,20)$, $(100,50)$, and $(120,50)$ are considered. Numerical solutions are obtained based on the finite difference method (for the details, see Maruhn et al. [41]). Three-dimensional space is incremented by 1.0 fm, and the unit time step is set to one-third of $10^{-23}$ s. Vacuum boxes are prepared as $24 \times 24 \times 24$ fm$^3$ for the stationary problems, and as $64 \times 32 \times 32$ fm$^3$ for the non-stationary problems. The center-of-mass of $^{A}Z$ and $^{A+4}Z$ are set to $(10, b/2, 0)$ and $(-10, b/2, 0)$, respectively, and the initial momentum of $^{A}Z$ and $^{A+4}Z$ to $(-\sqrt{2M_A E_K}, 0, 0)$ and $(\sqrt{2M_{A+4}E_K}, 0, 0)$, respectively. The parameter $b$ fm imitates the impact parameter. The quantities $M_A$ and $M_{A+4}$ denote the mass of $^{A}Z$ and $^{A+4}Z$, respectively. The periodic boundary condition is imposed in the three-dimensional Cartesian grid.

In **Table 2** the binding energies of initial states are shown to confirm the quality of the present calculations. The binding energy is not precisely the same as the experiment on the whole, but the difference is less than 15% for the lighter nuclei, and less than 5% is achieved for heavier nuclei. It simply shows the quality of the SV-bas parameter set. By changing $A$, $Z$ and the two control parameters, we can examine the mass and energy dependence of the final products. In particular, if the soliton wave is dominant, no nucleon transfer takes place between $^{A}Z$ and $^{A+4}Z$. If charge equilibrating wave is dominant, two neutron transfer from $^{A+4}Z$ to $^{A}Z$ is expected to be the most frequent reaction process. For an astrophysical comparison it is practical to define the typical temperature of collision using the kinetic energy per nucleon or the relative velocity of the collision. Based on the Bethe formula [42], the temperature of nuclear collision [7, 43] is defined by

$$E_K = \begin{cases} \kappa T_C T & (T < T_C), \\ \kappa T^2 & (T \geq T_C), \end{cases} \tag{31}$$

where $E_K$ is the total kinetic energy per nucleon, and $T_C = \kappa^{-1} = 7.2$ MeV is associated with the translation of the fermi energy of the many-nucleon system to the relativistic center-of-mass kinetic energy [44]. It shows that $E_K$ behaves linearly in low temperature and quadratically in high temperature. In this article the results are shown by the kinetic energy $E_K = 1, 2, 3, \cdots,$ 10 MeV.

According to the previous study [7], helium ($Z = 2$) and oxygen ($Z = 8$) isotopes have been proposed as candidates of nuclear soliton. This issue is examined from a stationary aspect. For nuclei with $Z \leq 20$, heavier nuclei become more stable than lighter nuclei, so that lighter nuclei tend to capture a neutron or proton easily. If this is also true for $^{4}$He and $^{16}$O, they cannot hold the soliton property. For the verification of the proposed mechanism, the single neutron addition energy and single proton addition energy are approximately calculated using the energies of even-even nuclei. From an energetic point of view, the following quantities are calculated.

$$\begin{aligned} \mathcal{E}_n(A,Z) &= \tfrac{E(A+2,Z)-E(A,Z)}{2}, \\ \mathcal{E}_p(A,Z) &= \tfrac{E(A+2,Z+2)-E(A,Z)}{2}, \end{aligned} \tag{32}$$

where $E(A,Z)$ means the binding energy for the ground state of a nucleus consisting of $Z$ protons and $A - Z$ neutrons. These quantities show the stability against adding one neutron ($\mathcal{E}_n(A,Z)$) or one proton ($\mathcal{E}_p(A,Z)$), respectively. Neutron capture or proton capture is not preferred if the value is positive. The upper panel of **Figure 3** shows that the formation of the density-functional field (a kind of mean-field) is not enough

for $Z \leq 8$ cases, and the directly-interacting few-body features are more important instead, where doubly-magic nuclei (helium and oxygen cases) show relatively good results comparable to experiments. The stability of $^4$He and $^{16}$O can be found in the lower panel of **Figure 3**. A nucleus is stable against the addition of nucleons, if both $\mathcal{E}_n(A,Z)$ and $\mathcal{E}_p(A,Z)$ are positive. $^4$He and $^{16}$O show the stability (lower panel of **Figure 3**), although heavier cases with $Z \geq 10$ will find a more stable bound system by adding neutrons. From an experimental point of view, $^4$He, $^{12}$C, and $^{16}$O are candidates of soliton, where $^8$Be itself is known to be an unbound system even before comparing it to its neighbor nuclei. From a theoretical and experimental point of view, $^4$He and $^{16}$O are the candidates of soliton in which $\mathcal{E}_q(A,Z)$ values are positive. Consequently, the stability of soliton candidates $^4$He and $^{16}$O are confirmed with respect to the stability of the stationary state in comparison to the neighbors.

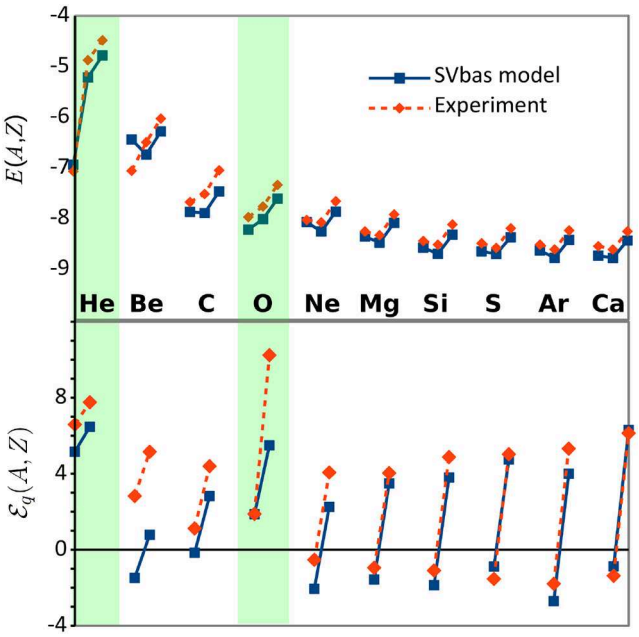


**FIGURE 3 |** Single particle energy and the corresponding energy differences are compared to experiments [40]. **(Upper)** For $Z \leq 20$ nuclei with $(A,Z)$=(4,2), (8,4), $\cdots$ (40,20), the binding energies $E(A,Z)$, $E(A+2,Z)$, $E(A+2,Z+2)$ are shown by the connected lines in this order in each column. **(Lower)** The corresponding energy difference $\mathcal{E}_n(A,Z)$ and $\mathcal{E}_p(A,Z)$ for each nucleus $^Z A$ is shown by the connected lines in this order.

A time evolution of $^8$He + $^4$He collision is shown in **Figure 4**. $^8$He is coming from the left hand side, and $^4$He is moving from the right hand side. It forms a rotating merged system around $t = 28/3 \times 10^{-22}$ s, and it is separated into two fragments as a result of collision. As for **Figure 4**, the collision energy is selected as the lowest energy at which the soliton wave component starts to appear. That is, taking this energy as the standard energy, for lower energies soliton cannot exist, and fusion reaction takes place; for higher energies almost perfect transparency with respect to both mass and momentum is realized. It is a non-central collision ($b \neq 0$) in which the axial symmetry along the collision axis is essentially violated. The shape (more precisely, non-spherical property of the density and momentum distribution) is an important factor in the multi-dimensional case, where a less-symmetric shape of the merged system is introduced by the parameter $b$. In addition to the internal excitation, a part of the total energy is delivered to the angular momentum of each nucleus in case of multi-dimensional and $b \neq 0$ cases. To a certain degree, the appearance of rotational motion of the merged nucleus is a specific factor for the multi-dimensional soliton existence.

The detail of the nucleon transfer depends on the impact parameter, therefore on the shape and geometry. For $^8$He + $^4$He collision transferred nucleon numbers are shown in **Figure 5**, where the impact parameter dependence is shown in an energy-dependent manner. By increasing the energy, nucleon transfer starts to disappear after $E_K$ =7.50 MeV. Indeed, for cases with

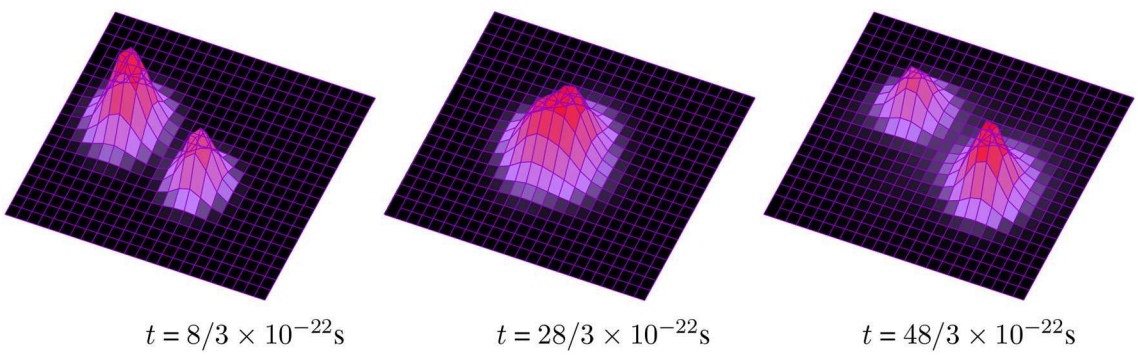


**FIGURE 4 |** Imperfect soliton including the spin degree of freedom, fermionic statistical property, the multi-dimensionality, and the effect due to the non-central collision. Time evolution of $^8$He + $^4$He for $E_K = 7.50$ MeV and $b = 3.0$ fm are shown. The collision energy is around the upper-limit energy of fast charge equilibration [36]. That is, by increasing the energy, the transparent component becomes dominant. For better sights, time evolution of total density is depicted by projecting them on the reaction plane ($z = 0$). The density is plotted on the vertical axis taken from 0 to 0.6 fm$^{-1}$, where the horizontal area is fixed to $(x,y) = 24 \times 20$ fm$^2$. In this situation, 0.29 protons are transferred from $^4$He to $^8$He, and 0.26 neutrons are transferred from $^8$He to $^4$He, where we can find a weak effect of dual-way type charge equilibration [45] leading to the contamination of pure soliton. The self-bound property of $^8$He and $^4$He contributes to recovering the original shape if the transparencies of both mass and momentum is sufficiently high (kinetic energy loss is less than 5 MeV, see **Figure 3**).

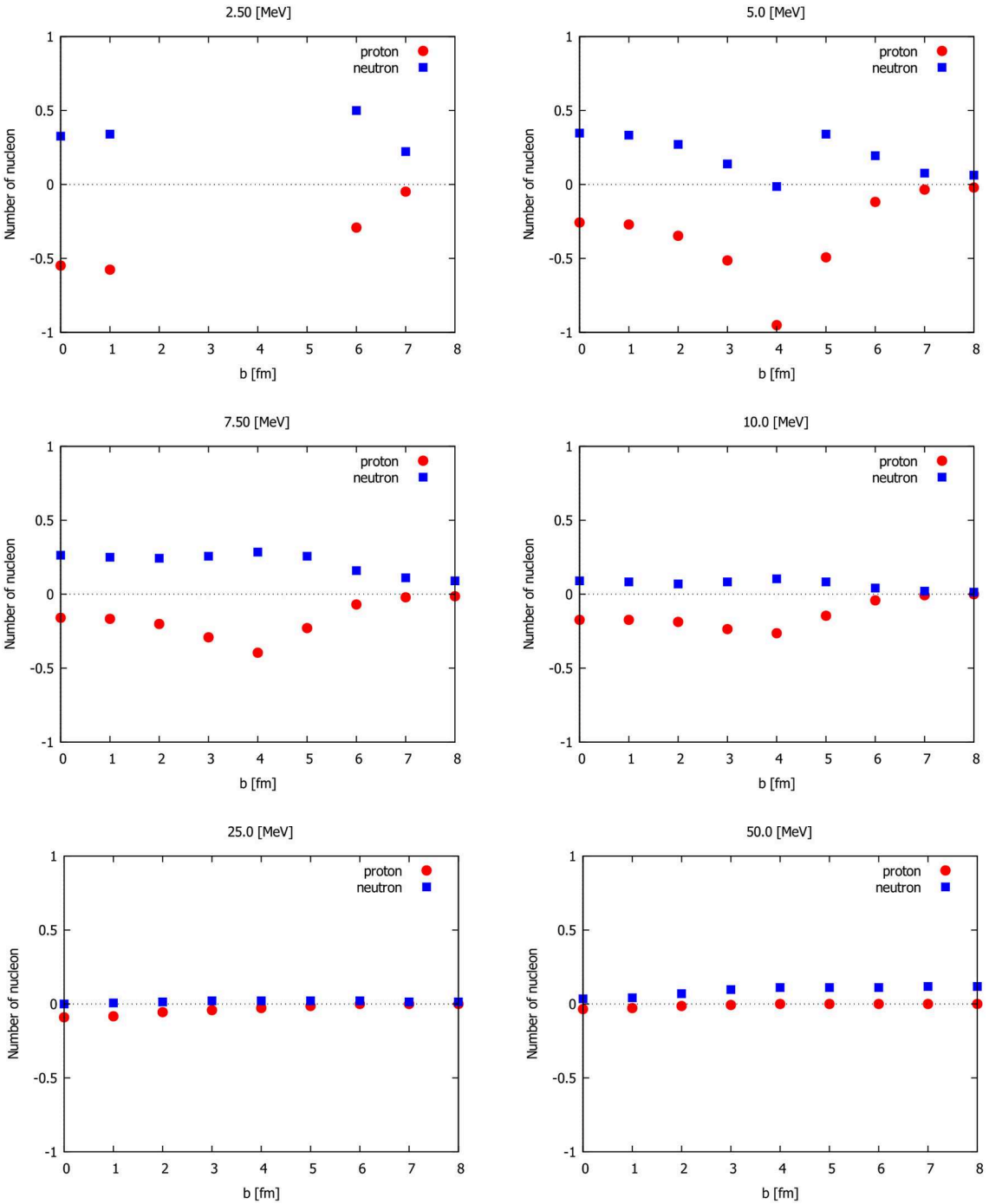


**FIGURE 5 |** For collisions $^{8}$He + $^{4}$He, transferred nucleon from $^{8}$He to $^{4}$He are shown depending on the relative velocity of the collisions. The impact parameter dependence with six different energies $E_K$ are shown. Red circles show the amounts of neutron transfer, and the blue squares show those of proton transfer. In a low energy case with $E_K$ = 2.50 MeV and $b$= 2, 3, 4, 5 fm, fusion appears.

$E_K$ =7.50, 10.0, 25.0, 50.0 MeV, the expectation value for the number of nucleon transfers are always less than 0.50, so that the soliton wave is concluded to be dominant in those cases.

With respect to the quantum mechanical observation, the calculated results are statistically summed up for a given collision energy (a given relative velocity). Indeed, we cannot divide possible events by the impact parameter. Using the concept of geometric cross section [46], the numbers of total cross sections of all the inelastic events (events with touching between two nuclei) for a given collision energy $E_K$ is

**TABLE 3 |** The observation probability [%] of soliton state of $^4$He calculated by $\mathcal{P}_m(E_K)$ and $\mathcal{P}_p(E_K)$ for given collision energies $E_K$.

| $\mathcal{P}_m(E_K)$ | | | $\mathcal{P}_p(E_K)$ | | |
|---|---|---|---|---|---|
| $E_K$ [MeV] | Proton | Neutron | $E_K$ [MeV] | Proton | Neutron |
| 2.50 | 68.3 | 61.4 | 2.50 | 74.5 | 72.5 |
| 5.00 | 75.2 | 69.4 | 5.00 | 60.2 | 56.2 |
| 7.50 | 86.5 | 82.1 | 7.50 | 64.6 | 62.4 |
| 10.0 | 90.7 | 95.0 | 10.0 | 76.9 | 73.7 |
| 25.0 | 98.5 | 98.2 | 25.0 | 95.0 | 93.5 |

*Since the positions of center-of-mass are not so different for protons and neutrons in the present cases, the momentum transfer is shown as the total momentum transfer of all nucleons. According to the preceding study, the soliton is suggested to exist around $E_K$ =25.0 MeV [7].*

calculated by

$$\pi(1.50)^2 T(b_0, E_K) + \sum_{b_i=1}^{10} (\pi(b_i + 0.50)^2 - \pi(b_i - 0.50)^2) T(b_i, E_K)) \tag{33}$$

where $b_i$ fm imitates the impact parameter; $T(b_i, E_K) = 1$ for touched cases, and $T(b_i, E_K) = 0$ for untouched cases. As readily understood by the definition, events with a large impact parameter hold a larger cross section. The rate of transparent events measured by the particle transparency for a given collision energy is calculated by

$$\mathcal{P}_m(E_K) = 1 - \frac{\pi(1.50)^2 |N(b_0,E_K))| + \sum_{b_i=1}^{10} (\pi(b_i+0.50)^2 - \pi(b_i-0.50)^2) |N(b_i,E_K))|}{\pi(1.50)^2 T(b_0,E_K) + \sum_{b_i=1}^{10} (\pi(b_i+0.50)^2 - \pi(b_i-0.50)^2) T(b_i,E_K))} \tag{34}$$

where $N(b_i)$ is the transferred nucleon numbers. This definition can be regarded as the probability, in which $|N(b_i, E_K)|$ is taken as 1 for $|N(b_i, E_K)| > 1$. According to this treatment, $\mathcal{P}_m(E_K)$ can be regarded as the probability for the particle transparency. Using the same definition in the geometric cross section, the transferred momentum rate is calculated. The rate of transparent events measured by the momentum transparency for a given collision energy is calculated by

$$\mathcal{P}_p(E_K) = 1 - \frac{\pi(1.50)^2 |M(b_0,E_K))| + \sum_{b_i=1}^{10} (\pi(b_i+0.50)^2 - \pi(b_i-0.50)^2) |M(b_i,E_K))|}{\pi(1.50)^2 T(b_0,E_K) + \sum_{b_i=1}^{10} (\pi(b_i+0.50)^2 - \pi(b_i-0.50)^2) T(b_i,E_K))} \tag{35}$$

where $-1 \leq M(b_i) \leq 1$ is the transferred momentum divided by the initial momentum.

The soliton probability for all the possible collisions at given energies is summarized in **Table 3**. To find the soliton events at the energy just above the charge equilibration upper limit energy, it is reasonable to focus on $E_K = 7.5$ MeV and $E_K = 10.0$ MeV cases. Indeed, for the reference case $E_K = 25$ MeV, single nucleon emission (neutron emission in most cases) took place during and after the collision, and the shapes are not well-conserved.

In case of helium collisions, almost 90% of the reaction is mass transparent for $E_K = 10.0$ MeV, and almost 80% is for $E_K = 7.5$ MeV. The corresponding momentum transparency rate is 89.6 % for $E_K$ =10.0 MeV, and 92.1 % for $E_K$ =7.5 MeV. Consequently, the probability for finding the soliton events calculated by the product

$$\mathcal{P}_p(E_K)\mathcal{P}_p(E_K)$$

are 81 % for $E_K$ =10.0 MeV, and 76 % for $E_K$ =7.5 MeV. In case of oxygen collisions, almost 70 % of the reaction is mass transparent for $E_K = 10.0$ MeV, and almost 60 % is for $E_K = 7.5$ MeV. The corresponding momentum transparency rate is 92.4 % for $E_K$ =10.0 MeV, and 87.8 % for $E_K$ =7.5 MeV. Consequently, the probability for finding the soliton events are 65 % for $E_K$ =10.0 MeV, and 53 % for $E_K$ =7.5 MeV. In both cases with helium and oxygen collisions, the cross section for soliton events is at the order of 1,000 mb (millibarn). The soliton observation probabilities are larger than 50 %, so that those collisions tend to be observed as the soliton time-reversible events.

## 5. SUMMARY

The soliton existence is nothing but the existence of perfect transparency, therefore the existence of perfect fluidity. The theoretical evidence for the imperfect nuclear soliton existence has been presented for the first time in a realistic setting. As a result, $^4$He is concluded to be a candidate of nuclear soliton. $^{16}$O also behaves like a soliton to a lesser degree. As the fermi energy can be different for different fermions, the present study brings about new insights on the validity of the different physics in different scales. Through the competition relation, the existence of nuclear soliton has been shown to depend essentially on the fermi energy of many-nucleon systems. An essential role of non-linearity in the formation of our material world is understood by the soliton propagation, since nucleon degree of freedom is related to the synthesis of chemical elements (H, He, Li, Be, $\cdots$). In conclusion, $^4$He and $^{16}$O are suggested to be candidates for nuclear soliton. From an applicational point of view, the soliton property of these nuclei will be utilized for the preservation of $^4$He matter, the condensation of $^4$He matter, and the production/synthesis of certain nucleus (by adding several $^4$He intentionally).

As seen in the competition mechanism between soliton wave propagation and charge equilibrating wave propagation, the conditions for the soliton propagation depend essentially on the fermi energy of the fermionic quantum system. Accordingly,

there are some conjectures that need to be confirmed in the near future. In quantum systems,

1. The fermionic soliton exists in different scales in different ways, as the fermi energy is determined by fixing effective degrees of freedom.
2. The solitons between fermionic and bosonic systems are essentially different.
3. The general and special relativity effects change the soliton existence.
4. Another type of the soliton appears in the event when fermions and bosons are tightly correlated (e.g., supersymmetric systems).
5. Another type of the soliton exists in anionic systems.

Where the first, second, and third conjectures are partly studied in this article. The third and fifth conjectures are also associated with clarifying the difference compared to the Maxwellian systems or anionic systems. That is, as in the present research, the soliton propagation in quantum systems should be examined by considering the spin degree of freedom and multi-dimensional spatial-degree of freedom. The fourth conjecture is expected to play a role in clarifying and identifying the theory of everything.

As a closing remark some related open problems should be pointed out. Although there are several unknown and interesting topics in nuclear physics, we focus on the soliton propagation in many-nucleon systems.

- Show the similarity/difference between the soliton "perfect fluidity" and the bosonic "superfluidity."
- Show quantitatively that the soliton propagation is suppressed/enhanced by the interaction terms other than $t_0$- and $t_3$-terms.
- Show the soliton existence probability under the influence of many-body dissipation (cf. one-body dissipation in the main text).
- Find the charge-parity symmetry breaking reaction in terms of the conditional/unconditional soliton existence (conditional/unconditional time-reversal symmetry).

These things will clarify the role of the imperfect soliton in many-nucleon systems. This kind of soliton should be different from the solitons in many-quark systems.

## DATA AVAILABILITY STATEMENT

All datasets generated for this study are included in the article/supplementary material.

## AUTHOR CONTRIBUTIONS

The author confirms being the sole contributor of this work and has approved it for publication.

## FUNDING

This work was partially supported by JSPS KAKENHI Grant No. 17K05440. Numerical computation was carried out at Yukawa Institute Computer Facility of Kyoto University, and a workstation system at Kansai University.

## ACKNOWLEDGMENTS

This article is a transcript of the seminar "The fundamentals of soliton theory and its applcation to many-nucleon systems" at the department of physics, Kyoto University, Japan on Nov. 21, 2019. Fruitful comments from Profs. K. Hagino, Y. Kanada-Enyo, N. Itagaki, K. Yoshida of Kyoto University and the other participants are acknowledged. The author is grateful to Editors Profs. C. Simenel, P. Stevenson, D. Lacroix, L. Guo, and N. Schank for giving him a chance to write this article.

## REFERENCES

1. Manton NS, Sutcliffe P. *Topological Solitons*. Cambridge University Press (2004). doi: 10.1017/CBO9780511617034
2. Weinberg EJ. *Classical Solutions in Quantum Field Theory*. Cambridge University Press (2012).
3. Lee TD, Pang Y. Nontopological solitons. *Phys Rep*. (1992) **221**:251. doi: 10.1016/0370-1573(92)90064-7
4. Ablowitz MJ. *Nonlinear Dispersive Waves: Asymptotic Analysis and Solitons*. Cambridge University Press (2011).
5. Greiner W, Maruhn JA. *Nuclear Models*. Berlin, Heidelberg: Springer-Verlag (1996). doi: 10.1007/978-3-642-60970-1
6. Ring P, Schuck P. *The Nuclear Many-Body Problem*. Berlin, Heidelberg: Springer-Verlag (1980). doi: 10.1007/978-3-642-61852-9
7. Iwata Y, Stevenson P. Conditional recovery of time-reversal symmetry in many nucleus systems. *New J Phys*. (2019) **21**:043010. doi: 10.1088/1367-2630/ab0e58
8. Bjorken JD, Drell SD. *Relativistic Quantum Mechanics*. New York, NY: McGraw-Hill Companies (1998).
9. Scott Russell J. *On Certain Effects Produced on Sound by the Rapid Motion of the Observer*. Report of the Eighteenth Meeting of the British (1848).
10. Zabusky NJ, Kruskal MD, Interaction of "Solitons" in a collisionless plasma and the recurrence of initial states. *Phys Rev Lett*. (1965) **15**:240. doi: 10.1103/PhysRevLett.15.240
11. Korteweg DJ, de Vries G, On the change of form of long waves advancing in a rectangular canal, and on a new type oflong stationary waves. *Philos Mag*. (1895) **39**:422–43. doi: 10.1080/14786449508620739
12. Lamb GL Jr. *Elements of Soliton Theory*. New York, NY: John Wiley & Sons (1980). Available online at: https://www.cambridge.org/core/journals/laser-and-particle-beams/article/g-l-lambjr-elements-of-soliton-theory-john-wiley-sons-new-york-1980-302-pages/B7746782CA289EFE25F3A17BD6DB3DB2
13. Scott W, Chu FY, Machlaughlin DW. The soliton: a new concept in applied science. *Proc IEEE*. (1973) **61**:1443. doi: 10.1109/PROC.1973.9296
14. Lax PD. Integrals of nonlinear equations of evolution and solitary waves. *Pure Appl Math*. (1968) **21**:467. doi: 10.1002/cpa.3160210503
15. Fetter L, Warecka JD. *Quantum Theory of Many-Particle Systems*. Mineola, NY: Dover (2003).
16. Dirac PAM. Note on exchange phenomena in the thomas atom. *Proc Camb Philos Soc*. (1930) **26**:376. doi: 10.1017/S0305004100016108
17. Engel YM, Brink DM, Goeke K, Krieger SJ, Vautherin D. Hartree-Fock calculations with Skyrme's interaction. I. Spherical nuclei. *Nucl Phys A*. (1975) **249**:215. doi: 10.1016/0375-9474(75)90184-0

18. Davey Stewartson K. On three-dimensional packets of surface waves. *Proc R Soc Lond A*. (1974) **338**:101. doi: 10.1098/rspa.1974.0076
19. Boiti M, Leon JJP, Penpinelli F. A new spectral transform for the Davey-Stewartson I equation. *Phys Lett A*. (1989) **141**:101. doi: 10.1016/0375-9601(89)90767-6
20. Hietarinta J, Hirota R. Multidromion solutions to the Davey-Stewartson equation. *Phys Lett A*. (1990) **145**:237. doi: 10.1016/0375-9601(90)90357-T
21. Bethe HA. On the theory of metals. *Z Phys*. (1931) **71**:205. doi: 10.1007/BF01341708
22. Dolan L. Scattering of quantized solitary waves in the cubic Schrödinger equation. *Phys Rev D*. (1976) **13**:528. doi: 10.1103/PhysRevD.13.528
23. McGuire JB. Study of exactly soluble one dimensional N body problems. *J Math Phys*. (1964) **5**:622. doi: 10.1063/1.1704156
24. Yang CN. Some exact results for the many-body problem in one dimension with repulsive delta-function interaction. *Phys Rev Lett*. (1967) **19**:1312. doi: 10.1103/PhysRevLett.19.1312
25. Yoon B, Negele JW. Time-dependent Hartree approximation for a one-dimensional system of bosons with attractive dfunction interactions. *Phys Rev A*. (1977) **16**:1451. doi: 10.1103/PhysRevA.16.1451
26. Zakharov VE, Shabat AB. Exact theory of two-dimensional self-focusing and onedimensional self-modulation of waves in nonlinear media. *Sov Phys JETP*. (1972) **34**:62.
27. Bonche P, Flocard H, Heenen PH. Solution of the Skyrme HF + BCS equation on a 3D mesh. *Comput Phys Commun*. (2005) **171**:49. doi: 10.1016/j.cpc.2005.05.001
28. Skyrme THR. The effective nuclear potential. *Philos Mag*. (1956) 1:1043; Nucl. Phys. (1956) 9:615. doi: 10.1080/14786435608238186
29. Vautherin D, Brink DM. Hartree-fock calculations with Skyrme's interaction. I. Spherical Nuclei. *Phys Rev*. (1972) **C5**:626. doi: 10.1103/PhysRevC.5.626
30. Klüpfel P, Reinhard P-G, Bürvenich TJ, Maruhn JA. Variations on a theme by Skyrme: a systematic study ofadjustments of model parameters. *Phys Rev C*. (2009) **79**:034310. doi: 10.1103/PhysRevC.79.034310
31. von Neumann-Cosel P. Complete electric dipole response in 120Sn 208Pb implications for neutron skin symmetry energy. *J Phys Conf Ser*. (2015) **590**:012017. doi: 10.1088/1742-6596/590/1/012017
32. Iwata Y. Energy-dependent existence of soliton in the synthesis of chemical elements. *Mod Phys Lett A*. (2015) **30**:155008. doi: 10.1142/S0217732315500881
33. Simenel C, Umar AS. Heavy-ions collisions and fission dynamics with the time-dependent Hartree-Fock theory and its extension. *Prog Part Nucl Phys*. (2018) **103**:19. doi: 10.1016/j.ppnp.2018.07.002
34. Stevenson P, Barton MC. Low-energy heavy-ion reactions and effective forces. *Prog Part Nucl Phys*. (2019) **104**:142. doi: 10.1016/j.ppnp.2018.09.002
35. Sekizawa K. TDHF theory and its extensions for the multinucleon transfer reaction: a mini review. *Front Phys*. (2019) **7**:20. doi: 10.3389/fphy.2019.00020
36. Iwata Y, Otsuka T, Maruhn JA, Itagaki N. Suppression of charge equilbration leading to the synthesis of exotic nuclei. *Phys Rev Lett*. (2010) **104**:252501. doi: 10.1103/PhysRevLett.104.252501
37. Iwata Y. Zero sound propagation in femto-scale quantum liquids. *J Mod Phys*. (2012) **6**:476. doi: 10.4236/jmp.2012.36064
38. Fermi E, Pasta JR, Ulam SM. *Studies of Nonlinear Problems*. I. Los Alamos report LA-1940 (1955). doi: 10.2172/4376203
39. Kim K-H, Otsuka T, Bonche P. Three-dimensional TDHF calculations for reactions of unstable nuclei. *J Phys G*. (1997) **23**:1267. doi: 10.1088/0954-3899/23/10/014
40. Nudat 2.7. Available online at: www.nndc.bnl.gov/nudat2/
41. Maruhn JA, Reinhard P-G, Stevenson PD, Umar AS. The TDHF code Sky3D. *Comput Phys Commun*. (2014) **185**:2195: doi: 10.1016/j.cpc.2014.04.008
42. Bethe HA. Nuclear physics nuclear dynamics B theoretical. *Rev Mod Phys*. (1937) **9**:69. doi: 10.1103/RevModPhys.9.69
43. Fröbrich P, Lipperheide R. *Theory of Nuclear Reactions*. Oxford: Oxford University Press (1996).
44. Iwata Y. Time-scaled scenario of low-energy heavy-ion collisions. *J Phys Conf Ser*. (2013) **445**:012017. doi: 10.1088/1742-6596/445/1/012017
45. Iwata Y, Otsuka T, Maruhn JA, Itagaki N. Geometric classification of nucleon transfer at moderate low-energies. *Nucl Phys A*. (2010) **836**:108. doi: 10.1016/j.nuclphysa.2010.01.242
46. Iwata Y. Reaction cross sections for time-dependent density functional calculations. In: *Fission and Properties of Neutron-Rich Nuclei - Proceedings of the Fifth International Conference on ICFN5*. Singapore: World Scientific. 643–649. Available online at: https://www.worldscientific.com/worldscibooks/10.1142/8910


**Conflict of Interest:** The author declares that the research was conducted in the absence of any commercial or financial relationships that could be construed as a potential conflict of interest.

frontiers in Physics

REVIEW
published: 03 July 2020
doi: 10.3389/fphy.2020.00233

# The Time-Dependent Generator Coordinate Method in Nuclear Physics

*Marc Verriere*[1,2]* *and David Regnier*[3,4]

[1] Nuclear and Chemical Sciences Division, Lawrence Livermore National Laboratory, Livermore, CA, United States, [2] Los Alamos National Laboratory, Los Alamos, NM, United States, [3] CEA, DAM, DIF, Arpajon, France, [4] Université Paris-Saclay, CEA, Laboratoire Matière en Conditions Extrêmes, Bruyères-le-Châtel, France

The emergence of collective behaviors and the existence of large amplitude motions are both central features in the fields of nuclear structure and reactions. From a theoretical point of view, describing such phenomena requires increasing the complexity of the many-body wavefunction of the system to account for long-range correlations. One of the challenges, when going in this direction, is to keep the approach tractable within our current computational resources while gaining a maximum of predictive power for the phenomenon under study. In the Generator Coordinate Method (GCM), the many-body wave function is a linear superposition of (generally non-orthogonal) many-body states (the generator states) labeled by a few collective coordinates. Such a method has been widely used in structure studies to restore the symmetries broken by single-reference approaches. In the domain of reactions, its time-dependent version (TDGCM) has been developed and applied to predict the dynamics of heavy-ion collisions or fission where the collective fluctuations play an essential role. In this review, we present the recent developments and applications of the TDGCM in nuclear reactions. We recall the formal derivations of the TDGCM and its most common approximate treatment, the Gaussian Overlap Approximation. We also emphasize the Schrödinger Collective-Intrinsic Model (SCIM) variant focused on the inclusion of quasiparticle excitations into the description. Finally, we highlight several exploratory studies related to a TDGCM built on time-dependent generator states.

**Keywords: nuclear reactions, energy density functional, configuration mixing, TDGCM, time-dependent, fission**

OPEN ACCESS

***Edited by:***
*Paul Denis Stevenson, University of Surrey, United Kingdom*

***Reviewed by:***
*J. Luis Egido, Autonomous University of Madrid, Spain*
*Marco La Cognata, Laboratori Nazionali del Sud (INFN), Italy*

***Correspondence:**
*Marc Verriere*
*verriere1@llnl.gov*

***Specialty section:***
*This article was submitted to Nuclear Physics?, a section of the journal Frontiers in Physics*

***Received:*** *17 April 2020*
***Accepted:*** *28 May 2020*
***Published:*** *03 July 2020*

***Citation:***
*Verriere M and Regnier D (2020) The Time-Dependent Generator Coordinate Method in Nuclear Physics. Front. Phys. 8:233. doi: 10.3389/fphy.2020.00233*

## 1. INTRODUCTION

Since the early days of nuclear physics, the variety of shapes that atomic nuclei can take is a core notion of our interpretation of nuclear processes. The fission reaction provides a typical example since it was quickly interpreted as the elongation of a charged liquid drop of nuclear matter, leading to a scission point [1]. Descriptions in terms of vibrations and rotations of the nuclear shape also lead to quantitative reproductions of the low energy spectra [2] of atomic nuclei. These successes of the theory suggest that the shape of the nuclear density is somehow a relevant degree of freedom (DoF) to describe several phenomena. In addition to the classical picture of the time evolution of a well defined nuclear shape, taking into account its associated quantum fluctuation is of particular importance. For instance, these fluctuations directly drive the width of the probability distribution of particles transferred during low energy heavy-ion collisions, as well as the modal characteristics

of the fragment distribution produced by fission. The incorporation of these fluctuations into a quantum description leads to a many-body wave function describing the system that is a mixture of states with different shapes. With this intuition, one may attempt a direct description of nuclei in terms of shape DoFs. However, transforming the $3A$ positions and $A$ spins of the nucleons into a new system of coordinates involving a set of deformations parameters is both cumbersome and problem-dependent [3, 4]. Another possibility consists in keeping the nucleons coordinates and build an *ad-hoc* quantum mixture of many-body states with different relevant shapes. This is precisely the starting point of the Generator Coordinate Method (GCM).

The GCM method was first developed in the seminal papers of Hill and Wheeler in the context of nuclear fission in 1953 [5], and later on generalized in [6]. The global philosophy is (i) to generate a set of many-body states parameterized by a set of shape variables (the generator states), (ii) to derive an equation of motion for the many-body wave function of the system in the restricted Hilbert space spanned by the generator states. The first applications of this method focused in introducing shape degrees of freedom, such as the multipole moments of the one-body density. It turns out to be very versatile and has been applied since with different families of generator states. The static GCM has demonstrated over the years its ability to describe the low excitation spectrum of nuclei [7, 8]. For this kind of application, the generator states are, in general, parameterized by some gauge variables associated with the breaking and restoration of symmetry groups (Euler angles for rotational symmetry, gauge angle for the particle-number symmetry) . Similar approaches based on generator states labeled by a few multipole moments of the one-body density also provided predictions of the giant monopole, dipole, and quadrupole resonances [9–14].

Studies based on the time-dependent flavor of the GCM are less abundant in the literature than the ones using its stationary counterpart. Therefore, the goal of this review is to recall the formal developments related to the Time-Dependent Generator Coordinate Method (TDGCM) and highlight their current applications in the field of nuclear physics. In section 2, we present some general aspects of the time-dependent generator coordinate method in its standard and full-fledged implementation. In section 3, we focus on the Gaussian overlap approximation framework that is commonly used in most of the state of the art applications of the TDGCM. In particular, we discuss the fact that such an approach has difficulties accounting for the diabatic aspects of nuclear collective motions. We then devote the two last sections to two possible extensions of the TDGCM that aim to overcome this issue. The section 4 highlights the Schrödinger Collective Intrinsic Model (SCIM), a framework based on the symmetric moment approximation of the TDGCM. Finally, section 5.1 reports alternative methods involving a TDGCM-like ansatz built on time-dependent generator states.

# 2. GENERAL FORMALISM OF THE TDGCM

## 2.1. Generator States

Predicting the structure and dynamics of medium to heavy nuclei starting from the nucleons degrees of freedom is a challenging task. The difficulty arises from a large number of correlations present in the many-body wave function of nuclear systems. A feature that helps us tackle this problem is the existence of two nearly separable time scales in nuclear processes. On the one hand, we have the typical time for the motion of individual nucleons inside the nucleus, which is roughly $10^{-22}$ s. On the other hand, the time scales associated with the system's collective deformations are roughly ten times bigger than the former (1 zs = $10^{-21}$ s). Such separation in time scale motivated attempts to describe the dynamics in terms of shape coordinates only. As mentioned in the introduction, one possibility is to transform the $3A$ positions of the nucleons into a set of collective coordinates plus some residual intrinsic DoFs. Such an approach could then be combined with an adiabatic approximation similar to the Born-Oppenheimer approximation in electronic systems to reduce the dynamics to the collective DoFs only. The GCM proceeds with an alternative approach that introduces collective deformations DoFs without relying on a transformation of the set of nucleons DoFs.

The first step of the method consists in building a family of many-body states $\{|\phi(\boldsymbol{q})\rangle\}$ parameterized by a vector of labels $\boldsymbol{q} = q_0 \cdots q_{m-1}$. We can summarize the essence of such a construction in the following few points:

- The labels $q_i$ are referred to as the generator coordinates or collective coordinates. They are continuous real numbers that can, for instance, characterize the shape of the nuclear density. The vector $\boldsymbol{q}$ takes arbitrary values in a $m$-dimensional subspace $E \subset \Re^m$.
- The states $\{|\phi(\boldsymbol{q})\rangle\}$ are the generator states. They are many-body states associated with the system of $A$ nucleons under study. In the standard TDGCM framework, these states are time-independent.
- The function $\boldsymbol{q} \rightarrow |\phi(\boldsymbol{q})\rangle$ should be continuous. In other words, for any sequence of collective coordinates $\{\boldsymbol{q}_k\}$ that converges to $\boldsymbol{q}$, the corresponding sequence $|\phi(\boldsymbol{q}_k)\rangle$ must converge to $|\phi(\boldsymbol{q})\rangle$. This property is required for a sound mathematical construction of the GCM framework as detailed in [15].

The choice of a family of generator states fulfilling these properties is then arbitrary, which gives great versatility to the GCM method[1]. The generator states should span a sub-Hilbert space that contains each stage of the exact dynamics to describe a physical process optimally. Therefore, building a pertinent family of generator states requires a good *a priori* knowledge of the dynamics of the system.

A standard procedure to handle nuclear deformations consists in the definition of the generator states as the solutions of a constrained Hartree-Fock-Bogoliubov equation. In this approach, each collective coordinate is typically associated with a multipole moment observable (i.e., the quadrupole moment of

[1]For some applications, it may be convenient to add one or several discrete generator coordinates. We will then note the generator states as $|\phi_{\boldsymbol{k}}(\boldsymbol{q})\rangle$ where $\boldsymbol{k}$ is a vector of discrete labels. A typical example of a discrete label could be the $K$ quantum number associated with the projection of the total spin onto a symmetry axis of the nucleus. Another example is provided in section 4.

the one-body density). The generator state $\left|\phi(\boldsymbol{q})\right\rangle$ is then obtained by minimizing the Routhian

$$R[\phi(\boldsymbol{q})] = E_{\mathrm{HFB}}[\phi(\boldsymbol{q})] - \sum_i \lambda_i \left(\left\langle\phi(\boldsymbol{q})\right|\hat{Q}_i\left|\phi(\boldsymbol{q})\right\rangle - q_i\right)^2, \quad (1)$$

where the $\hat{Q}_i$ refer to the chosen multipole operators and $\lambda_i$ are their associated Lagrange multipliers. This method presents the benefit of controlling the principal components of the shape of the states through a small set of DoFs. The other DoFs are determined automatically from the HFB variational principle. It is often qualified as an adiabatic method because the generator states will minimize their HFB energy under a small number of constraints. One drawback of this method is that it does not necessarily ensure the continuity of the function $\boldsymbol{q} \rightarrow \left|\phi(\boldsymbol{q})\right\rangle$. This could severely affect some applications as mentioned in sections 2.6, 3.3.

In the context of nuclear structure, the now-standard strategy of symmetry breaking and restoration provides a different yet natural way of building generator states. In this context, we typically define the generator states as the result of applying a parameterized group of symmetry operators on a reference (and symmetry breaking) HFB state $|\phi\rangle$. Typically, for the particle-number symmetry, the relevant collective coordinate is the gauge angle $\theta$ [16] and the generator states $\left|\phi(\theta)\right\rangle$ read

$$\left|\phi(\theta)\right\rangle = \exp\left(i\theta(\hat{A} - A)\right)|\phi\rangle\,. \quad (2)$$

Note that the two strategies mentioned above to create the generator states are often mixed when dealing with several collective coordinates [8].

## 2.2. Griffin-Hill-Wheeler Ansatz

Once the family of generator states is chosen, the Griffin-Hill-Wheeler (GHW) ansatz assumes that the many-body state of the system reads at any time

$$\left|\Psi(t)\right\rangle = \int_{\boldsymbol{q}\in E} \mathrm{d}\boldsymbol{q}\left|\phi(\boldsymbol{q})\right\rangle f(\boldsymbol{q},t). \quad (3)$$

The function $f(\boldsymbol{q},t)$ gives the complex-valued weights of this quantum mixture of states. It should belong to the space of square-integrable functions that we note here $L^2(E)$. The expectation value of any observable $\hat{O}$ for a GHW state has the compact form

$$\langle\hat{O}\rangle(t) = \iint \mathrm{d}\boldsymbol{q}\,\mathrm{d}\boldsymbol{q}' f^\star(\boldsymbol{q},t)\mathcal{O}(\boldsymbol{q},\boldsymbol{q}')f(\boldsymbol{q}',t). \quad (4)$$

We used here the notation $\mathcal{O}(\boldsymbol{q},\boldsymbol{q}')$ for the kernel of the observable defined by

$$\mathcal{O}(\boldsymbol{q},\boldsymbol{q}') = \left\langle\phi(\boldsymbol{q})\right|\hat{O}\left|\phi(\boldsymbol{q}')\right\rangle. \quad (5)$$

Significant kernels that we will discuss through this review are the norm kernel and the energy (or Hamiltonian) kernel. They are defined as

$$\mathcal{H}(\boldsymbol{q},\boldsymbol{q}') = \left\langle\phi(\boldsymbol{q})\right|\hat{H}\left|\phi(\boldsymbol{q}')\right\rangle \quad \text{(Hamiltonian)}, \quad (6)$$

$$\mathcal{N}(\boldsymbol{q},\boldsymbol{q}') = \left\langle\phi(\boldsymbol{q})\right|\hat{\mathbb{1}}\left|\phi(\boldsymbol{q}')\right\rangle \quad \text{(norm)}. \quad (7)$$

We emphasize that the choice of collective coordinates $\boldsymbol{q}$ is somehow arbitrary. From one choice of collective coordinate, we may switch to a different one while keeping invariant the space of GHW states. We can show this by defining a change of variable $\varphi$

$$\boldsymbol{a} = \varphi(\boldsymbol{q}). \quad (8)$$

Then we may consider the GHW ansatz built on the transformed generator states $\left|\tilde{\phi}(\boldsymbol{a})\right\rangle = \left|\phi(\varphi^{-1}(\boldsymbol{a}))\right\rangle$

$$\left|\tilde{\psi}(t)\right\rangle = \int_{\boldsymbol{a}\in\varphi(E)} \mathrm{d}\boldsymbol{a}\left|\tilde{\phi}(\boldsymbol{a})\right\rangle\tilde{f}(\boldsymbol{a},t). \quad (9)$$

Any GHW state defined by Equation (3) can be cast into Equation (9) with the weight function

$$\tilde{f}(\boldsymbol{a},t) = f(\varphi^{-1}(\boldsymbol{a}),t)|\det(J_\varphi(\boldsymbol{a}))|^{-1}. \quad (10)$$

Here $J_\varphi$ is the Jacobian matrix of the coordinate transformation. Also, the formula for the expectation value observables is invariant by this change of coordinate. Typically we have in the $\boldsymbol{a}$ representation

$$\langle\hat{O}\rangle(t) = \iint \mathrm{d}\boldsymbol{a}\,\mathrm{d}\boldsymbol{a}'\tilde{f}^\star(\boldsymbol{a},t)\mathcal{O}(\boldsymbol{a},\boldsymbol{a}')\tilde{f}(\boldsymbol{a}',t), \quad (11)$$

with

$$\mathcal{O}(\boldsymbol{a},\boldsymbol{a}') = \left\langle\tilde{\phi}(\boldsymbol{a})\right|\hat{O}\left|\tilde{\phi}(\boldsymbol{a}')\right\rangle. \quad (12)$$

Although applying such a change of variable does not change the physics of the ansatz, it does change intermediate quantities involved in the GCM framework. In some cases, it may be essential to change the variables to obtain valuable mathematical properties of the kernel operators [15, 16].

As a final remark, we would like to highlight that the integral of Equation (3) may not be well defined for some weight functions and family of generator states. The [15] gives a mathematically rigorous presentation of the GCM framework. We retain from this work that a sufficient condition for the GHW ansatz to be valid is that norm kernel defines a bounded linear operator on $L^2(E)$.

## 2.3. Griffin-Hill-Wheeler Equation

The time-dependent Schrödinger equation in the entire many-body Hilbert space,

$$\left(\hat{H} - i\hbar\frac{\mathrm{d}}{\mathrm{d}t}\right)\left|\Psi(t)\right\rangle = 0, \quad (13)$$

drives the exact time evolution of a many-body system $\left|\Psi(t)\right\rangle$. We assume here that all the interactions between the nucleons are encoded into the Hamiltonian $\hat{H}$ acting on the full many-body space. From this starting point, the TDGCM equation of motion can be obtained by assuming that at any time $t$:

1. the wave function of the system keeps the form of Equation (3),

2. the equality

$$\langle\Phi|\left(\hat{H}-i\hbar\frac{\mathrm{d}}{\mathrm{d}t}\right)\big|\Psi(t)\big\rangle=0 \tag{14}$$

is satisfied for every GHW state $|\Phi\rangle$.

In other words, we impose that the residual $(\hat{H}-i\hbar\mathrm{d}/\mathrm{d}t)\big|\Psi(t)\big\rangle$ is orthogonal to the space of GHW states. This last assumption is equivalent to a Frenkel's variational principle whose link to other time-dependent variational principles is discussed in [17]. By injecting the GHW ansatz (3) into (14), we obtain

$$\int\int \mathrm{d}\boldsymbol{q}\,\mathrm{d}\boldsymbol{q}' f_\Phi^\star(\boldsymbol{q}')\Big(\mathcal{H}(\boldsymbol{q}',\boldsymbol{q})-i\hbar\mathcal{N}(\boldsymbol{q}',\boldsymbol{q})\frac{\mathrm{d}}{\mathrm{d}t}\Big)f(\boldsymbol{q},t)=0. \tag{15}$$

Here $f_\Phi$ is the mixing function defining the GHW state $|\Phi\rangle$. Solving Equation (15) for any state $|\Phi\rangle$ is equivalent to look for a function $f$ verifying the so-called Griffin-Hill-Wheeler equation in its time-dependent form

$$\forall\boldsymbol{q}':\quad\int\mathrm{d}\boldsymbol{q}\Big(\mathcal{H}(\boldsymbol{q}',\boldsymbol{q})-i\hbar\mathcal{N}(\boldsymbol{q}',\boldsymbol{q})\frac{\mathrm{d}}{\mathrm{d}t}\Big)f(\boldsymbol{q},t)=0. \tag{16}$$

The time-evolution of the norm and the energy reads

$$\frac{\mathrm{d}}{\mathrm{d}t}\big\langle\Psi(t)\big|\Psi(t)\big\rangle=\frac{i}{\hbar}\big\langle\Psi(t)\big|(\hat{H}^\dagger-\hat{H})\big|\Psi(t)\big\rangle, \tag{17}$$

$$\frac{\mathrm{d}}{\mathrm{d}t}E(t)=\frac{i}{\hbar}\big\langle\Psi(t)\big|(\hat{H}^\dagger-\hat{H})\hat{H}\big|\Psi(t)\big\rangle. \tag{18}$$

Thus, this equation of motion preserves the norm of the wave function and the total energy of the system if the many-body Hamiltonian is Hermitian. However, it is not always the case. To simulate open systems, for instance in the context of nuclear reactions, a common practice consists in adding an imaginary absorption term to the Hamiltonian that acts in the neighborhood of the finite simulation box. Finally, the time-dependent GHW equation is a continuous system of integrodifferential equations. Its non-local nature in the $\boldsymbol{q}$ representation brings a serious hurdle to its numerical solving.

## 2.4. Mapping to the Collective Wave Functions

The equation of motion (15) and an initial condition for the system is sufficient to determine the dynamics in the TDGCM framework. It is possible to numerically integrate in time this equation with an implicit scheme such as Crank-Nicolson [18]. However, the TDGCM framework offers another natural approach that turns out to be both enlightening from the mathematical perspective and more stable from a numerical point of view. This method resorts on a mapping between the GHW states and some functions of the collective coordinate $\boldsymbol{q}$. The rigorous mathematical construction of this mapping in a general case is detailed in [15]. Here we will only build this mapping in the case where the norm kernel $\mathcal{N}$ is of Hilbert-Schmidt type [19]. It is the case as long as the domain $E$ of the collective coordinates is bounded, which is valid for a wide range of applications.

To start with, we recall that any kernel $\mathcal{O}(\boldsymbol{q},\boldsymbol{q}')$ also defines a linear operator acting on the space of functions $L^2(E)$

$$(\mathcal{O}f)(\boldsymbol{q})=\int_{\boldsymbol{q}'\in E}\mathrm{d}\boldsymbol{q}'\mathcal{O}(\boldsymbol{q},\boldsymbol{q}')f(\boldsymbol{q}'), \tag{19}$$

as long as this integral is mathematically defined. The Hilbert-Schmidt property of the norm operator implies the existence of a complete, discrete and orthonormal family of functions $\{u_i(\boldsymbol{q})\}_i$ of $L^2(E)$ that diagonalizes the linear operator associated with the norm kernel

$$\forall i>0:\quad\mathcal{N}u_i=\lambda_i u_i. \tag{20}$$

Since $\mathcal{N}$ is a Hermitian positive semidefinite operator, its eigenvalues are real and positives. We adopt here the convention where they are sorted by decreasing order and assume that only the first $r$ eigenvalues are not zero. From this diagonalization, we can split the space of functions $f$ into two orthogonal subspaces: the one associated with the vanishing eigenvalues and the one associated with the strictly positive eigenvalues. Formally, we write down the two projectors

$$\mathcal{Q}(\boldsymbol{q},\boldsymbol{q}')=\sum_{i\leq r}u_i(\boldsymbol{q})u_i^\star(\boldsymbol{q}') \tag{21}$$

$$\mathcal{P}(\boldsymbol{q},\boldsymbol{q}')=\sum_{i>r}u_i(\boldsymbol{q})u_i^\star(\boldsymbol{q}') \tag{22}$$

with

$$\mathcal{Q}+\mathcal{P}=\mathbb{1}_{L^2(E)}. \tag{23}$$

The projected space $\mathcal{P}L^2(E)$ is associated with the null eigenvalues of the norm operator $\mathcal{N}$. Any GHW state built from a weight function belonging to this space gives the null many-body state. Its orthogonal complement is the subspace $Q(E)=\mathcal{Q}L^2(E)$. We call collective wave functions, the functions living in this subspace.

We can define uniquely the positive hermitian square-root of $\mathcal{N}$ (which is also Hermitian) with

$$\mathcal{N}(\boldsymbol{q},\boldsymbol{q}')=\int_{\boldsymbol{a}\in E}\mathcal{N}^{1/2}(\boldsymbol{q},\boldsymbol{a})\mathcal{N}^{1/2}(\boldsymbol{a},\boldsymbol{q}')\,\mathrm{d}\boldsymbol{a}. \tag{24}$$

We can, therefore, associate to any GHW state its collective wave function $g(\boldsymbol{q})\in Q(E)$ by the equation

$$g=\mathcal{N}^{1/2}f. \tag{25}$$

Conversely, the operator $\mathcal{N}^{1/2}$ is invertible in $Q(E)$. Therefore, for any collective wave function $g\in Q(E)$, one can build its corresponding GHW state with the weight function

$$f=\mathcal{N}^{-1/2}g. \tag{26}$$

Finally, this mapping between $Q(E)$ and the GHW states is isometric as we may show that for any pair of GHW states $\Psi$ and $\Phi$ we have the property

$$\begin{aligned}\langle\Psi|\Phi\rangle&=\big\langle g_\Psi\big|g_\Phi\big\rangle\\&=\int_{\boldsymbol{q}\in E}g_\Psi^\star(\boldsymbol{q})g_\Phi(\boldsymbol{q})\,\mathrm{d}\boldsymbol{q}.\end{aligned} \tag{27}$$

Going further, any many-body observable $\hat{O}$ can be mapped into a collective operator $\tilde{\mathcal{O}}$ acting on the space $Q(E)$. This operator is defined by [2]

$$\tilde{\mathcal{O}} = \mathcal{N}^{-1/2}\mathcal{O}\mathcal{N}^{-1/2}. \tag{28}$$

The isometry of the mapping gives a simple mean to compute matrix elements of observables.

$$\langle\Psi|\hat{O}|\Phi\rangle = \langle g_\Psi|\tilde{\mathcal{O}}|g_\Phi\rangle \tag{29}$$

Finally, we can reduce the TDGCM equation of motion (Equation 16) in this language. It becomes a time-dependent Schrödinger equation for the collective wave function

$$i\hbar\dot{g} = \tilde{\mathcal{H}}g. \tag{30}$$

This equation of motion presents several practical advantages compared to Equation (16). The collective Hamiltonian $\tilde{\mathcal{H}}$ is, in general, still non-local, but the time derivative of $g$ has an explicit expression. It opens the possibility of using faster time integration schemes at the cost of computing first the collective Hamiltonian through Equation (28). Also, the collective wave function is expected to have a smoother behavior compared to the weight function $f$. This comes directly from Equation (26) where we see that eigenvalues of the norm kernel approaching zero add diverging components to $f$. The Equation (30) may be directly solved by discretizing the collective wave function $g(\boldsymbol{q})$. In many cases, it is appropriate to solve it directly in the representation given by the basis $\{u_i(\boldsymbol{q})\}_{i\leq r}$. The collective Hamiltonian $\tilde{\mathcal{H}}$, as well as other collective observables, are indeed easier to compute in this particular basis.

## 2.5. Difficulties Related to the Energy Kernel

We discussed general features of the TDGCM approach valid for any family of generator states. In nuclear physics, most applications of the GCM rely on families of Bogoliubov vacua. A crux of the GCM approach is then the determination of the norm and Hamiltonian kernels between such many-body states. The [20] provides a general and now-standard approach to fully determine the norm kernel between Bogoliubov vacua based on the calculation of a matrix Pfaffian. However, the evaluation of the energy kernel in nuclear physics applications suffers from several major difficulties. The origin of these flaws stems from the fact that our practical applications do not rely on a linear many-body Hamiltonian but some effective Hamiltonians or energy density functionals. This topic was extensively discussed in the context of static GCM for nuclear structure [21–25]. We briefly list here the pitfalls raised by the determinations of the energy kernel in practical nuclear applications.

[2]Note that such a definition is possible for any observable $\hat{O}$ due to the property

$$\mathcal{Q}\mathcal{O} = \mathcal{O}.$$

### 2.5.1. Neglecting Some Exchange Terms

A common practice to avoid unbearable numerical costs is the neglection or the approximation of parts of the many-body Hamiltonian. For instance, it is widespread to use the Slater approximation of the Coulomb exchange term or to neglect the exchange part of the pairing force between nucleons [26]. Although convenient from a numerical point of view, it was shown in [27] that such approximations may introduce poles in the expression of the energy kernel. These poles lead to a divergence when calculated between some Bogoliubov vacua. The [28, 29] illustrate this behavior in a case of particle number symmetry restoration.

### 2.5.2. Violation of Symmetries by Energy Density Functionals

In many practical applications, the nucleon-nucleon interaction is encoded in an energy density functional (EDF). Using such a formalism in combination with a GCM mixture of states requires a sound definition of a multireference energy density functional [22]. Such a definition is often provided and implemented in the form of the reduced energy kernel $h(\boldsymbol{q},\boldsymbol{q}') = \mathcal{H}(\boldsymbol{q},\boldsymbol{q}')/\mathcal{N}(\boldsymbol{q},\boldsymbol{q}')$ between two non-orthogonal Bogoliubov vacua. For a two-body Hamiltonian case, the reduced energy kernels may be expressed from the generalized Wick theorem

$$h(\boldsymbol{q},\boldsymbol{q}') = \sum_{ij} t_{ij}\rho_{ji}^{\boldsymbol{q}\boldsymbol{q}'} + \frac{1}{2}\sum_{ijkl}\bar{v}_{ijkl}\rho_{ki}^{\boldsymbol{q}\boldsymbol{q}'}\rho_{lj}^{\boldsymbol{q}\boldsymbol{q}'} + \frac{1}{4}\sum_{ijkl}\bar{v}_{ijkl}\kappa_{ij}^{\boldsymbol{q}\boldsymbol{q}'*}\kappa_{kl}^{\boldsymbol{q}\boldsymbol{q}'}. \tag{31}$$

It involves the matrix elements of the one- and two-body parts of the interaction $t$ and $\bar{v}$ as well as transition densities such as

$$\rho_{ij}^{\boldsymbol{q}\boldsymbol{q}'} = \frac{\langle\phi(\boldsymbol{q})|\hat{a}_j^\dagger\hat{a}_i|\phi(\boldsymbol{q}')\rangle}{\langle\phi(\boldsymbol{q})|\phi(\boldsymbol{q}')\rangle}. \tag{32}$$

In the practical implementations of the multireference EDF approach, such a kernel is defined by analogy as the same bilinear form whose coefficients come from a fit procedure. The main differences compared to the EDF case are:

1. the coefficients defining the EDF may depend on some densities of the system,
2. the coefficients in the particle-particle channels may differ from the ones in the particle-hole channels,
3. the matrix $\bar{v}$ may not be antisymmetric.

As detailed in [22, 30], the violation of these properties leads in some cases to a divergence of the reduced energy kernel that biases or prevents practical applications.

### 2.5.3. Density Dependent Terms of Energy Density Functionals

In an EDF framework, the coefficients of Equation (31) depend on the density of the system. The exact formulation of this dependency is yet subject to an arbitrary choice, especially for the non-diagonal part of the kernel. Several prescriptions have been developed and tested during the last two decades [31, 32]. A prescription that fulfills many important conditions

expected from a Hamiltonian is the transition density defined by Equation (32) (see [33]). However, this prescription yields to complex-valued densities. It is then incompatible with most of the EDFs developed at the mean-field level with terms that contain a non-integer power of the density. Finding a satisfying pair of density prescription and EDF valid for GCM calculations is still an open problem.

In conclusion, the current usage of the GCM formalism with effective Hamiltonian or energy density functionals suffers from several formal and practical flows when it comes to determining the energy kernel. This situation has been a major obstacle to the development of GCM applications in nuclear physics in the last years. Several ongoing efforts attempt to overcome this difficulty by building new energy functionals valid for multireference calculations [34] or going toward *ab initio* treatments [35].

## 2.6. Fission Dynamics With the Exact TDGCM

The exact solving of the time-dependent GHW equation in a realistic case has rarely been carried out. To our knowledge, the only published work tackling this task is presented in [36, 37] in the context of fission. It shows the challenges raised by an exact TDGCM calculation, especially when dealing with large collective coordinate domains.

In [36], the authors used the TDGCM to describe the reaction $^{239}$Pu(n,f). This study relies on two common collective coordinates for fission, namely $q_{20}$ and $q_{30}$, that are associated with the expectation value of the quadrupole and the octupole moments of the one-body density. The dynamics in this collective space accounts for the evolution from a compound to a fragmented system with, also, information on the mass asymmetry between the two fragments produced. It is well suited to determine the mass yields of the fragments. The set of constrained HFB solutions (a total of 20,212) obtained for a wide range of these collective coordinates forms the family of generator states. Each generator state is practically obtained with a finite-range Gogny interaction in its D1S parametrization. A two-center axial harmonic oscillator basis with 12 shells has been used where the parameters defining the basis have been optimized for each value of the collective coordinates.

The norm kernel has been calculated for each couple of generator states. The upper-left panel of **Figure 1** presents its values between the mean-field ground-state and the surrounding points, whereas the lower-left panel of the figure shows its values obtained for a more elongated configuration in the potential energy surface (PES). We see that the overlaps are above $\epsilon_{\text{thresh}} = 1.0 \times 10^{-4}$ only in a neighborhood of $\boldsymbol{q}_0$ in both cases. As noted in [16], it is due to the large number of nucleons in the system.

This behavior is at the heart of the Gaussian Overlap Approximation, discussed in more detail in section 3. The reduced Hamiltonian $h(\boldsymbol{q}_0, \boldsymbol{q})$, defined as the ratio between the collective Hamiltonian and the norm kernel

$$h(\boldsymbol{q}_0, \boldsymbol{q}) = \frac{\langle \phi(\boldsymbol{q}_0) | \hat{H} | \phi(\boldsymbol{q}) \rangle}{\langle \phi(\boldsymbol{q}_0) | \phi(\boldsymbol{q}) \rangle}, \tag{33}$$

has also been calculated for all overlaps greater than $\epsilon_{\text{thresh}}$. In this work, only the kinetic and central terms of the interaction were included. The right panels of **Figure 1** presents the slices of the reduced Hamiltonian for the same cases as in its left panels. The relative variation of the reduced Hamiltonian (where the norm kernel above the threshold) is almost constant, being only 2% around the ground state and 1% for the elongated configuration. In addition to the overlaps rapid decrease discussed above, it numerically justifies the standard second-degree polynomial approximation of this quantity (a further study with all the terms of the interaction is, however, required). The bottom panels highlight a discontinuous behavior around $q_{20} \approx 130$ b. This specific discontinuity is due to the existence of two competing valleys in the three-dimensional PES obtained by adding the hexadecapole moment $q_{40} = \langle \hat{Q}_{40} \rangle$ as a collective DoF [38]. Such a discontinuity gives a similar label in the collective space to two HFB states that are far in the full many-body space. The **Figure 2** is an illustration of such a discontinuity in a two-dimensional PES embedded in a three-dimensional collective space. It is not possible to reduce the loop $\mathcal{C}$ to a point: the discontinuity is a hole whose edges are highlighted by the red line of **Figure 2**. Such a discontinuity may add spurious boundary effects in the description of the reaction of interest. It is especially the case when the discontinuity appears in an area of the collective space that gives important contributions to the targeted observables. Note that in approximate treatments such as the ones based on the Gaussian Overlap Approximation, discontinuities are always neglected, leading to a spurious connection between distant regions of the full many-body space.

It is possible to determine the time evolution of the weight function $f(\boldsymbol{q}, t)$ of the GHW ansatz (3). In cases where the size of the discretized space of the collective coordinate is still tractable, this task has been achieved through a direct diagonalization of the collective Hamiltonian [37]. For this two-dimensional application, the straightforward diagonalization involves a prohibitive numerical cost. It is still possible to use a Crank-Nicolson method to integrate in time the GHW equation (16). **Figure 3** presents a snapshot at time $t = 0.55$ zs of the quantity $\mathbb{P}(\boldsymbol{q}, t)$ defined as

$$\mathbb{P}(\boldsymbol{q}, t) \equiv \langle \Psi(t) | \left( |\phi(\boldsymbol{q})\rangle \langle \phi(\boldsymbol{q})| \right) |\Psi(t)\rangle. \tag{34}$$

This corresponds to the probability to measure the system in the state $|\phi(\boldsymbol{q})\rangle$ [3]. Even though the simulation was a proof-of-concept, we see that the bottom of the asymmetric valley is slightly more populated than the other parts of the PES near scission. This leads mostly to asymmetric fission fragments, which is in agreement with experimental data [39, 40]. The GCM wavefunction evolves in a slightly non-local way in the collective space (in the range of the width of the overlaps along $\boldsymbol{q} - \boldsymbol{q}'$), leading to non-zero probability

[3] Note that due to the non-orthogonality of the generator states its sum over all the points $\boldsymbol{q}$ is not equal to 1.

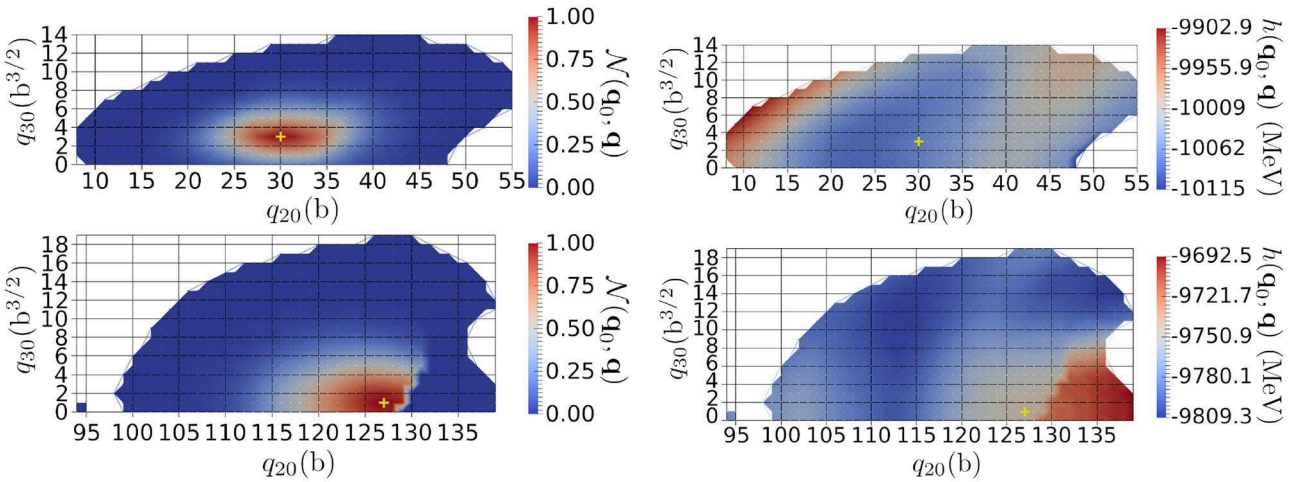


**FIGURE 1 | (Left)** Overlaps $\mathcal{N}(\boldsymbol{q}_0, \boldsymbol{q})$ as a function of $\boldsymbol{q}$ and where $\boldsymbol{q}_0 = (30, 3)$, in barn units, corresponds to the ground state (upper panel) or $\boldsymbol{q}_0 = (127, 1)$, in barn units, which corresponds to a point at higher elongation (lower panel). This was obtained for a $^{240}$Pu nucleus. The white parts correspond to values below a threshold of $1.0 \times 10^{-4}$. The yellow crosses correspond to $\boldsymbol{q}_0$. **(Right)** Same as the corresponding left panels for the reduced energy kernel $h(\boldsymbol{q}_0, \boldsymbol{q})$.

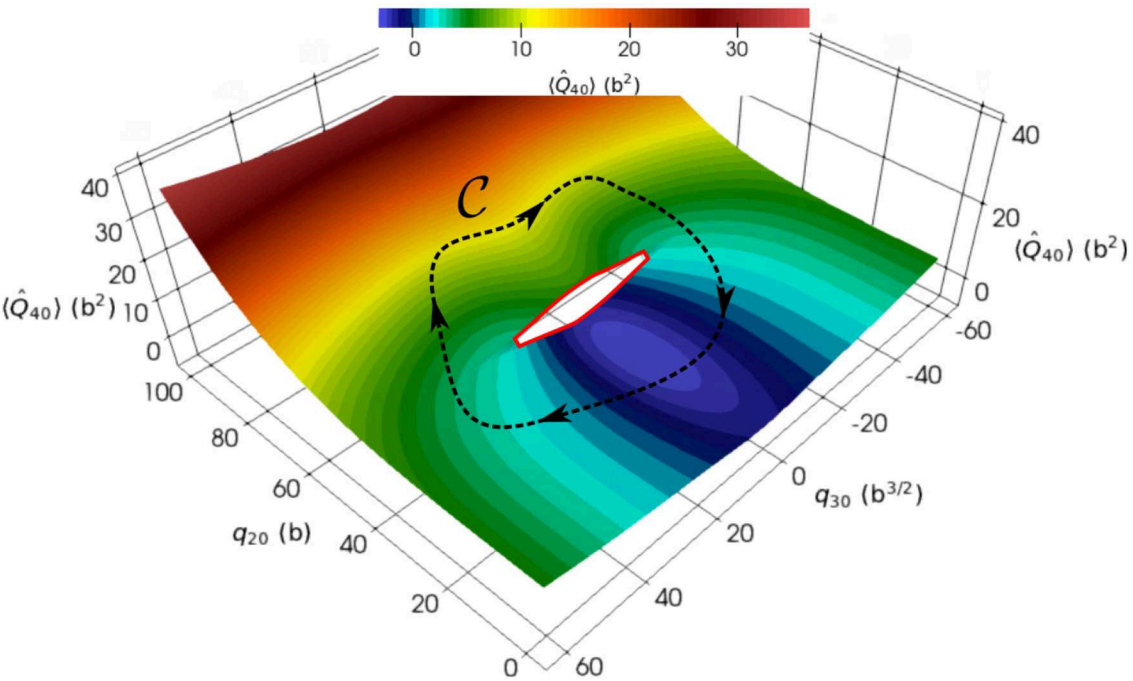


**FIGURE 2 |** Schematic representation of a discontinuity in two-dimensional calculations with constraints on $q_{20} = \langle\hat{Q}_{20}\rangle$ (x-axis) and $q_{30} = \langle\hat{Q}_{30}\rangle$ (y-axis). The z-axis and the color scale are associated with the average values of the unconstrained hexadecapole moment $\langle\hat{Q}_{40}\rangle$.

"drops" appearing and disappearing along the time-evolution of the system.

The most time-consuming part was the calculation of the norm and Hamiltonian kernels that required the use of 512 cpus for two weeks ($\sim$ 170,000 cpu.h). The calculation of the time-evolution of the weight function $f(\boldsymbol{q}, t)$ for times up to 0.55zs was done using 64 cpus for one week ($\sim$ 10,000 cpu.h). The short length of time for which the weight function was determined is not enough for the calculation of mass and charge probability distributions. A more realistic calculation would require at least 200,000 cpu.h, for the determination of the weight function up to 10zs only.

The principal difficulty of such an application stems from the big size of the discretized space of the collective coordinates

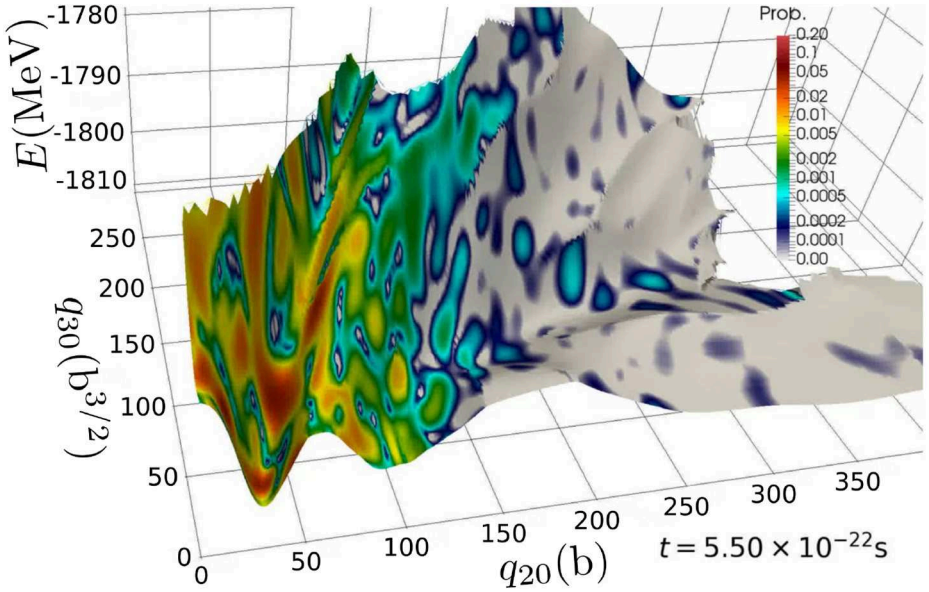


**FIGURE 3 |** The gray surface represents the generator states' HFB energy as a function of $q_{20}$ and $q_{30}$. On top of this, the color map gives the quantity $\mathbb{P}(\boldsymbol{q}, t = 0.550$ zs) in the same conditions than those of **Figure 1**.

(substantially bigger, for example, than in the case of the static GCM calculations for nuclear structure). This makes the computation of the norm and Hamiltonian kernel intensive but still embarrassingly parallel. Besides, in the case of fission, techniques to determine the post-scission observables of the fragments still need to be developed for the exact TDGCM. For instance, some simplifying hypotheses on the way to treat open domains of collective coordinates are commonly used under the Gaussian Overlap Approximation [41] but are no longer valid in the exact TDGCM framework.

## 3. GAUSSIAN OVERLAP APPROXIMATION (GOA)

In its straightforward application, the TDGCM leads to a non-local equation of motion that must be solved in a high-dimensional space in most of the practical calculations. As mentioned in Sec. 2, solving this equation involves a high numerical cost that strongly hurdles its applications in nuclear physics. Several approximate treatments of the TDGCM have been developed with the aim to build a local equation of motion for the collective wave function $g(\boldsymbol{q}, t)$ (cf. Equation 30). The Gaussian overlap approximation (GOA) is one of these approximations, which leverages the fact that the overlap and Hamiltonian kernels can, in some cases, be parameterized in terms of Gaussians of the variable $\boldsymbol{q}$. In its static form, the GOA has been largely used and applied for nuclear structure. Especially, it provides a nice bridge between the Bohr Hamiltonian equation that was first formulated in [42] and a quantum treatment based on the $3A + A$ nucleons degrees of freedom [43–47]. Extensive reviews of the static version of the GOA can be found in [16, 48]. We focus here on its time-dependent flavor.

### 3.1. TDGCM+GOA With Time Even Generator States

#### 3.1.1. Main Assumptions

In its most standard form, the GOA framework assumes the following situation:

1. we have a family of normed generator states $\{|\phi(\boldsymbol{q})\rangle\}$ parameterized by a vector of real coordinates $\boldsymbol{q} \in \Re^m$;
2. all the states of the set are time-even, i.e., they are their own symmetric by the time-reversal operation;
3. the function $\boldsymbol{q} \to |\phi(\boldsymbol{q})\rangle$ is continuous and twice derivable;
4. the overlap between two arbitrary generator states can be approximated by a Gaussian shape

$$\mathcal{N}(\boldsymbol{q}, \boldsymbol{q}') \simeq \exp\left[-\frac{1}{2}(\boldsymbol{q} - \boldsymbol{q}')^t G(\bar{\boldsymbol{q}})(\boldsymbol{q} - \boldsymbol{q}')\right], \qquad (35)$$

   with $\bar{\boldsymbol{q}} = (\boldsymbol{q} + \boldsymbol{q}')/2$ and $G(\bar{\boldsymbol{q}})$ a real positive definite matrix;
5. the Hamiltonian kernel can be approximated by

$$\mathcal{H}(\boldsymbol{q}, \boldsymbol{q}') \simeq \mathcal{N}(\boldsymbol{q}, \boldsymbol{q}')h(\boldsymbol{q}, \boldsymbol{q}'), \qquad (36)$$

   where $h(\boldsymbol{q}, \boldsymbol{q}')$, a polynomial of degree two in the collective variables $\boldsymbol{q}$ and $\boldsymbol{q}'$, is the reduced Hamiltonian.

In most applications of the TDGCM+GOA, the generator states are built as constrained Hartree-Fock-Bogoliubov states of even-even nuclei which ensures the time even property. The question is then: what are the situations where the Gaussian shape approximation is verified within a small error? Already from the

time-reversal symmetry, we can infer that the overlaps are real and symmetric in $(\boldsymbol{q}-\boldsymbol{q}')$. Therefore, the following relation is satisfied in the vicinity of $\boldsymbol{q}$

$$\left\langle \phi(\boldsymbol{q}+\frac{\boldsymbol{s}}{2})\middle|\phi(\boldsymbol{q}-\frac{\boldsymbol{s}}{2})\right\rangle = \exp\left[\ln\left(\left\langle \boldsymbol{q}+\frac{\boldsymbol{s}}{2}\middle|\boldsymbol{q}-\frac{\boldsymbol{s}}{2}\right\rangle\right)\right]. \tag{37}$$

A Taylor development of this expression up to order two in $\boldsymbol{s}$ already yields locally a Gaussian shape without any additional assumption

$$\left\langle \phi(\boldsymbol{q}+\frac{\boldsymbol{s}}{2})\middle|\phi(\boldsymbol{q}-\frac{\boldsymbol{s}}{2})\right\rangle = \exp\left[-\frac{1}{2}\boldsymbol{s}^t G(\boldsymbol{q})\boldsymbol{s}+o(\boldsymbol{s}^2)\right] \tag{38}$$

with

$$G_{ij}(\boldsymbol{q}) = \left\langle \partial_i\phi(\boldsymbol{q})\middle|\partial_j\phi(\boldsymbol{q})\right\rangle, \tag{39}$$

$$\left|\partial_i\phi(\boldsymbol{q})\right\rangle = \left.\frac{\partial\left|\phi(\boldsymbol{a})\right\rangle}{\partial \boldsymbol{a}_i}\right|_{\boldsymbol{q}}. \tag{40}$$

We used here some identities coming from the fact that generator states are normalized. In situations where the coordinates correspond to some collective deformations of the nucleus, it turns out that the Gaussian shape holds for larger values of $\boldsymbol{s}$. This is justified from the central limit theorem in [48] for Slater determinants or in [16] for Bogoliubov vacua. It especially holds for heavy nuclei.

Finally, note that although we limit here our description to the case of time-even generator states, it is possible to build a GOA framework without assuming this symmetry. Such a generalization can be found, for instance, in [48].

### 3.1.2. Equation of Motion

Starting from the GOA hypothesis, one can reduce the equation of motion (30) to a local equation involving the first and second-order derivatives of the collective wave function. In this section, we give only the main ideas to derive this local equation. For more exhaustive demonstrations, we refer the reader to [16, 48, 49].

In its historical version, the GOA framework assumes that the width of the Gaussian shape is constant. However, in most of the practical cases, this assumption is too restrictive. To overcome this issue, a series of papers published in the 70–80's generalized the GOA framework to account for a varying Gaussian width [49–51]. The idea is to perform a change of collective variables to recover the constant width case. The mapping between the new collective coordinates $\boldsymbol{\alpha}$ and the original ones $\boldsymbol{q}$ reads

$$\boldsymbol{\alpha}(\boldsymbol{q}) = \int_{\boldsymbol{a}\in C_0^{\boldsymbol{q}}} G^{\frac{1}{2}}(\boldsymbol{a})\,\mathrm{d}\boldsymbol{a} \tag{41}$$

where $C_0^{\boldsymbol{q}}$ is a path from the origin to $\boldsymbol{q}$. With this new labeling of the generator states, we get [4]

$$\left\langle \phi(\boldsymbol{\alpha})\middle|\phi(\boldsymbol{\alpha}')\right\rangle \simeq \exp\left[-\frac{1}{2}(\boldsymbol{\alpha}-\boldsymbol{\alpha}')^2\right]. \tag{42}$$

[4] Note that this assumes (i) that the integrals of $G^{1/2}(\boldsymbol{a})$ are independent of the integration path (ii) that its evaluation properly approximates the average of $G^{1/2}$ on the path at the central point of the path [51].

We can therefore perform all the derivations with the $\boldsymbol{\alpha}$ coordinates and make the inverse transformation on the final expressions only.

Starting with this simple form of the overlap, we seek an equation of motion involving a local collective Hamiltonian in the collective coordinate representation. The Gaussian shape of the norm kernel allows expressing its positive Hermitian square root analytically as

$$\mathcal{N}^{1/2}(\boldsymbol{\alpha},\boldsymbol{\alpha}') = C\cdot\exp\left[-(\boldsymbol{\alpha}-\boldsymbol{\alpha}')^2\right], \tag{43}$$

where the constant $C$ only depends on the dimension of the coordinate $\boldsymbol{\alpha}$. Additionally, there is a simple link, involving Hermite polynomials, between the successive derivatives of a Gaussian shape and its multiplication by polynomials. For instance, we have for the two first derivatives in $\boldsymbol{\alpha}$

$$\frac{\partial\mathcal{N}^{1/2}}{\partial\boldsymbol{\alpha}_k} = -2(\boldsymbol{\alpha}_k-\boldsymbol{\alpha'}_k)\mathcal{N}^{1/2}, \tag{44}$$

$$\frac{\partial^2\mathcal{N}^{1/2}}{\partial\boldsymbol{\alpha}_k\partial\boldsymbol{\alpha}_l} = [-2\delta_{kl}+4(\boldsymbol{\alpha}_k-\boldsymbol{\alpha}'_k)(\boldsymbol{\alpha}_l-\boldsymbol{\alpha}'_l)]\mathcal{N}^{1/2}. \tag{45}$$

In the following, we build a local collective Hamiltonian. After the change of variable (41), the Hamiltonian kernel between two arbitrary GHW states reads

$$\begin{aligned}&\left\langle\Psi\middle|\hat{H}\middle|\Phi\right\rangle \\ &= \int_{\boldsymbol{\alpha}\boldsymbol{\alpha}'\boldsymbol{\xi}} f^{\star}_{\Psi}(\boldsymbol{\alpha})\mathcal{N}^{1/2}(\boldsymbol{\alpha},\boldsymbol{\xi})h(\boldsymbol{\alpha},\boldsymbol{\alpha}')\mathcal{N}^{1/2}(\boldsymbol{\xi},\boldsymbol{\alpha}')f_{\Phi}(\boldsymbol{\alpha}')\,\mathrm{d}\boldsymbol{\alpha}\,\mathrm{d}\boldsymbol{\alpha}'\,\mathrm{d}\boldsymbol{\xi}.\end{aligned} \tag{46}$$

By assuming that the reduced Hamiltonian is a second-degree polynomial, we can write down for any point $\boldsymbol{\xi}$

$$\begin{aligned}h(\boldsymbol{\alpha},\boldsymbol{\alpha}') &= h(\boldsymbol{\xi},\boldsymbol{\xi}) + h_{\boldsymbol{\alpha}}(\boldsymbol{\alpha}-\boldsymbol{\xi}) + h_{\boldsymbol{\alpha}'}(\boldsymbol{\alpha}'-\boldsymbol{\xi}) \\ &+ \frac{1}{2}\left[h_{\boldsymbol{\alpha}\boldsymbol{\alpha}}(\boldsymbol{\alpha}-\boldsymbol{\xi})^2 + 2h_{\boldsymbol{\alpha}\boldsymbol{\alpha}'}(\boldsymbol{\alpha}-\boldsymbol{\xi})(\boldsymbol{\alpha}'-\boldsymbol{\xi}) + h_{\boldsymbol{\alpha}'\boldsymbol{\alpha}'}(\boldsymbol{\alpha}'-\boldsymbol{\xi})^2\right],\end{aligned} \tag{47}$$

where $h_{\boldsymbol{\alpha}}$ is a shorthand notation for the vector of the first derivatives of the reduced Hamiltonian estimated at $\boldsymbol{\xi}$

$$h_{\boldsymbol{\alpha}} \equiv \left(\left.\frac{\partial h(\boldsymbol{\alpha},\boldsymbol{\alpha}')}{\partial\boldsymbol{\alpha}_1}\right|_{\boldsymbol{\alpha}=\boldsymbol{\alpha}'=\boldsymbol{\xi}},\ldots,\left.\frac{\partial h(\boldsymbol{\alpha},\boldsymbol{\alpha}')}{\partial\boldsymbol{\alpha}_m}\right|_{\boldsymbol{\alpha}=\boldsymbol{\alpha}'=\boldsymbol{\xi}}\right). \tag{48}$$

Similarly $h_{\boldsymbol{\alpha}\boldsymbol{\alpha}}$, $h_{\boldsymbol{\alpha}\boldsymbol{\alpha}'}$, and $h_{\boldsymbol{\alpha}'\boldsymbol{\alpha}'}$ are the tensors of second derivatives with respect to the collective coordinates and evaluated at point $\boldsymbol{\xi}$. The idea is then to inject this local development into equation (46). Using the relation (44), we express the reduced kernel as a local operator containing derivatives acting on the right-hand side $\mathcal{N}^{1/2}$. Finally, after rearranging all the terms and performing some integrations by parts, we obtain the expected result

$$\left\langle\Psi\middle|\hat{H}\middle|\Phi\right\rangle = \int_{\boldsymbol{\alpha}\boldsymbol{\alpha}'} g^{\star}_{\Psi}(\boldsymbol{\alpha})\tilde{\mathcal{H}}(\boldsymbol{\alpha})\delta(\boldsymbol{\alpha}-\boldsymbol{\alpha}')g_{\Phi}(\boldsymbol{\alpha}')\,\mathrm{d}\boldsymbol{\alpha}\,\mathrm{d}\boldsymbol{\alpha}'. \tag{49}$$

The identification of this expression with (29) shows that the collective Hamiltonian is local. It reduces to a standard kinetic-plus-potential Hamiltonian acting on the collective wave function

$$\tilde{\mathcal{H}}(\boldsymbol{\alpha}) = -\frac{\hbar^2}{2}\nabla_{\boldsymbol{\alpha}} B(\boldsymbol{\alpha})\nabla_{\boldsymbol{\alpha}} + V(\boldsymbol{\alpha}). \tag{50}$$

The potential and inertia matrices in this coordinate representation are [5]

$$\begin{aligned} V(\boldsymbol{\alpha}) &= h(\boldsymbol{\alpha},\boldsymbol{\alpha}) - \frac{1}{2}\,\mathrm{Tr}(h_{\boldsymbol{\alpha}\boldsymbol{\alpha}'}) \\ B(\boldsymbol{\alpha}) &= \frac{1}{2\hbar^2}(h_{\boldsymbol{\alpha}\boldsymbol{\alpha}'} - h_{\boldsymbol{\alpha}\boldsymbol{\alpha}}). \end{aligned} \tag{51}$$

Injecting this expression of the collective Hamiltonian into (30) and solving the resulting equation gives the time-evolution of the unknown function $g(\boldsymbol{\alpha})$. The ultimate step is to transform back this equation of motion to another one acting on the original set of coordinates $\boldsymbol{q}$. Doing so, we get the same equation with a transformed local collective Hamiltonian

$$\tilde{\mathcal{H}}(\boldsymbol{q}) = -\frac{\hbar^2}{2\sqrt{\gamma(\boldsymbol{q})}}\nabla_{\boldsymbol{q}}\left[\sqrt{\gamma(\boldsymbol{q})}B(\boldsymbol{q})\right]\nabla_{\boldsymbol{q}} + V(\boldsymbol{q}). \tag{52}$$

The new collective Hamiltonian involves a metric $\gamma(\boldsymbol{q})$ defined by

$$\gamma(\boldsymbol{q}) = \det\left(G(\boldsymbol{q})\right). \tag{53}$$

The inertia tensor takes the more involved form

$$B(\boldsymbol{q}) = \frac{1}{2\hbar^2}G^{-1}(\boldsymbol{q})\Big[h_{\boldsymbol{q}\boldsymbol{q}'} - h_{\boldsymbol{q}\boldsymbol{q}} + \sum_n \Gamma^n(\boldsymbol{q})h_{\boldsymbol{q}_n}\Big]G^{-1}(\boldsymbol{q}). \tag{54}$$

The notation $\Gamma^n(\boldsymbol{q})$ stands for the Christoffel symbol. It is a matrix related to $G(\boldsymbol{q})$ through the relation

$$\Gamma^n_{kl}(\boldsymbol{q}) = \frac{1}{2}\sum_i G^{-1}_{ni}\left(\frac{\partial G_{ki}}{\partial \boldsymbol{q}_l} + \frac{\partial G_{il}}{\partial \boldsymbol{q}_k} - \frac{\partial G_{lk}}{\partial \boldsymbol{q}_i}\right). \tag{55}$$

Finally, the potential becomes in this set of coordinate

$$V(\boldsymbol{q}) = h(\boldsymbol{q},\boldsymbol{q}) - \frac{1}{2}\,\mathrm{Tr}\left(G^{-1}(\boldsymbol{q})h_{\boldsymbol{q}\boldsymbol{q}'}\right). \tag{56}$$

The first term is the HFB energy of the generator state $\left|\phi(\boldsymbol{q})\right\rangle$. The second term is a zero-point correction that contains second derivatives of the reduced Hamiltonian. With some additional work, it is possible to express this zero-point correction $\epsilon_{\mathrm{ZPE}}$ in a slightly more practical form that involves the inertia tensor and second derivatives of the energy $h(\boldsymbol{q},\boldsymbol{q})$ only

$$\begin{aligned} \epsilon_{\mathrm{ZPE}}(\boldsymbol{q}) \;=\; & -\frac{\hbar^2}{2}\,\mathrm{Tr}(BG) - \frac{1}{8}\,\mathrm{Tr}\left(G^{-1}\frac{\partial^2 h(\boldsymbol{q},\boldsymbol{q})}{\partial \boldsymbol{q}^2}\right) \\ & + \frac{1}{8}\,\mathrm{Tr}\left(G^{-1}\sum_n \Gamma^n \frac{\partial h(\boldsymbol{q},\boldsymbol{q})}{\partial a_n}\right). \end{aligned} \tag{57}$$

[5] Note that some higher-order correction terms in the potential are neglected here [see [48] for more details].

The equation of evolution (30) along with the expression of the collective Hamiltonian (52) and its components (53), (56), and (54) define the dynamics of the system in the TDGCM+GOA framework.

### 3.1.3. Inertia and Metric

The inertia tensor and the metric are quantities that depend on the derivatives of the generator states and the reduced Hamiltonian. One possibility could be to determine these derivatives numerically, for instance, with a finite difference method. In the standard situation where the generator states are constrained HFB solutions, one can find an analytical expression of the inertia and the metric. We recall here this result at any point $\boldsymbol{q}$

$$G = \frac{1}{2}[\mathbf{M}^{(1)}]^{-1}\mathbf{M}^{(2)}[\mathbf{M}^{(1)}]^{-1}. \tag{58}$$

$$B = \mathbf{M}^{(1)}[\mathbf{M}^{(2)}]^{-1}\tilde{\mathbf{M}}^{(1)}[\mathbf{M}^{(2)}]^{-1}\mathbf{M}^{(1)}. \tag{59}$$

The moments $\mathbf{M}^{(K)}$ and $\tilde{\mathbf{M}}^{(K)}$ involve the QRPA matrix $\mathcal{M}$ of the state $\left|\phi(\boldsymbol{q})\right\rangle$ and are defined in **Appendix 7.1**. For the complete derivation of these results, we refer the reader to [52] and references therein. Note that this result neglects the term involving the Christoffel symbol in the inertia. The argument for this approximation relies on the slow variation of the metric according to the collective coordinates. We are not aware of the systematic verification of the validity of this assumption in applications.

In all TDGCM+GOA practical applications, the so-called perturbative cranking approximation is used to avoid a costly inversion of the QRPA matrix required to compute the metric and inertia. It consists in approximating the QRPA matrix by a diagonal part only, in the quasiparticle basis that diagonalizes the generalized density matrix of $\left|\phi(\boldsymbol{q})\right\rangle$. This gives a simple and well known form for the moments $\mathbf{M}^{(K)}$

$$M^{(K)}_{ij} = \tilde{M}^{(K)}_{ij} = \mathfrak{Re}\sum_{\mu\nu}\frac{\langle\mu\nu|\hat{Q}_i|\phi(\boldsymbol{q})\rangle\langle\phi(\boldsymbol{q})|\hat{Q}_j|\mu\nu\rangle}{(E_\mu + E_\nu)^K}, \tag{60}$$

where $|\mu\nu\rangle$ is a two quasiparticles excitation built on top of the generator state, and $E_\mu$ and $E_\nu$ are the corresponding quasiparticle energies.

The GCM+GOA framework unambiguously defines the metric and inertia as functions of the successive derivatives of the generator states and reduced Hamiltonian. However, it is known that this inertia and its approximate perturbative cranking estimation is too low to describe several situations correctly. One example is the case of a translation motion [48]. Several studies compare the GOA inertia with inertia provided by other theories yielding an equivalent collective equation of motion, such as quantized ATDHFB [53–55]. In [56], the authors extend the TDGCM+GOA framework by introducing conjugate coordinates that bring time odd components into the generator states. In particular, they show that the resulting collective Hamiltonian takes the same form as Equation (52) but where the ATDHFB inertia replaces the GOA inertia. This justifies the

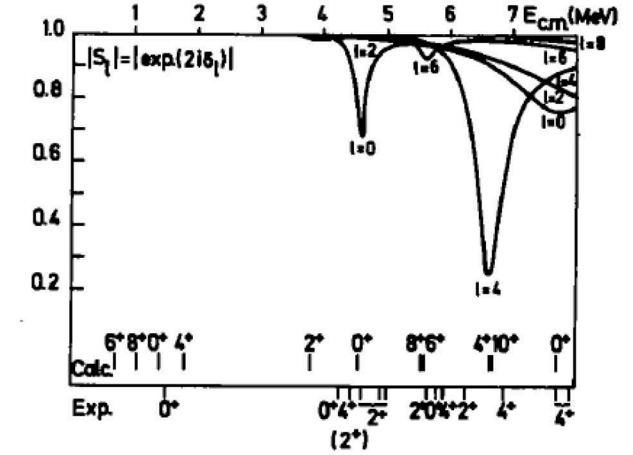


**FIGURE 4 |** Reflection coefficients as a function of the center of mass energy (in MeV) of a $^{12}C+^{12}C$ head-on collision. The position of the resonances estimated from a GCM+GOA framework are compared to a set of experimental data. Figure taken from [57].

common practice of using the ATDHFB inertia when solving the collective equation of motion.

## 3.2. Applications in Nuclear Reactions

### 3.2.1. Low Energy Ion Collisions

The force of TDGCM+GOA is its versatility in the choice of collective coordinates and its ability to treat in the same framework the nucleons DoFs as well as more collective DoFs. It seems an appropriate way to tackle the dynamics of low energy ion collisions where the principal degree of freedom is the relative distance between the two reaction partners and where the collision affects the internal organization of the nucleons. It is possible to build a family of generator states along this line, describing the two reaction partners and parameterizing them by their relative distance. Several papers followed this idea during the 1980s. In particular, Berger and Gogny [57] treated the frontal collision of $^{12}C+^{12}C$ within a GCM+GOA approach. This kind of study focuses on the determination of the cross-section resonances for some specific output channels of the reaction. **Figure 4** shows a typical result where the resulting positions of the resonances are compared to available experimental data. The predictions give a rough estimation of the position of the $0^+$ resonances, but they mostly fail to reproduce the presence of other resonances and their energy spacing. Many lacunae of the theory could explain such discrepancy, including the rough treatment of angular momentum, the breaking of some symmetries, or the mostly adiabatic characteristic of the GCM built on constrained HFB solutions.

Other similar studies have been performed on the base of the GCM (without the GOA) and have made the connection to the resonating group method. Baye and Salmon looked at the $^{16}O+^{40}Ca$ back angles scattering [58] along with the work of Friedrich et al. [59]. Also, Goeke et al. studied the $^{16}O+^{16}O$ collision in the framework of the quantized adiabatic time-dependent Hartree-Fock approach which yields a collective equation of motion identical to the one of TDGCM+GOA [60].

After this series of applications, treating collisions with the TDGCM+GOA framework was progressively abandoned to the profit of other methods such as the time-dependent Hartree-Fock plus pairing [61]. One difficulty that could explain this transition is the numerical cost required to build the generator states at the self-consistent mean-field level (note that this cost is nowadays completely acceptable). Beyond this, deeper problems raised, for instance, by the conservation of the total angular momentum of the collision or the generation of a continuous manifold of generator states appear with this method. Overall, the resulting cross-sections give only rough and qualitative estimations of the experimental data. The position of resonances, as well as the absolute value of cross-sections, are both observables that are very challenging to predict due to their extreme sensitivity to the kinematics of the reaction as well as the internal structure of the nuclei.

### 3.2.2. Fission Dynamics

The prediction of the fission fragments characteristics from a dynamical description is a domain where the TDGCM+GOA performs successfully. Fission involves heavy nuclei and begins with large collective motions that are mostly adiabatic. These two factors make the TDGCM+GOA framework built on constrained HFB solutions a suitable candidate. Moreover, the important width of the measured fission yields is the fingerprint of large quantum fluctuations of the one-body density of the compound system. Handling these fluctuations is precisely the purpose of the GCM.

The quest to predict fission yields from a dynamical TDGCM+GOA calculation began in the 1980s with the work of Berger et al. exploring the rupture of the neck between prefragments in terms of different collective coordinates [62, 63]. The first calculation of the mass distribution of fission fragments was later on performed among the same group for $^{238}U$ [41]. The authors have described the fissioning system's dynamics using the two collective coordinates: $q_{20}$ and $q_{30}$ associated with the quadrupole and octupole moments of the compound nucleus. The [64] reports the same technique applied to a few other actinides with a qualitative reproduction of the experimental values. Younes and Gogny further proposed an alternative set of collective variables in [65]. Still, an impediment to this approach was its numerical cost, from the determination of the generator states (up to 40,000 states in a 2-dimensional description) to the time integration of the collective Schrödinger equation. The development of new tools based on state-of-the-art numerical methods enables today's continuation of this work. For instance, the code FELIX [66, 67] solves the collective GOA dynamics efficiently based on a spectral element method. Also, the use of Bayesian processes to determine the best-suited parameters of a harmonic oscillator basis induced a significant speedup of some Hartree-Fock-Bogoliubov solvers.

In the last couple of years, we have seen a fast increase in the number of fission studies relying on this technique. All papers focused on the actinide region emphasize similar

results. In this region, the potential energy landscape presents mostly one asymmetric fission valley. The exact topology of this surface reflects the internal organization of the nucleons that would correspond to the shell effects in a microscopic-macroscopic picture. By starting from a collective state localized in the low deformation first potential well, the dynamics mostly populates the configurations of the asymmetric channel. The left panel of **Figure 5** shows the resulting yields obtained on an experimentally well-known nucleus, namely $^{240}$Pu.

The TDGCM+GOA captures within a few mass units the position of the asymmetric peaks that are, in fact, mostly determined by the position of the asymmetric valley in the collective space. A similar quality of results has been obtained with the same method for other actinides, such as $^{236}$U or $^{252}$Cf. Finally, this framework seems to be able to describe the transitions between symmetric and asymmetric fissions that are measured outside of the actinide region. The left panel of **Figure 6** shows the prediction versus experiment comparison of such a transition in the neutron-rich Fermium isotopes [70]. In this chain of isotopes, the addition of a few neutrons to $^{254}$Fm changes the dominant fragmentation mode completely. This can be interpreted as different shell effects occurring because of the new neutrons, that change the potential energy of the intermediate configurations leading to fission. This perturbation favors the population of the symmetric mode for $^{258}$Fm.

Several ingredients of the TDGCM+GOA framework for fission are still not adequately controlled and bring significant uncertainties on its predictions. Zdeb et al. [71] investigated in detail the impact of the choice of the initial state of the dynamics on the fission observables. They showed in particular that the global features of the fission yields (mostly the position and width of the peaks) are quite resilient to changes in the energy or the parity of the initial state. Furthermore, Tao et al. computed the fission yields from a relativistic mean-field approach [69] and looked at the sensitivity of the results to the pairing strength. The right panel of **Figure 5** gives a clue of their results, showing the variation of the charge yields induced by a 10% variation of their nominal pairing strength in the case of the multimodal fission of $^{226}$Th. For this nucleus, we see that the pairing strength is an essential factor that drives the ratio between the yields of the symmetric and asymmetric modes. Finally, the same team explored the inclusion of temperature into the generator states as a way to better account for the diabatic aspects of the dynamics [72, 73]. The **Figure 6** (right panel) shows that warming up the generator states changes slightly the topology of the potential energy surface. Increasing the temperature generally tends to smear out the shell effects and the structures in the potential energy surface. In the case of $^{226}$Th, it favors the symmetric fission and reduces the height of the asymmetric peaks of the mass yields by a factor $\simeq$1.4.

Other components or approximations of the TDGCM+GOA, such as the perturbative cranking approximation for the collective inertia, may also bring their source of bias and uncertainty on the prediction.

## 3.3. Main Limitations

Despite its success in determining the fission fragment distribution, the TDGCM+GOA framework suffers from several shortcomings.

First, on the same ground as the exact TDGCM, its derivation relies on the knowledge of a many-body Hamiltonian. However, in all practical applications, it is used with an energy density functional (cf. section 2.5). Indeed, the GOA method does not require an explicit calculation of the off-diagonal elements of the energy kernel responsible for divergent behavior in GCM. However, the GOA's formal construction still depends on the existence and sound mathematical definition of these matrix elements to be a valid framework. In that sense, the GOA suffers from the same flaws as the exact TDGCM concerning the use of energy density functionals.

A second issue comes from the requirement that the function $\boldsymbol{q} \rightarrow \left|\phi(\boldsymbol{q})\right\rangle$ is continuous and twice differentiable. The latter is a necessary condition to develop the formalism and, in particular, to compute the GOA metric and inertia. However, the standard construction of the family of generator states from constrained HFB solutions does not guaranty this property [38]. Different studies highlight discontinuities of this function in the treatment of fission, similar to the one visible in **Figure 1**. In the common $(q_{20}, q_{30})$ space of collective coordinates, a line of discontinuity is present in the vicinity of scission configurations. This feature limits the domain of validity of the collective dynamics and ultimately prevents the determination of the fission fragments characteristics after their complete separation.

Finally, we have seen that most of the current applications of TDGCM+GOA rely on constrained HFB solutions for the generator states. Certain diabatic aspects of the nuclear dynamics are then difficult to grasp with the corresponding GHW many-body wave function. This is the case of the dissipation as well as the viscosity of the shape dynamics predicted with Langevin methods [74, 75] or time-dependent Hartree-Fock-Bogoliubov calculations. Past and ongoing studies to improve the description of these effects include efforts to quantize the Langevin equation [76, 77], to couple the Langevin dynamics with the GCM [78] or to couple TDHFB trajectories with TDGCM [79]. Other techniques, such as the SCIM and TDGCM based on time-dependent generator states, are also promising avenues that we discuss in this review.

# 4. SCHRÖDINGER COLLECTIVE-INTRINSIC MODEL (SCIM)

Intrinsic degrees of freedom are often neglected in the microscopic modeling of the dynamics of reactions. However, including intrinsic degrees of freedom in a static GCM framework has already been performed, for instance, in [80, 81]. These studies show that taking into account two-quasiparticle excitations significantly improves the prediction of high spin levels, such as the $6^+$ states in medium mass isotopes as well as the prediction for $\beta$ excitation bands and its transition probabilities to other rotational bands in heavier systems. On

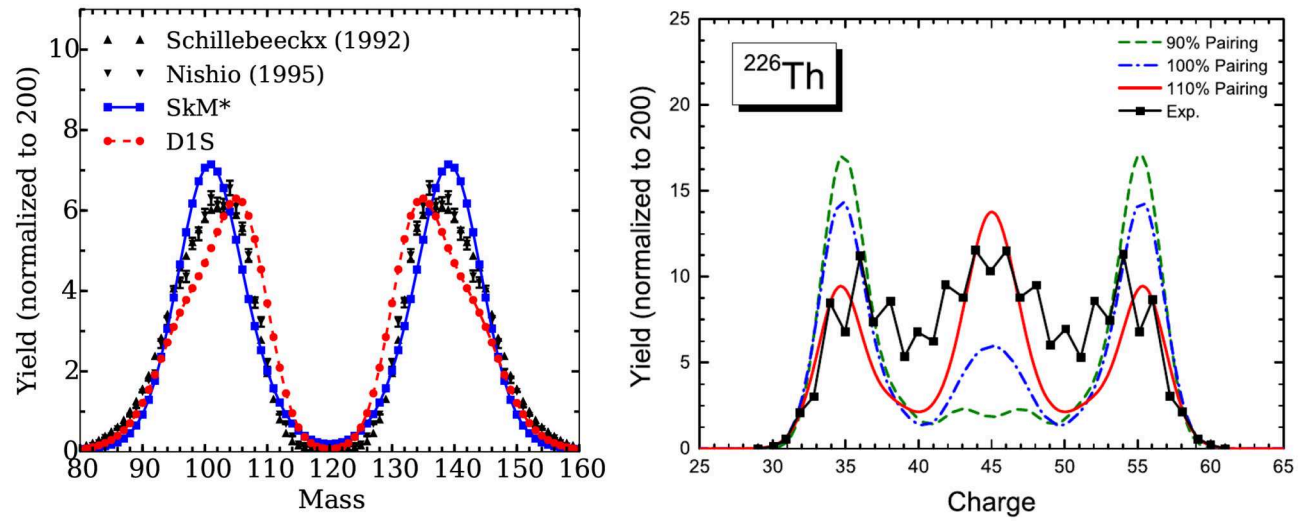


**FIGURE 5 | (Left)** Fragment mass distribution for the low energy neutron induced fission $^{239}$Pu(n,f). Two TDGCM results obtained with the Gogny D1S and Skyrme SkM* effective interactions are compared to two sets of experimental data. Reprinted figure with permission from [68]. Copyright 2016 by the American Physical Society. **(Right)** Fragment charge distribution obtained for a low energy fission of $^{226}$Th. The TDGCM+GOA results based on the relativistic mean field PC-PK1 with different pairing strengths are compared to experimental data (black line with points). Reprinted figure with permission from [69]. Copyright 2017 by the American Physical Society.

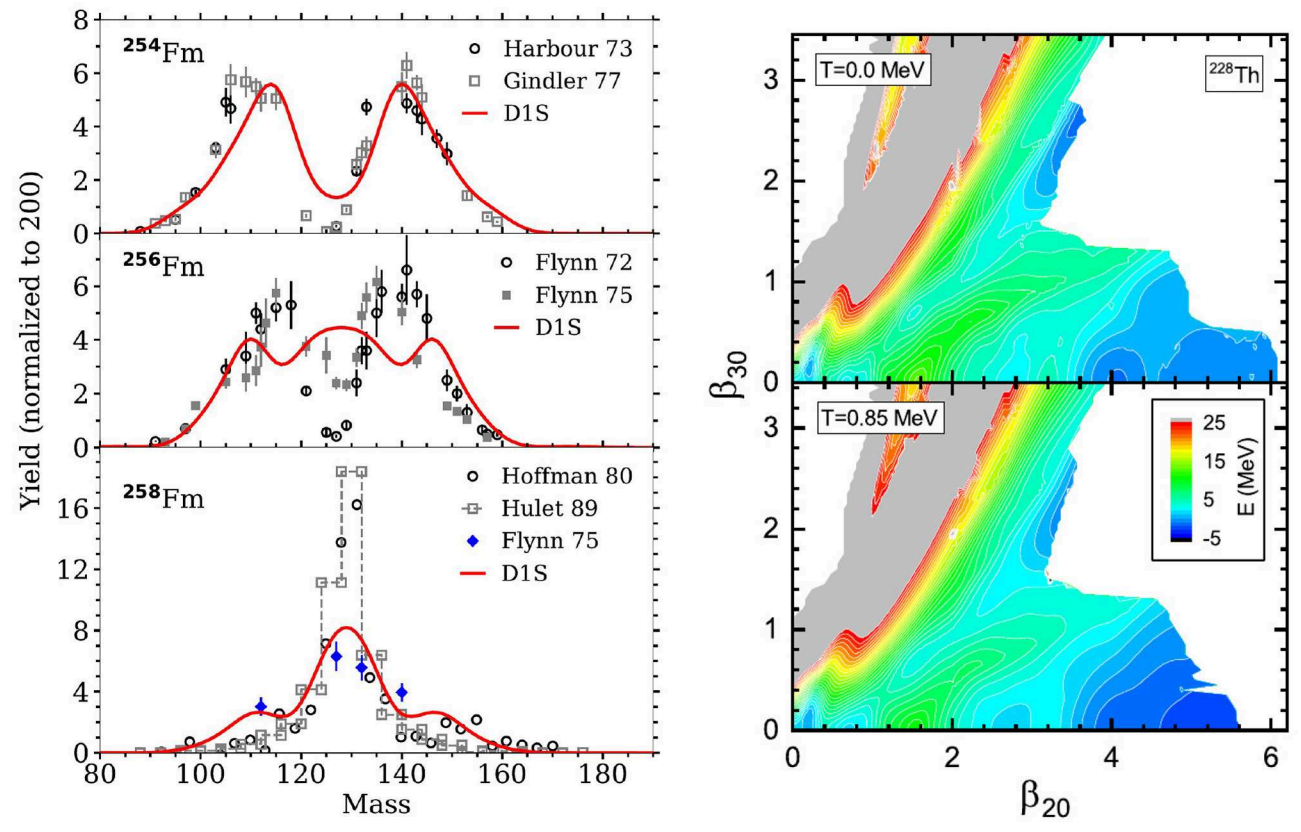


**FIGURE 6 | (Left)** Primary fragment mass yields of Fermium isotopes obtained with the Gogny D1S effective interaction and compared with various experimental data sets after neutron evaporation. The open symbols stand for experimental data associated with spontaneous fission, whereas full symbols are related to thermal neutron-induced fission. Reprinted figure with permission from [70]. Copyright 2019 by the American Physical Society. **(Right)** Effect of temperature on the free energy surface of $^{228}$Th in the plane of deformation ($\beta_{20}$, $\beta_{30}$). Reprinted figure with permission from [73]. Copyright 2019 by the American Physical Society.

another topic, the TDHFB/SLDA methods [82, 83] and semi-classical approaches to the description of fission [84, 85] clue that dissipation (and therefore intrinsic degrees of freedom) are necessary to describe the fission fragments properties correctly. Therefore, a few collective degrees of freedom are not enough to adequately model such a reaction. Several paths can be taken to overcome this limitation without resorting to the determination of an exact solution of the GHW Equation (16). A strategy in development consists in using the TDGCM+GOA with finite-temperature inertia tensors and collective potential. However, the inclusion of statistical mechanics on top of the TDGCM framework still lacks a solid formalization. The idea of the Schrödinger Collective-Intrinsic Model (SCIM) [86–88] is to derive a local Schrodinger-like equation from a generalization of the GHW ansatz (3) that contains individual quasiparticle degrees of freedom. The transformation to a local equation relies on the symmetric moment expansion method [89, 90]. The full SCIM formalism can be found in [86–88] in the stationary case. However, we would like to present here a derivation of the time-dependent SCIM equations consistent with the ones given for the TDGCM and the TDGCM+GOA equations.

## 4.1. Main Assumptions

The SCIM involves four main assumptions. The first one is the expression of the state $|\Psi(t)\rangle$ that describes the evolution of the many-body wavefunction associated with the reaction. This expression is assumed to be a generalization of the GHW ansatz

$$|\Psi(t)\rangle = \sum_k \int \mathrm{d}\boldsymbol{q}\, |\phi_k(\boldsymbol{q})\rangle f_k(\boldsymbol{q}, t). \tag{61}$$

In [87], the authors consider a family of generator states associated with one collective coordinate $q$ defined as the quadrupole moment of the system. The index $k$ iterates over the labels of the sheets of collective space which correspond, in this case, to two quasiparticle excitations. **Figure 7** shows the evolution of the excitation energies of the non-adiabatic points of the potential energy surface of $^{236}$U.

Note that the scope of expression (61) is broader than the only explicit inclusion of intrinsic DoF in the formalism. For example, it is used for $K$-mixing in the context of stationary angular-momentum-projected GCM on a triaxial configuration basis. In this case, the index $k$ iterates over the values of $K$. The second assumption is the analyticity of the weight function $f$ of the GCM ansatz (61) that allows the symmetrization of the GHW equations. The third assumption is the vanishing of the weight function and its derivatives at the boundaries of the integration domain. An implicit corollary of this property is the continuity of the functions $\boldsymbol{q} \to |\phi_k(\boldsymbol{q})\rangle$. It turns out that this assumption is in practice not verified for a broad range of applications, for example, in the actinide region, as emphasized in section 3.3. These three assumptions lead to the symmetrized GHW equation

$$\sum_k \int \mathrm{d}\boldsymbol{s}\, e^{i\boldsymbol{s}\mathcal{P}/2} \left[ \mathcal{H}[\boldsymbol{s}]_{lk}(\boldsymbol{q}) - i\mathcal{N}[\boldsymbol{s}]_{lk}(\boldsymbol{q}) \frac{\mathrm{d}}{\mathrm{d}t} \right] e^{i\boldsymbol{s}\mathcal{P}/2} f_k(\boldsymbol{q}, t) = 0, \tag{62}$$

where the following notations are introduced

$$\mathcal{H}[\boldsymbol{s}]_{lk}(\boldsymbol{q}) = \mathcal{H}_{lk}(\boldsymbol{q} + \boldsymbol{s}/2, \boldsymbol{q} - \boldsymbol{s}/2) \tag{63}$$

$$\mathcal{N}[\boldsymbol{s}]_{lk}(\boldsymbol{q}) = \mathcal{N}_{lk}(\boldsymbol{q} + \boldsymbol{s}/2, \boldsymbol{q} - \boldsymbol{s}/2), \tag{64}$$

and where the Hermitian operator

$$\mathcal{P} = i\frac{\partial}{\partial \boldsymbol{q}} \tag{65}$$

corresponds to the conjugate moment associated with the collective variables. The symmetrized GHW equation can be written in a more compact operator format as

$$\int \mathrm{d}\boldsymbol{s}\, e^{i\boldsymbol{s}\mathcal{P}/2} \left[ \mathcal{H}[\boldsymbol{s}] - i\mathcal{N}[\boldsymbol{s}] \frac{\mathrm{d}}{\mathrm{d}t} \right] e^{i\boldsymbol{s}\mathcal{P}/2} \mathrm{f}(t) = 0, \tag{66}$$

where $\mathrm{f}(t)$ denotes the function $\boldsymbol{q} \mapsto f_k(\boldsymbol{q}, t)$. The fourth and last assumption of the SCIM is the validity of the truncation of the symmetric moment expansion (SME) of the norm and Hamiltonian kernels of (66) up to order two. It was, for instance, verified numerically in the context of the study [87]. The SME of $\mathcal{K} = \mathcal{N}, \mathcal{H}$, in the case of one collective variable,

$$\mathcal{K} = \sum_n \frac{1}{n!} \left\{ \mathcal{K}^{(n)}, \mathcal{P} \right\}^{(n)}, \tag{67}$$

is obtained through the properties of the so-called Symmetric Ordered Product of Operators (SOPO) $\left\{ \mathcal{K}^{(n)}, \mathcal{P} \right\}^{(n)}$ presented in **Appendix 8** where $\mathcal{K}^{(n)}$ is the moment of order $n$ of $\mathcal{K}[s]$ in the variable $s$

$$\mathcal{K}^{(n)} \equiv i^n \int \mathrm{d}s s^n \mathcal{K}[s]. \tag{68}$$

The properties of the SOPO used to obtain these expressions are listed in **Appendix 8**.

The expression (67) can be generalized to the case of $m$ collective variables,

$$\mathcal{K} = \sum_{\boldsymbol{n}} \frac{1}{\boldsymbol{n}!} \left\{ \mathcal{K}^{(\boldsymbol{n})}, \mathcal{P} \right\}^{(\boldsymbol{n})}, \tag{69}$$

where the index $\boldsymbol{n}$ iterates over all the $m$-tuples of positive integers and where we have introduced the following notations

$$\boldsymbol{n}! \equiv n_0! n_1! \cdots n_{m-1}! \tag{70}$$

$$\{\mathcal{K}, \mathcal{P}\}^{(\boldsymbol{n})} \equiv \left\{ \cdots \left\{ \{\mathcal{K}, \mathcal{P}_0\}^{(n_0)}, \mathcal{P}_1 \right\}^{(n_1)} \cdots, \mathcal{P}_{m-1} \right\}^{(n_{m-1})} \tag{71}$$

$$\mathcal{K}^{(\boldsymbol{n})} \equiv \int \mathrm{d}\boldsymbol{s} \left[ \prod_k (is_k)^{n_k} \right] \mathcal{K}[\boldsymbol{s}]. \tag{72}$$

Their second-order approximation in their SME development is then given by

$$\mathcal{N} \approx \sum_{\tilde{\boldsymbol{n}} \leq 2} \frac{1}{\boldsymbol{n}!} \left\{ \mathcal{N}^{(\boldsymbol{n})}, \mathcal{P} \right\}^{(\boldsymbol{n})} \tag{73}$$

$$\mathcal{H} \approx \sum_{\tilde{\boldsymbol{n}} \leq 2} \frac{1}{\boldsymbol{n}!} \left\{ \mathcal{H}^{(\boldsymbol{n})}, \mathcal{P} \right\}^{(\boldsymbol{n})}, \tag{74}$$

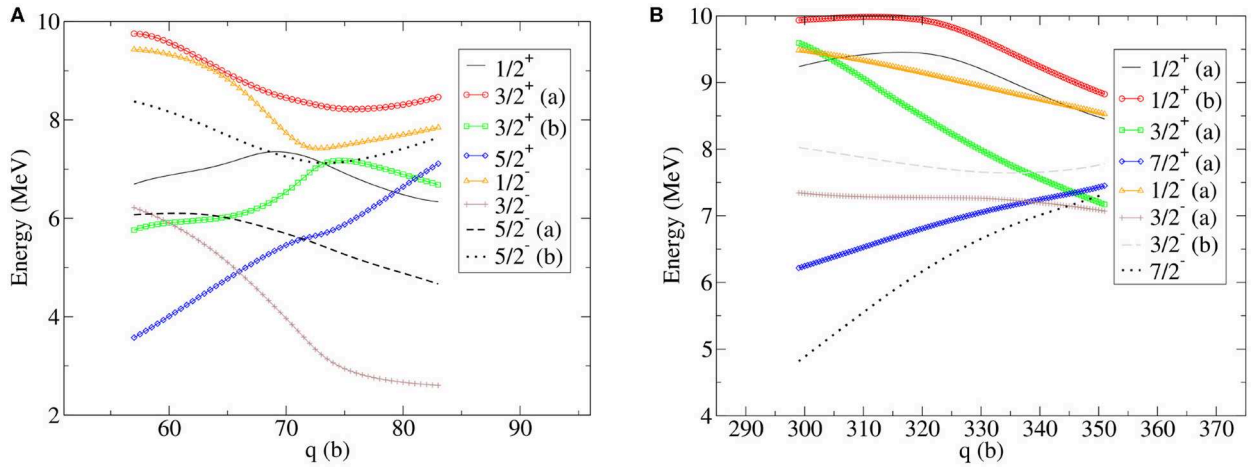


**FIGURE 7 |** (Color online) Excitation energies as a function of the quadrupole moment constraint $q$ and associated with 2-qp excitations of HFB states. The system under study is $^{236}$U around $\langle\hat{Q}_{20}\rangle = 70$ b **(A)** and $\langle\hat{Q}_{20}\rangle = 325$ b **(B)**. The figures are taken from [86].

where $\tilde{\boldsymbol{n}}$ is the sum of the elements of $\boldsymbol{n}$. In the one-dimensional case, the expressions reduce to.

$$\mathcal{N} \approx \sum_{n=0}^{2} \frac{1}{n!} \left\{\mathcal{N}^{(n)}, \mathcal{P}\right\}^{(n)}, \tag{75}$$

$$\mathcal{H} \approx \sum_{n=0}^{2} \frac{1}{n!} \left\{\mathcal{H}^{(n)}, \mathcal{P}\right\}^{(n)}. \tag{76}$$

## 4.2. Schrodinger Collective-Intrinsic Equation

The Schrödinger-like expression of the SCIM equations is given by

$$\left[\mathcal{H}^{\mathrm{CI}} - i\frac{\mathrm{d}}{\mathrm{d}t}\right] \mathrm{g}(t) = 0, \tag{77}$$

where $\mathrm{g}(t)$ is defined according to

$$\mathrm{g}(t) = \mathcal{N}^{1/2}\mathrm{f}(t) \tag{78}$$

and normalized as

$$\mathrm{g}^{\dagger}(t)\mathrm{g}(t) = \int \mathrm{d}\boldsymbol{q} g^{\star}(\boldsymbol{q}, t) g(\boldsymbol{q}, t) = 1. \tag{79}$$

The operator $\mathcal{N}^{1/2}$ is the only positive-definite hermitian square-root of $\mathcal{N}^{1/2}$ and $\mathcal{N}^{-1/2}$ is the inverse of the latter. Finally, using the hermicity of $\mathcal{N}^{-1/2}$, the collective-intrinsic Hamiltonian $\mathcal{H}^{\mathrm{CI}}$ has the expression

$$\mathcal{H}^{\mathrm{CI}} = \mathcal{N}^{-1/2}\mathcal{H}\mathcal{N}^{-1/2}. \tag{80}$$

An explicit form for $\mathcal{H}^{\mathrm{CI}}(q)$ is given by

$$\mathcal{H}^{\mathrm{CI}} = \frac{1}{2}\{\mathcal{B}, \mathcal{P}\}^{(2)} + \{\mathcal{T}, \mathcal{P}\}^{(1)} + \mathcal{V}, \tag{81}$$

where the expressions of $\mathcal{U} = \mathcal{B}/2, \mathcal{T}$ and $\mathcal{V}$ are given in [86–88]. By analogy with the TDGCM+GOA collective Hamiltonian (52), the first term of (81) can be interpreted as a kinetic term and $\mathcal{B}$ as the inertia tensor, related to the mass tensor $\mathcal{M}$ through the relation

$$\mathcal{B} = \mathcal{M}^{-1}. \tag{82}$$

Similarly, the third term of (81) is comparable to the potential term of the TDGCM+GOA. However, the last term

$$\{\mathcal{T}, \mathcal{P}\}^{(1)} = \frac{1}{2}\left[\mathcal{T}\frac{\partial}{\partial q} + \frac{\partial}{\partial q}\mathcal{T}\right], \tag{83}$$

contains first-order derivatives according to the collective variable, at the opposite of the TDGCM+GOA. In the Langevin equations, such a term corresponds to viscosity and arises in the SCIM from the coupling between intrinsic and collective degrees of freedom.

## 4.3. Choice of Quasiparticle Excitations

In [86–88], the generator states consist in

- constrained HFB states $\left|\phi_{k=0}(q = \langle\hat{Q}_{20}\rangle)\right\rangle$ describing the compound system at different elongations,
- intrinsic excitations of these HFB states

$$\left|\phi_{k>0}(q)\right\rangle = \hat{X}(q)_k \left|\phi_0(q)\right\rangle. \tag{84}$$

Note that the specific expression of $\hat{X}(q)_k$ is never used in the derivations of the Schrodinger-like equation, and it is only assumed that all the states in the collective space are time-reversal to avoid complex-valued overlaps. In practice, the intrinsic excitations taken into account in the existing developments of SCIM are considering 2-qp excitations. The included HFB states are breaking the rotational and particle number symmetries. In order to avoid restoring these symmetries, the quasiparticle excitations are chosen according to the following rules

1. the operators $\hat{X}_k$ are two quasiparticles operators,
2. all the states in the collective space have to be time-reversal invariant,
3. the chosen excitations have to preserve "as much as possible" the number of particles and $K$, the projection of the total angular moment on the symmetry axis,
4. and they must be associated with an excitation energy below 10 MeV.

The time-reversal condition limits the possible excitation operators to be

$$\hat{X}(q)_k = \alpha_k \hat{\eta}^{(q)\dagger}_{k_1} \hat{\eta}^{(q)\dagger}_{\bar{k}_2} - \hat{\eta}^{(q)\dagger}_{\bar{k}_1} \hat{\eta}^{(q)\dagger}_{k_2} \tag{85}$$

$$\alpha_k = \frac{1}{\sqrt{2}} \left( 1 + \delta_{k_1,k_2} \left( 1 - \frac{1}{\sqrt{2}} \right) \right), \tag{86}$$

where $\hat{\eta}^{(q)\dagger}_{k_1}$ is the creation operator of the quasiparticle $k_1$ associated with the HFB state

$$\left| \phi_0(q) \right\rangle = \prod_l \hat{\eta}^{(q)}_l \left| 0 \right\rangle . \tag{87}$$

Additionally, the selected quasiparticles in $\hat{X}(q)_k$ are assumed to have the same projection on the total angular moment on the symmetry axis $K_{k_1} = K_{k_2}$ so that the $K$ of the total system is unchanged. In case the HFB states are obtained with preserved parity, the same condition on $\pi$ is added.

Couplings between collective and intrinsic excitations play a major role in many reactions. For instance, it is known to play a crucial role in the distribution of excitation energy between the nascent fragments produced by fission. The TDGCM+GOA enables a microscopic description of nuclear reactions without internal degrees of freedom, while Langevin-based methods allow the semi-classical description of the reaction with the inclusion of thermal effects. The SCIM leads to a local Schrodinger-like equation, much simpler to solve than the exact, non-local, Griffin-Hill-Wheeler equation while being based on fewer assumptions than the TDGCM+GOA or Langevin. The collective-intrinsic Hamiltonian includes a viscosity term that is known to be relevant to the description of nuclear reaction from Langevin's calculations. However, the method still involves the full calculation of the norm and Hamiltonian kernels, which is extremely time-consuming. Furthermore, the formalism is rather complex compared to other methods such as the TDGCM+GOA. At present, this method did not lead to any application beyond the works presented in [86–88], and still needs to be tested thoroughly against experimental data.

## 5. QUANTUM MIXTURE OF TIME-DEPENDENT STATES

In its standard form, the TDGCM relies on the ansatz (3) that expands the many-body wave function on a family of time-independent generator states. The dynamics of the system is, therefore, entirely carried out by the time evolution of the collective wave function $g(\boldsymbol{q})$ driven by Equation 30. Although successful in describing some nuclear phenomena like collective vibrations, such an expansion suffers from two significant drawbacks.

The first one resides in the large dimension of the ensemble of generator states required to describe processes like nuclear reactions correctly. Despite the efforts reported in sections 3 and 4 to reduce the collective Hamiltonian to a local approximation, this high dimension quickly becomes a hindrance to the numerical applications of TDGCM. An origin of this difficulty is the fact that all the many-body configurations populated at any time of the reaction must be represented in the set of generator states. In many situations, this expansion is not optimal in the sense that most of the associated weights are close to zero at a given time. To give an example, we may consider the translation motion of a localized particle. While the translated states at any positions are to be incorporated in a TDGCM description of its motion, the collective wave function at a given time only has a small spatial expansion. A natural idea is then to express the wave function as a linear superposition of a few time-dependent states that follow the expected particle's translation motion. It may even happen that one well-chosen time-dependent basis state is enough to describe the dynamics of the system very accurately. The time-dependent energy density functional treatment of the giant resonances in nuclear physics provides such an example [91, 92].

The second drawback of the TDGCM is the construction of a family of generator states before the determination of the system evolution. The equation of motion provides only the probability of the system to populate parts of this predefined space. For this approach to work, the physicist must rely on an *a priori* knowledge of the relevant states for the dynamics. For nuclear reactions, it typically means that one should correctly guess what will be the reaction's output channels and include an ensemble of states representative of these channels in the working space. Beyond the difficulty to generate states representative of the systems far from the initial state, the typical risks of this method are

- to miss important channels/states in the construction of the set of generator states,
- to include states that will not be populated at all but will still increase the numerical cost.

A solution to overcome these difficulties is the expansion of the ansatz (3) on a set of time-dependent states, as shown schematically in **Figure 8**. In this case, the many-body wave function of the system reads

$$\left| \Psi(t) \right\rangle = \int_{\boldsymbol{q} \in E} f(\boldsymbol{q}, t) \left| \phi(\boldsymbol{q}, t) \right\rangle . \tag{88}$$

This very general ansatz brings more flexibility as the configuration basis can vary in time. However, this flexibility comes with additional complexity in the equation of motion for the collective wavefunction $g(\boldsymbol{q}, t)$ and the generator states $\left| \phi(\boldsymbol{q}, t) \right\rangle$. Studies in both chemistry and nuclear physics are exploring different strategies in the choice of generator states and

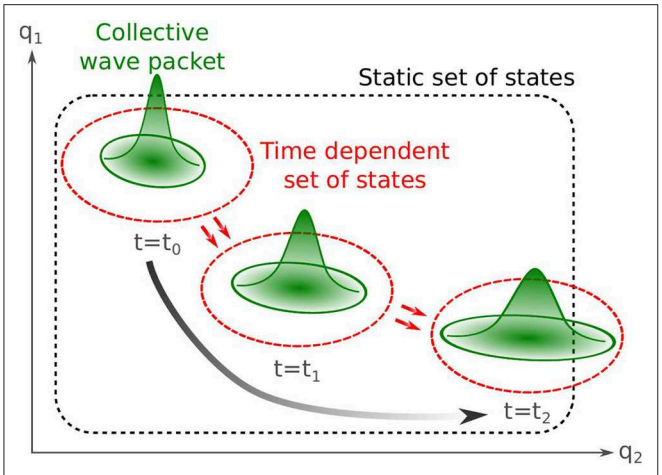


**FIGURE 8 |** Schematic dynamics of a localized collective wave packet. With the TDGCM strategy (static set of generator states), most of the working space does not contribute, and part of the final state is not captured. In contrast, a small, well-chosen set of time-dependent states is sufficient to capture the system's dynamics entirely.

the determination of the equation of motion of the system. We review these recent efforts in this section.

## 5.1. The Multiconfiguration Time-Dependent Hartree-Fock Approach

In 1990, Meyer et al. introduced the multiconfiguration time-dependent Hartree (MCTDH) approach to tackle the dynamics of molecules [93]. Contrary to the fermionic many-body problem, the system's degrees of freedom are distinct from each other and correspond typically to distances between some atoms of a molecule. Their associated wave function is assumed to be at any time a mixture of product states

$$\left|\Psi(x_1,\cdots,x_n,t)\right\rangle = \sum_{i_1=0}^{m_1-1}\cdots\sum_{i_n=0}^{m_n-1} c_{i_1\cdots i_n}\times\left|\varphi_{i_1}^{(1)}(t)\right\rangle\cdots\left|\varphi_{i_n}^{(n)}(t)\right\rangle, \tag{89}$$

where at any time, the $\{|\varphi_{i_k}^{(k)}(t)\}$ form a basis of the space associated with the $k$th degree of freedom, and the $c_{i_1\cdots i_n}$ are the mixing coefficients between all the product states. The equation of motion of both the individual states and the mixing coefficients can then be obtained from applying the Dirac-Frenkel variational principle. This method was since applied to different dynamical processes in chemistry [94–96] and up to five degrees of freedom in the treatment of the inelastic cross-section of $H_2O + H_2$ [97]. Note that in 2003, Wang et al. proposed an extension of this method referred to as multilayers MCTDHF to tackle more degrees of freedom (up to a few thousand) [98].

A natural extension of this work to the fermionic many-body problem is the replacement of the product states by Slater determinants in the trial wavefunction. This extension was introduced in [99] and the new ansatz reads

$$\left|\Psi(\boldsymbol{r}_1,\cdots,\boldsymbol{r}_n,t)\right\rangle = \sum_{i_1=0}^{m_1-1}\cdots\sum_{i_n=0}^{m_n-1} c_{i_1\cdots i_n}\left|\phi_{i_1\cdots i_n}(t)\right\rangle, \tag{90}$$

with the time-dependent Slater determinants

$$\left|\phi_{i_1\cdots i_n}(t)\right\rangle = \hat{a}_{i_1}^{\dagger}(t)\cdots\hat{a}_{i_n}^{\dagger}(t)\left|0\right\rangle. \tag{91}$$

In this expression, $\hat{a}_{i_k}^{\dagger}(t)$ stands for the fermionic creation operator of a particle in a single-particle state $\left|\varphi_{i_k}(\boldsymbol{r},t)\right\rangle$. This many-body wave function can then be injected into a time-dependent variational principle whose parameters are both the mixing coefficients $c_{i_1\cdots i_n}$ and the single-particle wave functions $\left|\varphi_{i_k}\right\rangle$. Note that there is no one-to-one mapping between the many-body state $\left|\psi(t)\right\rangle$ and the parameters of the right-hand side. In practical applications, the set of single-particle wave functions is assumed to be orthonormal at any time

$$\left\langle\varphi_i(t)\middle|\varphi_j(t)\right\rangle = \delta_{ij}. \tag{92}$$

This criterion lets some freedom in the choice of the $c_{i_k}$ and $\left|\varphi_{i_k}\right\rangle$ for a given many-body wave function, leading to an additional degree of freedom in their associated equation of motion. A usual convention to fix this freedom consists in imposing the additional constraint

$$\left\langle\varphi_i(t)\middle|\frac{\partial}{\partial t}\middle|\varphi_j(t)\right\rangle = 0. \tag{93}$$

This choice stabilizes the single-particle states against rotations among the occupied states. If such rotation has to be described, only the mixing coefficients will be affected while the single-particle states will stay constant. This convention yields to equations of motion that are often more suited for the numerical time integration.

With this criterion, the Dirac-Frenkel variational principle applied to a two-body Hamiltonian system leads to the equation of motion for both the coefficients and the single-particle states

$$i\hbar\,\dot{c}_{i_1\cdots i_n}(t) = \sum_{i_1=0}^{m_1-1}\cdots\sum_{i_n=0}^{m_n-1}\left\langle\phi_{i_1\cdots i_n}(t)\middle|\hat{H}\middle|\phi_{i_1\cdots i_n}(t)\right\rangle c_{i_1\cdots i_m}(t) \tag{94}$$

$$i\hbar\left|\dot{\varphi}_n(t)\right\rangle = \hat{P}\left\{\hat{t}\left|\varphi_n(t)\right\rangle + \sum_{pqrs}(\rho^{-1})_{np}\,\rho^{(2)}_{qspr}\,\hat{h}_{rs}\left|\varphi_q(t)\right\rangle\right\} \tag{95}$$

where $\hat{t}$ is the one-body part of the Hamiltonian, $\hat{h}$ is the mean-field potential that implicitly depends on the one-body density, $\rho$ and $\rho^{(2)}$ are the one- and two-body density matrices and $\hat{P}$ is a projection operator on the orthogonal complement of the occupied single-particle states. Such equation of motions have then been numerically solved for chemical systems with six valence electrons [99], to study the two photons ionization of helium [100] or the dynamics of di-molecular molecules [101, 102]. In nuclear physics, the multiconfiguration Hartree-Fock approach has been applied in its static version to determine

the structure of light nuclei mostly in the s-d shell [103, 104]. Such an expansion of the many-body state enables a good description of the low lying excitation spectrum with typically the first $2^+$ excitation reproduced within a few 100 keV. For the ground-state binding energy, this work still emphasizes a significant overestimation of the theory by 8.3 MeV in average in the s-d shell nuclei. This discrepancy would mostly come from (i) double-counting coming from the usage of energy functional that have been fitted at the mean-field level, (ii) the truncation of the configuration space that still cuts too early the population of single-particle states with the largest spatial expansion. Even though it would be interesting to study photoabsorption phenomena in light nuclei or diffusion between light nuclei, this method has not yet been applied in its dynamics version for nuclear physics. A generalization of the ansatz (90) to a superposition of Bogoliubov vacua and its corresponding equation of motion is yet to be formalized and tested.

## 5.2. Multiconfiguration With Time-Dependent Non Orthogonal States

The trial state of Equation (90) at the core of the MCTDHF method expands the wave function on a set of orthonormal Slater determinants. The orthonormality between such generator states simplifies the equation of motion as typically the norm kernel defined in Equation (6) is the identity at any time. In contrast, it may be more efficient in some situations to expand the many-body wave function on a set of non-orthogonal generator states (i.e., time-dependent Bogoliubov vacua with time-dependent deformations). Such a strategy was explored, for instance, in chemistry by mixing TDDFT trajectories with a shift in time to include memory effect [105] into the dynamics. This approach was proven to correctly include the description of dissipation in the two electrons dynamics of a Hooke's atom.

In nuclear physics, the idea of mixing time-dependent TDHF trajectories was already proposed in 1983 in the pioneering work of Reinhard et al. [106] to treat nuclear collisions. Starting back from the ansatz (90), the authors proposed to take as the time-dependent generator states a set of TDHF trajectories starting from different initial conditions. A time-dependent variational principle is then applied to obtain the equation of motion only for the mixing function $f(\boldsymbol{q}, t)$ (or the collective wave function $g(\boldsymbol{q}, t)$). Such a principle is schematically pictured in **Figure 9** (left panel).

The idea behind this scheme is that the TDHF trajectories will carry most of the one-body dynamics of the system, whereas the weight function will encompass part of the two-body collisional dynamics, in such importance as to account for additional dissipation and fluctuation. In this paper, a GOA approximation was performed to determine the evolution of the collective wave function in a one-dimensional nuclear collision model. The results showed in particular that the widths of the internal excitation energy of the collision partners after the collision were increased by a factor of seven compared to a TDHF trajectory alone. This additional fluctuation is directly coming from the additional correlations tackled by the enriched ansatz for the many-body wave function.

Even though promising, applications of this method to realistic systems were not carried out. One possible explanation is the numerical cost associated with TDHF trajectories. However, the advances in numerical methods and the recent development of supercomputers induced a surge of interest for such studies. In particular, the inclusion of superfluidity in our time-dependent mean-field codes [82, 108] opened the possibility to predict collisions between open-shell nuclei. Along this line, Scamps et al. attempted to predict the transfer of pairs of fermions in the contact between two superfluids based on a statistical mixing of TDHFB trajectories [109–111]. The idea is that the one-body dynamics of the nuclear processes would be already well accounted for by TDHFB like trajectories, while a statistical ensemble of such trajectories would account for the additional fluctuation induced by the residual two-body collisions terms of the dynamics. Up to now, these methods were only tested on toy-model cases and collisions between a few light systems such as $^{20}$O+$^{20}$O. Experimental data on such collisions still lack, which prevents a rigorous theory versus experiment comparison.

Nevertheless, the tests on exactly solvable models show that these semiclassical approaches manage to recover some crucial fluctuation related to the relative gauge angle between the reaction partners. In particular, they can predict the probability of one pair transfer with the proper order of magnitude in the perturbative regime where the nuclear interaction during the collision is weak compared to the pairing forces acting in each subsystem. Still, they partially miss the quantum interference between the TDHFB trajectories. Depending on the method's details, this may either lead to underestimating fluctuations of one-body observables or, in the worse case, predicting unphysical behavior such as particle transfer after the re-separation of the two reaction partners.

Coming back to a full quantum treatment of the problem, Regnier et al. recently attempted the full-fledged mixing of TDHFB trajectories in [107]. In this context, the time-dependent variational principle on the ansatz 90 leads to the equation of motion of the collective wave function $g(\boldsymbol{q}, t)$

$$i\hbar\dot{g} = \left(\tilde{\mathcal{H}} - \tilde{\mathcal{D}} + i\hbar\dot{\mathcal{N}}^{1/2}\mathcal{N}^{-1/2}\right) g. \tag{96}$$

This equation involves the collective operators $\tilde{\mathcal{H}}$ and $\tilde{\mathcal{D}}$ defined by the application of Equation (28) on the kernels

$$\mathcal{H}(\boldsymbol{q}, \boldsymbol{q}') = \left\langle \phi(\boldsymbol{q}, t) \right| \hat{H} \left| \phi(\boldsymbol{q}', t) \right\rangle, \tag{97}$$

$$\mathcal{D}(\boldsymbol{q}, \boldsymbol{q}') = \left\langle \phi(\boldsymbol{q}, t) \right| i\hbar \frac{\partial}{\partial t} \left| \phi(\boldsymbol{q}', t) \right\rangle. \tag{98}$$

All the kernels and collective operators involved now depend on time. Compared to the TDGCM on static generator states (Equation 30), this equation contains two additional terms. The first one contains the time derivative of the generator states, whereas the second one is linked to the time derivative of the norm kernel. These equations were numerically solved only in a simple case modeling the contact between two superfluid systems. The main results are summarized in the right panel of **Figure 9**. The full black line represents the system's exact many-body dynamics, and it is compared with a prediction

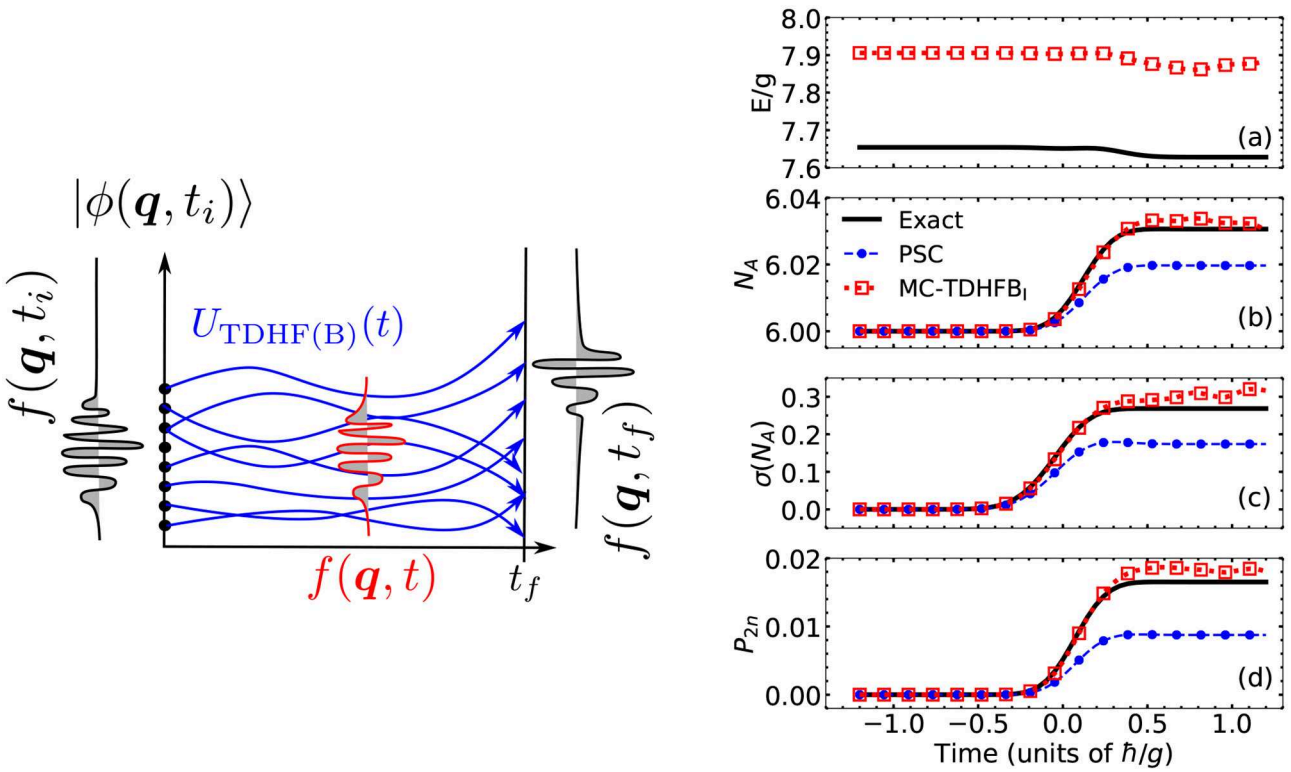


**FIGURE 9 | (Left)** Schematic picture of a GCM mixing of TDHF(B) trajectories. **(Right)** Evolution of several observables during the dynamics of a simple model of collision between two superfluids. The total energy (a), the number of particles in the left subsystem (b), and its dispersion (c) as well as the probability to transfer one pair of fermions during the collision (d) are plotted against the time of the collision for the exact many-body solution (black line), a statistical mixture of TDHFB trajectories (blue circles) and a quantum mixture of the same TDHFB trajectories (red squares). Reprinted figure with permission from [107]. Copyright 2019 by the American Physical Society.

obtained from a statistical mixture of TDHFB trajectories (the PSC method, dashed blue line) as well as the quantum mixing of the same TDHFB trajectories. While the statistical method recovers the good order of magnitude for most predictions, the inclusion of interference between the TDHFB trajectories significantly improves these results. In particular, a factor of two is highlighted between each method's predictions of the probability $P_{2n}$ to transfer a pair of fermions during the collision.

At a time where performing series of independent time-dependent mean-field calculations in nuclear physics becomes possible, such a method could be a suitable candidate to tackle nuclear reactions with a complex interplay between one-body and many-body degrees of freedom. The caveat to its direct application on a realistic nuclear collision would still be the difficulty that current implementations of the nuclear mean-field dynamics formalisms rely on energy density functionals instead of a linear Hamiltonian (cf. section 2.5).

## 6. CONCLUSION

This review presents four variants of the Time-Dependent Generator Coordinates Method that is rooted in a configuration-mixing principle. This class of methods is of particular interest to microscopically describe heavy-fermion systems. It allows the physicist to focus the description on the correlations of interest through the choice of the collective coordinates. Most of the time, the collective coordinates are related to some of the first multipole moments of the intrinsic one-body density or some groups of symmetry operators. Such freedom makes the TDGCM extremely versatile. Still, its practical applications in nuclear physics are plagued by the usage of effective Hamiltonians or energy density functionals that lead to misbehaviors of the energy kernel, an essential ingredient shared by all the TDGCM approaches.

The Time-Dependent Generator Coordinate Method is the most direct implementation of the configuration-mixing principle. In this case, the only approximations are the expression of the nuclear Hamiltonian, and the restriction of the total Fock space to the one spanned by the configuration basis. The Griffin-Hill-Wheeler (GHW) Equation (3) is the corresponding equation of motion. The main limitation of this method arises from the non-locality of the GHW equation in the collective coordinates representation, leading to intensive parallel computation. By resorting to some approximations, it is possible to rewrite the GHW equations into local equations, reducing hereafter substantially the calculation needs. The Gaussian Overlap Approximation (GOA) transforms

the GHW equations to a local Schrodinger-like equation essentially under the condition that the norm kernel is of Gaussian character. The TDGCM+GOA is the most widely used implementation of the TDGCM for the description of nuclear reactions and especially for fission. The Schrodinger Collective-Intrinsic Method is based on the truncation of the GHW equation in the second-order to obtain a local Schrodinger-like equation. In its current form, it still requires to calculate the full norm and Hamiltonian kernels. Finally, it is possible to generalize the standard TDGCM approach by expanding the many-body wave function on a set of time-dependent generator states. The recent progress of TDHFB solvers opens new possibilities for practical applications along this line.

Overall, most of these methods were first developed in the 1980s, at a time when they were quickly facing intractable numerical costs. The computational power at our disposal nowadays is an incentive to revisit the TDGCM approaches and look for new opportunities in the description of nuclear reactions. One of the most significant challenges in this path is the determination of energy density functionals or effective Hamiltonians, which are compatible with the GCM formalism and yield quantitative predictions of nuclear observables.

## AUTHOR CONTRIBUTIONS

All authors listed have made a substantial, direct and intellectual contribution to the work, and approved it for publication.

## FUNDING

This work was performed at Los Alamos National Laboratory under the auspices of the National Nuclear Security Administration of the U.S. Department of Energy at Los Alamos National Laboratory under Contract No. 89233218CNA000001. Support for this work was provided through the Fission In R-process Elements (FIRE) Topical Collaboration in Nuclear Theory of the U.S. Department of Energy. It was partly performed under the auspices of the U.S. Department of Energy by the Lawrence Livermore National Laboratory (LLNL) under Contract No. DE-AC52-07NA27344.

## ACKNOWLEDGMENTS

The authors would like to thank N. Schunck for his patience through the writing process of this paper as well as for fruitful comments on the manuscript.

## REFERENCES

1. Bohr N, Wheeler JA. The mechanism of nuclear fission. *Phys Rev*. (1939) **56**:426–450. doi: 10.1103/PhysRev.56.426
2. Bohr A, Mottelson BR. *Nuclear Structure*. Singapore; River Edge, NJ: World Scientific (1998). doi: 10.1142/3530-vol1
3. Scheid W, Greiner W. Theory of projection of spurious center of mass and rotational states from many-body nuclear wave functions. *Ann Phys*. (1968) **48**:493–525. doi: 10.1016/0003-4916(68)90143-7
4. Fink B, Kolb D, Scheid W, Greiner W. Spurious rotational states in deformed nuclear shell models. *Ann Phys*. (1972) **69**:375–99. doi: 10.1016/0003-4916(72)90182-0
5. Hill DL, Wheeler JA. Nuclear constitution and the interpretation of fission phenomena. *Phys Rev*. (1953) **89**:1102–45. doi: 10.1103/PhysRev.89.1102
6. Griffin JJ, Wheeler JA. Collective motions in nuclei by the method of generator coordinates. *Phys Rev*. (1957) **108**:311–27. doi: 10.1103/PhysRev.108.311
7. Bender M. Going beyond the self-consistent mean-field with the symmetry-restored generator coordinate method: from single-reference toward multi-reference energy density functional theory. *Eur Phys J Spec Top*. (2008) **156**:217–28. doi: 10.1140/epjst/e2008-00619-9
8. Egido JL. State-of-the-art of beyond mean field theories with nuclear density functionals. *Phys Scr*. (2016) **91**:073003. doi: 10.1088/0031-8949/91/7/073003
9. Krewald S, Rosenfelder R, Galonska JE, Faessler A. Selfconsistent generator coordinate method for giant monopole resonances. *Nucl Phys A*. (1976) **269**:112–24. doi: 10.1016/0375-9474(76)90400-0
10. Stoitsov MV, Ring P, Sharma MM. Generator coordinate calculations for breathing-mode giant monopole resonance in the relativistic mean-field theory. *Phys Rev C*. (1994) **50**:1445–55. doi: 10.1103/PhysRevC.50.1445
11. Caurier E, Bourotte-Bilwes B, Abgrall Y. Microscopic treatment of the coupled monopole and quadrupole vibrations in light nuclei. *Phys Lett B*. (1973) **44**:411–5. doi: 10.1016/0370-2693(73)90321-3
12. Flocard H, Vautherin D. Generator coordinate calculations of giant resonances with the Skyrme interaction. *Nucl Phys A*. (1976) **264**:197–220. doi: 10.1016/0375-9474(76)90428-0
13. Abgrall Y, Caurier E. On the monopole and quadrupole isoscalar giant resonances in 4He, 16O, 20Ne and 40Ca. *Phys Lett B*. (1975) **56**:229–31. doi: 10.1016/0370-2693(75)90381-0
14. Vretenar D, Lalazissis GA, Behnsch R, Pöschl W, Ring P. Monopole giant resonances and nuclear compressibility in relativistic mean field theory. *Nucl Phys A*. (1997) **621**:853–78. doi: 10.1016/S0375-9474(97)00192-9
15. De Toledo Piza A, De Passos E. The kinematics of generator co-ordinates. *Il Nuovo Cimento B*. (1978) **45**:1–30. doi: 10.1007/BF02904070
16. Ring P, Schuck P. *The Nuclear Many-Body Problem*. Berlin: Springer Science & Business Media (2004).
17. Löwdin PO, Mukherjee PK. Some comments on the time-dependent variation principle. *Chem Phys Lett*. (1972) **14**:1–7. doi: 10.1016/0009-2614(72)87127-6
18. Crank J, Nicolson P. A practical method for numerical evaluation of solutions of partial differential equations of the heat-conduction type. *Adv Comput Math*. (1996) **6**:207–26. doi: 10.1007/BF02127704
19. Reed M, Simon B. *Methods of Modern Mathematical Physics*. Princeton: Academic Press (1972).
20. Robledo LM. Sign of the overlap of hartree-fock-bogoliubov wave functions. *Phys Rev C*. (2009) **79**:021302. doi: 10.1103/PhysRevC.79.021302
21. Anguiano M, Egido JL, Robledo LM. Particle number projection with effective forces. *Nucl Phys A*. (2001) **696**:467–93. doi: 10.1016/S0375-9474(01)01219-2
22. Lacroix D, Duguet T, Bender M. Configuration mixing within the energy density functional formalism: removing spurious contributions from nondiagonal energy kernels. *Phys Rev C*. (2009) **79**:044318. doi: 10.1103/PhysRevC.79.044318
23. Bender M, Duguet T, Lacroix D. Particle-number restoration within the energy density functional formalism. *Phys Rev C*. (2009) **79**:044319. doi: 10.1103/PhysRevC.79.044319
24. Duguet T, Bender M, Bennaceur K, Lacroix D, Lesinski T. Particle-number restoration within the energy density functional formalism: nonviability of terms depending on noninteger powers of the density matrices. *Phys Rev C*. (2009) **79**:044320. doi: 10.1103/PhysRevC.79.044320
25. Sheikh JA, Dobaczewski J, Ring P, Robledo LM, Yannouleas C. Symmetry restoration in mean-field approaches. *arXiv [Preprint] arXiv:190106992*. (2019).

26. Ryssens W, Hellemans V, Bender M, Heenen PH. Solution of the Skyrme–HF+BCS equation on a 3D Mesh, II: a new version of the Ev8 code. *Comput Phys Commun*. (2015) **187**:175–94. doi: 10.1016/j.cpc.2014.10.001
27. Dönau F. Canonical form of transition matrix elements. *Phys Rev C*. (1998) **58**:872–7. doi: 10.1103/PhysRevC.58.872
28. Anguiano M, Egido JL, Robledo LM. Coulomb exchange and pairing contributions in nuclear Hartree–Fock–Bogoliubov calculations with the gogny force. *Nucl Phys A*. (2001) **683**:227–54. doi: 10.1016/S0375-9474(00)00445-0
29. Almehed D, Frauendorf S, Dönau F. Pairing correlations in high-K bands. *Phys Rev C*. (2001) **63**:044311. doi: 10.1103/PhysRevC.63.044311
30. Dobaczewski J, Stoitsov MV, Nazarewicz W, Reinhard PG. Particle-number projection and the density functional theory. *Phys Rev C*. (2007) **76**:054315. doi: 10.1103/PhysRevC.76.054315
31. Duguet T, Bonche P. Density dependence of two-body interactions for beyond-mean-field calculations. *Phys Rev C*. (2003) **67**:054308. doi: 10.1103/PhysRevC.67.054308
32. Robledo LM. Remarks on the use of projected densities in the density-dependent part of skyrme or gogny functionals. *J Phys G: Nucl Part Phys*. (2010) **37**:064020. doi: 10.1088/0954-3899/37/6/064020
33. Rodríguez-Guzmán R, Egido JL, Robledo LM. Correlations beyond the mean field in magnesium isotopes: angular momentum projection and configuration mixing. *Nucl Phys A*. (2002) **709**:201–35. doi: 10.1016/S0375-9474(02)01019-9
34. Bennaceur K, Idini A, Dobaczewski J, Dobaczewski P, Kortelainen M, Raimondi F. Nonlocal energy density functionals for pairing and beyond-mean-field calculations. *J Phys G*. (2017) **44**:045106. doi: 10.1088/1361-6471/aa5fd7
35. Yao JM, Bally B, Engel J, Wirth R, Rodríguez TR, Hergert H. Ab initio treatment of collective correlations and the neutrinoless double beta decay of 48Ca. *arXiv:190805424*. (2019). doi: 10.1103/PhysRevLett.124.232501
36. Verriere M. *Description de la Dynamique de la Fission Dans le Formalisme de la méthode de la Coordonnée génératrice dépendante du Temps*. Université Paris-Saclay (2017). Available online at: https://tel.archives-ouvertes.fr/tel-01559158/document
37. Verriere M, Dubray N, Schunck N, Regnier D, Dossantos-Uzarralde P. Fission description: first steps towards a full resolution of the time-dependent hill-wheeler equation. *EPJ Web Conf*. (2017) **146**:04034. doi: 10.1051/epjconf/201714604034
38. Dubray N, Regnier D. Numerical search of discontinuities in self-consistent potential energy surfaces. *Comput Phys Commun*. (2012) **183**:2035–41. doi: 10.1016/j.cpc.2012.05.001
39. Nishio K, Nakagome Y, Kanno I, Kimura I. Measurement of fragment mass dependent kinetic energy and neutron multiplicity for thermal neutron induced fission of plutonium-239. *J Nucl Sci Technol*. (1995) **32**:404–14. doi: 10.1080/18811248.1995.9731725
40. Tsuchiya C, Nakagome Y, Yamana H, Moriyama H, Nishio K, Kanno I, et al. Simultaneous measurement of prompt neutrons and fission fragments for 239Pu(nth,f). *J Nucl Sci Technol*. (2000) **37**:941–8. doi: 10.1080/18811248.2000.9714976
41. Goutte H, Berger JF, Casoli P, Gogny D. Microscopic approach of fission dynamics applied to fragment kinetic energy and mass distributions in U238. *Phys Rev C*. (2005) **71**:024316. doi: 10.1103/PhysRevC.71.024316
42. Bohr A. The coupling of nuclear surface oscillations to the motion of individual nucleons. *Dan Mat Fys Medd*. (1952) **26**:1–40.
43. Kumar K, Baranger M. Complete numerical solution of Bohr's collective Hamiltonian. *Nucl Phys A*. (1967) **92**:608–52. doi: 10.1016/0375-9474(67)90636-7
44. Libert J, Girod M, Delaroche JP. Microscopic descriptions of superdeformed bands with the Gogny force: configuration mixing calculations in the $A \simeq 190$ mass region. *Phys Rev C*. (1999) **60**:054301. doi: 10.1103/PhysRevC.60.054301
45. Delaroche JP, Girod M, Libert J, Goutte H, Hilaire S, Péru S, et al. Structure of even-even nuclei using a mapped collective Hamiltonian and the D1S Gogny interaction. *Phys Rev C*. (2010) **81**:014303. doi: 10.1103/PhysRevC.81.014303
46. Fu Y, Mei H, Xiang J, Li ZP, Yao JM, Meng J. Beyond relativistic mean-field studies of low-lying states in neutron-deficient krypton isotopes. *Phys Rev C*. (2013) **87**:054305. doi: 10.1103/PhysRevC.87.054305
47. Matsuyanagi K, Matsuo M, Nakatsukasa T, Yoshida K, Hinohara N, Sato K. Microscopic derivation of the Bohr–Mottelson collective Hamiltonian and its application to quadrupole shape dynamics. *Phys Scr*. (2016) **91**:063014. doi: 10.1088/0031-8949/91/6/063014
48. Reinhard P, Goeke K. The generator-coordinate method and quantized collective motion in nuclear systems. *Rep Prog Phys*. (1987) **50**:1–64. doi: 10.1088/0034-4885/50/1/001
49. Krappe HJ, Pomorski K. *Theory of Nuclear Fission*. Springer (2012). Available online at: http://www.springer.com/us/book/9783642235146.
50. Onishi N, Une T. Local Gaussian approximation in the generator coordinate method. *Prog Theor Phys*. (1975) **53**:504–15. doi: 10.1143/PTP.53.504
51. Gozdz A. An extended Gaussian overlap approximation in the generator coordinate method. *Phys Lett B*. (1985) **152**:281–3. doi: 10.1016/0370-2693(85)90495-2
52. Schunck N, Robledo LM. Microscopic theory of nuclear fission: a review. *Rep Prog Phys*. (2016) **79**:116301. doi: 10.1088/0034-4885/79/11/116301
53. Holzwarth G. Four approaches to the function of inertia in a solvable model. *Nucl Phys A*. (1973) **207**:545–64. doi: 10.1016/0375-9474(73)90861-0
54. Góźdź A, Pomorski K, Brack M, Werner E. The mass parameters for the average mean-field potential. *Nucl Phys A*. (1985) **442**:26–49. doi: 10.1016/0375-9474(85)90131-9
55. Baran A, Sheikh J, Dobaczewski J, Nazarewicz W, Staszczak A. Quadrupole collective inertia in nuclear fission: cranking approximation. *Phys Rev C*. (2011) **84**:054321. doi: 10.1103/PhysRevC.84.054321
56. Reinhard PG, Goeke K. The generation coordinate method with conjugate parameters and its relation to adiabatic time-dependent hartree-fock. *J Phys G*. (1978) **4**:L245. doi: 10.1088/0305-4616/4/9/006
57. Berger J, Gogny D. A self-consistent microscopic approach to the 12C+ 12C reaction at low energy. *Nucl Phys A*. (1980) **333**:302–32. doi: 10.1016/0375-9474(80)90235-3
58. Baye D, Salmon Y. Generator-coordinate study of elastic 40Ca+ 40Ca scattering. *Nucl Phys A*. (1979) **323**:521–39. doi: 10.1016/0375-9474(79)90123-4
59. Friedrich H, Langanke K, Weiguny A. Elastic scattering of 16O on 40Ca at backward angles. *Phys Lett B*. (1976) **63**:125–8. doi: 10.1016/0370-2693(76)90630-4
60. Goeke K, Grümmer F, Reinhard PG. Three-dimensional nuclear dynamics in the quantized ATDHF approach. *Ann Phys*. (1983) **150**:504–51. doi: 10.1016/0003-4916(83)90025-8
61. Sekizawa K. TDHF Theory and its extensions for the multinucleon transfer reaction: a mini review. *Front Phys*. (2019) **7**:20. doi: 10.3389/fphy.2019.00020
62. Berger JF, Girod M, Gogny D. Microscopic analysis of collective dynamics in low energy fission. *Nucl Phys A*. (1984) **428**:23–36. doi: 10.1016/0375-9474(84)90240-9
63. Berger JF, Girod M, Gogny D. Time-dependent quantum collective dynamics applied to nuclear fission. *Comput Phys Commun*. (1991) **63**:365–74. doi: 10.1016/0010-4655(91)90263-K
64. Younes W, Gogny D. *Fragment Yields Calculated in a Time-Dependent Microscopic Theory of Fission*. Livermore, CA: Lawrence Livermore National Laboratory (2012). doi: 10.2172/1053671
65. Younes W, Gogny D. *Collective Dissipation from Saddle to Scission in a Microscopic Approach*. Livermore, CA: Lawrence Livermore National Laboratory (2012). doi: 10.2172/1053675
66. Regnier D, Verriére M, Dubray N, Schunck N. FELIX-1.0: a finite element solver for the time dependent generator coordinate method with the Gaussian overlap approximation. *Comput Phys Commun*. (2016) **200**:350–63. doi: 10.1016/j.cpc.2015.11.013

67. Regnier D, Dubray N, Verriére M, Schunck N. FELIX-2.0: new version of the finite element solver for the time dependent generator coordinate method with the Gaussian overlap approximation. *Comput Phys Commun*. (2018) **225**:180–91. doi: 10.1016/j.cpc.2017.12.007
68. Regnier D, Dubray N, Schunck N, Verriére M. Fission fragment charge and mass distributions in $^{2}$39Pu(n,f) in the adiabatic nuclear energy density functional theory. *Phys Rev C*. (2016) **93**:054611. doi: 10.1103/PhysRevC.93.054611
69. Tao H, Zhao J, Li ZP, Nikšić T, Vretenar D. Microscopic study of induced fission dynamics of Th 226 with covariant energy density functionals. *Phys Rev C*. (2017) **96**:024319. doi: 10.1103/PhysRevC.96.024319
70. Regnier D, Dubray N, Schunck N. From asymmetric to symmetric fission in the fermium isotopes within the time-dependent generator-coordinate-method formalism. *Phys Rev C*. (2019) **99**:024611. doi: 10.1103/PhysRevC.99.024611
71. Zdeb A, Dobrowolski A, Warda M. Fission dynamics of $^{2}$52Cf. *Phys Rev C*. (2017) **95**:054608. doi: 10.1103/PhysRevC.95.054608
72. Zhao J, Nikšić T, Vretenar D, Zhou SG. Microscopic self-consistent description of induced fission dynamics: finite-temperature effects. *Phys Rev C*. (2019) **99**:014618. doi: 10.1103/PhysRevC.99.014618
73. Zhao J, Xiang J, Li ZP, Nikšić T, Vretenar D, Zhou SG. Time-dependent generator-coordinate-method study of mass-asymmetric fission of actinides. *Phys Rev C*. (2019) **99**:054613. doi: 10.1103/PhysRevC.99.054613
74. Usang MD, Ivanyuk FA, Ishizuka C, Chiba S. Correlated transitions in TKE and mass distributions of fission fragments described by 4-D Langevin equation. *Sci Rep*. (2019) **9**:1–9. doi: 10.1038/s41598-018-37993-7
75. Miyamoto Y, Aritomo Y, Tanaka S, Hirose K, Nishio K. Origin of the dramatic change of fission mode in fermium isotopes investigated using Langevin equations. *Phys Rev C*. (2019) **99**:051601. doi: 10.1103/PhysRevC.99.051601
76. Parisi G, Wu YS. Perturbation theory without gauge fixing. *Sci Sin*. (1981) **24**:483–96.
77. Damgaard P, Tsokos K. Stochastic quantization with fermions. *Nucl Phys B*. (1984) **235**:75–92. doi: 10.1016/0550-3213(84)90149-4
78. Sadhukhan J, Nazarewicz W, Schunck N. Microscopic modeling of mass and charge distributions in the spontaneous fission of $^{2}$40Pu. *Phys Rev C*. (2016) **93**:011304. doi: 10.1103/PhysRevC.93.011304
79. Bulgac A, Jin S, Roche KJ, Schunck N, Stetcu I. Fission dynamics of 240Pu from saddle to scission and beyond. *Phys Rev C*. (2019) **100**:034615. doi: 10.1103/PhysRevC.100.034615
80. Müther H, Goeke K, Allaart K, Faessler A. Single-particle degrees of freedom and the generator-coordinate method. *Phys Rev C*. (1977) **15**:1467–76. doi: 10.1103/PhysRevC.15.1467
81. Chen FQ, Egido JL. Triaxial shape fluctuations and quasiparticle excitations in heavy nuclei. *Phys Rev C*. (2017) **95**:024307. doi: 10.1103/PhysRevC.95.024307
82. Bulgac A, Magierski P, Roche KJ, Stetcu I. Induced fission of $^{2}$40Pu within a real-time microscopic framework. *Phys Rev Lett*. (2016) **116**:122504. doi: 10.1103/PhysRevLett.116.122504
83. Bulgac A, Jin S, Stetcu I. Unitary evolution with fluctuations and dissipation. *Phys Rev C*. (2019) **100**:014615. doi: 10.1103/PhysRevC.100.014615
84. Sierk AJ. Langevin model of low-energy fission. *Phys Rev C*. (2017) **96**:034603. doi: 10.1103/PhysRevC.96.034603
85. Wada T, Carjan N, Abe Y. Multi-dimensional Langevin approach to fission dynamics. *Nucl Phys A*. (1992) **538**:283–9. doi: 10.1016/0375-9474(92)90778-I
86. Bernard R. *Taking Into Account the Intrinsic Excitations and Their Couplings to Collective Modes in the Fission Process; Couplages Modes Collectifs - Excitations Intrinseques Dans le Processus de Fission*. Université Pierre et Marie Curie (2011).
87. Bernard R, Goutte H, Gogny D, Younes W. Microscopic and nonadiabatic Schrödinger equation derived from the generator coordinate method based on zero- and two-quasiparticle states. *Phys Rev C*. (2011) **84**:044308. doi: 10.1103/PhysRevC.84.044308
88. Younes W, Gogny DM, Berger JF. *A Microscopic Theory of Fission Dynamics Based on the Generator Coordinate Method. Lecture Notes in Physics*. Springer International Publishing (2019). Available online at: www.springer.com/us/book/9783030044220.
89. Holzwarth G. The connection between the generator coordinate method and bose expansions. *Nucl Phys A*. (1972) **185**:268–72. doi: 10.1016/0375-9474(72)90568-4
90. Kerman AK, Koonin SE. Quantum theory of dissipation for nuclear collective motion. *Phys Scr*. (1974) **10**:118–21. doi: 10.1088/0031-8949/10/A/020
91. Scamps G, Lacroix D. Systematics of isovector and isoscalar giant quadrupole resonances in normal and superfluid spherical nuclei. *Phys Rev C*. (2013) **88**:044310. doi: 10.1103/PhysRevC.88.044310
92. Scamps G, Lacroix D. Systematic study of isovector and isoscalar giant quadrupole resonances in normal and superfluid deformed nuclei. *Phys Rev C*. (2014) **89**:034314. doi: 10.1103/PhysRevC.89.034314
93. Meyer HD, Manthe U, Cederbaum LS. The multi-configurational time-dependent Hartree approach. *Chem Phys Lett*. (1990) **165**:73–8. doi: 10.1016/0009-2614(90)87014-I
94. Manthe U, Meyer HD, Cederbaum LS. Wave-packet dynamics within the multiconfiguration Hartree framework: general aspects and application to NOCl. *J Chem Phys*. (1992) **97**:3199–213. doi: 10.1063/1.463007
95. Beck MH, Jäckle A, Worth GA, Meyer HD. The Multiconfiguration Time-Dependent Hartree (MCTDH) method: a highly efficient algorithm for propagating wavepackets. *Phys Rep*. (2000) **324**:1–105. doi: 10.1016/S0370-1573(99)00047-2
96. Meyer HD, Gatti F, Worth GA. *Multidimensional Quantum Dynamics: MCTDH Theory and Applications*. John Wiley & Sons (2009). doi: 10.1002/9783527627400
97. Ndengué S, Scribano Y, Gatti F, Dawes R. State-to-state inelastic rotational cross sections in five-atom systems with the multiconfiguration time dependent Hartree method. *J Chem Phys*. (2019) **151**:134301. doi: 10.1063/1.5119381
98. Wang H, Thoss M. Multilayer formulation of the multiconfiguration time-dependent Hartree theory. *J Chem Phys*. (2003) **119**:1289–99. doi: 10.1063/1.1580111
99. Nest M, Klamroth T, Saalfrank P. The Multiconfiguration time-dependent Hartree–Fock method for quantum chemical calculations. *J Chem Phys*. (2005) **122**:124102. doi: 10.1063/1.1862243
100. Hochstuhl D, Bonitz M. Two-photon ionization of helium studied with the multiconfigurational time-dependent Hartree–Fock method. *J Chem Phys*. (2011) **134**:084106. doi: 10.1063/1.3553176
101. Kato T, Kono H. Time-dependent multiconfiguration theory for electronic dynamics of molecules in an intense laser field. *Chem Phys Lett*. (2004) **392**:533–40. doi: 10.1016/j.cplett.2004.05.106
102. Kato T, Kono H. Time-dependent multiconfiguration theory for electronic dynamics of molecules in intense laser fields: a description in terms of numerical orbital functions. *J Chem Phys*. (2008) **128**:184102. doi: 10.1063/1.2912066
103. Robin C, Pillet N, Pe na Arteaga D, Berger JF. Description of nuclear systems with a self-consistent configuration-mixing approach: theory, algorithm, and application to the C 12 test nucleus. *Phys Rev C*. (2016) **93**:024302. doi: 10.1103/PhysRevC.93.024302
104. Robin C, Pillet N, Dupuis M, Le Bloas J, Pe na Arteaga D, Berger JF. Description of nuclear systems with a self-consistent configuration-mixing approach. II. Application to structure and reactions in even-even s d -shell nuclei. *Phys Rev C*. (2017) **95**:044315. doi: 10.1103/PhysRevC.95.044315
105. Orestes E, Capelle K, da Silva ABF, Ullrich CA. Generator coordinate method in time-dependent density-functional theory: memory made simple. *J Chem Phys*. (2007) **127**:124101. doi: 10.1063/1.2768368
106. Reinhard PG, Cusson RY, Goeke K. Time evolution of coherent ground-state correlations and the TDHF approach. *Nucl Phys A*. (1983) **398**:141–88. doi: 10.1016/0375-9474(83)90653-X
107. Regnier D, Lacroix D. Microscopic description of pair transfer between two superfluid fermi systems. II. Quantum mixing of time-dependent Hartree-Fock-Bogolyubov trajectories. *Phys Rev C*. (2019) **99**:064615. doi: 10.1103/PhysRevC.99.064615
108. Scamps G. Pairing dynamics in particle transport. *Phys Rev C*. (2012) **85**:034328. doi: 10.1103/PhysRevC.85.034328

109. Scamps G, Hashimoto Y. Superfluid effects in collision between systems with small particle number. *EPJ Web Conf.* (2017) **163**:00049. doi: 10.1051/epjconf/201716300049
110. Scamps G. Transfer probabilities for the reactions. *Phys Rev C.* (2017) **96**:031602. doi: 10.1103/PhysRevC.96.031602
111. Regnier D, Lacroix D, Scamps G, Hashimoto Y. Microscopic description of pair transfer between two superfluid fermi systems: combining phase-space averaging and combinatorial techniques. *Phys Rev C.* (2018) **97**:034627. doi: 10.1103/PhysRevC.97.034627

**Conflict of Interest:** The authors declare that the research was conducted in the absence of any commercial or financial relationships that could be construed as a potential conflict of interest.

# 7. APPENDIX

## 7.1. Expression of the GOA Moments

The expression (58) involves some moments $M^{(K)}$ and $\tilde{M}^{(K)}$ that we define here. We recall that we consider generator states that are Bogoliubov vacua. Any generator state is then fully characterized by its generalized density matrix $\mathcal{R}(\boldsymbol{q})$

$$\mathcal{R} = \begin{bmatrix} \rho & \kappa \\ -\kappa^* & 1-\rho^* \end{bmatrix}. \tag{99}$$

Additionally, each collective coordinate $\boldsymbol{q}_i$ is associated to a one-body observable $\hat{Q}_i$ that is used as a constraint. Expressed in the basis of quasiparticles that diagonalizes $\mathcal{R}(\boldsymbol{q})$, this operator takes the matrix form

$$\mathcal{Q}_i = \begin{bmatrix} Q_i^{11} & Q_i^{12} \\ Q_i^{21} & Q_i^{22} \end{bmatrix}. \tag{100}$$

One can define the standard QRPA matrix $\mathcal{M}$ in this same basis as detailed in [16]. With these notations, the moments $M^{(K)}$ involved in the determination of the GOA inertia and metric tensors are

$$M_{ij}^{(K)} = \frac{1}{2}(Q_i^{12\,*},\ Q_i^{12})\mathcal{M}^{-K}\begin{pmatrix} Q_j^{12} \\ Q_j^{12\,*} \end{pmatrix}. \tag{101}$$

We also define the modified moments $\tilde{M}^{(K)}$ by,

$$\tilde{M}^{(K)} = \begin{bmatrix} 1 & 0 \\ 0 & -1 \end{bmatrix} M^{(K)} \begin{bmatrix} 1 & 0 \\ 0 & -1 \end{bmatrix}. \tag{102}$$

# 8. BESTIARY OF SOPO PROPERTIES

The Symmetric Ordered Product of Operators (SOPO) are defined, for any two operators $\mathcal{A}$ and $\mathcal{B}$, as

$$\{\mathcal{A},\mathcal{B}\}^{(n)} = \frac{1}{2^n}\sum_{k=0}^{n}\binom{n}{k}\mathcal{B}^k\mathcal{A}\mathcal{B}^{n-k}. \tag{103}$$

They can be equivalently defined recursively through their relation with the anti-commutator

$$\{\mathcal{A},\mathcal{B}\}^{(1)} = \frac{1}{2}\{\mathcal{A},\mathcal{B}\} \tag{104}$$

$$\{\mathcal{A},\mathcal{B}\}^{(n+1)} = \frac{1}{2}\left\{\{\mathcal{A},\mathcal{B}\}^{(n)},\mathcal{B}\right\}. \tag{105}$$

The SOPO are used to obtain the Symmetric Moment Expansion (SME) of the symmetrized GHW Equation (66), based on

$$e^{\alpha\mathcal{B}/2}\mathcal{A}e^{\alpha\mathcal{B}/2} = \sum_{p=0}^{\infty}\frac{\alpha^p}{p!}\{\mathcal{A},\mathcal{B}\}^{(p)}, \tag{106}$$

For any operators $\mathcal{A}$, $\mathcal{B}$, and $\mathcal{C}$, the following relation is satisfied

$$\mathcal{A}\{\mathcal{B},\mathcal{P}\}^{(n)}\mathcal{C} = \sum_{k=0}^{n}\left\{\mathcal{B}_{(n,k)}^{A,C},\mathcal{P}\right\}^{(k)}, \tag{107}$$

where the operators $\mathcal{B}_{(n,k)}^{A,C}$ are given by

$$\mathcal{B}_{(n,k)}^{A,C} = \frac{i^{n-k}}{2^{n-k}}\sum_{r=0}^{n-k}\left\{(-1)^r\binom{n}{k+r}\binom{k+r}{r}\mathcal{A}^{[r]}\,\mathcal{B}\,\mathcal{C}^{[n-k-r]}\right\}, \tag{108}$$

and where $\mathcal{A}^{[r]}$ the short-hand notation for the local operator associated with the kernel

$$\mathcal{A}^{[r]}(q) = \frac{\partial^r\mathcal{A}}{\partial q^r}(q). \tag{109}$$

frontiers in Physics

BRIEF RESEARCH REPORT
published: 11 September 2020
doi: 10.3389/fphy.2020.00351

# Shape Evolutions in Fission Dynamics Within Time-Dependent Hartree-Fock Approach

*Marko Pancic*[1,2], *Yu Qiang*[1], *Junchen Pei*[1]* *and Paul Stevenson*[2]

[1] State Key Laboratory of Nuclear Physics and Technology, School of Physics, Peking University, Beijing, China, [2] Department of Physics, University of Surrey, Guildford, United Kingdom

We studied the nuclear shape evolutions in fission process of $^{240}$Pu by the time-dependent Hartree-Fock approach with various Skyrme forces. Calculations are performed for the later phase of the fission with large initial deformations toward the scission. We show that calculations with Skyrme forces with large surface energies and large symmetry energies can have extremely long fission evolution time. The symmetry energy plays a role in the evolution of neutron-rich necks. In addition, we also demonstrated the shape oscillations of fission fragments after the fission. We see that particularly the heavy near-spherical fragments have remarkable octupole oscillations.

**Keywords: nuclear fission, TDHF method, Skyrme force, fission fragments, surface energy, symmetry energy**

OPEN ACCESS

***Edited by:***
*Dean Lee,*
*Michigan State University,*
*United States*

***Reviewed by:***
*Sait Umar,*
*Vanderbilt University, United States*
*Paul-Gerhard Reinhard,*
*University of Erlangen Nuremberg,*
*Germany*

***Correspondence:**
*Junchen Pei*
*peij@pku.edu.cn*

***Specialty section:***
*This article was submitted to Nuclear Physics, a section of the journal Frontiers in Physics*

***Received:*** *27 May 2020*
***Accepted:*** *24 July 2020*
***Published:*** *11 September 2020*

***Citation:***
*Pancic M, Qiang Y, Pei J and Stevenson P (2020) Shape Evolutions in Fission Dynamics Within Time-Dependent Hartree-Fock Approach. Front. Phys. 8:351. doi: 10.3389/fphy.2020.00351*

## 1. INTRODUCTION

Nuclear fission is a very complex and large amplitude collective motion of many-body quantum systems. Although fission was discovered in 1939, the development of a fully self-consistent and predictive microscopic fission theory is still very challenging [1, 2]. The earlier studies [3, 4] of nuclear fission are mainly based on macro-microscopic models, which have gained many insights about the fission mechanism. Thanks to the developments of supercomputing capabilities in recent years, microscopic fission theory has achieved remarkable progresses. The time-dependent Generator-Coordinate Method [5–7] as an adiabatic dynamical fission theory can describe reasonably well the mass distributions of fission yields, based on parallel calculations of complex potential energy surfaces. On the other hand, the time-dependent Hartree-Fock (TDHF) or time-dependent density functional theory [8–16] as a non-adiabatic dynamical theory is helpful for understanding fission mechanisms, particularly in the part of the trajectory close to scission.

There are extensive studies of real-time nuclear dynamics based on the time-dependent Hartree-Fock approach. Indeed, fusion and fission involving transitions between one-body and two-body quantum system are unique non-equilibrium processes. Nuclear dynamics in the TDHF framework provide an opportunity to probe effective nuclear interactions, many-body correlations and transport properties. TDHF has been extended to TDHF+BCS and TD-HFB approaches by including dynamical pairing [9, 17]. The pairing interactions has been demonstrated to increase the fission lifetime by allowing orbital exchanges [9]. On the other hand, the pairing can facilitate the fission at some initial deformations where fission doesn't occur within TDHF [17]. The effective nuclear forces have also been demonstrated to be important in heavy-ion collision reactions [18]. For example, the tensor force is expected to be crucial in nuclear dynamics [19, 20] and in the reproduction of fission barriers [21].

The effective forces are usually obtained by reproducing static nuclear properties. The SkM* force has been widely used for fission studies with good surface properties [22]. However, SkM* is not good at descriptions of global binding energies [23]. The static fission barriers due to different Skyrme forces can lead to significant differences in fission tunneling lifetimes [24–26]. In addition, the symmetry energy has been extensively studied in nuclear collision reactions for transport properties and equation of state [27–29]. It would be interesting to study the role of effective nuclear forces in the evolution of fission dynamics while static fission barriers are not observables in TDHF.

The real-time nuclear fission dynamics can be directly demonstrated by the evolution of nuclear density distributions. The fourier analysis of time-dependent deformations are connected to collective vibrations and damping effects. The non-adiabatic fission studies can only be performed after the saddle of the fission barrier. The nuclear shapes at the scission deformation and after scission are of particular interest. The octupole deformations and shell effects of fission fragments are essential for descriptions of fission yields [13]. The collective oscillations of fission fragments are also an interesting topic [10, 30]. The aim of the present work is to study the role of different Skyrme force in nuclear fission dynamics, as well as the oscillations of fission fragments based on the TDHF framework, which can capture the major features of real-time fission dynamics, at least close to scission. In this work, the studies are about the later phase of the fission with large initial deformations after the tunneling.

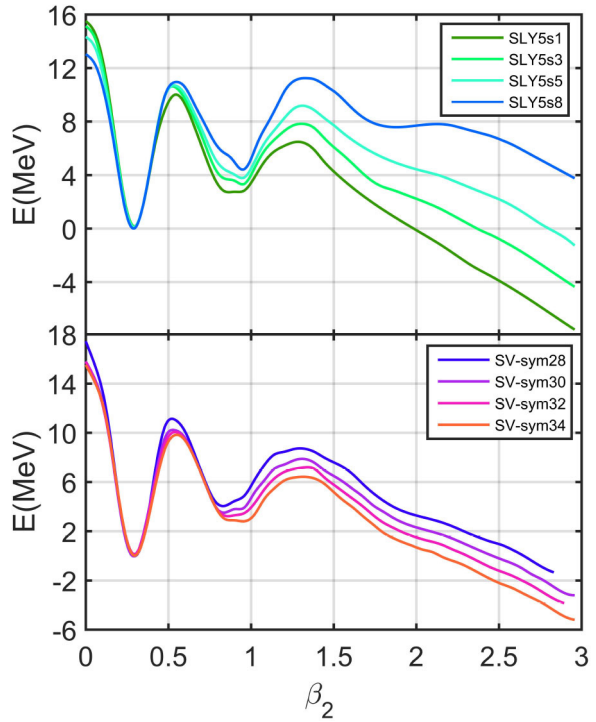


**FIGURE 1 |** The fission barriers of $^{240}$Pu calculated by Skyrme Hartree-Fock+BCS with SLy5s*X* and SV-sym forces, respectively. Calculations are performed with octupole deformations but without triaxial deformations.

## 2. THE TDHF THEORY

The TDHF equations can be formally derived from the time-dependent variational method. In the formalism of density matrices, TDHF is the approximation in which the two-body interaction term is approximated by a product of one-body terms [8, 18]. The TDHF equation is written as:

$$i\hbar\frac{\partial\varphi_k(\boldsymbol{r},t)}{\partial t} = h(\boldsymbol{r},t)\varphi_k(\boldsymbol{r},t) \tag{1}$$

where $\varphi_k$ are the time-dependent single-particle wave functions in coordinate spaces. The single-particle hamiltonian $h$ is also time dependent. The wave functions is always a Slater determinant during the evolution.

We utilize the 3D Skyrme-TDHF solver Sky3D [31, 32] and calculations are performed in the 3D uniform coordinate space. There are no symmetry restrictions on the wavefunctions. For the effective interactions, we adopted the series of SLy5s*X* [33] forces to study the influences of surface energies. In addition, we adopted the series of SV-sym forces [34] to study the influences of symmetry energies. The pairing has not been included in this work. The grid spacing is set to be 1 fm and the time step of dynamical evolution takes 0.2 fm/c. In Sky3D, the time propagator is evaluated by the Taylor series expansion up to the sixth order [31]. Computations with these settings have been demonstrated to be good enough for descriptions of dynamical properties. The static constrained calculations of $^{240}$Pu are firstly carried out to obtain the wave functions by the axial-symmetric Skyrme-Hartree-Fock solver SKYAX [35], which are inputs for time-evolution calculations. The 3D box size in static and dynamical calculations is taken as $50\times50\times70$ fm, along x, y, z-axis respectively. Note that the static wave functions are obtained by the SKYAX solver [35] in axial-symmetric cylindrical coordinate spaces and are transformed into 3D coordinate spaces by interpolations. The interpolation from a 2D grid to a 3D grid can result in small numerical errors, which are around 100 keV in binding energies. In this case, the initial wave functions at any constrained quadrupole and octupole deformations ($\beta_2$, $\beta_3$) can be obtained efficiently. The energies and density distributions as a function of time are the main outputs of the time-dependent solver.

## 3. RESULTS AND DISCUSSIONS

### 3.1. Influences of Surface Energies in Fission Dynamics

The surface energy coefficients of effective nuclear forces are critical properties as the fission is mainly determined by the competition between surface energies and Coulomb energies. To study the influences of surface energies in fission dynamics, we adopted the series of SLy5s*X* forces [33]. These Skyrme forces are obtained based on the SLy5 force but with varying surface energies in the fit protocol. The properties of equation of state (EoS) of SLy5s*X* forces are listed in the **Table 1**. The

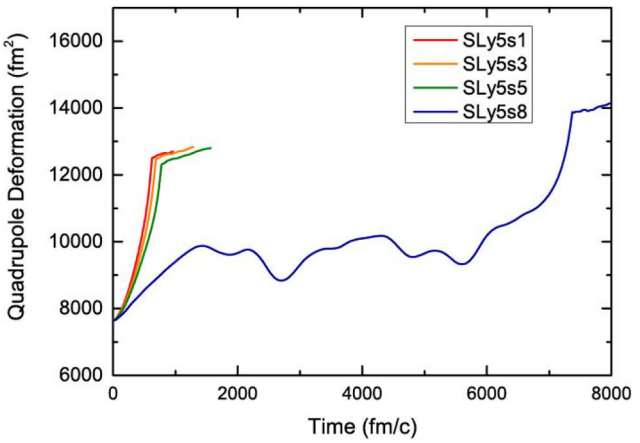


**FIGURE 2 |** The evolutions of quadrupole deformations in TDHF calculations with the SLy5s1, SLy5s3, SLy5s5, SLy5s8 forces.

**TABLE 1 |** The relevant EoS properties of SLy5s*X* [33] and SV-sym [34] forces are listed, including the incompressibility *K* (MeV), the symmetry energy $a_{sym}$ (MeV), the effective mass $m^*/m$, the slope of the symmetry energy *L* (MeV), the surface energy coefficient $a_{surf}$ (MeV).

| Forces | *K* | $a_{sym}$ | m*/m | *L* | $a_{surf}$ |
|---|---|---|---|---|---|
| SLy5s1 | 222.1 | 31.43 | 0.739 | 48.1 | 17.16 |
| SLy5s3 | 224.3 | 31.77 | 0.731 | 48.4 | 17.55 |
| SLy5s5 | 226.4 | 32.11 | 0.724 | 48.6 | 17.93 |
| SLy5s8 | 229.1 | 32.64 | 0.718 | 49.0 | 18.52 |
| SV-sym28 | 234 | 28 | 0.9 | 7 | 17.06 |
| SV-bas | 234 | 30 | 0.9 | 32 | 17.24 |
| SV-sym32 | 234 | 32 | 0.9 | 57 | 17.38 |
| SV-sym34 | 234 | 34 | 0.9 | 81 | 17.49 |

*For SV-sym forces, L and $a_{surf}$ are taken from [27] and [33], respectively.*

calculated potential energy curves of SLy5s*X* forces as a function of quadrupole deformations $\beta_2$ are shown in **Figure 1**. The two-dimensional potential energy surfaces of $^{240}$Pu from different calculations can be found in [5, 36, 37]. The SLy5s8 has the largest surface energy and SLy5s1 has the smallest surface energy. Consequently SLy5s8 has the highest fission barriers.

The TDHF calculations of the fission process of $^{240}$Pu are performed at the same initial deformations with SLy5s1, SLy5s3, SLy5s5, SLy5s8 forces. **Figure 2** shows that the evolutions of quadrupole deformations, in which initial deformations are $\beta_2$=2.4 and $\beta_3$=0.9 in four calculations. The multipole deformation $\beta_l$ is defined as [38],

$$\beta_l = \frac{4\pi}{3AR_0^l} < r^l Y_{l0} > \qquad (2)$$

where $R_0 = 1.2A^{1/3}$ fm. The quadrupole moment shown in **Figure 2** is defined as $< r^2 Y_{20} >$. We can see that in calculations with SLy5s1, SLy5s3, and SLy5s5, $^{240}$Pu goes to fission very quickly at time around 700 fm/c. With increasing surface energies, the fission lifetime increase slightly. However, in calculations with SLy5s8, the fission lifetime is extremely long. We see very slow and large-amplitude oscillations in the quadrupole deformation toward the fission. The results indicate that the fission would be strongly over-damped above a critical surface energy coefficient. This is understandable since the large surface tension would prohibit the fission movement.

## 3.2. Influences of Symmetry Energies in Fission Dynamics

The symmetry energy is expected to be crucial in the equation of state (EoS) of neutron stars and in exotic neutron-rich nuclei [39]. In Skyrme forces, the symmetry energy is density-dependent and is usually determined according to EoS properties at the saturated density. The larger symmetry energy coefficient indicates that neutron-rich systems are less stable. In the transport model, the large symmetry energy could lead to rapid isospin balance [28]. To study the role of symmetry energy in fission dynamics, we calculate the fission evolutions with Skyrme forces SV-sym28, SV-bas, SV-sym32, SV-sym34 [34], which differ in symmetry energy coefficients, but are otherwise similar. The calculated potential energy curves of SV-sym forces as a function of quadrupole deformations $\beta_2$ are shown in **Figure 1**. The EoS properties of SV-sym forces are listed in the **Table 1**. The fission barrier of SV-sym34 is slightly lower than that of SV-sym28, although the surface energy coefficient of SV-sym34 is slightly larger than that of SV-sym28. This is consistent with the results of fission barriers in [34]. Note that the surface symmetry energy is important for descriptions of fission barriers [40]. We also noticed that the slopes *L* of symmetry energies of SV-sym forces are very different, which are difficult to be constrained. The series of SV-sym forces have been used to study the influences of symmetry energies in nuclear fusion processes [27].

**Figure 3** shows that the quadrupole deformation evolutions with initial deformations of $\beta_2$=2.25 and $\beta_3$=0.9 in our calculations. The initial deformation $\beta_2$=2.25 used for SV-sym forces is slightly smaller than $\beta_2$=2.4 used for SLy5s*X* forces. This is because $^{240}$Pu doesn't fission in calculations with SLy5s8 if the initial deformation is $\beta_2$=2.25. We can see that in calculations with SV-sym28, SV-bas, SV-sym32, $^{240}$Pu goes to fission quickly. The fission time is longer than that with SLy5s1-3-5 forces (see **Figure 2**), since the initial deformation used for SLy5s*X* is slightly larger. The evolutions of SV-sym34 results are similar to three other cases at the beginning. However, just before the scission, the fission with SV-sym34 feels a strong restoring force that delays its fission. Such a restoring force has also subtle influences in SV-sym32 evolutions. The origin of such a restoring force can be understood that the formation of neutron-rich neck is not favored due to a large symmetry energy. Both symmetry energy and surface energy are positive contributions to total binding energies. During the fission process, the kinetic energy and Coulomb energy would decrease while total energies are conserved. Once the kinetic energies are strongly dissipated after several oscillations, the fission would finally occur. This is similar with the case of SLy5s8 with a large surface energy. The fission

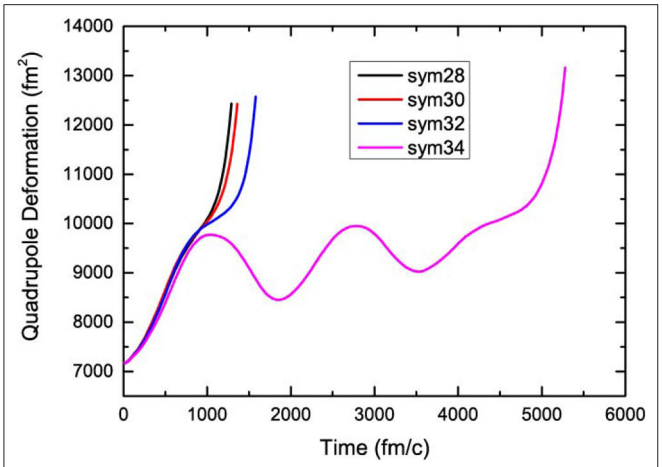


**FIGURE 3 |** The evolutions of quadrupole deformations in TDHF calculations with the SV-sym28, SV-bas, SV-sym30, SV-sym34 forces.

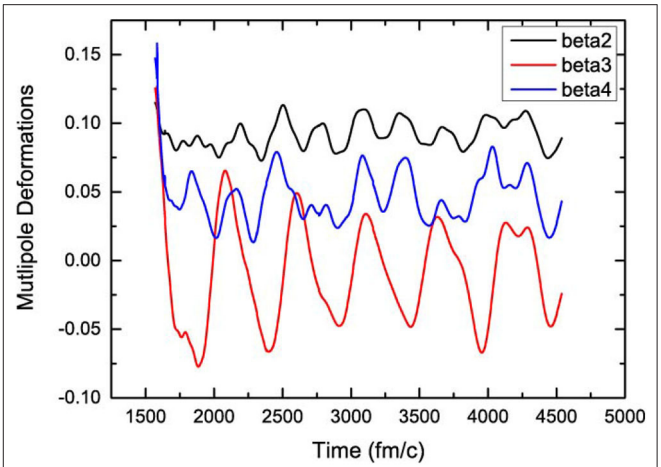


**FIGURE 4 |** The TDHF evolutions of quadrupole, octupole, and hexadecapole deformations of the heavy fragment after the $^{240}$Pu fission with the SV-sym32 force.

life times of SV-sym28, SV-bas, SV-sym32 are 1260, 1320, 1530 fm/c respectively. We see that with increased symmetry energies, the fission lifetimes increase non-linearly. This could be related the quantum critical point in dissipation dynamics [41]. Note that the over-damped fission phenomena with SV-sym34 would not appear if the initial deformation is very close to the scission point. The very different slopes of symmetry energies of SV-sym forces could also play a role in fission dynamics. In all cases, the octupole deformations increases very rapidly before 100 fm/c, then varies moderately before scission. At the scission, the octupole deformations increase more rapidly than quadruple deformations. The evolutions of hexadecapole deformations are similar to that of quadruple deformations before the scission.

## 3.3. The Collective Oscillations of Fission Fragments

The shapes of fission fragments at the scission point are far away from the equilibrium shapes. The octupole deformations of the fragments would strongly impact the fission yields [13]. For example, $^{144}$Ba with favorable octupole shell effects would play a significant role in asymmetric fission yields [13]. In fission dynamics, the oscillations of fission fragments can be connected to the low-lying multipole excitations [30].

**Figure 4** shows the multipole deformation oscillations of the heavy fission fragment after the $^{240}$Pu fission. The heavy fragment is around $^{132}$Sn and is nearly spherical at ground state which is resistant to octupole deformation. However, it can be seen that the oscillation amplitudes of octupole shapes are most significant compared to quadrupole and hexadecapole deformation oscillations. This is understandable since the initial octupole deformation is far from equilibrium. The hexadecapole oscillations are also significant compared to quadrupole oscillations since the initial hexadecapole deformation is very large. It is interesting to see that the large fragments have significant octupole oscillations. The dependence of the

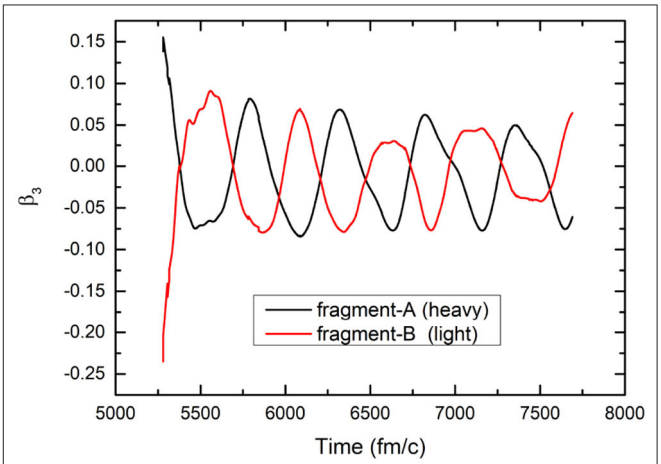


**FIGURE 5 |** The evolutions of octupole deformations in TDHF calculations of two fission fragments with the SV-sym34 force. The fragment-A is the heavy fragment and fragment-B is the light fragment.

octupole oscillation frequencies on different Skyrme forces is not significant.

**Figure 5** shows the octupole oscillations of both fragments of the $^{240}$Pu fission. The corresponding density evolutions are shown in **Figure 6**. **Figure 6** also shows that evolution of fission neck before scission in calculations with SV-sym34. We see that the neck is thin at 1000 fm/c and becomes thick at 1,900 fm/c. The main differences in nuclear shapes are the evolutions of neutron-rich necks, in which the symmetry energy can play a role. The shapes of fragments before scission don't change much. The small fragment around $^{107}$Mo has a significant octupole deformation before scission. The heavy fragment around $^{133}$Te which is close to $^{132}$Sn is nearly spherical but with an initial octupole deformation before scission. The sizes of the fragments can vary slightly with different Skyrme forces and initial deformations.

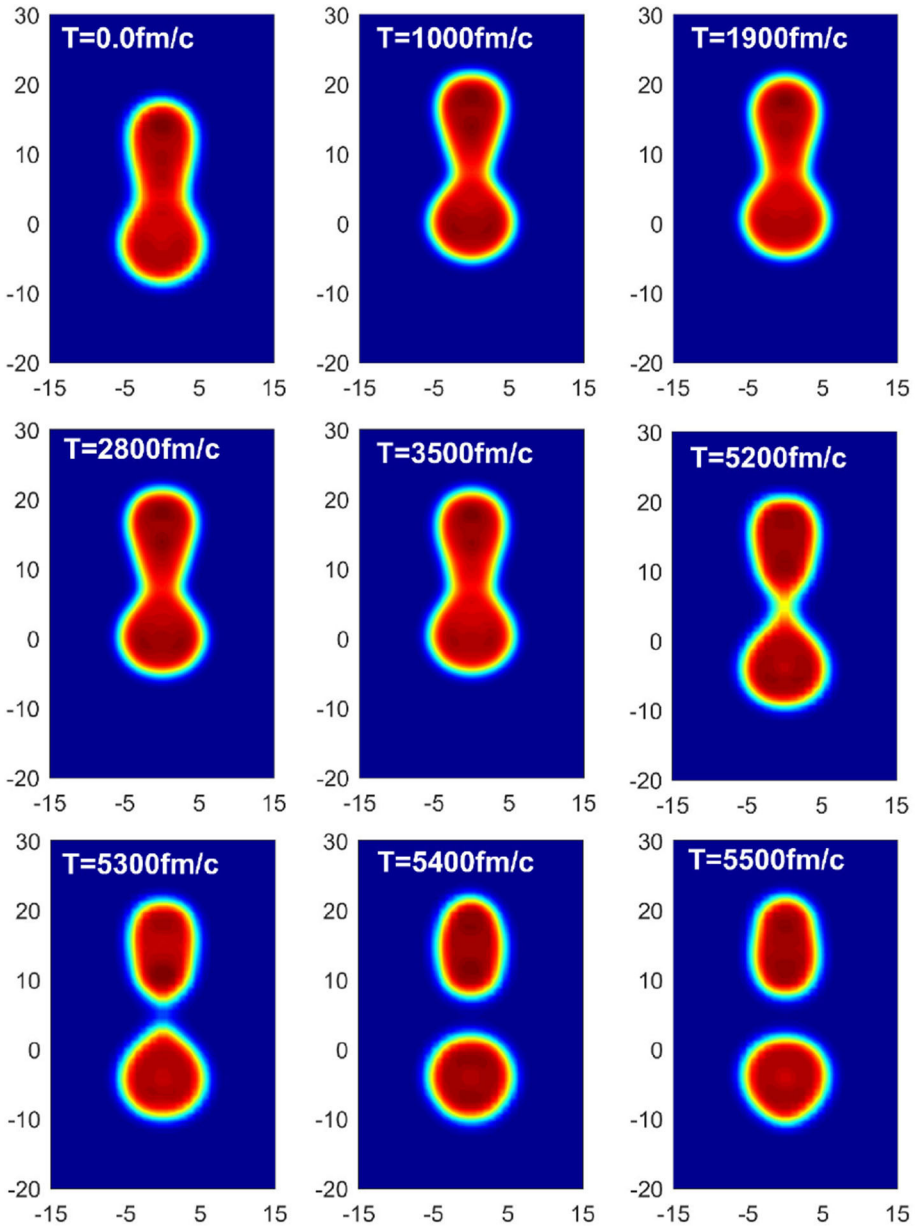


**FIGURE 6 |** The density evolutions of the $^{240}$Pu fission in TDHF calculations with the SV-sym34 force.

The amplitudes and frequencies of octupole oscillations of both fragments are comparable. The two fragments are oscillating with opposite octupole deformations. As shown in **Figure 6**, the small fragment has a significant quadrupole deformation at equilibrium. The heavy fragment has a spherical shape at equilibrium so that the octupole oscillation is very significant. The oscillation frequencies $\hbar\omega$ obtained by Fourier analysis are about 1.3 MeV, which is much lower than the typical experimental energies of the octupole vibration states of the fragments. For descriptions of vibrations of fragments, the finite-temperature QRPA [42] would be appropriate since the fragments are actually thermal excited.

## 4. CONCLUSION

In summary, we studied the shape evolutions in fission process of $^{240}$Pu with the TDHF approach. Firstly, the dependence of Skyrme forces in fission dynamics has been investigated. We found that Skyrme forces with large surface energy coefficients and large symmetry energy coefficients can result in extremely long fission times. Before the final scission, in these cases, the fission process would be over-damped with slow and small-amplitude shape oscillations. The symmetry energy can play a role in the evolution of neutron-rich necks before the scission. The evolutions of octupole deformations don't follow that of

quadrupole deformations. In addition, we also studied the shape oscillations of the fragments of the $^{240}$Pu fission. It is interesting to see that the heavy fragment which is close to spherical at equilibrium has significant octupole oscillations. Both fragments have comparable octupole oscillation amplitudes and frequencies. On the other hand, the quadrupole and hexadecapole oscillations of the fragments are less significant.

## AUTHOR CONTRIBUTIONS

MP did calculations and some figures. JP wrote the manuscript. YQ did part of the coding and figures. PS suggested the topic and worked on the manuscript.

## FUNDING

This work was supported by the National Natural Science Foundation of China under Grant Nos. 11975032, 11790325, 11835001, and 11961141003; the National Key R&D Program of China (Contract No. 2018YFA0404403). It was also supported by UK STFC under grant number ST/P005314/1.

## ACKNOWLEDGMENTS

We also acknowledge that computations in this work were performed in Tianhe-1A located in Tianjin.

## REFERENCES

1. Schunck N, Robledo LM. Microscopic theory of nuclear fission: a review. *Rep Prog Phys*. (2016) **79**:116301. doi: 10.1088/0034-4885/79/11/116301
2. Bender M, Bernard R, Bertsch G, Chiba S, Dobaczewski J, Dubray N, et al. Future of nuclear fission theory. *J Phys G*. (2020). doi: 10.1088/1361-6471/abab4f
3. Brosa U, Grossmann S, Müller A. Nuclear scission. *Phys Rep*. (1990) **197**:167. doi: 10.1016/0370-1573(90)90114-H
4. Nix JR. Summary: our 50-year Odyssey with fission. *Nucl Phys A*. (1989) **502**:609. doi: 10.1016/0375-9474(89)90693-3
5. Regnier D, Dubray N, Schunck N, Verriere M. Fission fragment charge and mass distributions in 239Pu(n,f) in the adiabatic nuclear energy density functional theory. *Phys Rev C*. (2016) **93**:054611. doi: 10.1103/PhysRevC.93.054611
6. Younes W, Gogny DM, Berger J-F. A microscopic theory of fission dynamics based on the generator coordinate method. In: *Lecture Notes on Physics 950*. Berlin: Springer (2019). doi: 10.1007/978-3-030-04424-4
7. Verriere M, Regnier D. The time-dependent generator coordinate method in nuclear physics. *Front Phys*. (2020) 8:233. doi: 10.3389/fphy.2020.00233
8. Simenel C. Nuclear quantum many-body dynamics: from collective vibrations to heavy-ion collisions. *Eur Phys J A*. (2012) **48**:152. doi: 10.1140/epja/i2012-12152-0
9. Bulgac A, Magierski P, Roche KJ, Stetcu I. Induced fission of 240Pu within a real-time microscopic framework. *Phys Rev Lett*. (2016) **116**:122504. doi: 10.1103/PhysRevLett.116.122504
10. Goddard P, Stevenson P, Rios A. Fission dynamics within time-dependent Hartree-Fock: deformation-induced fission. *Phys Rev C*. (2015) **92**:054610. doi: 10.1103/PhysRevC.92.054610
11. Goddard P, Stevenson P, Rios A. Fission dynamics within time-dependent Hartree-Fock. II. Boost-induced fission. *Phys Rev C*. (2016) **93**:014620. doi: 10.1103/PhysRevC.93.014620
12. Simenel C, Umar AS. Heavy-ions collisions and fission dynamics with the time-dependent Hartree-Fock theory and its extensions. *Prog Part Nucl Phys*. (2018) **103**:19. doi: 10.1016/j.ppnp.2018.07.002
13. Scamps G, Simenel C, Impact of pear-shaped fission fragments on mass-asymmetric fission in actinides, Nature (2018) **564**:382. doi: 10.1038/s41586-018-0780-0
14. Negele JW. The mean-field theory of nuclear structure and dynamics. *Rev Mod Phys*. (1982) **54**:9135. doi: 10.1103/RevModPhys.54.913
15. Nakatsukasa T, Matsuyanagi K, Matsuo M, Yabana K. Time-dependent density-functional description of nuclear dynamics. *Rev Mod Phys*. (2016) **88**:045004. doi: 10.1103/RevModPhys.88.045004
16. Ebata S. Studies on nuclear structure and nuclear dynamics using Cb-TDHFB. *Front Phys*. (2020) **8**:102. doi: 10.3389/fphy.2020.00102
17. Scamps G, Simenel C, Lacroix D. Dynamical description of the fission process using the TD-BCS theory. *AIP Conf Proc*. (2015) **1681**:040003. doi: 10.1063/1.4932264
18. Stevenson PD, Barton MC. Low-energy heavy-ion reactions and the Skyrme effective interaction. *Prog Part Nucl Phys*. (2019) **104**:142. doi: 10.1016/j.ppnp.2018.09.002
19. Stevenson PD, Suckling EB, Fracasso S, Barton MC, Umar AS. Skyrme tensor force in heavy ion collisions. *Phys Rev C*. (2016) **93**:054617. doi: 10.1103/PhysRevC.93.054617
20. Guo L, Godbey K, Umar AS. Influence of the tensor force on the microscopic heavy-ion interaction potential. *Phys Rev C*. (2018) **98**:064607. doi: 10.1103/PhysRevC.98.064607
21. Bernard RN, Pillet N, Robledo LM, Anguiano M. Description of the asymmetric to symmetric fission transition in the neutron-deficient thorium isotopes: role of the tensor force. *Phys Rev C*. (2020) **101**:044615. doi: 10.1103/PhysRevC.101.044615
22. Bartel J, Quentin P, Brack M, Guet C, Håkansson HB. Towards a better parameterisation of Skyrme-like effective forces: a critical study of the SkM force. *Nucl Phys A*. (1982) **386**:79. doi: 10.1016/0375-9474(82)90403-1
23. Zuo ZW, Pei JC, Xiong XY, Zhu Y. Global analysis of Skyrme forces with higher-order density dependencies. *Chin Phys C*. (2018) **42**:064106. doi: 10.1088/1674-1137/42/6/064106
24. Erler J, Langanke K, Loens HP, Martinez-Pinedo G, Reinhard P-G. Fission properties for r-process nuclei. *Phys Rev C*. (2012) **85**:025802. doi: 10.1103/PhysRevC.85.025802
25. Baran A, Kowal M, Reinhard PG, Robledo LM, Staszczak A, Warda M. Fission barriers and probabilities of spontaneous fission for elements with $Z \geqslant 100$. *Nucl Phys A*. (2015) **944**:442. doi: 10.1016/j.nuclphysa.2015.06.002
26. Zhu Y, Pei JC. Thermal fission rates with temperature dependent fission barriers. *Phys Rev C*. (2016) **94**:024329. doi: 10.1103/PhysRevC.94.024329
27. Reinhard P-G, Umar AS, Stevenson PD, Piekarewicz J, Oberacker VE, Maruhn JA. Sensitivity of the fusion cross section to the density dependence of the symmetry energy. Phys Rev C. (2016) **93**:044618. doi: 10.1103/PhysRevC.93.044618
28. Zhang Y, Tian J, Cheng W, Guan F, Huang Y, Li H, et al. Long-time drift of the isospin degree of freedom in heavy ion collisions. *Phys Rev C*. (2017) **95**:041602. doi: 10.1103/PhysRevC.95.041602
29. Li BA, Chen LW, Ko CM. Recent progress and new challenges in isospin physics with heavy-ion reactions. *Phys Rep*. (2008) **464**:113. doi: 10.1016/j.physrep.2008.04.005
30. Simenel C, Umar AS. Formation and dynamics of fission fragments. *Phys Rev C*. (2014) **89**:031601. doi: 10.1103/PhysRevC.89.031601
31. Maruhn JA, Reinhard P-G, Stevenson PD, Umar AS. The TDHF code Sky3D. *Comp Phys Commun*. (2014) **185**:2195. doi: 10.1016/j.cpc.2014.04.008
32. Schuetrumpf B, Reinhard P-G, Stevenson PD, Umar AS, Maruhn JA. The TDHF code Sky3D version 1.1. *Comp Phys Commun*. (2018) **229**:211. doi: 10.1016/j.cpc.2018.03.012
33. Jodon R, Bender M, Bennaceur K, Meyer J. Constraining the surface properties of effective Skyrme interactions. *Phys Rev C*. (2016) **94**:024335. doi: 10.1103/PhysRevC.94.024335

34. Klüpfel P, Reinhard P-G, Brvenich TJ, Maruhn JA. Variations on a theme by Skyrme: a systematic study of adjustments of model parameters *Phys Rev C*. (2009) **79**:034310. doi: 10.1103/PhysRevC.79.034310
35. Reinhard P-G. Computer Code SKYAX (unpublished).
36. Bulgac, Jin S, Roche KJ, Schunck N, Stetcu I. Fission dynamics of 240Pu from saddle to scission and beyond. *Phys Rev C*. (2019) **100**:034615. doi: 10.1103/PhysRevC.100.034615
37. Zhao J, Xiang J, Li ZP, Niksic T, Vretenar D, Zhou SG. Time-dependent generator-coordinate-method study of mass-asymmetric fission of actinides. *Phys Rev C*. (2019) **99**:054613. doi: 10.1103/PhysRevC.99.054613
38. Bender M, Heenen PH, Reinhard P-G. Self-consistent mean-field models for nuclear structure. *Rev Mod Phys*. (2003) **75**:121. doi: 10.1103/RevModPhys.75.121
39. Steiner AW, Prakash M, Lattimer JM, Ellis PJ. Isospin asymmetry in nuclei and neutron stars. *Phys*. Rep. (2005) **411**:325. doi: 10.1016/j.physrep.2005.02.004
40. Nikolov N, Schunck N, Nazarewicz W, Bender M, Pei J. Surface symmetry energy of nuclear energy density functionals. *Phys Rev C*. (2011) **83**:034305. doi: 10.1103/PhysRevC.83.034305
41. Tong D, Wong K. Fluctuation and dissipation at a quantum critical point. *Phys Rev Lett*. (2013) **110**:061602. doi: 10.1103/PhysRevLett.110.061602
42. Yüksel E, Colò G, Khan E, Niu YF, Bozkurt K. Multipole excitations in hot nuclei within the finite temperature quasiparticle random phase approximation framework. *Phys Rev C*. (2017) **96**:024303. doi: 10.1103/PhysRevC.96.024303


**Conflict of Interest:** The authors declare that the research was conducted in the absence of any commercial or financial relationships that could be construed as a potential conflict of interest.

frontiers in Physics

REVIEW
published: 06 October 2020
doi: 10.3389/fphy.2020.00330

# Nuclear Collective Dynamics in Transport Model With the Lattice Hamiltonian Method

*Rui Wang*[1,2], *Zhen Zhang*[3], *Lie-Wen Chen*[4]* *and Yu-Gang Ma*[1,2]

[1] Key Laboratory of Nuclear Physics and Ion-Beam Application (Ministry of Education), Institute of Modern Physics, Fudan University, Shanghai, China, [2] Shanghai Institute of Applied Physics, Chinese Academy of Sciences, Shanghai, China, [3] Sino-French Institute of Nuclear Engineering and Technology, Sun Yat-Sen University, Zhuhai, China, [4] Shanghai Key Laboratory for Particle Physics and Cosmology, School of Physics and Astronomy, Shanghai Jiao Tong University, Shanghai, China

We review recent progress in studying nuclear collective dynamics by solving the Boltzmann-Uehling-Uhlenbeck (BUU) equation with the lattice Hamiltonian method, treating the collision term with the full-ensemble stochastic collision approach. This lattice BUU (LBUU) method has recently been developed and implemented with a GPU parallel computing technique, and achieves rather stable nuclear ground-state evolution and high accuracy in evaluating the nucleon-nucleon (NN) collision term. This new LBUU method has been applied to investigate nuclear isoscalar giant monopole resonances and isovector giant dipole resonances. While calculations using the LBUU method without the NN collision term (i.e., the lattice Hamiltonian Vlasov method) provide a reasonable description of the excitation energies of nuclear giant resonances, the full LBUU calculations can well reproduce the width of the giant dipole resonance of $^{208}$Pb by including a collisional damping from NN scattering. The observed strong correlation between the width of the nuclear giant dipole resonance and the NN elastic cross-section suggests that the NN elastic scattering plays an important role in nuclear collective dynamics, and the width of the nuclear giant dipole resonance provides a good probe of the in-medium NN elastic cross-section.

**Keywords: Boltzmann-Uehling-Uhlenbeck equation, lattice Hamiltonian method, nuclear giant resonances, Thomas-Fermi initialization, stochastic collision approach**

OPEN ACCESS

***Edited by:***
*Paul Denis Stevenson, University of Surrey, United Kingdom*

***Reviewed by:***
*Armen Sedrakian, Frankfurt Institute for Advanced Studies, Germany*
*Norbert Kaiser, Technical University of Munich, Germany*

***Correspondence:**
*Lie-Wen Chen*
*lwchen@sjtu.edu.cn*

***Specialty section:***
*This article was submitted to Nuclear Physics, a section of the journal Frontiers in Physics*

***Received:*** *24 May 2020*
***Accepted:*** *16 July 2020*
***Published:*** *06 October 2020*

***Citation:***
*Wang R, Zhang Z, Chen L-W and Ma Y-G (2020) Nuclear Collective Dynamics in Transport Model With the Lattice Hamiltonian Method. Front. Phys. 8:330. doi: 10.3389/fphy.2020.00330*

## 1. INTRODUCTION

Transport models deal with the time evolution of the Wigner function or phase-space distribution function $f(\vec{r},\vec{p},t)$ that arises from the Wigner representation of the Schrödinger equation [1, 2], and provide a successful semi-classical time-dependent approach to studying nuclear dynamics, especially with regard to heavy-ion collisions (HICs). One of the main ingredients of transport models is the mean-field potential, which embodies information on the nuclear equation of state (EOS) or the in-medium effective nuclear interaction. Therefore, transport models serve as an important theoretical tool for investigating the EOS of asymmetric nuclear matter from observables in HICs. A good deal of information on the nuclear EOS, from sub-saturation [3–5] to supra-saturation densities of about 3–5 times saturation density [6–18], has been obtained from transport model analyses of various observables, such as collective flows and particle production, in intermediate- and high-energy HICs. Exact information about the nuclear EOS is crucial for describing reaction dynamics of exotic nuclei [19, 20], various properties of both finite nuclei

(e.g., neutron skin thickness [21–23] and drip lines [24, 25]) and neutron stars (e.g., masses and cooling mechanisms [26–30]), and astrophysical processes, such as supernova explosion scenarios [31–33]. In particular, it should be mentioned that the first gravitational wave signal GW170817 [34] of a binary neutron star merger has recently been observed and localized by the LIGO and Virgo observatories, inaugurating a new era of multimessenger astronomy and supplying important constraints on the dense nuclear matter EOS [35–39]. Moreover, very recently, using X-ray data from NASA's Neutron Star Interior Composition Explorer (NICER), the mass and radius of the millisecond pulsar PSR J0030+0451 have been simultaneously estimated [40, 41] and the implications for the dense nuclear matter EOS analyzed [42]. In addition, a new record for the maximum mass of neutron stars, namely a millisecond pulsar J0740+6620 with mass $2.14^{+0.10}_{-0.09}M_{\odot}$ (68.3% credibility interval), has been reported recently [43]; this heaviest neutron star observed so far can rule out many soft nuclear matter equations of state, and in particular, the supersoft high-density symmetry energy [44].

The time-dependent Hartree-Fock (TDHF) theory provides a very successful quantum many-body framework at the mean-field level for describing low-energy nuclear reaction dynamics, including the nuclear collective dynamics (see e.g., references [45, 46] for a review of recent work). Given that the Vlasov equation, i.e., the Boltzmann-Uehling-Uhlenbeck (BUU) equation without the nucleon-nucleon (NN) collision term, corresponds to the semi-classical limit of the TDHF equation, transport models can thus be seen as an efficient semi-classical approach to studying nuclear collective dynamics. In particular, the two-particle-two-hole ($2p$-$2h$) correlation beyond the mean-field approximation, which dominates the collisional damping of nuclear giant resonances, can be effectively taken into account in transport models via binary collisions. The literature contains many works that study nuclear giant resonances based on the pure Vlasov equation [47–49], the Vlasov equation with a collision relaxation time [50], and the full transport model with both the mean-field and the NN scatterings [51–53]. For example, based on simulations of transport models, the excitation energies of nuclear giant resonances have been used to extract information on the nuclear EOS and neutron-proton effective mass splitting [54], while the width of nuclear giant dipole resonance (GDR) has been proposed as an effective probe of the in-medium NN elastic cross-section [55]. The width of the nuclear GDR can also serve as a fingerprint of $\alpha$-particle clustering configurations in nuclei [56].

Although transport models have been extensively used in the study of nuclear giant resonances, the accurate description of giant resonances within transport models is still a challenge. In transport models, unlike in simulations of HICs at intermediate and high energies, the calculation of nuclear giant resonances, which are the collective excitation states with an excitation energy of about 20 MeV, requires a more proper description of nuclear ground states and an accurate implementation of Pauli blocking. In particular, Pauli blocking is intimately related to the collisional damping and hence the width of nuclear giant resonances in the transport model calculations. In this sense, studying the nuclear collective motion provides an ideal way to examine and improve transport models, since the effects of several deficiencies, such as the inaccurate treatment of Pauli blocking, are more pronounced in nuclear collective dynamics with small-amplitude oscillations. Transport models for HICs can be roughly divided into two categories, the BUU equation (see e.g., reference [2]) and the quantum molecular dynamics (QMD) model (see e.g., reference [57]). From the viewpoint of transport models, the essential difference between these two types is that the BUU-type models mimic $f(\vec{r},\vec{p},t)$ by having a large number of ensembles or test particles for each nucleon, while the QMD-type models use a Gaussian wave packet for each nucleon. Recently, the transport model community started a code comparison project [58–60] to try to understand the source of the discrepancies between various transport model codes and thus eventually reduce the uncertainties in transport models. For the issue of Pauli blocking, the QMD-type transport models seem not to be as good as the BUU-type models [59]; therefore the BUU-type transport models are more suitable for the study of nuclear collective motions, especially for the calculation of the spreading width, in which the accurate treatment of Pauli blocking is essential.

In order to study (near-)equilibrium nuclear dynamics within the framework of transport models, a BUU-type transport model, namely the lattice BUU (LBUU) method [55, 61], has recently been developed, which can achieve good stability for the ground-state evolution [61] and treat Pauli blocking with very high accuracy [55]. The resulting LBUU framework has the following features: (1) a smearing of the local density, which is commonly used in transport models to obtain a smooth mean field, is included self-consistently in the equations of motion through the lattice Hamiltonian (LH) method; (2) the ground state of a nucleus is obtained by varying the total energy with respect to the nucleon density distribution based on the same Hamiltonian that governs the system evolution; (3) the NN collision term in the BUU equation is implemented through a full-ensemble stochastic collision approach. The above features, as well as a sufficiently large number of ensembles, make it possible to solve the BUU equation almost exactly, and thus one can obtain very accurate results for the nuclear collective motions within the BUU equation. We note that the high accuracy of the LBUU method relies on a large amount of computational resources; therefore, high-performance GPU parallel computing [62] has been employed in the LBUU implementation to improve the computational efficiency.

This paper is organized as follows. In section 2, we first introduce the LBUU method for solving the BUU equation, including the mean field, the collision integral, and the initialization for the nuclear ground state, and then describe how to deal with the nuclear giant resonances within transport models. In section 3, we present results on the peak energies of the nuclear giant resonances obtained from lattice Hamiltonian Vlasov (LHV) calculations, i.e., LBUU calculations without the NN collision term, and then compare these with results from the random-phase approximation (RPA). In section 4, we give results on the strength function and the width of the GDR from the full LBUU calculations, and compare these with experimental data from the $^{208}\mathrm{Pb}(\vec{p},\vec{p}\,')$ reaction carried out at the Research Center for Nuclear Physics (RCNP) in

Osaka, Japan [63]. Finally we give a brief summary and outlook in section 5.

## 2. MODEL DESCRIPTION

The starting point for calculating the nuclear collective motion is the BUU equation with a momentum-dependent mean-field potential $U(\vec{r},\vec{p})$:

$$\frac{\partial f}{\partial t}+\frac{\vec{p}}{E}\cdot\nabla_{\vec{r}}f+\nabla_{\vec{p}}U(\vec{r},\vec{p})\cdot\nabla_{\vec{r}}f-\nabla_{\vec{r}}U(\vec{r},\vec{p})\cdot\nabla_{\vec{p}}f=I_{\rm c}, \quad (1)$$

where $f$ (the Wigner function) is the Fourier transform of the one-body density matrix $\rho(\vec{r}+\vec{s}/2,\vec{r}-\vec{s}/2)$, i.e.,

$$f(\vec{r},\vec{p})=\frac{1}{(2\pi\hbar)^3}\int\exp\Big(-i\frac{\vec{p}}{\hbar}\cdot\vec{s}\Big)\rho(\vec{r}+\vec{s}/2,\vec{r}-\vec{s}/2)\,d^3s. \quad (2)$$

In the local density approximation, $f(\vec{r},\vec{p})$ is reduced to the classical one-body phase-space distribution function. The collision term $I_{\rm c}$, which takes into account the Pauli principle due to nucleons' Fermi statistics, reads

$$I_{\rm c}=-g\int\frac{d^2p_2}{(2\pi\hbar)^3}\frac{d^3p_3}{(2\pi\hbar)^3}\frac{d^3p_4}{(2\pi\hbar)^3}\,|\mathcal{M}_{12\to34}|^2(2\pi)^4 \delta^4(p_1+p_2-p_3-p_4)\times[f_1f_2(1-f_3)(1-f_4)-f_3f_4(1-f_1)(1-f_2)], \quad (3)$$

where $g=2$ is the spin degeneracy factor and $\mathcal{M}_{12\to34}$ is the in-medium transition matrix element. Note that we have ignored the isospin index in the above three equations, but it can be restored easily. The BUU equation without the collision term $I_{\rm c}$ is referred to as the Vlasov equation, which is the semi-classical limit of the quantum transport theory with the system described by the one-body phase-space distribution function [1, 2], whereas the quantum corrections can be included perturbatively [64, 65].

We use the LH method, originally proposed by Lenk and Pandharipande [66] in 1989, to solve the BUU equation. The LH method has been successfully employed in the study of HICs [67, 68]. It improves the sample smoothing technique of the usual test particle approach [69] and conserves the total energy almost exactly. In the LH method, the phase-space distribution function $f_\tau(\vec{r},\vec{p},t)$ is mimicked by $A\times N_{\rm E}$ test nucleons with a form factor $S$ in the coordinate space to modify the relation between the test nucleons and the Wigner function, i.e.,

$$f_\tau(\vec{r},\vec{p},t)=\frac{1}{g}\frac{(2\pi\hbar)^3}{N_{\rm E}}\sum_i^{AN_{\rm E},\tau}S\big[\vec{r}_i(t)-\vec{r}\big]\delta\big[\vec{p}_i(t)-\vec{p}\big], \quad (4)$$

where $A$ is the mass number of the system and $N_{\rm E}$ is the number of ensembles or number of test particles, usually a very large number, used in the calculation. The sum in the above expression runs over all test nucleons with isospin $\tau$. The form factor $S$ can take a Gaussian form, or a certain form with a finite range that ensures the particle number conservation. By giving each test nucleon a form factor, the movement of a test nucleon leads to a continuous variation of the local nucleon density of nearby lattice sites, which is useful for smoothing the nucleon distribution functions in phase space. A similar form factor in momentum space [here the $\delta$-function is used in Equation (4)] could be introduced and might help to reduce fluctuations if a momentum-dependent mean-field potential is employed, and in the future it would be interesting to carry out a systematic investigation of the effects of a form factor in momentum space. The equations of motion of the test nucleons are governed by the total Hamiltonian, and we approximate the latter by the lattice Hamiltonian, i.e.,

$$H=\int\mathcal{H}(\vec{r})\,d\vec{r}\approx l_xl_yl_z\sum_\alpha\mathcal{H}(\vec{r}_\alpha)\equiv H_L, \quad (5)$$

where $\vec{r}_\alpha$ denotes the coordinates of lattice site $\alpha$, and $l_x$, $l_y$, and $l_z$ are the lattice spacings. Therefore, in the LH method only the values of the phase-space distribution function at lattice sites $f_\tau(\vec{r}_\alpha,\vec{p},t)$ need to be calculated.

By solving the BUU equation or Vlasov equation using the LH method, one obtains the time evolution of $f(\vec{r},\vec{p},t)$, or the test nucleons' coordinates $\vec{r}_i$ and momenta $\vec{p}_i$, and then the time evolution of other physical quantities can be calculated accordingly.

### 2.1. Mean Fields

We employ the Skyrme pseudopotential to calculate the lattice Hamiltonian in Equation (5). The next-to-next-to-next leading order (N3LO) Skyrme pseudopotential [70], which is a mapping of the N3LO local energy density functional [71], generalizes the standard Skyrme interaction [72] and can reproduce the empirical nuclear optical potential up to about 1 GeV in kinetic energy [73], which the standard Skyrme interactions fail to describe. The Hamiltonian density from the N3LO Skyrme pseudopotential contains the kinetic term $\mathcal{H}^{\rm kin}(\vec{r})$, the local term $\mathcal{H}^{\rm loc}(\vec{r})$, the momentum-dependent term $\mathcal{H}^{\rm MD}(\vec{r})$, the density-dependent term $\mathcal{H}^{\rm DD}(\vec{r})$, and the gradient term $\mathcal{H}^{\rm grad}(\vec{r})$. The kinetic term

$$\mathcal{H}^{\rm kin}(\vec{r})=\sum_{\tau=n,p}\int d^3p\,\frac{p^2}{2m_\tau}f_\tau(\vec{r},\vec{p}) \quad (6)$$

and the local term

$$\mathcal{H}^{\rm loc}(\vec{r})=\frac{t_0}{4}\Big[(2+x_0)\rho^2-(2x_0+1)\sum_{\tau=n,p}\rho_\tau^2\Big] \quad (7)$$

are the same as those from the standard Skyrme interaction. The momentum-dependent term is written in the form

$$\mathcal{H}^{\rm MD}(\vec{r})=\int d^3p\,d^3p'\,\mathcal{K}_s(\vec{p},\vec{p}')f(\vec{r},\vec{p})f(\vec{r},\vec{p}') +\sum_{\tau=n,p}\int d^3p\,d^3p'\,\mathcal{K}_v(\vec{p},\vec{p}')f_\tau(\vec{r},\vec{p})f_\tau(\vec{r},\vec{p}'), \quad (8)$$

with $f(\vec{r},\vec{p})=f_n(\vec{r},\vec{p})+f_p(\vec{r},\vec{p})$. The quantities $\mathcal{K}_{\rm s}(\vec{p},\vec{p}')$ and $\mathcal{K}_{\rm v}(\vec{p},\vec{p}')$ in Equation (8) represent the isoscalar and isovector kernels of the momentum-dependent part of the mean-field

potential, respectively; $\mathcal{K}_s(\vec{p},\vec{p}')$ and $\mathcal{K}_v(\vec{p},\vec{p}')$ for the N3LO Skyrme pseudopotential are expressed as

$$\mathcal{K}_s(\vec{p},\vec{p}') = \frac{C^{[2]}}{16\hbar^2}(\vec{p}-\vec{p}')^2 + \frac{C^{[4]}}{32\hbar^2}(\vec{p}-\vec{p}')^4 + \frac{C^{[6]}}{16\hbar^2}(\vec{p}-\vec{p}')^6, \tag{9}$$

$$\mathcal{K}_v(\vec{p},\vec{p}') = \frac{D^{[2]}}{16\hbar^2}(\vec{p}-\vec{p}')^2 + \frac{D^{[4]}}{32\hbar^2}(\vec{p}-\vec{p}')^4 + \frac{D^{[6]}}{16\hbar^2}(\vec{p}-\vec{p}')^6. \tag{10}$$

If we keep only the $C^{[2]}$ and $D^{[2]}$ terms, the N3LO Skyrme pseudopotential reduces to the standard Skyrme effective interaction. For the sake of simplicity in performing numerical derivatives, we truncate at the second order of the spatial gradient of $\rho(\vec{r})$,

$$\begin{aligned}\mathcal{H}^{\rm grad}(\vec{r}) &= \frac{1}{8}E^{[2]}\Big\{\rho(\vec{r})\nabla^2\rho(\vec{r}) - \big[\nabla\rho(\vec{r})\big]^2\Big\} \\ &+ \frac{1}{8}F^{[2]}\sum_{\tau=n,p}\Big\{\rho_\tau(\vec{r})\nabla^2\rho_\tau(\vec{r}) - \big[\nabla\rho_\tau(\vec{r})\big]^2\Big\} \\ &= \frac{1}{8}g^{[2]}\Big\{\rho(\vec{r})\nabla^2\rho(\vec{r}) - \big[\nabla\rho(\vec{r})\big]^2\Big\} \\ &+ \frac{1}{8}g^{[2]}_{\rm iso}\Big\{\rho_\delta(\vec{r})\nabla^2\rho_\delta(\vec{r}) - \big[\nabla\rho_\delta(\vec{r})\big]^2\Big\}. \end{aligned} \tag{11}$$

In the second line we have introduced $g^{[2]} = E^{[2]} + \frac{1}{2}F^{[2]}$, $g^{[2]}_{\rm iso} = \frac{1}{2}F^{[2]}$, and $\rho_\delta = \rho_n - \rho_p$. We neglect the second term in Equation (11) since it is much smaller than the first term; in other words, we keep only the second-order spatial derivative of the total nucleon density $\rho(\vec{r})$. The density-dependent term for the N3LO Skyrme pseudopotential takes its form in the standard Skyrme interaction,

$$\mathcal{H}^{\rm DD}(\vec{r}) = \frac{t_3}{24}\Big[(2+x_3)\rho^2 - (2x_3+1)\sum_{\tau=n,p}\rho_\tau^2\Big]\rho^\alpha. \tag{12}$$

One can see that the Hamiltonian density $\mathcal{H}(\vec{r})$, expressed as the sum of Equations (6)–(8), (11), and (12), is explicitly dependent on $f_\tau(\vec{r},\vec{p})$ as well as on the densities $\rho_\tau(\vec{r})$ and their derivatives.

In the above expressions, the parameters $C^{[n]}$, $D^{[n]}$, $E^{[n]}$, and $F^{[n]}$ are recombinations of the Skyrme parameters $t_1^{[n]}$, $t_2^{[n]}$, $x_1^{[n]}$ and $x_2^{[n]}$, which are related to the derivative terms of the Skyrme two-body potential $v_{\rm Sk}(\vec{r}_1,\vec{r}_2)$, i.e.,

$$C^{[n]} = t_1^{[n]}(2+x_1^{[n]}) + t_2^{[n]}(2+x_2^{[n]}), \tag{13}$$

$$D^{[n]} = -t_1^{[n]}(2x_1^{[n]}+1) + t_2^{[n]}(2x_2^{[n]}+1), \tag{14}$$

$$E^{[n]} = \frac{i^n}{2^n}\Big[t_1^{[n]}(2+x_1^{[n]}) - t_2^{[n]}(2+x_2^{[n]})\Big], \tag{15}$$

$$F^{[n]} = -\frac{i^n}{2^n}\Big[t_1^{[n]}(2x_1^{[n]}+1) + t_2^{[n]}(2x_2^{[n]}+1)\Big]. \tag{16}$$

Specifically, we obtain the coefficient of the gradient term,

$$g^{[2]} = E^{[2]} + \frac{1}{2}F^{[2]} = -\frac{1}{8}\Big[3t_1^{[2]} - t_2^{[2]}(5+4x_2^{[2]})\Big]. \tag{17}$$

Substituting $f(\vec{r},\vec{p},t)$ as expressed in Equation (4) into Equations (6)–(12) and noting that the local nucleon density $\rho_\tau(\vec{r})$ is given by the integral of $f_\tau(\vec{r},\vec{p},t)$ with respect to momentum,

$$\rho_\tau(\vec{r},t) = g\int f_\tau(\vec{r},\vec{p},t)\frac{d^3p}{(2\pi\hbar)^3} = \frac{1}{N_{\rm E}}\sum_i^{\alpha,\tau} S\big[\vec{r}_i(t)-\vec{r}\big], \tag{18}$$

we can express the lattice Hamiltonian $H_L$ in Equation (5) in terms of the coordinates and momenta of the test nucleons. Since the coordinates and momenta of the test nucleons $\vec{r}_i$ and $\vec{p}_i$ can be regarded as the canonical variables of the lattice Hamiltonian, their time evolution is then governed by the Hamilton equation for all ensembles,

$$\begin{aligned}\frac{d\vec{r}_i}{dt} &= N_{\rm E}\frac{\partial H_L\big[\vec{r}_1(t),\ldots,\vec{r}_{A\times N_{\rm E}}(t);\vec{p}_1(t),\ldots,\vec{p}_{A\times N_{\rm E}}(t)\big]}{\partial\vec{p}_i} \\ &= \frac{\vec{p}_i(t)}{m} + N_{\rm E}l_xl_yl_z\sum_{\alpha\in V_i}\frac{\partial\mathcal{H}^{\rm MD}_\alpha}{\partial\vec{p}_i}, \end{aligned} \tag{19}$$

$$\begin{aligned}\frac{d\vec{p}_i}{dt} &= -N_{\rm E}\frac{\partial H_L\big[\vec{r}_1(t),\ldots,\vec{r}_{A\times N_{\rm E}}(t);\vec{p}_1(t),\ldots,\vec{p}_{A\times N_{\rm E}}(t)\big]}{\partial\vec{r}_i} \\ &= -N_{\rm E}l_xl_yl_z \\ &\times\sum_{\alpha\in V_i}\Bigg\{\sum_\tau^{n,p}\Bigg[\frac{\partial(\mathcal{H}^{\rm loc}_\alpha+\mathcal{H}^{\rm Cou}_\alpha+\mathcal{H}^{\rm DD}_\alpha)}{\partial\rho_{\tau,\alpha}} \\ &+\sum_{n=0}(-1)^n\nabla^n\frac{\partial\mathcal{H}^{\rm grad}_\alpha}{\partial\nabla^n\rho_{\tau,\alpha}}\Bigg]\frac{\partial\rho_{\tau,\alpha}}{\partial\vec{r}_i} + \frac{\partial\mathcal{H}^{\rm MD}_\alpha}{\partial\vec{r}_i}\Bigg\}. \end{aligned} \tag{20}$$

In the above two equations, the subscript $\alpha$ refers to values at lattice site $\alpha$. The $V_i$ under the summation sign represents the volume that the form factor of the $i$th test nucleon covers, and the sums run over all lattice sites inside $V_i$. The Coulomb interaction contributes to the Hamiltonian density through the term

$$\begin{aligned}\mathcal{H}^{\rm Cou}(\vec{r}_\alpha) &= e^2\rho_p(\vec{r}_\alpha)\Bigg\{\frac{1}{2}\int\frac{\rho_p(\vec{r}')}{|\vec{r}_\alpha-\vec{r}'|}\,d\vec{r}' - \frac{3}{4}\Big[\frac{3\rho_p(\vec{r}_\alpha)}{\pi}\Big]^{1/3}\Bigg\} \\ &\approx e^2\rho_p(\vec{r}_\alpha)\Bigg\{\frac{1}{2}\sum_{\alpha'\neq\alpha}\frac{\rho_p(\vec{r}_{\alpha'})l_xl_yl_z}{|\vec{r}_\alpha-\vec{r}_{\alpha'}|} - \frac{3}{4}\Big[\frac{3\rho_p(\vec{r}_\alpha)}{\pi}\Big]^{1/3}\Bigg\}, \end{aligned} \tag{21}$$

where the second term represents the contribution from the Coulomb exchange energy. Further tests show that the Coulomb energy $\mathcal{H}^{\rm Cou}(\vec{r}_\alpha)$ converges at the lattice spacing of $l_x = l_y = l_z =$ 0.5 fm used in the present LBUU simulations. The gradient term $\mathcal{H}^{\rm grad}_\alpha$ in Equation (20) is obtained by considering

$$\begin{aligned}\delta\int\mathcal{H}^{\rm grad}(\vec{r})\,d^3r &= \sum_\tau^{n,p}\int\Bigg[\frac{\partial\mathcal{H}^{\rm grad}(\vec{r})}{\partial\rho_\tau(\vec{r})}\delta\rho_\tau(\vec{r}) \\ &+ \frac{\partial\mathcal{H}^{\rm grad}(\vec{r})}{\partial\nabla\rho_\tau(\vec{r})}\delta\nabla\rho_\tau(\vec{r}) + \frac{\partial\mathcal{H}^{\rm grad}(\vec{r})}{\partial\nabla^2\rho_\tau(\vec{r})}\delta\nabla^2\rho_\tau(\vec{r}) + \cdots\Bigg]d^3r \\ &= \sum_\tau^{n,p}\int\sum_{n=0}(-1)^n\nabla^n\frac{\partial\mathcal{H}^{\rm grad}(\vec{r})}{\partial\nabla^n\rho_\tau(\vec{r})}\delta\rho_\tau(\vec{r})\,d^3r, \end{aligned} \tag{22}$$

where we have integrated by parts to obtain the second line. The spatial derivative of $\rho_{\tau,\alpha}$ in Equation (20) is related to the spatial derivative of $S$ through

$$\frac{\partial \rho_{\tau,\alpha}}{\partial \vec{r}_i} = \frac{\partial}{\partial \vec{r}_i} \sum_{\vec{r}_j \in V_\alpha}^{\tau_j=\tau} S(\vec{r}_j - \vec{r}_\alpha) = \begin{cases} \frac{\partial S(\vec{r}_i - \vec{r}_\alpha)}{\partial \vec{r}_i}, & \tau_i = \tau, \\ 0, & \tau_i \neq \tau. \end{cases} \quad (23)$$

Substituting the $f_\tau(\vec{r},\vec{p})$ from Equation (4) into Equation (8), we obtain the momentum-dependent parts of the equation of motion for the test nucleons, and these are expressed in terms of the sums over the test nucleons as

$$\begin{aligned} \frac{\partial \mathcal{H}^{\mathrm{MD}}(\vec{r}_\alpha)}{\partial \vec{r}_i} &= 2\frac{\partial S\big[\vec{r}_i(t) - \vec{r}_\alpha\big]}{\partial \vec{r}_i} \\ &\times \Bigg\{ \sum_{j \in V_\alpha} S\big[\vec{r}_j(t) - \vec{r}_\alpha\big] \mathcal{K}_{\mathrm{s}}\big[\vec{p}_i(t), \vec{p}_j(t)\big] \\ &+ \sum_{j \in V_\alpha}^{\tau_j=\tau_i} S\big[\vec{r}_j(t) - \vec{r}_\alpha\big] \mathcal{K}_{\mathrm{v}}\big[\vec{p}_i(t), \vec{p}_j(t)\big] \Bigg\}, \end{aligned} \quad (24)$$

$$\begin{aligned} \frac{\partial \mathcal{H}^{\mathrm{MD}}(\vec{r}_\alpha)}{\partial \vec{p}_i} &= 2S\big[\vec{r}_i(t) - \vec{r}_\alpha\big] \\ &\times \Bigg\{ \sum_{j \in V_\alpha} S\big[\vec{r}_j(t) - \vec{r}_\alpha\big] \frac{\partial \mathcal{K}_{\mathrm{s}}\big[\vec{p}_i(t), \vec{p}_j(t)\big]}{\partial \vec{p}_i} \\ &+ \sum_{j \in V_\alpha}^{\tau_j=\tau_i} S\big[\vec{r}_j(t) - \vec{r}_\alpha\big] \frac{\partial \mathcal{K}_{\mathrm{v}}\big[\vec{p}_i(t), \vec{p}_j(t)\big]}{\partial \vec{p}_i} \Bigg\}. \end{aligned} \quad (25)$$

Using Equations (19)–(25), one can evaluate the time evolution of the coordinates $\vec{r}_i(t)$ and momenta $\vec{p}_i(t)$ of the test nucleons, and then obtain $f(\vec{r},\vec{p},t)$ from Equation (4), based on which physical observables can be calculated.

The choice of the form factor $S(\vec{r}_i - \vec{r})$ should ensure particle number conservation,

$$\sum_\alpha \rho(\vec{r}_\alpha) l_x l_y l_z = \frac{1}{N_{\mathrm{E}}} \sum_\alpha \sum_i S(\vec{r}_i - \vec{r}_\alpha)\, l_x l_y l_z = A. \quad (26)$$

In the present LBUU framework, we use a triangular form

$$\begin{aligned} S(\vec{r}_i - \vec{r}) &= \frac{1}{(nl/2)^6}\, g(\Delta x) g(\Delta y) g(\Delta z), \\ g(q) &= \Big(\frac{nl}{2} - |q|\Big)\theta\Big(\frac{nl}{2} - |q|\Big), \end{aligned} \quad (27)$$

where $\theta$ is the Heaviside function and $n$ is an integer that determines the range of $S$. Generally speaking, calculations on lattices violate momentum conservation since they break Galilean invariance. Early studies have shown that the total momentum can be conserved to a high degree of accuracy if $n \geq 4$ [66].

It should be mentioned that compared with the conventional test particle method, in which the equations of motion for the test nucleons are derived from *single-particle* Hamiltonians, the equations of motion for the test nucleons in the LH method, Equations (19) and (20), are derived from the *total* Hamiltonian of the system. In the former approach it is difficult to conserve energy exactly [2, 66], while the latter approach can ensure exact energy conservation in the dynamic process [66].

## 2.2. Collision Integral

In the present LBUU method, the stochastic collision method [74], instead of the commonly used geometric method, is implemented for the NN collision term in the BUU equation. In the stochastic collision approach, the collision probability of two test nucleons can be derived directly from the NN collision term, $I_{\mathrm{c}}$ in Equation (3), as follows. Considering nucleons around lattice site $\vec{r}_\alpha$ from two momentum space volume elements $V_{\vec{p}_1} = \vec{p}_1 \pm \frac{1}{2}\Delta^3\vec{p}_1$ and $V_{\vec{p}_2} = \vec{p}_2 \pm \frac{1}{2}\Delta^3\vec{p}_2$, one can average over momentum space volume $V_{\vec{p}_i}$ to obtain the distribution function $f(\vec{r}_\alpha,\vec{p}_i)$ according to Equation (4):

$$f(\vec{r}_\alpha,\vec{p}_i) \approx \frac{1}{\Delta^3\vec{p}_i} \frac{(2\pi\hbar)^3}{gN_{\mathrm{E}}} \sum_j^{\vec{p}_j \in V_{\vec{p}_i}} S(\vec{r}_j - \vec{r}_\alpha). \quad (28)$$

The number of collisions between nucleons from these two momentum space volumes that happen in a time interval $\Delta t$ is

$$\begin{aligned} \Delta N^{\mathrm{coll}}(\vec{r}_\alpha,\vec{p}_1,\vec{p}_2) &= g\frac{\Delta^3\vec{p}_1}{(2\pi\hbar)^3} \Big|\frac{df(\vec{r}_\alpha,\vec{p}_1)}{dt}\Big|^{\mathrm{coll}}_{\vec{p}_2} l_x l_y l_z \Delta t \\ &= g\frac{\Delta^3\vec{p}_2}{(2\pi\hbar)^3} \Big|\frac{df(\vec{r}_\alpha,\vec{p}_2)}{dt}\Big|^{\mathrm{coll}}_{\vec{p}_1} l_x l_y l_z \Delta t. \end{aligned} \quad (29)$$

The quantities $\big|\frac{df(\vec{r}_\alpha,\vec{p}_1)}{dt}\big|^{\mathrm{coll}}_{\vec{p}_2}$ and $\big|\frac{df(\vec{r}_\alpha,\vec{p}_2)}{dt}\big|^{\mathrm{coll}}_{\vec{p}_1}$ are the changing rates of $f(\vec{r}_\alpha,\vec{p}_1)$ and $f(\vec{r}_\alpha,\vec{p}_2)$, respectively, caused by two-body scatterings between the nucleons in $V_{\vec{p}_1}$ and $V_{\vec{p}_2}$. These terms can be obtained directly from Equation (3), i.e., the NN collision term in the BUU equation, as

$$\begin{aligned} \Big|\frac{df(\vec{r}_\alpha,\vec{p}_1)}{dt}\Big|^{\mathrm{coll}}_{\vec{p}_2} &= g\frac{\Delta^3\vec{p}_2}{(2\pi\hbar)^3} f(\vec{r}_\alpha,\vec{p}_1) f(\vec{r}_\alpha,\vec{p}_2) \\ &\int \frac{d^3p_3}{(2\pi\hbar)^3}\frac{d^3p_4}{(2\pi\hbar)^3} |\mathcal{M}_{12\to34}|^2 (2\pi)^4 \\ &\delta^4(p_1 + p_2 - p_3 - p_4) \\ &= g\frac{\Delta^3\vec{p}_2}{(2\pi\hbar)^3} f(\vec{r}_\alpha,\vec{p}_1) f(\vec{r}_\alpha,\vec{p}_2) v_{\mathrm{rel}} \sigma^*_{\mathrm{NN}}, \end{aligned} \quad (30)$$

where we have substituted in the definition of the cross-section,

$$\begin{aligned} \sigma^*_{\mathrm{NN}} &= \tfrac{1}{v_{\mathrm{rel}}} \int \tfrac{d^3p_3}{(2\pi\hbar)^3}\tfrac{d^3p_4}{(2\pi\hbar)^3} |\mathcal{M}_{12\to34}|^2 (2\pi)^4 \\ &\delta^4(p_1 + p_2 - p_3 - p_4), \end{aligned} \quad (31)$$

with $v_{\mathrm{rel}}$ being the relative velocity of the test nucleons in the two momentum space volumes and $\sigma^*_{\mathrm{NN}}$ the scattering cross-section in the *two-nuclei* center-of-mass frame. Here, we obtain the in-medium NN cross-section $\sigma^*_{\mathrm{NN}}$ by multiplying the free NN cross-section $\sigma^{\mathrm{free}}_{\mathrm{NN}}$ by a medium-correction factor. The NN elastic scattering cross-section in free space, $\sigma^{\mathrm{free}}_{\mathrm{NN}}$, is taken from the parameterization in reference [75] with a cutoff of

$\sigma_{\rm NN}^{\rm free}(p_{\rm lab} \leq 0.1\ {\rm GeV}/c) = \sigma_{\rm NN}^{\rm free}(p_{\rm lab} = 0.1\ {\rm GeV}/c)$ for neutron-neutron (*nn*) or proton-proton (*pp*) scatterings and a cutoff of $\sigma_{\rm NN}^{\rm free}(p_{\rm lab} \leq 0.05\ {\rm GeV}/c) = \sigma_{\rm NN}^{\rm free}(p_{\rm lab} = 0.05\ {\rm GeV}/c)$ for neutron-proton (*np*) scatterings, since the parameterization is shown to be valid for nucleon momentum $p_{\rm lab}$ down to the corresponding cutoff [75]. We note that the $p_{\rm lab}$ cutoff actually corresponds to only a few MeV of incident kinetic energy (i.e., 1.3 MeV for $p_{\rm lab} = 0.05\ {\rm GeV}/c$ and 5.3 MeV for $p_{\rm lab} = 0.1\ {\rm GeV}/c$), and these very low-energy scatterings are not important in the present transport model calculations. Since this parameterization of $\sigma_{\rm NN}^*$ is given in the *two-nucleon* center-of-mass frame, its value in the *two-nuclei* center-of-mass frame can be obtained through the Lorentz invariant quantity $E_1E_2v_{\rm rel}\sigma_{\rm NN}^*$. From Equations (28)–(30) one obtains

$$\Delta N^{\rm coll}(\vec{r}_\alpha,\vec{p}_1,\vec{p}_2) = \sum_{i,j}^{\substack{\vec{p}_i\in V_{\vec{p}_1}\\ \vec{p}_j\in V_{\vec{p}_2}}} \Delta N_{ij}^{\rm coll}$$
$$= \sum_{i,j}^{\substack{\vec{p}_i\in V_{\vec{p}_1}\\ \vec{p}_j\in V_{\vec{p}_2}}} \frac{1}{N_{\rm E}^2} v_{\rm rel}\sigma_{\rm NN}^* S(\vec{r}_i-\vec{r}_\alpha)S(\vec{r}_j-\vec{r}_\alpha)l_xl_yl_Z\Delta t, \quad (32)$$

where $\Delta N_{ij}^{\rm coll}$ denotes the number of physical collisions from the scattering of the *i*th and *j*th test nucleons. Given that every test nucleon is $1/N_{\rm E}$ of a physical nucleon, one obtains the collision probability of the *i*th and *j*th test nucleons as

$$P_{ij} = \frac{\Delta N_{ij}^{\rm coll}}{(1/N_{\rm E})^2} = v_{\rm rel}\sigma_{\rm NN}^* S(\vec{r}_i-\vec{r}_\alpha)S(\vec{r}_j-\vec{r}_\alpha)l_xl_yl_z\Delta t. \quad (33)$$

One can reduce statistical fluctuations of the collision events by allowing collisions of test nucleons that come from different ensembles. In this case the collision probability is reduced, $P_{ij} \to P_{ij}/N_{\rm E}$, via the scaling $\sigma_{\rm NN}^* \to \sigma_{\rm NN}^*/N_{\rm E}$. In our case, the NN scattering probabilities are very small within one time step, so instead of evaluating the probabilities of all possible collisions of test nucleons, we randomly divide the test nucleons that are available for scattering around the lattice site $\alpha$ into many pairs for scattering, and amplify the corresponding scattering probabilities accordingly, which is a common practice when one allows the scattering of test nucleons from different ensembles [74, 76]. The amplified scattering probabilities are given by

$$P'_{ij} = P_{ij}\frac{N_\alpha(N_\alpha-1)/2}{N'_\alpha/2}, \quad (34)$$

where $N_\alpha$ is the number of test nucleons that contribute to lattice site $\vec{r}_\alpha$ and $N'_\alpha$ is the number of test nucleons available for scattering. Since we choose a finite-range form factor for coordinates in the LBUU framework, one test nucleon can be involved in different collision events at different lattice sites. Those test nucleons that have already collided at another lattice site are excluded from the scattering at the present lattice site, so $N'_\alpha$ is not necessarily equal to $N_\alpha$. The time step $\Delta t$ needs to be sufficiently small to pin down the effect of such an exclusion by suppressing the chance of multi-scattering attempts, as well as to keep $P'_{ij}$ less than unity. In the present LBUU framework, we choose $\Delta t = 0.2\ {\rm fm}/c$ for the full LBUU calculations and $\Delta t = 0.4\ {\rm fm}/c$ for the Vlasov calculations (i.e., the LBUU calculations without the NN scatterings).

To verify the accuracy of the stochastic collision treatment within the present LBUU framework, we simulate collisions of nucleons confined in a cubic box of volume $V = 10\times10\times10\ {\rm fm}^3$ with periodic boundary conditions. In this simulation, we ignore the nuclear mean-field potential and the quantum nature of nucleons. Initially, 80 neutrons and 80 protons are uniformly distributed over the box, corresponding to a nucleon density of $\rho = 0.16\ {\rm fm}^3$. Their momenta are generated according to the relativistic Boltzmann distribution,

$$P(p) \propto p^2 \exp\left[\frac{\sqrt{m^2+p^2}}{T}\right], \quad (35)$$

where $m = 939$ MeV is the free nucleon mass. Here, the temperature $T$ is taken to be 14.24 MeV so that the system has the same kinetic energy density as the zero-temperature isospin-symmetric Fermi gas of nucleons.

Using the NN elastic scattering cross-section in free space [75], we simulate the time evolution of this system up to $1\ {\rm fm}/c$ with a time step of $0.2\ {\rm fm}/c$ and $N_{\rm E} = 1,000$. It is constructive to see the collision rate as a function of the center-of-mass energy $\sqrt{s}$ of the colliding nucleon pair. The $\sqrt{s}$ distributions of the collision rates for *np* and for *nn* plus *pp* are plotted as red circles in the left and right panels of **Figure 1**, respectively. Theoretically, considering two species of particles following relativistic Boltzmann distributions, the $\sqrt{s}$ distributions of their collision rates can be derived as

$$\frac{dN_{\rm coll}}{dt\,ds^{1/2}} = \frac{1}{1+\delta_{ij}}\frac{N_iN_j}{V}\frac{s(s-4m^2)K_1(s^{1/2}/T)\sigma(s^{1/2})}{4m^4T_{\rm B}K_2^2(m/T)}, \quad (36)$$

where $K_n$ is the *n*th order modified Bessel function, $N_i$ ($N_j$) is the number of particles *i* (*j*) in the volume $V$, and $\sigma$ is their scattering cross-section. The expected distributions are shown as black solid lines in **Figure 1** for comparison. It is seen that the LBUU calculations are in excellent agreement with the expected results.

Given the quantum nature of nucleons, we handle Pauli blocking in the LBUU method as follows. If the NN scattering between the *i*th and *j*th test nucleons happens at the lattice site $\vec{r}_\alpha$ according to $P_{ij}$ or $P'_{ij}$, the directions of their final momenta $\vec{p}_3$ and $\vec{p}_4$ are determined by the differential cross-section given in reference [75], and then the Pauli blocking factor $[1-f(\vec{r}_\alpha,\vec{p}_3)]\times[1-f(\vec{r}_\alpha,\vec{p}_4)]$ is used to determine whether the collision is blocked by the Pauli principle. The distribution function $f_\tau(\vec{r}_\alpha,\vec{p})$ is calculated according to Equation (28). For the momentum space volume $\Delta^3\vec{p}_i$, we take a sphere with radius $R_\tau^p(\vec{r}_\alpha,\vec{p})$ centered at $\vec{p}_i$. In typical BUU transport models, $R_\tau^p(\vec{r}_\alpha,\vec{p})$ is a constant of about a hundred MeV. For the calculation of small-amplitude nuclear collective dynamics near the ground state, a specifically proposed $R_\tau^p(\vec{r}_\alpha,\vec{p})$ is more suitable [51], i.e.,

$$R_\tau^p(\vec{r}_\alpha,\vec{p}) = \max[\Delta p, p_\tau^F(\vec{r}_\alpha) - |\vec{p}|], \quad (37)$$

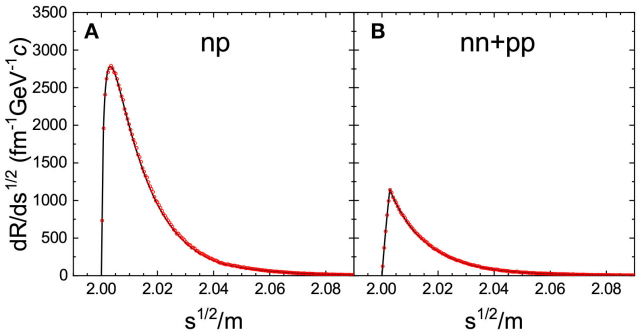


**FIGURE 1 |** The $\sqrt{s}$ distribution of **(A)** *np* and **(B)** $nn + pp$ elastic collision rates for the Boltzmann distribution at $T = 14.24$ MeV, with 80 neutrons and 80 protons in a cube of volume $V = 10 \times 10 \times 10$ fm$^3$, for theoretical predictions (black solid line) and LBUU calculations (red circles). In both calculations, we choose free NN cross-sections as parameterized in reference [75].

where $\Delta p$ is a constant that should be sufficiently small and $p_\tau^F = \hbar(3\pi^2\rho_\tau)^{1/3}$ is the nucleon Fermi momentum.

## 2.3. Ground State Initialization and Evolution Stability

In the present LBUU method, we obtain the ground state of nuclei at zero temperature by varying the Hamiltonian with respect to the nuclear radial density, which is sometimes called Thomas-Fermi (TF) initialization [51, 66, 77, 78] in the one-body transport model. We assume that for a ground-state nucleus at zero temperature, its Wigner function satisfies

$$f_\tau(\vec{r},\vec{p}) = \frac{2}{(2\pi\hbar)^3}\,\theta\big[|\vec{p}| - p_\tau^F(\vec{r})\big], \tag{38}$$

where $p_\tau^F(\vec{r})$ is the local Fermi momentum given by

$$p_\tau^F(\vec{r}) = \hbar\big[3\pi^2\rho_\tau(\vec{r})\big]^{1/3}. \tag{39}$$

It should be noted that, in principle, with the inclusion of NN scatterings, which goes beyond mean-field correlations, the nucleon momentum distribution in the ground state may differ slightly from the zero-temperature Fermi distribution. If we assume for simplicity that the nucleus is spherical, the total energy of a ground-state nucleus at zero temperature can be regarded as a functional of the radial density $\rho_\tau(r)$ and its spatial gradients,

$$E = \int \mathcal{H}\big[r, \rho_\tau(r), \nabla\rho_\tau(r), \nabla^2\rho_\tau(r), \dots\big]\,dr. \tag{40}$$

The neutron (proton) radial density in a ground-state nucleus can be obtained, by varying the total energy with respect to $\rho_\tau(r)$ [note that for protons the contribution from the Coulomb interaction in Equation (21) should also be included in the Hamiltonian density], as

$$\frac{1}{2m}\big\{p_\tau^F\big[\rho_\tau(r)\big]\big\}^2 + U_\tau\big\{p_\tau^F\big[\rho_\tau(r)\big], r\big\} = \mu_\tau, \tag{41}$$

where $\mu_\tau$ is the chemical potential of a proton or neutron inside the nucleus, with value determined by the given proton number $Z$ or neutron number $N$. The quantity $U_\tau\big\{p_\tau^F\big[\rho_\tau(r)\big], r\big\}$ refers to the single nucleon potential of the nucleon with local Fermi momentum. The single nucleon potential is derived by varying the Hamiltonian density in Equations (6)–(12) with respect to the phase-space distribution function and density gradients, and its detailed expression for the N3LO Skyrme pseudopotential is given in reference [73]. The physical significance of Equation (41) is very intuitive: in a classical picture, in a ground-state nucleus at zero temperature, the nucleons in the Fermi surface at different radial positions have the same chemical potential. The local density $\rho_\tau(\vec{r})$ for a ground-state spherical nucleus is obtained by solving Equation (41) subject to the following boundary conditions on the total local density $\rho(r) = \rho_n(r) + \rho_p(r)$:

$$\left.\frac{\partial\rho(r)}{\partial r}\right|_{r=0} = \left.\frac{\partial\rho(r)}{\partial r}\right|_{r=r_B} = 0. \tag{42}$$

Here, $r_B$ is the boundary of the nucleus and it satisfies $\rho(r_B) = 0$.

In the present LBUU framework, the initial coordinates of test nucleons are generated according to the obtained $\rho_\tau(\vec{r})$, while their initial momenta are generated from a zero-temperature Fermi distribution with the Fermi momentum given in Equation (39). Owing to the presence of the form factor $S(\vec{r}-\vec{r}')$ introduced in Equation (4), the density is smeared slightly in the LBUU calculations compared with the realistic local density. Thus the initial ground-state radial density distribution is slightly different from the solution of Equation (41). Unlike the Gaussian wave packet that is used to mimic the Wigner function in QMD model [57], the form factor $S(\vec{r}-\vec{r}')$ does not have any physical meaning; it can be regarded as a numerical technique introduced in the test-particle approach so that one can obtain well-defined densities and mean fields. As shown in the following, an additional gradient term in the local density can compensate for the effects caused by the smearing of the local density due to the form factor. In this subsection, we will denote by $\tilde{\rho}(\vec{r})$ the local density in the LBUU calculation and by $\rho(\vec{r})$ the realistic local density. The local density $\tilde{\rho}(\vec{r})$ can be regarded as a convolution of the realistic local density with the form factor,

$$\tilde{\rho}(\vec{r}) = \int \rho(\vec{r}\,')S(\vec{r}-\vec{r}')\,d^3r'. \tag{43}$$

To express $\rho(\vec{r})$ in terms of $\tilde{\rho}(\vec{r})$, we have formally

$$\begin{aligned}\rho(\vec{r}) &= \int \tilde{\rho}(\vec{r}\,')S^{-1}(\vec{r}\,'-\vec{r})\,d^3r' \\ &= \int \Big[\sum_{n=0}^{\infty}\frac{1}{n!}\nabla^n\tilde{\rho}(\vec{r})(\vec{r}\,'-\vec{r})^n\Big]S^{-1}(\vec{r}\,'-\vec{r})\,d^3r' \\ &\approx \tilde{\rho}(\vec{r}) + c\nabla^2\tilde{\rho}(\vec{r}),\end{aligned} \tag{44}$$

where we have truncated at next-to-leading order [the $\nabla\tilde{\rho}(\vec{r})$ term vanishes because of the symmetry of the integral] and $S^{-1}(\vec{r}-\vec{r}')$ is the inverse of $S(\vec{r}-\vec{r}')$, which satisfies

$$\int S(\vec{r}-\vec{r}'')S^{-1}(\vec{r}''-\vec{r}')\,d^3r'' = \delta(\vec{r}-\vec{r}'). \tag{45}$$

The parameter $c$, defined by

$$c \equiv \int \frac{1}{2}(\vec{r}\,' - \vec{r})^2 S^{-1}(\vec{r}\,' - \vec{r})\, d^3r', \tag{46}$$

is a small constant that depends only on the form of $S$. In the LBUU framework, to obtain $\rho(\vec{r})$ by direct correction of $\tilde{\rho}(\vec{r})$ is not feasible since numerically the density in Equation (44) is not always positive. If we substitute Equation (44) into the total Hamiltonian, with several necessary approximations, we obtain an additional term that is proportional to $c\tilde{\rho}(\vec{r})\nabla^2\tilde{\rho}(\vec{r})$. This term leads to an additional gradient term $\tilde{E}^{[2]}\nabla^2\tilde{\rho}$ in the equations of motion (20). Therefore, in practice we can add the extra gradient terms $\tilde{E}^{[2]}\nabla^2\tilde{\rho}$ to the equations of motion, to compensate for the smearing of density due to the form factor. In principle, the parameter $\tilde{E}^{[2]}$ should contain higher-order effects, so we adjust it to roughly obtain the ground-state root-mean-square (rms) radius evolution with the smallest oscillation, since the rms radius in the exact ground state should not change with time. Normally $\tilde{E}^{[2]}$ is a small parameter, around 15 MeV for various (N3LO) Skyrme parameter sets. It should be mentioned that this correction of the density gradient term improves the stability of the ground-state evolution (rms radius and radial density profile) only slightly, and does not lead to much difference in the results for collective motions. In ideal cases with $N_E \to \infty$ and $l_x, l_y, l_z \to 0$, the local density in the LBUU calculation will approach the physical local density, and $\tilde{E}^{[2]}$ will become zero. Since all the LBUU calculations are based on $\tilde{\rho}(\vec{r})$, we do not distinguish between $\tilde{\rho}(\vec{r})$ and $\rho(\vec{r})$, and $\rho(\vec{r})$ should be interpreted as $\tilde{\rho}(\vec{r})$ in the rest of the article.

We first examine the ground-state evolution stability of the LHV calculation, i.e., the LBUU calculation without the collision term, since in principle all NN scatterings should be blocked in the ground state. We show in **Figure 2** the time evolution of the radial density profile from the LHV calculation for the nucleus $^{208}$Pb in ground state up to 1,000 fm/$c$, obtained with $N_E = 10,000$ and a time step of $\Delta t = 0.4$ fm/$c$ by using the N3LO Skyrme pseudopotential SP6m. We notice from **Figure 2** that the profile of the radial density exhibits only very small variations with time, which indicates the success of the above initialization method. It also shows that the smearing of the local density caused by the inclusion of the form factor $S$ does not affect the dynamic evolution significantly. Such features indicate that the present LBUU method of solving the BUU equation can be used to study long-time nuclear processes, such as nuclear spallation and heavy-ion fusion reactions.

Apart from the radial density profile, other properties of the ground-state evolution stability are also examined. In **Figure 3** we present the time evolution of the rms radius, the fraction of bound nucleons, and the binding energy of the LHV calculation (i.e., the LBUU calculation without NN scatterings). The calculations are performed with time step $\Delta t = 0.4$ fm/$c$ and with $N_E = 5,000$ and 10,000. The test nucleons for which the form factor does not overlap with that of others are considered free test nucleons, and they are excluded when calculating the fraction of bound nucleons and the rms radius. We notice from **Figure 3A** that although in the $N_E = 5,000$ case the rms radius starts to decrease after about 800 fm/$c$, the LHV calculation gives a fairly stable time evolution of the rms radius. The observed decrease is due to the evaporation of test nucleons from the bound nuclei, which is illustrated in **Figure 3B**. Such evaporation of test nucleons is inevitable in transport model calculations because of the limited precision of the numerical realization, but it can be suppressed by increasing $N_E$, as seen in **Figure 3B**, though the result with $E_E = 5,000$ is already satisfactory [61]. As **Figure 3C** shows, the LH method ensures the energy conservation to a very high degree. The difference between the cases of $N_E = 5,000$ and $N_E = 10,000$ is mainly due to the numerical precision of the gradient term in the Hamiltonian. It is seen from **Figure 3** that the present LBUU framework can give a fairly stable ground-state time evolution. Owing to the high efficiency of GPU parallel computing, it becomes possible to include more ensembles or test particles in the LBUU calculation. As one will see in the following, to obtain the correct GDR width, as many as 30,000 ensembles are needed in the full LBUU calculation with NN scatterings.

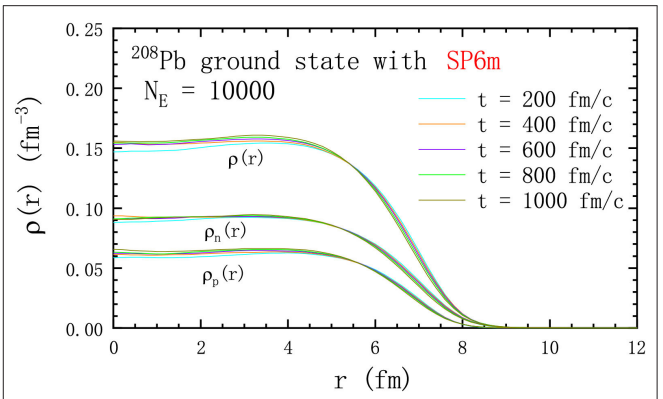


**FIGURE 2 |** Time evolution of the radial density profile of the ground state of $^{208}$Pb based on the LHV calculation (i.e., the LBUU calculation without NN scatterings) with the N3LO Skyrme pseudopotential SP6m up to 1,000 fm/$c$. Reproduced from reference [61] with permission from the American Physical Society.

For the stability of the ground-state evolution in the full LBUU calculation, we note that for $\sigma_{NN}^{free}$ with $N_E = 30,000$, the rms radius and the ground-state energy of $^{208}$Pb vary <3.6% (0.2 fm) and 3.2% (50 MeV), respectively, during the time evolution of 0–500 fm/$c$ [55]. The stability of the rms radius in the full LBUU calculation is not as good as in the LHV case, and this may be due to the fact that with the inclusion of NN scatterings, i.e., beyond mean-field correlations, the nucleon momentum distribution in the ground state may differ slightly from the zero-temperature Fermi distribution. Apart from this, although the LH method can conserve the energy almost exactly for the mean-field evolution without NN collisions, the non-perfect energy conservation in the LBUU calculation could be caused by the NN scattering processes, which usually violate energy conservation when the momentum-dependent mean-field potentials are used. Both problems require further investigation of transport model calculations in the future.

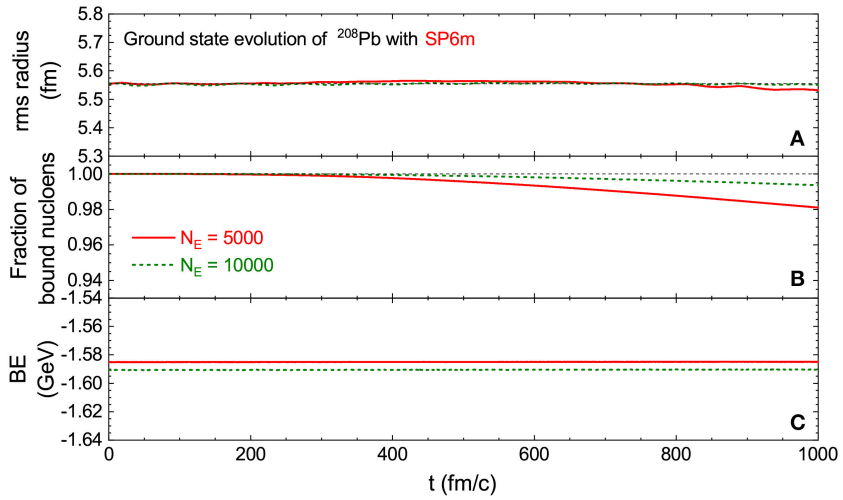


**FIGURE 3 |** Time evolution of **(A)** rms radius, **(B)** fraction of bound nucleons, and **(C)** binding energy of the $^{208}$Pb ground state from the LHV calculation (i.e., the LBUU calculation without NN scatterings) with the N3LO Skyrme pseudopotential SP6m up to 1,000 fm/$c$. Calculations are performed with a time step of $\Delta t = 0.4$ fm/$c$ and with $N_E = 5,000$ and 10,000. Reproduced from reference [61] with permission from the American Physical Society.

## 2.4. Nuclear Giant Resonances Within Transport Models

We consider a small excitation of the Hamiltonian,

$$\hat{H}_{\rm ex}(t) = \lambda \hat{Q}\delta(t - t_0), \tag{47}$$

where $\hat{Q}$ is the excitation operator for a given mode and $\lambda$ is the initial excitation parameter, which is assumed to be small. In linear response theory [79], the response of the excitation operator $\hat{Q}$ as a function of time is given by

$$\begin{aligned}\Delta\langle\hat{Q}\rangle(t) &= \langle 0'|\hat{Q}|0'\rangle(t) - \langle 0|\hat{Q}|0\rangle(t) \\ &= -\frac{2\lambda\theta(t)}{\hbar}\sum_F |\langle F|\hat{Q}|0\rangle|^2 \sin\frac{(E_F - E_0)t}{\hbar},\end{aligned} \tag{48}$$

where $|0\rangle$ is the unperturbed nuclear ground state with energy $E_0$, $|0'\rangle$ is the nuclear state after the perturbation, and $|F\rangle$ is the energy eigenstate of the excited nucleus with eigen-energy $E_F$. The strength function, which is defined as

$$S(E) = \sum_F |\langle F|\hat{Q}|0\rangle|^2\, \delta(E - E_F + E_0), \tag{49}$$

can be expressed as a Fourier integral of $\Delta\langle\hat{Q}\rangle(t)$ in Equation (48):

$$S(E) = -\frac{1}{\pi\lambda}\int_0^\infty dt\, \Delta\langle\hat{Q}\rangle(t) \sin\frac{Et}{\hbar}. \tag{50}$$

By evaluating the time evolution of $\Delta\langle\hat{Q}\rangle(t)$ within the transport model, we can obtain the strength function and, subsequently, other quantities, such as the peak energy, width, and energy-weighted sum rules. The time evolution of $\Delta\langle\hat{Q}\rangle(t)$ can be expressed in terms of the Wigner function $f(\vec{r},\vec{p})$ as follows.

If we assume that $\hat{Q}$ is a one-body operator, then it can be written as the sum of single-particle operators $\hat{q}$ acting on each nucleon, $\hat{Q} = \sum_i^A \hat{q}$, and the expectation value of $\hat{Q}$ for a given state is evaluated as

$$\begin{aligned}\langle\hat{Q}\rangle = \langle\Phi|\hat{Q}|\Phi\rangle = \int &\langle\Phi|\vec{r}_1\cdots\vec{r}_N\rangle\langle\vec{r}_1\cdots\vec{r}_N|\hat{Q}|\vec{r}'_1\cdots\vec{r}'_N\rangle \\ &\langle\vec{r}'_1\cdots\vec{r}'_N|\Phi\rangle\, d^3r_1\cdots d^3r_N\, d^3r'_1\cdots d^3r'_N,\end{aligned} \tag{51}$$

where we have added two identity operators. Considering the definition of the one-body density matrix,

$$\rho(\vec{r}_1,\vec{r}'_1) = A\int \langle\vec{r}_1\vec{r}_2\cdots\vec{r}_N|\Phi\rangle\langle\Phi|\vec{r}'_1\vec{r}_2\cdots\vec{r}_N\rangle\, d^3r_2\cdots d^3r_N,$$

and combining it with the one-body operator condition $\hat{Q} = \sum_i^A \hat{q}$, we can rewrite Equation (51) as

$$\langle\hat{Q}\rangle = \int \rho(\vec{r}'_1,\vec{r}_1)\langle\vec{r}_1|\hat{q}|\vec{r}'_1\rangle\, d^3r_1\, d^3r'_1. \tag{52}$$

The density matrix can be expressed in coordinate space as the inverse Fourier transform of $f(\vec{r},\vec{p})$,

$$\rho\left(\vec{r} - \frac{\vec{s}}{2}, \vec{r} + \frac{\vec{s}}{2}\right) = \int f(\vec{r},\vec{p}) \exp\left(i\frac{\vec{p}}{\hbar}\vec{s}\right) d^3p. \tag{53}$$

In the above equation we have changed the integration variables: $\vec{r}_1 = \vec{r} + \frac{\vec{s}}{2}$ and $\vec{r}'_1 = \vec{r} - \frac{\vec{s}}{2}$. We define the Wigner transform of $\hat{q}$ in coordinate space,

$$q(\vec{r},\vec{p}) \equiv \int \exp\left(-i\frac{\vec{p}}{\hbar}\cdot\vec{s}\right) q\left(\vec{r} + \frac{\vec{s}}{2}, \vec{r} - \frac{\vec{s}}{2}\right) d^3s, \tag{54}$$

where $q\left(\vec{r} + \frac{\vec{s}}{2}, \vec{r} - \frac{\vec{s}}{2}\right) = \left\langle\vec{r} + \frac{\vec{s}}{2}|\hat{q}|\vec{r} - \frac{\vec{s}}{2}\right\rangle$ represents the matrix element of $\hat{q}$ in coordinate space. By substituting Equation (53)

and the inverse transform of Equation (54) into Equation (52), the expectation of $\hat{Q}$ can be written in the form

$$\langle \hat{Q} \rangle = \int f(\vec{r},\vec{p}) q(\vec{r},\vec{p})\, d^3r\, d^3p, \tag{55}$$

which means that the time evolution of $\langle \hat{Q} \rangle$ can be calculated through the time evolution of $f(\vec{r},\vec{p})$.

In the transport model, different external excitations $\lambda \hat{Q} \delta(t - t_0)$ can be generated by changing the positions and momenta of the test nucleons as follows [47]:

$$\vec{r}_i \to \vec{r}_i + \lambda \frac{\partial q(\vec{r}_i,\vec{p}_i)}{\partial \vec{p}_i}, \quad \vec{p}_i \to \vec{p}_i - \lambda \frac{\partial q(\vec{r}_i,\vec{p}_i)}{\partial \vec{r}_i}. \tag{56}$$

The detailed forms of $q(\vec{r}_i,\vec{p}_i)$ for different collective modes and their corresponding initializations in the transport model will be given later.

## 3. LATTICE HAMILTONIAN VLASOV CALCULATIONS

In this section we compare the peak energy of nuclear giant resonances obtained from LBUU calculations without the NN scatterings, i.e., LHV calculations, with that obtained from the RPA, since the 2*p*-2*h* correlation is absent in both cases. Both the isoscalar monopole and isovector dipole modes of $^{208}$Pb are examined.

### 3.1. Isoscalar Monopole Mode

Since the isoscalar giant monopole resonance (ISGMR) provides information about the nuclear matter incompressibility [80–85], which is a fundamental quantity that characterizes the EOS of symmetric nuclear matter, it is interesting to study the ISGMR within the transport model to make a cross-check with the incompressibility extracted from the HICs.

From the point of view of the one-body transport model, the isoscalar monopole mode is regarded as a compressional breathing of the nuclear fluid. The excitation operator $\hat{Q}_{\rm ISM}$ for the isoscalar monopole mode and its one-body operator $\hat{q}_{\rm ISM}$ take the forms

$$\hat{Q}_{\rm ISM} = \frac{1}{A}\sum_i^{\rm A} \hat{r}_i^2, \quad \hat{q}_{\rm ISM} = \frac{\hat{r}^2}{A}. \tag{57}$$

From Equation (54) we obtain the Wigner transform of $\hat{q}_{\rm ISM}$ as

$$q_{\rm ISM}(\vec{r},\vec{p}) = \frac{\vec{r}^2}{A}. \tag{58}$$

According to Equation (56), we can generate in the transport model the initial isoscalar monopole excitation by changing the initial phase-space information of test nucleons with respect to that of the ground state:

$$\vec{p}_i \to \vec{p}_i - 2\lambda \frac{\vec{r}_i}{A}. \tag{59}$$

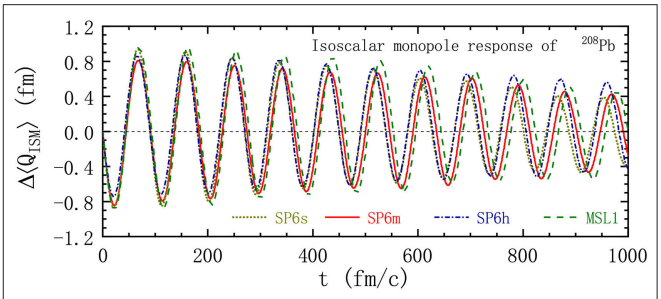


**FIGURE 4 |** Time evolution of $\Delta\langle \hat{Q}_{\rm ISM}\rangle$ of $^{208}$Pb after a perturbation by $\hat{H}_{\rm ex}(t) = \lambda \hat{Q}_{\rm ISM}\delta(t - t_0)$ with $\lambda = 100$ MeV $\cdot$ fm$^{-1}/c$ in the LHV calculations. The results correspond to three N3LO Skyrme pseudopotentials, SP6s, SP6m, and SP6h, and one conventional Skyrme interaction MSL1. Reproduced from reference [61] with permission from the American Physical Society.

The spatial coordinates of the test nucleons remain unchanged since $q_{\rm ISM}$ in Equation (58) is independent of momentum. Note that the rms radius of a nucleus, shown in **Figure 3**, is given by the square root of the expectation value of $\hat{Q}_{\rm ISM}$.

We show in **Figure 4** the time evolution of $\Delta\langle \hat{Q}_{\rm ISM}\rangle$, i.e., the difference between the expectation values of $\langle \hat{Q}_{\rm ISM}\rangle$ for the excited state and the ground state from the LHV calculations. The results are from one conventional Skyrme interaction MSL1 and three N3LO Skyrme pseudopotentials, SP6s, SP6m, and SP6h. In the calculation, we set the number of ensembles $N_{\rm E}$ to 5,000, and the initial excitation parameter $\lambda$ is taken to be 100 MeV $\cdot$ fm$^{-1}/c$. One sees from the figure that the time evolution of $\Delta\langle \hat{Q}_{\rm ISM}\rangle$, or equivalently the rms radius, displays a very regular oscillation, and the rapid increase of the radius with time that is generally seen in most BUU calculations using the conventional test particle method does not show up here. Besides that, since the only damping mechanism in the LHV calculation is Landau damping, the amplitude of the oscillation only decreases slightly. Landau damping is caused by one-body dissipation, which is governed by a coupling of single-particle and collective motions. It should be mentioned that in the RPA framework, the damping also comes only from one-body dissipation, since the coupling to more complex states, such as 2*p*-2*h* states, is missing in RPA [86]. We obtain the peak energy of the giant monopole resonance through Fourier transform of the time evolution of $\Delta\langle \hat{Q}_{\rm ISM}\rangle$ shown in **Figure 4**. The obtained peak energy is 13.8 MeV for SP6s, 13.6 MeV for SP6m, 13.9 MeV for SP6h, and 13.5 MeV for MSL1. In order to compare the result from the LHV calculation with that from RPA, we calculate the strength function of the giant monopole resonance using the Skyrme-RPA code of Colo et al. [87] with the MSL1 interaction. The obtained peak energy of 14.1 MeV is comparable to that from the LHV calculation with MSL1, and the small discrepancy may reflect the difference between their semi-classical and quantum natures.

### 3.2. Isovector Dipole Mode

The isovector giant dipole resonance (IVGDR) of finite nuclei is the earliest observed nuclear collective excitation. Systematic

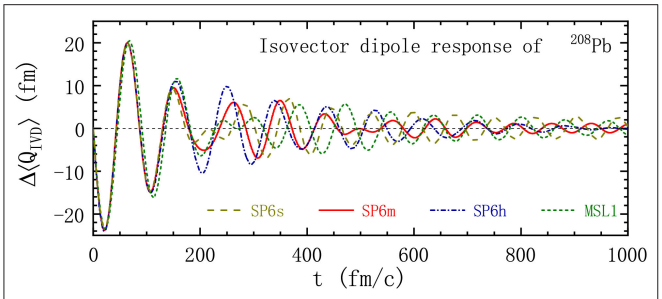


**FIGURE 5 |** Same as **Figure 4** but for the isovector dipole mode with $\lambda = 25$ MeV/$c$. Reproduced from reference [61] with permission from the American Physical Society.

experimental investigation of the IVGDR with photon-nuclear reactions was conducted decades ago [88]. Recent precise measurements of the isovector dipole response have been performed at the RCNP for $^{48}$Ca [89], $^{120}$Sn [90], and $^{208}$Pb [63] with inelastic proton scattering, as well as at GSI for $^{68}$Ni [91] by using Coulomb excitation in inverse kinematics. Recently, a low-lying mode called pygmy dipole resonance (PDR) has been observed experimentally [92–95], and this effect has already been studied based on the Vlasov equation [47]. The IVGDR [54, 96, 97], PDR [98, 99], and electric dipole polarizability $\alpha_D$ [100–103], which are dominated by these isovector dipole modes, provide sensitive probes to constrain the density dependence of the nuclear symmetry energy.

For the isovector dipole mode, the external perturbation can be written in the form

$$\hat{Q}_{\rm IVD} = \frac{N}{A}\sum_i^Z \hat{z}_i - \frac{Z}{A}\sum_i^N \hat{z}_i. \tag{60}$$

The coefficients in front of the single-particle position operator are chosen so as to keep the center of mass of the nucleus at rest. According to Equation (56), in transport models the excited nucleus can be obtained by changing the initial phase-space coordinates of test nucleons:

$$p_z \to \begin{cases} p_z - \lambda\frac{N}{A} & \text{for protons,} \\ p_z + \lambda\frac{Z}{A} & \text{for neutrons.} \end{cases} \tag{61}$$

We show in **Figure 5** the time evolution of $\Delta\langle\hat{Q}_{\rm IVD}\rangle$ for $^{208}$Pb with the interactions SP6s, SP6m, SP6h, and MSL1 of the LHV calculations. The number of ensembles $N_{\rm E}$ and the initial excitation parameter $\lambda$ are set to 5,000 and 25 MeV/$c$, respectively. Based on the time evolution of $\Delta\langle\hat{Q}_{\rm IVD}\rangle$ shown in **Figure 5**, the obtained peak energies for SP6s, SP6m, SP6h, and MSL1 are 13.4 MeV, 13.5 MeV, 13.7 MeV, and 13.1 MeV, respectively. The peak energy of MSL1 from the RPA calculation is 13.3 MeV, which is comparable to that obtained from the LBUU calculation without the NN collision term.

## 4. SPREADING WIDTH OF THE GIANT DIPOLE RESONANCE AND COLLISIONAL DAMPING

It is generally thought that in low-energy HICs with incident energies of only a few MeV/nucleon, the NN scatterings can be safely neglected since they are mostly blocked by the Pauli principle. However, when it comes to the width of the GDR, the collisional damping caused by NN scatterings is an essential mechanism for enhancing the insufficient GDR width obtained through the pure Vlasov calculation [55]. Nevertheless, to properly implement the damping mechanism caused by NN scatterings in transport models requires a rather accurate treatment of the Pauli blocking, which is a challenge in transport model calculations. The main difficulty lies in accurately calculating local momentum distributions $f_\tau(\vec{r}_\alpha,\vec{p})$ in transport models. Inaccuracy of $f_\tau(\vec{r}_\alpha,\vec{p})$ negatively affects the accuracy of the Pauli blocking and leads to spurious collisions, which enhance the collisional damping and thus overestimate the width of nuclear giant resonances. There are three main origins of the inaccuracy of the calculated $f_\tau(\vec{r}_\alpha,\vec{p})$ and hence the spurious collisions in transport models:

(1) fluctuations in calculating $f_\tau(\vec{r}_\alpha,\vec{p})$ through Equation (28) caused by too-small $N_{\rm E}$;
(2) a spurious temperature caused by a finite $\Delta p$ in calculating $f_\tau(\vec{r}_\alpha,\vec{p})$ (also see reference [51]);
(3) the finite lattice spacing $l$ causing diffusion in local momentum space due to the averaging of different local lattice densities in the nuclear surface region.

In order to obtain the spreading width with high accuracy from the BUU equation, one should choose a large $N_{\rm E}$ together with sufficiently small $l$ and $\Delta p$. After a careful test, it is found [55] that to get a convergent GDR width, $l$ should be smaller than 0.5 fm, $\Delta p$ smaller than 0.05 GeV, and $N_{\rm E}$ larger than 30,000. Further reducing $\Delta p$ and $l$ or increasing $N_{\rm E}$ leads to only a negligible decrease of the calculated GDR width. Therefore, in the following full LBUU calculations of the GDR width, we take $l = 0.5$ fm, $\Delta p = 0.05$ GeV, and $N_{\rm E} = 30,000$.

The collisional damping or NN scattering can have a significant effect on the width of nuclear giant resonances. **Figure 6** shows the time evolution of the isovector dipole response $\Delta\langle\hat{Q}_{\rm IVD}\rangle$ of $^{208}$Pb and its strength function obtained from the LHV calculation and the full LBUU calculation with the free NN elastic scattering cross-section [55]. In both cases, the N3LO Skyrme pseudopotential SP6h is adopted, and the same initial excitation with $\lambda = 15$ MeV/$c$ is employed (we note that varying $\lambda$ by 2/3 leads to almost the same value of the GDR width). The dotted line in the left panel of **Figure 6** is the time evolution of the expectation value $\langle 0|\hat{Q}_{\rm IVD}|0\rangle$ in the ground state of $^{208}$Pb as obtained from the LBUU calculation with the free-space NN cross-section. The expectation value $\langle 0|\hat{Q}_{\rm IVD}|0\rangle$ in the ground state of $^{208}$Pb is negligible compared with that in the GDR cases with and without NN scatterings. It is seen that including NN scatterings significantly increases the damping of the oscillations and leads to a much larger width. From the

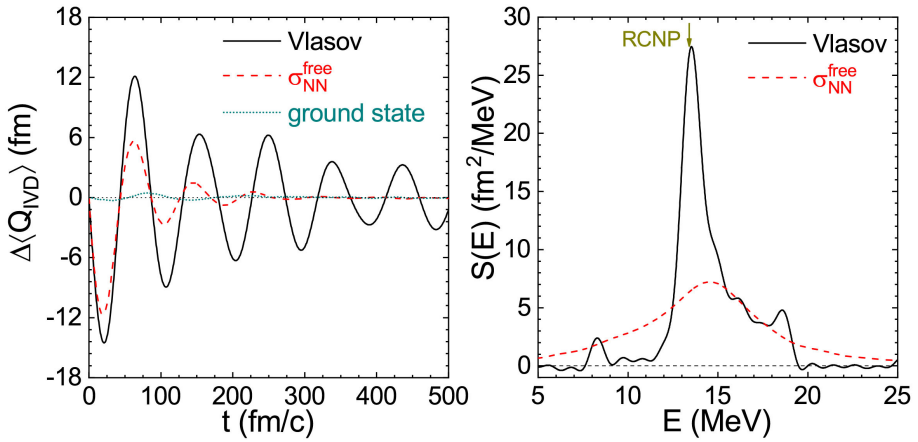


**FIGURE 6 |** Time evolution of $\Delta\langle\hat{Q}_{IVD}\rangle$ (left) and its strength function (right) for $^{208}$Pb after a perturbation $\hat{H}_{ex} = \lambda\hat{Q}_{IVD}\delta(t - t_0)$ with $\lambda = 15$ MeV/$c$ obtained from the LHV (Vlasov) calculation and the LBUU calculation with the free NN cross-section $\sigma_{NN}^{free}$. The dotted line in the left panel is the expectation value of $\hat{Q}_{IVD}$ in the ground state from the LBUU calculation with $\sigma_{NN}^{free}$. Reproduced from reference [55] under the Creative Commons CCBY license.

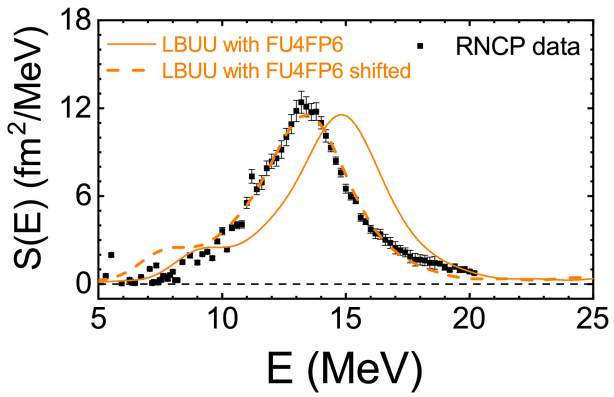


**FIGURE 7 |** Strength function of the GDR in $^{208}$Pb after a perturbation $\hat{H}_{ex} = \lambda\hat{Q}_{IVD}\delta(t - t_0)$ with $\lambda = 15$ MeV/$c$ obtained from the LBUU calculation using the FU4FP6 parameterization [107] for the in-medium NN scattering cross-section. The strength function measured in the RCNP experiment [63] is also shown for comparison.

strength functions, the obtained GDR width of $^{208}$Pb is 1.5 MeV in the Vlasov calculation and 6.5 MeV in the LBUU calculation with NN scatterings. We also notice from the right panel of **Figure 6** that the peak shifts to a higher energy when the NN scatterings are included. The impact that the NN scatterings have on the width indicates that they may also affect some particular observables in low-energy HICs, such as the nuclear stopping of HICs in the Fermi energy region, which merit further study.

Recent experiments performed at the RCNP on the $^{208}$Pb$(\vec{p},\vec{p}')$ reaction [63] have measured the GDR width of $^{208}$Pb accurately, giving a value of 4.0 MeV. Therefore, the LBUU calculation with the free NN elastic cross-section (which predicts a GDR width of 6.5 MeV) significantly overestimates the GDR width of $^{208}$Pb. It is well-known that the NN elastic cross-section is suppressed in the nuclear medium, so the overestimation of the GDR width with $\sigma_{NN}^{free}$ is understandable since the medium effects on the NN elastic cross-section will weaken the collisional damping and thus result in smaller GDR width. As shown in reference [55], in order to reproduce the experimental GDR width of $^{208}$Pb obtained at the RCNP, a strong medium reduction of the NN cross-section is needed. There are many parameterizations for the medium reduction of the NN cross-section [104–107], which could be dependent on density, collision energy, or isospin. As an example, we choose the FU4FP6 parameterization [107] for the medium reduction of the cross-section to calculate the strength function and width of the GDR in $^{208}$Pb. The FU4FP6 parameterization of the medium reduction is density-, momentum-, and isospin-dependent; it is preferred by the nucleon induced nuclear reaction cross-section data [107] and predicts a very strong in-medium reduction of NN scattering cross-sections. The strength function of the GDR in $^{208}$Pb from the LBUU calculation is shown in **Figure 7** and compared with the RCNP data [63]. The GDR width obtained from the LBUU calculation through the full width at half maximum (FWHM) of the strength function is 4.32 MeV, which is consistent with the value of 4.0 MeV found in the RCNP experiment. However, the Skyrme pseudopotential SP6h used in the calculation overestimates the peak energy by about 1.5 MeV. Using effective interactions with a different symmetry energy slope parameter $L$ or different nuclear effective masses can easily reproduce the correct peak energy [54]. In order to compare the shape of the strength function and the value of the width of the GDR in $^{208}$Pb, we shift the strength function from the LBUU calculation to match the experimental peak energy. We conclude from **Figure 7** that the present LBUU method with the FU4FP6 parameterization [107] for the medium reduction of the NN scattering cross-section can well reproduce the measured shape of the strength function and the width of the GDR in $^{208}$Pb. It should be stressed that the FU4FP6 parameterization suggests a very strong in-medium reduction

of NN scattering cross-sections, consistent with the conclusions obtained in reference [55].

## 5. SUMMARY AND OUTLOOK

We have reviewed recent progress in calculating nuclear collective motions by solving the BUU equation with the LH method. In order to calculate the nuclear collective motions accurately with the BUU equation, the present LBUU framework includes the following features: (1) the smearing of the local density is incorporated in the equations of motion self-consistently through the lattice Hamiltonian method; (2) the initialization of a ground state nucleus is carried out according to a nucleon radial density distribution obtained by varying the same Hamiltonian that governs the evolution; (3) the NN collision term in the BUU equation is implemented through a full-ensemble stochastic collision approach; (4) high-performance GPU parallel computing is employed to increase the computational efficiency. The present LBUU framework with these features affords a new level of precision in solving the BUU equation.

Within the LBUU framework, it has been shown that the peak energies of the ISGMR and IVGDR obtained from the pure Vlasov calculation are consistent with those from the RPA calculation, and the full LBUU calculation can yield a reasonable GDR strength function compared with the experimental data. The peak energies can be used to extract information about the nuclear EOS, while the width of the GDR can constrain the medium reduction of the elastic NN scattering cross-section.

The success of the present LBUU framework in describing the nuclear collective motions has demonstrated its capability in treating the stability of ground-state nuclei and the nuclear dynamics near equilibrium. Thus the present LBUU framework provides a solid foundation for studying long-time processes of heavy-ion reactions at low energies, such as heavy-ion fusion and multi-nucleon transfer reactions at near-barrier energies, based on solving the BUU equation. The significant effects of the collisional damping on the width of the nuclear GDR indicate that NN scatterings should play a crucial role in nuclear collective dynamics with small-amplitude oscillations.

The present LBUU framework has been shown to significantly reduce the uncertainties in transport model simulations of HICs in various respects, especially with regard to the stability of the nuclear ground-state evolution and the accurate treatment of NN scatterings as well as the Pauli blocking. This is very important for various studies of HICs based on transport model calculations, such as the extraction of the nuclear EOS and the in-medium NN scattering cross-sections. Further studies of HICs from low to intermediate energies within the present LBUU framework are in progress, and it is expected that more reliable information on the nuclear EOS, the in-medium NN scattering cross-sections, and the effective nuclear interactions will be gained in near future.

## AUTHOR CONTRIBUTIONS

All authors listed have made a substantial, direct and intellectual contribution to the work, and approved it for publication.

## FUNDING

This work was partially supported by the National Natural Science Foundation of China under Contracts Nos. 11947214, 11905302, 11890714, 11625521, and 11421505, the Key Research Program of Frontier Sciences of the CAS under Grant No. QYZDJ-SSW-SLH002, the Strategic Priority Research Program of the CAS under Grants Nos. XDB16 and XDB34000000, and the Major State Basic Research Development Program (973 Program) in China under Contract No. 2015CB856904.

## ACKNOWLEDGMENTS

We thank Pawel Danielewicz, Che Ming Ko, Bao-An Li, and Jun Su for helpful discussions, as well as Meisen Gao, Jie Pu, Xiaopeng Zhang, Chen Zhong, and Ying Zhou for setting up and maintaining the GPU servers.

## REFERENCES

1. Carruthers P, Zachariasen F. Quantum collision theory with phase-space distributions. *Rev Mod Phys.* (1983) **55**:245–85. doi: 10.1103/RevModPhys.55.245
2. Bertsch G, Das Gupta S. A guide to microscopic models for intermediate energy heavy in collisions. *Phys Rep.* (1988) **160**:189–233. doi: 10.1016/0370-1573(88)90170-6
3. Li BA. Neutron-proton differential flow as a probe of isospin-dependence of the nuclear equation of state. *Phys Rev Lett.* (2000) **85**:4221–4. doi: 10.1103/PhysRevLett.85.4221
4. Chen LW, Ko CM, Li BA. Determination of the stiffness of the nuclear symmetry energy from isospin diffusion. *Phys Rev Lett.* (2005) **94**:032701. doi: 10.1103/PhysRevLett.94.032701
5. Tsang MB, Zhang Y, Danielewicz P, Famiano M, Li Z, Lynch WG, et al. Constraints on the density dependence of the symmetry energy. *Phys Rev Lett.* (2009) **102**:122701. doi: 10.1103/PhysRevLett.102.122701
6. Danielewicz P, Lacey RA, Gossiaux PB, Pinkenburg C, Chung P, Alexander JM, et al. Disappearance of elliptic flow: a new probe for the nuclear equation of state. *Phys Rev Lett.* (1998) **81**:2438. doi: 10.1103/PhysRevLett.81.2438
7. Li BA. Probing the high density behavior of the nuclear symmetry energy with high energy heavy-ion collisions. *Phys Rev Lett.* (2002) **88**:192701. doi: 10.1103/PhysRevLett.88.192701
8. Danielewicz P, Lacey R, Lynch WG. Determination of the equation of state of dense matter. *Science.* (2002) **298**:1592–6. doi: 10.1126/science.1078070
9. Xiao Z, Li BA, Chen LW, Yong GC, Zhang M. Circumstantial evidence for a soft nuclear symmetry energy at suprasaturation densities. *Phys Rev Lett.* (2009) **102**:062502. doi: 10.1103/PhysRevLett.102.062502
10. Feng ZQ, Jin GM. Probing high-density behavior of symmetry energy from pion emission in heavy-ion collisions. *Phys Lett B.* (2010) **683**:140–4. doi: 10.1016/j.physletb.2009.12.006
11. Russotto P, Wu PZ, Zoric M, Chartier M, Leifels Y, Lemmon RC, et al. Symmetry energy from elliptic flow in $^{197}$Au + $^{197}$Au. *Phys Lett B.* (2011) **697**:471–6. doi: 10.1016/j.physletb.2011.02.033

12. Xie WJ, Su J, Zhu L, Zhang FS. Symmetry energy and pion production in the Boltzmann–Langevin approach. *Phys Lett B.* (2013) **718**:1510–4. doi: 10.1016/j.physletb.2012.12.021
13. Cozma MD, Leifels Y, Trautmann W, Li Q, Russotto P. Toward a model-independent constraint of the high-density dependence of the symmetry energy. *Phys Rev C.* (2013) **88**:044912. doi: 10.1103/PhysRevC.88.044912
14. Russotto P, Gannon S, Kupny S, Lasko P, Acosta L, Adamczyk M, et al. Results of the ASY-EOS experiment at GSI: the symmetry energy at suprasaturation density. *Phys Rev C.* (2016) **94**:034608. doi: 10.1103/PhysRevC.94.034608
15. Cozma MD. Feasibility of constraining the curvature parameter of the symmetry energy using elliptic flow data. *Eur Phys J A.* (2018) **54**:40. doi: 10.1140/epja/i2018-12470-1
16. Feng ZQ. Nuclear dynamics and particle production near threshold energies in heavy-ion collisions. *Nucl Sci Tech.* (2018) **29**:40. doi: 10.1007/s41365-018-0379-z
17. Li PC, Wang YJ, Li QF, Zhang HF. Collective flow and nuclear stopping in heavy ion collisions in Fermi energy domain. *Nucl Sci Tech.* (2018) **29**:177. doi: 10.1007/s41365-018-0510-1
18. Wolter H. The high-density symmetry energy in heavy-ion collisions and compact stars. *Universe.* (2018) **4**:72. doi: 10.3390/universe4060072
19. Baran V, Colonna M, Greco V, Di Toro M. Reaction dynamics with exotic nuclei. *Phys Rep.* (2005) **410**:335–466. doi: 10.1016/j.physrep.2004.12.004
20. Li BA, Chen LW, Ko CM. Recent progress and new challenges in isospin physics with heavy-ion reactions. *Phys Rep.* (2008) **464**:113–281. doi: 10.1016/j.physrep.2008.04.005
21. Brown BA. Neutron radii in nuclei and the neutron equation of state. *Phys Rev Lett.* (2000) **85**:5296. doi: 10.1103/PhysRevLett.85.5296
22. Typel S, Brown BA. Neutron radii and the neutron equation of state in relativistic models. *Phys Rev C.* (2001) **64**:027302. doi: 10.1103/PhysRevC.64.027302
23. Yoshida S, Sagawa H. Neutron skin thickness and equation of state in asymmetric nuclear matter. *Phys Rev C.* (2004) **69**:024318. doi: 10.1103/PhysRevC.69.024318
24. Oyamatsu K, Iida K, Koura H. Neutron drip line and the equation of state of nuclear matter. *Phys Rev C.* (2010) **82**:027301. doi: 10.1103/PhysRevC.82.027301
25. Wang R, Chen LW. Positioning the neutron drip line and the r-process paths in the nuclear landscape. *Phys Rev C.* (2015) **92**:031303. doi: 10.1103/PhysRevC.92.031303
26. Prakash M, Ainsworth TL, Lattimer JM. Equation of state and the maximum mass of neutron stars. *Phys Rev Lett.* (1988) **61**:2518–21. doi: 10.1103/PhysRevLett.61.2518
27. Lattimer JM, Pethick CJ, Prakash M, Haensel P. Direct URCA process in neutron stars. *Phys Rev Lett.* (1991) **66**:2701–4. doi: 10.1103/PhysRevLett.66.2701
28. Lattimer JM, Prakash M. The physics of neutron stars. *Science.* (2004) **304**:536. doi: 10.1126/science.1090720
29. Steiner A, Prakash M, Lattimer J, Ellis P. Isospin asymmetry in nuclei and neutron stars. *Phys Rep.* (2005) **411**:325–75. doi: 10.1016/j.physrep.2005.02.004
30. Lattimer J, Prakash M. Neutron star observations: prognosis for equation of state constraints. *Phys Rep.* (2007) **442**:109–65. doi: 10.1016/j.physrep.2007.02.003
31. Sumiyoshi K, Toki H. Relativistic equation of state of nuclear matter for the supernova explosion and the birth of neutron stars. *Astrophys J.* (1994) **422**:700. doi: 10.1086/173763
32. Oertel M, Hempel M, Klähn T, Typel S. Equations of state for supernovae and compact stars. *Rev Mod Phys.* (2017) **89**:015007. doi: 10.1103/RevModPhys.89.015007
33. Pais H, Gulminelli F, Providencia C, and Ropke G. Light and heavy clusters in warm stellar matter. *Nucl Sci Tech.* (2018) **29**:181. doi: 10.1007/s41365-018-0518-6
34. Abbott BP et al. GW170817: Observation of gravitational waves from a binary neutron star inspiral. *Phys Rev Lett.* (2017) **119**:161101. doi: 10.1103/PhysRevLett.119.161101
35. Zhou EP, Zhou X, Li A. Constraints on interquark interaction parameters with GW170817 in a binary strange star scenario. *Phys Rev D.* (2018) **97**:083015. doi: 10.1103/PhysRevD.97.083015
36. De S, Finstad D, Lattimer JM, Brown DA, Berger E, Biwer CM. Tidal deformabilities and radii of neutron stars from the observation of GW170817. *Phys Rev Lett.* (2018) **121**:091102. doi: 10.1103/PhysRevLett.121.091102
37. Zhang NB, Li BA. Astrophysical constraints on a parametric equation of state for neutron-rich nucleonic matter. *Nucl Sci Tech.* (2018) **29**:178. doi: 10.1007/s41365-018-0515-9
38. Li BA, Krastev PG, Wen DH, and Zhang NB. Towards understanding astrophysical effects of nuclear symmetry energy. *Eur Phys J A.* (2019) **55**:117. doi: 10.1140/epja/i2019-12780-8
39. Zhou Y, Chen LW, Zhang Z. Equation of state of dense matter in the multimessenger era. *Phys Rev D.* (2019) **99**:121301. doi: 10.1103/PhysRevD.99.121301
40. Riley TE, Watts AL, Bogdanov S, Ray PS, Ludlam RM, Guillot S, et al. A NICER view of PSR J0030+0451: millisecond pulsar parameter estimation. *Astrophys J Lett.* (2019) **887**:L21. doi: 10.3847/2041-8213/ab481c
41. Miller MC, Lamb FK, Dittmann AJ, Bogdanov S, Arzoumanian Z, Gendreau KC, et al. PSR J0030+0451 mass and radius from NICER data and implications for the properties of neutron star matter. *Astrophys J Lett.* (2019) **887**:L24. doi: 10.3847/2041-8213/ab50c5
42. Raaijmakers G, Riley TE, Watts AL, Greif SK, Morsink SM, Hebeler K, et al. A NICER view of PSR J0030+0451: implications for the dense matter equation of state. *Astrophys J Lett.* (2019) **887**:L22. doi: 10.3847/2041-8213/ab451a
43. Cromartie HT et al. Relativistic Shapiro delay measurements of an extremely massive millisecond pulsar. *Nat. Astron.* (2019) **4**:72–6. doi:10.1038/s41550-019-0880-2
44. Zhou Y, Chen LW. Ruling out the supersoft high-density symmetry energy from the discovery of PSR J0740+6620 with mass $2.14^{+0.10}_{-0.09}M_{\odot}$. *Astrophys J.* (2019) **886**:52. doi: 10.3847/1538-4357/ab4adf
45. Simenel C, Umar AS. Heavy-ion collisions and fission dynamics with the time-dependent Hartree-Fock theory and its extensions. *Prog Part Nucl Phys.* (2018) **103**:19–66. doi: 10.1016/j.ppnp.2018.07.002
46. Stevenson PD, Barton MC. Low-energy heavy-ion reactions and the Skyrme effective interaction. *Prog Part Nucl Phys.* (2019) **104**:142–64. doi: 10.1016/j.ppnp.2018.09.002
47. Urban M. Pygmy resonance and torus mode within Vlasov dynamics. *Phys Rev C.* (2012) **85**:034322. doi: 10.1103/PhysRevC.85.034322
48. Baran V, Colonna M, Di Toro M, Frecus B, Croitoru A, Dumitru D. Nuclear collective dynamics within Vlasov approach. *Eur Phys J D.* (2014) **68**:356. doi: 10.1140/epjd/e2014-50171-x
49. Zheng H, Burrello S, Colonna M, Baran V. Dipole response in neutron-rich nuclei with new Skyrme interactions. *Phys Rev C.* (2016) **94**:014313. doi: 10.1103/PhysRevC.94.014313
50. Smerzi A, Bonasera A, DiToro M. Damping of giant resonances in hot nuclei. *Phys Rev C.* (1991) **44**:1713–6. doi: 10.1103/PhysRevC.44.1713
51. Gaitanos T, Larionov AB, Lenske H, Mosel U. Breathing mode in an improved transport approach. *Phys Rev C.* (2010) **81**:054316. doi: 10.1103/PhysRevC.81.054316
52. Tao C, Ma YG, Zhang GQ, Cao XG, Fang DQ, Wang HW, et al. Isoscalar giant monopole resonance in Sn isotopes using a quantum molecular dynamics model. *Phys Rev C.* (2013) **88**:064615. doi: 10.1103/PhysRevC.88.064615
53. Wang K, Ma YG, Zhang GQ, Cao XG, He WB, Shen WQ. Giant dipole resonance in proton capture reactions using an extended quantum molecular dynamics model. *Phys Rev C.* (2017) **95**:014608. doi: 10.1103/PhysRevC.95.014608
54. Kong HY, Xu J, Chen LW, Li BA, Ma YG. Constraining simultaneously nuclear symmetry energy and neutron-proton effective mass splitting with nucleus giant resonances using a dynamical approach. *Phys Rev C.* (2017) **95**:034324. doi: 10.1103/PhysRevC.95.034324
55. Wang R, Zhang Z, Chen LW, Ko CM, Ma YG. Constrains on the in-medium nucleon-nucleon cross-section from the width of nuclear giant dipole resonance. *Phys Lett B.* (2020) **807**:135532. doi: 10.1016/j.physletb.2020.135532
56. He WB, Ma YG, Cao XG, Cai XZ, Zhang GQ. Giant dipole resonance as a fingerprint of $\alpha$ clustering configurations in $^{12}$C and $^{16}$O. *Phys Rev Lett.* (2014) **113**:032506. doi: 10.1103/PhysRevLett.113.032506

57. Aichelin J. "Quantum" molecular dynamics—a dynamical microscopic n-body approach to investigate fragment formation and the nuclear equation of state in heavy ion collisions. *Phys Rep.* (1991) **202**:233–360. doi: 10.1016/0370-1573(91)90094-3
58. Xu J, Chen LW, Tsang MB, Wolter H, Zhang YX, Aichelin J, et al. Understanding transport simulations of heavy-ion collisions at 100*A* and 400*A* MeV: comparison of heavy-ion transport codes under controlled conditions. *Phys Rev C.* (2016) **93**:044609. doi: 10.1103/PhysRevC.93.044609
59. Zhang YX, Wang YJ, Colonna M, Danielewicz P, Ono A, Tsang MB, et al. Comparison of heavy-ion transport simulations: collision integral in a box. *Phys Rev C.* (2018) **97**:034625. doi: 10.1103/PhysRevC.97.034625
60. Ono A, Xu J, Colonna M, Danielewicz P, Ko CM, Tsang MB, et al. Comparison of heavy-ion transport simulations: collision integral with pions and Δ resonances in a box. *Phys Rev C.* (2019) **100**:044617. doi: 10.1103/PhysRevC.100.044617
61. Wang R, Chen LW, Zhang Z. Nuclear collective dynamics in the lattice Hamiltonian Vlasov method. *Phys Rev C.* (2019) **99**:044609. doi: 10.1103/PhysRevC.99.044609
62. Ruetsch G, Fatica M. *CUDA Fortran for Scientists and Engineers: Best Practices for Efficient CUDA Fortran Programming.* Waltham, MA: Morgan Kaufmann (2013).
63. Tamii A, Poltoratska I, von Neumann-Cosel P, Fujita Y, Adachi T, Bertulani CA, et al. Complete electric dipole response and the neutron skin in $^{208}$Pb. *Phys Rev Lett.* (2011) **107**:062502. doi: 10.1103/PhysRevLett.107.062502
64. Bonasera A, Kondratyev VN, Smerzi A, Remler EA. Nuclear dynamics in the Wigner representation. *Phys Rev Lett.* (1993) **71**:505–8. doi: 10.1103/PhysRevLett.71.505
65. Kondratyev V, Smerzi A, Bonasera A. Dynamics of a quantal system. *Nucl Phys A.* (1994) **577**:813–28. doi: 10.1016/0375-9474(94)90946-6
66. Lenk RJ, Pandharipande VR. Nuclear mean field dynamics in the lattice Hamiltonian Vlasov method. *Phys Rev C.* (1989) **39**:2242–9. doi: 10.1103/PhysRevC.39.2242
67. Xu HM, Lynch WG, Danielewicz P, Bertsch GF. Disappearance of fusionlike residues and the nuclear equation of state. *Phys Rev Lett.* (1990) **65**:843–6. doi: 10.1103/PhysRevLett.65.843
68. Xu HM. Disappearance of flow in intermediate-energy nucleus-nucleus collisions. *Phys Rev Lett.* (1991) **67**:2769–72. doi: 10.1103/PhysRevLett.67.2769
69. Wong CY. Dynamics of nuclear fluid. VIII. Time-dependent Hartree-Fock approximation from a classical point of view. *Phys Rev C.* (1982) **25**:1460–75. doi: 10.1103/PhysRevC.25.1460
70. Raimondi F, Carlsson BG, Dobaczewski J. Effective pseudopotential for energy density functionals with higher-order derivatives. *Phys Rev C.* (2011) **83**:054311. doi: 10.1103/PhysRevC.83.054311
71. Carlsson BG, Dobaczewski J, Kortelainen M. Local nuclear energy density functional at next-to-next-to-next-to-leading order. *Phys Rev C.* (2008) **78**:044326. doi: 10.1103/PhysRevC.78.044326
72. Chabanat E, Bonche P, Haensel P, Meyer J, Schaeffer R. A Skyrme parametrization from subnuclear to neutron star densities. *Nucl Phys A.* (1997) **627**:710–46. doi: 10.1016/S0375-9474(97)00596-4
73. Wang R, Chen LW, Zhou Y. Extended Skyrme interactions for transport model simulations of heavy-ion collisions. *Phys Rev C.* (2018) **98**:054618. doi: 10.1103/PhysRevC.98.054618
74. Danielewicz P, Bertsch GF. Production of deuterons and pions in a transport model of energetic heavy-ion reactions. *Nucl Phys A.* (1991) **533**:712–48. doi: 10.1016/0375-9474(91)90541-D
75. Cugnon J, L'Hôte D, Vandermeulen J. Simple parametrization of cross-sections for nuclear transport studies up to the GeV range. *Nucl Instrum Methods Phys Res Sect B Beam Interact Mater At* (1996) **111**:215–20. doi: 10.1016/0168-583X(95)01384-9
76. Xu Z, Greiner C. Thermalization of gluons in ultrarelativistic heavy ion collisions by including three-body interactions in a parton cascade. *Phys Rev C.* (2005) **71**:064901. doi: 10.1103/PhysRevC.71.064901
77. Danielewicz P. Determination of the mean-field momentum-dependence using elliptic flow. *Nucl Phys A.* (2000) **673**:375–410. doi: 10.1016/S0375-9474(00)00083-X
78. Lin H, Danielewicz P. One-body Langevin dynamics in heavy-ion collisions at intermediate energies. *Phys Rev C.* (2019) **99**:024612. doi: 10.1103/PhysRevC.99.024612
79. Fetter A, Walecka JD. *Quantum Theory of Many-Particle Systems.* New York, NY: McGraw-Hill (1971).
80. Youngblood DH, Clark HL, Lui YW. Incompressibility of nuclear matter from the giant monopole resonance. *Phys Rev Lett.* (1999) **82**:691–4. doi: 10.1103/PhysRevLett.82.691
81. Shlomo S, Youngblood DH. Nuclear matter compressibility from isoscalar giant monopole resonance. *Phys Rev C.* (1993) **47**:529–36. doi: 10.1103/PhysRevC.47.529
82. Li T, Garg U, Liu Y, Marks R, Nayak BK, Rao PVM, et al. Isotopic dependence of the giant monopole resonance in the even-$A^{112-124}$Sn isotopes and the asymmetry term in nuclear incompressibility. *Phys Rev Lett.* (2007) **99**:162503. doi: 10.1103/PhysRevLett.99.162503
83. Patel D, Garg U, Fujiwara M, Akimune H, Berg GPA, Harakeh MN, et al. Giant monopole resonance in even-A Cd isotopes, the asymmetry term in nuclear incompressibility, and the "softness" of Sn and Cd nuclei. *Phys Lett B.* (2012) **718**:447–450. doi: 10.1016/j.physletb.2012.10.056
84. Patel D, Garg U, Fujiwara M, Adachi T, Akimune H, Berg G, et al. Testing the mutually enhanced magicity effect in nuclear incompressibility via the giant monopole resonance in the 204,206,208Pb isotopes. *Phys Lett B.* (2013) **726**:178–81. doi: 10.1016/j.physletb.2013.08.027
85. Gupta YK, Garg U, Howard KB, Matta JT, Şenyiğit M, Itoh M, et al. Are there nuclear structure effects on the isoscalar giant monopole resonance and nuclear incompressibility near A∼90? *Phys Lett B.* (2016) **760**:482–5. doi: 10.1016/j.physletb.2016.07.021
86. Bertsch GF, Bortignon PF, Broglia RA. Damping of nuclear excitations. *Rev Mod Phys.* (1983) **55**:287–314. doi: 10.1103/RevModPhys.55.287
87. Colò G, Cao L, Van Giai N, Capelli L. Self-consistent RPA calculations with Skyrme-type interactions: the skyrme_rpa program. *Comput Phys Commun.* (2013) **184**:142–61. doi: 10.1016/j.cpc.2012.07.016
88. Berman BL, Fultz SC. Measurements of the giant dipole resonance with monoenergetic photons. *Rev Mod Phys.* (1975) **47**:713–61. doi: 10.1103/RevModPhys.47.713
89. Birkhan J, Miorelli M, Bacca S, Bassauer S, Bertulani CA, Hagen G, et al. Electric dipole polarizability of $^{48}$Ca and implications for the neutron skin. *Phys Rev Lett.* (2017) **118**:252501. doi: 10.1103/PhysRevLett.118.252501
90. Hashimoto T, Krumbholz AM, Reinhard PG, Tamii A, von Neumann-Cosel P, Adachi T, et al. Dipole polarizability of $^{120}$Sn and nuclear energy density functionals. *Phys Rev C.* (2015) **92**:031305. doi: 10.1103/PhysRevC.92.031305
91. Rossi DM, Adrich P, Aksouh F, Alvarez-Pol H, Aumann T, Benlliure J, et al. Measurement of the dipole polarizability of the unstable neutron-rich nucleus $^{68}$Ni. *Phys Rev Lett.* (2013) **111**:242503. doi: 10.1103/PhysRevLett.111.242503
92. Ryezayeva N, Hartmann T, Kalmykov Y, Lenske H, von Neumann-Cosel P, Ponomarev VY, et al. Nature of low-energy dipole strength in nuclei: the case of a resonance at particle threshold in $^{208}$Pb. *Phys Rev Lett.* (2002) **89**:272502. doi: 10.1103/PhysRevLett.89.272502
93. LAND-FRS Collaboration, Adrich P, Klimkiewicz A, Fallot M, Boretzky K, Aumann T, et al. Evidence for Pygmy and giant dipole resonances in $^{130}$Sn and $^{132}$Sn. *Phys Rev Lett.* (2005) **95**:132501. doi: 10.1103/PhysRevLett.95.132501
94. Wieland O, Bracco A, Camera F, Benzoni G, Blasi N, Brambilla S, et al. Search for the Pygmy dipole resonance in $^{68}$Ni at 600MeV/nucleon. *Phys Rev Lett.* (2009) **102**:092502. doi: 10.1103/PhysRevLett.102.092502
95. Endres J, Litvinova E, Savran D, Butler PA, Harakeh MN, Harissopulos S, et al. Isospin character of the Pygmy dipole resonance in $^{124}$Sn. *Phys Rev Lett.* (2010) **105**:212503. doi: 10.1103/PhysRevLett.105.212503
96. Yildirim S, Gaitanos T, Toro MD, Greco V. Relativistic transport approach to collective nuclear dynamics. *Phys Rev C.* (2005) **72**:064317. doi: 10.1103/PhysRevC.72.064317
97. Trippa L, Colò G, Vigezzi E. Giant dipole resonance as a quantitative constraint on the symmetry energy. *Phys Rev C.* (2008) **77**:061304. doi: 10.1103/PhysRevC.77.061304
98. Carbone A, Colò G, Bracco A, Cao LG, Bortignon PF, Camera F, et al. Constraints on the symmetry energy and neutron skins from

pygmy resonances in $^{68}$Ni and $^{132}$Sn. *Phys Rev C.* (2010) **81**:041301. doi: 10.1103/PhysRevC.81.041301
99. Baran V, Colonna M, Di Toro M, Croitoru A, Dumitru D. Connecting the pygmy dipole resonance to the neutron skin. *Phys Rev C.* (2013) **88**:044610. doi: 10.1103/PhysRevC.88.044610
100. Piekarewicz J, Agrawal BK, Colò G, Nazarewicz W, Paar N, Reinhard PG, et al. Electric dipole polarizability and the neutron skin. *Phys Rev C.* (2012) **85**:041302. doi: 10.1103/PhysRevC.85.041302
101. Roca-Maza X, Brenna M, Colò G, Centelles M, Viñas X, Agrawal BK, et al. Electric dipole polarizability in $^{208}$Pb: insights from the droplet model. *Phys Rev C.* (2013) **88**:024316. doi: 10.1103/PhysRevC.88.024316
102. Roca-Maza X, Viñas X, Centelles M, Agrawal BK, Colò G, Paar N, et al. Neutron skin thickness from the measured electric dipole polarizability in $^{68}$Ni, $^{120}$Sn, and $^{208}$Pb. *Phys Rev C.* (2015) **92**:064304. doi: 10.1103/PhysRevC.92.064304
103. Zhang Z, Chen LW. Electric dipole polarizability in Pb 208 as a probe of the symmetry energy and neutron matter around $\rho$ 0/3. *Phys Rev C.* (2015) **92**:031301. doi: 10.1103/PhysRevC.92.031301
104. Lopez O, Durand D, Lehaut G, Borderie B, Frankland JD, Rivet MF, et al. In-medium effects for nuclear matter in the Fermi-energy domain. *Phys Rev C.* (2014) **90**:064602. doi: 10.1103/PhysRevC.90.064602
105. Li P, Wang Y, Li Q, Guo C, Zhang H. Effects of the in-medium nucleon-nucleon cross-section on collective flow and nuclear stopping in heavy-ion collisions in the Fermi-energy domain. *Phys Rev C.* (2018) **97**:044620. doi: 10.1103/PhysRevC.97.044620
106. Barker B, Danielewicz P. Shear viscosity from nuclear stopping. *Phys Rev C.* (2019) **99**:034607. doi: 10.1103/PhysRevC.99.034607
107. Ou L, He Xy. In-medium nucleon-nucleon elastic cross-sections determined from the nucleon induced reaction cross-section data. *Chinese Phys C.* (2019) **43**:044103. doi: 10.1088/1674-1137/43/4/044103

**Conflict of Interest:** The authors declare that the research was conducted in the absence of any commercial or financial relationships that could be construed as a potential conflict of interest.

frontiers in Physics

REVIEW
published: 29 October 2020
doi: 10.3389/fphy.2020.567171

# Microscopic Theory for Spontaneous Fission

*Jhilam Sadhukhan**

*Variable Energy Cyclotron Centre & Homi Bhabha National Institute, Kolkata, India*

Nuclear fission is a fascinating field of research that involves large-amplitude collective dynamics of a microscopic many-body system. Specifically, the process of spontaneous-fission decay can only be explained within the quantum tunneling phenomenon. The present review discusses recent advancements in the theoretical understanding of spontaneous fission. These concern precise prediction of the spontaneous fission observables like fission lifetime and distribution of fragment yields. The theoretical developments presented here are based on a coherent coupling between the adiabatic collective dynamics and the static inputs obtained from the nuclear energy density functional formalism.

**Keywords: spontaneous fission, density functional theory, heavy and superheavy nuclei, fission fragment mass distribution, quantum tunneling**

OPEN ACCESS

***Edited by:***
*Cedric Simenel,*
*Australian National University, Australia*

***Reviewed by:***
*Yoritaka Iwata,*
*Kansai University, Japan*
*Armen Sedrakian,*
*Frankfurt Institute for Advanced Studies, Germany*

***Correspondence:**
*Jhilam Sadhukhan*
*jhilam@vecc.gov.in*

***Specialty section:***
*This article was submitted to Nuclear Physics, a section of the journal Frontiers in Physics*

***Received:*** *29 May 2020*
***Accepted:*** *25 August 2020*
***Published:*** *29 October 2020*

***Citation:***
*Sadhukhan J (2020) Microscopic Theory for Spontaneous Fission. Front. Phys. 8:567171. doi: 10.3389/fphy.2020.567171*

## 1. INTRODUCTION

Nuclear spontaneous fission (SF) is a unique decay mechanism that has crucial applications in both basic and applied sciences [1–3]. Particularly, the stability of very heavy and superheavy nuclei strongly depends on the SF probability [4–6]. Although superheavy nuclei predominantly decay via $\alpha$-emission at the beginning of a decay chain, SF leads to terminate the chain. This type of decay sequences are experimentally observed for isotopes of Fl and Ts [7, 8]. Moreover, in comparison to $\alpha$-emission, SF is predicted to be the preferred decay mode for neutron-rich superheavy nuclei [5, 9, 10]. In the case of nuclear astrophysics, SF strongly impacts the abundances of heavy elements in stars by participating in the *r*-process recycling mechanism [11–13]. Specifically, distributions of fission-fragment yields from different fission modes (SF, beta-delayed fission, and neutron-induced fission) are essential components of the *r*-process abundances [9, 14–19] and, therefore, very accurate prediction of these yields is required to improve the *r*-process network calculations. Further, as suggested in a recent study [20], the precise estimation of fission yields is indispensable for a better understanding of the chemical evolution of *r*-process elements produced in binary neutron-star mergers. In the application frontier, SF data are important to calibrate the nuclear material counting techniques relevant to power generation and international safeguards [21, 22]. However, measurements in actinide nuclei are restricted due to safety issues. Therefore, for both basic science and applications, predictive modeling of SF observables is of utmost interest. The present scenario and the prospects of fission theory are described in a recent review [23].

In the SF process, a fissioning nucleus undergoes quantum tunneling through a single or multiple potential barriers generated by the coherent motion of strongly interacting nucleons. Ideally, the time-dependent density functional theory (TDDFT) provides the most realistic microscopic framework to deal with such large amplitude collective dynamics [24–27]. Specifically, in the characterization of fission yields, nuclear dissipation plays a crucial role near the scission configuration and would be best accounted for by TDDFT. Albeit very promising, TDDFT poses several limitations in its application to SF. Primarily, the quantum tunneling is energetically

forbidden within this semiclassical approach. Besides, current implementations of TDDFT simulate only a single fission path for a given initial condition; reconstruction of a full yield distribution requires large-scale Monte Carlo sampling, which is beyond the current computational capabilities. The exascale computing platforms may open up the avenues to overcome such restrictions [23].

In general, the collective dynamics of a nucleus is believed to be a much slower process than the random motion of the constituent nucleons. Consequently, majority of the fission models are implemented within the adiabatic approximation that segregates the collective degrees of freedom from the intrinsic coordinates. The same approach is adopted in a static nuclear density functional theory (DFT) based model [28], where the collective motion is simulated by incorporating the DFT inputs within an appropriate equation of motion. Specifically, in case of SF, the dynamics of a fissioning system can be divided into two successive steps as depicted in **Figure 1** [29]. In the first step, the system tunnels through a multidimensional space of collective coordinates. This process is mainly governed by the potential energy profile and the collective inertia, which is often calculated within the adiabatic time-dependent Hartree-Fock-Bogoliubov (ATDHFB) formalism [30, 31]. The region beyond the outer turning point ("out" in **Figure 1**) is energetically accessible and the time-evolution in this space can be followed with a simple classical prescription, e.g., the Langevin dynamical model. Finally, the system breaks into two fragments at the scission configuration. The dynamics in the second phase involves the collective inertia and the dissipative forces as well. The SF half-life is primarily decided by the tunneling phase as, for most of the relevant nuclei, it is significantly slower than the subsequent propagation outside the barrier. The second dynamical phase controls the fission fragment properties like yield and total kinetic energy (TKE) distributions.

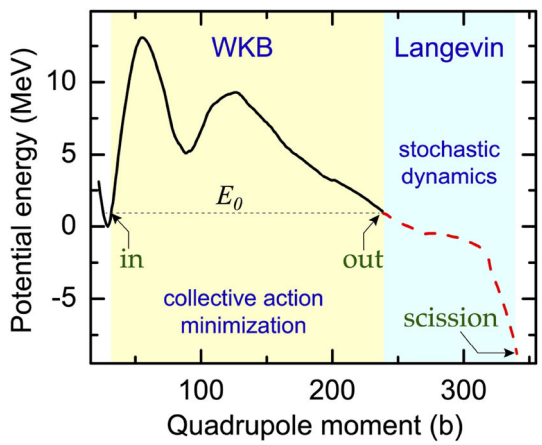


**FIGURE 1 |** Variation in potential energy calculated along the most-probable fission path of $^{240}$Pu. The region marked as WKB is classically forbidden as the fission excitation energy $E_0$ is less than the potential energy. Shape evolution: the collective action is minimized between the turning points "in" and "out" by using the WKB method and, from "out" to scission, dynamics is governed by Langevin dynamics. The figure is adapted from Sadhukhan et al. [29].

Apart from the standard inputs discussed in the previous paragraph, paring correlations play a critical role in controlling the SF lifetime and the connected fission pathway. The individual nucleonic motion leads to shell structures that guide both the nuclear shape and the potential energy along a fission path. Moreover, crossings of single-particle levels can modify the collective inertia through associated changes in the single-particle configurations [32–34]. The residual interaction among these crossing configurations is strongly influenced by the pairing force. Precisely, a larger pairing gap $\Delta$ helps the collective motion to be more adiabatic [35–40]. The enhancement of pairing fluctuations along the fission path was first postulated in Moretto and Babinet [41] by using a simple parabolic potential. In fact, the collective inertia and potential energy show opposite trends as $\Delta$ changes. The potential energy increases as $\Delta$ deviates from the static value $\Delta_s$, obtained from the self-consistent energy minimization procedure. In contrast, the collective inertia varies as $\Delta^{-2}$ [35, 42–45] and, therefore, the dynamic $\Delta$, corresponding to the minimum collective action, may differ from $\Delta_s$. This suggests that the parameter $\Delta$ should be implemented as an independent dynamical variable to determine the least action trajectory. Indeed, a reduction in the collective action due to pairing fluctuations is observed in many macroscopic-microscopic studies [46–49]. In addition, the pairing fluctuations are recently treated as dynamical variables in microscopic models based on the DFT formalism [50, 51].

## 2. A MODEL FOR SPONTANEOUS FISSION HALF-LIFE

### 2.1. Fission Half-Life

The SF mechanism involves a very wide range of timescales depending on the choice of the fissioning nucleus. For example, the observed SF half-life for actinides varies from a few ms to $10^{20}$ yrs. Therefore, it is impractical to develop a SF model based on the real-time quantum dynamics. The most common approach for the calculation of SF half-life is rooted in the one-dimensional WKB approximation to the quantum tunneling process. The corresponding half-life can be expressed as [52, 53], $T_{1/2} = \ln 2/(nP)$, where $n$ is the rate of collision on the fission barrier and $P$ is the barrier penetration probability given by

$$P = \left(1 + \exp\left[2S(L)\right]\right)^{-1}. \tag{1}$$

In the above equation, $S(L)$ is the action integral calculated along a predefined fission path $L(s)$ in the multidimensional collective space. The expression for $S(L)$ is given by,

$$S(L) = \int_{s_{\rm in}}^{s_{\rm out}} \frac{1}{\hbar}\sqrt{2\mathcal{M}_{\rm eff}(s)\left(V(s) - E_0\right)}\, ds, \tag{2}$$

where $V(s)$ and $\mathcal{M}_{\rm eff}(s)$ are the potential energy and collective inertia, respectively, along the path $L(s)$. Here, $s_{\rm in}$ and $s_{\rm out}$ indicate the classical turning points defined by $V(s) = E_0$; $E_0$ being the zero-point energy at the ground state configuration. We can define different fission paths $[L(s)]$ by choosing different values of $q_i(s)$ along the path's length $s$. The minimum of $S(L)$

corresponds to the most probable fission path [35, 54]. The $\mathcal{M}_{\rm eff}$ can be expressed in terms of the multidimensional collective inertia tensor $\mathcal{M}_{ij}(q_1, q_2, ...)$ as [52, 53, 55]:

$$\mathcal{M}_{\rm eff}(s) = \sum_{ij} \mathcal{M}_{ij}(q_1, q_2, ...) \frac{dq_i}{ds} \frac{dq_j}{ds}. \quad (3)$$

Generalization of the WKB method to several dimensions is recently recommended as a future goal [23].

The potential energy $V$ is obtained by subtracting the vibrational zero-point energy $E_{\rm ZPE}$ [56] from the Hartree-Fock-Bogoliubov (HFB) energy $E_{\rm HFB}(= \langle \hat{H}_{\rm HFB} \rangle)$. In the DFT formalism, $E_{\rm HFB}$ can be computed self-consistently by solving the constrained HFB equations for the Routhian:

$$\hat{H}' = \hat{H}_{\rm HFB} - \sum_{ij} \lambda_{ij} \hat{Q}_{ij} - \sum_{\tau=n,p} \left( \lambda_\tau \hat{N}_\tau - \lambda_{2\tau} \Delta \hat{N}_\tau^2 \right), \quad (4)$$

where $\hat{H}_{\rm HFB}$, $\hat{Q}_{ij}$, and $\hat{N}_\tau$ represent the HFB hamiltonian, the mass multipole moment operators, and particle-number operators for neutrons ($\tau = n$) and protons ($\tau = p$), respectively. The Lagrange multipliers $\lambda_{2\tau}$ can be used to control the particle-number fluctuation terms: $\Delta \hat{N}_\tau^2 = \hat{N}_\tau^2 - \langle \hat{N}_\tau \rangle^2$. Pairing correlations in nucleons are interconnected to the particle-number fluctuations [57, 58] and, hence, expected to be stronger for $\lambda_{2\tau} > 0$, compared to its static value obtained with $\lambda_{2\tau} = 0$. Further, the overall magnitude of pairing correlations is linked to the average pairing gap [31, 59]. Therefore, $\lambda_{2n}$ and $\lambda_{2p}$ can be utilized as dynamical coordinates [50] to scan the configuration space over a wide range of $\Delta$. It is indeed more physical to select the isoscalar ($\lambda_{2n} + \lambda_{2p}$) and the isovector ($\lambda_{2n} - \lambda_{2p}$) variations as independent coordinates. Consequently, a one-dimensional path $L(s)$ can be identified with the collective variables $\{q_i\} \equiv \{Q_{20}, Q_{22}, Q_{30}, ..., \lambda_{2n} + \lambda_{2p}, \lambda_{2n} - \lambda_{2p}\}$ as functions of path's length $s$. In a recent study [50], the role of dynamical isovector pairing is found to be negligible and, therefore, the associated coordinate $\lambda_{2n} - \lambda_{2p}$ can be set to zero. I denote $\lambda_{2n} + \lambda_{2p}$ as $\lambda_2$ in the subsequent discussions. Also, I should mention that an appropriate normalization scheme for all the coordinates must be adopted to make $ds$ dimensionless in Equation (2) [50].

Minimum-action paths can be simulated by using two different techniques named as the dynamic-programming method (DPM) [52, 56] and the Ritz method (RM) [53, 56]. In DPM, the dynamical space is first discretized into a multi-dimensional mesh. Then, at any intermediate step, minimum action paths are calculated for all the mesh points on a hypersurface perpendicular to the elongation coordinate ($Q_{20}$). Calculation is propagated along the $Q_{20}$ direction and finally the hypersurface of the desired outer-turning point is reached. In this method, path lengths are further divided into smaller segments whenever the distance between two adjacent mesh points is large. This is essential to ensure numerical accuracy as the collective inertia may vary quite sharply in certain regions of the collective space. In the case of RM, trial paths are defined in terms of Fourier series of dynamical coordinates and the coefficients of different Fourier components are obtained by minimizing the action. Although RM is easier to implement numerically, efficiency of this method depends on the number of Fourier components needed to reproduce the actual fission path. On the other hand, DPM is free of such limitations.

The HFB energy $E_{\rm HFB}$ can be calculated by employing either covariant or non-relativistic energy density functionals (EDFs). In the case of non-relativistic EDFs, the SkM* parametrization [60] of the zero range Skyrme functionals is commonly used in fission studies together with the density-dependent mixed pairing interaction [61], where the pairing strengths are calculated locally by reproducing the odd-even mass differences around $^{240}$Pu [62]. The parameters of this parametrization are benchmarked for large deformations relevant to fission. Recent optimizations of the Skyrme functionals are performed within the UNEDF project [63] and one of its variants, UNEDF1$_{\rm HFB}$, Schunck et al. [64] is successfully applied to fission works [65–67]. Apart from these, other microscopic interactions like the finite-range Gogny interaction [68–70] and the Barcelona-Catania-Paris-Madrid EDFs [9, 69, 71, 72] are widely used in the SF calculations. Despite different groups of EDFs exist, appropriate benchmarking with the experimental data are performed to ensure the consistency of model predictions. For example, it is recently shown that the SF yields of the superheavy $^{294}$Og nucleus are robust against different choices of EDFs [66]. Covariant EDFs [51, 73–78] based frameworks for large-amplitude collective dynamics are becoming more accessible with the increasing computational resources. Interestingly, SF pathways, calculated within covariant EDFs [51, 74], are found to be in close agreement with the non-relativistic results.

## 2.2. Calculation of Fission-Fragment Yields

It is desirable to use the TDDFT framework to study the evolution of a fissioning system in the collective space beyond the outer-turning point (**Figure 1**: region in-between "out" and "scission"). However, as pointed out in a recent study [79], the dynamics near scission is strongly dissipative and existing versions of TDDFT are not adequate since they are lacking fluctuations in collective coordinates. Also, an advanced TDDFT framework is recently proposed that incorporates fluctuations to generate TKE and yield distributions of fission fragments. In this approach, density fluctuations are assumed to prepare an ensemble of different configurations outside the barrier region and the subsequent propagation is followed with the standard TDDFT [80]. However, the fluctuations are considered in a somewhat restricted configuration space and a more exhaustive calculation may require huge computations. A feasible alternative to TDDFT is the time-dependent generator coordinate method (TDGCM) [77, 81–84]. However, in this approach, the Gaussian overlap approximation [81, 85] is additionally assumed to derive simple expressions for the parameters of the collective Hamiltonian. As a result, structural details like large fluctuations in the collective inertia are diluted [86]. It is also pointed out in the recent proposal [23] by Bender et al. that a stochastic mean-field approach with large fluctuations is more suitable for calculating fragment yields. Furthermore, the requirement of strongly dissipative dynamics for yield distributions of excited nuclei is well-established [87].

The stochastic Langevin dynamical model is a plausible option to avoid all the above-mentioned difficulties. It is quite straightforward to implement this model even in a complicated multidimensional collective space. In Langevin dynamics, the intrinsic motion of the nucleons is assumed to form a heat bath. The collective coordinates interact with the heat bath through random and dissipative forces. This decoupling of the collective coordinates from the internal degrees of freedom is performed under the adiabatic approximation. Fluctuations (random forces) introduce stochasticity in the collective dynamics and dissipation hinders the motion by transferring collective energy to the heat bath. Also, the collective motion experiences the standard conservative force exerted by potential energy. First, a family of SF probabilities $P(s_{\rm out})$ is obtained on the hypersurface of outer turning points $s_{\rm out}$. The hypersurface should contain mass octupole moment $Q_{30}$ as one of the coordinates since this variable defines different realizations of the fragment mass and charge. Subsequently, fission paths are computed for all the $s_{\rm out}$s by solving the Langevin equations [88, 89]:

$$\frac{dp_i}{dt} = -\frac{p_j p_k}{2}\frac{\partial}{\partial q_i}(\mathcal{M}^{-1})_{jk} - \frac{\partial V}{\partial q_i} - \eta_{ij}(\mathcal{M}^{-1})_{jk}p_k + g_{ij}\Gamma_j(t), \qquad (5)$$

$$\frac{dq_i}{dt} = (\mathcal{M}^{-1})_{ij}p_j,$$

where $p_i$ is the momentum conjugate to $q_i$. $\eta_{ij}$ and $g_{ij}$ represent the dissipation tensor and the strength of the random force, respectively, and these two quantities are connected through Einstein's fluctuation-dissipation theorem: $\sum_k g_{ik}g_{jk} = \eta_{ij}k_{\rm B}T$. Here, $T$ is the temperature of the nucleus. It is calculated at each instant of the Langevin evolution by assuming the nucleus as a non-interacting Fermi gas and the resulting formula is $T = \sqrt{E^*/a}$ ($T$ in MeV); $a$ being the level density parameter and $E^* = V(s_{\rm out}) - V(s) - \frac{1}{2}\sum(\mathcal{M}^{-1})_{ij}p_ip_j$. In the case of SF studies, $a$ can be approximated as a shape independent constant given by $a = A/10$ MeV$^{-1}$ [29, 66]. The stochastic variable $\Gamma_j(t)$ signifies the Markovian nature of the random force with the time correlation property: $\langle\Gamma_k(t)\Gamma_l(t')\rangle = 2\delta_{kl}\delta(t-t')$. The excitation energy $E^*$ increase as the system slides down to lower potential resulting stronger effects from fluctuations. The scission configuration is defined with the condition that the number of neck-particles ($N_q$) in the fissioning system is less than a critical value [28]. Each point on the scission hypersurface uniquely identifies the particle numbers of two fission fragments and these numbers can be calculated by integrating the nucleonic density distributions [62]. Owing to the random force, an ensemble of Langevin events with the same initial configuration (i.e., same $s_{\rm out}$) yields different fission pathways. Finally, the charge and mass distributions of the yields can be extracted by counting the number of events terminating at a given fragmentation. The numbers are weighted with $P(s_{\rm out})$ to account for the tunneling phase. Further, to incorporate the uncertainties in $N_q$, Langevin yields are convoluted with Gaussian functions [90].

Although the Langevin model does not explicitly simulate the time evolution of nucleonic degrees of freedom, it incorporates all the essential microscopic effects through the input quantities like PES and collective inertia which are obtained from effective nucleon-nucleon interactions. A special characteristic of the Langevin formalism is the presence of fluctuating and dissipative forces. In the case of induced fission, the importance of fluctuations and dissipation is well-established [87, 91] as the compound system is produced at least with a reasonable amount of excitation energy. In SF, the ground-state zero-point vibration is the initial source of excitation energy and it is inadequate to trigger any noticeable randomness in the collective motion. However, for all the relevant nuclei, potential energy drops rapidly below its ground state value as the deformation grows beyond the tunneling region. Consequently, nuclei acquire sufficient excitation energy that enhances fluctuations to a considerable level. In the following section, I have demonstrated the impact of the random force in Equation (5) on SF pathways.

## 2.3. Nucleonic Localization Function and Pre-fragments

For a better understanding of the structural evolution in a fissioning nucleus, nucleonic localization functions (NLF) are calculated [25, 92, 93]. NLF measures the probability of finding two nucleons with the same spin $\sigma$ and isospin $q$ at the same spatial localization. It is computed as described in references [93, 94]:

$$C_{q\sigma} = \left[1 + \left(\frac{\tau_{q\sigma}\rho_{q\sigma} - \frac{1}{4}|\nabla\rho_{q\sigma}|^2 - \boldsymbol{j}_{q\sigma}^2}{\rho_{q\sigma}\tau_{q\sigma}^{\rm TF}}\right)^2\right]^{-1}, \qquad (6)$$

where $\rho_{q\sigma}$, $\tau_{q\sigma}$, $\boldsymbol{j}_{q\sigma}$ and $\nabla\rho_{q\sigma}$ are the particle density, kinetic energy density, current density, and density gradient, respectively. The Thomas-Fermi kinetic energy density $\tau_{q\sigma}^{\rm TF} = \frac{3}{5}(6\pi^2)^{2/3}\rho_{q\sigma}^{5/3}$ is introduced as a normalization parameter. A value of $C \sim 1$ indicates a large nucleon's localization, i.e., a low probability of finding two nucleons with the same quantum numbers at the same spatial location. On the other hand, $C = 1/2$ corresponds to the limit of a homogeneous Fermi gas. The concept of NLF was originally applied to characterize chemical bonds in electronic systems. In nuclear physics, it is first used to visualize the cluster structures in light nuclei [94]. As illustrated in references [93, 94], the clustering of nucleons inside a nucleus can be predicted more precisely by NLFs in comparison to the scalar density distributions given by $\rho_{q\sigma}$. This is because the spatial distributions of NLFs exhibit pattern of concentric rings that reflect the underlying shell structure, but such patterns are averaged out in the density distributions. Recent studies [66, 67, 92, 93] suggest that NLFs can be utilized to identify prefragments in a fissioning nucleus. The method is described in Sadhukhan et al. [92] for a typical case of elongated $^{240}$Pu. The corresponding NLFs are shown in **Figure 2**. Evidently, the parts of NLFs for $z \geq z_{\rm L}$ and $z \leq z_{\rm H}$ contain ring-like patterns delineating the presence of localized nucleons inside the deformed $^{240}$Pu. This finding is further extended to define prefragments by integrating the densities of the localized portions and doubling the result to account for reflection symmetry. As replicated in **Figure 2**, the compound nuclear NLFs were found to be in remarkable agreement with the ground-state

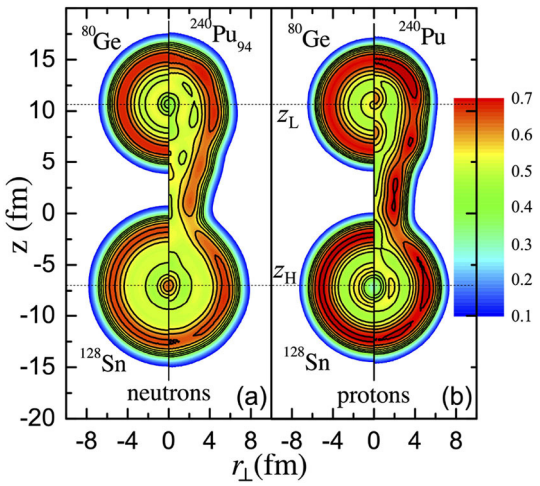


**FIGURE 2 |** Right of each panel: neutron **(a)** and proton **(b)** localization functions in a deformed configuration on the fission path of $^{240}$Pu. Left of each panel: NLFs of the localized prefragments, $^{80}$Ge and $^{128}$Sn, as indicated. Vertical lines are symmetry axes. Maximum extensions of the NLFs along the radial coordinate $r_\perp(z)$ are marked with horizontal dotted lines: $z = z_L$ and $z = z_H$. The figure is adapted from Sadhukhan et al. [92].

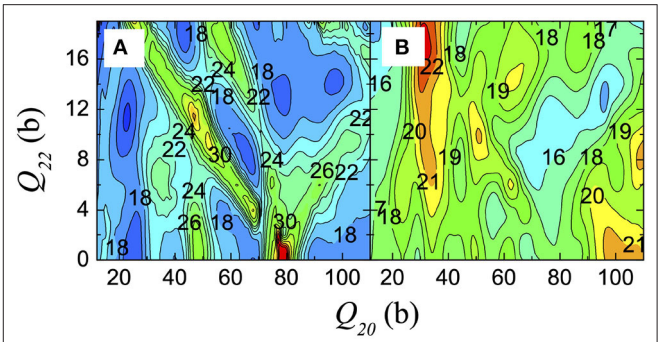


**FIGURE 3 |** Square-root-determinant of inertia tensors **(A)** $|\mathcal{M}^C|^{1/2}$ and **(B)** $|\mathcal{M}^{Cp}|^{1/2}$ (both in $\hbar^2$ MeV$^{-1}$ b$^{-2}$/1,000) calculated for $^{264}$Fm. The figure is modified from Sadhukhan et al. [56].

NLFs of the predicted prefragments ($^{128}$Sn and $^{80}$Ge) [92]. Similarly, prefragments are predicted successfully by comparing the scalar densities [95, 96]. Here, I should mention that the notion of prefragments is a purely theoretical concept as it cannot be measured experimentally. Moreover, other definitions of pre-fragment exist [25, 97]. Therefore, the validity of a pre-fragment based description depends on its ability to reproduce the experimental observables.

## 3. RESULTS ON DIFFERENT ASPECTS OF SPONTANEOUS FISSION

Calculation of SF observables is a very active field of research as the theoretical capability is increasing. In parallel, appropriate sets of fission observables are required to benchmark theoretical models [98]. In the rest of this review, I will discuss selected results from the recent theoretical achievements pertinent to both of these aspects.

### 3.1. Effect of Collective Inertia in Fission Pathway

In recent studies [56, 74], it is demonstrated that the SF pathways are strongly influenced by the characteristics of the collective inertia. The microscopic collective inertia is usually calculated within the ATDHFB formalism [30, 31] and it is commonly known as the cranking inertia $\mathcal{M}^C$ [86]. An exact calculation of $\mathcal{M}^C$ requires derivatives of the particle and pairing densities with respect to the dynamical coordinates. These can be achieved by employing the three-point or a higher-order Lagrange formula [99, 100]. On the other hand, in case of the commonly used perturbative cranking inertia $\mathcal{M}^{Cp}$ [86], these derivatives are reduced to matrix elements of mass multipole moments ($Q_{ij}$). **Figure 3** demonstrates the variations of square-root-determinants of both $\mathcal{M}^C$ and $\mathcal{M}^{Cp}$ calculated for $^{264}$Fm in a two-dimensional collective space of ($Q_{20}$, $Q_{22}$). As discussed in 1, $\left|\mathcal{M}^C\right|^{1/2}$ shows large fluctuations as an outcome of crossings in single-particle levels at the Fermi energy [39]. To affirm this, single-particle energies for $^{264}$Fm are displayed in **Figure 4** along two straight lines defined by $Q_{22} = 0$ and $Q_{20} = 61$ b. Multiple level crossings near the Fermi energy are clearly visible at deformations where $\mathcal{M}^C$ changes sharply. Similar features of the inertia tensor are observed within the covariant EDF formalism [74].

The dynamical minimum-action paths (or equivalently most probable paths), obtained with $\mathcal{M}^C$ and $\mathcal{M}^{Cp}$, are drawn in **Figure 5**. The same figure also shows the static path that traverses the minimized collective potential [56]. Due to strong dynamical hindrance by the perturbative inertia the corresponding minimum-action path avoids large triaxial shapes. $\mathcal{M}^{Cp}$ varies rather smoothly along both the deformation coordinates and, therefore, the minimum in the action integral in Equation (2) is achieved by minimizing the path-length. This weaker dependency on the triaxial shapes, imposed by collective inertia, is also observed in older fission studies [101–105]. On the other hand, due to localized large variations in $\mathcal{M}^C$, the non-perturbative path passes through the triaxial shapes that are fairly close to the static pathway. Apparently, both the non-perturbative and static trajectories always adhere to a configuration that tries to minimize the density of single-particle levels on the Fermi energy by avoiding level crossings. In short, the underestimation of structural details in $\mathcal{M}^{Cp}$ results in an artificial restoration of axial symmetry, which is broken in both static and non-perturbative approaches. This conclusion is also verified within the relativistic mean-field formalism [74]. Although the inertia strongly influences the topology of the minimum action path near the first fission barrier in actinides, it is rather simple in the space outside the fission isomer. Here, the SF path usually follows the minimum distance from a mass-symmetric configuration to the nearest outer turning point [29] (shown in the following figure, **Figure 8**).

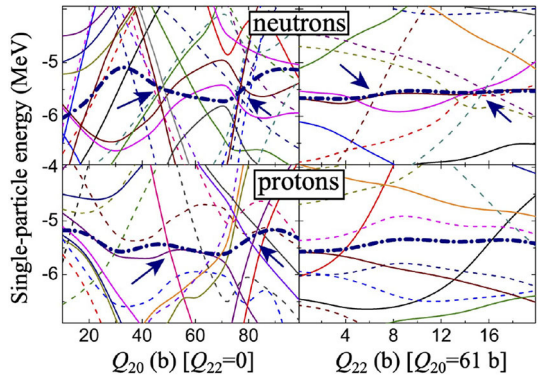


**FIGURE 4 |** Variation in single-particle energies of neutron (top) and proton (bottom) calculated for $^{264}$Fm along $Q_{20}$ (left, at $Q_{22} = 0$) and $Q_{22}$ (right, at $Q_{20} = 61$ b). The Fermi energies are marked with thick dash-dotted lines. The arrows indicate regions of level-crossings near Fermi energy. The figure is adapted from Sadhukhan et al. [56].

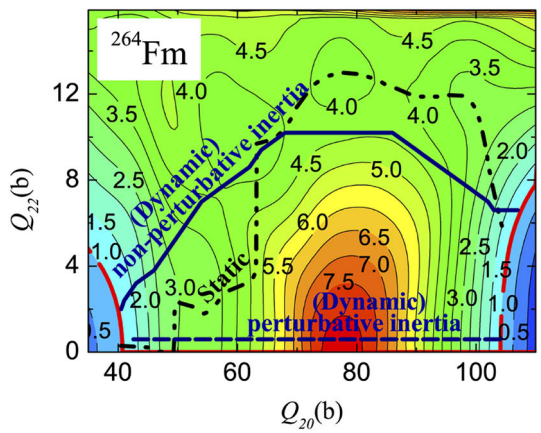


**FIGURE 5 |** Minimum-action (or most-probable) fission paths of $^{264}$Fm [56], calculated for $\mathcal{M}^C$ (solid line) and $\mathcal{M}^{Cp}$ (dashed line) using the DPM technique. cranking inertia using DMP technique. The static pathway is shown by the dash-dotted line. The loci of turning points are marked by thick solid lines. The PES (in MeV) is plotted for reference. The figure is modified from Sadhukhan et al. [56].

Most importantly, apart from modifying the fission pathways, collective inertia strongly impacts the fission lifetime. The SF half-life changes by orders of magnitude depending on the choice of collective inertia, even for the same fission trajectory [56]. For example, values of $T_{1/2}$ and $S(L)$ corresponding to different selections of the fission path and inertia are given in **Table 1**.

## 3.2. Role of Pairing Correlations

In the previous subsection, I demonstrated that a fissioning system tries to always follow single-particle configurations with comparatively lower level density. This can be fulfilled by avoiding the regions of level-crossing. In contrast, pairing correlations increases with the single-particle level density and, as I have discussed in 1, it affects the potential and collective inertia

**TABLE 1 |** Values of the action integral (2) and half-lives for different spontaneous fission pathways shown in **Figure 5**.

| Path | $S(L)$ | $\log(T_{1/2}/\text{yr})$ |
|---|---|---|
| Static + $\mathcal{M}^C$ | 23.4 | −7.7 |
| Static + $\mathcal{M}^{Cp}$ | 20.8 | −10.0 |
| Dynamic + $\mathcal{M}^C$ | 19.1 | −11.4 |
| Dynamic + $\mathcal{M}^{Cp}$ | 16.8 | −13.4 |

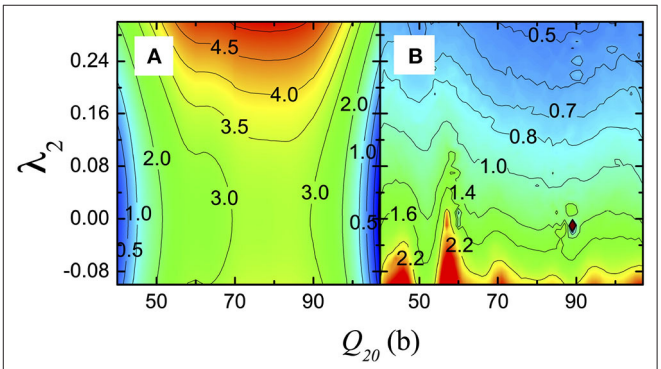


**FIGURE 6 |** Projections of **(A)** potential energy (in MeV) after subtracting the ground state value, and **(B)** $|\mathcal{M}^C|^{1/3}$ (in $\hbar^2$ MeV$^{-1}$/1,000). Both are calculated for $^{264}$Fm in the three-dimensional space of $(Q_{20}, Q_{22}, \lambda_2)$ and then projected on the $Q_{22} = 0$ plane. The figure is modified from Sadhukhan et al. [50].

in the opposite way. The potential energy use to increase with pairing fluctuations, while the collective inertia diminishes as the pairing correlations become stronger than self-consistent values. The least-action path is determined dynamically by the interplay between these two inverse effects. Typical nature of a PES and $\mathcal{M}^C$ along the pairing coordinate is shown in **Figure 6** [50]. It portrays clear evidence of the opposite tendencies discussed above. Minimum action paths for two different nuclei are calculated in Sadhukhan et al. [50] by including the pairing degrees of freedom. Corresponding projections onto the $(Q_{20}, Q_{22})$ and $(Q_{20}, \lambda_2)$ planes are shown in **Figure 7**. Also, two-dimensional (2D) fission paths calculated without pairing fluctuations are compared in this figure. In the case of $^{264}$Fm, the three-dimensional (3D) pathway, calculated with pairing fluctuations, closely follows triaxial configurations of the corresponding 2D path. However, this scenario changes for $^{240}$Pu, where the difference between the axial and triaxial barrier-heights is small and, as a result, pairing correlations could enforce the axial symmetry of the path in the region between the ground state configuration and superdeformed fission isomer. Nevertheless, irrespective of this system dependence, the pairing fluctuations are substantially enhanced in both the cases. Therefore, the dynamic coupling between pairing and deformation coordinates can produce dramatic changes in the SF process. Relativistic mean-field calculation [51] for Fm isotopes also shows a similar behavior of the fission pathway under the influence of dynamic paring fluctuations. Moreover, owing to the associated reduction in the action integral, the calculated SF

half-life decreases by as much as three decades. These strong dynamical effects, predicted for SF, are however expected to disappear at higher excitation energies of the compound system. The subsection is concluded by demonstrating the average pairing gaps ($\Delta_n$ and $\Delta_p$), in **Figure 8**, along the SF path of $^{240}$Pu [29]. Although the dynamic (3D) path overlaps with the static pathway in the ($Q_{20}$, $Q_{30}$) space, average pairing gaps are always higher in case of the 3D path except near the outer turning line where pairing correlations are quenched.

## 3.3. Fission-Fragment Yield Distributions

Stochastic Langevin dynamics is widely used to study fission fragment yield distributions of excited compound systems [89, 91, 106, 107]. Only recently, it is successfully applied to calculate SF yields [29]. The detailed formalism is described in 1. Since the dynamics is stochastic in nature, it is difficult to understand the time evolution from a single fission event. Therefore, the concept of effective fission path (EFP) is devised in Sadhukhan et al. [92] for a better realization of the post-tunneling dynamics. First, for a given initial configuration, the local density of Langevin trajectories [108] is computed by counting the number of tracks in a small volume element of the collective space. Such distributions for two initial configurations are presented in **Figure 9**. Evidently, these two distributions are quite distinct in nature. The spreading of distribution is mainly governed by the interplay between the conservative and fluctuating forces. As I explained in 1, fluctuations become dominant near the scission and it leads to broader trajectory distributions.

Next, the EFP is calculated by tracing the maxima in a trajectory-density distribution. Effectively, an EFP guides to the most probable fragmentation for the associated initial configuration. Eleven distinct EFPs are calculated in Sadhukhan et al. [92] for the representative system $^{240}$Pu, and these are further shown in **Figure 9**. Also, the partial contribution

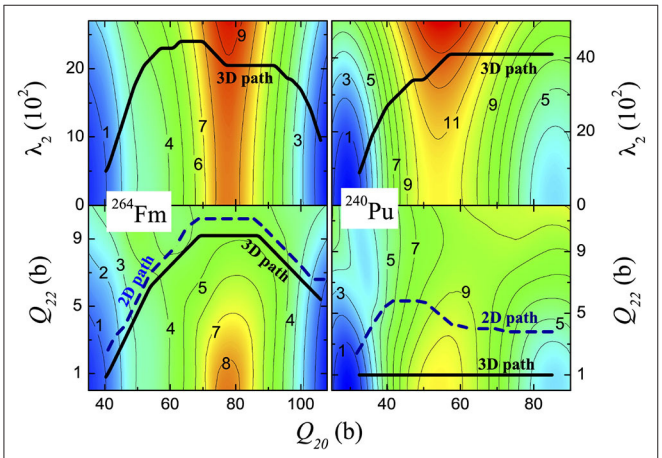


**FIGURE 7 |** Thick solid lines: projections of the three-dimensional (3D) minimum-action paths for $^{264}$Fm (left) and $^{240}$Pu (right) on the ($Q_{20}$, $\lambda_2$; $Q_{22} = 0$) (top) and ($Q_{20}$, $Q_{22}$; $\lambda_2 = 0$) (bottom) planes. Thick dashed lines: two-dimensional (2D) paths computed without pairing fluctuations. The PES corresponding to $Q_{22} = 0$ (top) and static pairing, i.e., $\lambda_2 = 0$, (bottom) are shown for reference. The figure is modified from Sadhukhan et al. [50].

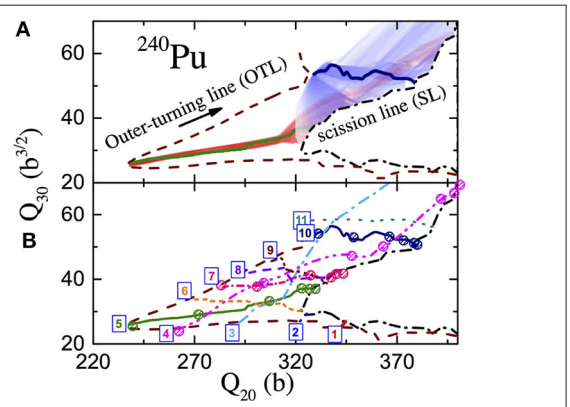


**FIGURE 9 | (A)** The density of Langevin trajectories for two different initial configurations and the corresponding EFPs in the ($Q_{20}$, $Q_{30}$) plane. The loci of outer turning-points land scission configurations are shown by dashed and dash-dotted lines, respectively. **(B)** Eleven EFPs marked according to their initial coordinates. The figure is adapted from Sadhukhan et al. [92].

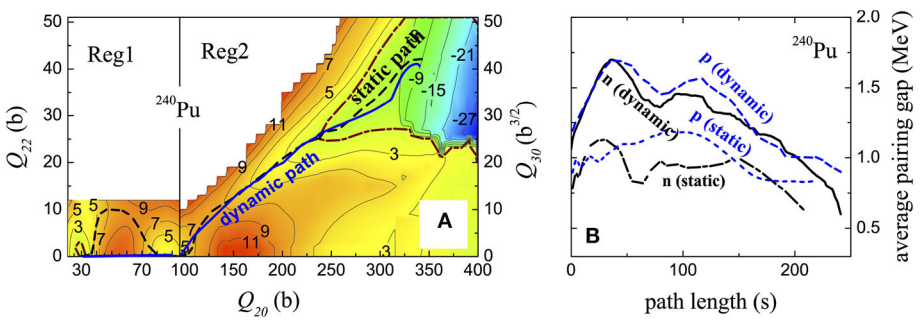


**FIGURE 8 | (A)** The 3D dynamic path (solid line), projected on the $\lambda_2 = 0$ surface, and the 2D static path (dashed line) in the two considered regions (Reg1: ($Q_{20}$, $Q_{22}$, $\lambda_2$), Reg2: ($Q_{20}$, $Q_{30}$, $\lambda_2$)) of the collective space. The reason for this choice of 3D-3D configuration space is explained in Sadhukhan et al. [29]. The contours of inner and outer turning points are shown by dash-dotted lines. **(B)** Average pairing gaps, for neutrons (*n*) and protons (*p*), along the 3D dynamic (with pairing fluctuations) and 2D static ($\lambda_2 = 0$) pathways shown in **(A)**. The figure is modified from Sadhukhan et al. [29].

of each EFP to the total mass distribution is extracted by weighing the corresponding distribution with the appropriate tunneling probability. All the eleven partial mass distributions are plotted in **Figure 10** along with the overall distribution. Due to higher tunneling probability, the peak region of the cumulative distribution is mostly contributed by EFPs close to the most probable path (EFP 5). On the other hand, contributions are negligible from those EFPs which originate far away from the most-probable outer turning point. For example, EFP 1 and EFP 11 hardly alters the total mass distribution. Most interestingly, certain EFPs (e.g., EFP 3 and EFP 4), associated with high tunneling probability, end up at large mass asymmetries and these constitute the tail part of the yield distribution. Such fission trajectories can only appear due to the presence of the random force in the Langevin dynamics.

In addition to the isolated yield distributions corresponding to either mass or charge of the fission fragments, DFT inputs enable the Langevin model to predict the correlation between mass and charge numbers of the fragments. In a recent study [66], it is calculated for the heaviest discovered element $^{294}_{118}$Og. Three different EDFs are used for this purpose and, as shown in **Figure 11**, all of them predict a strongly asymmetric fission, or cluster emission, to be the dominant decay mode for this nucleus.

## 3.4. Uncertainties in Yield Distributions

It is necessary to estimate the uncertainties due to different model parameters [112]. In case of SF yield distributions, predicted within the hybrid WKB + Langevin method, uncertainties are primarily associated to the three input quantities: ground state zero-point energy $E_0$, dissipation tensor $\eta_{ij}$ in Equation (5), and scission configuration which is defined with the neck-particle number $N_q$. Moreover, the use of a particular EDF may induce additional bias in the results. In practice, the SF half-life is reproduced by tuning the free parameter $E_0$ [5, 29] that effectively shifts the location of the inner and outer turning-points. As a result, both $P(s_{\rm out})$ and fission paths are modified. Secondly, the fragment properties are expected to strongly depend on the scission configuration. However, no method exists that defines the scission configuration uniquely within the static adiabatic description of fission. Usually, different values of $N_q$ are used to identify the scission hypersurface in a multidimensional space. In the case of $\eta_{ij}$, a microscopic theory is still missing and it is considered as an adjustable parameter in the SF model [29, 66]. Considering all these limitations, a sensitivity analysis of the yield distributions with respect to all the model parameters is essential. Calculations are performed in Sadhukhan et al. [29] to illustrate the uncertainties in the yield distributions produced by $E_0$, $N_q$, and $\eta_{ij}$. As demonstrated in **Figure 12**, the mass and charge distributions of $^{240}$Pu are found to be robust against wide variations of all these input quantities. A similar response to the dissipation tensor is observed for the yield distributions of $^{294}_{118}$Og [66]. Further, as plotted in **Figure 13**, both mass and charge distributions show weak dependency on the choice of the EDF and also on the dimensionality of the configuration space.

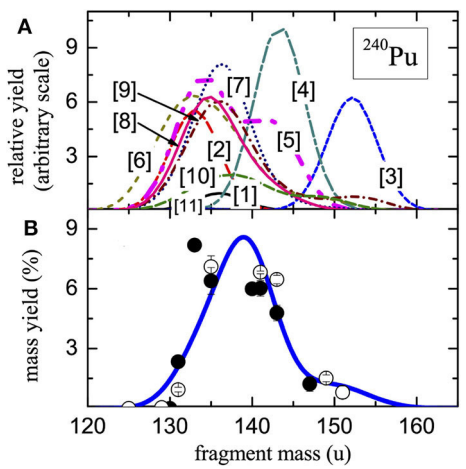


**FIGURE 10 | (A)** Partial mass distributions for different EFPs of **Figure 9B** as indicated. The distribution corresponding to the most-probable fission path, i.e., EFP 5, is shown by a thick line. **(B)** The mass distribution for the SF of $^{240}$Pu obtained by counting contributions from all the Langevin trajectories, in addition to the eleven selected EFPs. The experimental data [109, 110] are shown by circles that include mirror points (open circles). Only the heavy-fragment parts are plotted in both **(A,B)**. The figure is partially adapted from Sadhukhan et al. [92].

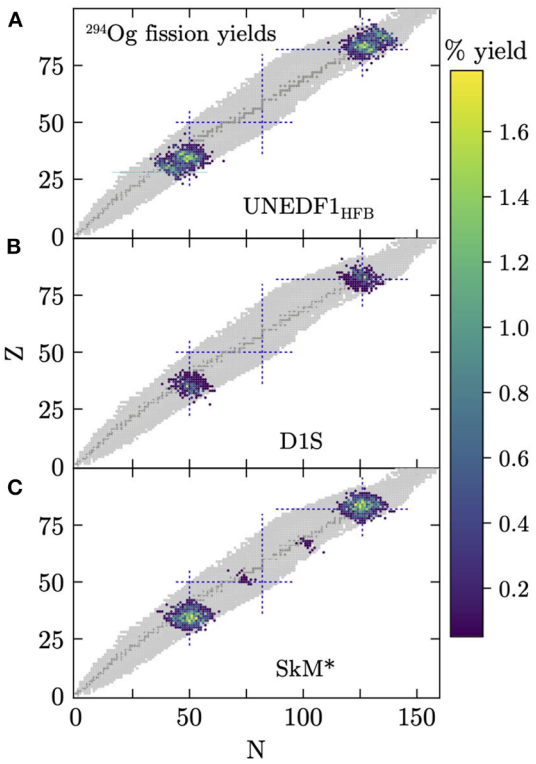


**FIGURE 11 |** Fission fragment distributions for $^{294}_{118}$Og$_{176}$ obtained in UNEDF1$_{\rm HFB}$ **(A)**, D1S **(B)**, and SkM* **(C)** EDFs using the non-perturbative cranking ATDHFB inertia and a standard value of dissipation strength [66]. Known isotopes are marked in gray [111]. Dotted lines indicate the magic numbers: 50, 82, and 126. The figure is adapted from Matheson et al. [66].

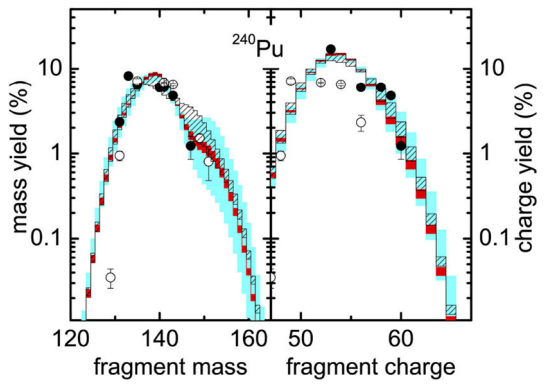


**FIGURE 12 |** Mass (left) and charge (right) distributions of heavier fragment in the SF of $^{240}$Pu. The symbols are experimental values as shown in **Figure 10**. The shaded regions describe uncertainties in the yield distributions corresponding to different values of the model parameters: $E_0$ (narrow red band), dissipation tensor (wider cyan band), and scission configuration (linear hatch pattern). See Sadhukhan et al. [29] for details. The figure is adapted from Sadhukhan et al. [29].

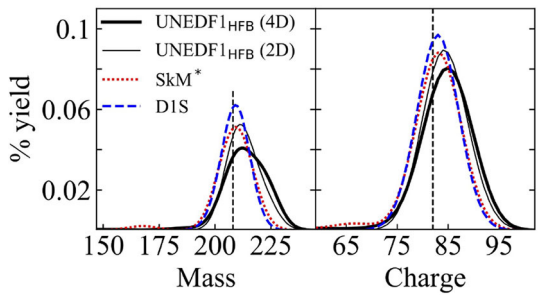


**FIGURE 13 |** Predicted heavy-fragment mass and charge yields of $^{294}$Og obtained by employing UNEDF1$_{HFB}$ functional in the 4D ($Q_{20}, Q_{22}, Q_{30}, \lambda_2$) and the 2D ($Q_{20}, Q_{30}$) spaces, and in the 2D ($Q_{20}, Q_{30}$) space for other functionals (SkM* and D1S). The figure is adapted from Matheson et al. [66].

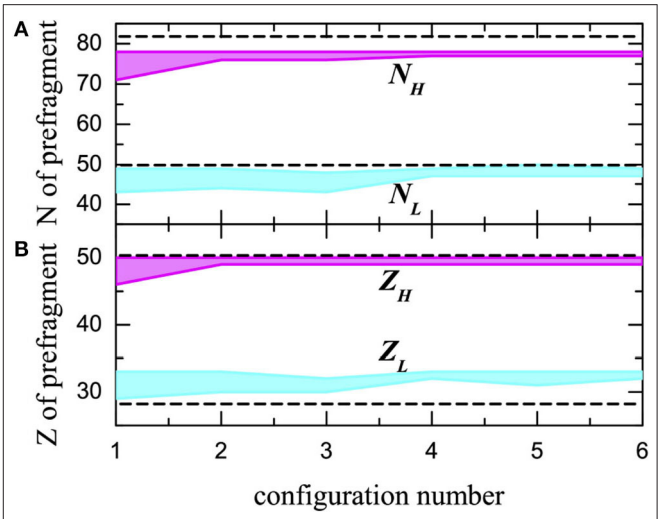


**FIGURE 14 |** The ranges for the number of localized neutrons **(A)** and protons **(B)** for heavier ($N_H$, $Z_H$) and lighter ($N_L$, $Z_L$) prefragments as a function of the configurations along the EFPs marked in **Figure 9B** by circles. The magic numbers are marked by horizontal dotted lines.

Therefore, the hybrid model, with reasonable values of the input parameters, can be used for a reliable prediction of the SF yields. Of course, theoretical progresses toward a more precise calculation of input parameters is required [23].

## 3.5. Prediction of Fragments From Localized Pre-fragment

I have already argued how a pre-fragment can be defined from NLFs (see section 1). Properties of such prefragments are needed to be scrutinized very carefully to validate their applicability in predicting the fission fragments. To this end, the particle numbers of the prefragments are extracted along the EFPs shown in **Figure 9** [92]. The results are reiterated here in **Figure 14** and it displays that the pre-fragment particle-numbers remain remarkably stable as the deformation increases toward scission. Moreover, variations in these numbers, indicated by the bands in **Figure 14**, become fairly narrow ($< \pm 2$ particles) at large deformations. This suggests that the prefragments formed in an initial configuration of the fissioning nucleus hardly change. This early development of the prefragments is a manifestation of the freeze-out of single-particle energies along the fission pathway [25, 39, 56, 113], since the system tries to retain its microscopic configuration by escaping the level crossings. The concept is further extended to predict the particle numbers of the fission fragments. This is accomplished by distributing the neck nucleons to each pre-fragments following a statistical prescription. The predicted yield distributions are found to agree well with the experimental data [67].

This fast and efficient method of fission-fragment identification will be very useful in the *r*-process network calculations that predict the astrophysical abundances of more than half of the elements heavier than iron. In a very neutron-rich environment, such at those exists in the ejecta of neutron-star mergers, neutron-induced and $\beta$-delayed fission are highly probable. It is speculated that nuclear fission terminates the *r*-process paths near $A \sim 300$. The location of the *r*-process endpoint can significantly influence the final yield distribution [114]. Since these superheavy nuclei can not be studied with a standard laboratory procedure, reliable theoretical predictions are of utmost interest. Hence, the density functional formalism, which is deeply rooted in the underlying nucleon-nucleon interactions, provides an ideal platform. Moreover, there can be multiple fission cycles along the *r*-process path and these cycles involve a wide variety of fissioning nuclei. Therefore, the theoretical method needs to be very time-efficient. The model prescribed in Sadhukhan et al. [67] fulfills both the requirements. In parallel, precise measurements of fission fragment yield distributions of neutron rich actinides and heavier elements may help to minimize the theoretical uncertainties associated with model parameters.

## 4. CONCLUSION

In this review, I have elaborated on a successful theoretical model for the spontaneous fission yields and lifetime. It is developed in a hybrid manner by combining the WKB approximation for quantum tunneling with the stochastic Langevin dynamics. Several recent advancements to enhance the predictive capabilities of this hybrid model are presented. In particular, I elucidated the intricate role of collective inertia and pairing correlations in guiding the dynamics during the tunneling phase. The inevitable presence of fluctuation and dissipation in the final stage of the fission dynamics is explained in connection with the calculation of fragment yields. This approach could be a prospective candidate for large-scale applications to a wide range of fissioning nuclei. In parallel, further improvements in different aspects of the model are in queue [23].

Although an accurate prediction of the fission observables is the foremost priority for a fission model, global calculations of fragment properties related to stellar nucleosynthesis processes additionally demand a faster and more reliable technique compared to existing models. This is because such calculations involve a large variety of fissioning nuclei most of which are outside the valley of nuclear stability. For this purpose, a quicker method [67] is recently proposed that utilizes the idea of shell-stabilized/localized prefragments. This model enables the identification of fragments by performing self-consistent calculations within a very localized domain of the configuration space. Clearly, theoretical investigation of the fission process is a diverse field of research with a broad perspective.

## AUTHOR CONTRIBUTIONS

The author confirms being the sole contributor of this review work and has approved it for publication.

## ACKNOWLEDGMENTS

The author acknowledges useful discussions with Witold widows.

## REFERENCES


1. Krappe HJ, Pomorski K. *Theory of Nuclear Fission: A Textbook*. New York, NY: Springer (2012).
2. Shultis JK, Faw RE. *Fundamentals of Nuclear Science and Engineering*. 2nd ed. Boca Raton, FL: CRC Press (2007).
3. Wagemans C. *The Nuclear Fission Process*. Boca Raton, FL: CRC Press (1991).
4. Oganessian YT. Heaviest nuclei from $^{48}$Ca-induced reactions. *J Phys G*. (2007) 34:R165. doi: 10.1088/0954-3899/34/4/R01
5. Staszczak A, Baran A, Nazarewicz W. Spontaneous fission modes and lifetimes of superheavy elements in the nuclear density functional theory. *Phys Rev C*. (2013) 87:024320. doi: 10.1103/PhysRevC.87.024320
6. Giuliani SA, Matheson Z, Nazarewicz W, Olsen E, Reinhard PG, Sadhukhan J, et al. Colloquium: superheavy elements: Oganesson and beyond. *Rev Mod Phys*. (2019) 91:011001. doi: 10.1103/RevModPhys.91.011001
7. Khuyagbaatar J, Yakushev A, Düllmann CE, Ackermann D, Andersson LL, Asai M, et al. $^{48}$Ca $+^{249}$ Bk fusion reaction leading to element $Z = 117$: long-lived $\alpha$-decaying $^{270}$Db and discovery of $^{266}$Lr. *Phys Rev Lett*. (2014) 112:172501. doi: 10.1103/PhysRevLett.112.172501
8. Utyonkov VK, Brewer NT, Oganessian YT, Rykaczewski KP, Abdullin FS, Dmitriev SN, et al. Neutron-deficient superheavy nuclei obtained in the $^{240}$Pu $+^{48}$ Ca reaction. *Phys Rev C*. (2018) 97:014320. doi: 10.1103/PhysRevC.97.014320
9. Giuliani SA, Martínez-Pinedo G, Robledo LM. Fission properties of superheavy nuclei for *r*-process calculations. *Phys Rev C*. (2018) 97:034323. doi: 10.1103/PhysRevC.97.034323
10. Afanasjev AV, Agbemava SE, Gyawali A. Hyperheavy nuclei: existence and stability. *Phys Lett B*. (2018) 782:533. doi: 10.1016/j.physletb.2018.05.070
11. Arnould M, Goriely S, Takahashi K. The r-process of stellar nucleosynthesis: Astrophysics and nuclear physics achievements and mysteries. *Phys Rep*. (2007) 450:97. doi: 10.1016/j.physrep.2007.06.002
12. Panov IV, Korneev IY, Rauscher T, Martínez-Pinedo G, Kelic-Heil A, Zinner NT, et al. Neutron-induced astrophysical reaction rates for translead nuclei. *Astron Astrophys*. (2010) 513:A61. doi: 10.1051/0004-6361/200911967
13. Erler J, Langanke K, Loens HP, Martinez-Pinedo G, Reinhard PG. Fission properties for *r*-process nuclei. *Phys Rev C*. (2012) 85:025802. doi: 10.1103/PhysRevC.85.025802
14. Horowitz CJ, Arcones A, Côté B, Dillmann I, Nazarewicz W, Roederer IU, et al. r-process nucleosynthesis: connecting rare-isotope beam facilities with the cosmos. *J Phys G*. (2019) 46:083001. doi: 10.1088/1361-6471/ab0849
15. Goriely S, Sida JL, Lemaître JF, Panebianco S, Dubray N, Hilaire S, et al. New fission fragment distributions and r-process origin of the rare-earth elements. *Phys Rev Lett*. (2013) 111:242502. doi: 10.1103/PhysRevLett.111.242502
16. Eichler M, Arcones A, Kelic A, Korobkin O, Langanke K, Marketin T, et al. The role of fission in neutron star mergers and its impact on the r-process peaks. *Astrophys J*. (2015) 808:30. doi: 10.1088/0004-637X/808/1/30
17. Goriely S. The fundamental role of fission during r-process nucleosynthesis in neutron star mergers. *Eur Phys J A*. (2015) 51:22. doi: 10.1140/epja/i2015-15022-3
18. Vassh N, Vogt R, Surman R, Randrup J, Sprouse TM, Mumpower MR, et al. Using excitation-energy dependent fission yields to identify key fissioning nuclei in r-process nucleosynthesis. *J Phys G*. (2019) 46:065202. doi: 10.1088/1361-6471/ab0bea
19. Vassh N, Mumpower MR, McLaughlin GC, Sprouse TM, Surman R. Co-production of light and heavy *r*-process elements via fission deposition. *Astrophys J*. (2019) 896:28. doi: 10.3847/1538-4357/ab91a9
20. Côté B, Fryer CL, Belczynski K, Korobkin O, Chruślińska M, Vassh N, et al. The origin of r-process elements in the milky way. *Astrophys J*. (2017) 855:99. doi: 10.3847/1538-4357/aaad67
21. Nichols A, Aldama D, Verpelli M. *Handbook for Nuclear Data for Safeguards: Database Extensions, August 2008*. INDC(NDS)-0534. Vienna: International Atomic Energy Agency (2008).
22. Murray R, Holbert KE. *Nuclear Energy: An Introduction to the Concepts, Systems, and Applications of Nuclear Processes*. Elsevier (2014).
23. Bender M, Bernard R, Bertsch G, Chiba S, Dobaczewski JJ, Dubray N, et al. Future of nuclear fission theory. *J Phys G*. (2020) arXiv:2005.10216. doi: 10.1088/1361-6471/abab4f
24. Nakatsukasa T, Matsuyanagi K, Matsuo M, Yabana K. Time-dependent density-functional description of nuclear dynamics. *Rev Mod Phys*. (2016) 88:045004. doi: 10.1103/RevModPhys.88.045004
25. Scamps G, Simenel C. Impact of pear-shaped fission fragments on mass-asymmetric fission in actinides. *Natute*. (2018) 564:382. doi: 10.1038/s41586-018-0780-0
26. Simenel C, Umar AS. Formation and dynamics of fission fragments. *Phys Rev C*. (2014) 89:031601. doi: 10.1103/PhysRevC.89.031601
27. Scamps G, Simenel C, Lacroix D. Superfluid dynamics of $^258\mathrm{Fm}$ fission. *Phys Rev C*. (2015) 92:011602. doi: 10.1103/PhysRevC.92.011602
28. Schunck N, Robledo LM. Microscopic theory of nuclear fission: a review. *Rep Prog Phys*. (2016) 79:116301. doi: 10.1088/0034-4885/79/11/116301

29. Sadhukhan J, Nazarewicz W, Schunck N. Microscopic modeling of mass and charge distributions in the spontaneous fission of $^{240}$Pu. *Phys Rev C*. (2016) 93:011304. doi: 10.1103/PhysRevC.93.011304
30. Baranger M, Véneroni M. An adiabatic time-dependent Hartree-Fock theory of collective motion in finite systems. *Ann Phys*. (1978) 114:123. doi: 10.1016/0003-4916(78)90265-8
31. Dobaczewski J, Flocard H, Treiner J. Hartree-Fock-Bogoliubov description of nuclei near the neutron-drip line. *Nucl Phys A*. (1984) 422:103–39. doi: 10.1016/0375-9474(84)90433-0
32. Hill DL, Wheeler JA. Nuclear constitution and the interpretation of fission phenomena. *Phys Rev*. (1953) 89:1102. doi: 10.1103/PhysRev.89.1102
33. Wilets L. Surface coupling mechanism for approaching statistical equilibrium in compound nucleus formation, with application to fission. *Phys Rev*. (1959) 116:372. doi: 10.1103/PhysRev.116.372
34. Hasse RW. Approaches to nuclear friction. *Rep Prog Phys*. (1978) 41:1027. doi: 10.1088/0034-4885/41/7/002
35. Brack M, Damgaard J, Jensen AS, Pauli HC, Strutinsky VM, Wong CY. Funny Hills: the shell-correction approach to nuclear shell effects and its applications to the fission process. *Rev Mod Phys*. (1972) 44:320. doi: 10.1103/RevModPhys.44.320
36. Schütte G, Wilets L. Dynamics and non-adiabaticity in the fission process. *Nucl Phys A*. (1975) 252:21. doi: 10.1016/0375-9474(75)90598-9
37. Schütte G, Wilets L. Excitation during collective deformation: how simple it is. *Z Phys A*. (1978) 286:313. doi: 10.1007/BF01408263
38. Strutinsky VM. Collective motion at large amplitudes and finite velocities. *Z Phys A*. (1977) 280:99. doi: 10.1007/BF01438114
39. Nazarewicz W. Diabaticity of nuclear motion: problems and perspectives. *Nucl Phys A*. (1993) 557:489. doi: 10.1016/0375-9474(93)90565-F
40. Nakatsukasa T, Walet NR. Diabatic and adiabatic collective motion in a model pairing system. *Phys Rev C*. (1998) 57:1192. doi: 10.1103/PhysRevC.57.1192
41. Moretto LG, Babinet RP. Large superfluidity enhancement in the penetration of the fission barrier. *Phys Lett B*. (1974) 49:147. doi: 10.1016/0370-2693(74)90494-8
42. Urin MG, Zaretsky DF. On the spontaneous fission of nuclei. *Nucl Phys*. (1966) 75:101. doi: 10.1016/0029-5582(66)90749-8
43. Ledergerber T, Pauli HC. On the dynamics of fission: the role of reflection asymmetry in the nuclear shape. *Nucl Phys A*. (1973) 207:1–32. doi: 10.1016/0375-9474(73)90022-5
44. Lazarev YA. Influence of pairing correlations on the probability and dynamics of tunnelling through the barrier in fission and fusion of complex nuclei. *Phys Scr*. (1987) 35:255. doi: 10.1088/0031-8949/35/3/007
45. Pomorski K. Pairing as a collective mode. *Int J Mod Phys E*. (2007) 16:237. doi: 10.1142/S0218301307005685
46. Staszczak A, Baran A, Pomorski K, Böning K. Coupling of the pairing vibrations with the fission mode. *Phys Lett B*. (1985) 161:227. doi: 10.1016/0370-2693(85)90750-6
47. Staszczak A, Piłat S, Pomorski K. Influence of the pairing vibrations on spontaneous fission probability. *Nucl Phys A*. (1989) 504:589. doi: 10.1016/0375-9474(89)90559-9
48. Łojewski Z, Staszczak A. Role of pairing degrees of freedom and higher multipolarity deformations in spontaneous fission process. *Nucl Phys A*. (1999) 657:134. doi: 10.1016/S0375-9474(99)00328-0
49. Mirea M, Bobulescu RC. Cranking mass parameters for fission. *J Phys G*. (2010) 37:055106. doi: 10.1088/0954-3899/37/5/055106
50. Sadhukhan J, Dobaczewski J, Nazarewicz W, Sheikh JA, Baran A. Pairing-induced speedup of nuclear spontaneous fission. *Phys Rev C*. (2014) 90:061304. doi: 10.1103/PhysRevC.90.061304
51. Zhao J, Lu BN, Niksic T, Vretenar D, Zhou SG. Multidimensionally-constrained relativistic mean-field study of spontaneous fission: coupling between shape and pairing degrees of freedom. *Phys Rev C*. (2016) 93:044315. doi: 10.1103/PhysRevC.93.044315
52. Baran A, Pomorski K, Lukasiak A, Sobiczewski A. A dynamic analysis of spontaneous-fission half-lives. *Nucl Phys A*. (1981) 361:83. doi: 10.1016/0375-9474(81)90471-1
53. Baran A. Some dynamical aspects of the fission process. *Phys Lett B*. (1978) 76:8. doi: 10.1016/0370-2693(78)90085-0
54. Skalski J. Nuclear fission with mean-field instantons. *Phys Rev C*. (2008) 77:064610. doi: 10.1103/PhysRevC.77.064610
55. Baran A, Łojewski Z, Sieja K, Kowal M. Global properties of even-even superheavy nuclei in macroscopic-microscopic models. *Phys Rev C*. (2005) 72:044310. doi: 10.1103/PhysRevC.72.044310
56. Sadhukhan J, Mazurek K, Baran A, Dobaczewski J, Nazarewicz W, Sheikh JA. Spontaneous fission lifetimes from the minimization of self-consistent collective action. *Phys Rev C*. (2013) 88:064314. doi: 10.1103/PhysRevC.88.064314
57. Vaquero NL, Rodríguez TR, Egido JL. On the impact of large amplitude pairing fluctuations on nuclear spectra. *Phys Lett B*. (2011) 704:520. doi: 10.1016/j.physletb.2011.09.073
58. Vaquero NL, Egido JL, Rodríguez TR. Large-amplitude pairing fluctuations in atomic nuclei. *Phys Rev C*. (2013) 88:064311. doi: 10.1103/PhysRevC.88.064311
59. Dobaczewski J, Nazarewicz W, Werner TR. Closed shells at drip-line nuclei. *Phys Scr*. (1995) 1995:15. doi: 10.1088/0031-8949/1995/T56/002
60. Bartel J, Quentin P, Brack M, Guet C, Håkansson HB. Towards a better parametrisation of Skyrme-like effective forces: a critical study of the SkM force. *Nucl Phys A*. (1982) 386:79. doi: 10.1016/0375-9474(82)90403-1
61. Dobaczewski J, Nazarewicz W, Stoitsov MV. Nuclear ground-state properties from mean-field calculations. *Eur Phys J A*. (2002) 15:21. doi: 10.1140/epja/i2001-10218-8
62. Schunck N, Duke D, Carr H, Knoll A. Description of induced nuclear fission with Skyrme energy functionals: static potential energy surfaces and fission fragment properties. *Phys Rev C*. (2014) 90:054305. doi: 10.1103/PhysRevC.90.054305
63. Nam H, Stoitsov M, Nazarewicz W, Bulgac A, Hagen G, Kortelainen M, et al. UNEDF: advanced scientific computing collaboration transforms the low-energy nuclear many-body problem. *J Phys Conf Ser*. (2012) 402:012033. doi: 10.1088/1742-6596/402/1/012033
64. Schunck N, McDonnell JD, Sarich J, Wild SM, Higdon D. Error analysis in nuclear density functional theory. *J Phys G*. (2015) 42:034024. doi: 10.1088/0954-3899/42/3/034024
65. Tsekhanovich I, Andreyev AN, Nishio K, Denis-Petit D, Hirose K, Makii H, et al. Observation of the competing fission modes in 178Pt. *Phys Lett B*. (2019) 790:583. doi: 10.1016/j.physletb.2019.02.006
66. Matheson Z, Giuliani SA, Nazarewicz W, Sadhukhan J, Schunck N. Cluster radioactivity of $^{294}_{118}$Og$_{176}$. *Phys Rev C*. (2019) 99:041304. doi: 10.1103/PhysRevC.99.041304
67. Sadhukhan J, Giuliani SA, Matheson Z, Nazarewicz W. Efficient method for estimation of fission fragment yields of *r*-process nuclei. *Phys Rev C*. (2020) 101:065803. doi: 10.1103/PhysRevC.101.065803
68. Rodríguez-Guzmán R, Robledo LM. Microscopic description of fission in uranium isotopes with the Gogny energy density functional. *Phys Rev C*. (2014) 89:054310. doi: 10.1103/PhysRevC.89.054310
69. Giuliani SA, Robledo LM, Rodríguez-Guzmán R. Dynamic versus static fission paths with realistic interactions. *Phys Rev C*. (2014) 90:054311. doi: 10.1103/PhysRevC.90.054311
70. Bernard RN, Pillet N, Robledo LM, Anguiano M. Description of the asymmetric to symmetric fission transition in the neutron-deficient thorium isotopes: role of the tensor force. *Phys Rev C*. (2020) 101:044615. doi: 10.1103/PhysRevC.101.044615
71. Baldo M, Robledo LM, Schuck P, Viñas X. New Kohn-Sham density functional based on microscopic nuclear and neutron matter equations of state. *Phys Rev C*. (2013) 87:064305. doi: 10.1103/PhysRevC.87.064305
72. Giuliani SA, Robledo LM. Fission properties of the BCPM functional. *Phys Rev C*. (2013) 88:054325. doi: 10.1103/PhysRevC.88.054325
73. Abusara H, Afanasjev AV, Ring P. Fission barriers in covariant density functional theory: extrapolation to superheavy nuclei. *Phys Rev C*. (2012) 85:024314. doi: 10.1103/PhysRevC.85.024314
74. Zhao J, Lu BN, Niksic T, Vretenar D. Multidimensionally constrained relativistic Hartree-Bogoliubov study of spontaneous nuclear fission. *Phys Rev C*. (2015) 92:064315. doi: 10.1103/PhysRevC.92.064315
75. Agbemava SE, Afanasjev AV, Ray D, Ring P. Assessing theoretical uncertainties in fission barriers of superheavy nuclei. *Phys Rev C*. (2017) 95:054324. doi: 10.1103/PhysRevC.95.054324

76. Zhao J, Niksic, Vretenar D, Zhou SG. Microscopic self-consistent description of induced fission dynamics: finite-temperature effects. *Phys Rev C*. (2019) 99:014618. doi: 10.1103/PhysRevC.99.014618
77. Zhao J, Xiang J, Li ZP, Niksic T, Vretenar D, Zhou SG. Time-dependent generator-coordinate-method study of mass-asymmetric fission of actinides. *Phys Rev C*. (2019) 99:054613. doi: 10.1103/PhysRevC.99.054613
78. Shi Z, Afanasjev AV, Li ZP, Meng J. Superheavy nuclei in a microscopic collective Hamiltonian approach: the impact of beyond-mean-field correlations on ground state and fission properties. *Phys Rev C*. (2019) 99:064316. doi: 10.1103/PhysRevC.99.064316
79. Bulgac A, Jin S, Roche KJ, Schunck N, Stetcu I. Fission dynamics of $^{240}$Pu from saddle to scission and beyond. *Phys Rev C*. (2019) 100:034615. doi: 10.1103/PhysRevC.100.034615
80. Tanimura Y, Lacroix D, Ayik S. Microscopic phase-space exploration modeling of $^{258}$Fm spontaneous fission. *Phys Rev Lett*. (2017) 118:152501. doi: 10.1103/PhysRevLett.118.152501
81. Reinhard PG, Goeke K. The generator coordinate method and quantised collective motion in nuclear systems. *Rep Prog Phys*. (1987) 50:1. doi: 10.1088/0034-4885/50/1/001
82. Goutte H, Berger JF, Casoli P, Gogny D. Microscopic approach of fission dynamics applied to fragment kinetic energy and mass distributions in $^{238}$U. *Phys Rev C*. (2005) 71:024316. doi: 10.1103/PhysRevC.71.024316
83. Regnier D, Dubray N, Schunck N, Verriére M. Fission fragment charge and mass distributions in $^{239}$Pu$(n,f)$ in the adiabatic nuclear energy density functional theory. *Phys Rev C*. (2016) 93:054611. doi: 10.1103/PhysRevC.93.054611
84. Regnier D, Dubray N, Schunck N. From asymmetric to symmetric fission in the fermium isotopes within the time-dependent generator-coordinate-method formalism. *Phys Rev C*. (2019) 99:024611. doi: 10.1103/PhysRevC.99.024611
85. Ring P, Schuck P. The Nuclear Many-Body Problem. Berlin; Heidelberg: Springer-Verlag (2000).
86. Baran A, Sheikh JA, Dobaczewski J, Nazarewicz W, Staszczak A. Quadrupole collective inertia in nuclear fission: cranking approximation. *Phys Rev C*. (2011) 84:054321. doi: 10.1103/PhysRevC.84.054321
87. Randrup J, Möller P. Brownian shape motion on five-dimensional potential-energy surfaces: nuclear fission-fragment mass distributions. *Phys Rev Lett*. (2011) 106:132503. doi: 10.1103/PhysRevLett.106.132503
88. Abe Y, Ayik S, Reinhard PG, Suraud E. On stochastic approaches of nuclear dynamics. *Phys Rep*. (1996) 275:49. doi: 10.1016/0370-1573(96)00003-8
89. Fröbrich P, Gontchar II. Langevin description of fusion, deep-inelastic collisions and heavy-ion-induced fission. *Phys Rep*. (1998) 292:131. doi: 10.1016/S0370-1573(97)00042-2
90. Younes W, Gogny D. *Fragment Yields Calculated in a Time-Dependent Microscopic Theory of Fission*. LLNL-TR-586678. Livermore, CA: Lawrence Livermore National Laboratory (LLNL) (2012).
91. Sierk AJ. Langevin model of low-energy fission. *Phys Rev C*. (2017) 96:034603. doi: 10.1103/PhysRevC.96.034603
92. Sadhukhan J, Zhang C, Nazarewicz W, Schunck N. Formation and distribution of fragments in the spontaneous fission of **$^{240}$Pu**. *Phys Rev C*. (2017) 96:061301. doi: 10.1103/PhysRevC.96.061301
93. Zhang CL, Schuetrumpf B, Nazarewicz W. Nucleon localization and fragment formation in nuclear fission. *Phys Rev C*. (2016) 94:064323. doi: 10.1103/PhysRevC.94.064323
94. Reinhard PG, Maruhn JA, Umar AS, Oberacker VE. Localization in light nuclei. *Phys Rev C*. (2011) 83:034312. doi: 10.1103/PhysRevC.83.034312
95. Warda M, Staszczak A, Nazarewicz W. Fission modes of mercury isotopes. *Phys Rev C*. (2012) 86:024601. doi: 10.1103/PhysRevC.86.024601
96. Warda M, Zdeb A. Fission fragment mass yield deduced from density distribution in the pre-scission configuration. *Phys Scr*. (2015) 90:114003. doi: 10.1088/0031-8949/90/11/114003
97. Scamps G, Simenel C. Effect of shell structure on the fission of sub-lead nuclei. *Phys Rev C*. (2019) 100:041602. doi: 10.1103/PhysRevC.100.041602
98. Bertsch GF, Loveland W, Nazarewicz W, Talou P. Benchmarking nuclear fission theory. *J Phys G*. (2015) 42:077001. doi: 10.1088/0954-3899/42/7/077001
99. Giannoni MJ, Quentin P. Mass parameters in the adiabatic time-dependent Hartree-Fock approximation. II. Results for the isoscalar quadrupole mode. *Phys Rev C*. (1980) 21:2076. doi: 10.1103/PhysRevC.21.2076
100. Yuldashbaeva EK, Libert J, Quentin P, Girod M. Mass parameters for large amplitude collective motion: a perturbative microscopic approach. *Phys Lett B*. (1999) 461:1. doi: 10.1016/S0370-2693(99)00836-9
101. Smolańczuk R, Klapdor-Kleingrothaus HV, Sobiczewski A. Role of the deformation space admitted in the analysis of spontaneous fission. *Acta Phys Pol B*. (1993) 24:685.
102. Smolańczuk R, Skalski J, Sobiczewski A. Spontaneous-fission half-lives of deformed superheavy nuclei. *Phys Rev C*. (1995) 52:1871. doi: 10.1103/PhysRevC.52.1871
103. Gherghescu RA, Skalski J, Patyk Z, Sobiczewski A. Non-axial shapes in spontaneous fission of superheavy nuclei. *Nucl Phys A*. (1999) 651:237. doi: 10.1016/S0375-9474(99)00126-8
104. Warda M, Egido JL. Fission half-lives of superheavy nuclei in a microscopic approach. *Phys Rev C*. (2012) 86:014322. doi: 10.1103/PhysRevC.86.014322
105. Delaroche JP, Girod M, Goutte H, Libert J. Structure properties of even-even actinides at normal and super deformed shapes analysed using the Gogny force. *Nucl Phys A*. (2006) 771:103. doi: 10.1016/j.nuclphysa.2006.03.004
106. Karpov AV, Nadtochy PN, Vanin DV, Adeev GD. Three-dimensional Langevin calculations of fission fragment mass-energy distribution from excited compound nuclei. *Phys Rev C*. (2001) 63:054610. doi: 10.1103/PhysRevC.63.054610
107. Nadtochy PN, Ryabov EG, Gegechkori AE, Anischenko YA, Adeev GD. Four-dimensional Langevin dynamics of heavy-ion-induced fission. *Phys Rev C*. (2012) 85:064619. doi: 10.1103/PhysRevC.85.064619
108. Pal S, Chaudhuri G, Sadhukhan J. The role of neck degree of freedom in nuclear fission. *Nucl Phys A*. (2008) 808:1. doi: 10.1016/j.nuclphysa.2008.05.001
109. Laidler JB, Brown F. Mass distribution in the spontaneous fission of 240Pu. *J Inorg Nucl Chem*. (1962) 24:1485. doi: 10.1016/0022-1902(62)80001-3
110. Thierens H, De Clercq A, Jacobs E, De Frenne D, D'hondt P, De Gelder P, et al. Kinetic energy and fragment mass distributions for $^{240}$Pu(s.f.), $^{239}$Pu$(n_{\rm th},f)$, and $^{240}$Pu$(\gamma,f)$. *Phys Rev C*. (1981) 23:2104. doi: 10.1103/PhysRevC.23.2104
111. *Interactive Chart of Nuclides*. NuDat 2.7. Available online at: https://www.nndc.bnl.gov/nudat2/
112. Dobaczewski J, Nazarewicz W, Reinhard PG. Error estimates of theoretical models: a guide. *J Phys G*. (2014) 41:074001. doi: 10.1088/0954-3899/41/7/074001
113. Negele JW. Microscopic theory of fission dynamics. *Nucl Phys A*. (1989) 502:371. doi: 10.1016/0375-9474(89)90676-3
114. Kajino T, Aoki W, Balantekin AB, Diehl R, Famiano MA, Mathews GJ. Current status of r-process nucleosynthesis. *Prog Part Nucl Phys*. (2019) 107:109. doi: 10.1016/j.ppnp.2019.02.008


**Conflict of Interest:** The author declares that the research was conducted in the absence of any commercial or financial relationships that could be construed as a potential conflict of interest.

# Advantages of publishing in Frontiers

**OPEN ACCESS**
Articles are free to read for greatest visibility and readership

**FAST PUBLICATION**
Around 90 days from submission to decision

**HIGH QUALITY PEER-REVIEW**
Rigorous, collaborative, and constructive peer-review

**TRANSPARENT PEER-REVIEW**
Editors and reviewers acknowledged by name on published articles

**Frontiers**
Avenue du Tribunal-Fédéral 34
1005 Lausanne | Switzerland

**Visit us:** www.frontiersin.org
**Contact us:** frontiersin.org/about/contact

**REPRODUCIBILITY OF RESEARCH**
Support open data and methods to enhance research reproducibility

**DIGITAL PUBLISHING**
Articles designed for optimal readership across devices

**FOLLOW US**
@frontiersin

**IMPACT METRICS**
Advanced article metrics track visibility across digital media

**EXTENSIVE PROMOTION**
Marketing and promotion of impactful research

**LOOP RESEARCH NETWORK**
Our network increases your article's readership